International Journal of Antennas and Propagation

Array Signal Processing with Model Errors

Lead Guest Editor: Fangqing Wen
Guest Editors: Jin He, Liangtian Wan, Xianpeng Wang, and Wei Liu

Array Signal Processing with Model Errors

International Journal of Antennas and Propagation

Array Signal Processing with Model Errors

Lead Guest Editor: Fangqing Wen
Guest Editors: Jin He, Liangtian Wan, Xianpeng Wang, and Wei Liu

Chief Editor

Associate Editors

Academic Editors

Contents

Retracted: A FJSSP Method Based on Dynamic Multi-Objective Squirrel Search Algorithm
International Journal of Antennas and Propagation
Retraction (1 page), Article ID 9842357, Volume 2023 (2023)

Retracted: Channel Estimation for Switch-Based Millimeter-Wave Communications via Atomic Norm
International Journal of Antennas and Propagation
Retraction (1 page), Article ID 9838045, Volume 2023 (2023)

Retracted: The System Research and Implementation for Autorecognition of the Ship Draft via the UAV
International Journal of Antennas and Propagation
Retraction (1 page), Article ID 9834050, Volume 2023 (2023)

Retracted: DOA Estimation of an Enhanced Generalized Nested Array with Increased Degrees of Freedom and Reduced Mutual Coupling
International Journal of Antennas and Propagation
Retraction (1 page), Article ID 9810256, Volume 2023 (2023)

Retracted: Construction and Application of Media Corpus Based on Big Data
International Journal of Antennas and Propagation
Retraction (1 page), Article ID 9786725, Volume 2023 (2023)

Retracted: Research on Quantization Error Influence of Millimeter-Wave Phased Array Antenna
International Journal of Antennas and Propagation
Retraction (1 page), Article ID 9769872, Volume 2023 (2023)

Retracted: HR Management Big Data Mining Based on Computational Intelligence and Deep Learning
International Journal of Antennas and Propagation
Retraction (1 page), Article ID 9840409, Volume 2023 (2023)

Retracted: Research on Interactive Art Online Teaching System Based on BS Mode and Internet of Things
International Journal of Antennas and Propagation
Retraction (1 page), Article ID 9768912, Volume 2023 (2023)

[Retracted] Design of the School-Enterprise Cooperation Management Information Platform Based on the B/S Architecture
Qiang Zhang
Research Article (7 pages), Article ID 2651936, Volume 2021 (2021)

A Sliding Window Data Compression Method for Spatial-Time DOA Estimation
Pin-Jiao Zhao, Guo-Bing Hu, and Li-Wei Wang
Research Article (8 pages), Article ID 9705617, Volume 2021 (2021)

[Retracted] A Motion Image Pose Contour Extraction Method Based on B-Spline Wavelet
Chen chen and Daohui Bi
Research Article (8 pages), Article ID 4553143, Volume 2021 (2021)

Contents

Hindawi
International Journal of Antennas and Propagation
Volume 2024, Article ID 9843957, 1 page
https://doi.org/10.1155/2024/9843957

Retraction

Retracted: Research on Behavior Monitoring of Elderly Living Alone Based on Wearable Devices and Sensing Technology

International Journal of Antennas and Propagation

Received 30 January 2024; Accepted 30 January 2024; Published 31 January 2024

This article has been retracted by Hindawi following an investigation undertaken by the publisher [1]. This investigation has uncovered evidence of one or more of the following indicators of systematic manipulation of the publication process:

(1) Discrepancies in scope
(2) Discrepancies in the description of the research reported
(3) Discrepancies between the availability of data and the research described
(4) Inappropriate citations
(5) Incoherent, meaningless and/or irrelevant content included in the article
(6) Manipulated or compromised peer review

The presence of these indicators undermines our confidence in the integrity of the article's content and we cannot, therefore, vouch for its reliability. Please note that this notice is intended solely to alert readers that the content of this article is unreliable. We have not investigated whether authors were aware of or involved in the systematic manipulation of the publication process.

In addition, our investigation has also shown that one or more of the following human-subject reporting requirements has not been met in this article: ethical approval by an Institutional Review Board (IRB) committee or equivalent, patient/participant consent to participate, and/or agreement to publish patient/participant details (where relevant).

Wiley and Hindawi regrets that the usual quality checks did not identify these issues before publication and have since put additional measures in place to safeguard research integrity.

We wish to credit our own Research Integrity and Research Publishing teams and anonymous and named external researchers and research integrity experts for contributing to this investigation.

The corresponding author, as the representative of all authors, has been given the opportunity to register their agreement or disagreement to this retraction. We have kept a record of any response received.

References

[1] M. Yin, "Research on Behavior Monitoring of Elderly Living Alone Based on Wearable Devices and Sensing Technology," *International Journal of Antennas and Propagation*, vol. 2021, Article ID 4200137, 10 pages, 2021.

Hindawi
International Journal of Antennas and Propagation
Volume 2024, Article ID 9872025, 1 page
https://doi.org/10.1155/2024/9872025

Retraction

Retracted: Design of the School-Enterprise Cooperation Management Information Platform Based on the B/S Architecture

International Journal of Antennas and Propagation

Received 23 January 2024; Accepted 23 January 2024; Published 24 January 2024

This article has been retracted by Hindawi following an investigation undertaken by the publisher [1]. This investigation has uncovered evidence of one or more of the following indicators of systematic manipulation of the publication process:

(1) Discrepancies in scope
(2) Discrepancies in the description of the research reported
(3) Discrepancies between the availability of data and the research described
(4) Inappropriate citations
(5) Incoherent, meaningless and/or irrelevant content included in the article
(6) Manipulated or compromised peer review

The presence of these indicators undermines our confidence in the integrity of the article's content and we cannot, therefore, vouch for its reliability. Please note that this notice is intended solely to alert readers that the content of this article is unreliable. We have not investigated whether authors were aware of or involved in the systematic manipulation of the publication process.

In addition, our investigation has also shown that one or more of the following human-subject reporting requirements has not been met in this article: ethical approval by an Institutional Review Board (IRB) committee or equivalent, patient/participant consent to participate, and/or agreement to publish patient/participant details (where relevant).

Wiley and Hindawi regrets that the usual quality checks did not identify these issues before publication and have since put additional measures in place to safeguard research integrity.

We wish to credit our own Research Integrity and Research Publishing teams and anonymous and named external researchers and research integrity experts for contributing to this investigation.

The corresponding author, as the representative of all authors, has been given the opportunity to register their agreement or disagreement to this retraction. We have kept a record of any response received.

References

[1] Q. Zhang, "Design of the School-Enterprise Cooperation Management Information Platform Based on the B/S Architecture," *International Journal of Antennas and Propagation*, vol. 2021, Article ID 2651936, 7 pages, 2021.

Hindawi
International Journal of Antennas and Propagation
Volume 2024, Article ID 9869817, 1 page
https://doi.org/10.1155/2024/9869817

Retraction

Retracted: Design of Chinese-English Wireless Simultaneous Interpretation System Based on Speech Recognition Technology

International Journal of Antennas and Propagation

Received 23 January 2024; Accepted 23 January 2024; Published 24 January 2024

This article has been retracted by Hindawi following an investigation undertaken by the publisher [1]. This investigation has uncovered evidence of one or more of the following indicators of systematic manipulation of the publication process:

(1) Discrepancies in scope
(2) Discrepancies in the description of the research reported
(3) Discrepancies between the availability of data and the research described
(4) Inappropriate citations
(5) Incoherent, meaningless and/or irrelevant content included in the article
(6) Manipulated or compromised peer review

The presence of these indicators undermines our confidence in the integrity of the article's content and we cannot, therefore, vouch for its reliability. Please note that this notice is intended solely to alert readers that the content of this article is unreliable. We have not investigated whether authors were aware of or involved in the systematic manipulation of the publication process.

In addition, our investigation has also shown that one or more of the following human-subject reporting requirements has not been met in this article: ethical approval by an Institutional Review Board (IRB) committee or equivalent, patient/participant consent to participate, and/or agreement to publish patient/participant details (where relevant).

Wiley and Hindawi regrets that the usual quality checks did not identify these issues before publication and have since put additional measures in place to safeguard research integrity.

We wish to credit our own Research Integrity and Research Publishing teams and anonymous and named external researchers and research integrity experts for contributing to this investigation.

The corresponding author, as the representative of all authors, has been given the opportunity to register their agreement or disagreement to this retraction. We have kept a record of any response received.

References

[1] F. Liu, "Design of Chinese-English Wireless Simultaneous Interpretation System Based on Speech Recognition Technology," *International Journal of Antennas and Propagation*, vol. 2021, Article ID 7346984, 9 pages, 2021.

Hindawi
International Journal of Antennas and Propagation
Volume 2024, Article ID 9867141, 1 page
https://doi.org/10.1155/2024/9867141

Retraction

Retracted: Risk Prediction Algorithm of Social Security Fund Operation Based on RBF Neural Network

International Journal of Antennas and Propagation

Received 23 January 2024; Accepted 23 January 2024; Published 24 January 2024

This article has been retracted by Hindawi following an investigation undertaken by the publisher [1]. This investigation has uncovered evidence of one or more of the following indicators of systematic manipulation of the publication process:

(1) Discrepancies in scope

(2) Discrepancies in the description of the research reported

(3) Discrepancies between the availability of data and the research described

(4) Inappropriate citations

(5) Incoherent, meaningless and/or irrelevant content included in the article

(6) Manipulated or compromised peer review

The presence of these indicators undermines our confidence in the integrity of the article's content and we cannot, therefore, vouch for its reliability. Please note that this notice is intended solely to alert readers that the content of this article is unreliable. We have not investigated whether authors were aware of or involved in the systematic manipulation of the publication process.

In addition, our investigation has also shown that one or more of the following human-subject reporting requirements has not been met in this article: ethical approval by an Institutional Review Board (IRB) committee or equivalent, patient/participant consent to participate, and/or agreement to publish patient/participant details (where relevant).

Wiley and Hindawi regrets that the usual quality checks did not identify these issues before publication and have since put additional measures in place to safeguard research integrity.

We wish to credit our own Research Integrity and Research Publishing teams and anonymous and named external researchers and research integrity experts for contributing to this investigation.

The corresponding author, as the representative of all authors, has been given the opportunity to register their agreement or disagreement to this retraction. We have kept a record of any response received.

References

[1] L. Yang, "Risk Prediction Algorithm of Social Security Fund Operation Based on RBF Neural Network," *International Journal of Antennas and Propagation*, vol. 2021, Article ID 6525955, 8 pages, 2021.

Hindawi
International Journal of Antennas and Propagation
Volume 2024, Article ID 9853970, 1 page
https://doi.org/10.1155/2024/9853970

Retraction

Retracted: Design of English Mobile Learning Platform Based on GSM-R Wireless Network Communication System

International Journal of Antennas and Propagation

Received 23 January 2024; Accepted 23 January 2024; Published 24 January 2024

This article has been retracted by Hindawi following an investigation undertaken by the publisher [1]. This investigation has uncovered evidence of one or more of the following indicators of systematic manipulation of the publication process:

(1) Discrepancies in scope
(2) Discrepancies in the description of the research reported
(3) Discrepancies between the availability of data and the research described
(4) Inappropriate citations
(5) Incoherent, meaningless and/or irrelevant content included in the article
(6) Manipulated or compromised peer review

The presence of these indicators undermines our confidence in the integrity of the article's content and we cannot, therefore, vouch for its reliability. Please note that this notice is intended solely to alert readers that the content of this article is unreliable. We have not investigated whether authors were aware of or involved in the systematic manipulation of the publication process.

In addition, our investigation has also shown that one or more of the following human-subject reporting requirements has not been met in this article: ethical approval by an Institutional Review Board (IRB) committee or equivalent, patient/participant consent to participate, and/or agreement to publish patient/participant details (where relevant).

Wiley and Hindawi regrets that the usual quality checks did not identify these issues before publication and have since put additional measures in place to safeguard research integrity.

We wish to credit our own Research Integrity and Research Publishing teams and anonymous and named external researchers and research integrity experts for contributing to this investigation.

The corresponding author, as the representative of all authors, has been given the opportunity to register their agreement or disagreement to this retraction. We have kept a record of any response received.

References

[1] X. Liu and H. Liu, "Design of English Mobile Learning Platform Based on GSM-R Wireless Network Communication System," *International Journal of Antennas and Propagation*, vol. 2021, Article ID 9944169, 9 pages, 2021.

Hindawi
International Journal of Antennas and Propagation
Volume 2024, Article ID 9850361, 1 page
https://doi.org/10.1155/2024/9850361

Retraction

Retracted: Research on Design and Application of Online English Education Platform Based on Web

International Journal of Antennas and Propagation

Received 23 January 2024; Accepted 23 January 2024; Published 24 January 2024

This article has been retracted by Hindawi following an investigation undertaken by the publisher [1]. This investigation has uncovered evidence of one or more of the following indicators of systematic manipulation of the publication process:

(1) Discrepancies in scope
(2) Discrepancies in the description of the research reported
(3) Discrepancies between the availability of data and the research described
(4) Inappropriate citations
(5) Incoherent, meaningless and/or irrelevant content included in the article
(6) Manipulated or compromised peer review

The presence of these indicators undermines our confidence in the integrity of the article's content and we cannot, therefore, vouch for its reliability. Please note that this notice is intended solely to alert readers that the content of this article is unreliable. We have not investigated whether authors were aware of or involved in the systematic manipulation of the publication process.

In addition, our investigation has also shown that one or more of the following human-subject reporting requirements has not been met in this article: ethical approval by an Institutional Review Board (IRB) committee or equivalent, patient/participant consent to participate, and/or agreement to publish patient/participant details (where relevant).

Wiley and Hindawi regrets that the usual quality checks did not identify these issues before publication and have since put additional measures in place to safeguard research integrity.

We wish to credit our own Research Integrity and Research Publishing teams and anonymous and named external researchers and research integrity experts for contributing to this investigation.

The corresponding author, as the representative of all authors, has been given the opportunity to register their agreement or disagreement to this retraction. We have kept a record of any response received.

References

[1] Y. Huang, "Research on Design and Application of Online English Education Platform Based on Web," *International Journal of Antennas and Propagation*, vol. 2021, Article ID 7648856, 10 pages, 2021.

Hindawi
International Journal of Antennas and Propagation
Volume 2024, Article ID 9785482, 1 page
https://doi.org/10.1155/2024/9785482

Retraction

Retracted: Iris Localization Algorithm based on Effective Area

International Journal of Antennas and Propagation

Received 23 January 2024; Accepted 23 January 2024; Published 24 January 2024

This article has been retracted by Hindawi following an investigation undertaken by the publisher [1]. This investigation has uncovered evidence of one or more of the following indicators of systematic manipulation of the publication process:

(1) Discrepancies in scope

(2) Discrepancies in the description of the research reported

(3) Discrepancies between the availability of data and the research described

(4) Inappropriate citations

(5) Incoherent, meaningless and/or irrelevant content included in the article

(6) Manipulated or compromised peer review

The presence of these indicators undermines our confidence in the integrity of the article's content and we cannot, therefore, vouch for its reliability. Please note that this notice is intended solely to alert readers that the content of this article is unreliable. We have not investigated whether authors were aware of or involved in the systematic manipulation of the publication process.

Wiley and Hindawi regrets that the usual quality checks did not identify these issues before publication and have since put additional measures in place to safeguard research integrity.

We wish to credit our own Research Integrity and Research Publishing teams and anonymous and named external researchers and research integrity experts for contributing to this investigation.

The corresponding author, as the representative of all authors, has been given the opportunity to register their agreement or disagreement to this retraction. We have kept a record of any response received.

References

[1] J. Yu, L. Zhang, and Z. Wang, "Iris Localization Algorithm based on Effective Area," *International Journal of Antennas and Propagation*, vol. 2021, Article ID 2049646, 11 pages, 2021.

Hindawi
International Journal of Antennas and Propagation
Volume 2024, Article ID 9784903, 1 page
https://doi.org/10.1155/2024/9784903

Retraction

Retracted: A Motion Image Pose Contour Extraction Method Based on B-Spline Wavelet

International Journal of Antennas and Propagation

Received 23 January 2024; Accepted 23 January 2024; Published 24 January 2024

This article has been retracted by Hindawi following an investigation undertaken by the publisher [1]. This investigation has uncovered evidence of one or more of the following indicators of systematic manipulation of the publication process:

(1) Discrepancies in scope
(2) Discrepancies in the description of the research reported
(3) Discrepancies between the availability of data and the research described
(4) Inappropriate citations
(5) Incoherent, meaningless and/or irrelevant content included in the article
(6) Manipulated or compromised peer review

The presence of these indicators undermines our confidence in the integrity of the article's content and we cannot, therefore, vouch for its reliability. Please note that this notice is intended solely to alert readers that the content of this article is unreliable. We have not investigated whether authors were aware of or involved in the systematic manipulation of the publication process.

In addition, our investigation has also shown that one or more of the following human-subject reporting requirements has not been met in this article: ethical approval by an Institutional Review Board (IRB) committee or equivalent, patient/participant consent to participate, and/or agreement to publish patient/participant details (where relevant).

Wiley and Hindawi regrets that the usual quality checks did not identify these issues before publication and have since put additional measures in place to safeguard research integrity.

We wish to credit our own Research Integrity and Research Publishing teams and anonymous and named external researchers and research integrity experts for contributing to this investigation.

The corresponding author, as the representative of all authors, has been given the opportunity to register their agreement or disagreement to this retraction. We have kept a record of any response received.

References

[1] Chen chen and D. Bi, "A Motion Image Pose Contour Extraction Method Based on B-Spline Wavelet," *International Journal of Antennas and Propagation*, vol. 2021, Article ID 4553143, 8 pages, 2021.

Hindawi
International Journal of Antennas and Propagation
Volume 2023, Article ID 9895714, 1 page
https://doi.org/10.1155/2023/9895714

Retraction

Retracted: Three-Dimensional Inversion of Borehole-Surface Resistivity Method Based on the Unstructured Finite Element

International Journal of Antennas and Propagation

Received 19 December 2023; Accepted 19 December 2023; Published 20 December 2023

This article has been retracted by Hindawi following an investigation undertaken by the publisher [1]. This investigation has uncovered evidence of one or more of the following indicators of systematic manipulation of the publication process:

(1) Discrepancies in scope

(2) Discrepancies in the description of the research reported

(3) Discrepancies between the availability of data and the research described

(4) Inappropriate citations

(5) Incoherent, meaningless and/or irrelevant content included in the article

(6) Manipulated or compromised peer review

The presence of these indicators undermines our confidence in the integrity of the article's content and we cannot, therefore, vouch for its reliability. Please note that this notice is intended solely to alert readers that the content of this article is unreliable. We have not investigated whether authors were aware of or involved in the systematic manipulation of the publication process.

Wiley and Hindawi regrets that the usual quality checks did not identify these issues before publication and have since put additional measures in place to safeguard research integrity.

We wish to credit our own Research Integrity and Research Publishing teams and anonymous and named external researchers and research integrity experts for contributing to this investigation.

The corresponding author, as the representative of all authors, has been given the opportunity to register their agreement or disagreement to this retraction. We have kept a record of any response received.

References

[1] Z. Wang and S. Fang, "Three-Dimensional Inversion of Borehole-Surface Resistivity Method Based on the Unstructured Finite Element," *International Journal of Antennas and Propagation*, vol. 2021, Article ID 5154985, 13 pages, 2021.

Hindawi
International Journal of Antennas and Propagation
Volume 2023, Article ID 9864861, 1 page
https://doi.org/10.1155/2023/9864861

Retraction

Retracted: 2D-DOA Estimation for EMVS Array with Nonuniform Noise

International Journal of Antennas and Propagation

Received 19 December 2023; Accepted 19 December 2023; Published 20 December 2023

This article has been retracted by Hindawi following an investigation undertaken by the publisher [1]. This investigation has uncovered evidence of one or more of the following indicators of systematic manipulation of the publication process:

(1) Discrepancies in scope

(2) Discrepancies in the description of the research reported

(3) Discrepancies between the availability of data and the research described

(4) Inappropriate citations

(5) Incoherent, meaningless and/or irrelevant content included in the article

(6) Manipulated or compromised peer review

The presence of these indicators undermines our confidence in the integrity of the article's content and we cannot, therefore, vouch for its reliability. Please note that this notice is intended solely to alert readers that the content of this article is unreliable. We have not investigated whether authors were aware of or involved in the systematic manipulation of the publication process.

Wiley and Hindawi regrets that the usual quality checks did not identify these issues before publication and have since put additional measures in place to safeguard research integrity.

We wish to credit our own Research Integrity and Research Publishing teams and anonymous and named external researchers and research integrity experts for contributing to this investigation.

The corresponding author, as the representative of all authors, has been given the opportunity to register their agreement or disagreement to this retraction. We have kept a record of any response received.

References

[1] C.-X. Cai, G.-J. Huang, F.-Q. Wen, X.-H. Wang, and L. Wang, "2D-DOA Estimation for EMVS Array with Nonuniform Noise," *International Journal of Antennas and Propagation*, vol. 2021, Article ID 9053864, 9 pages, 2021.

Hindawi
International Journal of Antennas and Propagation
Volume 2023, Article ID 9842357, 1 page
https://doi.org/10.1155/2023/9842357

Retraction

Retracted: A FJSSP Method Based on Dynamic Multi-Objective Squirrel Search Algorithm

International Journal of Antennas and Propagation

Received 19 December 2023; Accepted 19 December 2023; Published 20 December 2023

This article has been retracted by Hindawi following an investigation undertaken by the publisher [1]. This investigation has uncovered evidence of one or more of the following indicators of systematic manipulation of the publication process:

(1) Discrepancies in scope

(2) Discrepancies in the description of the research reported

(3) Discrepancies between the availability of data and the research described

(4) Inappropriate citations

(5) Incoherent, meaningless and/or irrelevant content included in the article

(6) Manipulated or compromised peer review

The presence of these indicators undermines our confidence in the integrity of the article's content and we cannot, therefore, vouch for its reliability. Please note that this notice is intended solely to alert readers that the content of this article is unreliable. We have not investigated whether authors were aware of or involved in the systematic manipulation of the publication process.

Wiley and Hindawi regrets that the usual quality checks did not identify these issues before publication and have since put additional measures in place to safeguard research integrity.

We wish to credit our own Research Integrity and Research Publishing teams and anonymous and named external researchers and research integrity experts for contributing to this investigation.

The corresponding author, as the representative of all authors, has been given the opportunity to register their agreement or disagreement to this retraction. We have kept a record of any response received.

References

[1] Y. Wang and J. Han, "A FJSSP Method Based on Dynamic Multi-Objective Squirrel Search Algorithm," *International Journal of Antennas and Propagation*, vol. 2021, Article ID 6062689, 19 pages, 2021.

Hindawi
International Journal of Antennas and Propagation
Volume 2023, Article ID 9838045, 1 page
https://doi.org/10.1155/2023/9838045

Retraction

Retracted: Channel Estimation for Switch-Based Millimeter-Wave Communications via Atomic Norm

International Journal of Antennas and Propagation

Received 19 December 2023; Accepted 19 December 2023; Published 20 December 2023

This article has been retracted by Hindawi following an investigation undertaken by the publisher [1]. This investigation has uncovered evidence of one or more of the following indicators of systematic manipulation of the publication process:

(1) Discrepancies in scope

(2) Discrepancies in the description of the research reported

(3) Discrepancies between the availability of data and the research described

(4) Inappropriate citations

(5) Incoherent, meaningless and/or irrelevant content included in the article

(6) Manipulated or compromised peer review

The presence of these indicators undermines our confidence in the integrity of the article's content and we cannot, therefore, vouch for its reliability. Please note that this notice is intended solely to alert readers that the content of this article is unreliable. We have not investigated whether authors were aware of or involved in the systematic manipulation of the publication process.

Wiley and Hindawi regrets that the usual quality checks did not identify these issues before publication and have since put additional measures in place to safeguard research integrity.

We wish to credit our own Research Integrity and Research Publishing teams and anonymous and named external researchers and research integrity experts for contributing to this investigation.

The corresponding author, as the representative of all authors, has been given the opportunity to register their agreement or disagreement to this retraction. We have kept a record of any response received.

References

[1] T. Ma, X. Fan, and X. Wu, "Channel Estimation for Switch-Based Millimeter-Wave Communications via Atomic Norm," *International Journal of Antennas and Propagation*, vol. 2021, Article ID 7356963, 9 pages, 2021.

Hindawi
International Journal of Antennas and Propagation
Volume 2023, Article ID 9834050, 1 page
https://doi.org/10.1155/2023/9834050

Retraction

Retracted: The System Research and Implementation for Autorecognition of the Ship Draft via the UAV

International Journal of Antennas and Propagation

Received 19 December 2023; Accepted 19 December 2023; Published 20 December 2023

This article has been retracted by Hindawi following an investigation undertaken by the publisher [1]. This investigation has uncovered evidence of one or more of the following indicators of systematic manipulation of the publication process:

(1) Discrepancies in scope

(2) Discrepancies in the description of the research reported

(3) Discrepancies between the availability of data and the research described

(4) Inappropriate citations

(5) Incoherent, meaningless and/or irrelevant content included in the article

(6) Manipulated or compromised peer review

The presence of these indicators undermines our confidence in the integrity of the article's content and we cannot, therefore, vouch for its reliability. Please note that this notice is intended solely to alert readers that the content of this article is unreliable. We have not investigated whether authors were aware of or involved in the systematic manipulation of the publication process.

Wiley and Hindawi regrets that the usual quality checks did not identify these issues before publication and have since put additional measures in place to safeguard research integrity.

We wish to credit our own Research Integrity and Research Publishing teams and anonymous and named external researchers and research integrity experts for contributing to this investigation.

The corresponding author, as the representative of all authors, has been given the opportunity to register their agreement or disagreement to this retraction. We have kept a record of any response received.

References

[1] W. Zhan, S. Hong, Y. Sun, and C. Zhu, "The System Research and Implementation for Autorecognition of the Ship Draft via the UAV," *International Journal of Antennas and Propagation*, vol. 2021, Article ID 4617242, 11 pages, 2021.

Hindawi
International Journal of Antennas and Propagation
Volume 2023, Article ID 9810256, 1 page
https://doi.org/10.1155/2023/9810256

Retraction

Retracted: DOA Estimation of an Enhanced Generalized Nested Array with Increased Degrees of Freedom and Reduced Mutual Coupling

International Journal of Antennas and Propagation

Received 19 December 2023; Accepted 19 December 2023; Published 20 December 2023

This article has been retracted by Hindawi following an investigation undertaken by the publisher [1]. This investigation has uncovered evidence of one or more of the following indicators of systematic manipulation of the publication process:

(1) Discrepancies in scope

(2) Discrepancies in the description of the research reported

(3) Discrepancies between the availability of data and the research described

(4) Inappropriate citations

(5) Incoherent, meaningless and/or irrelevant content included in the article

(6) Manipulated or compromised peer review

The presence of these indicators undermines our confidence in the integrity of the article's content and we cannot, therefore, vouch for its reliability. Please note that this notice is intended solely to alert readers that the content of this article is unreliable. We have not investigated whether authors were aware of or involved in the systematic manipulation of the publication process.

Wiley and Hindawi regrets that the usual quality checks did not identify these issues before publication and have since put additional measures in place to safeguard research integrity.

We wish to credit our own Research Integrity and Research Publishing teams and anonymous and named external researchers and research integrity experts for contributing to this investigation.

The corresponding author, as the representative of all authors, has been given the opportunity to register their agreement or disagreement to this retraction. We have kept a record of any response received.

References

[1] Y. Zhang, G. Hu, J. Shi, H. Zhou, C. Zhan, and F. Zhao, "DOA Estimation of an Enhanced Generalized Nested Array with Increased Degrees of Freedom and Reduced Mutual Coupling," *International Journal of Antennas and Propagation*, vol. 2021, Article ID 7233651, 13 pages, 2021.

Hindawi
International Journal of Antennas and Propagation
Volume 2023, Article ID 9786725, 1 page
https://doi.org/10.1155/2023/9786725

Retraction

Retracted: Construction and Application of Media Corpus Based on Big Data

International Journal of Antennas and Propagation

Received 19 December 2023; Accepted 19 December 2023; Published 20 December 2023

This article has been retracted by Hindawi following an investigation undertaken by the publisher [1]. This investigation has uncovered evidence of one or more of the following indicators of systematic manipulation of the publication process:

(1) Discrepancies in scope

(2) Discrepancies in the description of the research reported

(3) Discrepancies between the availability of data and the research described

(4) Inappropriate citations

(5) Incoherent, meaningless and/or irrelevant content included in the article

(6) Manipulated or compromised peer review

The presence of these indicators undermines our confidence in the integrity of the article's content and we cannot, therefore, vouch for its reliability. Please note that this notice is intended solely to alert readers that the content of this article is unreliable. We have not investigated whether authors were aware of or involved in the systematic manipulation of the publication process.

Wiley and Hindawi regrets that the usual quality checks did not identify these issues before publication and have since put additional measures in place to safeguard research integrity.

We wish to credit our own Research Integrity and Research Publishing teams and anonymous and named external researchers and research integrity experts for contributing to this investigation.

The corresponding author, as the representative of all authors, has been given the opportunity to register their agreement or disagreement to this retraction. We have kept a record of any response received.

References

[1] B. Yin and L. Fu, "Construction and Application of Media Corpus Based on Big Data," *International Journal of Antennas and Propagation*, vol. 2021, Article ID 9317018, 7 pages, 2021.

Hindawi
International Journal of Antennas and Propagation
Volume 2023, Article ID 9769872, 1 page
https://doi.org/10.1155/2023/9769872

Retraction

Retracted: Research on Quantization Error Influence of Millimeter-Wave Phased Array Antenna

International Journal of Antennas and Propagation

Received 19 December 2023; Accepted 19 December 2023; Published 20 December 2023

This article has been retracted by Hindawi following an investigation undertaken by the publisher [1]. This investigation has uncovered evidence of one or more of the following indicators of systematic manipulation of the publication process:

(1) Discrepancies in scope

(2) Discrepancies in the description of the research reported

(3) Discrepancies between the availability of data and the research described

(4) Inappropriate citations

(5) Incoherent, meaningless and/or irrelevant content included in the article

(6) Manipulated or compromised peer review

The presence of these indicators undermines our confidence in the integrity of the article's content and we cannot, therefore, vouch for its reliability. Please note that this notice is intended solely to alert readers that the content of this article is unreliable. We have not investigated whether authors were aware of or involved in the systematic manipulation of the publication process.

Wiley and Hindawi regrets that the usual quality checks did not identify these issues before publication and have since put additional measures in place to safeguard research integrity.

We wish to credit our own Research Integrity and Research Publishing teams and anonymous and named external researchers and research integrity experts for contributing to this investigation.

The corresponding author, as the representative of all authors, has been given the opportunity to register their agreement or disagreement to this retraction. We have kept a record of any response received.

References

[1] H. Yang, L. Zhu, Z. Xia et al., "Research on Quantization Error Influence of Millimeter-Wave Phased Array Antenna," *International Journal of Antennas and Propagation*, vol. 2021, Article ID 1874537, 19 pages, 2021.

Hindawi
International Journal of Antennas and Propagation
Volume 2023, Article ID 9840409, 1 page
https://doi.org/10.1155/2023/9840409

Retraction

Retracted: HR Management Big Data Mining Based on Computational Intelligence and Deep Learning

International Journal of Antennas and Propagation

Received 15 August 2023; Accepted 15 August 2023; Published 16 August 2023

This article has been retracted by Hindawi following an investigation undertaken by the publisher [1]. This investigation has uncovered evidence of one or more of the following indicators of systematic manipulation of the publication process:

(1) Discrepancies in scope

(2) Discrepancies in the description of the research reported

(3) Discrepancies between the availability of data and the research described

(4) Inappropriate citations

(5) Incoherent, meaningless and/or irrelevant content included in the article

(6) Peer-review manipulation

The presence of these indicators undermines our confidence in the integrity of the article's content and we cannot, therefore, vouch for its reliability. Please note that this notice is intended solely to alert readers that the content of this article is unreliable. We have not investigated whether authors were aware of or involved in the systematic manipulation of the publication process.

Wiley and Hindawi regrets that the usual quality checks did not identify these issues before publication and have since put additional measures in place to safeguard research integrity.

We wish to credit our own Research Integrity and Research Publishing teams and anonymous and named external researchers and research integrity experts for contributing to this investigation.

The corresponding author, as the representative of all authors, has been given the opportunity to register their agreement or disagreement to this retraction. We have kept a record of any response received.

References

[1] G. Zhao and Z. Xue, "HR Management Big Data Mining Based on Computational Intelligence and Deep Learning," *International Journal of Antennas and Propagation*, vol. 2021, Article ID 1657236, 13 pages, 2021.

Hindawi
International Journal of Antennas and Propagation
Volume 2023, Article ID 9768912, 1 page
https://doi.org/10.1155/2023/9768912

Retraction

Retracted: Research on Interactive Art Online Teaching System Based on BS Mode and Internet of Things

International Journal of Antennas and Propagation

Received 15 August 2023; Accepted 15 August 2023; Published 16 August 2023

This article has been retracted by Hindawi following an investigation undertaken by the publisher [1]. This investigation has uncovered evidence of one or more of the following indicators of systematic manipulation of the publication process:

(1) Discrepancies in scope

(2) Discrepancies in the description of the research reported

(3) Discrepancies between the availability of data and the research described

(4) Inappropriate citations

(5) Incoherent, meaningless and/or irrelevant content included in the article

(6) Peer-review manipulation

The presence of these indicators undermines our confidence in the integrity of the article's content and we cannot, therefore, vouch for its reliability. Please note that this notice is intended solely to alert readers that the content of this article is unreliable. We have not investigated whether authors were aware of or involved in the systematic manipulation of the publication process.

Wiley and Hindawi regrets that the usual quality checks did not identify these issues before publication and have since put additional measures in place to safeguard research integrity.

We wish to credit our own Research Integrity and Research Publishing teams and anonymous and named external researchers and research integrity experts for contributing to this investigation.

The corresponding author, as the representative of all authors, has been given the opportunity to register their agreement or disagreement to this retraction. We have kept a record of any response received.

References

[1] Y. Ying and W. Hongyan, "Research on Interactive Art Online Teaching System Based on BS Mode and Internet of Things," *International Journal of Antennas and Propagation*, vol. 2021, Article ID 7391634, 9 pages, 2021.

Hindawi
International Journal of Antennas and Propagation
Volume 2024, Article ID 9872025, 1 page
https://doi.org/10.1155/2024/9872025

Retraction

Retracted: Design of the School-Enterprise Cooperation Management Information Platform Based on the B/S Architecture

International Journal of Antennas and Propagation

Received 23 January 2024; Accepted 23 January 2024; Published 24 January 2024

This article has been retracted by Hindawi following an investigation undertaken by the publisher [1]. This investigation has uncovered evidence of one or more of the following indicators of systematic manipulation of the publication process:

(1) Discrepancies in scope
(2) Discrepancies in the description of the research reported
(3) Discrepancies between the availability of data and the research described
(4) Inappropriate citations
(5) Incoherent, meaningless and/or irrelevant content included in the article
(6) Manipulated or compromised peer review

The presence of these indicators undermines our confidence in the integrity of the article's content and we cannot, therefore, vouch for its reliability. Please note that this notice is intended solely to alert readers that the content of this article is unreliable. We have not investigated whether authors were aware of or involved in the systematic manipulation of the publication process.

In addition, our investigation has also shown that one or more of the following human-subject reporting requirements has not been met in this article: ethical approval by an Institutional Review Board (IRB) committee or equivalent, patient/participant consent to participate, and/or agreement to publish patient/participant details (where relevant).

Wiley and Hindawi regrets that the usual quality checks did not identify these issues before publication and have since put additional measures in place to safeguard research integrity.

We wish to credit our own Research Integrity and Research Publishing teams and anonymous and named external researchers and research integrity experts for contributing to this investigation.

The corresponding author, as the representative of all authors, has been given the opportunity to register their agreement or disagreement to this retraction. We have kept a record of any response received.

References

[1] Q. Zhang, "Design of the School-Enterprise Cooperation Management Information Platform Based on the B/S Architecture," *International Journal of Antennas and Propagation*, vol. 2021, Article ID 2651936, 7 pages, 2021.

Hindawi
International Journal of Antennas and Propagation
Volume 2021, Article ID 2651936, 7 pages
https://doi.org/10.1155/2021/2651936

Research Article

Design of the School-Enterprise Cooperation Management Information Platform Based on the B/S Architecture

Qiang Zhang

Kavidi National University of the Philippines, Linyi 276000, Shandong, China

Correspondence should be addressed to Qiang Zhang; 201814040003@zknu.edu.cn

Received 18 August 2021; Revised 29 September 2021; Accepted 8 October 2021; Published 31 October 2021

Academic Editor: Fangqing Wen

The SEC teaching management platform provides a good support for school-enterprise cooperation. This paper conducts research on the SEC management information platform based on the B/S architecture. On the basis of the analysis of the relevant functional needs of the system, the overall functional framework of the system includes the college management platform, enterprise management platform, resource-sharing platform, and user login platform, then the B/S architecture is used to develop the SEC teaching management platform, and the test experiments of the SEC teaching management platform are carried out. The maximum number of concurrent tests shows that the maximum number of concurrencies of the platform is 989. Through the system response time test, the system response time is between 0.2 and 0.45, which meets the system response time requirements. In the CPU use test, the CPU share of the system was between 25% and 31%, meeting the needs of the system. From the above experimental results, the system is relatively high.

1. Introduction

With the rapid development of our country's information technology industry, various information technology-related enterprises continue to develop and grow, and the demand for employment is increasing year by year because colleges have undertaken most of the talent training work [1, 2]. However, from the analysis of the employment situation of students in recent years, the employment situation of students is not optimistic, and the pressure of students' employment is increasing [3, 4]. By investigating the reasons of some talent training objectives in universities and the actual situation of enterprise recruitment, in universities, the school wants self-taught students to seamlessly connect with businesses [5, 6]. In enterprises, talents who can work smoothly are needed, and students who need to work are turned into employees who can operate business for the successful realization of SEC for both parties. However, the development of this work did not develop smoothly in the university. This is mainly reflected in the difficulty in achieving cooperation and difficulty in determining and implementing the cooperation plan. Therefore, it is particularly important to build a school-enterprise information management collaboration platform [7, 8].

Regarding the research on the SEC management information platform, some researchers used the UML method to analyze the system functions from the perspective of SEC talent training information and constructed the internet and SEC talent training model [9]. From the perspective of system management, the problems existing in system management at this stage are explained, and relevant suggestions and countermeasures to deepen SEC are put forward to effectively play the role of the SEC management information platform [10]. Some researchers have integrated the human resource training model and system design of SEC and put forward an information management idea based on the SaaS MOOC platform. First, the overall system architecture is designed, then the needs of the system are analyzed, the system thinking map is drawn, and Alibaba Cloud, Apache, PHP, MySQL, and other tools are used to realize the development of the platform [11]. Researchers have also designed a system of innovation and entrepreneurship training management based on SEC. The system uses B/S architecture technology to realize the basic

management of user training for students. Users can provide information to colleges and students. Management of basic information can also realize the information management of student training management [12].

This paper studies the SEC management information platform based on the B/S architecture, expounds the significance of developing the SEC information platform based on related documents, and expounds the necessity of the information platform design. Have a comprehensive understanding of the application of the B/S architecture, then design the SEC management information platform based on the B/S architecture, and test the designed platform to verify the effectiveness of the platform.

2. Research on the Information Platform of SEC Management

2.1. The Significance of the Development of a SEC Management Information Platform

(1) The school-enterprise joint running of schools has achieved a win-win complementarity between the school and the enterprise. On the one hand, the school trains graduates who can be employed, provides services for enterprises, and contributes to the development of enterprises. The school is guided by the needs of enterprises, which can enable students to quickly adapt to the needs of enterprises, and the economic and social benefits of enterprises will be greatly improved. On the other hand, for higher vocational colleges, this not only ensures the employment of students but also expands the social influence and further enhances the image of universities. At the same time, the company submitted the talent training requirements, providing a guarantee for the school's practical teaching. School-enterprise cooperation can introduce the latest commercial, scientific, and technological achievements into vocational teaching, making the curriculum and content more advanced, applicable, and relevant. The new knowledge, new technology, and new business concepts can be timely integrated into the teaching content so that better development of the curriculum can be made. The cooperation between the school and the company school has fundamentally broken the exclusive social status of education and enhanced the training of students' work adaptability and comprehensive quality. For schools and enterprises, this is a win-win and complementary engineering.

(2) The key to the success or failure of vocational training and teaching: only with the recognition and participation of enterprises, vocational training can always pay attention to the society's demand for technical application talents in the process of talent training and can ensure the pertinence and application of talent training. In order to improve the relevance of vocational training and social economy and enhance the practicality of occupations, vocational colleges need to understand the market economy's requirements for specific professional teams and the ever-changing needs of knowledge, quality, technology, and abilities after employment. Targeted arrangements, curriculum, and textbook updates have created a professional-focused teaching system. Through communication with enterprises, higher vocational colleges can connect education goals and employment standards, curriculum settings and corporate needs, and skills' training and job requirements, and the cutting-edge information support that enterprises can provide has a higher starting point and certainty. The forward-looking nature has effectively improved the professional adaptability of vocational training.

(3) Using this network platform can promote cooperation and interaction between universities, promote the promotion and transformation of scientific and technological achievements of universities, and promote cooperation between the industry, university, and research.

(4) Efforts have been made to create a professional information platform for the exchange and placement of batch professional graduates and order education and training between colleges and enterprises and realize the zero-distance and low-cost information transmission between schools and enterprises and serving students' employment.

2.2. Application of the B/S Architecture in the SEC Management Information Platform. In terms of B/S architecture, the software installation and maintenance can be completed on the server side at the same time, and corresponding modifications can also be made. With this structure, the client can be used without the client app, and upgrade operations can be performed during operation. The reason is that, at this time, the user only needs to access the browser to make all the modules work. For the structure of the system, it provides the most realistic and developmental basis. Through this foundation, it can provide networking, integrated services, and online services for heterogeneous applications, heterogeneous networks, and heterogeneous machines.

2.3. Platform Search Algorithm. The attribute words in the attribute set are not representative. If an accurate attribute word weight can be calculated from it, it needs to be evaluated using an attribute selection algorithm. This evaluation process uses the construction evaluation function. After the evaluation of this function, a representative set of feature words and their corresponding weights will be obtained. Therefore, an important central factor in the process is the evaluation function. This paper mainly studies two commonly used evaluation functions.

(1) Information gain method: (1) count the number of positive and negative classified documents: N, N_z. (2) Count the number of occurrences of positive

documents for each word (A), the number of occurrences of negative documents (B), positive documents and negative documents Times C and D do not appear. (3) The formula for calculating information entropy (1) is as follows. (4) Calculate the information gain of each word. (5) Sort each word according to the information gain value from large to small, and select the top K, the word is the feature, and K is the feature dimension

$$\text{Entropy}(S) = -\left(\frac{N_1}{N_1+N_2}\right)\log\left(\frac{N_1}{N_1+N_2}\right) + \frac{N_2}{N_1+N_2}\log\left(\frac{N_2}{N_1+N_2}\right). \quad (1)$$

(2) Mutual information method: it is mainly based on the probability that a feature and category coexist to measure the relevance of a feature and category. For a feature t and category c, the calculation formula of mutual information is expressed as follows:

$$\text{MI}(t,c) = \log\frac{p(t,c)}{p(t)\times p(c)} = \log\frac{p(t|c)}{p(t)}, \quad (2)$$

where $p(t, c)$ represents the probability of the text containing attribute t and category c in the training set, $p(t)$ represents the probability of text containing attribute t in the training set, and $p(c)$ represents the category probability of text c in the training set. The attribute t has a higher probability of appearing in category c, while the probability of appearing in other categories is lower, that is, attribute t and category c; if the correlation is large, the mutual information value MI (t, c) will be obtained. Sort each word according to the information gain value from high to low, and select the first few words K as the attribute.

3. Design of a SEC Management Information Platform Based on the B/S Architecture

3.1. System Requirements' Analysis

(1) Query function: the SEC information service platform has designed user sections such as personal job hunting intentions, collaborative recruitment, SEC, promotion of scientific and technological achievements, technical requirements, and batches. Expert information database and other user modules are convenient for different users to ask questions according to their needs. In the corresponding information, the platform has created a variety of effective query modules.

(2) Functional navigation: in order to make the target user feel more perfect when navigating, the design of the platform application adopts page rotation and sorting editing methods, which can effectively navigate the information released on the platform.

(3) Management function: the back-end maintenance administrator of the school-enterprise collaborative information service platform must perform effective authentication when processing and deleting platform data information. When deleting data information, one needs to back up the deleted content to avoid accidental deletion. At the same time, any modification and deletion operations must be recorded.

(4) User management: according to the division of labor, the authorized administrators at all levels of the platform system have different levels of data and information management permissions, such as repair and deletion, which also include the supervision of the back-end administrator and back-end maintenance.

(5) Help feedback: includes specific operating system issues of the platform, sent to the platform through messages and emails.

3.2. Overall System Architecture. According to the aforementioned system function requirement analysis, the overall architecture of the SEC management information platform is proposed as shown in Figure 1.

3.3. College Management Platform. School management is applied to enterprise users. The user groups are teaching quality support supervisors and teaching quality support teachers. They are mainly used to initialize the information of each partner institution, set professional information, grade information, class information, and student information, and set up the enterprise and the distribution of contact personnel among various institutions.

3.4. Enterprise Management Platform. Companies can effectively retain the specific information and data they publish on the system platform, and they can also apply for the first-stage talents including the needs of graduates and experts. Including points of operation are as follows: input and release of graduate student requirements information and maintain relevant information on the needs of college graduates in the province (including modification, deletion, cancellation, and release of information).

3.5. Resource-Sharing Platform. After individuals, companies, or college members have released their personal job search, corporate recruitment, result recommendation, technical requirements, and other related information in their management module, ordinary users can choose among personal job search, corporate recruitment, and recommendation results. One can also query and search information in the technical requirements column, talent database, information center, and expert teachers. For example, the talent search in the personal job search column can be searched by position, gender, graduation time, etc. In the corporate recruitment column, one can search for positions by company or by position or by industry classification.

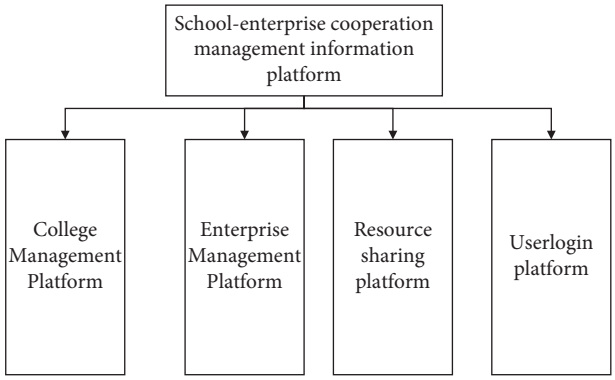

Figure 1: System overall architecture diagram.

3.6. User Login Platform

(1) Except for administrators, enterprise users, university users, and individual users must register and log in through the system home page to complete their specific functions. After the user enters the user name and password and selects the user type, the system searches for the user based on the entered data and judges whether it is a registered legal user based on the user name and password. If you meet the requirements, you can log in to the system management page after passing the authentication. At the same time, write the user name and user role in the Session, and the corresponding section will be automatically uploaded according to the user's type and permissions, and the corresponding page will be inserted to create a unique personalized service for your members. User registration and management can be completed through a browser, which greatly simplifies the traditional customer-based management methods.

3.7. Platform Architecture. The school-enterprise collaborative service platform technology adopts relatively mature J2EE technology and B/S architecture for research and development. The system is divided into four levels: system user access level, technology application level, information data resource level, and application network level. The network layer is the basic network facilities and hardware and software infrastructure that support the operation of the business platform. The data resource level is the main level of the project construction content. The main purpose of data resources is to share and interact with the data and information uploaded by each target user in accordance with the system standards and to create a database for the SEC information service platform: cooperative enterprise database, professional and technical personnel database, application equipment database, scientific and technological achievements' database, and data resource databases such as cooperative enterprise databases. The application layer should provide various applications for colleges, enterprises, governments, and park users, mainly college management platforms, enterprise management platforms, resource-sharing platforms, and user docking platforms. The access layer is to centrally display the information of each application system through the website platform and WeChat platform and create different default access interfaces for different users. The schematic diagram is shown in Figure 2.

4. Based on the Detection of the SEC Management Information Platform Based on the B/S Architecture

4.1. Performance Testing. It mainly conducted detailed performance tests on the SEC teaching management platform in terms of the maximum concurrent access and the response time of the system.

4.2. Analysis of the Experimental Results of the Maximum Concurrent Number Detection. This article uses Apache ab as a stress test tool to detect the maximum number of concurrencies of the SEC teaching management platform designed in this article. The relevant experimental data results are shown in Table 1.

It can be seen from Table 1 that 90% of the responders of the system are 907, 95% of the responders are 931, and the maximum concurrent number of 99% is 989. It can be seen that the maximum concurrent number of the system is better, close to the high-performance number of 1100 responders.

4.3. System Response Time. The response time performance test is mainly for the data throughput operation when the amount of data is large. For example, the information retrieval of the large amount of data involved in this system, the import and export operations of a large amount of data, and the upload and download operations of a large amount of resources all require big data. Quantity test is shown in Table 2.

4.3.1. Response Time Performance Test. The system was tested repeatedly for 3 times, and the response time of 200 users, 400 users, 600 users, and 800 users was calculated each time. The relevant data results are shown in Table 3.

It can be seen from Figure 3 that when the system has 200 users, the system response time is about 0.3 s. When there are 800 users, the average response time is 0.45 s. The corresponding response time is shown in Table 2. It can be seen that the response time is relatively short.

4.3.2. CPU Usage. The system is subjected to 3 repeated experimental tests, and the CPU usage rates of 200 users, 400 users, 600 users, and 800 users are calculated each time. The relevant data results are shown in Table 4.

It can be seen from Figure 4 that when the system has 200 users, the average CPU usage rate of the system is 25%, and when there are 800 users, the average CPU usage rate of the system is 31%, which corresponds to the CPU usage rate in Table 2. The comparison shows that the system CPU usage is still relatively low.

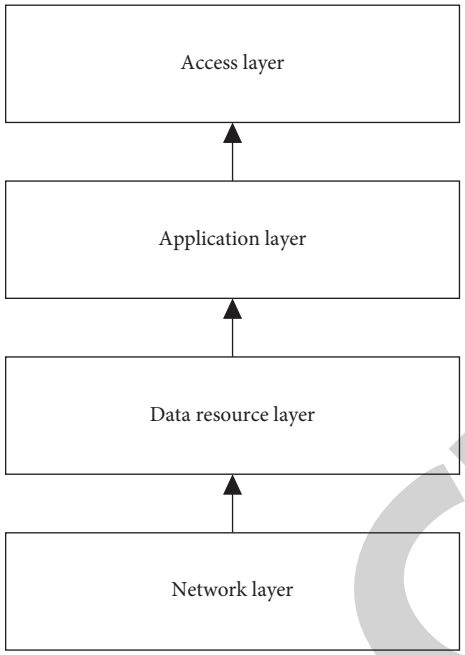

Figure 2: Platform architecture diagram.

Table 1: Analysis of the experimental results of the maximum concurrent number detection.

	90% line	95% line	99% line
HTTP request	907	931	989
Transaction controller	907	931	989
Total	907	931	989

Table 2: Test case table.

Number of users	Response time	CPU (%)	Throughput rate (b/s)	Click-through rate (h/s)
200	< 1	< 45	> 844, 595, 200	> 290
400	< 2	< 45	> 1,689, 190, 400	> 290.150
600	< 2.5	< 45	> 2,533, 785, 600	> 302.115
800	< 3	< 45	> 3,378, 380, 800	> 317.266

Table 3: Response time performance test.

	Experiment 1	Experiment 2	Experiment 3
200	0.2	0.4	0.3
400	0.4	0.3	0.2
600	0.3	0.3	0.5
800	0.5	0.5	0.2

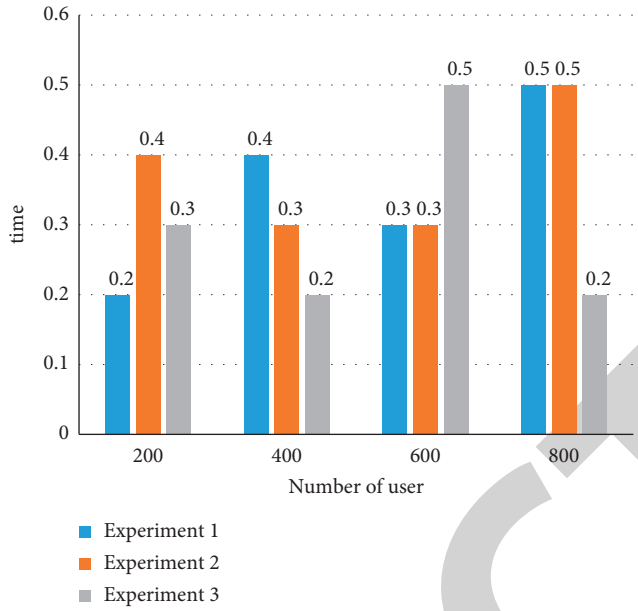

Figure 3: Response time performance test.

Table 4: CPU usage.

	Experiment 1 (%)	Experiment 2 (%)	Experiment 3 (%)
200	23	25	26
400	24	26	25
600	34	28	27
800	35	29	28

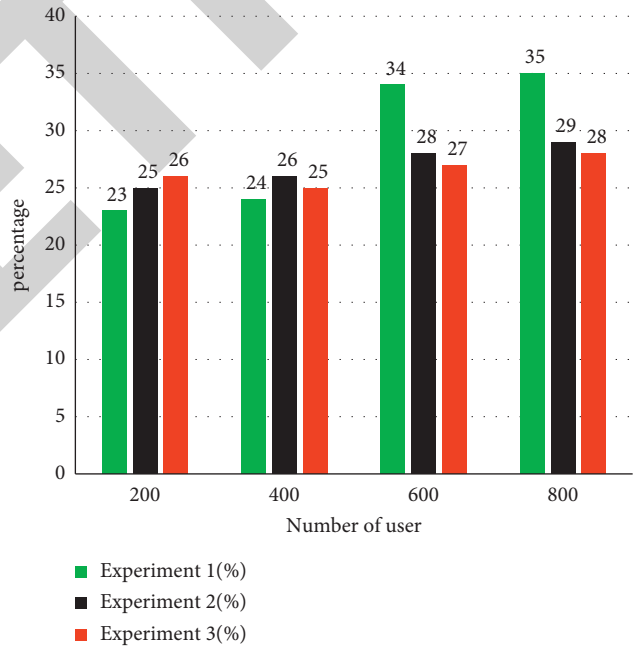

Figure 4: CPU usage.

Hindawi
International Journal of Antennas and Propagation
Volume 2021, Article ID 9705617, 8 pages
https://doi.org/10.1155/2021/9705617

Research Article

A Sliding Window Data Compression Method for Spatial-Time DOA Estimation

Pin-Jiao Zhao,[1] **Guo-Bing Hu**,[1] **and Li-Wei Wang**[2]

[1]*Department of Electronic and Information Engineering, Jinling Institute of Technology, Nanjing 211169, China*
[2]*Nanjing Electronic Devices Institute, Nanjing 210007, China*

Correspondence should be addressed to Pin-Jiao Zhao; zhaopinjiao@hrbeu.edu.cn

Received 10 September 2021; Accepted 7 October 2021; Published 28 October 2021

Academic Editor: Fangqing Wen

This paper presents a sliding window data compression method for spatial-time direction-of-arrival (DOA) estimation using coprime array. The signal model is firstly formulated by jointly using the temporal and spatial information of the impinging sources. Then, a sliding window data compression processing is performed on the array output matrix to realize fast calculation of time average function, and the computational burden has been reduced accordingly. Based on the concept of sum and difference co-array (SDCA), the vectorized conjugate augmented MUSIC is adopted, with which more sources than twice of the physical sensors can be resolved. Additionally, the sparse array robustness to sensor failure has been evaluated by introducing the concept of essential sensors. The theoretical analysis and numerical simulations are provided to confirm the effectiveness performance of the proposed method.

1. Introduction

Direction-of-arrival (DOA) estimation has been a crucial topic in various practical applications, such as radar, navigation, and wireless communication [1–4], where the antenna arrays are utilized for collecting the spatial sampling of impinging electromagnetic waves. In comparison to the typical uniform linear array (ULA) [5, 6], the emerging sparse arrays [7–9] have remarkable advantages in terms of sensor layout, degrees of freedom (DOF), and virtual array aperture, with which more sources than the number of the physical sensors can be resolved.

Nested array (NA) [10] and coprime array (CPA) [11] are the two most typical sparse array configurations, which have closed form expressions for array geometry and achievable DOF as compared with the minimum redundancy array (MRA) and the minimum hole array (MHA). NA is composed of two concatenated subarrays with increasing element spacing, which is capable of providing $\mathcal{O}(L^2)$ DOF with $\mathcal{O}(L)$ physical sensors, but the existing small interelement spacing in the subarray of NA would cause severe mutual coupling. As for the CPA, the mutual coupling can be alleviated for the configuration is constructed by a pair of coprime ULAs, which can offer $\mathcal{O}(MN)$ DOF with $\mathcal{O}(M+N)$ sensors, but has holes in the virtual co-array. Recently, lots of modified versions have been further developed, such as super NA [12], enhanced NA [13], augmented NA [14], generalized CPA [15], and thinned CPA [16], to increase the consecutive DOF and reduce the mutual coupling. The sparse arrays mentioned above construct virtual co-array from the view of difference co-array (DCA) and realize the multitarget DOA estimation by exploiting vector MUSIC method or compressed sensing (CS) approach; nevertheless, the number of resolvable sources cannot exceed twice of the physical aperture.

Motivated by the sum co-array (SCA) originating from active sensing [17–19], the concept of sum and difference co-array (SDCA) has provided a new perspective for DOA estimation [20], where the vectorized conjugate augmented MUSIC (VCAM) is presented by jointly using the temporal and spatial information of the impinging sources. The CPA configuration based on SDCA is firstly proposed for spatial-time DOA estimation [21]. Following this, a modified NA configuration named as sum-diff NA (SdNA) is proposed in

[22] for the purpose of resolving more sources. In [23], combining with the VCAM method, the unfold CPA configuration on the basis of SDCA is developed to provide more DOF and larger array aperture, and the DOA estimation accuracy is improved accordingly. However, the above spatial-time DOA estimation methods based on SDCA involve high-dimensional data processing of multiple pseudo snapshots, which has high computational load. Additionally, another limitation of the above methods is that the case of sensor failure [24–26] always occurring in the actual direction-finding system has been ignored. The failure of some sensors or receiving channels may destroy the virtual array structure of sparse array and reduce the number of consecutive DOF and the effective array aperture, which results in the performance degradation.

To tackle these problems, a sliding window data compression method for spatial-time DOA estimation is proposed in this paper. The coprime array is adopted from the perspective of SDCA, which can provide more DOF and larger effective array aperture. Then, a sliding window data compression processing is performed on array output matrix to realize fast calculation of time average function. Afterwards, the vectorized conjugate augmented MUSIC is adopted by jointly using the temporal and spatial information of the impinging sources. Moreover, the sparse array robustness to sensor failure has been evaluated by introducing the concept of essential sensors.

Notations: vectors and matrices are denoted by lowercase and uppercase bold-face letters, respectively. $(\cdot)^T$, $(\cdot)^H$, and $(\cdot)^*$ and $|\cdot|$ denote transpose, conjugate transpose, conjugate, and the norm of the embraced matrix, respectively. $\mathbf{0}_{m\times n}$ represents an $m \times n$ null matrix and $\mathbf{I}_m$ represents an $m \times m$ identity matrix. The symbol $\otimes$ denotes the Kronecker product and $\odot$ denotes the Khatri–Rao product.

2. Problem Formulation

2.1. Sparse Array Configuration. Referring to [11], a prototype CPA is composed of two uniform linear subarrays: one is a N-element ULA with interspacing being Md (d denotes the unit interspacing) and the other is an M-element ULA with interspacing being Nd, where N and M are coprime integers satisfying $M < N$. Intuitively, an example of 8-element CPA with $M = 4$ and $N = 5$ is illustrated in Figure 1, where white circles and black circles, respectively, denote the sensor locations of subarray 1 and subarray 2 and shaded circles denote the overlapping sensor between subarray 1 and subarray 2. For the reason that the two uniform linear subarrays share the same antenna sensor placing at zero position, the CPA have $M + N - 1$ physical sensors, whose locations are given by

$$\mathbb{P}_{CPA} = \{Mnd | n \in \mathbb{Z}(N-1)\} \cup \{Nmd | m \in \mathbb{Z}(M-1)\}, \tag{1}$$

where $\mathbb{Z}(m)$ denotes a set of positive integers ranging from 1 to m and the unit interspacing d is generally set to be half of the wavelength.

2.2. Signal Model. Assume that K far-field narrowband sources from directions $\{\theta_1, \theta_2, \ldots, \theta_K\}$ impinge on an L-element CPA configuration with $\theta_k \in (-\pi/2, \pi/2]$, where $L = M + N - 1$. Then, the antenna array output at time t can be expressed as

$$\mathbf{x}(t) = \mathbf{A}\mathbf{s}(t) + \mathbf{n}(t) = \sum_{k=1}^{K} \mathbf{a}(\theta_k) s_k(t) + \mathbf{n}(t), \tag{2}$$

where $\mathbf{a}(\theta_k) = e^{j\pi \mathbf{l} \sin\theta_k}$ is the steering vector with respect to the direction θ_k with the sensor location vector being $\mathbf{l} = [l_1, l_2, \ldots, l_L]^T$. By stacking all the $\mathbf{a}(\theta_k)$ for $k = 1, 2, \ldots, K$, the array manifold matrix $\mathbf{A} = \{\mathbf{a}(\theta_k)\}_{k=1}^{K}$ can be obtained. $s_k(t) = G_k e^{j\omega_k t}$ denotes the kth impinging source with G_k and ω_k being the deterministic complex amplitude and the small frequency offset, respectively. Accordingly, $\mathbf{s}(t) = \{s_k(t)\}_{k=1}^{K}$ is the source vector. $\mathbf{n}(t)$ is the Gaussian white noise vector with zero mean and variance being σ_n^2.

Define the ith and the jth ($1 \le i, j \le L$) row of $\mathbf{x}(t)$ as $x_i(t)$ and $x_j(t)$, respectively; then, the time average function for T_P samples can be calculated by

$$R_{x_i^* x_j}(\tau) = \frac{1}{T_P} \sum_{t=1}^{T_P} x_i^*(t) x_j(t+\tau) \approx \sum_{k=1}^{K} e^{j\pi (l_j - l_i) \sin\theta_k} R_{s_k^* s_k}(\tau) + R_{n_i^* n_j}(\tau), \tag{3}$$

where $\tau \neq 0$ is the time lag ranging from 1 to T_s with T_s being the number of pseudo snapshots, $l_j - l_i$ denotes the generated virtual sensor with $l_i, l_j \in \mathbf{l}$, $R_{s_i^* s_j}(\tau) = |E_k|^2 e^{j\omega_k t}$ can be seen as an equivalent source with amplitude $|E_k|^2$ and frequency offset ω_k, which has the similar form as $s_k(t) = G_k e^{j\omega_k t}$. Since $\mathbf{n}(t)$ is assumed to be the Gaussian white noise, $R_{n_i^* n_j}(\tau) \approx 0$ holds. As compared with the covariance matrix widely used in spatial DOA estimation methods, $R_{x_j^* x_j}(\tau)$ is constructed by jointly using both temporal and spatial information of the impinging sources, which has potential to expand the effective array aperture and improve the DOA estimation accuracy and angle resolution. Nevertheless, it is worth pointing that (3) involves the sampling of array output matrix with a dimension of

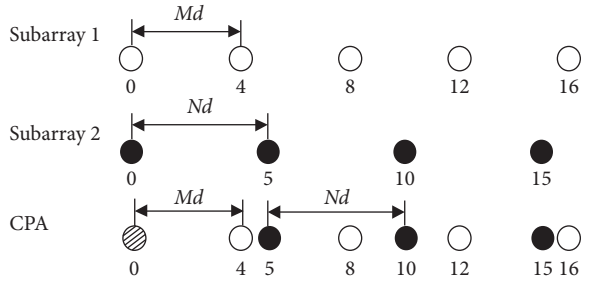

FIGURE 1: Example of 8-element CPA with $M = 4$ and $N = 5$.

$L \times T_s T_P$, which is computationally expensive. Toward this end, a data compression processing method based on sliding window principle is proposed in Section 3.

3. DOA Estimation Based on Sliding Window Data Compression

For the purpose of realizing the fast calculation of time average function and the corresponding pseudo data matrix, the sliding window data compression processing is performed on $x_i(t)$ and $x_j(t)$ $(1 \le i, j \le L)$ with a period of T_P, which is given by

$$\begin{cases} x_o(t) = x_i(t) * \left[\mathbf{0}_{T_s \times T_P}; \mathbf{I}_{T_P}; \mathbf{0}_{T_s \times T_P}\right], \\ x_{\tau+}(t) = x_j(t) * \left[\mathbf{0}_{(T_s+\tau)\times T_P}; \mathbf{I}_{T_P}; \mathbf{0}_{(T_s-\tau)\times T_P}\right], \\ x_{\tau-}(t) = x_j(t) * \left[\mathbf{0}_{(T_s-\tau)\times T_P}; \mathbf{I}_{T_P}; \mathbf{0}_{(T_s+\tau)\times T_P}\right]. \end{cases} \tag{4}$$

With the sliding window data compression processing in (4), the sampling of the array output matrix with a dimension of $L \times T_s T_P$ can be transformed into the sampling of an equivalent one with a dimension of $L \times (T_P + 2T_s)$; thus, the computational burden can be reduced accordingly. Moreover, notice that the data information is not lost during the process of sliding window data compression, which ensures the DOA estimation accuracy and angle resolution. For the convenience of analysis, we choose the first sensor to be the reference, i.e., $i = 1$. Then, (3) can be written as

$$\begin{cases} R_{ij}^*(\tau) = \dfrac{1}{T_P} \displaystyle\sum_{t=1}^{T_P} x_o^*(t) x_{\tau+}(t), \\ R_{ij}^*(-\tau) = \dfrac{1}{T_P} \displaystyle\sum_{t=1}^{T_P} x_o^*(t) x_{\tau-}(t). \end{cases} \tag{5}$$

More intuitively, an example of a short data sequence with $T_p = 3$ and $T_s = 4$ is depicted in Figure 2 for the convenience of description, where the data in blue sliding window stands for the reference, the sliding windows on its right side stand for the cases of $\tau > 0$, and the sliding windows on its left side stand for the cases of $\tau < 0$. It should be noted that the proposed sliding window data compression method involves a long data sequence, which has the same processing principle as the given example of short data sequence.

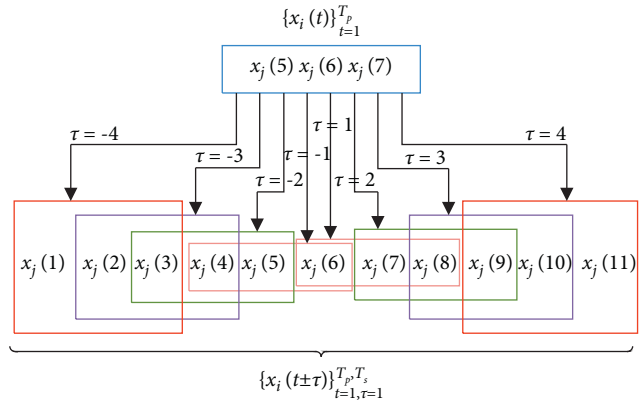

FIGURE 2: Example of sliding window data compression processing.

Since j varies from 1 to L, the conjugate augmented vector can be obtained as

$$\mathbf{g}(\tau) = \left[\mathbf{g}_x^H(-\tau), \mathbf{g}_x^T(\tau)\right]^T = \left[\mathbf{A}^H, \mathbf{A}^T\right]^T \mathbf{g}_s(\tau), \tag{6}$$

where the time average vector $\mathbf{g}(\tau)$ and its mirrored version $\mathbf{g}_x(-\tau)$ are given as

$$\begin{cases} \mathbf{g}_x(\tau) = \mathbf{A}\mathbf{g}_s(\tau) = \left[R_{11}^*(\tau), R_{12}^*(\tau), \ldots, R_{1L}^*(\tau)\right]^T, \\ \mathbf{g}_x(-\tau) = \mathbf{A}\mathbf{g}_s(-\tau) = \left[R_{11}^*(-\tau), R_{12}^*(-\tau), \ldots, R_{1L}^*(-\tau)\right]^T, \end{cases} \tag{7}$$

with $\mathbf{g}_s(\tau) = [R_{s_1^* s_1}(\tau), R_{s_2^* s_2}(\tau), \ldots, R_{s_K^* s_K}(\tau)]^T$ and $\mathbf{g}_s(-\tau) = [R_{s_1^* s_1}(-\tau), R_{s_2^* s_2}(-\tau), \ldots, R_{s_K^* s_K}(-\tau)]^T$.

Then, for the T_s pseudo snapshots, the pseudo data matrix can be constructed as

$$\mathbf{G} = \left\{\mathbf{g}(n_s P_s)\right\}_{n_s=1}^{T_s} = \left[\mathbf{A}^H, \mathbf{A}^T\right]^T \mathbf{E}\boldsymbol{\Omega}, \tag{8}$$

where P_s is the pseudo sampling period satisfying Nyguist sampling principle, $\mathbf{E}$ is a diagonal matrix with main diagonal elements being $|E_k|^2$ and zeros elsewhere, and Ω is a $K \times T_s$ matrix with the (k, n)th element being $e^{jw_k n P_s}$. By calculating the covariance matrix of $\mathbf{G}$ and then vectorizing it, we have

$$\mathbf{v}_G = \left(\overline{\mathbf{A}}^H \odot \overline{\mathbf{A}}^T\right)\mathbf{q}_s, \tag{9}$$

where $\overline{\mathbf{A}} = [\mathbf{A}^{\mathrm{H}}, \mathbf{A}^{\mathrm{T}}]$ is the generated array manifold matrix and $\mathbf{q}_s$ can be seen as an equivalent impinging source vector $K \times 1$ with the kth element being $|E_k|^4$. Additionally, the kth column of $(\overline{\mathbf{A}}^H \odot \overline{\mathbf{A}}^T)$ can be denoted as

$$\tilde{\mathbf{a}}(\theta_k) = \begin{bmatrix} \mathbf{a}(\theta_k) \otimes \mathbf{a}^*(\theta_k) \\ \mathbf{a}(\theta_k) \otimes \mathbf{a}(\theta_k) \\ \mathbf{a}^*(\theta_k) \otimes \mathbf{a}^*(\theta_k) \\ \mathbf{a}^*(\theta_k) \otimes \mathbf{a}(\theta_k) \end{bmatrix}, \tag{10}$$

where the term $\tilde{\mathbf{a}}(\theta_k)$ in (10) behaves like a longer virtual steering vector that can provide more DOF for DOA estimation. More specifically, the union of $\mathbf{a}(\theta_k) \otimes \mathbf{a}^*(\theta_k)$ and $\mathbf{a}^*(\theta_k) \otimes \mathbf{a}(\theta_k)$, respectively, are corresponding to the DCA

Table 1: Main steps of the proposed method.

(1) Calculate the time average function $R_{x_i^* x_j}(\tau)$ using (3)
(2) Perform sliding window data compression processing on $x_i(t)$ and $x_j(t)$ via (4) and rewrite (3) using (5)
(3) Construct the conjugate augmented vector $\mathbf{g}(\tau)$using (6)
(4) Construct the pseudodata matrix $\mathbf{G}$ using (8) and calculate its covariance matrix
(5) Vectorize the covariance matrix of $\mathbf{G}$ using (9)
(6) Perform spatial smoothing MUSIC method or sparse construction techniques on $\mathbf{q}_s$

and its mirror version and the union of $\mathbf{a}(\theta_k) \otimes \mathbf{a}(\theta_k)$ and $\mathbf{a}^*(\theta_k) \otimes \mathbf{a}^*(\theta_k)$, respectively, are corresponding to the SCA and its mirror version. Then, the spatial smoothing MUSIC method or sparse construction techniques can be performed for DOA estimation. To conclude, the main steps of the proposed method are given in Table 1.

4. Array Robustness Analysis

The array robustness to sensor failure directly affects the DOA estimation performance in the practical direction-finding system and the relevant analysis is discussed in detail in this section. For a sparse array with known array configuration, if the distribution of SDCA changes when one or more sensors are deleted from the physical array (PA), then these sensors are termed as essential sensors. Mathematically, for the sparse array $\mathscr{A}$ and the corresponding SDCA $\mathscr{S}$, when the lth sensor is deleted from $\mathscr{A}$, the remaining array becomes $\mathscr{A}_{-l} = \mathscr{A} \backslash \{l\}$ and the corresponding SDCA becomes $\mathscr{S}_{-l}$. If $\mathscr{S} \neq \mathscr{S}_{-l}$ holds, then the lth sensor is essential for the sparse array $\mathscr{A}$, but not vice versa.

An example of detecting essential sensor with $\mathscr{A}_1 = \{0, 1, 2, 3, 4, 6\}$ is given in Figure 3, where the red circles and black circles, respectively, denote the locations of PA and SDCA. As can be seen from Figure 3, after removing the sensor 1, the PA becomes $\mathscr{A}_2 = \{0, 2, 3, 4, 6\}$; then, the corresponding SDCA has holes at ± 1, which implies that sensor 1 is essential. On the contrary, after removing the sensor 2, the PA becomes $\mathscr{A}_3 = \{0, 1, 3, 4, 6\}$; then, the corresponding SDCA is the same as the original one; hence, the sensor 2 of PA is inessential.

Then, the evaluation function of sparse array robustness is calculated as

$$\mathscr{F}_k = \left|\mathrm{E}_k\right| / |\mathbb{A}|, \tag{11}$$

where $|\mathrm{E}_k|$ is the number of essential sensors for sparse array $\mathbb{A}$ and $|\mathbb{A}|$ is the number of the whole sparse array $\mathbb{A}$. According to (10), the values of $\mathscr{F}_k$ ranges from 0 to 1. More specifically, if $\mathscr{F}_k \longrightarrow 0$, then the sparse array has strong robustness, but the number of essential sensors is small; if $\mathscr{F}_k \longrightarrow 1$, almost all the sensors in sparse array are essential, which is economic, but the array robustness is low. Therefore, several strategies, such as reducing the failure probability of essential sensors and introducing a certain number of inessential sensors, can be adopted to improve the robustness of sparse array and meanwhile ensure the economic benefits.

5. Numerical Simulations

In this section, numerical simulations are performed to evaluate the performance of the proposed method. Consider $K = 20$ narrowband sources uniformly distributed between -60° and 60° and impinge on an 8-sensor CPA with SNR being 0 dB and pseudo snapshot number $T_s = 400$, where the sensor locations of CPA is $\mathbb{P}_{CPA} = \{0, 4, 5, 8, 10, 12, 15, 16\}$. To demonstrate the computational efficiency of the proposed method, the averaged CPU times of the proposed sliding window data compression (SWDC) and VCAM [21] *versus* snapshot number T_P over 200 independent Monte Carlo trials are compared in Table 2, where the software used for implementation is MATLAB R2014a (version 8.3) and executed in PC Intel(R) Core(TM) i7-8550U processor with 8.0 GB RAM. It can be observed from Table 2 that the operation time of the proposed SWDC method is significantly reduced in comparison to VCAM, which is mainly attributed to reason that sliding window data compression can transform the antenna received matrix with a dimension of $L \times T_s T_P$ into an $L \times (T_P + 2T_s)$ equivalent one, and the computational load is reduced accordingly.

Then, array robustness to sensor failure is discussed in this simulation. For the 8-element CPA with $\mathbb{P}_{CPA} = \{0, 4, 5, 8, 10, 12, 15, 16\}$, we model the sensor failure by deleting the sensors of CPA one by one; then, the remaining array location, holes of SDCA, and the consecutive DOF are listed in Table 3. As can be seen from Table 3 that if sensor failure occurs to sensor 0, the distribution of SDCA remains unchanged, which implies that sensor "0" is an inessential sensor for the 8-element CPA. Apart from sensor "0," if sensor failure occurs to other sensors, the corresponding SDCA has more holes and less consecutive DOF. Thus, all the sensors in the 8-element CPA are essential, except for sensor "0." Moreover, the importance of each essential sensor is different, e.g., the failure of sensor "5", "10", "12," or "15" would cause more "holes" than the other essential sensors.

The third simulation investigates the DOA estimation performance via MUSIC spectrum. All the conditions are the same as the first simulation except that the snapshot number T_P is set to be 300. In addition, the searching step of MUSIC spectrum is set to be 0.5°. Figure 4 depicts the MUSIC spectrum of the proposed method, where the blue solid line represents the angle estimates and the red dotted line represents incident sources. As can be seen from Figure 4, the proposed method can resolve 20 impinging sources with only 8 sensors and the MUSIC spectrum has sharp and high power peaks in the vicinity of the true impinging sources.

In the last simulation, the DOA estimation performance of the proposed SWDC, VCAM [21], and CPA-MUSIC [11] *versus* SNR and the number of snapshots are compared via 200 independent Monte Carlo trials, where the root mean square error (RMSE) is chosen for evaluating the DOA estimation performance:

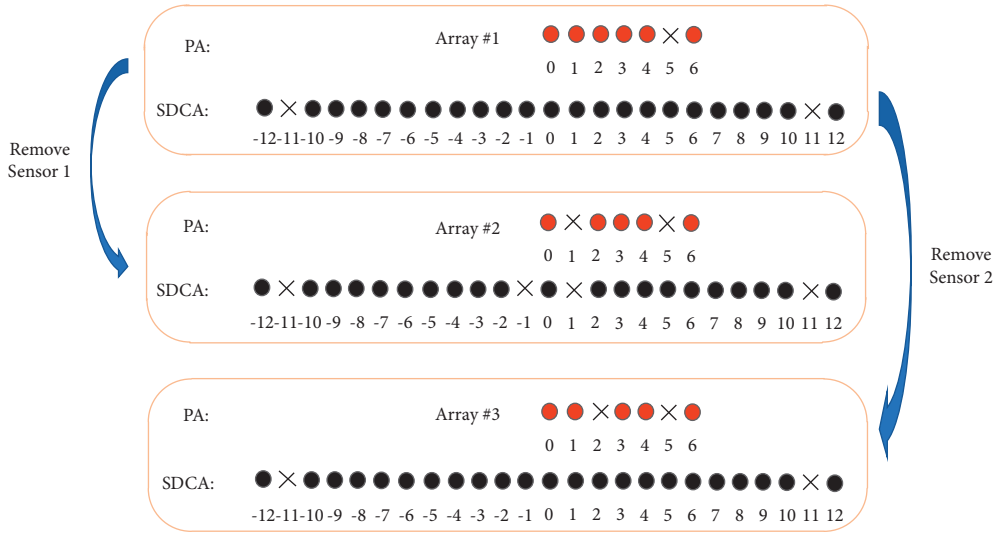

Figure 3: Example of detecting essential sensors.

Table 2: Averaged CPU times.

Time(sec)	$T_P = 200$	$T_P = 300$	$T_P = 400$	$T_P = 500$	$T_P = 600$
SWDC	0.0544	0.0666	0.0761	0.0852	0.0962
VCAM	0.0995	0.1368	0.1747	0.1950	0.1990

Table 3: The array robustness to sensor failure.

Sensor failure	Remaining array	Holes in SDCA	Consecutive DOF
Null	{0, 4, 5, 8, 10, 12, 15, 16}	{−29, 29}	57
"0"	{4, 5, 8, 10, 12, 15, 16}	{−29, 29}	57
"4"	{0, 5, 8, 10, 12, 15, 16}	{−29, −19, −14, 14, 19, 29}	27
"5"	{0, 4, 8, 10, 12, 15, 16}	{−29, −21, −17, −13, −9, 9, 13, 17, 21, 29}	17
"8"	{0, 4, 5, 10, 12, 15, 16}	{−29, −23, −18, −13, 13, 18, 23, 29}	25
"10"	{0, 4, 5, 8, 12, 15, 16}	{−29, −26, −25, −22, −18, −14, −6, −2, 2, 6, 14, 18, 22, 25, 26, 29}	9
"12"	{0, 4, 5, 8, 10, 15, 16}	{−29, −28, −27, −22, −17, 17, 22, 27, 28, 29}	33
"15"	{0, 4, 5, 8, 10, 12, 16}	{−29, −27, −25, −23, −19, 19, 23, 25, 27, 29}	37
"16"	{0, 4, 5, 8, 10, 12, 15}	{−29, −28, −26, −21, 21, 26, 28, 29}	41

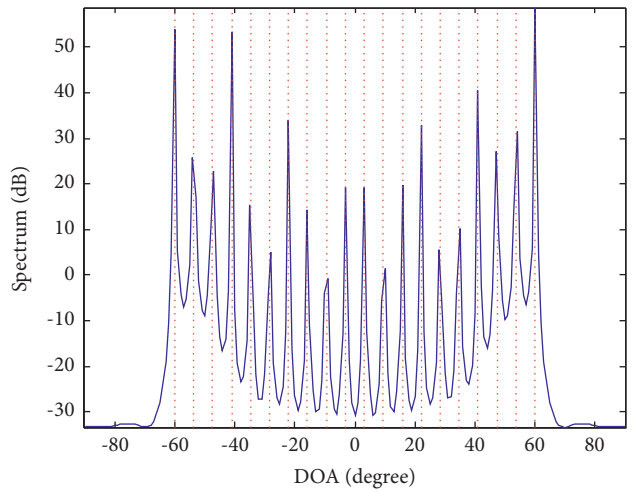

Figure 4: MUSIC spectrum with SNR = 0 dB, T_P = 300, and T_s = 400.

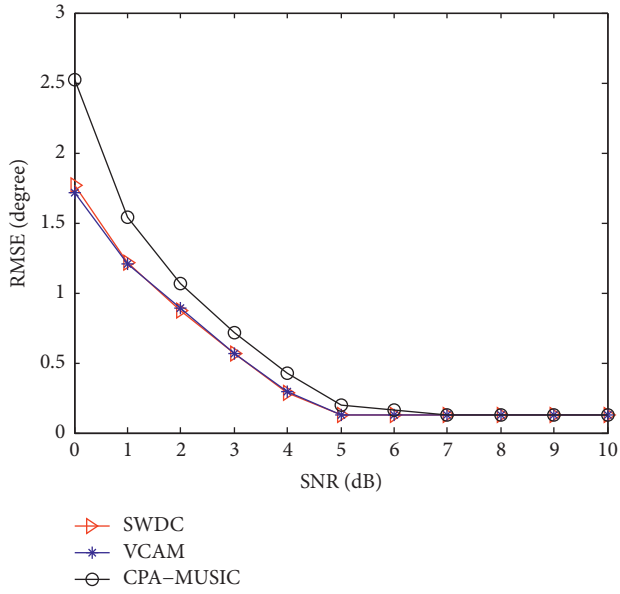

Figure 5: RMSE *versus* SNR with the number of snapshots being 600.

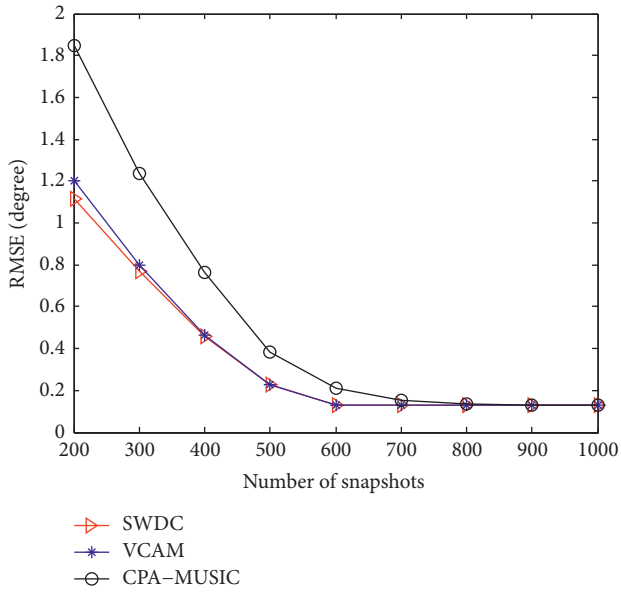

Figure 6: RMSE *versus* the number of snapshots with SNR being 5 dB.

$$\text{RMSE} = \sqrt{\frac{1}{200K}\sum_{i=1}^{200}\sum_{k=1}^{K}\left(\widehat{\theta}_{k,i} - \theta_k\right)^2}, \tag{12}$$

where $\widehat{\theta}_{k,i}$ is the estimate of θ_k for the ith Monte Carlo trial. The source distribution in this simulation is the same as that in the third simulation. The results from Figures 5 and 6 show that the DOA estimation accuracy of the proposed SWDC method is similar to that of VCAM, which is superior to the CPA-MUSIC. The reason is that the data information is not lost for the sliding window data compression processing, which implies that the proposed SWDC method and the VCAM method exploit the same data for DOA estimation, and the estimation accuracy is almost the same accordingly. By contrast, the CPA-MUSIC is performed based on DCA, where the available DOF and virtual array aperture are reduced.

6. Conclusions

In this paper, we have proposed a sliding window data compression method to reduce the computational burden of high-dimensional data processing for the spatial-time DOA estimation. By jointly using the temporal and spatial information of the impinging sources, the signal model is firstly formulated based on CPA from the perspective of

SDCA. Then, a sliding window data compression processing is applied to the array output vector. Afterwards, we resort to the VCAM approach for DOA estimation. In addition, the sparse array robustness to sensor failure has been evaluated by introducing the concept of essential sensors. Simulation results have confirmed that the proposed method can resolve more sources than twice of physical sensors and has notable performance advantages in terms of computational load and DOA estimation accuracy.

Data Availability

No data were used in this study.

Conflicts of Interest

The authors declare that there are no conflicts of interest regarding the publication of this paper.

Acknowledgments

This work was supported by the National Natural Science Foundation of China, under Grant no. 62101223, and Natural Science Foundation of the Jiangsu Higher Education Institutions of China, under Grant nos. 20KJB510027 and 20KJA510008.

References

[1] H. Krim and M. Viberg, "Two decades of array signal processing research: the parametric approach," *IEEE Signal Processing Magazine*, vol. 13, no. 4, pp. 67–94, 1996.

[2] B. Ottersten, M. Viberg, P. Stoica, and A. Nehorai, *Exact and Large Sample Maximum Likelihood Techniques for Parameter Estimation and Detection in Array Processing*, Springer, Berlin, Germany, 1993.

[3] L. Wan, M. Zhang, L. Sun, and X. Wang, "Machine learning empowered IoT for intelligent vehicle location in smart cities," *ACM Transactions on Internet Technology*, vol. 21, no. 3, pp. 1–25, 2021.

[4] J. He, L. Li, and T. Shu, "Sparse nested arrays with spatially spread orthogonal dipoles: high accuracy passive direction finding with less mutual coupling," *IEEE Transactions on Aerospace and Electronic Systems*, vol. 57, no. 4, pp. 2337–2345, 2021.

[5] Z. Zhongfu Ye, J. Jisheng Dai, X. Xu Xu, and fnm Xiaopei Wu, "DOA estimation for uniform linear array with mutual coupling," *IEEE Transactions on Aerospace and Electronic Systems*, vol. 45, no. 1, pp. 280–288, 2009.

[6] R. Cao, B. Liu, F. Gao, and X. Zhang, "A low-complex one-snapshot DOA estimation algorithm with massive ULA," *IEEE Communications Letters*, vol. 21, no. 5, pp. 1071–1074, 2017.

[7] C.-L. Liu and P. P. Vaidyanathan, "Cramér-Rao bounds for coprime and other sparse arrays, which find more sources than sensors," *Digital Signal Processing*, vol. 61, pp. 43–61, 2017.

[8] Z. Zheng, W.-Q. Wang, Y. Kong, and Y. D. Zhang, "MISC array: a new sparse array design achieving increased degrees of freedom and reduced mutual coupling effect," *IEEE Transactions on Signal Processing*, vol. 67, no. 7, pp. 1728–1741, 2019.

[9] A. M. Elbir, "Two-dimensional DOA estimation via shifted sparse arrays with higher degrees of freedom," *Circuits, Systems, and Signal Processing*, vol. 38, no. 12, pp. 5549–5575, 2019.

[10] P. Pal and P. P. Vaidyanathan, "Nested arrays: a novel approach to array processing with enhanced degrees of freedom," *IEEE Transactions on Signal Processing*, vol. 58, no. 8, pp. 4167–4181, 2010.

[11] P. P. Vaidyanathan and P. Pal, "Sparse sensing with co-prime samplers and arrays," *IEEE Transactions on Signal Processing*, vol. 59, no. 2, pp. 573–586, 2011.

[12] C.-L. Liu and P. P. Vaidyanathan, "Super nested arrays: linear sparse arrays with reduced mutual coupling-part I: Fundamentals," *IEEE Transactions on Signal Processing*, vol. 64, no. 15, pp. 3997–4012, 2016.

[13] P. Zhao, G. Hu, Z. Qu, and L. Wang, "Enhanced nested array configuration with hole-free co-array and increasing degrees of freedom for DOA estimation," *IEEE Communications Letters*, vol. 23, no. 12, pp. 2224–2228, 2019.

[14] J. Liu, Y. Zhang, Y. Lu, S. Ren, and S. Cao, "Augmented nested arrays with enhanced DOF and reduced mutual coupling," *IEEE Transactions on Signal Processing*, vol. 65, no. 21, pp. 5549–5563, 2017.

[15] S. Qin, Y. D. Zhang, and M. G. Amin, "Generalized coprime array configurations for direction-of-arrival estimation," *IEEE Transactions on Signal Processing*, vol. 63, no. 6, pp. 1377–1390, 2015.

[16] A. Raza, W. Liu, and Q. Shen, "Thinned coprime array for second-order difference co-array generation with reduced mutual coupling," *IEEE Transactions on Signal Processing*, vol. 67, no. 8, pp. 2052–2065, 2019.

[17] L. Wan, K. Liu, Y.-C. Liang, and T. Zhu, "DOA and polarization estimation for non-circular signals in 3-D millimeter wave polarized massive MIMO systems," *IEEE Transactions on Wireless Communications*, vol. 20, no. 5, pp. 3152–3167, 2021.

[18] W. Zheng, X. Zhang, Y. Wang, M. Zhou, and Q. Wu, "Extended coprime array configuration generating large-scale antenna co-array in massive MIMO system," *IEEE Transactions on Vehicular Technology*, vol. 68, no. 8, pp. 7841–7853, 2019.

[19] F. Wen, J. Shi, and Z. Zhang, "Closed-form estimation algorithm for EMVS-MIMO radar with arbitrary sensor geometry," *Signal Processing*, vol. 186, p. 108117, 2021.

[20] X. Wang, X. Wang, and X. Lin, "Co-prime array processing with sum and difference co-array," *" in 2015 49th Asilomar Conference on Signals, Systems and Computers*, pp. 380–384, 2015.

[21] X. Wang, Z. Chen, S. Ren, and S. Cao, "DOA estimation based on the difference and sum coarray for coprime arrays," *Digital Signal Processing*, vol. 69, pp. 22–31, 2017.

[22] W. Si, Z. Peng, C. Hou, and F. Zeng, "Improved nested arrays with sum-difference coarray for DOA estimation," *IEEE Sensors Journal*, vol. 19, no. 16, pp. 6986–6997, 2019.

[23] P. Zhao, K. Wang, G. Hu, and L. Wan, "Underdetermined DOA estimation using unfold coprime array from the perspective of sum-difference co-array," *IEEE Access*, vol. 7, pp. 168557–168564, 2019.

[24] A. Alexiou and A. Manikas, "Investigation of array robustness to sensor failure," *Journal of the Franklin Institute*, vol. 342, no. 3, pp. 255–272, 2005.

[25] C.-L. Liu and P. P. Vaidyanathan, "Robustness of difference coarrays of sparse arrays to sensor failures-Part I: a theory

motivated by coarray MUSIC," *IEEE Transactions on Signal Processing*, vol. 67, no. 12, pp. 3213–3226, 2019.

[26] C.-L. Liu and P. P. Vaidyanathan, "Robustness of difference coarrays of sparse arrays to sensor failures-Part II: array geometries," *IEEE Transactions on Signal Processing*, vol. 67, no. 12, pp. 3227–3242, 2019.

Hindawi
International Journal of Antennas and Propagation
Volume 2024, Article ID 9784903, 1 page
https://doi.org/10.1155/2024/9784903

Retraction

Retracted: A Motion Image Pose Contour Extraction Method Based on B-Spline Wavelet

International Journal of Antennas and Propagation

Received 23 January 2024; Accepted 23 January 2024; Published 24 January 2024

This article has been retracted by Hindawi following an investigation undertaken by the publisher [1]. This investigation has uncovered evidence of one or more of the following indicators of systematic manipulation of the publication process:

(1) Discrepancies in scope
(2) Discrepancies in the description of the research reported
(3) Discrepancies between the availability of data and the research described
(4) Inappropriate citations
(5) Incoherent, meaningless and/or irrelevant content included in the article
(6) Manipulated or compromised peer review

The presence of these indicators undermines our confidence in the integrity of the article's content and we cannot, therefore, vouch for its reliability. Please note that this notice is intended solely to alert readers that the content of this article is unreliable. We have not investigated whether authors were aware of or involved in the systematic manipulation of the publication process.

In addition, our investigation has also shown that one or more of the following human-subject reporting requirements has not been met in this article: ethical approval by an Institutional Review Board (IRB) committee or equivalent, patient/participant consent to participate, and/or agreement to publish patient/participant details (where relevant).

Wiley and Hindawi regrets that the usual quality checks did not identify these issues before publication and have since put additional measures in place to safeguard research integrity.

We wish to credit our own Research Integrity and Research Publishing teams and anonymous and named external researchers and research integrity experts for contributing to this investigation.

The corresponding author, as the representative of all authors, has been given the opportunity to register their agreement or disagreement to this retraction. We have kept a record of any response received.

References

[1] Chen chen and D. Bi, "A Motion Image Pose Contour Extraction Method Based on B-Spline Wavelet," *International Journal of Antennas and Propagation*, vol. 2021, Article ID 4553143, 8 pages, 2021.

Hindawi
International Journal of Antennas and Propagation
Volume 2021, Article ID 4553143, 8 pages
https://doi.org/10.1155/2021/4553143

Research Article

A Motion Image Pose Contour Extraction Method Based on B-Spline Wavelet

Chen chen[1] and Daohui Bi[1,2]

[1]*Physical Culture Institute, Henan University of Technology, Zhengzhou 450001, China*
[2]*Journal Editorial Department, Henan University of Technology, Zhengzhou 450001, China*

Correspondence should be addressed to Daohui Bi; 2016122370@jou.edu.cn

Received 19 August 2021; Revised 8 October 2021; Accepted 12 October 2021; Published 26 October 2021

Academic Editor: Fangqing Wen

In order to improve the accuracy of traditional motion image pose contour extraction and shorten the extraction time, a motion image pose contour extraction method based on B-spline wavelet is proposed. Moving images are acquired through the visual system, the information fusion process is used to perform statistical analysis on the images containing motion information, the location of the motion area is determined, convolutional neural network technology is used to preprocess the initial motion image pose contour, and B-spline wavelet theory is used. The preprocessed motion image pose contour is detected, combined with the heuristic search method to obtain the pose contour points, and the motion image pose contour extraction is completed. The simulation results show that the proposed method has higher accuracy and shorter extraction time in extracting motion image pose contours.

1. Introduction

Sports image pose contour extraction refers to the process of finding the required contours of sports targets in all frame images in a certain video sequence [1]. With the increasing requirements for the accuracy of image information in related fields, the maturity of the target contour extraction technology has been further enhanced. With the rapid development of science and technology today, sports image pose contour extraction technology is an important research content in the field of computer vision and artificial intelligence. This technology has an important role in many fields, such as medicine, transportation, and military [2]. At present, people's lives are inseparable from portable communication devices with camera functions. These devices produce a large amount of video information every day. These videos are processed through image pose contour extraction methods to extract valuable information and improve work efficiency in various fields. In sports images, the most basic feature is the edge. The edge is the junction of the image area and the attribute area and is the place where the image information is most concentrated. The extraction of sports image pose contours is a prerequisite for realizing sports target detection, and it is also an important content in the field of digital image processing. Only by accurately extracting pose contour features can it be used for subsequent sports target recognition, motion trajectory tracking, sports target behavior, and so on. The work lays a theoretical foundation. Therefore, extracting the contours of sports images has more research value and challenge [3].

Literature [4] proposes a method for extracting pose contours of nonrigid human motion images. First, preprocessing of the scale-invariant feature transform (SIFT) is removed in the human motion image sequence, the human body feature extraction map is obtained, and a sequence probabilistic graph model continuity of feature sequence extraction is designed. Second, the human body appearance model is constructed. Based on the appearance model, the contour line of the current human motion frame is extracted by the high-precision contour extraction method of sequence images. The experimental results show that this method can extract continuous feature sequences, and the extracted human pose contours are more accurate and have higher efficiency and robustness. However, the extraction of

the posture contour of the human motion image in the above method takes a long time, resulting in low extraction efficiency. Literature [5] proposed a method for extracting the correct posture contour of a motion image. The correct posture area of the motion image was extracted by the adjacent frame difference method. On this basis, the snake model method was introduced, which extracts the correct posture contour of the motion image. The problem is converted to the minimization of the energy function. The level set method is analyzed, and the evolution curve is implicitly described as the zero level set of the three-dimensional continuous function surface on the motion image. When the level set function is 0, the result is contour extraction result. Through experiments comparing the effectiveness of the two proposed methods, it is found that the contour extraction effect, completeness, and information loss of the snake model method are better than other methods but inferior to the level set method. Literature [6] proposed an image-based secondary feature extraction method for abnormal gait. According to the pressure change value of the sole of the foot under different postures, a feature extraction of the abnormal gait image was completed. The feature variable data are used to construct the gait energy map of the walking contour of the target individual. At the same time, combined with the KPCA kernel method, the gait contour data after the primary feature extraction are processed for dimensionality reduction, and the secondary feature extraction of the abnormal gait is completed. The simulation results show that, under normal gait and abnormal gait, the proposed method can effectively extract the abnormal gait of the image and has a high feature extraction effect, indicating that the proposed method has strong practicability. However, the motion image pose contour extraction accuracy of the above two methods is low, resulting in unsatisfactory extraction results. The spline curve is commonly used for describing the contour of the target object in the field of image-based visual servo (IBVS). However, this method has the disadvantage of low sensitivity and poor precision when facing the camera's rotational motions. To solve this problem, literature [7] presented a visual servo system with rotational pose compensation. Literature [8] presented a multipose human detection system based on unmanned aerial vehicle (UAV) imageries in real-time. A satisfying detection accuracy of multipose human detection in complex outdoor environments can be achieved with no accelerating hardware like graphics processing unit.

Aiming at the problems of the above methods, this paper proposes a B-spline wavelet-based sports image pose contour extraction method, and the effectiveness and practicability of this method are verified through simulation experiments, which solve the problems of traditional methods and lay a foundation for sports career base.

2. Sports Image Acquisition

Aiming at the problem of the poor accuracy of image pose contour extraction in the original image pose contour extraction method, this design is carried out. In order to ensure the accuracy of the extraction results, firstly the acquisition of sports images is completed. Setting the posture of the sports image as the directional feature of the image can well reflect the edge state of the image. The direction vector is one of the important characteristics of the image [9].

In the process of acquiring sports images, the visual system is used to perceive the direction information in the sports images. In the process of acquiring sports image poses, four sets of Gabor filters with different directions of light are used to extract the direction information in the pictures. The filter function is set in the filter as a Gaussian function modulated by a sine function, which has a certain direction selectivity and spatial connectivity [10]. The filter function can be embodied by the following formula:

$$\begin{aligned} \overline{x} &= x \cos \alpha + y \sin \alpha, \\ \overline{y} &= -x \sin \alpha + y \cos \alpha. \end{aligned} \tag{1}$$

In the above formula, $\overline{x}$ and $\overline{y}$, respectively, represent the weighted average of sports image coordinate points x and y and α represents the direction of the filter. In the extraction of sports image pose contours, n is set to 4; that is, there are 4 directions in the image, and the values are, respectively, 0°, 60°, 120°, and 180°. Based on the characteristics of the filter, the extracted direction vector is the direction information perpendicular to the current filter direction in the image [11]. The direction vector of the sports image is set as the center-peripheral operator, and then the Gaussian pyramid is used to perform multiangle transformation on the image's posture direction vector feature. The multiscale angle feature difference information $\delta(A, B, \alpha)$ can be expressed as follows:

$$\delta(A, B, \alpha) = |\overline{x}(A \cdot B \cdot \alpha) - \overline{y}(B \cdot \alpha)|. \tag{2}$$

In the above formula, A and B, respectively, represent the characteristic difference value, and its value is the same [12]. Through the above formula, sports images can be obtained and used as the data basis for contour extraction.

3. Analysis and Preprocessing of Initial Sports Image Pose Contour

3.1. Analysis of Initial Sports Image Pose Contour. If you want to achieve the extraction of sports image posture contours, first the initial sports image posture contours are analyzed based on the sports image acquisition, the position of the sports area is determined, and the initial sports image posture contours are preprocessed [13]. Under normal circumstances, the location of the region segmented by the sports detection process contains the position information of the target in the previous frame and also contains the shape of the current frame, and the result of the sports segmentation indicates the current image position of the target. Therefore, the image difference method based on the statistical model is used to complete the sports segmentation. In the process of assuming that the target is moving, the camera equipment is still, the image noises of the two frames before and after are not correlated, and the mixed noise of the lens and the environment obeys the Gaussian

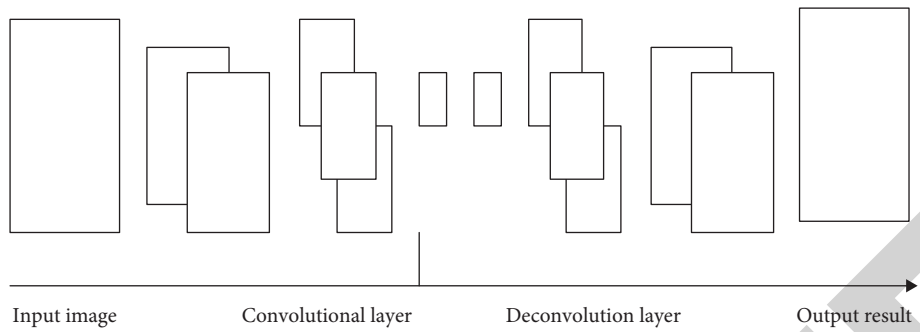

Figure 1: Model building process.

distribution of $\sigma^2/2$, and $D(k)$ is assumed to be the difference image of the two frames before and after. Among them, k represents a random pixel in the image. If $D(k)$ is accumulated in the field $w(k)$, σ is used for normalization processing. The specific structure is as follows:

$$\Delta^2(k) = \sum_{i \in w(k)} \left(\frac{D(k)}{\sigma} \right)^2. \tag{3}$$

Assuming that none of the pixels in $w(k)$ are moving, then the normalized difference $D(k)/\sigma$ of all pixels in this window will all obey the $N(0,1)$ distribution, then the difference sub and Δ^2 needs to obey the x_m^2 distribution, and the degree of freedom m represents w number of pixels in the middle. In this way, the probability distribution $p(\Delta^2|H_0)$ can be obtained, in which H_0 represents that the pixel position has no movement [14].

An appropriate small confidence level $10^{-6} \le a < 10^{-2}$ is chosen, and the corresponding threshold l_a according to the X^2 distribution table is obtained, so that $a = p(\Delta^2 > l_a|H_0)$ can be considered that $\Delta^2 > l_a$ pixels are relative motion [15].

Through the above statistical process, the position of the sports area of the sports image is obtained, and the initial sports image posture contour analysis is completed. Morphological processing is performed on it, noise is removed, and this is used as the contour data of the initial sports image.

3.2. Convolutional Neural Processing. Through the above settings, the initial sports image posture contour is analyzed, and the convolutional neural network technology is used to complete the preprocessing of the initial sports image posture contour. The pixel processing of the acquired sports image is expanded, the image feature size is reduced and restored layer by layer, and the deconvolution layer is used to obtain the human contour feature map of the image [16]. The operation process is displayed as shown in Figure 1.

The convolutional layer and the pooling layer are combined to extract the posture features of the sports image. The fully connected layer and the Softmax layer complete the extraction of global features and the classification output. In order to ensure the effectiveness of the image model acquisition, the largest pooling form in the VGG16 grid pooling is selected, as shown in Figure 2. The pooling window is set to the size of $4 * 4$, and the moving step is set to 4.

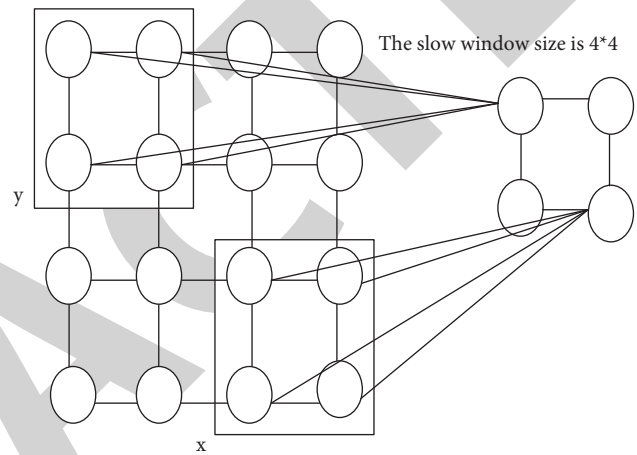

Figure 2: Schematic diagram of maximum pooling.

The sports image processed by the maximum pooling network is transformed into a one-dimensional feature vector after multiple connection layers, and the Softmax layer is used to complete the category processing, and then the posture in the sports image is obtained. The image information obtained by using the convolution network is not accurate enough. In this design, a deconvolution process is added, and the process is realized by bilinear interpolation by merging the multistage output results of the neural network. The corresponding feature points of the image contour acquired for the first time are set, and its pixel value is obtained, and the interpolation method is used to obtain the pixel value of the middle point of the image. The above pixel values are used to fill the pooled graphics to the original image size [17].

Through the above settings, the magnified image quality is improved, and the problem of missing pixel values due to convolutional neural processing is avoided. This setting has its own filter attribute, which can reduce the occurrence of unclear image posture contours and improve the detection accuracy of post-processing motion image pose contours.

4. Pose Contour Detection of Sports Images Based on B-Spline Wavelet

Through the preprocessed initial sports image posture contour obtained above, B-spline wavelet theory is used to detect it. The wavelet transform of the known signal $f(X)$ at any scale S and direction X is defined as follows:

$$W_S f(X) = f * \psi_S(x) = \int f(t)\psi_S(x-t)\mathrm{d}t. \quad (4)$$

In the formula, $\psi_S(x)$ is the expansion of the mother wavelet $\psi(x)$ on the scale factor S, which is called the wavelet function. The wavelet function $\psi(x)$ is used as the first and second derivatives of the smoothing function $\theta(x)$:

$$\psi(x) = \frac{\mathrm{d}\theta(x)}{\mathrm{d}x}. \quad (5)$$

When using the maximum point edge detection method (canny), the wavelet transform multiscale edge detection is actually convolution smoothing the image surface with a smooth function $\theta(x)$ expansion, and then the canny edge detection method is used. Generally speaking, the extreme point detection is more advantageous than the zero-crossing detection because the zero-crossing detection is more susceptible to noise interference, and sometimes the zero-crossing response is not the sudden change point but the turning point of the signal in the slow-changing interval.

Taking $\beta_{2^{-1}}^{n+1}(x)$ as the smoothing function $\theta(x)$, corresponding to the local extremum detection, the Fourier transform is as follows:

$$\psi^n(w) = iw\left(\sin c\frac{w}{4}\right)^{n+2}. \quad (6)$$

According to the derivative properties of convolution,

$$\frac{\mathrm{d}}{\mathrm{d}x}\beta^{n+1}(x) = \beta^n * \frac{\mathrm{d}}{\mathrm{d}x}\beta^0(x). \quad (7)$$

The cubic spline is used as the smoothing function $\theta(x)$ to obtain a discrete algorithm for efficient multiscale edge detection. Using cubic spline function as smoothing function and its first derivative as wavelet function, then cubic spline $\beta^3(x)$ is as follows:

$$\beta^3(x) = \begin{cases} \dfrac{(x+2)^3}{6}, & x \in [-2,-1], \\ \dfrac{-x^3}{2} - x^2 + \dfrac{2}{3}, & x \in [-1,0], \\ \dfrac{-x^3}{2} - x^2 + \dfrac{2}{3}, & x \in [0,1), \\ \dfrac{(2-x)^3}{6}, & x \in [1,2). \end{cases} \quad (8)$$

According to the determination of the cubic spline coefficients, the sports image is adjusted through a smoothing filter to adjust the parameters, through the convolution with the appropriate horizontal and vertical templates to complete the estimation of the sampling value in the image gradient direction, and then the gradient for the modulus maximum in the direction is determined, and all local nonmaximum points in the gradient direction are set to zero to realize the detection of the sports image pose contour. The expression is as follows:

$$U(x,y) = \sum f(i,j)\beta_k(x-i)\beta_l(y-j). \quad (9)$$

5. Sports Image Pose Contour Extraction

According to the detection result of the abovementioned sports image posture contour, the image posture contour is extracted. According to the highest gradient contour point obtained in the search process, it is the contour line of the first frame of the sports image pose, and other contour lines are obtained by the heuristic search method. The specific process is as follows:

(1) Calculate the normal line of the contour point: The contour line of the sports action is set as shown in Figure 3.

Assuming that the target contour point is $p(x,y)$, the specific relation formula of the normal line of the contour point is as follows:

$$\begin{cases} x = S\cos\theta + x_0, \\ y = S\cos\theta + y_0. \end{cases} \quad (10)$$

Setting θ to represent the inclination angle of the straight line and the length from the point to $p(x,y)$ is S, then the normal vector of the contour point is shown in Figure 4.

It can be seen from Figure 4 that the normal vector 1 of straight line AB and the normal vector 2 of BC are first obtained. According to the addition and subtraction of vectors, the sum of vectors 1 and 2 can be obtained, which is the normal vector of B.

(2) Gradient threshold: The normals of points A, B, and C are calculated. Through the method shown in Figure 5, first look for 15 points along the upper and lower parts of each line and calculate the gradient value. Then, the gradient statistical histogram is used to calculate the gradient value.

(3) Determine the outline point of the current frame: First, Fourier transform on the first image is performed, and the Gaussian low-pass filtering method is used to reduce noise on the previous image. In the first image, a certain point is searched in the outer normal to calculate the gradient threshold. A search is performed on the points in the normal direction, the first point is stored higher than the gradient value, and it is treated as a new contour point in the immediate frame, so that the posture contour of the sports image can be obtained.

6. Simulation Experiment Analysis

In the process of this research, the design work of sports image pose contour extraction method based on B-spline wavelet was completed. In order to ensure the effectiveness of the method design in this paper, the Matlab simulation tool was used to operate in VS2010+OpenCV2.4.13, Windows10 System Intel(R) Xeon(R) CPU E5-2603v4@2.20 GHz, memory is 32 GB, and resolution is

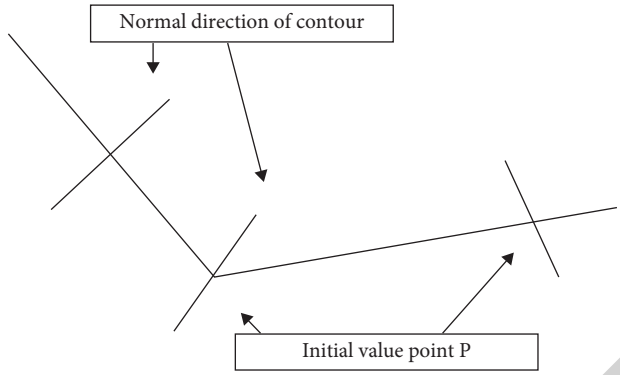

Figure 3: Contour of the target part.

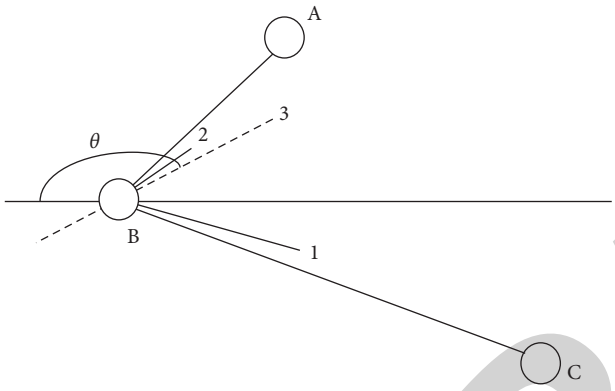

Figure 4: Normal vector of contour points.

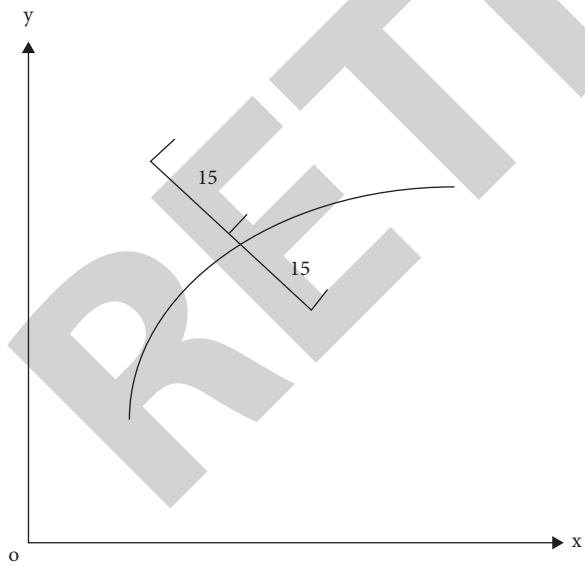

Figure 5: Search 15 points up and down in the direction of the normal.

800 ∗ 600 in an environment, using comparative experiments to complete the comparison between the method in this article and the traditional method, so as to obtain the method difference.

In this experiment, a simulation experiment was used to complete the experiment. The data used in the experiment came from the Baidu gallery, and some sports pictures totaling 10,000. Unqualified images are eliminated, 1,000 images are selected as the training set for this experiment, and the image format is set in the database to 400 ∗ 400. The 1000 images are randomly divided into 5 groups of test data, and the specific settings are shown in Table 1.

The above sample settings are used as the data basis for this experiment, and aerobics action images are selected from the Baidu gallery as the experimental samples. The original images are shown in Figure 6.

The original aerobics action image in Figure 6 is denoised, and the output result is shown in Figure 7.

Using the B-spline wavelet-based sports image pose contour extraction method proposed in this paper, the nonrigid human motion image pose contour extraction method proposed in literature [4], and the correct pose contour extraction method of sports motion image proposed in literature [5], the posture contour extraction is performed on the image samples, respectively, to verify the accuracy of the sports image posture contour extraction of the three methods. The comparison results are shown in Table 2.

According to the comparison results in Table 2, it can be seen that the sports image pose contour extraction method based on the B-spline wavelet proposed in this paper has a maximum accuracy of 98.9%, rather than rigid body movement [4]. The sports image pose contour extraction accuracy of the motion image pose contour extraction method is only 89.3%, and the sports image pose contour extraction accuracy of the motion image correct pose contour extraction method proposed in [5] is only 74.6%. The proposed method is a motion image pose contour extraction method based on B-spline wavelet, which is better than the non-rigid human motion image pose contour extraction method proposed in [4] and the motion motion image proposed in [4]. The contour extraction method is more accurate.

In order to further verify the effectiveness of the method in this paper, the B-spline wavelet-based sports image pose contour extraction method proposed in this paper, the

Table 1: Experimental data sample settings.

Experiment sample number	Number of samples	Sample format
S1	250	.jpg
S2	150	.jpg
S3	200	.jpg
S4	270	.jpg
S5	130	.jpg

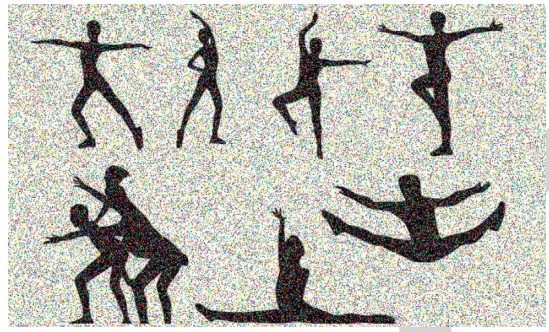

Figure 6: Original image.

Figure 7: Denoising output image of aerobics action image.

Table 2: Comparison results of the three methods of sports image pose contour extraction accuracy.

Number of experiments	Literature [4] method (%)	Literature [5] method (%)	Literature [7] method (%)	Literature [8] method (%)	Method of this article (%)
10	82.3	71.7	61.6	84.8	93.6
20	82.1	70	60	80	92.4
30	84.5	70.4	60.4	80.4	92.8
40	84.9	71.9	61.1	84.9	92.6
50	85.9	70.1	60.1	80.4	92.5
60	88.4	72.5	64.3	82.5	94.1
70	81.1	73.2	63.4	83.2	93.5
80	81.8	74.6	64.7	84.5	95.8
90	89.3	72.6	64.2	82.9	96.4
100	88	73.4	63.4	83.4	98.9

nonrigid human motion image pose contour extraction method proposed in document [4], and the method proposed in document [5], the correct posture contour extraction method of the sports action image compares the extraction time of the posture contour of the sports image. The comparison result is shown in Figure 8.

According to Figure 8, this paper proposes a motion image pose contour extraction method based on B-spline wavelet, the sports image pose contour extraction time is within 30 s, the document [4] proposed the nonrigid human motion image pose contour extraction method, and Reference [5] proposed the correct posture contour extraction

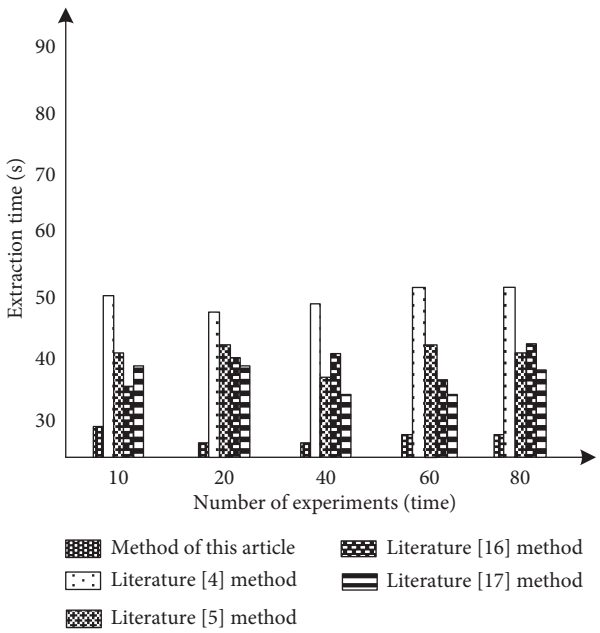

Figure 8: Comparison results of sports image posture contour extraction time.

method of the sports image. The extraction time of the sports image pose contour is within 55 s and 40 s. The sports image pose based on the B-spline wavelet-based sports image pose contour extraction method is proposed in this paper. The contour extraction time is shorter than that of the literature method.

7. Conclusion

In the conventional sports image detection process, the target contour feature extraction is a very complicated process, and it is necessary to study a method that is convenient for calculation. For this reason, this paper proposes a B-spline wavelet-based sports image pose contour extraction method, through B-spline wavelet theory detects the posture contours of sports images, calculates the normals of the contour points, obtains the posture contours of the sports images, and completes the image posture contour extraction. The simulation results show that the proposed method of sports image pose contour extraction effect is better, and the extraction efficiency is higher. However, with the rapid development of deep learning today, there may still be some gap between our method and deep learning method in performance. Therefore, in the future work, we need to try to integrate deep learning methods for modeling.

Data Availability

The data used to support the findings of this study are available from the corresponding author upon request.

Conflicts of Interest

The authors declare that they have no conflicts of interest.

References

[1] X. Yu, Y. Chu, F. Jiang, Y. Guo, and D. Gong, "SVMs classification based two-side cross domain collaborative filtering by inferring intrinsic user and item features," *Knowledge-Based Systems*, vol. 141, pp. 80–91, 2018.

[2] C. W. Peng and Z. Yang, "Image feature extraction and object recognition based on vision neural mechanism," *International Journal of Pattern Recognition and Artificial Intelligence*, vol. 34, no. 06, pp. 3340–3342, 2020.

[3] S. Yamakawa and K. Shimada, "Feature edge extraction via angle-based edge-collapsing and recovery," *Journal of Computing & Information Science in Engineering*, vol. 18, no. 2, pp. 021001.1–021001.18, 2018.

[4] X. Leng and H. Jiang, "An algorithm for extracting pose contours from non-rigid human motion images," *Journal of Jilin University: Science Edition*, vol. 56, no. 06, pp. 1453–1460, 2018.

[5] W. Fatau, L. Ding, H. Yu, and Y. Zhao, "Big data analytics on enterprise credit risk evaluation of e-Business platform," *Information Systems and e-Business Management*, vol. 18, pp. 311–350, 2020.

[6] X. Jiang and H. Zhan, "Simulation of secondary feature extraction algorithm for abnormal gait based on image," *Computer Simulation*, vol. 037, no. 003, pp. 381–384, 2020.

[7] Y. Zhang, N. Wang, H. Wang, X. Lu, Z. Zhang, and C. Sheng, "Curve control points-based feature extraction for visual servo with rotational pose compensation," *Proceedings of the 2020 Chinese Control And Decision Conference (CCDC)*, IEEE, pp. 450–454, August 2020.

[8] Q. Wu and Y. Zhou, "Multi-pose moving human detection based on unmanned aerial vehicle in real-time," in *Proceedings of the 2019 14th IEEE Conference on Industrial Electronics and Applications (ICIEA)*, pp. 608–613, IEEE, Xian, China, June 2019.

[9] Q. Nie, Y. B. Zou, and C. W. Lin, "Feature extraction for medical CT images of sports tear injury," *Mobile Networks and Applications*, no. 3, pp. 1–11, 2020.

[10] X. Ni, H. Liu, Z. Ma, C. Wang, and J. Liu, "Detection for rail surface defects via partitioned edge feature," *IEEE Transactions on Intelligent Transportation Systems*, vol. 5, no. 99, pp. 1–17, 2021.

[11] M. Koeshardianto, E. M. Yuniarno, and M. Hariadi, "Automatic matting using edge feature-based scribbles," *IAENG Internaitonal Journal of Computer Science*, vol. 46, no. 3, pp. 459–466, 2019.

[12] V. B. S. Prasath, R. Pelapur, G. Seetharaman, and K. Palaniappan, "Multiscale structure tensor for improved feature extraction and image regularization," *IEEE Transactions on Image Processing*, vol. 28, no. 12, pp. 6198–6210, 2019.

[13] Q. Guo, M. He, and L. An, "High-resolution remote-sensing image registration based on angle matching of edge point features," *IEEE Journal of Selected Topics in Applied Earth Observations and Remote Sensing*, vol. 6, pp. 1–15, 2018.

[14] F. Yousefiyan, H. Ebadi, and A. Sedaghat, "Shadow extraction of building using fusion of edge and point feature orientation from high resolution satellite imagery," *Journal of Geospatial Information Technology*, vol. 6, no. 3, pp. 123–145, 2018.

[15] J. Tang, Y. Wang, Y. Wang, C. Huang, H. Liu, and N. Al-Nabhan, "Image edge detection based on singular value feature vector and gradient operator," *Mathematical Biosciences and Engineering*, vol. 17, no. 4, pp. 3721–3735, 2020.

[16] F. Hang, G. Sun, J. Zabalza, A. Zhang, J. Ren, and X. Jia, "A novel spectral-spatial singular spectrum analysis technique for

Hindawi
International Journal of Antennas and Propagation
Volume 2023, Article ID 9840409, 1 page
https://doi.org/10.1155/2023/9840409

Retraction

Retracted: HR Management Big Data Mining Based on Computational Intelligence and Deep Learning

International Journal of Antennas and Propagation

Received 15 August 2023; Accepted 15 August 2023; Published 16 August 2023

This article has been retracted by Hindawi following an investigation undertaken by the publisher [1]. This investigation has uncovered evidence of one or more of the following indicators of systematic manipulation of the publication process:

(1) Discrepancies in scope

(2) Discrepancies in the description of the research reported

(3) Discrepancies between the availability of data and the research described

(4) Inappropriate citations

(5) Incoherent, meaningless and/or irrelevant content included in the article

(6) Peer-review manipulation

The presence of these indicators undermines our confidence in the integrity of the article's content and we cannot, therefore, vouch for its reliability. Please note that this notice is intended solely to alert readers that the content of this article is unreliable. We have not investigated whether authors were aware of or involved in the systematic manipulation of the publication process.

Wiley and Hindawi regrets that the usual quality checks did not identify these issues before publication and have since put additional measures in place to safeguard research integrity.

We wish to credit our own Research Integrity and Research Publishing teams and anonymous and named external researchers and research integrity experts for contributing to this investigation.

The corresponding author, as the representative of all authors, has been given the opportunity to register their agreement or disagreement to this retraction. We have kept a record of any response received.

References

[1] G. Zhao and Z. Xue, "HR Management Big Data Mining Based on Computational Intelligence and Deep Learning," *International Journal of Antennas and Propagation*, vol. 2021, Article ID 1657236, 13 pages, 2021.

Hindawi
International Journal of Antennas and Propagation
Volume 2021, Article ID 1657236, 13 pages
https://doi.org/10.1155/2021/1657236

Research Article

HR Management Big Data Mining Based on Computational Intelligence and Deep Learning

Genliang Zhao[1] **and Zhe Xue**[2]

[1]*School of International Business and Tourism, Anhui Business College, Wuhu 241002, Anhui, China*
[2]*The Greater Bay Area Huizhou Development Research Institute, Huizhou University, Huizhou 516007, Guangdong, China*

Correspondence should be addressed to Genliang Zhao; zhaogenliang528@abc.edu.cn

Received 17 August 2021; Accepted 28 September 2021; Published 23 October 2021

Academic Editor: Fangqing Wen

Decomposing the structure of a large number of existing posts through data mining will greatly improve the effect of enterprise human resource structure optimization. To this end, this paper proposes an end-to-end competency-aware job requirement generation framework to automate the job requirement generation, and the prediction based on competency themes can realize the skill prediction in job requirements. Then an encoder-decoder LSTM is proposed to implement job requirement generation, and a competency-aware attention mechanism and a replication mechanism are proposed to guide the generation process to ensure that the generated job requirement descriptions comprehensively cover the relevant and representative competency and job skill requirements. A competency-aware strategy gradient training algorithm is then proposed to further enhance the rationality of the generated job requirement descriptions. Finally, extensive experiments on real-world HR data sets clearly validate the effectiveness and interpretability of the proposed framework and its variants compared to state-of-the-art benchmarks.

1. Introduction

In order to achieve long-term development, enterprises need to put the advantages of HRs to better use. The modern human capital theory consensus points out that the most valuable asset of an enterprise and the trump card that can win long-term profit in the competitive market and gain maximum benefit for the enterprise is human capital [1]. If an enterprise wants to achieve long-term sustainable development and formulate a more permanent development strategy, it must take precise and detailed HR planning as the first priority, and especially in the current situation of rising human resource costs, only the accurate deployment of human resource costs in advance can reduce costs [2]. Only by making the HR cost planning precise and detailed in advance can, we reduce the cost of manpower and shift to a more efficient cost allocation model [3].

Even if the labor productivity of the best employees in the same position is much higher than that of the average or poor employees, the best employees in the same position should not be taken as the standard for staffing [4]. Only by systematically screening and judging the skills, experience, and level of different employees as well as the needs of the position can we find the most suitable employees for the position so as to achieve the best overall organizational effectiveness [5, 6]. However, it is worth noting that the process of HR allocation is not a simple selection process but only relies on scientific methods to achieve the best results of the system.

In the use of HR computing intelligence, enterprises are able to access all the contents that are closely related to HR [7]. The relevant data and information on the practical application, on the one hand, and easy to grasp specific information of enterprise development, on the other hand, can provide a reference for the enterprise to make the corresponding management decisions. When data mining technology is applied to HR management, the main content can be divided into three categories: The first category is real-time data. This type of data is mainly reflected in the personnel roster, including individual and organizational levels, where the individual level contains the number of personnel, personnel structure, work experience, age structure, education structure, skills and specialties, certification structure, and family background [8]. The organization level contains

six modules, including HR management, HR strategy management, payroll, and performance management. The second category is dynamic data. This part of data is usually reflected in data reports, such as labor cost tables, and so on [9]. In the management of such data, statistical calculations and tracking records are required. The third category is integrated data. It mainly refers to the information in the form of designed questionnaires and so on and after integration and analysis, such as employee satisfaction.

There are a limited number of personnel at different levels, and too many or too few will affect the stable operation of the company [10, 11]. Therefore, the ratio of supervisors to employees should be kept within a reasonable range. At the same time, in HR management, different management methods are implemented for a given number of employees, and there are differences in the management effect. At the same time, the same management style for different quality and able employees will also make a difference in management efficiency. Therefore, it is crucial for enterprises to adopt scientific and effective management methods according to different information in HR management, while using traditional management methods, it is difficult to realize the use and effective mastering of corresponding information care. In contrast, the management with the assistance of data mining technology in the new era can improve the effect of carrying out the relevant work [12]. For example, if a company controls the proportion of employees who are responsible for the corresponding functions, by analyzing information such as the work capacity of the personnel concerned and the number of people served, it is possible to quickly determine whether the staffing should be increased, maintained, or reduced and improve the rational use of HR [13].

Further, this paper proposes an end-to-end competency-aware neural job requirement generation framework to automate the generation of job requirements, and the prediction based on competency themes enables the prediction of skill words in job requirements. A neural theme model is first designed to explore various competency and skill-related information from real-world HR data. Then an encoder-decoder recurrent neural network is proposed to implement job requirement generation, and a competency-aware attention mechanism and a replication mechanism are proposed to guide the generation process to ensure that the generated job requirement descriptions comprehensively cover the relevant and representative competencies and skill requirements of the job. A competency-aware strategy gradient training algorithm is then proposed to further enhance the rationality of the generated job requirement descriptions. Finally, extensive experiments on real-world HR data sets clearly validate the effectiveness and interpretability of the proposed framework and its variants compared to state-of-the-art benchmarks. Thus, the proposed framework can be effectively applied to talent attraction scenarios in HR services.

2. Related Work

Following the commonly used definition, computational intelligence refers to the nontrivial process of identifying novel, potentially useful, and valid patterns in data [9, 14]. During this period, there is a wide range of data mining application areas and corresponding research fields, which also include the field of business management, as well as well-established subfields such as customer management, manufacturing management, or financial management [14].

Recently, these enterprise application domains seem to be complemented by HRM. In the last few years, an increasing number of research contributions aim to support the practical adoption of data mining in HRM. Contributions are various activities and processes of HRM, such as selecting employees or predicting employee turnover [15], to determine the competencies of employees in development, or predicting and evaluating employee performance in performance management [16–18]. To provide these functions, a whole range of data mining methods such as classification trees [19], clustering [20], association analysis [21], support vector machines [22], or neural networks [12, 23] are used, while system improvements and customizations [24] are also presented. In short, browsing the literature gives the impression of a flourishing new field of data mining research that fits the specific requirements of the HR field and is therefore very useful for HR practice.

However, the large number of relevant contributions and different results complicate the overview of the current state of research. Therefore, this thesis aims to design a rational architecture for HRM to be effectively applied to talent attraction scenarios in HR services.

3. Data-Mining-Based Multifactor HR Requirements

3.1. Data Mining. Data mining is also the effective use of all mathematical algorithms to discover potential patterns from the resulting information. Therefore, it can also be said that the process of finding out the inner laws of the company's HR needs and other influencing elements that interact with each other is to make demand forecasts for the process of data mining in the context of both internal and external effects of the company [25].

Machine learning uses statistics to uncover general patterns that exist in various types of input data and builds training models based on them to predict new input outcomes. For example, support vector machines are based on statistical learning theory, which can reduce structural risk and have the advantages of being theoretically adequate and easy to operate [26].

Initially, support vector machines were proposed in the context of data classification, but the role of kernel functions and support vectors in support vector machines led to the extension of the problem to the field of regression analysis, giving birth to the problem of vector regression machines, also known as support vector regression. The minimum deviation of all sampling points can be obtained in the sample space, and thus, the effect of nonlinear regression in the original space can be derived. The SVR-based features can explore the outstanding performance in the sample data, so it is very useful for enterprises to predict HRs.

The equation defining the regression function is as follows:

$$f(x) = w \times \phi(x) + b. \tag{1}$$

In the high-dimensional eigenspace, the SVR represents the input quantity better by means of the kernel function, while the penalty coefficient C and the relaxation variable ε are introduced together to optimize the daily function as follows:

$$\min \frac{1}{2}\|\omega\|^2 + C\sum\left(\xi_i + \xi_j^+\right). \tag{2}$$

The calculation of the extremal point is achieved mainly by means of the Lagrangian function.

3.2. Variable Weight Support Vector Regression Machines. When forecasting the demand for HRs, it is necessary to effectively enter the historical data of the time series, which is characterized by a gradual decline with time regression [27, 28]. In the process of regression, the regression error between the earlier data and the new data is almost zero. The weight of the slack variables in the traditional SVR model is the same, and the large variance samples are absolutely dominant in the regression super flat, which allows the regression distortion to appear. With the help of the weight coefficient vector $\{\lambda_1, \lambda_2, \ldots, \lambda_n\}$, an identical small penalty strength is taken for all samples, and the importance of early and recent data in the sample series is effectively distinguished so that the regression effects in each sample are scientifically integrated.

The weighting coefficients can be indexed, that is,

$$\lambda_i = ke^{i-N}, \tag{3}$$

where N is the total number of years of historical data.

4. HR Demand Forecasting Case

Taking a company dealing with automobiles as an example, if the HR demand of the company is analyzed, the results generated under this method are tested for prediction. Based on the analysis of correlation, the relevant factors are reasonably selected, and the total output value, total profit, sales situation, and model number are used as the core elements to forecast the HR demand [13, 21].

4.1. Preprocessing of Data. If the difference between the numerical magnitudes of the key factors is very obvious, it will cause a serious impact on the serial variance gap of each factor, and if the use is carried out directly, the influences with a large variance will cause a direct impact on the regression results, so it is necessary to preprocess all the data [28]. When processing each group of data, the z-score method can be used, and its formula is as follows:

$$y_i = \frac{(x_i - \overline{x})}{\delta_\lambda}, \tag{4}$$

where x is the original data, y is the predicted value, and δ_λ is the distribution factor. After preprocessing, the approximate numerical magnitude of all core factors was effectively obtained.

4.2. Forecasting Variable-Weight SVR HR Requirements. The kernel function is filled by a Gaussian function as follows:

$$K\left(x_i, x_j\right) = \exp\left[\frac{-1}{\delta^2\left(x_i - x_j\right)^2}\right]. \tag{5}$$

The experimental findings are carefully analyzed, while the experience accumulated over the years is effectively combined, and the kernel width is set to $\delta^2 = 2$, so that the high-dimensional nonlinearity of the data is better represented. When the penalty factor $C = 100$, the penalty factor can be avoided, which results in deterioration of performance and generalization of the data. When the base of the relaxation variable in the model is set to 0.01, the accuracy of the data points is very high and the number of support vectors in the training model is minimal, which results in a better extrapolation of the model. In order to enable the prediction accuracy of the method, five years of historical data from 2015 to 2019 were synthesized into a training set [26, 29], which allowed the regression model to be created in a reasonable manner. The actual situation of the company's HRs in 2019 has met the company's strategy implementation needs to the greatest extent, which fully demonstrates the effectiveness of the forecasting method. This is a good indication of the effectiveness of the method. Using this method to forecast the company's HR demand in 2020, the six years of historical data from 2015 to 2020 were combined into a training set, and all key factors for 2020 were entered into the SVR model, resulting in an HR demand of 5,963 people in 2020, with a shortfall of more than 300 people.

5. The Proposed Framework

5.1. Problem Definition. The goal of this paper is to automate the generation of job requirement descriptions. Given a set C of job requirement documents for $|c|$ different jobs, that is, $c = \{C_i = (X_i, Y_i)\}_{i=1}^{|c|}$, where X_i is the job duties, which describe the duties of the i-th job, and Y_i is the job requirements, which describe the various competency needs of the job. Specifically, for each job responsibility X_i, it is assumed to contain M^d words, that is, $X_i = \{x_1, x_2, \ldots, x_{M^d}\}$ requirements typically contain multiple sentences to describe different competency requirements, so Y_i each job requirement is represented as $Y_i = \{y_1, y_2, \ldots, y_N\}$, where y_j is the j-th sentence. For example, Figure 1 contains five job requirement statements, that is, $N = 5$, which correspond to the introduction of education, programming, machine learning, audio processing, and teamwork; the different colors in Figure 1 represent different neurons.

In addition, it is assumed that each y_j contains M_j^c words, that is, $y_j = \left\{y_{j,1}, y_{j,2}, \ldots, y_{j,M_j^c}\right\}$. In order to analyze the fine-grained competency requirements of each job, the idea of the paper is followed here to train a neural model

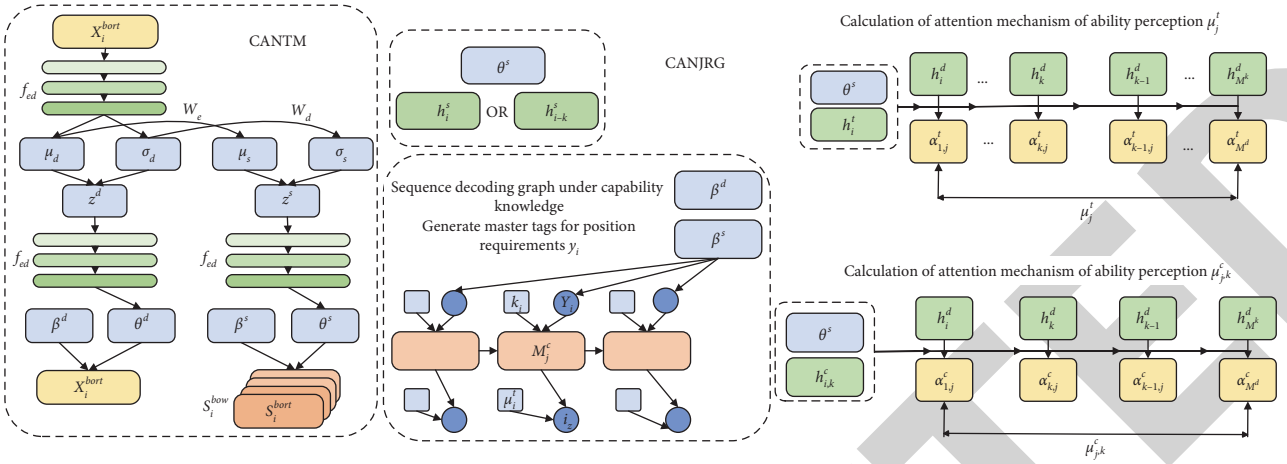

Figure 1: Schematic diagram of the framework of this paper (without CAPGTA).

to extract the skill words in each job requirement. Based on the annotation of these words, a list of competency words corresponding to each y_j can be generated, that is, $s_j = \{s_{j,1}, s_{j,2}, \ldots, s_{j,M_j^s}\}$. Based on this idea, the following job requirement description generation problem is defined in this section.

Problem definition: given a set of HR text blocks C. Each $c_i \in c$ contains a job responsibility X_i and a job requirement Y_i. The goal of job requirement description generation is to learn a model M whose smooth and reasonable job requirements Y_{new} can be generated when a new job responsibility X_{new} is given.

The proposed automatic job requirement generation framework (Cajon) based on skill prediction contains three main components: capability-aware under neural topic model (CANTM), the neural model for job requirement generation under ability perception (CANJRG), and the policy gradient training algorithm under ability perception (CAPGTA). Figure 1 shows a schematic diagram of the framework without the CAPGTA training algorithm.

5.2. CANTM. This subsection proposes a novel CANTM for mining potential competence topics in job responsibilities and job requirements, as shown in Figure 2. Next, the generation process and the inference process in CANTM are described separately. CANTM generation process: in order to model the potential semantics in job responsibilities and job requirements, we assume that there exists two topic spaces with the number of potential topics of K^d and K^s. Each topic is divided into K_j^d and K_j^s, respectively.

Word distributions β_j^d and β_j^s can be expressed as

$$\begin{aligned} \beta_j^d &= \text{soft max}\left(v_d \cdot (t_d)_j^\top\right), \\ \beta_j^s &= \text{soft max}\left(v_s \cdot (t_s)_j^\top\right), \end{aligned} \tag{6}$$

where $t_d \in R^{K^d \times H}$ and $t_S \in R^{K^S \times H'}$ are topic-based parameters, respectively, and $v_d \in R^{V^d \times H}$ and $v_S \in R^{V^S \times H'}$ are word-based parameters, respectively, all of which will be learned during the training process. The other V^d and V^S are the word list sizes for

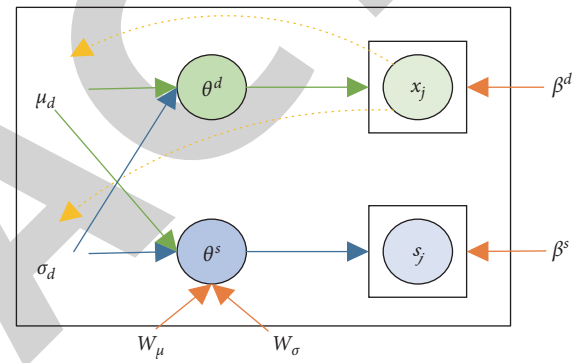

Figure 2: Schematic diagrams of CANTM probability diagram (the solid line represents the generation process, and the dashed line represents the variational inference process).

job responsibilities and job requirements, respectively. And only the list of competency words s_i is considered here as data input for the job requirement part of CANTM, which can reduce input noise and improve the performance of learning potential competency topics in job requirements.

Similar to the LAD topic model [30], it is assumed here that each job duty X_i and list of competency words s_i in the job requirements Y_i have topic vectors θ^d and θ^S, respectively, where $\theta^d \in R^{K^d}$ and $\theta^S \in R^{K^s}$. Here, θ^d and θ^S are generated based on Gaussian softmax, respectively. Specifically, the generation process for post X_i is as follows:

Sampling hidden variables $z^d \sim \mathcal{N}(\mu_d, \sigma_d^2)$:

$$\theta^d = \text{soft max}\left(f_{\theta^d}\left(z^d\right)\right). \tag{7}$$

For the L-th word in X_i: sampled word $x_l \sim \theta^d \cdot \beta^d$, where μ_d and σ_d^d are a priori parameter and $f_{\theta^d}(\cdot)$ is a neuron activated by a nonlinear function.

The difference is that for the generation process of competency word lists S_i in job requirements Y_i, usually, only one competency topic is designed. Based on this, the generation process is as follows:

Sampling hidden variables $z^s \sim \mathcal{N}(\mu_d, \sigma_d^s)$:

$$\theta^s = \text{soft max}\left(f_{\theta^s}(z^s)\right). \tag{8}$$

The probability of the word s_j in the j-th sentence can be expressed as

$$p\left(s_j \mid \theta^s, \beta^s\right) = \theta^s \cdot \prod_{k=1}^{M_j^s} \beta^s_{*,s_{j,k}}, \tag{9}$$

where μ_s and σ_s are a priori parameters and $\beta^s_{*,s_{j,k}}$ represents the column vector of ability words in β^s. In this paper, an end-to-end competency-aware neural job requirement generation framework is proposed to automate the generation of job requirements, and the prediction of skill words in job requirements can be achieved based on the prediction of competency themes. A neural topic model is first designed; then an encoder-decoder LSTM is proposed to implement a job requirement generation, followed by a competency-aware policy gradient-based training algorithm to further enhance the rationality of the generated job requirement descriptions. Finally, extensive experiments on real-world HR data sets clearly validate the effectiveness and interpretability of the proposed framework and its variants in comparison with state-of-the-art benchmarks.

In addition, in order to model the strong correlation between each job position X_i and the competency term S_i in the job requirements Y_i, the following mapping relationship is assumed here for the a priori parameters of their potential topics.

$\mu_s = W_\mu \mu_d$, $\log \sigma_s = W_\sigma (\log \sigma_d)$ CANTM Inference Process: the edge likelihood [31] of the CANTM-based generation process is as follows:

$$\begin{aligned} &p\left(X_i, S_i \mid \mu_d, \mu_s, \sigma_d, \sigma_s, \beta^d, \beta^s\right) \\ &= \int p\left(\theta^d \mid \mu_d, \sigma_d^2\right) \int_{k=1}^{M^d} p\left(x_k \mid \theta^d, \beta^d\right) \mathrm{d}\theta^d \\ &\cdot \int p\left(\theta^s \mid \mu_s, \sigma_s^2\right) \prod_{j=1}^{N} p\left(s_j \mid \theta^s, \beta^s\right) \mathrm{d}\theta^s. \end{aligned} \tag{10}$$

The neural variational method is used here to approximate the posterior distribution on θ^d and θ^s. Based on equation (10), the variational lower bound for the log-likelihood is as follows:

$$\begin{aligned} \mathscr{L} &= \mathbb{E}_{q(\theta^d)}\left[\sum_{k=1}^{M} \log p\left(x_k \mid \theta^d, \beta^d\right)\right] - D_{KL}\left(q\left(\theta^d\right) \| p\left(\theta^d \mid \mu_d, \sigma_d\right)\right) \\ &+ \mathbb{E}_{q(\theta^s)}\left[\sum_{j=1}^{M} \log p\left(s_j \mid \theta^s, \beta^s\right)\right] - D_{KL}\left(q\left(\theta^s\right) \| p\left(\theta^s \mid \mu_s, \sigma_s\right)\right), \end{aligned} \tag{11}$$

where $q(\theta^s)$ and $q(\theta^d)$ are estimates of the variance distribution of the true posterior $p(\theta^d \mid X_i, S_i)$ and $p(\theta^S \mid X_i, S_i)$, respectively. D_{KL} represents the Kullback–Leibler divergence [5, 32]. The proof is derived as follows:

$$\begin{aligned} \mathscr{L} &= \log \int p\left(\theta^d \mid \mu_d, \sigma_d^2\right) \prod_{k=1}^{M^d} p\left(x_k \mid \theta^d, \beta^d\right) \mathrm{d}\theta^d + \log \int p\left(\theta^s \mid \mu_s, \sigma_s^2\right) \prod_{j=1}^{N} p\left(s_j \mid \theta^s, \beta^s\right) \mathrm{d}\theta^s \\ &= \log \int \frac{q\left(\theta^d\right)}{q\left(\theta^d\right)} p\left(\theta^d \mid \mu_d, \sigma_d^2\right) \prod_{k=1}^{M^d} p\left(x_k \mid \theta^d, \beta^d\right) \mathrm{d}\theta^d + \log \int \frac{q(\theta^s)}{q(\theta^s)} p\left(\theta^s \mid \mu_s, \sigma_s^2\right) \prod_{j=1}^{N} p\left(s_j \mid \theta^s, \beta^s\right) \mathrm{d}\theta^s \\ &\geq \int q\left(\theta^d\right) \log \left[p\left(\theta^d \mid \mu_d, \sigma_d^2\right) \prod_{k=1}^{M^d} p\left(x_k \mid \theta^d, \beta^d\right)\right] \mathrm{d}\theta^d \\ &+ \int q(\theta^s) \log \left[p\left(\theta^s \mid \mu_s, \sigma_s^2\right) \prod_{j=1}^{N} p\left(s_j \mid \theta^s, \beta^s\right)\right] \mathrm{d}\theta^s \\ &- \int q\left(\theta^d\right) \log q\left(\theta^d\right) \mathrm{d}\theta^d - \int q(\theta^s) \log q(\theta^s) \mathrm{d}\theta^s \\ &= \mathbb{E}_{q(\theta^d)}\left[\sum_{k=1}^{M^d} \log p\left(x_k \mid \theta^d, \beta^d\right)\right] - D_{\mathrm{KL}}\left(q\left(\theta^d\right) \| p\left(\theta^d \mid \mu_d, \sigma_d^2\right)\right) \\ &+ \mathbb{E}_{q(\theta^r)}\left[\sum_{j=1}^{N} \log p\left(s_j \mid \theta^s, \beta^s\right)\right] - D_{\mathrm{KL}}\left(q(\theta^s) \| p\left(\theta^s \mid \mu_s, \sigma_s^2\right)\right). \end{aligned} \tag{12}$$

We generate the variance parameters $\mu_d(X_i, S_i)$, $\log \sigma_d(X_i, S_i)$, $\mu_s(X_i, S_i)$, and $\log \sigma_S(X_i, S_i)$ here based on the idea of the paper to estimate μ_d, σ_d, μ_s, and σ_s through input X_i. This allows the CANTM model to explore potential competency thematic representations through job duties only θ_d and θ_s. Therefore, an inferential network based on the observed job duties X_i is introduced here, combined with equation (12) to generate the above variance parameters as follows:

$$\begin{aligned}
\mu_d(X_i, S_i) &= f_{\mu_d}\left(f_{e_d}\left(X_i^{\text{bow}}\right)\right),\\
\mu_s(X_i, S_i) &= W_{\mu}\mu_d(X_i, S_i),\\
\log \sigma_d(X_i, S_i) &= f_{\sigma_d}\left(f_{e_d}\left(X_i^{\text{bow}}\right)\right),\\
\log \sigma_s(X_i, S_i) &= W_{\sigma}\log \sigma_d(X_i, S_i),
\end{aligned} \tag{13}$$

where (X_i^{bow}) is the bag-of-words vector of X_i, $(f_{e_d}(\cdot))$ is a neuron activated by a nonlinear function, and $(f_{\mu_d}(\cdot))$ and $(f_{\sigma_d}(\cdot))$ are linear neural perceptual functions.

Based on this, the following loss function can be directly minimized for each set of instances (X_i, S_i) during the training process:

$$\mathscr{L}_{\text{CANTM}} = -\sum_{k=1}^{M^d} \log\left(\theta^d \cdot \beta^d_{*,x_k}\right) + D_{KL}\left(q\left(\theta^d\right)\middle\|p\left(\theta^d\right)\right). \tag{14}$$

Therefore, all parameters in CANTM can be inferred, and the potential competency themes involved in each position can be further explored.

5.3. CANJRG. After learning about the potential competency themes through CANTM, this subsection describes how to use the encoder-decoder neural model to generate job requirements. As shown in Figure 3, it contains two main components, including a sequence encoder that extracts semantic information from the input job responsibilities X_i, and a sequence decoder under competency awareness, which can generate each word in the job requirements Y_i by the guidance of potential competency themes.

Sequence encoder: first use an embedding layer to find the embedding vector e_k^d for each word x_k in X_i and then use a Bi-LSTM [5, 33] to encode the sequence $\left\{e_1^d, e_2^d, \ldots, e_{M^d}^d\right\}$: $\overrightarrow{h_k^d} = \text{LSTM}(e_k^d, \overrightarrow{h_{k-1}^d})$, $\overleftarrow{h_k^d} = \text{LSTM}(e_k^d, \overleftarrow{h_{k+1}^d})$, where $e_k^d = W_{e^d}x_k$ is the word vector of x_k and the LSTM is a unidirectional LSTM network. Finally, $h_k^d = [\overrightarrow{h_k^d}; \overleftarrow{h_k^d}]$ is used to represent the final hidden vector of the x_k sequence encoder.

Competency-aware sequence decoder: the following describes how to construct a decoder to generate each word in job requirement Y_i. In the generation process, the competency topic t_j is first estimated for each sentence y_j in Y_i, and then each word is predicted the following probability $y_{j,k}$:

$$p\left(y_{j,k} \mid X_i\right) = p\left(y_{j,k} \mid y_{<j}, y_{j,<k}, \mathscr{H}, \theta^s, t_j\right), \tag{15}$$

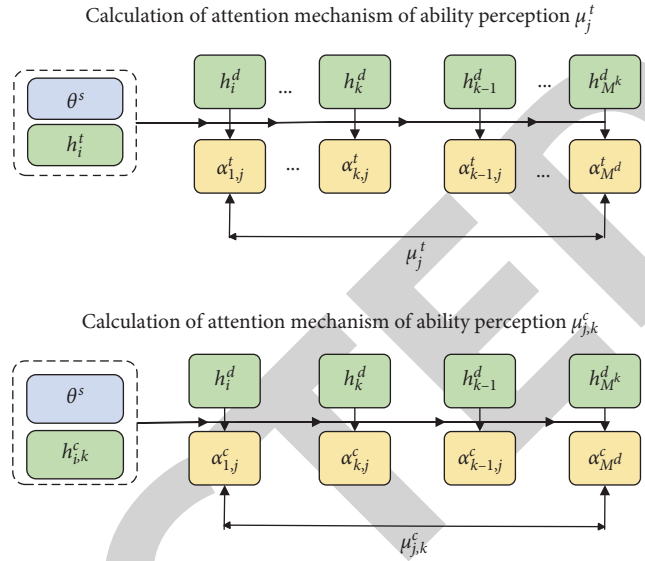

Figure 3: Schematic diagrams of the attention mechanism under ability perception: (a) calculation of attention mechanism of ability perception μ_j^t and (b) calculation of attention mechanism of ability perception $\mu_{j,k}^c$.

where $y < j$ represents the sequence $\left\{y_1, y_2, \ldots, y_{j-1}\right\}$, $y_{j,<k}$ and represents $\left\{y_{j,1}, y_{j,2}, \ldots, y_{j,k-1}\right\}$ and $\mathscr{H} = \{h_1^d, h_2^d, \ldots, h\, M^{dd}\}$ represents the implicit state of all sequence encoders. θ^s is Y_i; the implicit capability topic vector learned through CANTM, and $t_j \in [1, K^s]$ is the topic label for each utterance y_j.

Specifically, the sequence decoder under capability awareness is constructed based on two one-way LSTMs [34]. h_j^t and $h_{j,k}^c$ represent the implicit status of the competent topics t_j and words $y_{j,k}$ computed by the LSTM, respectively.

$$\begin{aligned}
h_j^t &= \text{LSTM}\left(\left[e_{j-1}^t; \theta^s; h_{j-1,M_{j-1}^c}^c\right], h_{j-1}^t\right)h_{j,k}^c\\
&= \text{LSTM}\left(\left[e_{j,k-1}^c; \theta^s; h_j^t\right], h_{j,k-1}^c\right),\\
e_j^t &= W_{e^t}t_j, e_{j,k}^c = W_{e^c}y_{j,k},
\end{aligned} \tag{16}$$

where e_j^t and $e_{j,k}^c$ is the embedded representations of t_j and $y_{j,k}$. M_j^c is the length of statement y_j. Also, implicit states h_0^t and $h_{1,0}^c$ are initialized by $h_{M^d}^d$, and $h_{j,0}^c$ is initialized by $h_{j-1,M_{j-1}^c}^c$. In addition, two capability-aware attention mechanisms are designed here to capture contextual features from H to enhance the performance of the generation process as follows:

$$\begin{aligned}
\alpha_{l,j}^t &= \frac{\exp\left(g_{l,j}^t\right)}{\sum_{p=1}^{N}\exp\left(g_{p,j}^t\right)},\\
\alpha_{l,j,k}^c &= \frac{\exp\left(g_{l,j,k}^c\right)}{\sum_{p=1}^{M_j^c}\exp\left(g_{p,j,k}^c\right)},\\
g_{l,j}^t &= v_{\alpha^1}^{\top}\tanh\left(W_{\alpha^1}\left[h_l^d; h_j^t; \theta^s\right] + b_{\alpha'}\right),\\
g_{l,j,k}^c &= v_{\alpha^c}^{\top}\tanh\left(W_{\alpha^c}\left[h_l^d; h_{j,k}^c; \theta^s\right] + b_{\alpha^c}\right).
\end{aligned} \tag{17}$$

The capability-aware context vectors u_j^t and $u_{j,k}^c$ can then be calculated by the following equations:

$$u_j^t = \sum_{l=1}^{N} \alpha_{l,j}^t h_l^d,$$
$$u_{j,k}^c = \sum_{l=1}^{M_j^c} \alpha_{l,j,k}^c h_l^d. \tag{18}$$

The ability theme labels can then be predicted. t_j and y_j for each word in $y_{j,k}$ as follows:

$$p\left(t_j \mid t_{<j}, \mathcal{H}, \theta^s\right) = \text{soft max}\left(W_t\left[h_j^t; u_j^t; \theta^s\right] + b_t\right),$$
$$p\left(y_{j,k} \mid y_{<j}, y_{j,<k}, \mathcal{H}, \theta^s, t_j\right) = \text{soft max}\left(W_c\left[h_{j,k}^c; u_{j,k}^c; \theta^s\right] + b_c\right). \tag{19}$$

In addition, an ability-aware replication mechanism is designed such that the proposed decoder can directly replicate the words in the ability vocabulary. Specifically, a generation probability is defined here when y_j generates the k-th word: $y_{j,k}$; $p_{\text{gen}} \in [0, 1]$.

The probability distribution of the predicted words based on the ability word list can then be updated with the following equation:

$$p\left(y_{j,k} \mid y_{<j}, y_{j,<k}, \mathcal{H}, \theta^s, t_j\right) = p_{\text{gen}} \text{soft max}\left(W_c\left[h_{j,k}^c; u_{j,k}^c; \theta^s\right] + b_c\right) + \left(1 - p_{\text{gen}}\right)\left(\beta^s\right)_{t_j}, \tag{20}$$

where $(\beta^s)_{t_j}$ is the word distribution in topic.

Finally, in the heterogeneous model, for each group of training instances (X_i, Y_i), the parameters in the model are learned by minimizing the following cross-entropy loss function:

$$\mathcal{L}_{\text{CTL}} = -\sum_{j=1}^{N} \log p\left(t_j \mid X_i, \theta_s\right),$$
$$\mathcal{L}_{\text{GJR}} = -\sum_{j=1}^{N} \sum_{k=1}^{M_j^s} \log p\left(y_{j,k} \mid X_i, \theta_s\right). \tag{21}$$

5.4. Capability-Aware Policy Gradient Training Algorithm (CAPGTA). Before introducing CAPGTA, a basic end-to-end training approach will be shown to learn all the parameters in the above two models. Specifically, because of the CANTM neural variation, the loss functions $\mathcal{L}_{\text{CANTM}}$, $\mathcal{L}_{\text{CTL}}$ and $\mathcal{L}_{\text{GJR}}$, can be trained jointly at the same time.

$\mathcal{L}^* = \mathcal{L}_{\text{GJR}} + \lambda_1 \mathcal{L}_{\text{CANTM}} + \lambda_2 \mathcal{L}_{\text{CTL}}$, where λ_1 and λ_2 are hypermastigote to balance each model. The teacher forcing algorithm is used in the training process, that is, the previous real word $y_{j,k-1}$ is used in the training to calculate h_j^t and $h_{j,k}^c$. For the ability topic t_{j-1}, the following is used for generation:

$$t_{j-1} = \arg\max_l \left\{ \left(\theta^s\right)_l \left(\prod_{k=1}^{M_{j-1}^s} \beta_{*, s_{j-1,k}}^s \right)_l \right\}_{l=1}^{K^s}. \tag{22}$$

And the predicted values are used as input in the testing sessions.

Direct minimization $\mathcal{L}^*$ does not always generate the best job requirements because it does not directly optimize discrete assessment metrics such as ROUGE and BLKJ [35]. In addition, it is desired here that the accuracy of the competencies involved in the generated job requirements can be optimized more intuitively, so that the rationality and validity of the generated results can be better ensured.

Some recent reinforcement learning techniques can be used to solve this nondifferentiable task metric problem. Here, the combination of CANTM and CANJRG can be considered as an agent [30, 36], which interacts with the environment, that is, the training instances. Given an input job duty X, strategy $(\text{pol} - \text{icy}) p_\theta(y_{j,k} X, \hat{y}_{<j}, y_{j<k})$ is determined by the parameter 0 of the intelligence for each action, that is, predicting the next word based on the current state. Until the end position (EOS) of the sequence of job requirements is generated, a reward will be observed. The goal of the whole training is to learn the strategy by minimizing the negative expected reward of

$$\mathcal{L}^{\text{RL}} = -\mathbb{E}_{\hat{Y} \sim p_\theta(\hat{Y} \mid X)}[r(\hat{Y})]. \tag{23}$$

Based on reinforcement learning algorithm, it obtains that

$$\nabla_\theta \mathcal{L}^{\text{RL}} = -\mathbb{E}_{\hat{Y} \sim p_\theta(\hat{Y} \mid X)}\left[r(\hat{Y}) \nabla_\theta \log p_\theta(\hat{Y} \mid X)\right]. \tag{24}$$

It is possible to use a simple Monte–Carlo sampling $\hat{Y}$ based strategy p_θ as follows:

$$\begin{aligned} \nabla_\theta \mathcal{L}^{\text{RL}} &\approx -r(\hat{Y}) \nabla_\theta \log p_\theta(\hat{Y} \mid X) \\ &= -r(\hat{Y}) \nabla_\theta \sum_{j=1}^{N} \sum_{k=1}^{M_j^c} \log p_\theta\left(y_{j,k} X, \hat{y}_{<j}, y_{j<k}\right) \\ &= -r(\hat{Y}) \nabla_\theta \sum_{j=1}^{N} \Big(\log p_\theta\left(\hat{t}_j \mid X, \quad \hat{t} < j\right) \\ &\quad + \sum_{k=1}^{M_j^c} \log p_\theta\left(\left(y_{j,k} X, \hat{y}_{<j}, y_{j<k}\right)\right) \Big), \end{aligned} \tag{25}$$

where $(\hat{t}_1, \ldots, \hat{t}_N)$ is a Monte–Carlo [37] sample of the capability label. $p_\theta(\hat{t}_j \mid X, \hat{t} < j)$ and $p_\theta((y_{j,k} X, \hat{y}_{<j}, y_{j<k}))$ are calculated from equations (23) and (24), respectively.

$$\nabla_\theta \mathcal{L}^{\text{RL}} \approx \left(r\left(\hat{Y}^g\right) - r(\hat{Y})\right) \nabla_\theta \sum_{j=1}^{N} \left(\log p_\theta\left(\hat{t}_j \mid X, \hat{t}_{<j}\right) + \sum_{k=1}^{M_j^c} \log p_\theta\left(y_{j,k} X, \hat{y}_{<j}, y_{j<k}\right) \right). \tag{26}$$

As mentioned earlier, here, it is desired to directly optimize the accuracy of the competencies in the generated job requirements. Therefore, we use the $F1$ values [38] of the generated skill terms as a reward function, that is,

$$r_{\text{capability}}(\widehat{Y}) = \frac{2\text{Card}(\widehat{S} \cap S)}{\text{Card}(\widehat{S}) + \text{Card}(S)}, \tag{27}$$

where S is the set of skill words in the actual job requirements and $\widehat{S}$ is the set of skill words in $\widehat{Y}$, representing the set size. The ROUGE-1 score is also incorporated into the reward function, which is used to measure statistical information based on the longest common subsequence between the actual and model-generated job requirements. This allows a direct optimization of the similarity of the sentence hierarchy to authenticity, which helps improve the fluency of the generated text. The reward function can then be set to

$$r(\widehat{Y}) = \lambda_3 r_{\text{capability}}(\widehat{Y}) + \text{Rouge} - 1(\widehat{Y}, Y). \tag{28}$$

Finally, $\mathscr{L}^*$ and $\mathscr{L}^{\text{RL}}$ are used jointly to obtain the overall learning objective function as follows:

$$\mathscr{L} = (1 - \gamma)\mathscr{L}^* + \gamma\mathscr{L}^{\text{RL}}, \tag{29}$$

where γ is the dynamic hypernatremia during the training process. It is first set to 0 for a period of training alone $\mathscr{L}^*$, and then the value is gradually increased.

6. Experimental Analysis

This section presents the results of extensive experiments of quantitative analysis and manual evaluation on real-world HR data sets [4, 12] to demonstrate the effectiveness of the proposed Cajon in job skill prediction and job requirement generation.

6.1. Experimental Data. Two real-world HR data sets [4, 12], including technical (T) and product (P) related job data sets, are used here. Specifically, 3,475 and 2,351 different jobs were collected, respectively, including their job responsibilities and corresponding job requirement texts, which have been carefully proofread by six HR experts to ensure fluency and reasonableness. Some statistics are shown in Table 1 and Figures 4 and 5. In the experiments, 80% of the data set were randomly selected as training data, another 10% as test data to verify the performance, and the last 10% was used to tune the parameters.

In addition to generating reasonable skill words in job requirements, LSTM-CRF [15, 25] model was trained to extract possible competency words based on the method of the paper. With the help of HR experts, a final vocabulary containing 4,825 skill entities was obtained.

6.2. Training Parameters and Environment Setting. In the competency-aware neural topic model, the raw input of job responsibilities and competency words from the job descriptions is first converted into a bag-of-words vector [4, 23]. And before that, deactivated words and high- and low-frequency words are removed to enhance the model. The performance of the model is enhanced by removing the discontinued words and high- and low-frequency words. Here, the number of topics (K^d, K^s) is set to (30, 50) and (30, 30) for the T and P data sets, respectively. In addition, we add batch normalization in computing $\mu_d(X_i, S_i), \mu_s(X_i, S_i)$, $\log \sigma_d(X_i, S_i)$, and $\log \sigma_s(X_i, S_i)$ to avoid the problem that KL divergence disappears during training.

In the capability-aware postrequirement generation model, the embedding layer sizes of word x_k, $y_{j,k}$, and topic tag t_k are 128, 128, and 50, respectively. Sequence encoder is implemented by a bidirectional LSTM, and the hidden layer size of each LSTM layer is 256. Capability-aware sequence decoder is implemented by two unidirectional LSTMs, both of which have a hidden layer size of 256. In addition, the size of the hidden layer states in both the capability-aware attention mechanism and the capability-aware replication mechanism are also set to 256.

During the training of the complete Cajon framework, the parameters are initialized using the Xavier strategy.

Then 200 rounds of pretraining are performed on CANTM. After that, we set $\lambda_1 = 1$ and $\lambda_2 = 1$ to train the part of Cajon other than the reinforcement learning loss function. Finally, we set $\lambda_3 = 1$ and incrementally increase to train our model by equation (12). In addition, Adam is used as the optimizer, and the initial learning rate is set to 0.001. And, the gradient crop is also set to 1.0 to stabilize the training process. In the test phase of generation, we used the Beam Search algorithm and set the cluster size to 4.

The overall experiments were performed on a Linux server configured with RedHat 4.8.536, 2.40 G Hz Intel(R) Xeon(R) Gold6148 CPU; models were developed based on the tensor flow framework.

6.3. Benchmarking Algorithm. To evaluate the effectiveness of the proposed approach, several state-of-the-art text generation methods are compared here, and these methods are adapted to fit the problem definition setting.

Seq2Seq [14] is a classical text-to-text generation model, which was proposed in the paper with the aim of implementing neural machine translation. In the experiments of this section, a concat-based approach to compute attention mechanisms is also applied, which is similar to the approach proposed in this chapter.

Kit [18] is a variant of Seq2Seq, a model that implements a pointer network and an overlay mechanism to handle the automatic digest problem.

Kid is a natural language generation model based on transformer networks, which are proposed to solve the sequence-to-sequence generation problem.

In addition, state-of-the-art automated job description writing methods are compared.

SAMA [19, 21] is the state-of-the-art automated job description writing model, which is presented in the paper. For a fair comparison with the proposed model, the characteristics of the additional information it uses (e.g., company size) are removed in this section of the experiments.

In addition, four variants of the Cajon framework are compared to assess the impact of each component of the

Table 1: Statistical description of T and P data sets.

Data set	Statistical indicators	Value
T	Total number	3,475
	Average number of words for job duties	50.11
	Average word count of job requirements	100.10
	Average number of words of ability for job requirements	25.72
	Average number of sentences for job requirements	6.95
P	Total number	2,351
	Average number of words for job duties	74.98
	Average word count of job requirements	75.80
	Average number of words of ability for job requirements	15.58
	Average number of sentences for job requirements	4.98

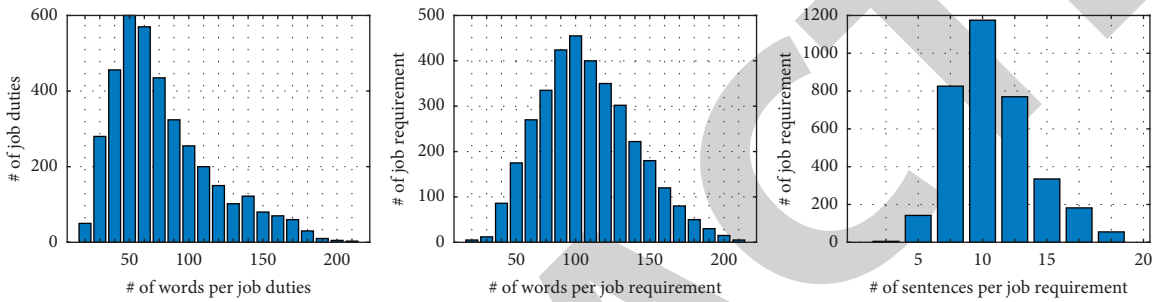

Figure 4: Text statistics of the technology (T) data set.

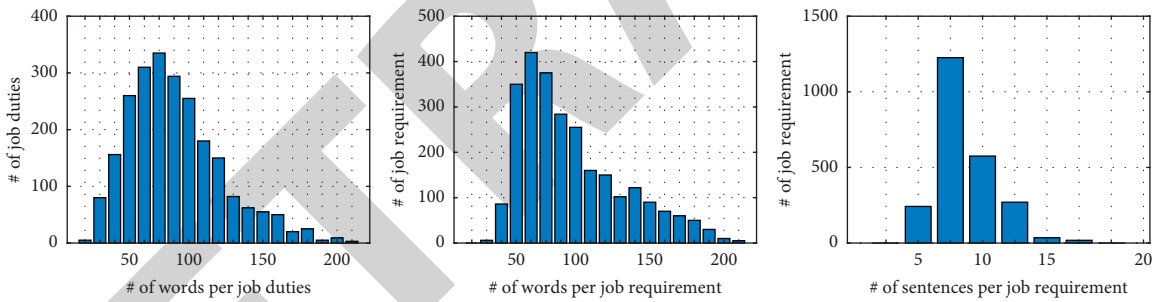

Figure 5: Text statistics of the product (P) data set.

model on the generated results: Cajon (w/o RL) is a variant of Cajon in which the CAPGTA is removed from the training, that is, the training is done directly by the formula. Cajon (w/o RL, $\mathscr{L}_{\text{CANTM}}$) is a variant of Cajon (w/o RL, $\mathscr{L}_{\text{CTL}}$) that removes the ability topic label related part of the sequence decoder, that is, only θ^s is used to introduce ability topic information.

Cajon (w/o RL, topic-copy) is a variant of Cajon (w/o RL), which removes the capability-aware replication-based mechanism.

6.4. Evaluation Indicators. In order to evaluate the effectiveness of job requirement generation, both automatic and manual assessments were used.

In the automatic evaluation, standard ROUGE metrics were used, including ROUGE-1, ROUGE-2, and ROUGE-L, which measure the statistics of unary word overlap, binary word overlap, and longest common subsequence (LCS) [31] in the comparison of real and automatically generated results, respectively. The BLEU evaluation metric, which measures the cooccurrence of n-words, was also used. Finally, the precision rate, recall rate, and F1 value of skill words in job requirements are used to automatically verify the rationality and validity of the generated results, as shown in Table 2.

Figure 6 shows the accuracy, recall, and $F1$ value data set of Cajon and its variants; the proposed model improves 1.06% and 4.60% in automatic metrics ROUGE-1 and BLEU-1, and 3.00% and 7.16% in manual metrics Fluency and Validity, respectively, compared to the best available techniques. This result clearly demonstrates the effectiveness of the proposed model in generating fluent and reasonable job requirements [39].

In addition, Figure 6 shows the precision, recall, and F1 values of the generated competency words in the job requirements. Here, it can be found that the proposed model outperforms the best results of all benchmarks of 9.49%,

Table 2: Experimental results of Cajon and comparison methods.

Data set	Method	ROUGE			BLEU		Manual evaluation metrics	
		ROUGE-1	ROUGE-2	ROUGE-L	BLEU-1 (%)	BLEU-4 (%)	Fluency	Validity
T	Seq2Seq	0.6389	0.4151	0.5996	37.32	16.22	3.66	3.58
	pGNet	0.6413	0.4246	0.6061	38.14	16.75	3.70	3.61
	UniLM	0.6167	0.3965	0.5863	34.64	12.29	3.52	3.14
	SAMA	0.6004	0.3277	0.5455	39.30	15.07	3.47	3.52
	Cajon	0.6531	0.4296	0.6077	41.81	19.41	3.73	3.81
P	Seq2Seq	0.7236	0.5085	0.7138	32.02	7.28	3.63	3.34
	pGNet	0.7421	0.5410	0.7331	32.72	8.28	3.67	3.41
	UniLM	0.7542	0.5439	0.7452	31.43	6.42	3.46	3.28
	SAMA	0.7160	0.4788	0.7074	34.76	9.00	3.55	3.49
	Cajon	0.7522	0.5757	0.7531	36.46	10.84	3.78	3.74

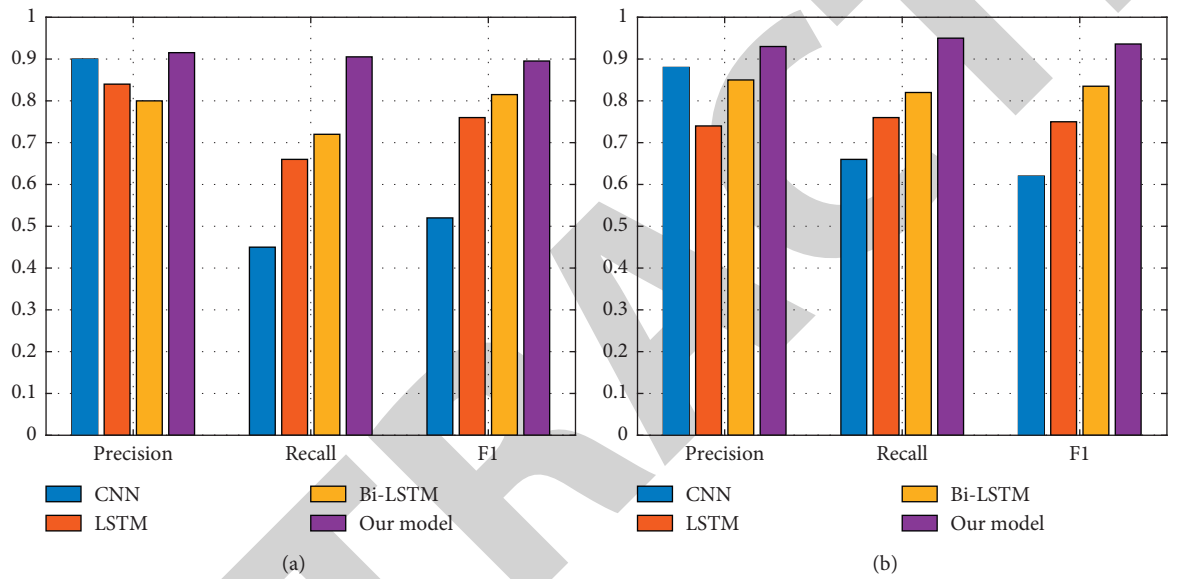

Figure 6: Different model performance: (a) technology (*T*) data set and (b) product (*P*) data set.

3.55%, and 6.73% in the technical data and 20.62%, 5.29%, and 17.69% in the product data set, respectively. It clearly validates that the generated results of the proposed framework can more accurately capture the relevant and representative skill requirements of the position.

Ablation experiments: here, the effects of the proposed model and its variants are compared. And Seq2Seq can also be used as a variant of the proposed method, that is, the CANTM model is removed. Obviously, it is clear from the results that all model components can enhance the effect. Specifically, the performance decreases rapidly when only potential capability topic information is considered, which proves the importance of predicting potential capability topic labels for the decoder. As shown in Figure 7, the capability-awareness-based attention mechanism can improve about 2.61% and 1.38% of ROUGE-1 and BLEU-I, respectively, in the technology data set, and 2.53% and 4.83% in the product data set, respectively. Meanwhile, the capability-awareness-based replication mechanism can improve 1.87% and 0.84% in the technical data set on ROUGE-1 and BLEU-1 white spoon effect and 2.92% and 1.54% in the product data set, respectively. In addition, Figure 8 shows that the proposed CAPGTA can effectively improve the precision, recall, and F1 values of skill words in generating job requirements.

Subject number parameter experiments: as shown in Figure 8, to evaluate the parameter sensitivity, Cajon is trained here by tuning parameters K^d and K^s, 0 to 100, whose other ones are fixed at $K^d = 30$ and $K^s = 50$ in the technical data set and $K^d = 30$ and $K^s = 30$ in the product data set. Here, it can be clearly observed that the best results can be obtained in the technical data set $K^d = 30$ and $K^s = 30$ and in the product data set $K^s = 30$ and $K^d = 30$.

6.5. Generating Example Studies and Discussion. To further illustrate the effectiveness and interpretability of the proposed framework, an example of job requirements generated by Cajon is given in Figure 9. Given the position to hire a data mining algorithm engineer, it can be found that the generated results are fluent and include competency requirements regarding education, work experience, data mining algorithms, basic programming language, and

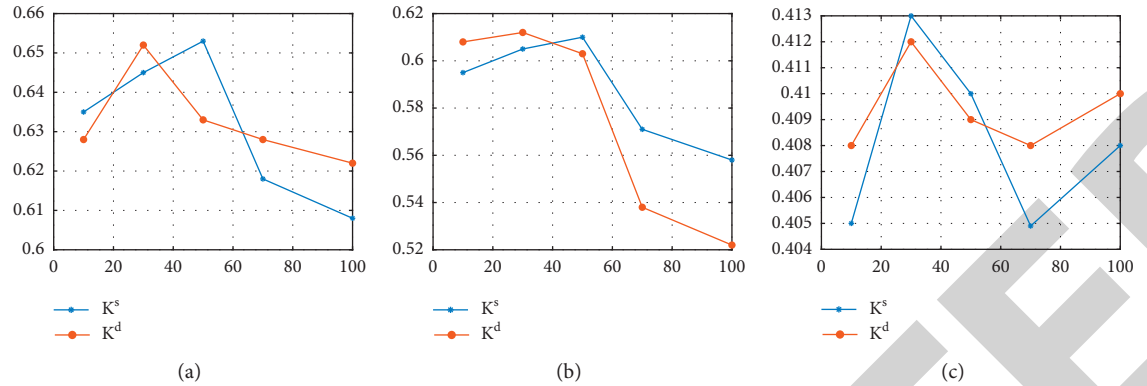

Figure 7: Effect of technical data sets K^d and K^s on model effects: (a) ROUGE-1, (b) ROUGE-L, and (c) BLEU-1.

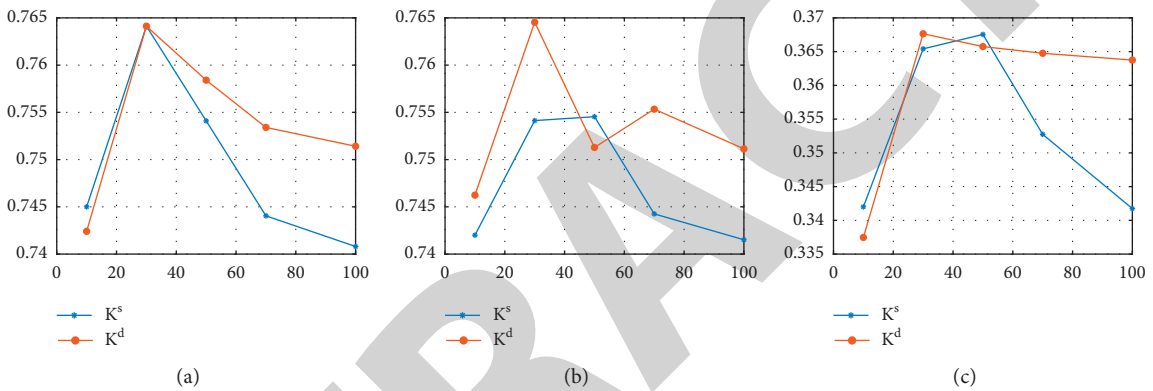

Figure 8: Effect of product data sets K^d and K^s on model effects: (a) ROUGE-1, (b) ROUGE-L, and (c) BLEU-1.

Figure 9: Case study diagrams generated from job requirements, with skill words highlighted.

teamwork, most of which are mentioned in the job requirements written by experts. This proves that the proposed model is effective in generating fluent and reasonable job requirements. In addition when generating each job requirement statement, a word cloud representation corresponding to the predicted competency topic is shown. For this reason, it can be seen that the proposed CANTM can effectively learn meaningful competency themes, demonstrating that potential competency themes can effectively guide the generation of job requirement texts, thus demonstrating the interpretability of the proposed framework.

7. Conclusions

In this paper, an end-to-end competency-aware neural job requirement generation framework is proposed to automate the generation of job requirements, and the prediction of skill words in job requirements can be achieved based on the prediction of competency themes. Then an encoder-decoder recurrent neural network is proposed to implement a job requirement generation, followed by a competency-aware policy gradient-based training algorithm to further enhance the rationality of the generated job requirement descriptions. Finally, extensive experiments on real-world HR data sets clearly validate the effectiveness and interpretability of the proposed framework and its variants in comparison with state-of-the-art benchmarks.

Data Availability

The data sets used in this paper are available from the corresponding author upon request.

Conflicts of Interest

The authors declare that they have no conflicts of interest regarding this work.

Acknowledgments

This work was supported by the Outstanding Young Scholars Program (2020): "Research on the Driving Mechanism, Model Selection and Path Optimization of the Transformation and Upgrading of the Human Resource Service Industry in Anhui Province in the AI Era" under grant no. gxyq2020229.

References

[1] R. Iqbal, F. Doctor, B. More, S. Mahmud, and U. Yousuf, "Big data analytics and computational intelligence for cyber-physical systems: recent trends and state of the art applications," *Future Generation Computer Systems*, vol. 105, pp. 766–778, 2020.

[2] R. Iqbal, F. Doctor, B. More, S. Mahmud, and U. Yousuf, "Big data analytics: computational intelligence techniques and application areas," *Technological Forecasting and Social Change*, vol. 153, p. 119253, 2020.

[3] Y. E. Zhang, S. Liu, and S. Xu, "Integrating the split/analyze/meta-analyze (SAM) approach and a multilevel framework to advance big data research in psychology," *Zeitschrift für Psychologie*, vol. 226, 2019.

[4] R. Li, Q. Liu, and J. Gui, "Indoor relocalization in challenging environments with dual-stream convolutional neural networks," *IEEE Transactions on Automation Science and Engineering*, vol. 15, pp. 651–662, 2017.

[5] N. Chen, W. Liu, R. Bai, and A. Chen, "Application of computational intelligence technologies in emergency management: a literature review," *Artificial Intelligence Review*, vol. 52, no. 3, pp. 2131–2168, 2019.

[6] A. Chadha, A. Abbas, and Y. Andreopoulos, "Video classification with CNNs: using the codec as a spatio-temporal activity sensor," *IEEE Transactions on Circuits and Systems for Video Technology*, vol. 29, no. 2, pp. 475–485, 2017.

[7] R. Arandjelovic, P. Gronat, and A. Torii, "NetVLAD: CNN architecture for weakly supervised place recognition," in *Proceedings of the IEEE Conference on Computer Vision and Pattern Recognition*, pp. 5297–5307, Las Vegas, NV, USA, June 2016.

[8] F. L. Oswald, T. S. Behrend, D. J. Putka, and E. Sinar, "Big data in industrial-organizational psychology and human resource management: forward progress for organizational research and practice," *Annual Review of Organizational Psychology and Organizational Behavior*, vol. 7, no. 1, pp. 505–533, 2020.

[9] N. Nawaz, "Exploring artificial intelligence applications in HR management," *Journal of Management Information and Decision Sciences*, vol. 23, no. 5, pp. 552–563, 2020.

[10] I. Harris and M. B. Küssner, "Come on baby, light my fire: sparking further research in socio-affective mechanisms of music using computational advancements," *Frontiers in Psychology*, vol. 11, p. 3274, 2020.

[11] G. Nagarajan and R. I. Minu, "Multimodal fuzzy ontology creation and knowledge information retrieval," in *Proceedings of the International Conference on Soft Computing Systems*, pp. 697–706, Delhi, India, November 2016.

[12] J. Ock and H. An, "Machine learning approach to personality assessment and its application to personnel selection," *Korean Journal of Industrial and Organizational Psychology*, vol. 34, no. 2, pp. 213–236, 2021.

[13] Z. Gao, P. Wang, H. Wang, M. Xu, and W. Li, "A review of dynamic maps for 3D human motion recognition using ConvNets and its improvement," *Neural Processing Letters*, vol. 52, no. 2, pp. 1501–1515, 2020.

[14] A. Agus, S. K. Krishnan, and S. L. S. A. Kadir, "The structural impact of total quality management on financial performance relative to competitors through customer satisfaction: a study of Malaysian manufacturing companies," *Total Quality Management*, vol. 11, no. 4-–6, pp. 808–819, 2000.

[15] Y. Zhao, M. K. Hryniewicki, F. Cheng, B. Fu, and X. Zhu, "Employee turnover prediction with machine learning: a reliable approach," in *Proceedings of the SAI Intelligent Systems Conference*, pp. 737–758, London, UK, September 2018.

[16] L. Wang, C. Zhang, and Q. Chen, "A communication strategy of proactive nodes based on loop theorem in wireless sensor networks," in *Proceedings of the 2018 Ninth International Conference on Intelligent Control and Information Processing (ICICIP)*, pp. 160–167, Wanzhou, China, November 2018.

[17] H. He, C. Maple, and T. Watson, "The security challenges in the IoT enabled cyber-physical systems and opportunities for evolutionary computing & other computational intelligence," in *Proceedings of the 2016 IEEE Congress on Evolutionary Computation (CEC)*, pp. 1015–1021, Vancouver, Canada, July 2016.

[18] S. N. Mishra and D. R. Lama, "A decision making model for HR management in organizations using data mining and predictive analytics," *International Journal of Computer Science and Information Security*, vol. 14, no. 5, p. 217, 2016.

[19] N. Hajiheydari, S. H. Khabiri, and M. Talafi Daryani, "A framework for data mining approach applications in HR management," *Iranian Journal of Management Sciences*, vol. 12, no. 47, pp. 21–50, 2017.

[20] Y. Zhang, S. Xu, L. Zhang, and M. Yang, "Big data and human resource management research: an integrative review and new directions for future research," *Journal of Business Research*, vol. 133, pp. 34–50, 2021.

[21] R. Etukudo, *Strategies for Using Analytics to Improve HR Management*, Walden University, Minneapolis, Minnesota, 2019.

[22] X. Wang, S. Wang, Z. Huang, and Y. Du, "Condensing the solution of support vector machines via radius-margin bound," *Applied Soft Computing*, vol. 101, p. 107071, 2021.

[23] M. Ameer, S. P. Rahul, and S. Manne, "HR analytics using power Bi visualization tool," in *Proceedings of the 2020 4th International Conference on Intelligent Computing and Control Systems (ICICCS)*, pp. 1184–1189, Madurai, India, May 2020.

[24] J. Okolita, *Moving from Instincts to Insights: Leaders Behavioral Intention to Use People Analytics*, The Chicago School of Professional Psychology, Chicago, IL, USA, 2019.

[25] D. J. M. Reddy, S. Regella, and S. R. Seelam, "Recruitment prediction using machine learning," in *Proceedings of the 2020 5th International Conference on Computing, Communication and Security (ICCCS)*, pp. 1–4, Bihar, India, October 2020.

[26] N. A. Rahmad, N. A. J. Sufri, N. H. Muzamil, and M. A. As'ari, "Badminton player detection using faster region convolutional neural network," *Indonesian Journal of Electrical Engineering and Computer Science*, vol. 14, no. 3, pp. 1330–1335, 2019.

Hindawi
International Journal of Antennas and Propagation
Volume 2024, Article ID 9850361, 1 page
https://doi.org/10.1155/2024/9850361

Retraction

Retracted: Research on Design and Application of Online English Education Platform Based on Web

International Journal of Antennas and Propagation

Received 23 January 2024; Accepted 23 January 2024; Published 24 January 2024

This article has been retracted by Hindawi following an investigation undertaken by the publisher [1]. This investigation has uncovered evidence of one or more of the following indicators of systematic manipulation of the publication process:

(1) Discrepancies in scope
(2) Discrepancies in the description of the research reported
(3) Discrepancies between the availability of data and the research described
(4) Inappropriate citations
(5) Incoherent, meaningless and/or irrelevant content included in the article
(6) Manipulated or compromised peer review

The presence of these indicators undermines our confidence in the integrity of the article's content and we cannot, therefore, vouch for its reliability. Please note that this notice is intended solely to alert readers that the content of this article is unreliable. We have not investigated whether authors were aware of or involved in the systematic manipulation of the publication process.

In addition, our investigation has also shown that one or more of the following human-subject reporting requirements has not been met in this article: ethical approval by an Institutional Review Board (IRB) committee or equivalent, patient/participant consent to participate, and/or agreement to publish patient/participant details (where relevant).

Wiley and Hindawi regrets that the usual quality checks did not identify these issues before publication and have since put additional measures in place to safeguard research integrity.

We wish to credit our own Research Integrity and Research Publishing teams and anonymous and named external researchers and research integrity experts for contributing to this investigation.

The corresponding author, as the representative of all authors, has been given the opportunity to register their agreement or disagreement to this retraction. We have kept a record of any response received.

References

[1] Y. Huang, "Research on Design and Application of Online English Education Platform Based on Web," *International Journal of Antennas and Propagation*, vol. 2021, Article ID 7648856, 10 pages, 2021.

Hindawi
International Journal of Antennas and Propagation
Volume 2021, Article ID 7648856, 10 pages
https://doi.org/10.1155/2021/7648856

Research Article

Research on Design and Application of Online English Education Platform Based on Web

Yijuan Huang

School of Foreign Languages, Nanyang Institute of Technology, Nanyang 473004, China

Correspondence should be addressed to Yijuan Huang; hyj@nyist.edu.cn

Received 20 August 2021; Accepted 8 October 2021; Published 22 October 2021

Academic Editor: Giuseppe Castaldi

Aiming at the problems of low user satisfaction and long response time in traditional online English education platforms, this paper designs a web-based online English education platform and carries out relevant application tests. With the support of the web, the hardware and software of the platform are designed. The hardware of the platform is composed of student module, teacher module, administrator module, and database module. On this basis, the *K*-means clustering method is used to cluster the learner data in the web, to determine their English level, and the collaborative filtering algorithm is combined to recommend relevant course materials for learners so as to complete the platform software design. The application test results show that the platform has the advantages of superior function and security, high user satisfaction, and short response time and has certain practical application value.

1. Introduction

With the continuous updating of knowledge, the rapid development of science and technology and the popularization of the application of network information in education, colleges, and universities are increasingly demanding to realize the modernization of teaching, so it is imperative to use computers to realize the management of online teaching. The development of information technology has brought a revolutionary impact on education. Online teaching has become an important teaching method. With the development of web technology, relevant learners can easily use multimedia network technology to build such an ideal learning environment. Web technology is not only an auxiliary tool but also a basic knowledge carrier, teaching media, and communication tool. For students and teachers, using computers to realize online teaching is a necessary condition for adapting to the requirements of the modern education system and promoting scientific and standardized teaching [1].

Different courses have different teaching modes and different teaching methods, and different students' acceptance of knowledge is also different. In the past, a teacher and dozens of students studied together in a large classroom, and the class hours were fixed, which may lead to students cannot fully digest the lessons taught by the teacher in class and teachers cannot do a timely review after class, which may lead to the negative consequences of student weariness [2]. Facing the current situation, there is an urgent need to develop a new, real-time platform to solve these problems. The emergence of online education platforms has become the best vehicle to solve these problems. Students can check the learning materials they need at any time through the Internet and consult teachers or have online discussions with classmates for learning problems anytime and anywhere so that problems can be solved in time [3].

With the continuous development of China's economy, culture, science, and technology, society has put forward higher requirements on college students' English level, and the reform of college English teaching has become one of the hot topics of social concern. English teaching reform and making full use of the web will change the past passive classroom teaching, teaching model of one-way infusion, and closed and enable it to active, two-way communication, open teaching mode, the resulting teaching materials, teaching methods and means, the effect of classroom

atmosphere, classroom teaching and social relations, and a similar series of innovations. The realization of this series of innovations is the perfect combination of the innovation of educational ideas, concepts, methods, means, modes, and technological progress [4]. With the continuous enrollment expansion of colleges and universities and the increase of the number of students, the teaching pressure of teachers is increasing. Often, the teaching method of large classes brings some adverse factors to ensure the teaching effect. As a basic course, English class is a very difficult task to help students answer questions and correct homework. The repetition rate of questions raised by different students is very high, but teachers need to answer one to one. Teachers have to face a lot of homework to correct every week, and most of these jobs are simple and repetitive work, which will take up a lot of valuable time of teachers and students. In order to ensure the quality of teaching and improve efficiency and liberate teachers, let them organize teaching better and create an online English education platform, publish teachers' teaching content on the Internet, solve common problems, and provide a convenient environment for discussion and communication between teachers and students.

Yan [5] designed an online English education platform based on small programs, mainly studied the design of online English learning small programs and the implementation of background management programs, completed the online playback of foreign teachers' voices, the corresponding text viewing, etc., through PHP + MySQL implements front-end user functions such as course purchases and small programs for back-end management functions such as course content list, WeChat member user management, audio upload, and course unlocking. However, it is found in practical application that the platform has a long response time. Reference [6] design an online English education platform based on the FBM. Through the analysis of the current status of online education platforms and online learning behavior characteristics of online learning users, combined with quantitative and qualitative analysis such as user questionnaires, interviews, and surveys, and according to the user journey map of online learners, the problems of the online learning experience of users in online education platforms are summarized. Coupled with the FBM behavior model proposed by Stanford University's Behavioral Science Professor Fogg, the model conducts interaction design from three aspects: increasing user incentives, increasing user capacity, and increasing trigger mechanisms, and the ideal application effect has a large gap. Reference [7] designed an online learning platform based on mobile Internet. Based on the design and analysis of the overall structure, functions, and execution process of the online learning system, the key technology of Android development, database design, and personalized recommendation algorithm are emphatically studied. On this basis, the system is implemented by using the Android platform and C/S structure, combined with the SQLite database. However, in the actual application, it is found that the platform has the problems of low user satisfaction and long response time, and the actual application effect is not good.

In order to solve the above-mentioned problems, this paper designs a new online English education platform based on the web and verifies the practical application effect of the platform through simulation experiments.

2. Online English Education Platform

2.1. Platform Hardware Design

2.1.1. Student Modules. Student module including teachers information consulting, courses available announcements, course learning, course information consult, course assignments and BBS discussion, teaching video review, personal Settings, registration, information query, interactive online grammar teaching, online discussion, and student module work process is shown in Figure 1.

Firstly, students submit their registration requests to the platform. Secondly, the administrator can view the user registration request in the module and judge whether it is authorized according to the registration information submitted by the student. If authorized, the last student will be sent after receiving the student email notification. After you log in successfully, you can log in with the application account and password. On the platform, students need to start course learning, and then enter the course learning environment to learn. Students can access the course bulletin board to view the latest announcements issued by the teacher of the course; open courseware and conduct online course study. The students can go to the course assignments section, select the assignments that the teacher has posted, do them online or download them, and then submit them. The students can also choose a test paper for online testing; if they encounter problems, they can enter the online discussion and directly communicate with other students or teachers. They can also post their problems in the course forum, discuss common problems with other students, and set their own personal password. Information about courses, assignments, tests, and grades can also be searched.

2.1.2. Teacher Module. Teacher module functions include teaching application, course announcement, course file maintenance, course preview: preview their own taught courses, course Q&A, course question bank management, course work, personal setting, registration application, information query, homework query, test paper management, and video resources. The workflow of the teacher module is shown in Figure 2.

From the analysis of the figure above, it can be seen that firstly, teachers submit registration requests to the platform, and secondly, administrators can view the registration requests of users and decide whether to grant authorization according to the registration information submitted by teachers. If authorized, a notice will be sent to the teacher's e-mail. After receiving the notice, the teacher can log in to the platform with his/her own account and password [8]. The procedure is the same as when a student submits an application. After the successful login, the first thing the teacher needs to do is to choose the course to teach. If it is the first time for the teacher to use the course,

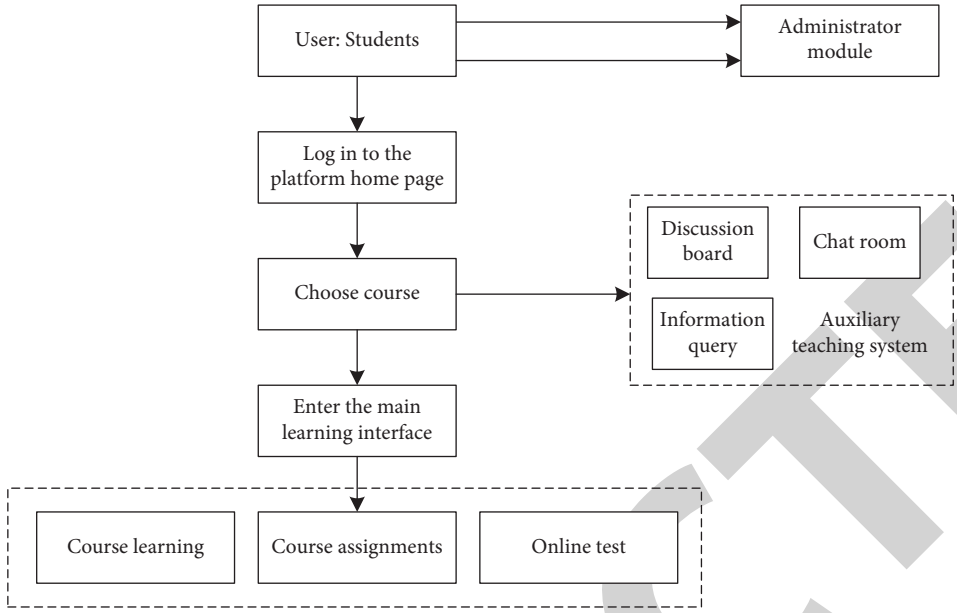

Figure 1: Workflow of student module.

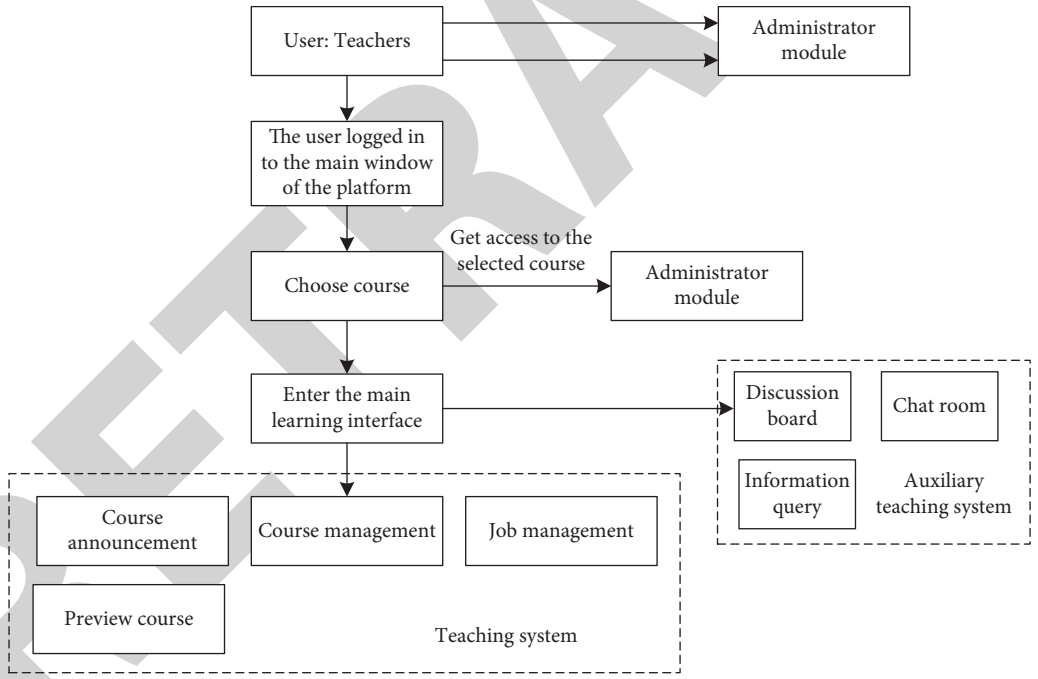

Figure 2: Workflow of teacher module.

he/she needs to apply to open the course and fill in some information about the course before completing the application. By entering the course maintenance module, teachers can directly maintain the course files; upload, download, and delete files; or upload a compressed package and decompress it [9]. They can also set the first file executed in the hypertext courseware and can browse their own courses, through the entry of the question bank maintenance module and the establishment and modification of the course question bank. They can maintain the homework library, correct the homework online, respond to students' questions, manage the articles in the course forum, and discuss with them. They can also set up their own personal password and find out about courses, assignments, tests, and grades.

2.1.3. Administrator Module. Administrator module functions include student management, announcement management, administrator management, teacher management,

course library management, test paper library management, question bank management, interactive plug-in management, professional information management, test score management, homework score management, and information query. The administrator module workflow is shown in Figure 3.

The administrator can log in to the platform management module, manage students, teachers, and administrators by entering the user management, add and delete users, and authorize the registration application of students or teachers. Through the announcement management module, the administrator can publish, modify, and delete the announcement and can view or delete the announcement of all courses. Through the course management module, the administrator can authorize the teacher's course application or delete a course from the system [10]. Through the basic table management module, the administrator can maintain the basic table of the platform through the question bank, job bank, test paper bank management respectively to the question bank, job bank, and test paper bank to maintain.

2.1.4. Database Module. Various kinds of data need to be stored and managed in the database of a web-based online English education platform. Database design also affects the design of the online English education platform, a lot of data according to certain organizations together in the database; the database not only can provide storage and maintenance functions but also can provide retrieval data function so that the platform can be more accurately extract the needed information and more convenient than the original more timely, [11]. Therefore, the development and operation of online English education platform are directly affected by the database; database design is a very important aspect of the online English education platform development and design.

Based on the analysis of entities, the relationship between the tables in the database is formed. According to the corresponding relational model, the physical design of the database is carried out, and the data design software Power Designer 10.0 is used for the physical structure design of the database [12]. The database table of online English education platform will be designed according to Table 1.

2.2. Platform Software Design. On this basis, the *K*-means clustering method is used to cluster the learner data in the web, to determine their English level, and the collaborative filtering algorithm is combined to recommend relevant course materials for learners so as to complete the platform software design.

2.2.1. Classification of Student Grades Based on K-Means Clustering. Clustering is to find out the similarities between some data from a large number of data and gather these familiar data together. This process is usually called clustering. The data objects in one cluster have similar characteristics, but the data objects in different clusters have no correlation with each other. The purpose of clustering is to classify and study data objects, find out the characteristics of a group of objects, and draw research rules or conclusions without studying each object individually so as to save research manpower or material resources. In education, cluster analysis of learners is usually used to distinguish different learning groups, outline the basic characteristics of each group, reveal the characteristics of each group, conduct in-depth analysis of each group, arrange personalized curriculum, implement personalized education, and improve the learning efficiency of each group [13]. There are many kinds of clustering algorithms, which can be roughly divided into a split clustering algorithm, hierarchical clustering algorithm, density-based clustering algorithm, mesh-based clustering algorithm, and so on. The algorithm adopted in this paper is one of the split clustering algorithms: *K*-means clustering algorithm. The core idea of the K-means clustering algorithm is K, given the number of clusters in advance, find K data objects as the initial cluster centers, calculate other centers that enter the data cluster through a certain method, calculate the average value of each cluster, and then change to the cluster center value until the cluster center gets fixed. [14].

In this paper, *K*-means clustering algorithm is adopted to cluster learners on the English online education platform, scientifically determine their English level, and then arrange appropriate learning content for them combined with the collaborative filtering method. Before students study, they have to take a proficiency test, which includes five parts: listening score, speaking score, reading score, writing score, and total score.

Common European Framework of Reference for Languages (CEFR) was developed by the Council of Europe and consists of six levels, which are currently used as a reference standard in the field of language learning and teaching. Each level represents the level that a student should achieve. This classification standard is adopted in the English online education platform studied in this paper [15]. The six grades are *A*1, *A*2, *B*1, *B*2, *C*1, and *C*2. Table 2 describes the language proficiency required for each level [16].

(1) Data Collection. On most English online education platforms, students take a proficiency test to determine their current English level before the formal study. In the process of *K*-means clustering, a certain number of students' level test data were randomly selected from the database of the English online education platform in the study. The level test data were divided into four modules, namely listening, speaking, reading, and writing, and the score of each module was calculated on a scale of 100. At the same time, the basic data of these students should be selected as the analysis basis of cluster mining results, including age, gender, occupation, position, and study reasons. The sample of students should be limited according to the purpose of the study. Since this paper mainly studies online learning, the learning objects are all adults. The age limit of the selected research objects is 18 years or above. The ranges of occupations, positions, and study reasons are all based on the classification criteria in the selected cases.

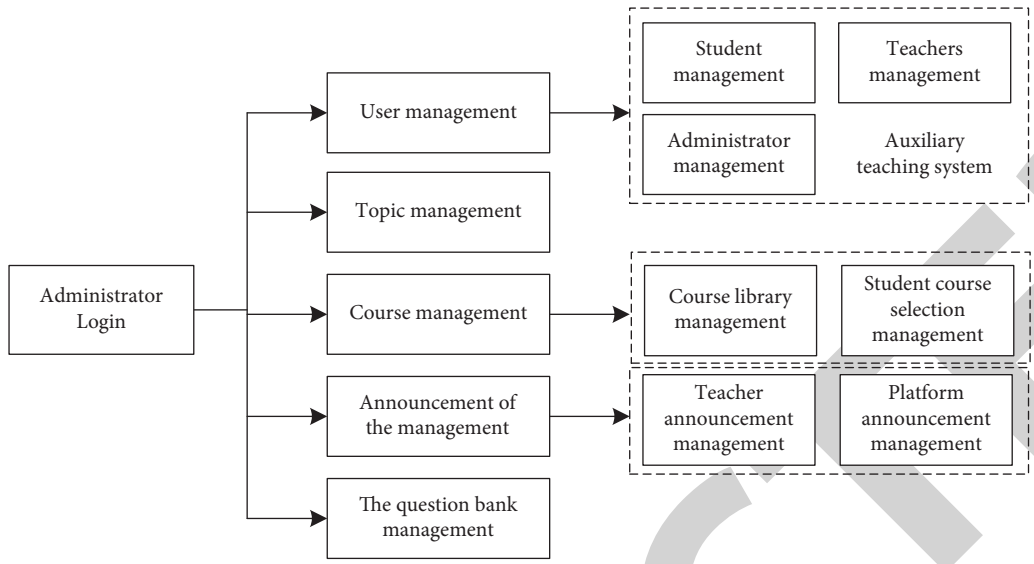

Figure 3: Administrator module workflow.

Table 1: Overall design table of database physical structure.

The name of the table	Instructions
Users	This table stores administrator and teacher information
Student info	This table stores basic information about students
Exam manage	This table holds information about each test schedule
Subject info	This table stores course information for each major
Paper manage	This table holds information about each test
Score manage	This table holds information about students' scores for each test
Single questions	This table holds all the multiple-choice information
Mul questions	This table holds all the multiple-choice information
YN questions	This table holds all true or false information
Fill questions	This table holds information about all the fill-in-the-blank questions

YN: yes or no.

Table 2: Six levels of CEFR.

Level	Ability to describe
*A*1 (initiation and discovery stage)	Students can understand and use popular and commonly used phrases to make simple statements to meet specific requirements. Students are able to introduce themselves, introduce a person, and ask a person questions about that person where they live, their relationships, and what they own.
*A*2 (intermediate and continuation)	Students can understand individual sentences and common phrases that describe simple activities personal and family information, shopping, familiar environment, and work. Students are able to carry out simple and direct information exchange on familiar and habitual content while completing simple and habitual tasks.
*B*1 (entry stage)	Students can understand the general meaning when the other person speaks clearly and in standard terms and when the speech is about familiar topics such as work, study, and hobbies. Students are able to describe an event, describe a desire or goal, and give short reasons for, or explain, a plan or idea.
*B*2 (advanced or independent stage)	Students are able to understand the main points of a complex text, both concrete and abstract, and to discuss their own areas of expertise. Students are able to express their views clearly and in detail on a wide range of topics, present opinions on current issues, and express the benefits and disadvantages of something.
*C*1 (autonomous stage)	Students can understand many articles with long and large vocabularies and understand the hidden meanings. Students are able to express their ideas freely and fluently without struggling to find the right words to use. Students are able to articulate their ideas on complex topics in a clear and well-organized manner, speaking in a well-organized, articulating, and coherent manner.
*C*2 (mastery stage)	Students can understand almost everything they read or hear without struggling. Students are able to make organized summaries of a variety of information from written or oral sources. Students can express their opinions freely, fluently and accurately, and can use different levels of words to express themselves.

The flowchart of applying *K*-means clustering in the English online education platform is shown in Figure 4.

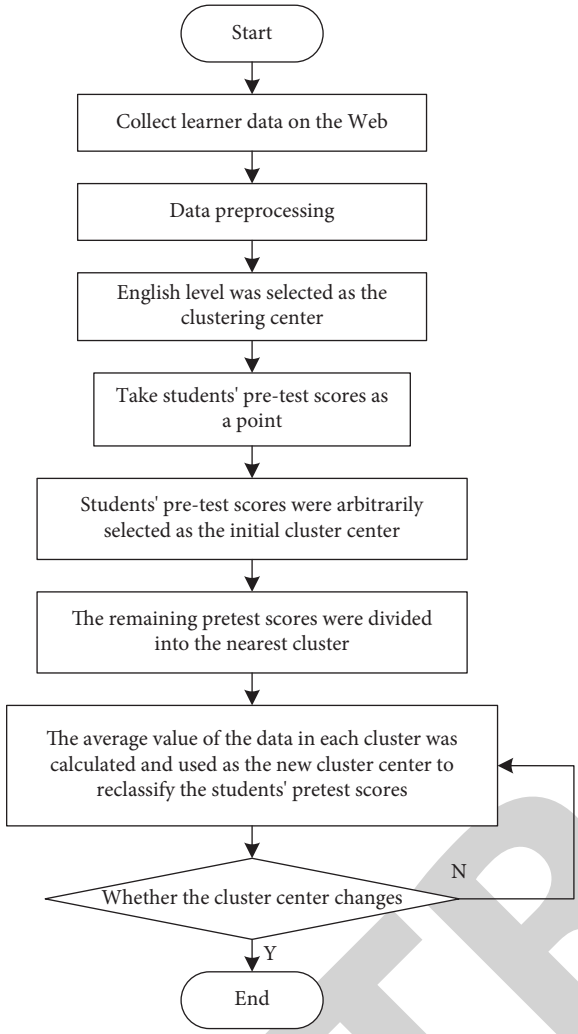

Figure 4: Flowchart of K-means clustering.

(2) Data Preprocessing. After obtaining the data of learners' level test, the next step is to preprocess the data, make its format meet the requirements of the clustering algorithm, and then store it. The data used for K-means clustering in this paper are the scores of listening, speaking, reading, and writing sections of students' proficiency tests, and these data will be counted according to the percentage system in the clustering analysis. In addition, according to the case studied, the English level must be divided into certain standards. English is divided into six levels, which are entry, elementary, intermediate, intermediate, advanced, and proficient levels. English proficiency is the number of cluster categories, and the cluster category a student belongs to is the level of English proficiency [17].

(3) Analysis of Clustering Results. According to the clustering results of the previous step, the clustering analysis is carried out on the learners, the English level of the learners is determined, and the learning content suitable for their own level is arranged for them so that the learning effect will be relatively significant [18]. In addition, the clustering results can also be applied in the organization of learning content, combining with the basic situation of learners to organize personalized learning content for them. After clustering learners, it can also help teachers arrange students' oral classes or other teaching activities [19].

2.2.2. Course Recommendation Based on Collaborative Filtering Algorithm. Based on users' learning records, this paper analyzes the similarity between users and evaluates users' interest preference for unlearned courses according to similar users' learning conditions [20]. The similarity between users will be calculated according to the user-item matrix. The similarity calculation formula of user u and user v is as follows:

$$\mathrm{sim}(u,v) = \frac{r_u r_v'}{\sqrt{(r_u r_u')(r_v r_v')}}, \tag{1}$$

where r_u and r_v, respectively, represent two users' rating vectors for all items and r_v' and r_u', respectively, represent the transpose matrix of two rating vectors for similarity calculation [21].

In this paper, the nearest neighbor recommendation algorithm based on users is mainly used, that is, the scores of users and items are predicted according to the scores of the K users most similar to the target users [22]. The similarity calculation uses cosine similarity, and the size of K values will be determined through experiments. After the similarity between two users is obtained, the collaborative filtering preference value of user u for course i is defined as follows, and the final result is obtained by weighting the scores and similarity of the K users. The specific calculation formula is as follows:

$$\mathrm{pref}_{\mathrm{CF}} = \frac{\sum_{v=1}^{K} \mathrm{sim}(u,v) \cdot r(u,v)}{\sum_{v=1}^{K} \mathrm{sim}(u,v)}, \tag{2}$$

where $r(u,v)$ represents user u's rating of course i.

By calculating the similarity between the user feature vector and the course feature vector, the preferences of users to courses can be obtained. We define the feature vectors of users and the theme-based user preferences as follows:

$$\theta_u = \frac{1}{u}\sum_{i=1}^{n} \theta_i,$$
$$\mathrm{pref}_{\mathrm{LDA}} = \frac{\theta_u \theta_i'}{\sqrt{(\theta_u \theta_u')(\theta_i \theta_i')}}, \tag{3}$$

where θ_i represents the feature vector of course i; when calculating the user's feature vector θ_u, n represents the number of courses that the user has learned [23].

The popularity characteristics of a course are calculated by taking into account the number of students studying the course, the number of users who rate it, and the number of students who rate it. In the cloud classroom data, general courses are rated on a scale of 1 to 5. Assuming that c_i represents the number of students in course i, s_i represents the number of students marking course i, and d_i represents the average score of course i, the course popularity can be calculated as follows:

$$\text{var}_{\text{HOT}}(u,i) = c_i + s_i \cdot d_i. \quad (4)$$

Since the absolute value of the popularity of courses is not of practical significance, but the relative value between courses is more important; after calculating the popularity of each course, it is necessary to rank the scores from highest to lowest [24]. Because the number of students in courses under different classifications varies greatly, it is of little significance to sort all courses in the data set, so the sorting is carried out separately for courses under each secondary classification [25]. After the sorted list is obtained, the following formula is used to calculate the final course popularity eigenvalue to be used:

$$\text{pref}_{\text{HOT}}(u,i) = 1 - \frac{R_i}{N}. \quad (5)$$

where N represents the total number of courses in the corresponding category, R_i represents the ranking of course i, and the course with R_i as 1 is the course with the highest value, that is, the most popular course in this category. After this calculation, the course popularity eigenvalues in the range of 0 to 1 can be obtained [20].

Due to the lack of personal information of course lecturers, it is impossible to make a good judgment on their influence [26]. However, lecturers have rich data in their course records. Therefore, this paper will quantify the influence of lecturers mainly according to the popularity of their courses. The lecturer impact factor is defined as follows:

$$\text{pref}_{\text{TEACH}}(u,i) = C \cdot \frac{1}{n} \sum_{k=1}^{n} \text{pref}_{\text{HOT}}(u,i), \quad (6)$$

where n for the total number of other courses i; course instructor name C is about the relationship between the user and the lecturer. The relationship between users and mentors is usually the degree of attention, of course, there are not three types. The three relationships reflect the trust of potential users to the mentor, so we also divide the value of the coefficient C into different levels (2.0, 1.5, 1.0).

The above four features influencing recommendation results are summarized from the original data, and they are extracted quantitatively. Next, the ranking function will be used to integrate these features and calculate the predicted score of user u to course i. The calculation method is to carry out a weighted linear combination of these features. In this paper, the weight calculation of the combination function is modeled as a ranking learning problem. In the course recommendation problem, there are only two relationships between users and the course: learning and not learning. For this binary scoring problem, the ranking SVM method is used to carry out the ranking learning [27].

For a given user and object, each pair of relationships will be represented as a vector x in which each dimension corresponds to different extracted features, and the dimension of the vector is the number of features [28]. The sorting function $f(x) = wx$ and w is the weight vector, which is also the parameter to be trained. In the model training stage, according to the user's learning situation of the course in the training data, the two courses are combined into item pairs. The representation of the i-th group of data in the training set is as follows:

$$\left(x_i^{(1)} - x_i^{(2)}, y_i\right), \quad i = 1, 2, \ldots, n. \quad (7)$$

Each set of data in the training set is for the same user, where n is the number of samples in the training set. The value of marking value y_i of the training sample includes +1 and −1. For two items $x^{(1)}$ and $x^{(2)}$, the difference of their eigenvectors will be used to mark the samples. If the user has studied course 1 but not course 2, it can be assumed that course 1 should precede course 2 in the sorted list, so $x^{(1)} - x^{(2)}$ is marked as a positive sample and $x^{(2)} - x^{(1)}$ as a negative sample. In the same way, all the courses learned by the users in the training sample are grouped with the courses not learned. If the user has learned or not learned the two courses, the training sample will be ignored because the ordering relationship cannot be judged [29].

After marking the training samples, the SVM model was used to conduct sorting training on them, and its loss function was set as follows:

$$L(i) = \min \sum_{i=1}^{n} \max\left(1 - \omega^T\left(x_i^{(1)} - x_i^{(2)}\right), 0\right) + \frac{1}{2}\|\omega\|^2. \quad (8)$$

After learning and training the sorting function, the model can be used to get the sorting situation of the list of courses to be recommended, and then the courses with the highest ranking can be selected and recommended to users.

3. Application Test and Analysis

In order to verify the practical application effect of the web-based online English education platform designed in this paper, the application test is carried out.

3.1. Application Effect Test. The platform is deployed on an IBM System X3200 M2 (CPU: Intel Xeon 2.83 GHz, DDR2 2 GB), Microsoft Windows Server 2003. Microsoft's stress test software was used to simulate 6000 users to stress test the main page of the platform, and the main performance indicators of the monitoring server are shown in Table 3.

The functional test results are shown in Table 4.

The main areas for security testing of the platform are: you must log in with a valid user name and password, and there is no background page that can be directly viewed without login. The user name and password are sensitive to uppercase and lowercase letters, and the user password is stored in ciphertext in the database. The platform has a login timeout limit. In other words, a user does not perform any operations within 15 minutes after logging in to the platform. In this way, resources can be saved. The platform has log files that can be traced.

From the perspective of the function of the platform, the platform correctly realizes the functional requirements of the demand analysis and can complete the course management, user management, teaching resources

Table 3: Main performance specifications and detection values of the server.

Counter	Minimum value	Maximum value	Average
%Processor time	3.9%	2.%	11.6%
Memory available MBytes	1287	1296	1291
Requests current	212	687	411
Request execute time	0	15 ms	2 ms
Request wait time	0	0	0
Request queued	0	0	0

Table 4: Functional test results.

Test the name	The test content	The test results	Conclusion
User authentication	Log in as administrator, teacher, and student respectively. Different identities can access the corresponding operation page.	Can fully verify the registered users, accurately judge the permission, and enter the corresponding operation page.	Implement design functions
File upload and browse	Upload picture information and can query and browse.	Multiple formats of files can be uploaded. By querying the filter, you can view the information about the uploaded portfolio according to the user permission.	Implement design functions
Homework upload and browse	Teachers and students log in, teachers upload, and students browse.	Teachers publish homework; students view and download	Implement design functions
Student testing module	Students log in to test; the platform can automatically set questions.	The platform can automatically set questions.	Implement design functions

Table 5: Satisfaction test results.

Grouping situation	Education platform based on small program	Education platform based on FBM behavior model	Education platform based on web
Group 1	6.6	7.5	9.6
Group 2	6.1	7.8	9.5
Group 3	5.9	8.2	9.4
Group 4	6.3	8.6	9.2
Group 5	6.8	8.4	9.4
Group 6	5.9	7.1	9.3
Group 7	6.4	7.1	9.1
Group 8	6.1	7.5	9.7
Group 9	5.5	8.2	9.3
Group 10	6.9	8.3	9.1
Average	6.3	7.9	9.4

management, homework management and online testing, and other functions. From the use of the platform, the existing platform interface is beautiful; the operation is simple; and the consistency of query, delete, and modify operation-related prompt information and the correctness, understandability, and consistency of input limit prompt information is realized. From the perspective of platform security, security issues under the control of the existing platform, without logging in, directly entering the URL of a page cannot open the corresponding page, indicating that the platform is safe and stable, and can effectively assist English teaching through the network. This can improve teaching efficiency and effectively reduce the economic burden of teachers.

3.2. Comparison Test. The education platform based on a small program, the education platform based on the FBM behavior model, and the education platform based on the web are taken as the experimental platforms, and the user satisfaction and response time of different platforms are tested as the evaluation indicators.

A total of 1,000 volunteers were selected as the experimental subjects. They logged in to different online English education platforms as administrators, teachers, and students and conducted functional tests. The corresponding test scores were given, with the highest score being 10 and the lowest score being 0. The valid evaluation results are divided into 10 groups, and the user satisfaction test results of the three platforms are shown in Table 5.

According to the data in Table 5, the average user satisfaction of the education platform based on a small program is 6.3, which is the lowest among the three platforms. The average user satisfaction of the education platform based on the FBM behavior model is 7.9, and that of the education platform based on the web is 9.4, which is the highest among the three platforms. It shows that the platform is more popular and recognized by users.

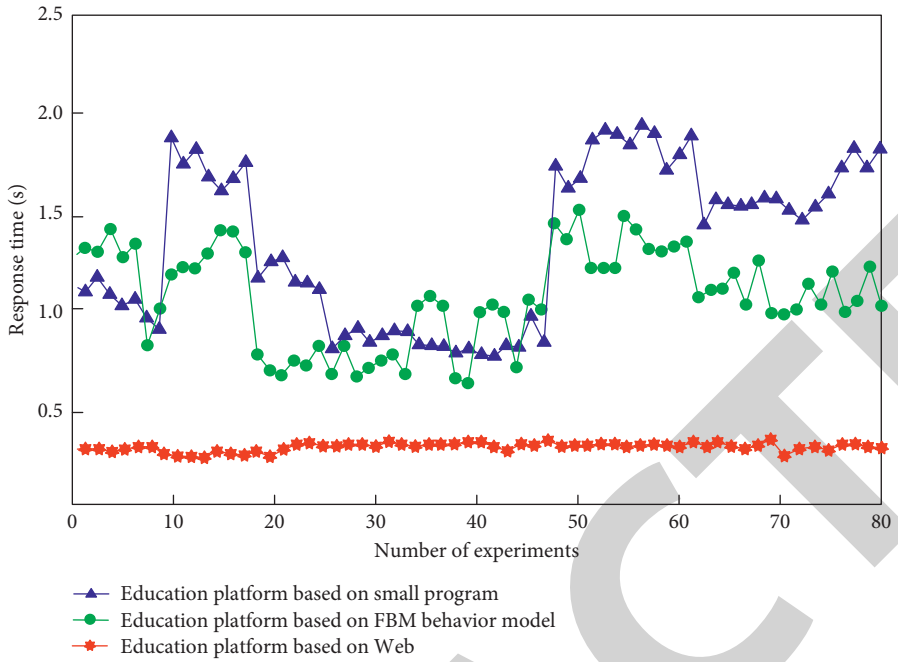

Figure 5: Response time comparison results.

On the basis of the above, the response time of the education platform based on a small program, the education platform based on the FBM behavior model, and the education platform based on the web is compared. The specific comparison results are shown in Figure 5.

By analyzing the data in Figure 5, it can be seen that the response time of the education platform based on small program varies between 0.6 s and 1.6 s; the response time of the education platform based on the FBM behavior model varies between 0.8 s and 2.9 s; and the response time of the education platform based on the web is always below 0.4 s, indicating that the response speed of the platform designed in this paper is faster. The practical application results are better.

4. Conclusion

With the rapid development of the Internet, people pay more and more attention to various applications based on the Internet. In the field of education, traditional teaching methods have changed dramatically. The modern education mode under the web environment appeared. Computer-aided instruction (CAI) is a new educational technology. With the development of educational reform and the advancement of social information, it is required to popularize CAI vigorously. Online English education platform has broken the time and space limit and regional limit of traditional education and can make full use of educational resources. Therefore, the online English education platform has become an important practical content and one of the research directions of educational informatization, and it is also an important and urgent subject to promote the process of educational informatization. Therefore, increasing web-based teaching and developing various kinds of information teaching software have become an increasing concern of educators. Therefore, this paper developed a web-based online English education platform. The practical application results show that the platform has better functions and security, and compared with traditional platforms, with high user satisfaction and short response time, the platform can fully solve the problems existing in the traditional platform, and the practical application effect is better.

Data Availability

The data used to support the findings of this study are available from the corresponding author upon request.

Conflicts of Interest

The authors declare that they have no known competing financial interests or personal relationships that could have appeared to influence the work reported in this paper.

Acknowledgments

No funding was used in this study.

References

[1] L. A. Zhi, "Simulation of English education translation platform based on web remote embedded platform and 5G network-ScienceDirect," *Microprocessors and Microsystems*, vol. 81, no. 1, pp. 1–12, 2020.

[2] Z. Sun, M. Anbarasan, and D. P. Kumar, "Design of online intelligent English teaching platform based on artificial intelligence techniques," *Computational Intelligence*, vol. 86, no. 2, pp. 235–246, 2020.

[3] H. Chen, "The influence of online English writing platform on writing metacognitive strategies and writing

Hindawi
International Journal of Antennas and Propagation
Volume 2023, Article ID 9786725, 1 page
https://doi.org/10.1155/2023/9786725

Retraction

Retracted: Construction and Application of Media Corpus Based on Big Data

International Journal of Antennas and Propagation

Received 19 December 2023; Accepted 19 December 2023; Published 20 December 2023

This article has been retracted by Hindawi following an investigation undertaken by the publisher [1]. This investigation has uncovered evidence of one or more of the following indicators of systematic manipulation of the publication process:

(1) Discrepancies in scope

(2) Discrepancies in the description of the research reported

(3) Discrepancies between the availability of data and the research described

(4) Inappropriate citations

(5) Incoherent, meaningless and/or irrelevant content included in the article

(6) Manipulated or compromised peer review

The presence of these indicators undermines our confidence in the integrity of the article's content and we cannot, therefore, vouch for its reliability. Please note that this notice is intended solely to alert readers that the content of this article is unreliable. We have not investigated whether authors were aware of or involved in the systematic manipulation of the publication process.

Wiley and Hindawi regrets that the usual quality checks did not identify these issues before publication and have since put additional measures in place to safeguard research integrity.

We wish to credit our own Research Integrity and Research Publishing teams and anonymous and named external researchers and research integrity experts for contributing to this investigation.

The corresponding author, as the representative of all authors, has been given the opportunity to register their agreement or disagreement to this retraction. We have kept a record of any response received.

References

[1] B. Yin and L. Fu, "Construction and Application of Media Corpus Based on Big Data," *International Journal of Antennas and Propagation*, vol. 2021, Article ID 9317018, 7 pages, 2021.

Hindawi
International Journal of Antennas and Propagation
Volume 2021, Article ID 9317018, 7 pages
https://doi.org/10.1155/2021/9317018

Research Article

Construction and Application of Media Corpus Based on Big Data

Bochun Yin[1] **and Lei Fu**[2]

[1]*School of Foreign Languages, Changsha University, Changsha 410205, China*
[2]*The First Clinical College, Changsha Medical University, Changsha 410205, China*

Correspondence should be addressed to Bochun Yin; z20200811@ccsu.edu.cn

Received 17 August 2021; Revised 17 September 2021; Accepted 28 September 2021; Published 21 October 2021

Academic Editor: Fangqing Wen

Aiming at the problems of poor data quality and low application rate in the construction of existing media corpus, this paper proposes the construction and application research of media corpus based on big data. Media corpus data are collected, the data are divided into four categories, the heuristic data item column sorting algorithm is introduced to sort all collection processes, the minimum value of data item collection rate is determined, on this basis, the maximum value of quantity in media corpus is determined, and data collection is realized in media corpus data through sliding window. Then, the state characteristics and probability distribution of feature data are determined by dynamic Bayesian network, the relationship between the state variables and dimensions of media corpus data is determined, and the media corpus data state is processed by component to complete the preprocessing of media corpus data; finally, through the application research of storage and encryption of the designed database through big data technology, the storage structure data and encryption secret key are designed to realize the construction and application of media corpus. The experimental results show that the data quality of the media corpus constructed by the proposed method is high, and its application rate has been improved to a certain extent.

1. Introduction

With the rapid development of Internet technology, database is becoming more and more important in people's mind. As the core of future technology development, database has attracted much attention. Different software companies have developed different database software, and the data models of the same software are also different. Because the data models are not unified, it is difficult to transmit data between database software. Data conversion between heterogeneous databases is an important means needed at present. The conversion between heterogeneous data can effectively improve work efficiency and reduce cost [1]. The timeliness of language database is an important attribute of data. In data mining, data analysis, and data value-added applications, accurate data timeliness determines the effect of a series of algorithms such as time series analysis, association, and recommendation. Relevant scholars have studied the problem of data quality by means of direct observation, social investigation, and theoretical derivation. The properties that have a great impact on data availability are accuracy, integrity, consistency, timeliness, and entity identity. In the field of business data, due to the change of customer information, 2% of business data are outdated every month. A large number of imprecise data are filled in the data set. If you cannot identify which is the latest, data query may return wrong results, and data analysis may produce contrary conclusions, followed by the decline of data quality and data value. In the era of big data, people's various data are distributed in various platforms and systems, forming data islands. The problems caused by inaccurate data timeliness and outdated data are becoming more and more serious. In the era of big data and artificial intelligence, personal big data contain immeasurable social and economic value. The personal data banking model is a new model that can effectively sort and integrate personal data, improve the quality and value of personal data, enhance the controllability and availability of personal data, and effectively protect personal data privacy [2]. In the process of data aggregation, due to the high dispersion of personal data at the same time, personal data are typical dynamic data, and various data reflecting

personal attributes and status are constantly changing. This feature is also the biggest challenge in the process of personal data cleaning. In the data mode, in order to ensure data quality and improve data value, it is necessary to gather data from many sources, and its time attribute is often inaccurate [3]. For some attributes of data, different times correspond to different values or states, such as a person's educational background change and marital status change. If the timestamp is incomplete or inaccurate, it is impossible to determine the sequence of records, which will bring great difficulties to data value-added applications. Therefore, how to improve the construction effect of media corpus and widely apply it has become the focus of current research [4]. Therefore, relevant researchers have conducted research on the construction of media corpus and obtained some results.

Literature [5] designed a database selection based on the hesitant language information aggregation algorithm and studied the construction and application of media corpus. In order to improve the efficiency of database selection, a database selection method based on the hesitation language multiattribute group decision-making algorithm is proposed for multiattribute group decision-making. Firstly, a database selection model based on generalized hesitation language Heronian average (GHLHM) operator is constructed; secondly, Archimedean norm is introduced into hesitation language environment, and a new hesitation language algorithm is defined; thirdly, based on the new algorithm and Heronian average, GHLHM operator is proposed, some basic properties of GHLHM operator are discussed, several common operator forms of GHLHM operator are studied, and generalized hesitant language weighted Heronian average (GHLWHM) operator is proposed; and finally, a new hesitant language multiattribute group decision-making method based on GHLWHM operator is constructed and applied to database selection. Experiments show that this method can realize the comprehensive optimization and ranking of database performance and has a wide application prospect in other fields. However, this method still needs some improvement in order to consider too much data security and storage occupancy. Literature [6] designed a method for automatic conversion of heterogeneous data in language database. This method provides an important method and means to operate the database for the database management system. In view of the problems of long data conversion time, low information utilization, and conversion accuracy after data conversion in the traditional data conversion method, a new heterogeneous data conversion method is proposed, which is based on the automatic heterogeneous data conversion method in the language database. The language data with the same collection cycle are placed in the corresponding data column, the heuristic algorithm is introduced to sort the data column, and each data item is adjusted according to the arrangement order to complete the automatic heterogeneous data collection in the language database. The experimental results show that the proposed method can effectively reduce the time-consuming of data conversion and improve the utilization and accuracy of data conversion. However, the amount of data and safety performance in the construction of this method has not been effectively controlled, and there are some deficiencies. Through the investigation of 33 Arabic language corpora, reference [7] found that although Arabic language corpus has made great progress, the Saudi dialect corpus still needs to be further expanded. This paper makes a contribution to the literature of SD corpus by creating the Saudi Corpus (KSUSC) of King Saud University, the largest corpus in Saudi Arabia. The total number of words in this corpus is +1 B, in which SD words are +119 M. KSUSC is not only the latest and largest SD corpus in China but also a corpus with rich and diverse contents, covering 26 fields from 5 different sources. Reference [7] proposed a method to semiautomatically construct a corpus that includes Japanese youth slang called Wakamono Kotoba. The process of semiautomatic corpus construction is composed of the first step which is automatic collection of example sentence, the second step is tag annotation to collected sentences, and the final step is manually modifying tag and noise reduction.

Therefore, this paper proposes a media corpus construction and application research method based on big data. Firstly, the media corpus data are collected, the data are divided into four categories, the heuristic data item column sorting algorithm is introduced to sort the whole collection process, and the minimum value of the collection rate of the data item is determined. On this basis, the maximum value of the number in the media corpus is determined, and the data collection in the media corpus data is realized through the interaction window; then, the state characteristics and probability distribution of feature data are determined by dynamic Bayesian network, the relationship between the state variables and dimensions of media corpus data is determined, and the media corpus data state is processed by component to complete the preprocessing of media corpus data; finally, the designed database is effectively applied through big data technology. The technical route of this paper is as follows:

(i) Step 1: collect media corpus data, divide the data into four categories, introduce the heuristic data item column sorting algorithm to sort all collection processes, determine the minimum value of data item collection rate, on this basis, determine the maximum value of quantity in media corpus, and realize data collection in media corpus data through interactive window.

(ii) Step 2: determine the state characteristics and probability distribution of feature data through dynamic Bayesian network, determine the relationship between media corpus data state variables and dimensions, process the media corpus data state by components, and complete the preprocessing of media corpus data.

(iii) Step 3: effectively apply the designed database through big data technology.

(iv) Step 4: analysis of the experimental process.

(v) Step 5: experimental conclusions and future prospects.

Our contribution includes the following three points:

(1) Aiming at the problems of poor data quality and low application rate in the construction of existing media corpus, this paper proposes the construction and application research of media corpus based on big data.

(2) Media corpus data are collected, the data are divided into four categories, the heuristic data item column sorting algorithm is introduced to sort all collection processes, the minimum value of data item collection rate is determined, and on this basis, the maximum value of quantity in media corpus is determined.

(3) The state characteristics and probability distribution of feature data are determined by dynamic Bayesian network, the relationship between the state variables and dimensions of media corpus data is determined, and the media corpus data state is processed by component to complete the preprocessing of media corpus data.

2. Research on the Media Corpus Construction

2.1. Media Corpus Data Collection. Data collection of media corpus is the most critical mitigation in the construction process. Only complete and massive data support can make the construction of media language database more complete. Only by fully ensuring the real-time and effectiveness of the collected data can we fully understand the operation status of the whole media corpus and better apply it [8].

Data items in the media corpus are composed of different separate cells, each with their own attribute characteristics. Therefore, in the process of building the media corpus, setting up the collected data consists of four categories. Express its attributes based on different language data as $S/T/T_d/D$. Among them, S represents the data in the media corpus, T represents the sampling cycle, T_d represents the heterogeneous data acquisition time delay, and D represents the collection of data items in the media corpus. Heuristic data items are introduced to the column sorting algorithm to sort all the collection processes, and then the common relationship of different data items is sorted. In the process of sorting, the collection rate of "reused" data items is the lowest, that is:

$$A = \left(a_{ij}\right)_{n\times m}. \tag{1}$$

After obtaining the most effective frequency of data acquisition in the media corpus data, it is necessary to determine the number of data items required by the media corpus [9], and the maximum number of media corpus obtained is as follows:

$$R_{\max} = \sum_{j=1}^{m}\left(\sum_{i=1}^{n} a_{ij} - 1\right). \tag{2}$$

After the quantity of data in the media corpus data is determined, reflect the data relationship existing in the database and reflect the data relationship through the relationship matrix to obtain the following:

$$B = \left(x_{ij}\right)_{n\times m}. \tag{3}$$

According to the determined data relationship matrix in the media corpus data, the data collection in the media corpus data is completed through the sliding window, that is:

$$R = \sum_{j=1}^{m}\sum_{i=1}^{n} c_{ij}\delta_{ij} - 1. \tag{4}$$

In the process of media corpus construction, first collect the data of media corpus, divide the data into four categories, introduce the heuristic data item column sorting algorithm to sort all the collection processes, determine the minimum value of data item collection rate, on this basis, determine the maximum value of quantity in media corpus, and realize data collection in media corpus data through interactive window.

2.2. Media Corpus Data Preprocessing. According to the media corpus data obtained above, there are many data in the data collected in the media corpus, and there are great differences between the data, which affects the construction of the media corpus. Therefore, it is necessary to preprocess the media corpus data. In the obtained media corpus data, the characteristics of media corpus data cannot become the key data due to the rapid change of media corpus data [10]. Therefore, this paper preprocesses the differences in media corpus data. In this paper, dynamic Bayesian network is used to preprocess feature data.

Assume that the p-dimensional implied state variable in the media corpus data can be expressed as follows:

$$P = \{p_1, p_2, \ldots, p_{n-1}\}. \tag{5}$$

Here, the probability distribution is expressed as follows:

$$Q = \{q_1, q_2, \ldots, q_n\}. \tag{6}$$

The relationship between the media corpus data state variables and the dimension can be expressed as follows:

$$G(P,Q) = \varepsilon\prod_{i=1}^{P-1} P\left(p_n \mid q_n\right)Q\left(p_n \mid q_n\right). \tag{7}$$

In formula, $P(p_n \mid q_n)$ represents the state transition probability distribution, $Q(p_n \mid q_n)$ represents the actual information volume of the media corpus data, and ε represents the initial state of the media corpus data.

Based on this basis, the media corpus data state is processed, and the preprocessing of the data characteristics of the media corpus is completed.

$$D_i(u) = \frac{1}{N}\sum_{i=1}^{N} Q(t). \tag{8}$$

In formula, $D_i(u)$ represents the acquired media corpus data.

The media corpus data preprocessing process is shown in Figure 1.

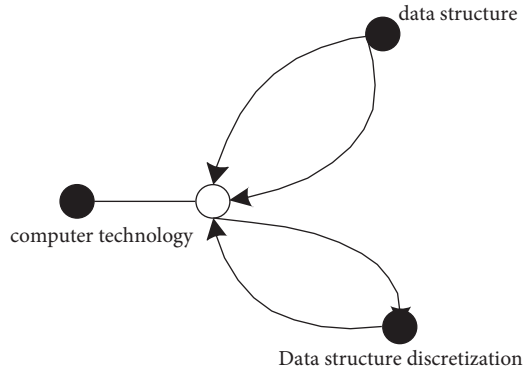

Figure 1: Data preprocessing process of the media corpus.

In the media corpus data preprocessing, the characteristic data state characteristics and probability distribution are determined through the dynamic Bayesian network, the relationship between the media corpus data state variables and the dimensions is determined, the media corpus data state is carried out for component processing, and the preprocessing of the media corpus data is completed [11].

3. Application Study of the Media Corpus Based on Big Data

3.1. Media Corpus Storage Applications. Based on the construction of the above media corpus data, the storage and application of the database are studied. By constructing the data information flow model of media corpus, the data storage of media corpus is studied by using nonlinear time series analysis [12]. In the media corpus data storage, the time model of media corpus data storage and scheduling information flow is as follows:

$$s(t) = \sum_{i=1}^{n} a_{\min} g_{\min}. \tag{9}$$

In formula, $s(t)$ represents the media corpus data storage space envelope amplitude.

In order to improve the efficiency of media corpus data storage application and meet the needs of media corpus data structure, the fitness function of constructing media corpus data storage point with the multiple regressive regression model is as follows:

$$f_{ij} = w_i \delta_t + w_c + \delta_t + w_q \delta_q. \tag{10}$$

In formula, f_{ij} represents the scheduling time for storage and access, δ_t represents the time cost of the storage, w_i represents the quality of storage of media corpus data, and w_q represents the database security performance.

Based on this basis, using the phase space reconstruction model, reorganize the storage subsets of the media corpus data for spatial characteristics and determine the probability distribution [13] of the fitness function satisfied by the media corpus data storage node, that is:

$$x_p(u) = \sqrt{\frac{1-\mu}{2\pi}} dt\ . \tag{11}$$

In formula, $x_p(u)$ represents the number of stages of the media corpus data storage structure. Data information flow characteristics in the media corpus data are classified as noninteger times of a. According to this calculation, the information flow time series reconstruction [11] in the database storage system is reconstructed by the nonlinear time series system analysis method, and the reconstruction expression is as follows:

$$F^p = F^4[f(t)]v. \tag{12}$$

According to the above reconstruction data flow time series, complete the media corpus data storage application as follows

$$F^p = x_p(u)(u - v \sin a). \tag{13}$$

In formula, F^p represents the spectral analysis features of the data store, v represents the distributed structure scaling properties, and equation (13) represents the orthogonal odd function of fractional transformation.

3.2. Media Corpus Data Encryption Application. In the application of media corpus data, its encryption is also a key link. Therefore, in the application of this paper, the encryption of media corpus data is studied. The secure encryption design of media corpus information is carried out under the advanced encryption standard protocol. The random linear coding scheme is adopted to construct the encryption key model of media corpus data storage information. The ciphertext construction and key design of database storage information are carried out under the logistics chaotic mapping, and the optimal encryption of database storage information is realized under the piecewise linear combination model [15].

The encryption and decryption key of the media corpus data storage information is set to H, the random phase reorganization method is used to encode and design the key of media corpus data information, the ciphertext protocol is constructed in logistics chaotic mapping, the block encryption method is used to encode the symbols of media corpus data, and the entanglement state model of media corpus data is established.

$$\beta \in H_1 \mid \beta \in H_1, \ldots, \mid \in H_n. \tag{14}$$

The cumulative probability distribution interval of the media corpus data encryption within the statistical interval I_i meets the following conditions:

$$\begin{aligned} \sum_{i=1}^{n} Q_i &= 1, \\ I_i\left[\sum_{i=1}^{n} Q_i = 1\right] &= \sum_{i=1}^{n} Q_j. \end{aligned} \tag{15}$$

The security key for media corpus data encryption is built, adaptive feature classification and vector quantification coding design with arithmetic coding design scheme are conducted, combined with the segmented Logistics encryption public key [16] of media corpus data, and the media corpus data encryption is completed. According to the Hash ciphertext distribution, the cryptographic coding protocol is used to design the media corpus data in the finite domain, improve the stability of the encryption process, and realize the research of encryption application.

4. Experimental Analysis

4.1. Experimental Design. In order to verify the effectiveness of the proposed method in the construction and application of media corpus data, simulation experiments are carried out. Assuming that the block length of media corpus data is 100, the sampling length of time series samples of media corpus data is 1200, the bandwidth of statistical feature sequence distribution set of media corpus is 14 dB, the number of layers of media corpus data encryption is set, and 30, 50, 60, 70, and 75 are used as the segmented sample set size of information coding stored in media corpus. The intensity of media corpus data attack is 20 dB. The waveform shape of sample media corpus data is shown in Figure 2.

4.2. Experimental Index Design. Based on the experimental scheme designed above, the indexes of this experiment are set as the space occupation of media corpus data storage and the security of media corpus data encryption. In order to promote the effectiveness of the experiment, the experiment is carried out in the form of comparison. The methods in this paper, literature [5], and literature [6] are compared, respectively. Many iterations are carried out in the comparison process to improve the accuracy of the experiment.

4.3. Analysis of Experimental Results. In order to verify the effectiveness of the design method in this paper, the experiment compares the method in this paper, the method in literature [5], and the method in literature [6] and compares the space occupation of sample media corpus data storage. The results are shown in Figure 3.

By analyzing the data in Figure 3, it can be seen that there are some differences in the space occupation of sample media corpus data stored by this method, literature [5] method, and literature [6] method under the same data

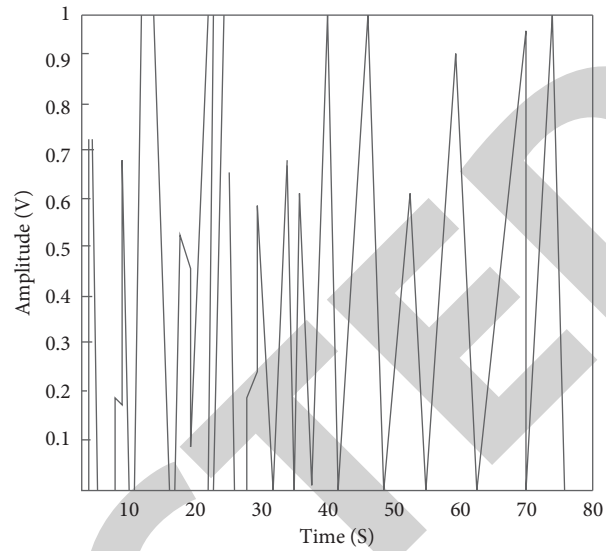

Figure 2: Waveform form of the sample media corpus data.

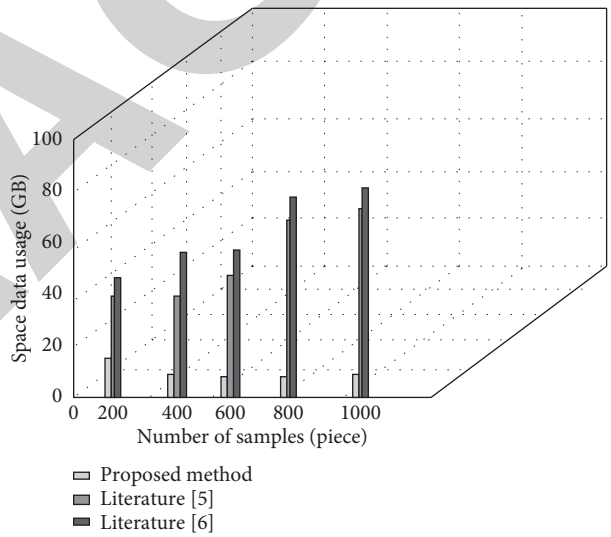

Figure 3: Comparison of space occupation of media corpus data storage by different methods.

volume. Among them, the space occupation of sample media corpus data storage in this method is always less than 20 GB, while the space occupation of sample media corpus data storage in the other two methods is always higher than that in this method. This is because this method has processed the data in the construction of data to verify the effectiveness of this method.

In order to further verify the effectiveness of the proposed method, the experiment compares the method in this paper, the method in literature [5], and the method in literature [6] to analyze the security of data encryption of sample media corpus. Taking the encrypted security coefficient as the measurement standard, the value range of the security coefficient is [0, 1]. The closer the security coefficient is to 1, the better the security is. The security results after encryption by the three methods are shown in Figure 4.

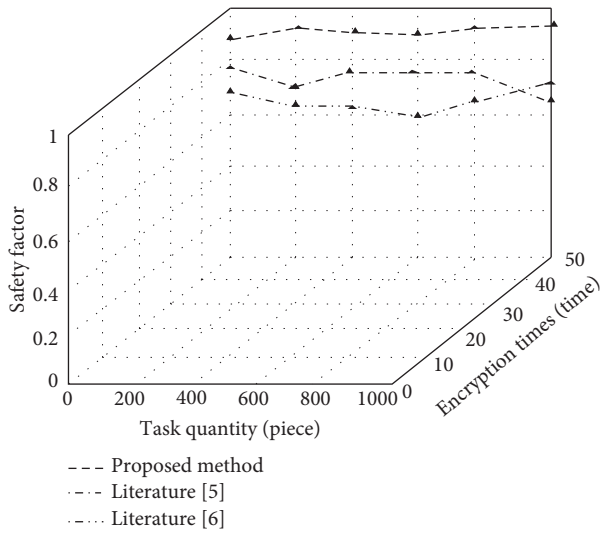

Figure 4: Comparison of data security coefficients of media corpora with different methods.

By analyzing the curve trend in Figure 4, it can be seen that under the same experimental conditions, the security of data encryption of sample media corpus is analyzed by using the methods of this paper, literature [5], and literature [6], and it can be seen that there are some differences in the security coefficients of the three methods. Among them, the security factor of sample media corpus data encryption by this method is higher than 0.9, while the security factor of sample media corpus data encryption by the other two methods is lower than that by this method. This is because this method uses big data technology to design the encryption key on the basis of the media corpus, which improves the security of the media corpus data and has a certain reliability. As can be seen from Figure 4, our method is more stable and fulfils our expected assumptions. In addition, the results in the figure also reflect the effective improvement of big data storage and encryption technology to our model.

5. Conclusion

This paper proposes the construction and application of media corpus based on big data. Media corpus data are collected, the data are divided into four categories, the heuristic data item column sorting algorithm is introduced to sort all collection processes, the minimum value of data item collection rate is determined, on this basis, the maximum value of quantity in media corpus is determined, and data collection in media corpus data through sliding window is determined; then, the state characteristics and probability distribution of feature data are determined by dynamic Bayesian network, the relationship between the state variables and dimensions of media corpus data is determined, and the media corpus data state is processed by component to complete the preprocessing of media corpus data; finally, through the application research of storage and encryption of the designed database through big data technology, the storage structure data and encryption secret key are designed to realize the construction and application of media corpus. The experimental results show that the data quality of the media corpus constructed by the proposed method is high, and its application rate has been improved to a certain extent.

Data Availability

The data used to support the findings of this study are available from the corresponding author upon request.

Conflicts of Interest

The authors declare that they have no conflicts of interest or personal relationships that could have appeared to influence the work reported in this paper.

References

[1] P. Aprent, "Eine digitale analyse sterreichischer printmedien auf basis des Austrian media corpus," *Zeitgeschichte*, vol. 46, no. 4, pp. 501–534, 2018.

[2] S. Coats, "Language choice and gender in a nordic social media corpus," *Nordic Journal of Linguistics*, vol. 42, no. 1, pp. 1–25, 2019.

[3] S. Goodman and S. Kirkwood, "Political and media discourses about integrating refugees in the UK," *European Journal of Social Psychology*, vol. 49, no. 7, pp. 1145–1152, 2019.

[4] M. T. Odenkirk, D. M. Reif, and E. S. Baker, "Multiomic big data analysis challenges: increasing confidence in the interpretation of artificial intelligence assessments," *Analytical Chemistry*, vol. 93, no. 11, pp. 45–53, 2021.

[5] T. Gao and X. Wang, "The database selection based on hesitant linguistic information aggregation algorithm," *Control Engineering of China*, vol. 26, no. 8, pp. 1444–1449, 2019.

[6] Y. Wu, "Research on automatic conversion method of heterogeneous data in language database," *Computer Simulation*, vol. 36, no. 7, pp. 380–384, 2019.

[7] H. Elgibreen, M. Faisal, M. A. Sulaiman et al., "An incremental approach to corpus design and construction: application to a large contemporary saudi corpus," *IEEE Access*, vol. 9, pp. 88405–88428, 2021.

[8] L. Zhang, Y. Guan, and S. C. Jiang, "Investigations of soil autotrophic ammonia oxidizers in farmlands through genetics and big data analysis," *Science of the Total Environment*, vol. 777, no. 3, Article ID 146091, 2021.

[9] M. J. Y. Suh, H. J. Yi, H. J. Kim, and S. H. Kim, "Is asymmetric hearing loss a risk factor for vestibular dysfunction? lesson from big data analysis based on the Korean national health and nutrition survey," *Otology & Neurotology*, vol. 40, no. 10, pp. 1339–1345, 2019.

[10] P. Kumar and A. Kumar Bhatt, "Enhancing multi-tenancy security in the cloud computing using hybrid ECC-based data encryption approach," *IET Communications*, vol. 14, no. 18, pp. 3212–3222, 2020.

[11] R. Geetha, T. Padmavathy, T. Thilagam, and A. Lallithasree, "Tamilian cryptography: an efficient hybrid symmetric key encryption algorithm," *Wireless Personal Communications*, vol. 112, no. 1, pp. 21–36, 2020.

[12] H. Zhang, Z. Xu, F. Tao, Y. Li, Y. Cui, and X. Li, "New barbituric acid derivatives for data encryption and decryption based on the mechanochromic fluorescence effect," *Analyst*, vol. 145, no. 12, pp. 1109–1121, 2020.

Hindawi
International Journal of Antennas and Propagation
Volume 2023, Article ID 9842357, 1 page
https://doi.org/10.1155/2023/9842357

Retraction

Retracted: A FJSSP Method Based on Dynamic Multi-Objective Squirrel Search Algorithm

International Journal of Antennas and Propagation

Received 19 December 2023; Accepted 19 December 2023; Published 20 December 2023

This article has been retracted by Hindawi following an investigation undertaken by the publisher [1]. This investigation has uncovered evidence of one or more of the following indicators of systematic manipulation of the publication process:

(1) Discrepancies in scope

(2) Discrepancies in the description of the research reported

(3) Discrepancies between the availability of data and the research described

(4) Inappropriate citations

(5) Incoherent, meaningless and/or irrelevant content included in the article

(6) Manipulated or compromised peer review

The presence of these indicators undermines our confidence in the integrity of the article's content and we cannot, therefore, vouch for its reliability. Please note that this notice is intended solely to alert readers that the content of this article is unreliable. We have not investigated whether authors were aware of or involved in the systematic manipulation of the publication process.

Wiley and Hindawi regrets that the usual quality checks did not identify these issues before publication and have since put additional measures in place to safeguard research integrity.

We wish to credit our own Research Integrity and Research Publishing teams and anonymous and named external researchers and research integrity experts for contributing to this investigation.

The corresponding author, as the representative of all authors, has been given the opportunity to register their agreement or disagreement to this retraction. We have kept a record of any response received.

References

[1] Y. Wang and J. Han, "A FJSSP Method Based on Dynamic Multi-Objective Squirrel Search Algorithm," *International Journal of Antennas and Propagation*, vol. 2021, Article ID 6062689, 19 pages, 2021.

Hindawi
International Journal of Antennas and Propagation
Volume 2021, Article ID 6062689, 19 pages
https://doi.org/10.1155/2021/6062689

Research Article

A FJSSP Method Based on Dynamic Multi-Objective Squirrel Search Algorithm

Yanjiao Wang and Jieru Han

School of Electrical Engineering, Northeast Electric Power University, Jilin 132000, China

Correspondence should be addressed to Jieru Han; jieru_han@163.com

Received 1 September 2021; Accepted 30 September 2021; Published 15 October 2021

Academic Editor: Fangqing Wen

This paper comprehensively analyzes the characteristics of flexible job shop scheduling problem (FJSSP), takes the dynamic factors in the actual scheduling process such as the arrival and departure of jobs, the breakdown and recovery of machines into account at the same time, and establishes a new dynamic multi-objective mathematical model. Take the Squirrel Search Algorithm (SSA) as the core evolution strategy, and combine the multi-objective framework and the dynamic processing technology to solve the established mathematical model. Experimental results show that the mathematical model proposed in this paper can solve the flexible job shop scheduling problem effectively. Compared with other mathematical models, the mathematical model established in this paper can keep better balance between the efficiency and stability.

1. Introduction to Flexible Job Shop Scheduling Problem

The purpose of flexible job shop scheduling problem (FJSSP) is to allocate machines rationally to all the processes that arrive at the workshop to be processed, so as to achieve one or more goals concerning operation efficiency and system stability [1]. FJSSP is a complex combinatorial optimization problem. The amount of computation increases exponentially with the increase in the numbers of machines and jobs. Intelligent evolutionary algorithms are not constrained by the constraints of search space and do not rely on other auxiliary knowledge, they only need to decide the optimization objective and corresponding fitness function of the search direction, and they are suitable for solving large-scale optimization problems, such as polarization estimation, estimation, and cooperative localization [2–6]. Many scholars have used swarm intelligence and evolutionary algorithms, including the traditional intelligent optimization algorithm, such as Genetic Algorithm [7], and new intelligent evolutionary algorithms, such as Shuffled Frog Leaping Algorithm, the Swarm Spider Optimization algorithm, and so on, to solve FJSSP large-scale combinatorial optimization problems. The completion time of scheduling scheme is minimum, which is the initial optimization goal of FJSSP, and it is the most common optimization objective [8–10]; however, the actual working environment is often dynamic, i.e., new events may occur at any time, such as the arrival of new jobs, the departure of completed jobs, and the sudden breakdown of machines. Obviously, the best scheduling scheme matching the original system state is unsuitable for the new working environment. Rescheduling the jobs in the new environment is necessary. For the scheduling scheme in the new environment, if the highest efficiency is the goal, the machine with the highest efficiency for the process to be chosen may cause the load imbalance of the system, and the new scheduling scheme may have a great difference from the historical scheduling scheme, which will affect the system stability. If the system stability is the optimization objective, the gap between new and old scheduling schemes can be reduced, but the processes needed may not be performed by the most efficient machines corresponding to them, resulting in low operation efficiency. In summary, flexible job shop scheduling should consider the efficiency and stability of the system at the same time to ensure the scheduling efficiency after changing the working environment, and a mutual

exclusion relationship exists between the two. Scholars have proposed new flexible job shop scheduling methods after environmental change.

For instance, Lei and Jensen, respectively, aimed at the shortest completion time and the best robustness, and solved the task-scheduling problem with machine failure [11, 12]. Chryssolouris and Zhang used the weighted sum of completion time and delay time as the optimization target for production-scheduling scheme [13, 14], although the operation efficiency and system stability were considered in the optimization process; when solving the problem, multiple targets could be transformed into single targets by using the weighted summation method, and the reasonable weight values could not be set in accordance with the actual situation of the environment; consequently, the most suitable scheduling scheme was difficult to generate, and the universality was weak. Huang Zhiqing et al. set up an energy consumption model for the FJSSP problem and improved the genetic algorithm with the idea of particle swarm optimization and simulated annealing algorithm. The completion time and energy consumption were regarded as optimization objectives, and the efficiency and stability were optimized simultaneously. Nevertheless, the model ignored the difference between the old and new scheduling schemes before and after machine failure, and the system stability at fault time was poor [15]. Shi et al. solved the FJSSP problem by using the discrete multi-population invasive weed optimization algorithm, adaptive mutation, and domain search strategy to improve the algorithm's ability to search and use the concept of rolling window to schedule the system operation at a certain time. In essence, the static FJSSP problem is divided into several time periods, and it is not applied to the dynamic situation of the task sequence leaving at any time [16]. Chen et al., used delay and deviation as efficiency indicators and stability indicators, respectively. They used NSGA-II to optimize the two targets simultaneously. The deviation degree was evaluated by the rescheduling scheme at the time of failure. The stability of the system is improved to a certain extent before and after machine failure, but it is not applied to the dynamic environment where the operation is arriving at any time [17].

To sum up, firstly, FJSSP has natural dynamics. When establishing flexible job shop scheduling model, work efficiency is usually measured by the completion time of the task to be processed, and the stability of the system is measured by the machine load state of the workshop. Although the existing mathematical model can cope with the change in some working environments, they still cannot deal with the random arrival of task sequence, the departure of completed tasks, sudden machine failure, and the repair of failed machines at the same time. Secondly, the efficiency and stability of flexible workshop systems are mutually exclusive; therefore, in the essence of mathematics, FJSSP is a dynamic multi-objective optimization problem [18]. Compared with the method of transforming multiple targets into a single objective through weighted summation, multi-objective evolutionary algorithm can simultaneously consider efficiency and stability, and it is the main method to solve flexible job shop scheduling. Thus, the performance of multi-objective algorithm is also the key to solve DJSSP. In order to get a scheduling scheme with both efficiency and stability in dynamic environment, it is necessary to establish a mathematical model conforming to the dynamic characteristics of DFJSSP and a dynamic multi-objective evolutionary algorithm with excellent performance.

Based on the above analysis, this paper proposes a flexible shop scheduling method based on dynamic multi-objective squirrel algorithm. The main innovations are as follows: First, in consideration of the changes in an actual workshop environment, including the random arrival of task sequences, the departure of completed tasks, sudden machine failure, and the repair of failed machines, a new dynamic multi-objective flexible shop scheduling model is proposed, with the completion time, load balance (LB), and fault rescheduling deviation as the objective functions, to address working efficiency and system stability. Second, in order to effectively solve the above established mathematical model, an improved dynamic multi-objective squirrel search algorithm based on decomposition is proposed in this paper. It adopts operation and machine coding for individual coding and improves individual evolutionary strategy of SSA according to the characteristics of FJSSP. In addition, a new dynamic processing technology including the establishment and update of the external population and the initialization of the population at the time of rescheduling is proposed, which can respond quickly to changes by regenerating initial population at rescheduling time.

The remaining sections are arranged as follows: Section 2 introduces the establishment process of the mathematical model of dynamic multi-objective flexible shop scheduling problem; the third part introduces the principle of the flexible shop scheduling method based on dynamic multi-objective squirrel search algorithm; the fourth part gives the experimental results and analysis; and the fifth part summarizes the whole paper.

2. The Establishment of a Mathematical Model for Dynamic Multi-Objective Flexible Job Shop Scheduling Problem

2.1. Description of Flexible Job Shop Scheduling Problem. The flexible job shop scheduling problem can be described as: there are n jobs $J = \{J_1, J_2, \ldots, J_n\}$, each operation J_i is composed of n_i processes, and the number of multi-objective steps per operation is n_i. The processing time t_{ij} of each process is subject to certain distribution. The purpose of the FJSSP is to assign the operation machine to each process, so that the process of arriving at the workshop is processed in a certain order, and after processing is finished, the operation machine leaves the workshop. A new mathematical model for flexible job shop scheduling problem is established to realize flexible job shop dynamic scheduling. Firstly, the variables involved in flexible job shop scheduling problem are introduced as follows:

t_1: rescheduling cycle, time $t = nt_l$ (n is a positive integer), update the state of the workshop, including new task, machine idle time, etc.

t_b: the time when the machine breaks down.

t_r: the time for recovering from machinery breakdowns.

Mtbf: the average breakdown time.

Mttr: the average recovery time.

J_i: the task *i-th* that arrives at the workshop.

N_l: the number of tasks arriving at the workshop before the time of nt_l.

n_i: the number of Ji's processes.

O (i, j): the *j-th* process of task J_i.

m: the total number of machines in workshop.

M: the set of machines in workshop, $M = \{M_1, M_2, \ldots, M_m\}$.

M (i, j): a set of all machines that can handle *O (i, j)*.

F (i, j): the number of machines contained in the alternative machine set *M (i, j)* of *O (i, j)*, flexible degree.

t (i, j, k): the processing time of *O (i, j)* on machine M_k.

S_i: the beginning time of job *i*.

C_i: the completion time of job *i*. *S (i, j)*: the beginning time of process *O (i, j)*.

C (i, j): the completion time of process *O (i, j)*.

C_{k_last}: *O (i, j)* is processed by M_k, the completion time of the last procedure of M_k processing before *O (i, j)* starts.

S (i, j) *: the beginning time of O_{ij} in rescheduling processes.

C (i, j) *: the completion time of O_{ij} in rescheduling processes.

I_k: the earliest available time of machine M_k;

L_k: the total working time of machine M_k;

Task scheduling requirements for Flexible Job Shop:

(1) At the initial time, all machines are available, i.e., $t = 0$, $I_k = 0$.

(2) A process can only be processed by one machine at a time, that is, *O (i, j)* can only be processed by one machine in *M (i, j)* at a time.

(3) One machine can handle only one process at a time.

(4) There is no precedence constraint between different tasks.

(5) The process in the same task has no priority, that is, *O (i, j-1)* can only deal with *O (i, j)* after processing.

(6) All processes have no priority for the same machine, that is, the machine must deal with the current process before it can handle the next process.

(7) When the machine is not out of order, the operation system is scheduled at a fixed cycle according to the completion and arrival of the operation. When the machine breaks down, no matter whether the fault machine is executing the procedure or whether the procedure is to be executed soon, in the rescheduling plan, all the remaining procedures corresponding to the fault machine are arranged to be executed by the nonfault machine. After the fault is fixed, the repaired machine can continue to perform job scheduling.

For the periodic rescheduling time nt_l, the rescheduling time t_b and the task to be processed at the recovery time of rescheduling t_r, if the procedure *O (i, j)* is processed on machine M_k, then the beginning time *S (i, j)* and the ending time *C (i, j)* of *O (i, j)* are, respectively, shown in formulas (1) and (2). The beginning time Si and the ending time C_i of J_i are shown in formulas (3) and (4), respectively.

$$S_{ij} = \begin{cases} \max\{nt_l, I_k\}, & j = 1, \\ \max\{C(i, j-1), I_k\}, & j > 1. \end{cases} \quad (1)$$

Among them: $I_k = \max\{nt_l, t_b, t_r, C_{k\_last}\}$,

$$C(i, j) = S(i, j) + t(i, j, k), \quad (2)$$

$$S_i = \max\{S(i, 1), \ldots, S(i, n_i)\}, \quad (3)$$

$$C_i = \max\{C(i, 1), \ldots, C(i, n_i)\}. \quad (4)$$

The scheduling example in [19] is illustrated to have an enhanced understanding of the rules of flexible job shop scheduling. As shown in Table 1, "/" means that the process cannot be executed on the corresponding machine. Figure 1 is a Gantt chart corresponding to a specific scheduling plan for the data in Table 1.

As shown in Figure 1, when $t = 0$, O_{31}, O_{41}, and O_{21} are treated using M_1, M_3, and M_5, respectively. Given that O_{31}, O_{41}, and O_{21} are the first processes of J_3, J_4, and J_2, respectively, all machines are idle when $t = 0$; thus, $S_{31} = S_{41} = S_{21} = 0$. O_{11} is selected to be treated using M_1. Although O_{11} is the first step of J_1, given no priority constraint among different tasks, M_1 has started processing O_{31} when $t = 0$. O_{11} can start after O_{31} ends; therefore, $S_{11} = I_1 = C_{31} = S_{31} + t_{311} = 5$. O_{12} is processed using M_4. Given that the process in the same task has no priority, O_{12} can only start after O_{11} ends, and O_{11} ends at $t = C_{11} = S_{11} + t_{111} = 7$. However, when $t = 7$, M_4 handles O_{32}, and M_4 is idle after O_{32} is finished, i.e., $I_4 = C_{32} = S_{32} + t_{324} = 8$; consequently, $S_{12} = I_4 = 8$. O_{13} is processed using M_2. Although M_2 has been idle at $t = 5$ when O_{22} ends, O_{12} has not started yet when $t = 5$, and the process in the same task has no priority. Accordingly, $S_{13} = C_{12} = S_{12} + t_{124} = 10$.

2.2. Characteristic Analysis of FJSSP. For the scheduling problem of flexible job workshops, even for exactly the same scheduling tasks, multiple scheduling schemes often exist. Figure 2 is a Gantt chart corresponding to Table 1 and another scheduling scheme different from Figure 1.

For FJSSP, the efficiency and stability of the system are usually considered. On this basis, we compare and analyze the scheduling schemes in Figures 1 and 2 from these two perspectives. For the tasks in Table 1, the final completion time of the two scheduling schemes is 17, indicating that the efficiency of the two scheduling schemes is equivalent. However, in the scheduling scheme corresponding to Figure 1, all machines participate in the scheduling process, and the machine load is

Table 1: Six task scheduling examples.

Job number	Process number	Machine number and corresponding processing time of each process					
		1	2	3	4	5	6
1	1	2	3	4	—	—	—
1	2	—	3	—	2	4	—
1	3	1	4	5	—	—	—
2	1	3	—	5	—	2	—
2	2	4	3	—	—	6	—
2	3	—	—	4	—	7	11
3	1	5	6	—	—	—	—
3	2	—	4	—	3	5	—
3	3	—	—	13	—	9	12
4	1	9	—	7	9	—	—
4	2	—	6	—	4	—	5
4	3	1	—	3	—	—	3

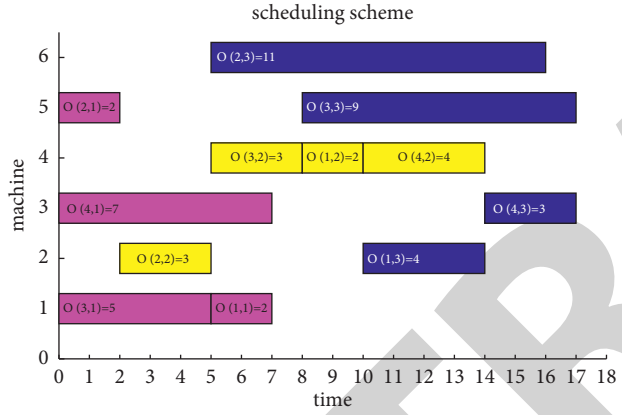

Figure 1: Scheduling plan 1.

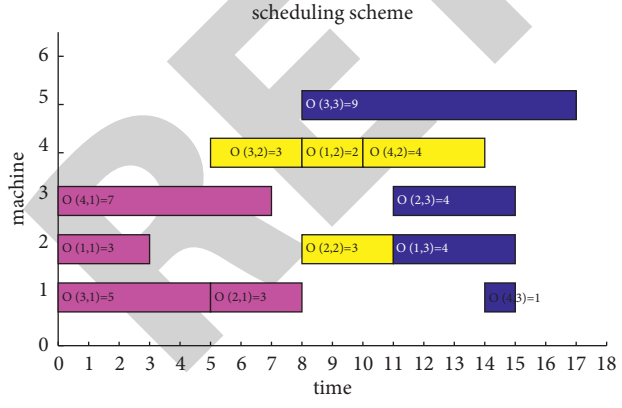

Figure 2: Scheduling plan 2.

balanced. For the scheduling scheme in Figure 2, M_6 is not involved in the scheduling process. All processes are completed using M_1–M_5, and the LB of the machine is poor. The unbalanced load of machines in the workshop may cause some machines to be idle and others to be in working state for a long time. The machines in working state for a long time are prone to failure, thus affecting the system stability. Therefore, compared with the scheduling scheme in Figure 2, the scheduling scheme in Figure 1 is better while ensuring efficiency and considering system stability.

The machine failure mentioned above is also one of the important factors that affect the system stability, and the specific analysis is as follows. When a machine in the workshop breaks down, the process in the same task has no priority, except for the process that is being implemented or has not been implemented on the failed machine. $O(i, j)$ can only be processed after $O(i, j\text{-}1)$ is processed, and the processes arranged on no-fault machines in the original scheduling plan will also be affected. Figure 2 is regarded as an example, i.e., if M_4 breaks down at $t = 9$. Process O (1, 2) being handled on M_4 and process O (4, 2) that has not yet been handled on M_4 need to be rescheduled. O (1, 3) and O (4, 3) cannot be executed in accordance with the original scheduling plan due to the changes in O (1, 2) and O (4, 2). Although O (2, 3) in the original scheduling scheme is unaffected by the failed machine, the machine failure changes the system state, and the scheduling of O (2, 3) will also have a new impact on the system state. Nonetheless, the workshop still maintains an efficient and stable operation at the time of failure. Except for the processes that have been started on no-fault machines and the process that has been completed on the fault machine, all the other processes need to be rescheduled. At the time of recovery, all the remaining untreated processes need to be rescheduled, except for the processes that have been completed and started. The smaller the deviation between the rescheduling scheme and the original scheduling scheme is, the smaller the system changes, and the better the stability will be. Conversely, the greater the difference between the new and old scheduling schemes is, the worse the system stability will be.

To sum up, if we want to ensure the operation efficiency, the most efficient machines in all processes can lead to some machines being idle for a long time, while some machines are in a state of work for a long time, resulting in unbalanced load. If we want to ensure the LB of machines, some jobs may not be processed by the most efficient machines, resulting in low efficiency. Some processes do not match the most efficient machines, and the efficiency of the machines may still be reduced. If the work efficiency is to be guaranteed, the new scheduling scheme may be larger than the historical scheduling scheme, but the system stability will be worse.

2.3. Dynamic Multi-Objective Mathematical Model of FJSSP. Subsection 2.2 indicates that operation efficiency and system stability are conflicted. To consider the efficiency and stability of the workshop at the same time, this paper regards the completion time, LB, and rescheduling deviation as the objective functions and establishes a multi-objective optimization mathematical model. The completion time is used to evaluate the workshop efficiency, while LB and fault rescheduling deviation are used to measure the system stability. The details are as follows:

2.3.1. Work Efficiency. A short completion time means high work efficiency. To ensure the workshop work efficiency, this paper regards the shortest completion time as the

optimization objective, and the objective function is shown in Formula (5).

$$\min CT = \max\{C_i, i = 1, 2, \ldots, N_l\}. \tag{5}$$

2.3.2. System Stability. This study measures the system stability from two aspects: the machine LB and rescheduling deviation. LB is measured using the variance of machine utilization shown in Formula (6); the smaller the variance is, the more balanced the machine load and the better the system stability will be. When machines break down or recover, the average deviation (AD) between the new and old scheduling schemes shown in Formula (8) indicates the rescheduling deviation. Small AD indicates a small difference between the rescheduling and original scheduling schemes, and improved stability.

$$\min LB = \frac{1}{m}\sum_{k=1}^{m}\left[\frac{L_k}{\max\{L_1, \ldots, L_m\}} - \frac{1}{m}\sum_{k=1}^{m}\frac{L_k}{\max\{L_1, \ldots, L_m\}}\right]^2. \tag{6}$$

In (6),

$$L_k = \sum_{i=1}^{N_l}\sum_{j=1}^{n_i} x(i, j, k) * t(i, j, k),$$
$$x(i, j, k) = \begin{cases} 1, & O(i, j) \text{is handle using } M_k, \\ 0, & \text{other.} \end{cases} \tag{7}$$

The smaller the LB is, the more balanced the system will be.

$$\min AD = \frac{\sum_{i=1}^{N_l}\sum_{j=1}^{n_i}\left(\left|S(i, j) - S^*(i, j)\right| + \left|C(i, j) - C^*(i, j)\right|\right)}{n_{\text{res}}}. \tag{8}$$

In (8), n_{res} is the total number of operations to be rescheduled; for the operations that have started or been completed on the working machines, $S(i, j) = S^*(i, j)$ and $C(i, j) = C^*(i, j)$.

In summary, to consider the efficiency and stability of the system, a dynamic multi-objective mathematical model of FJSSP is established:

$$\begin{cases} \min CT = \max\{C_i, i = 1, 2, \ldots, N_l\}, \\ \min LB = \dfrac{1}{m}\displaystyle\sum_{k=1}^{m}\left[\frac{L_k}{\max\{L_1, \ldots, L_m\}} - \frac{1}{m}\sum_{m}^{1}\frac{L_k}{\max\{L_1, \ldots, L_m\}}\right]^2, \\ \min AD = \dfrac{\left(\sum_{i=1}^{N_l}\sum_{j=1}^{n_i}\left(\left|S(i, j) - S^*(i, j)\right| + \left|C(i, j) - C^*(i, j)\right|\right)\right)}{n_{\text{res}}}. \end{cases} \tag{9}$$

In the mathematical model above, the first objective function guarantees the shortest completion time of all tasks arriving at time nt_1; the second objective function guarantees that all machines will be loaded as evenly as possible until nt_1; the third objective function ensures that when machines break down or get back to work, the deviation between the rescheduling scheme and the original scheduling scheme is the smallest. When no machine breaks down or a machine is not recovered, only the objective functions one and two are considered, and the mathematical model is considered a two-objective optimization problem. If a machine breaks down or the faulty machine is recovered, the three objectives are all needed to be optimized, and the mathematical model is regarded as a three-objective optimization problem.

Compared with existing mathematical models of FJSSP, the mathematical model established in this paper considers the dynamic characteristics of the departure of completed tasks, the arrival of new tasks, the failure of workshop machines, and the repair of machine faults. The mathematical model adjusts the optimization objective automatically in accordance with the machine state, which will shorten the working time and balance the load of the machine when no machine breaks down or a machine is not recovered. Meanwhile, the established mathematical model minimizes the deviation of the new and old scheduling schemes when a machine breaks down or the faulty machine is recovered, which gives consideration to the working efficiency and system stability in real time.

3. Dynamic Multi-Objective SSA For Solving FJSSP

When solving a dynamic multi-objective optimization problem, the dynamic environment is divided into several transient environments; a dynamic processing technology is used to deal with environmental changes, and a multi-objective algorithm is used to solve static multi-objective optimization problems in a transient environment. Squirrel Search Algorithm (SSA) is a new swarm intelligence evolutionary algorithm [20]. Compared with traditional evolutionary algorithms, SSA has higher convergence speed and accuracy. Wang et al. propose an Improved Squirrel Search Algorithm for global function optimization (ISSA), which improves the convergence of SSA. Besides, Zhang et al.

proposed MOEA/D, which can solve the multi-objective optimization problem in a transient environment and has high solving speed and efficiency [21]. Therefore, to expand the application of SSA in the engineering field, this paper regards ISSA as the core evolutionary strategy, considers the multi-objective framework of MOEA/D, and integrates a dynamic processing technology to solve FJSSP. Figure 3 is the flowchart of the dynamic multi-objective SSA for solving FJSSP.

Figure 3 illustrates that at the end of each transient environment, the final scheduling scheme under the current environment in the nondominated solution set should be selected, and the scheduling under the new environment is based on the selected scheduling scheme. In this study, the TOPSIS method [22] is used to determine the final scheduling scheme for each transient environment. In addition, considering that FJSSP is a discrete optimization problem, this study adopts the individual coding method [23]. In accordance with the characteristics of FJSSP, the dynamic processing technology and evolution strategy for FJSSP are designed as follows.

3.1. Individual Coding Method. The individual coding method includes two parts: operation and machine coding. The operation coding is determined using the job number to be processed at the rescheduling time. Operation *O (i, j)* is represented by its task number J_i. The first occurrence of J_i corresponds to operation *O (i, 1)*, the second occurrence of J_i corresponds to operation *O (i, 2)*, and so on. The *j-th* occurrence of J_i corresponds to operation *O (i, j)*; therefore, the frequency of occurrence of J_i is the same as the total operation number of J_i. Each operation code corresponds to one machine code. A machine is selected from the candidate machine set of *O (i, j)* randomly, and the number of the selected machine is the machine code corresponding to *O (i, j)*.

The task data in Table 1 are regarded as an example. The complete code corresponding to the scheduling scheme shown in Figure 1 is 342133221144/135145264243, i.e., $O_{31} \longrightarrow M_1$, $O_{41} \longrightarrow M_3$, $O_{21} \longrightarrow M_5$, $O_{11} \longrightarrow M_1$, $O_{32} \longrightarrow M_4$, $O_{33} \longrightarrow M_5$, $O_{22} \longrightarrow M_2$, $O_{23} \longrightarrow M_6$, $O_{12} \longrightarrow M_4$, $O_{13} \longrightarrow M_2$, $O_{42} \longrightarrow M_4$, $O_{43} \longrightarrow M_3$.

3.2. Dynamic Processing Technology

3.2.1. Establishment and Renewal of External Population. The solution principle of MOEA/D indicates that when offspring individual y' cannot replace any individual in the neighbourhood, y' is abandoned directly. Thus, this study establishes an external population *Ey* for each individual to make the abandoned y' participate in the evolution. The specific way is as follows. An external population with the same size is set as the neighbourhood *T*. num_alt is used to record the number of individuals in the neighbourhood replaced with y'. y', whose num_alt is equal to 0, enters the external population.

When the scale of *Ey* is smaller than the upper limit *T*, if num_alt = 0, the corresponding y' enters *Ey*; if $0 <$ num_alt $\leq T/2$, *Ey* remains unchanged; if num_alt $> T/2$, *Ey* is emptied because the current subproblem and its neighbour subproblems are far from the optimal solution.

When the scale of *Ey* is up to the upper limit *T*, if num_alt = *0*, the population has evolved to a certain extent, and the current individual is close to its neighbour individual. To maintain the population diversity, the individual with the smallest Euclidean distance to the current individual in *Ey* is deleted, and y' enters *Ey*.

3.2.2. Generation of Initial Population at Rescheduling Time. Two cases needing to reschedule tasks are considered in this paper. The first one is related to workshop working time, which is called periodic rescheduling. The second one is related to machine state, including fault and fault recovery rescheduling. In consideration of the two situations above, two different dynamic processing technologies are designed, and the details are as follows.

At the time of periodic rescheduling nt_l, the new tasks are recorded, the machine state is updated, and the initial population under the new period is generated in accordance with the coding method in Subsection 3.1.

If a machine breaks down or operates again, i.e., $t = t_b$ or $t = t_r$, the new population of t_b or t_r is generated in accordance with the implementation of the original scheduling scheme. The details are as follows. If $t = t_b$, in the current scheduling scheme, operations to be rescheduled contain all the unfinished operations arranged on the broken machine and all the operations that have not started until t_b. If $t = t_r$, in the current scheduling scheme, operations to be rescheduled contain all the operations that have not started until t_r. The set of all operations to be rescheduled is named O_{re}. When $t = t_b$ or $t = t_r$, for each individual in the original population, if $Ey = \varnothing$, all operations in O_{re} should be reinitialized as the new individual in the new environment in accordance with the coding method above; if $Ey \neq \varnothing$, for each scheduling scheme in *Ey*, the set of operations that need to be rescheduled is recorded and named O_{ey}; if memory individuals with exactly the same O_{ey} and O_{re} exist, one is selected randomly, the scheduling order of all operations is kept in O_{ey}, and the corresponding machine code is mutated and regarded as the initial individual in the new environment. Given the high similarity between the scheduling scheme in memory population and the currently executing scheduling scheme, the new individuals generated using memory individuals are more suitable for the current working state, which is conducive to the system stability.

3.3. Core Evolutionary Strategy. In the scheduling process of each transient environment, the core evolutionary strategy SSA is used to update the population. An individual contains operation and machine codes, but the machine code is determined by the operation code. Therefore, the updating strategy of the population is aimed only at the operation code, rather than the machine code. The specific updating process is described below.

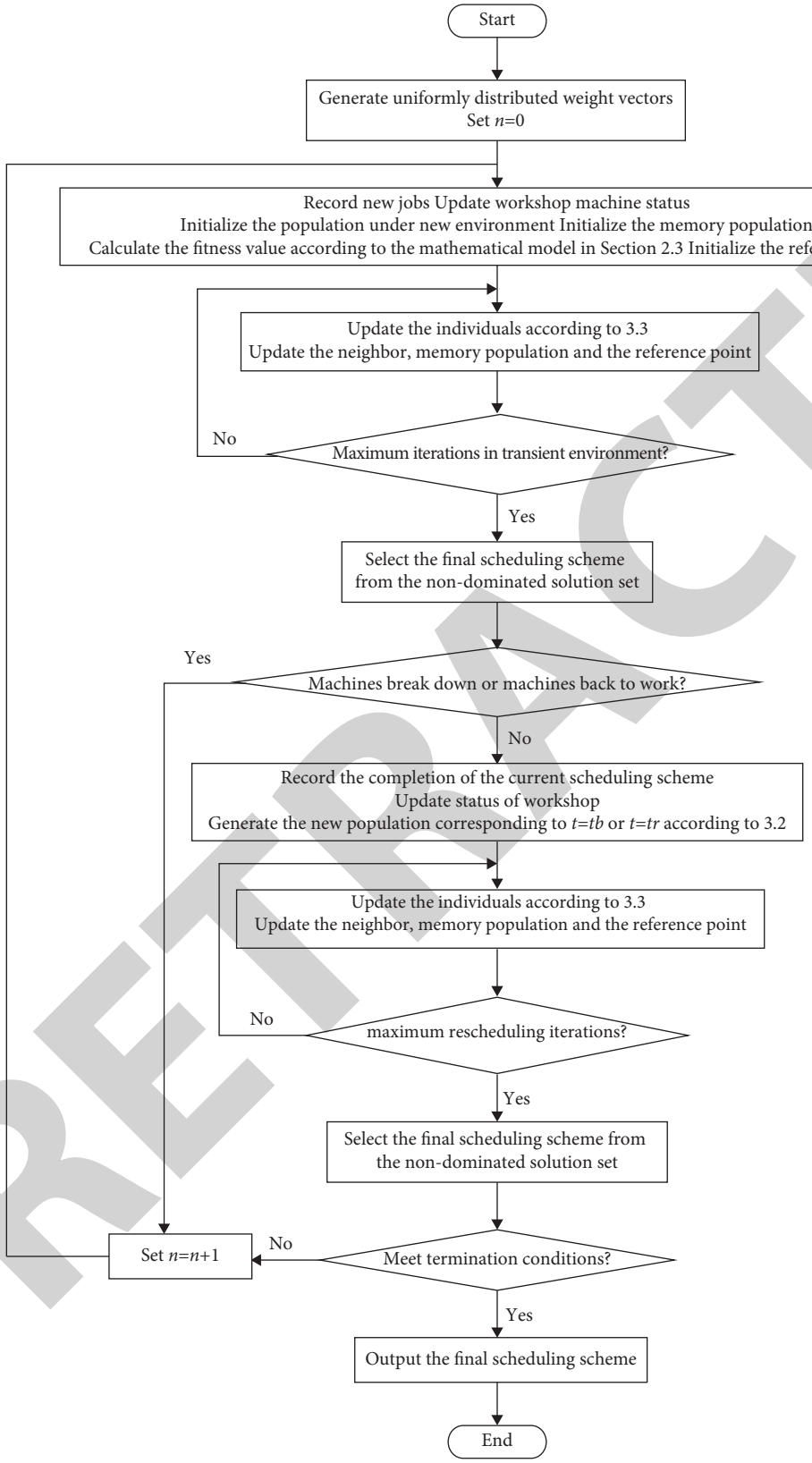

Figure 3: Flowchart for solving FJSSP.

3.3.1. Related Variables

F_d: Learning target in accordance with the standard SSA; the details have been introduced in Reference [20].

n_same: When the operation codes of FS_i and F_d are matched one by one, n_same is the total number of the same operation codes.

n_j_l: Total number of new jobs at t_l.

Fr_1, Fr_2: If $Ey = \varnothing$, Fr_1 and Fr_2 are two individuals different from F_d and FS_i randomly selected in their neighbor; if $Ey \neq \varnothing$, Fr_1 is any individual in its neighborhood different from FS_i, and Fr_2 is randomly selected in Ey.

S_c^g and $S_{\min}$ are calculated according to Reference [20], and the winter search strategy is selected when $S_c^g > S_{\min}$.

(1) Winter search strategy

① No predators exist when $r > P_{dp}$.
The jump search method is selected when $n\_same > n\_j_l/2$, and the progressive search method is decided when $n\_same \leq n\_j_l/2$.
The jump search method: FS_i and F_d have high similarity when $n\_same > n\_j_l/2$, and the individual is updated using Formula (10).

$$FS_i^{g+1} = FS_i^g + \left[d_g \times G_c \times \left(F_d^t - FS_i^t\right)\right]. \quad (10)$$

In the formula above, "[.]" means to carry out rounding operation, which ensures that the individual code of each dimension is a positive integer. d_g and G_c have been introduced in Reference [20].
The progressive search method: FS_i and F_d have low similarity when $n\_same \leq n\_j_l/2$. To maintain population diversity, r_{ds} dimensions are selected randomly in accordance with Formula (11) and then rearranged also randomly.

$$r_{ds} = \left[r \times \left(n\_j_l - n\_same\right)\right]. \quad (11)$$

In the formula above, r is a random number between 0 and 1; the lower the similarity between FS_i and F_d is, the more dimensions can be rearranged, and the search space can be developed more sufficiently.

② A predator occurs when $r \leq P_{dp}$.
FS_i is considered dead, and the offspring is generated via F_{r1} and F_{r2} in accordance with the POX introduced in Reference [24].

(2) Summer search strategy

① No predators exist when $r > P_{dp}$.
The jump search method is selected when $n\_same > n\_j_l/2$, and the progressive search method is chosen when $n\_same \leq n\_j_l/2$.
The jump search method: FS_i and F_d have high similarity when $n\_same > n\_j_l/2$, and the individual is updated using Formula (12).

$$FS_i^{t+1} = F_d^t + \left[d_g \times G_c \times \left(FS_i^t - F_d^t\right)\right]. \quad (12)$$

Formula (12) regards F_d as the basic vector, improves the convergence speed at the beginning of environmental change, and deeply develops the search space after the population evolves to a certain extent.
The progressive search method is the same as that in the winter search method. If $n\_same \leq n\_j_l/2$, r_{ds} dimensions are selected randomly in accordance with Formula (10) and then rearranged also randomly.

② A predator occurs when $r \leq P_{dp}$.

FS_i is considered dead, and the offspring is generated using F_{r1} and F_{r2} in accordance with the POX introduced in Reference [24].

FJSSP requires that the value of each dimension is the job number corresponding to the operation, and the total occurrence time of each job number should be the same as its total operations. Therefore, the operation code of the offspring obtained using the updating strategy above should be modified. The task in Table 1 is regarded as an example to introduce the modification process, and the details are as follows.

The redundant job numbers are determined and recorded in vector "more." If number i of job J_i occurs $n_i + c$ times, then i occurs in "more" c times. Figure 4 is considered an example. For the problem in Table 1, the operation code of the offspring is 134312214131, more = {1, 1}.

The missing job numbers are identified and recorded in vector "*less.*" If number i of job J_i occurs n_i-c times, then i occurs in "less" c times. Figure 4 is regarded as an example. For the problem in Table 1, the operation code of the offspring is 134312214131, less = {2, 4}.

The redundant job numbers occurring in "more" in the offspring are selected randomly to replace the missing job numbers in "less." All elements in "less" are arranged randomly, and the modification is completed. Figure 4 is regarded as an example, the 5-th dimension of the offspring operation code changes from 1 to 4, and the 10th dimension changes from 1 to 2.

An operation machine is selected randomly in the alternative machine set after the operation code of each offspring is determined, and the operation code constitutes a complete offspring scheduling scheme.

4. Experimental Simulation and Result Analysis

To verify the effectiveness of the dynamic multi-objective SSA for solving the FJSSP mathematical model established in this paper, the FJSSP model and the dynamic multi-objective SSA are applied to solve an actual FJSSP. All the tests are implemented on a computer CPU: Intel (R) Core (TM) i5-7200U, 4 G memory, and 2.70 GHz main frequency. The program is implemented in MATLAB R2016a. The experiment includes two parts: effectiveness validation and advanced verification.

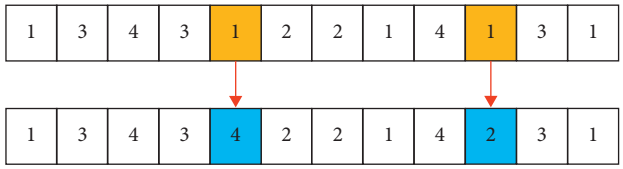

Figure 4: Modification of the operation code.

4.1. Effectiveness Validation. To investigate the FJSSP mathematical model established in this paper and the effect of the designed scheduling method, the following FJSSPs are tested: the number of machines is $m = 6$; the rescheduling cycle is $t_l = 1$; the time intervals between two adjacent tasks arrive at an exponential distribution of mean 0.5; the number of jobs per task n_j obeys the uniform distribution between $[m/2, m]$; the flexibility of each process is subject to a uniform distribution between $[m/2, m]$; the processing time of each process obeys the exponential distribution with a mean value of 1; *MTBF* obeys the exponential distribution of mean *mtb*, and *mtb* obeys the uniform distribution between [20, 40]; *MTTR* obeys the exponential distribution of mean *MTR*, and *MTR* obeys the uniform distribution of [5, 10] and randomly selects a fault machine. The task to be processed at the initial time is shown in Table 2. The algorithm parameters are set as follows: SSA's $N_{fs} = 2$; population size $N = 300$; the upper limit of neighbourhood size and positive memory population size is 20; the maximum iteration number of each transient environment is $g_{\max} = 100$; POX cross mode cross probability $p_c = 1$; mutation probability $p_m = 1$; when $N_{l=}100$, the total number of scheduling tasks is terminated.

Table 3 is a part of the nondominated solutions obtained from the fault free time $t = 5$, the first failure time $t = 15.7633$, and the first fault repair time $t = 23.7424$ or the rescheduling task optimization. Figures 5–7 are, respectively, the nondominated graphs obtained from the task to be processed or the rescheduling task optimization of t = 52.1802 at the time of failure free t = 30, the second failure time t = 43.6123, and the second fault repair time.

From the above chart, the mathematical model proposed in this paper is a two-objective optimization problem when all the machines in the workshop are free of failure. The nondominated solution is distributed in the same plane. When the fault occurs or restores, the mathematical model is a three-objective optimization problem, and the nondominated solution is dispersed in a three-dimensional space.

Figures 8 and 9 are the Gantt charts of the shop scheduling plan during $t = 10$–30 and $t = -55$, respectively. J_i is the task number. Purple, yellow, blue, orange, cyan, and gray represent the 1–6 processes of each task, respectively. Red represents the rescheduling process after a machine fails, and green represents the rescheduling process after the machine fails to recover. When machine M_2 breaks down at $t = 15.7633$–23.7424, the fault machine does not perform any operation. When machine M breaks down at $t = 43.6123$–52.1802, the fault machine does not perform any operation. After the machine breaks down, the fault machine is in working state again.

In order to further verify the FJSSP mathematical model established in this paper and the effect of the designed scheduling method, we carry out the following experiments. Set the number of machines to 8, and the rescheduling period $t_l = 15$; the time interval between two adjacent tasks follows an exponential distribution with a mean of 0.625. The parameter settings and algorithm settings of other scheduling environments are consistent with those mentioned above. The tasks to be processed at the initial time are shown in Table 4. Figures 10 and 11 are the Gantt charts of the shop scheduling plan during $t = 15$–25 and $t = 30$–40, respectively.

It can be seen from Figures 10 and 11, when machine M_1 breaks down at $t = 15.5810$–$t = 17.7670$, the fault machine does not perform any operation. When machine M_2 breaks down at $t = 33.9251$–$t = 39.2939$, the fault machine does not perform any operation. After the machine breaks down, the fault machine is in working state again.

To sum up, the FJSSP mathematical model and the scheduling method established in this paper can effectively cope with the changes in an actual workshop environment, including the task of reaching or leaving at any time and the occurrence of faults. This condition can effectively solve FJSSP.

4.2. Advanced Verification. The dynamic multi-objective SSA is used to optimize the mathematical models established in this paper and Reference [23] to solve FJSSP by satisfying the following conditions: the number of machines is $m = 6$; rescheduling cycle $t_l = 30$; the time intervals between two adjacent tasks arrive at an exponential distribution of mean 3; the number of jobs per task n_j obeys the uniform distribution between $[m/2, m]$; the degree of flexibility of each process obeys the uniform distribution between $[m/2, m]$; the processing time of each process obeys the exponential distribution of mean 5; *MTBF* obeys the exponential distribution of mean *mtb*, and *mtb* obeys the uniform distribution of [100, 200]; *MTTR* obeys the exponential distribution of mean *mtr*, and *mtr* obeys the uniform distribution of [30, 60] and randomly selects a fault machine at the time of failure. The rest of the parameter settings are consistent with the previous ones. The task to be processed at the initial time is shown in Table 5.

For a dynamic scheduling environment, the scheduling scheme is different, and the workshop state at the end of each transient environment is diverse. That is, the initial state of the workshop at the beginning of the next new environment is different. Comparing the optimization capability of different mathematical models for FJSSP requires the same initial workshop state and the same task to be optimized. The following parts are tested in this study.

(1) The mathematical model in Reference [23] is used to optimize the dynamic environment continuously. The workshop state at the beginning of each new scheduling cycle is recorded. Several different initial states and transient scheduling cycles are obtained. The new task to be processed in each scheduling cycle is recorded, and the mathematical model built in this

Table 2: Tasks to be processed at $t = 0$.

Job number	Process number	Machine number and corresponding processing time of each process					
		1	2	3	4	5	6
1	1	1.5278	0.5901	1.1614	0.7246	0.4811	0.4691
1	2	0.3956	0.4539	1.0810	1.0675	0.6425	0.5351
1	3	0.5129	0.6446	0.3990	—	0.3562	—
2	1	0.3668	0.1866	3.7728	0.5068	1.4320	1.0902
2	2	1.2446	0.6315	—	0.2521	—	0.2403
2	3	0.4178	0.6454	—	0.5130	0.4797	0.1741
3	1	1.0332	0.4689	1.0538	0.5362	0.5307	1.0737
3	2	1.4766	0.6708	0.6258	0.5990	3.4804	—
3	3	—	0.5051	0.5074	0.4874	0.4436	1.9361
3	4	0.5011	3.0418	0.3736	—	0.5299	1.4914
3	5	0.5034	1.0831	0.4777	0.3409	—	—
4	1	—	—	0.6324	2.4931	0.6410	0.4427
4	2	0.4982	0.5326	0.5844	0.0977	1.7782	1.0170
4	3	1.0407	0.3432	2.2131	2.3234	—	0.3157
4	4	0.4482	0.5209	2.5250	6.4491	—	0.6933
5	1	0.4508	—	0.4902	0.7867	0.4561	—
5	2	—	—	0.3664	—	0.6246	0.5435
5	3	—	0.4329	0.3010	—	0.7159	—
6	1	0.4204	0.5577	1.0348	2.8571	—	0.7716
6	2	1.7587	1.5530	0.6008	—	0.7694	—
6	3	0.5188	0.3955	—	0.6630	2.4961	1.07434
6	4	1.5050	1.6941	0.6725	—	0.7614	0.5686
7	1	2.5187	3.7462	0.2872	0.4990	—	0.5650
7	2	3.7646	—	1.7037	—	0.7952	3.1828
7	3	1.0688	0.3720	0.6191	—	—	0.2297
8	1	0.6037	0.4592	—	1.0678	0.7454	0.4188
8	2	0.4884	0.4996	0.4361	—	1.8487	0.4254
8	3	0.4996	0.4550	—	—	0.1078	3.6344
8	4	0.3247	0.5305	—	0.6690	—	0.3700
9	1	0.5065	0.5234	0.7427	—	2.3589	0.3925
9	2	0.4606	0.5201	0.2577	0.6951	0.5649	1.4906
9	3	1.1232	—	0.5104	1.3293	1.0829	0.3600
9	4	—	—	—	1.8475	2.4910	0.7087
10	1	1.0394	—	0.5291	0.4944	0.3455	—
10	2	0.5875	—	0.4925	0.5101	—	0.7072
10	3	—	—	0.3822	3.9409	0.3874	0.5002
10	4	0.6164	0.2521	0.6785	—	—	—
10	5	2.9608	0.4550	0.6386	0.4971	2.3437	2.0466
10	6	0.4888	—	0.4568	2.4233	1.7440	0.6625

Table 3: Nondominated solutions retained at different times.

$t = 5$			$t = 15.7633$			$t = 24.7424$		
CT	LB	AD	CT	LB	AD	CT	LB	AD
9.7185	0.0547	0	20.3301	0.0495	7.2194	27.1586	0.0539	1.5871
10.5680	0.0529	0	20.5133	0.0401	7.2194	27.3802	0.0539	0.9745
10.7969	0.0511	0	21.5258	0.0367	7.2194	27.3130	0.0537	1.4474
11.2463	0.0453	0	22.4842	0.0541	4.8224	27.3263	0.0548	0.9963
11.4612	0.0435	0	25.0291	0.0503	4.8224	27.6919	0.0537	0.9963
12.1650	0.0398	0	26.6129	0.0411	4.7628	27.7270	0.0528	1.1974
13.2902	0.0307	0	27.8853	0.0270	5.7375	27.4832	0.0559	0.9328
14.8153	0.0243	0	29.8500	0.0232	3.7171	27.5886	0.0531	1.0079

paper is used to optimize the corresponding workshop initial state. The completion time and maximum machine load of two scheduling indexes in Reference [23] are compared. Figure 12 is a comparison chart of the maximum scheduling time obtained from the optimization of the two models. Figure 13 is a comparison diagram of the maximum machine load obtained from the two models.

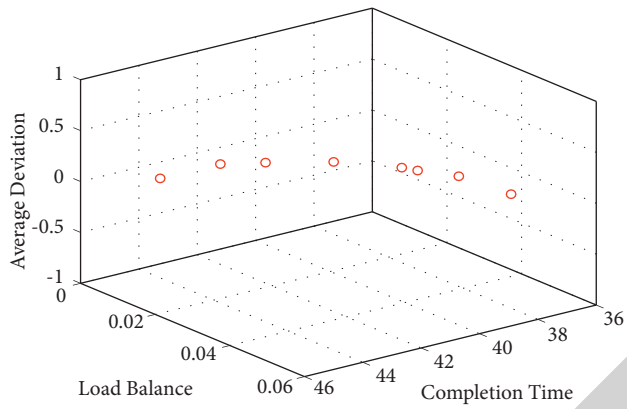

Figure 5: Nondominated graph for the optimization of tasks to be processed at $t = 30$.

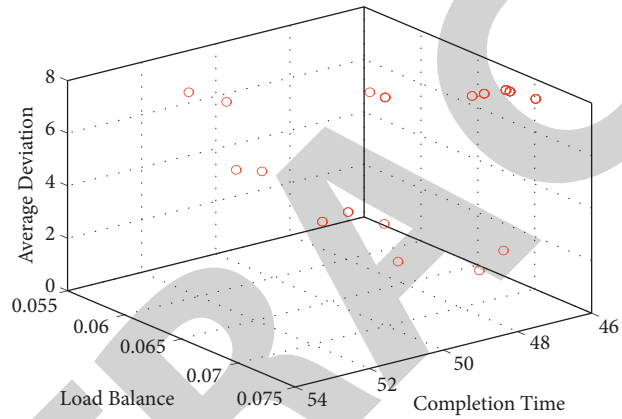

Figure 6: Nondominated graph optimization for rescheduling tasks at $t = 43.6123$.

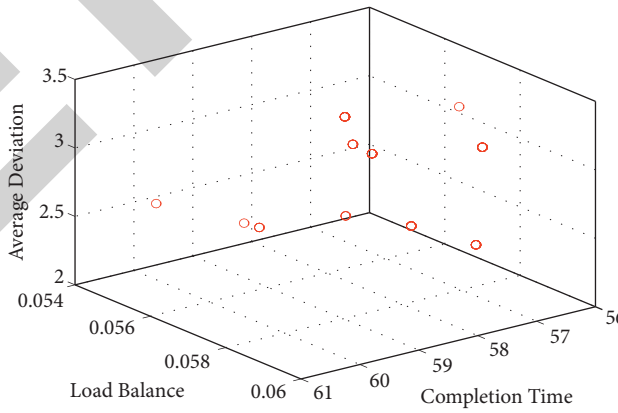

Figure 7: Nondominated graph optimization for rescheduling tasks at $t = 52.1802$.

(2) Figure 12 shows that when the mathematical model in Reference [23] is used to optimize FJSSP continuously, the completion time increases with the increase in the number of tasks to be processed. At the initial time, the mathematical model in Reference [23] achieves shorter completion time at the fourth scheduling cycle, but a minimal difference exists between the two mathematical models at the ninth scheduling cycle. In the rest of the scheduling cycles, the mathematical models in this paper achieve shorter completion time. Therefore, compared with the mathematical model in Reference [23], the mathematical model in this paper is more efficient in solving FJSSP. In Figure 13, the maximum machine

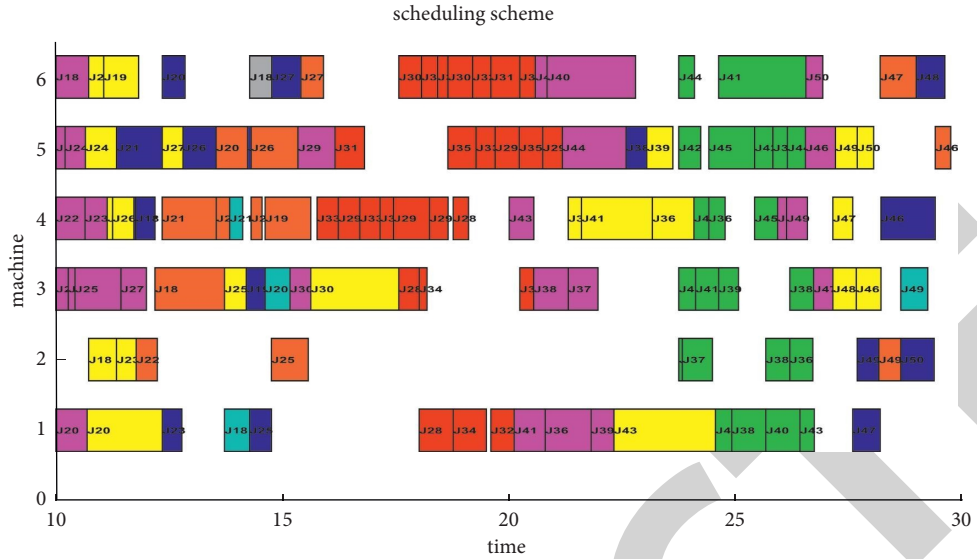

Figure 8: Gantt chart of $t = 10–30$ scheduling scheme.

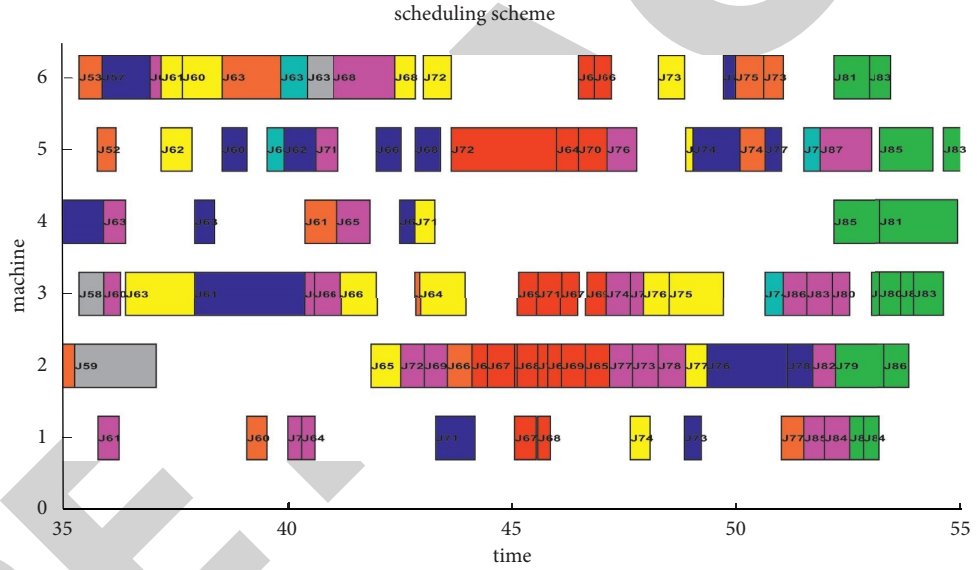

Figure 9: Gantt chart of $t = 35–55$ scheduling scheme.

Table 4: Tasks to be processed at $t = 0$.

Job number	Process number	Machine number and corresponding processing time of each process							
		1	2	3	4	5	6	7	8
1	1	—	0.6382	1.2681	1.0710	—	1.3042	0.8963	—
1	2	0.5019	0.8400	1.3880	1.0160	0.3989	0.8541	0.4708	0.3358
1	3	1.6475	—	0.8298	—	1.2152	0.2717	1.5794	1.5971
1	4	2.8928	1.4613	—	1.1014	0.9968	2.1039	—	—
1	5	1.1864	1.3696	1.2559	0.1734	—	—	—	—
1	6	1.2120	0.6545	0.6413	—	1.2581	1.0654	—	0.7189
2	1	0.6815	0.8164	0.9751	—	1.0529	2.3129	—	0.2768
2	2	0.4422	—	0.4240	—	1.5143	1.5095	2.0199	0.8215
2	3	2.7416	2.6740	—	1.7388	1.3254	0.0500	2.1685	0.3425
2	4	—	0.9891	2.0880	2.2006	0.4174	0.5254	1.9515	0.4033
2	5	2.3676	0.3323	0.7549	1.8217	0.1319	0.5349	1.8295	0.3132
3	1	2.0371	0.7917	1.5249	0.5102	1.7024	1.4674	0.5818	0.5744
3	2	2.1183	—	0.5471	0.9859	0.5768	1.0352	0.6740	1.9032
3	3	0.9638	0.6347	1.1081	0.9293	1.1082	1.4623	0.8659	0.4380

Table 4: Continued.

Job number	Process number	Machine number and corresponding processing time of each process							
		1	2	3	4	5	6	7	8
3	4	—	—	1.4176	0.2305	—	—	—	2.2456
4	1	2.0491	1.6558	—	1.0707	1.5561	0.3166	1.3802	0.7998
4	2	0.3704	0.7575	1.2038	—	—	0.5326	—	—
4	3	—	1.2657	—	—	0.8511	0.8744	2.9220	1.4142
4	4	1.3512	1.4050	0.4743	2.6791	2.8502	1.1182	2.9756	0.3806
4	5	0.9679	—	1.3229	1.2626	1.8965	0.4182	1.3583	0.5312
4	6	—	0.3225	1.9250	—	1.6030	0.9702	2.5834	—
5	1	0.4691	2.1852	0.7140	0.9937	1.2777	2.7375	3.0324	0.4996
5	2	2.9772	—	1.8705	—	—	—	—	1.1175
5	3	—	1.8562	0.1373	1.0024	0.7281	—	—	0.8232
5	4	1.3402	0.6634	0.0999	0.6004	0.2650	—	—	—
5	5	0.9894	1.9170	2.1850	2.9171	—	0.3045	0.5929	0.3364
5	6	0.6517	0.7840	—	0.2839	0.9946	0.2948	—	0.4172
6	1	1.1747	—	—	—	—	0.2649	0.7974	1.7007
6	2	1.0199	0.6806	0.4107	1.6766	—	0.7231	1.2838	2.3242
6	3	—	—	—	1.6511	0.5025	—	—	1.3843
6	4	0.2826	—	—	1.8508	—	—	0.5031	—
7	1	0.8562	0.4408	1.2425	—	—	0.9039	1.7611	2.9910
7	2	0.5652	0.8330	1.2936	0.6021	—	0.9480	1.9891	2.9164
7	3	—	0.5842	1.4921	—	0.5617	—	0.6148	—
7	4	—	—	0.7785	—	0.6716	1.6041	1.9949	0.0982
7	5	—	0.5235	1.4898	—	1.3141	0.0204	—	—
8	1	—	0.5735	—	—	0.1725	—	1.3313	0.4930
8	2	0.3275	—	—	—	0.9262	—	—	0.6194
8	3	—	2.2066	0.8222	0.9665	0.6131	0.2283	1.1873	1.7934
8	4	0.5493	0.6385	0.5536	—	0.6374	0.5601	1.1408	—
8	5	0.9098	—	—	—	1.4946	0.6431	—	0.7129
8	6	1.6085	3.3016	3.1581	0.3536	1.1893	0.4541	0.3692	—
9	1	1.5629	0.3463	1.0989	1.6513	—	—	—	—
9	2	0.2841	0.7069	2.4057	1.3018	1.1407	0.4920	1.9512	2.9612
9	3	0.0736	—	1.7815	1.3833	0.1368	1.5720	2.1434	0.4936
9	4	—	1.6847	3.0446	—	—	3.0226	0.5515	—
9	5	0.4957	1.7989	—	1.2870	0.4484	2.8027	—	0.0536
10	1	0.4631	2.9016	—	0.8857	0.1663	—	—	—
10	2	0.1600	—	1.0278	—	0.4837	—	—	—
10	3	—	2.0967	1.3427	—	—	0.3534	0.1632	1.3010
10	4	0.5864	1.3044	2.0412	0.6325	1.8661	0.4146	—	—
10	5	1.8594	0.5863	0.6037	0.2186	0.6127	0.1225	3.1598	—
10	6	2.2898	1.4587	—	0.1752	0.4326	0.3804	1.9046	0.9512

load increases with the increase in the number of tasks to be processed. The first scheduling cycle and the seventh scheduling period in the literature yield a smaller maximum machine load. The optimization results of the two mathematical models at the fifth scheduling cycle are similar to each other. In the rest of the scheduling cycles, the mathematical models proposed in this paper achieve a smaller maximum machine load. Hence, compared with the mathematical model in Reference [23], the mathematical model in this paper has better stability when solving FJSSP.

(3) The mathematical model established in this paper is used to optimize the above dynamic environment continuously. The workshop state at the beginning of each new scheduling cycle is recorded. Several different initial states and transient scheduling cycles are obtained. The new task to be processed in each scheduling cycle is recorded, and the mathematical model in Reference [23] is optimized in the initial state of the corresponding workshop. The completion time, LB, and deviation degree of the three scheduling indexes optimized in this paper are compared. Figure 14 shows a comparison of the maximum scheduling time obtained from the optimization of the two models, and Figure 15 depicts a comparison of the LB obtained from the optimization of the two models. Figure 14 shows the two models at the time of failure or recovery (M_2 breaks down at $t = 85.7705$, 108.0616; M_5 breaks down at $t = 137.4366$ and recovers at $t = 196.8504$; M_6 breaks down at $t = 253.2210$ and recovers at $t = 261.4715$). Figure 16 is a Gantt chart of the final scheduling scheme obtained by optimizing the mathematical model established in this paper.

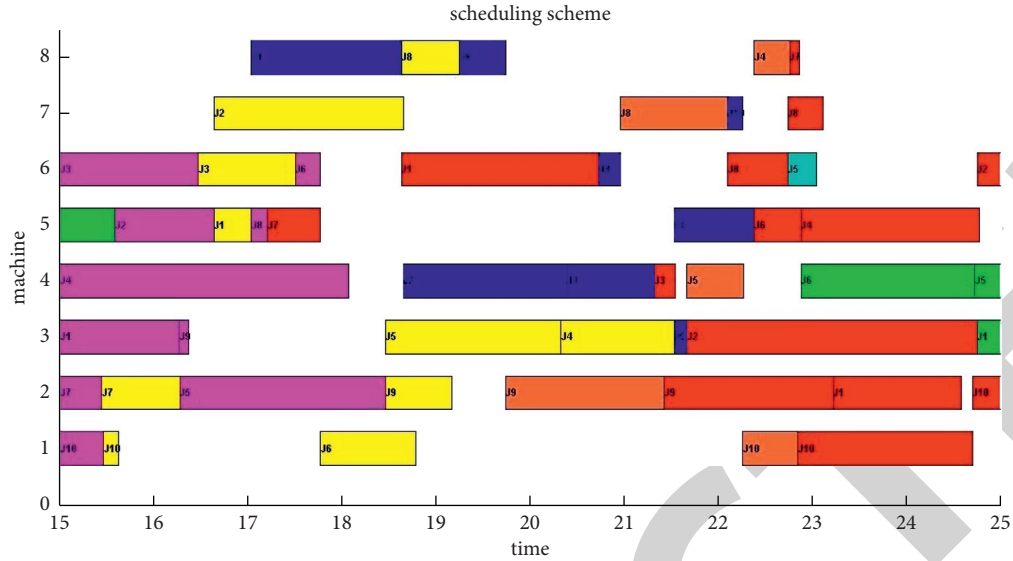

Figure 10: Gantt chart of $t = 15 \sim t = 25$ scheduling scheme.

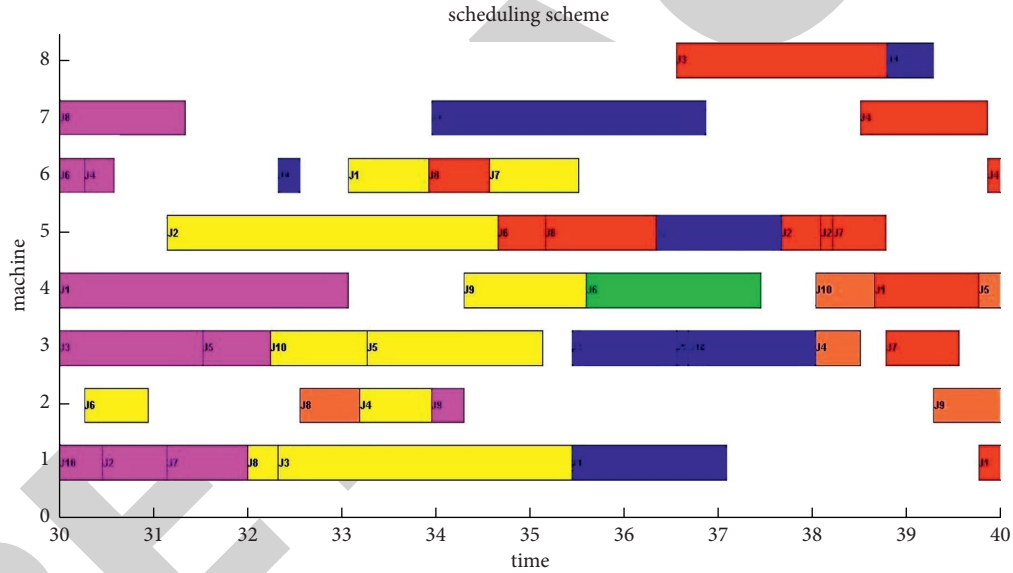

Figure 11: Gantt chart of $t = 30 \sim t = 40$ scheduling scheme.

Table 5: Tasks to be processed at $t = 0$.

Job number	Process number	Machine number and corresponding processing time of each process					
		1	2	3	4	5	6
1	1	—	—	9.8238	5.6066	2.3884	—
1	2	—	8.7614	0.1616	—	4.5111	3.6049
1	3	2.2260	—	1.0555	5.9327	—	—
1	4	6.8426	5.3029	—	—	0.3179	2.4924
2	1	—	—	8.7605	3.2139	0.8977	2.2408
2	2	1.8753	27.4468	6.7044	5.2220	—	0.1501
2	3	1.0321	0.4354	0.4033	3.8629	0.2432	0.7356
2	4	4.1349	3.6649	—	4.2966	0.3085	0.7078
2	5	5.1805	—	6.7070	0.0218	6.3798	1.4679
3	1	7.4515	—	8.7112	11.4423	0.5015	0.4604
3	2	3.4696	—	0.1401	3.4382	—	0.8415

Table 5: Continued.

Job number	Process number	Machine number and corresponding processing time of each process					
		1	2	3	4	5	6
3	3	0.8281	—	12.5823	0.9464	—	14.4992
3	4	5.4673	—	3.5510	—	3.7151	4.3297
3	5	—	2.3391	—	2.3792	6.5705	0.4136
4	1	1.0062	3.9873	0.2861	6.3271	2.9692	0.7711
4	2	3.1558	0.3706	3.3700	—	4.1528	0.5581
4	3	15.1522	6.1692	—	5.3464	0.2628	—
5	1	1.3501	2.3151	6.9586	6.3153	3.9388	0.5668
5	2	—	7.8409	0.4757	—	7.1685	11.6505
5	3	1.5864	1.6647	2.4072	1.1779	—	0.3065
5	4	1.6864	4.8608	—	2.6172	—	4.6677
6	1	6.3858	—	9.5675	8.1202	—	1.0911
6	2	10.0866	4.2997	—	14.2298	2.1821	—
6	3	—	3.9033	0–.6444	8.5418	3.8565	—
6	4	0.9869	—	0.7095	2.5105	11.3434	21.0465
6	5	2.1080	—	5.2743	2.0611	1.2416	6.9164
7	1	1.2192	2.0500	4.6593	—	—	2.3203
7	2	13.4036	0.3065	6.4845	4.5084	0.1403	0.7197
7	3	12.0271	7.5283	2.3252	8.6630	2.1088	4.8157
7	4	3.4707	2.7486	—	6.7813	2.5525	10.2010
8	1	10.9951	9.7286	2.7084	8.0656	—	4.2686
8	2	6.5468	3.4921	1.6932	4.2582	2.3376	9.5210
8	3	1.2771	7.0129	—	—	0.0317	9.7530
8	4	10.1690	0.3012	4.4865	3.8201	3.8540	3.9938
9	1	—	0.8426	4.9192	—	16.1560	18.1553
9	2	3.9587	1.8530	—	—	0.8106	—
9	3	0.6760	—	—	2.2566	—	7.2321
9	4	0.3468	11.8284	0.2563	2.6967	—	—
10	1	0.6787	2.9536	1.5828	4.1907	0.8061	1.9341
10	2	11.2861	0.9612	3.3480	4.2695	—	5.6762
10	3	—	3.3068	5.3467	8.9140	—	1.1600
10	4	1.9494	—	—	3.0254	0.2133	—
10	5	9.7772	0.2504	1.4523	3.7225	11.8949	0.9377
10	6	4.8633	1.2156	10.1277	2.1841	4.6520	0.2748

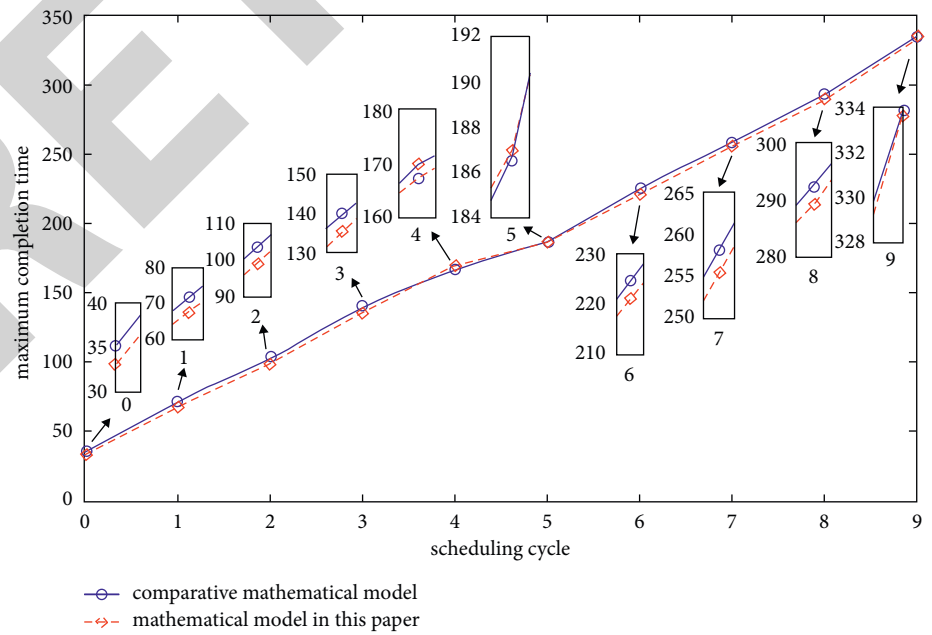

Figure 12: Comparison of the maximum completion time of each scheduling cycle.

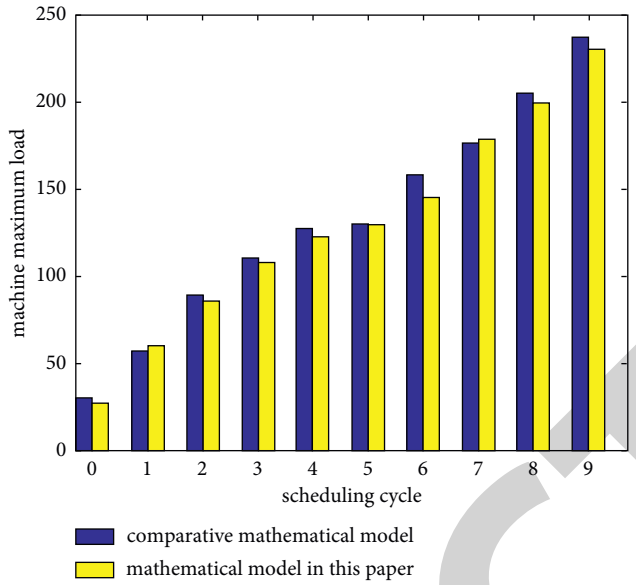

Figure 13: Comparison of the maximum load of machines in each scheduling cycle.

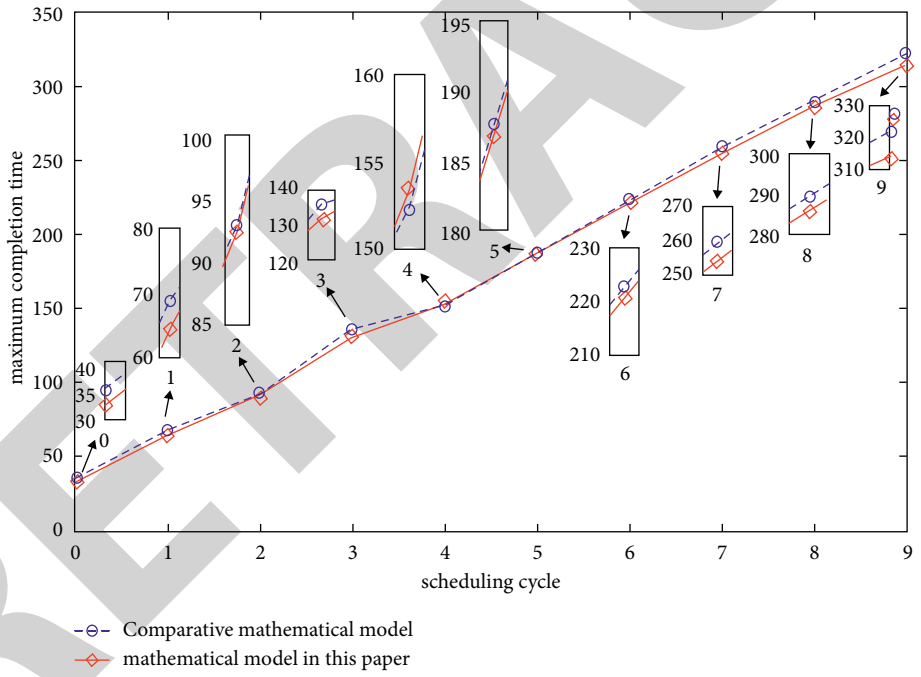

Figure 14: Comparison of the maximum completion time of each scheduling cycle.

Figure 14 demonstrates that when the mathematical model established in this paper continuously optimizes FJSSP, the completion time increases with the number of tasks to be processed. Except at the fourth scheduling cycle, the mathematical model in this paper achieves a smaller completion time in the rest of the scheduling cycles. Thus, compared with the mathematical model in Reference [23], the mathematical model in this paper is more efficient in solving FJSSP. In Figure 15, with the progress of the scheduling process, the stability of the workshop is enhanced. Except at the sixth scheduling cycle, the mathematical model in this paper achieves a smaller LB in the rest of the scheduling cycles. Accordingly, compared with the mathematical model in Reference [23], the current model achieves better system stability when solving FJSSP. Figure 14 illustrates that at the time of failure and the time of recovery, the mathematical model established in this paper can achieve smaller deviations of the old and new schemes. Therefore, the mathematical model proposed in this paper can maintain better stability in the rescheduling process after the workshop machine failure or machine failure recovery. A comprehensive observation of Figures 14–17 shows that machine M_5 fails at the fourth

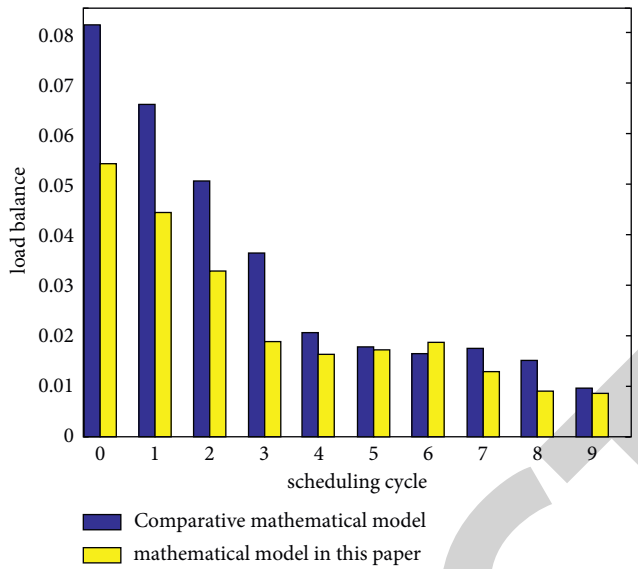

Figure 15: Comparison of LB for each scheduling cycle.

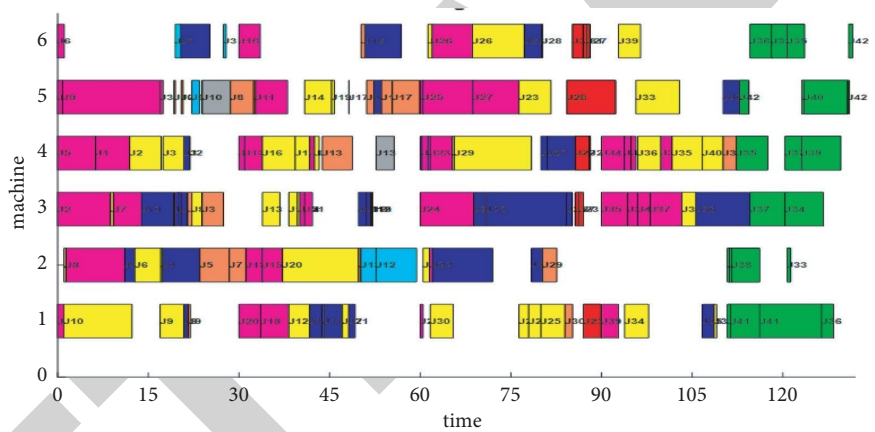

(a)

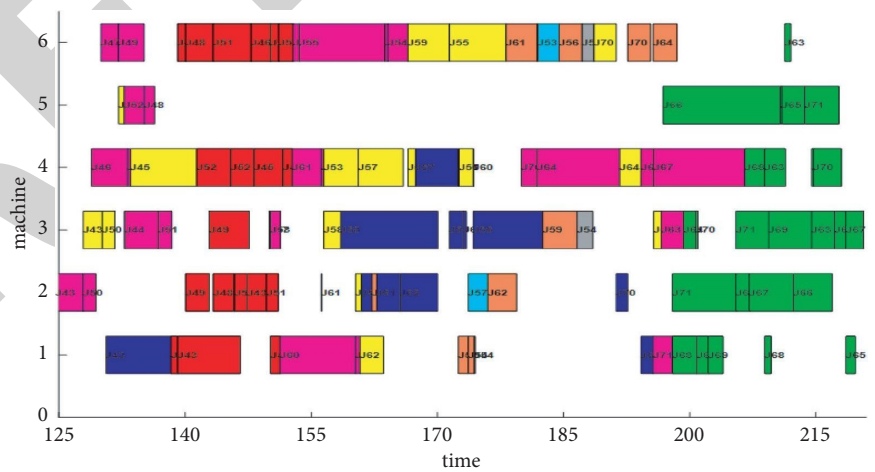

(b)

Figure 16: Continued.

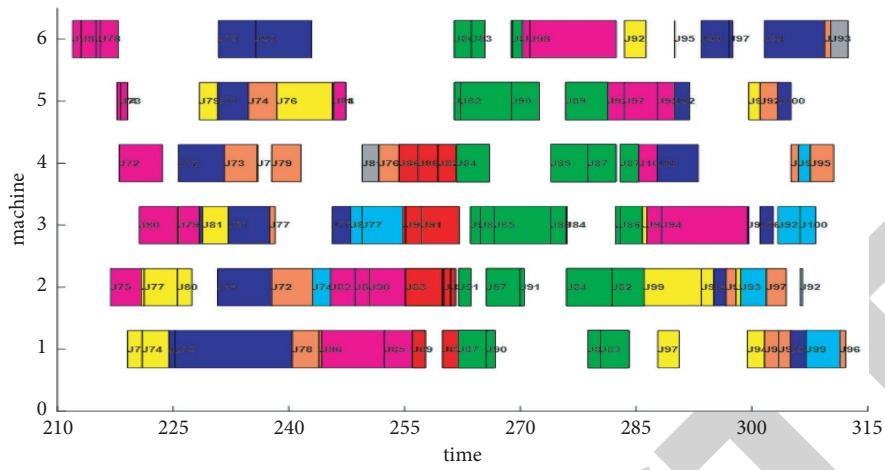

Figure 16: Final scheduling scheme in this paper. (a) $t = 0$–$3t_1$. (b) $t = 4t_1$–$6t_1$. (c) $t = 7t_1$–$9t_1$.

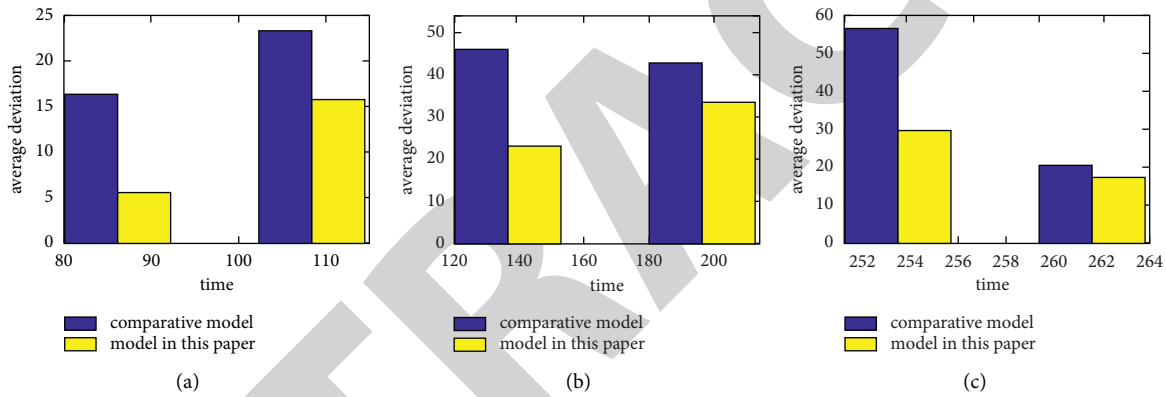

Figure 17: Comparison of deviations between old and new scheduling schemes during machine failure and failure recovery. (a) M2 failure. (b) M5 failure. (c) M6 failure.

scheduling cycle. Although the final scheduling scheme optimized by the mathematical model established in this paper is longer, it maintains better system stability, especially when the machine fault rescheduling achieves a smaller deviation; *M5* is recovered at the sixth scheduling cycle. Although the LB of the final scheduling scheme optimized using the mathematical model established in this paper is poor, the completion time is shorter, and a smaller deviation degree is achieved during machine fault rescheduling.

In summary, the mathematical model established in this paper has higher efficiency and better system stability when solving FJSSP. Moreover, in the workshop machine failure or failure recovery, it can pay attention to efficiency and stability at the same time. It has certain advantages for FJSSP optimization.

5. Conclusions

In this study, the characteristics and current research status of FJSSP are comprehensively analysed. A new mathematical model is established on the basis of three objectives: completion time, LB, and AD between new and old scheduling schemes. A dynamic multi-objective SSA is used to optimize the established model. The experimental results show that the dynamic multi-objective SSA can be used to solve FJSSP. The mathematical model established in this paper has improved efficiency and stability in solving dynamic multi-objective FJSSP. Especially when a workshop machine breaks down or gets back to work, the established model can keep enhanced balance between efficiency and stability. In the future, convergence rate of flexible job shop scheduling algorithms should be improved.

Data Availability

The data used to support the findings of this study are available from the corresponding author upon request.

Conflicts of Interest

The authors declare that there are no conflicts of interest regarding the publication of this paper.

Hindawi
International Journal of Antennas and Propagation
Volume 2024, Article ID 9843957, 1 page
https://doi.org/10.1155/2024/9843957

Retraction

Retracted: Research on Behavior Monitoring of Elderly Living Alone Based on Wearable Devices and Sensing Technology

International Journal of Antennas and Propagation

Received 30 January 2024; Accepted 30 January 2024; Published 31 January 2024

This article has been retracted by Hindawi following an investigation undertaken by the publisher [1]. This investigation has uncovered evidence of one or more of the following indicators of systematic manipulation of the publication process:

(1) Discrepancies in scope
(2) Discrepancies in the description of the research reported
(3) Discrepancies between the availability of data and the research described
(4) Inappropriate citations
(5) Incoherent, meaningless and/or irrelevant content included in the article
(6) Manipulated or compromised peer review

The presence of these indicators undermines our confidence in the integrity of the article's content and we cannot, therefore, vouch for its reliability. Please note that this notice is intended solely to alert readers that the content of this article is unreliable. We have not investigated whether authors were aware of or involved in the systematic manipulation of the publication process.

In addition, our investigation has also shown that one or more of the following human-subject reporting requirements has not been met in this article: ethical approval by an Institutional Review Board (IRB) committee or equivalent, patient/participant consent to participate, and/or agreement to publish patient/participant details (where relevant).

Wiley and Hindawi regrets that the usual quality checks did not identify these issues before publication and have since put additional measures in place to safeguard research integrity.

We wish to credit our own Research Integrity and Research Publishing teams and anonymous and named external researchers and research integrity experts for contributing to this investigation.

The corresponding author, as the representative of all authors, has been given the opportunity to register their agreement or disagreement to this retraction. We have kept a record of any response received.

References

[1] M. Yin, "Research on Behavior Monitoring of Elderly Living Alone Based on Wearable Devices and Sensing Technology," *International Journal of Antennas and Propagation*, vol. 2021, Article ID 4200137, 10 pages, 2021.

Hindawi
International Journal of Antennas and Propagation
Volume 2021, Article ID 4200137, 10 pages
https://doi.org/10.1155/2021/4200137

Research Article

Research on Behavior Monitoring of Elderly Living Alone Based on Wearable Devices and Sensing Technology

Mulin Yin

Jiangsu Food & Pharmaceutical Science College, Huai'an, Jiangsu 223003, China

Correspondence should be addressed to Mulin Yin; 20031020@jsfpc.edu.cn

Received 18 August 2021; Revised 29 September 2021; Accepted 8 October 2021; Published 15 October 2021

Academic Editor: Fangqing Wen

Human behavior recognition and status monitoring are current research hotspots, especially in the fields of medical monitoring, smart home, and elderly care. With the development of sensor technology, low-power IC chips, and wireless body sensors, miniature sensor networks can be popularized and applied in daily life. Since the energy consumption of sensor networks is a bottleneck problem that limits its development, this paper designs a multimodal collaborative sensing method for the application scenarios of elderly people living alone to reduce energy consumption in the process of daily behavior perception of the elderly. This method subdivides behavior perception into behavior recognition and status monitoring, determines the optimal sensor combination for identifying monitoring different behaviors based on information theory, and then uses a behavior recognition model modeled by a multiclassifier and a status model modeled by a plurality of two classifiers that are used to perceive user behavior. A large number of experimental results show that compared with the traditional sensor network method, our proposed solution can achieve effective sensing while reducing the energy consumption in the process of data transmission and model calculation, thereby prolonging the working life of the sensing network and realizing long-term and reliable daily behavior perception.

1. Introduction

Human behavior recognition [1, 2] and status monitoring are the current research hotspots in the field of artificial intelligence and pattern recognition. Human behavior recognition is classified by the method of obtaining human behavior data and can be divided into behavior recognition methods based on computer vision and behavior recognition methods based on sensor devices. Among them, the main application areas of human behavior recognition based on computer vision include intelligent video surveillance, virtual reality, smart home, user interface, and automobile driving [3–5]. Human behavior recognition based on sensor equipment is mainly used in the fields of medical monitoring, sports medicine, elderly care, and gait analysis [6].

The development of wireless communication technology, sensor technology, low-power embedded technology, and nanotechnology has enabled the integration of miniature sensor networks with our daily life environment, and the difficulty and cost of developing miniature sensor devices such as wearable smart devices have been greatly reduced. At present, various miniature sensor devices (such as wearable sensors devices) have become very popular. Because they are not restricted by the place of use, they are simple to operate, easy to carry, small in size, beautiful, and fashionable. In the field of mobile health, wearable devices and other miniature sensor devices have become an indispensable part of daily life [7]. These wearable sensor products can detect human sleep and movement and can provide a data reference for our daily life or whether the amount of exercise is reasonable. Human physiological characteristics monitoring systems based on wearable sensors have also been widely used in the medical field. The detected data includes the patient's body temperature, heart rate, brain activity, muscle movements, and other important physiological data [8, 9]. These human physiological data can be obtained through wearable heart rate sensors, temperature sensors, blood pressure sensors, acceleration sensors, and so on. These

sensors can provide a lot of accurate and reliable data about human activities and behaviors. Through the monitoring data provided by the sensors, the nursing staff can know whether the patient is in a relatively healthy condition in real time. If one or more of the physical characteristics of the patient is abnormal during the monitoring process, such as Parkinson's syndrome or sudden heart disease, the monitoring systems will trigger the alarm mechanism that enables the patient to be treated as soon as the unexpected situation is sent.

The development of wireless body sensor networks (WBSN) [10, 11] has greatly reduced the difficulty of developing a mobile human body monitoring system. The sensor nodes distributed in the human body and space form the WBSN through self-organization or multihop. The sensing node in WBSN is used to detect human physiological parameters such as body temperature, blood pressure, and heart rate and send the collected information to the base station or data processing center through the wireless network in a cooperative manner. Commonly used communication protocols in wireless body sensor networks include Bluetooth, WI-FI [12, 13], RFID [14–18], Zigbee, and so on. In various fields, WBSNs have been widely used, including medical care, disease monitoring and prevention, and smart homes. With the more in-depth research and wide application of WBSNs, it will inevitably penetrate into many fields in our real life.

Also, with the development of various technologies, multiparameters, intelligence, miniaturization, and low power consumption have become the main directions for the development of wireless medical sensor nodes, and wireless sensor networks have also been widely used in the medical field. The development of community-wide human characteristics monitoring systems and the establishment of intelligent wards are two of the current development trends in the medical field. The architecture of the physiological characteristic monitoring system based on a wireless sensor network is shown in Figure 1. In Figure 1, the patient's physiological characteristic parameters are collected by wearable sensors, and their data are sent to the monitoring center of the upper computer, and the upper computer determines the patient's health status through the threshold judgment of the parameters.

With the further promotion of the research and application of wearable devices, WBSN composed of multimodal sensors can achieve comprehensive and continuous detection of human behavior through long-term wear in daily life so as to help elderly people living alone, especially those suffering from Parkinson's disease (PD), and provide solutions. At present, not only the continuous detection of human behavior using WBSN through the continuous working mechanism of all sensors in the network consumes a lot of energy and computing resources, but the limited computing resources, wireless transmission, and power of the sensor network also greatly limit WBSN's monitoring and evaluation of PD motor symptoms in daily life. At present, whether it is using wearable sensor devices or BSNs to continuously monitor human behaviors, all sensors or devices in the network will continue to work. Therefore, they not only consume a lot of energy and computing resources but also greatly limit the BSN's monitoring and evaluation of monitored objects. In order to reduce the resource and energy consumption in the process of user behavior perception, this paper proposes a Parkinson's disease-oriented multimodal collaborative perception method. While the proposed method realizes the perception of user behavior, it minimizes the number of working sensors and the amount of data transmitted, thereby reducing the energy and resource consumption of the entire network.

2. Related Work

Because wearable device-based behavior recognition methods have advantages in many aspects, they have received widespread attention. The acceleration sensor is a necessary sensor for wearable devices, and it is also that the most widely used sensor in human behavior recognition. By analyzing the acceleration of certain positions of the human body, work such as fall monitoring [19], human posture analysis [20], and movement type analysis [21] can be performed. In the human body behavior recognition methods based on the acceleration sensor, two basic issues must be considered first: the number of acceleration sensor nodes and the nodes. In order to improve the accuracy of behavior recognition, early researchers usually used more acceleration sensors to obtain a large amount of human behavior data. Laerhoven installed 30 acceleration sensors on their clothes [22], which are mainly placed on the joints and torso of the human body, and centrally processed the data collected by the acceleration sensors. Subsequently, Kern used 12 acceleration sensors in the behavior recognition experiment, mainly placing the sensors at the joints of the arms and legs, and finally achieved relatively ideal results [23]. In the research work of Varkey, only two acceleration sensors were used, which were placed on the wrist and ankle [24], and Khan only used one acceleration sensor, which was placed on the chest [25]. In the process of behavior recognition, when the number of acceleration sensors is large, in order to reduce the amount of data transmitted by the network in WBSN and reduce the processing of redundant data, an appropriate sensor work scheduling strategy is needed at this time. When the behavior of the human body in a certain state can get the correct recognition result using a small number of sensors, the data of other sensors are redundant at this moment. Zappi solves this problem by dynamically selecting the sensor needed to recognize the current human behavior. The sensor will only be awakened when the current behavior recognition requires data from a certain sensor node [26]. Veltink et al.'s research work shows that a small number of sensor nodes can correctly recognize a behavior set [27]. In the process of behavior recognition, only when the data collected by the current sensor node cannot uniquely identify the current behavior, the system will start a new sensor node to collect human behavior data. Given a specific behavior set, it is easy to select the number of sensors needed and the placement position of the sensors. If a larger behavior set is given and the number of sensors working is also required to be ensured, distributed

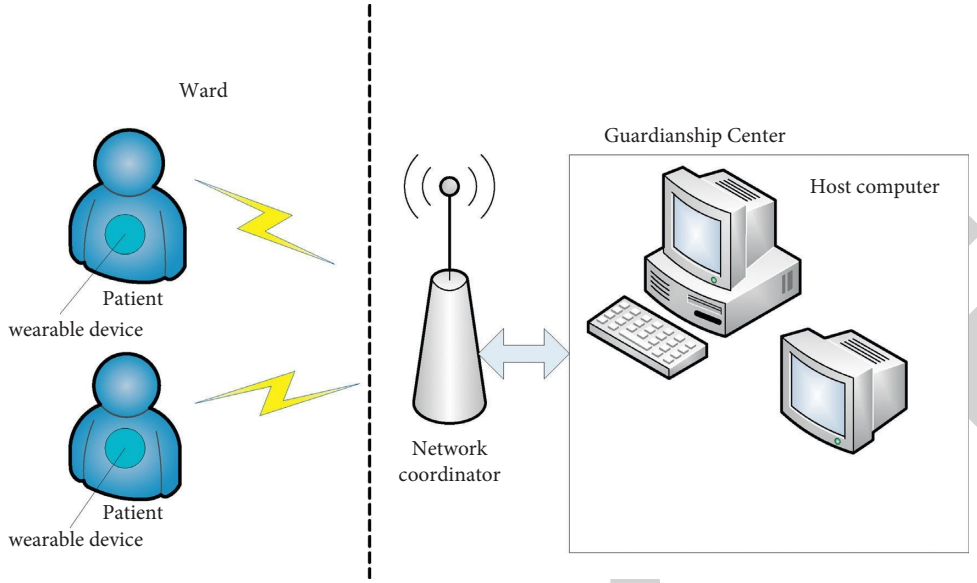

Figure 1: The physiological feature monitoring system architecture diagram based on WSN.

recognition mode is a good solution. The distributed recognition mode only needs to collect the node data of some sensors. Ghasemzadeh et al. [28] proposed a distributed behavior recognition method based on string matching. Each sensor node recognizes the current behavior of the human body through the sensor data collected by itself and the processing results of other sensor nodes and sends the generated preselected set of human behavior to neighboring nodes. When there is only one behavior in the preselected set of generated behaviors, this behavior is regarded as the target behavior of the current human body. Yang et al. [29] proposed a distributed human behavior recognition framework based on a low-bandwidth wearable sensor network (distributed sparse classification method). This method uses human behavior sample training motion sequences as prior samples and can mark those behaviors that are not within the recognition range. In the process of using WBSN for data perception, limited computing resources, electricity, and energy have gradually become one of the bottlenecks restricting its application and development and have become hot research topics. Gedik et al. [30] dynamically select a part of the sensor for sampling, while the rest of the sensor data is generated by the probabilistic model trained in advance, reducing power consumption by reducing the number of working sensors. Willett et al. [31] first roughly recognizes the current environment through a small number of sensors and then dynamically activates the sensors based on the recognition results so as to maintain high sampling frequency and accuracy while reducing the number of activated sensors to reduce the overall network power consumption and communication overhead. Ngai and Xiong [32] proposed a method for evaluating the quality of perceived data for the WBSN composed of the mobile phone's own sensors and fixed sensors, dynamically adjusting the sampling rate of the sensor, so as to reduce power consumption while ensuring data quality. In addition, there are some other types of IoT sensing such as motion sensing [33] by using MIMO radar signals.

However, the currently proposed model not only ignores the collaborative relationship between sensors, but also does not consider the power consumption caused by the complexity of the model calculation process. In order to further reduce the energy and resource consumption caused by behavior perception and model calculation, this paper proposes a collaborative sensing mechanism that uses a multisensor-multiclassification model to identify behaviors and a few-sensor-two-classification model to monitor state.

3. Multimodal Collaborative Sensing Method for Elderly Living Alone

In order to effectively reduce the power consumption in the process of WBSN perceiving users' daily behaviors, this paper proposes a multimodal collaborative sensing method (MMCS-EPLA) for elderly people living alone. The diagram of multimodal collaborative sensing method is illustrated in Figure 2.

3.1. Sensor Selection Method Based on Information Gain. The basis of the method proposed in this paper is to select the optimal sensor combination for behavior recognition and status monitoring models, which not only effectively characterizes user behavior but also reduces the power consumption of WBSN by optimizing the sensor combination and prolongs the lifetime of sensors.

Information gain is one of the commonly used metrics to measure the importance of a node. It is an evaluation method based on entropy. It measures the contribution of feature F to the classification model. It is generally defined as each category set A before and after the feature appears. The difference in the information entropy of the category is shown in the following formulas:

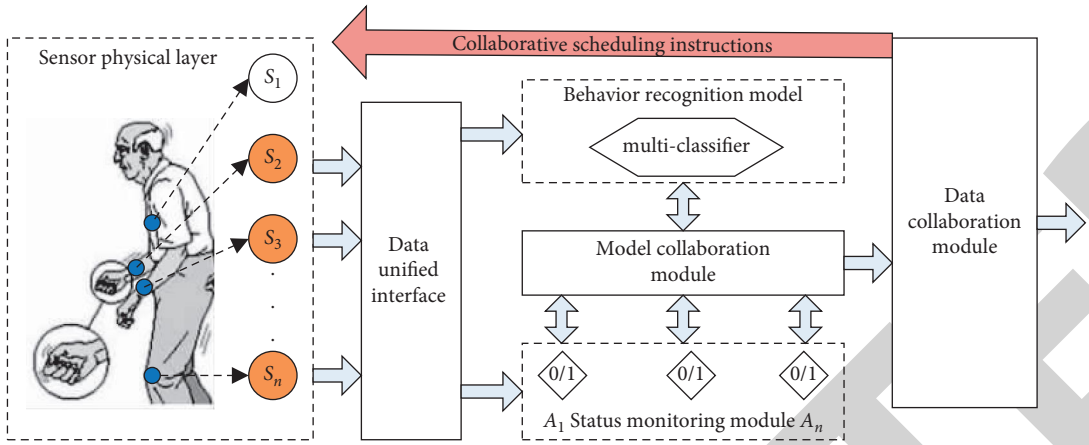

Figure 2: The diagram of the multimodal collaborative sensing method.

$$\text{InfoGain}(F, A) = H(A) - H(A|F), \tag{1}$$

$$H(A) = -\sum_{j=1}^{m} P_r(A_j)\log P_r(A_j), \tag{2}$$

$$H\left(\frac{A}{F}\right) = -\sum_{j}\sum_{v} P_r(A_j|F = v) \log P_r(A_j|F = v), \tag{3}$$

where $H(A/F)$ and $H(A)$ are the information entropy of each category when the feature F appears or not, and the probability of each category appearing $P_r(A_j)$ is estimated using the posterior probability. Inspired by the feature information gain, we propose a method to measure the contribution of the sensor, that is, the contribution of the sensor S is measured by the sum of the information gain of its related features, and the calculation method is shown in the following formula:

$$\text{InfoGain}(S) = \sum_{j} \text{InfoGain}(F_j), \tag{4}$$

where F_j represents the j-th behavior feature extracted from the sensor data.

We use a greedy strategy to combine multimodal sensors in descending order of information gain and find the optimal sensor combination as the sensor that should be activated under this model.

3.2. Collaborative Sensing Model. The multimodal collaborative sensing model for elderly people living alone with Parkinson's disease uses the continuity of PD-related daily behaviors and divides behavior sensing into two submodels: behavior recognition and status monitoring, as shown in Figure 3.

After we use the behavior recognition (multiclassification problem) model to perceive user behavior, we use a simpler status monitoring (two-classification problem) model to determine whether user behavior has changed. Since the lightweight model is used in the status monitoring process, less sensor data and resources will be used, and the overall power consumption of WBSN can be reduced.

Assuming that the number of user behaviors that need to be recognized is m, the task of the behavior recognition model is to recognize what behavior the user is in, which can be characterized by a multiclass classifier (MC). The task of the status monitoring module is to determine whether the user's behavior status has changed, which can be characterized by m binary classifier (BC). It is to be determined which status monitoring model to use based on the result of the behavior recognition model, and the result of the status monitoring model determines whether to call the behavior recognition model.

Let f^{mc} denote the classification result of MC, $f^{mc} = \{1, \ldots, m\}$. f_i^{bc} denote the classification result of i-th BC, $f_i^{bc} = \{0, 1\}$. The collaborative working mechanism of the behavior recognition model and status monitoring model is shown in the following formulas:

$$\text{flag}_i^{bc} = \begin{cases} 1, & f^{mc} = i, \\ 0, & f^{mc} \neq i, \end{cases} \tag{5}$$

$$\text{flag}^{mc} = \left\{ 1, \quad \bigcap_{i=1}^{m} f_i^{bc} = 0, 0, \bigcap_{i=1}^{m} f_i^{bc} \neq 0, \right. \tag{6}$$

where flag_i^{bc} represents the cosign of the i-th BC of the status model and flag^{mc} denotes the cosign of the behavior recognition model.

4. Experiment and Analysis

4.1. Experiment Setup. This paper uses a desktop computer equipped with Intel Core i5-2320 CPU (Quad-Core, 3.0 GHz) and 16 GB RAM as the experimental platform. The system used is Windows 10, and the simulation software is MATLAB 2015b. We use the public data sets MHEALTH [34, 35] and PAMAP2 [36, 37] for experiments, which include daily behaviors of 10 and 9 subjects, including sitting, standing, lying, walking, and going upstairs. The types of multimodal sensors and their wearing positions are shown in Table 1. The sampling frequency of all sensors is greater than 50 Hz, which can meet the requirements of user behavior recognition. All experiments are independently performed, and the results are averaged [38, 39].

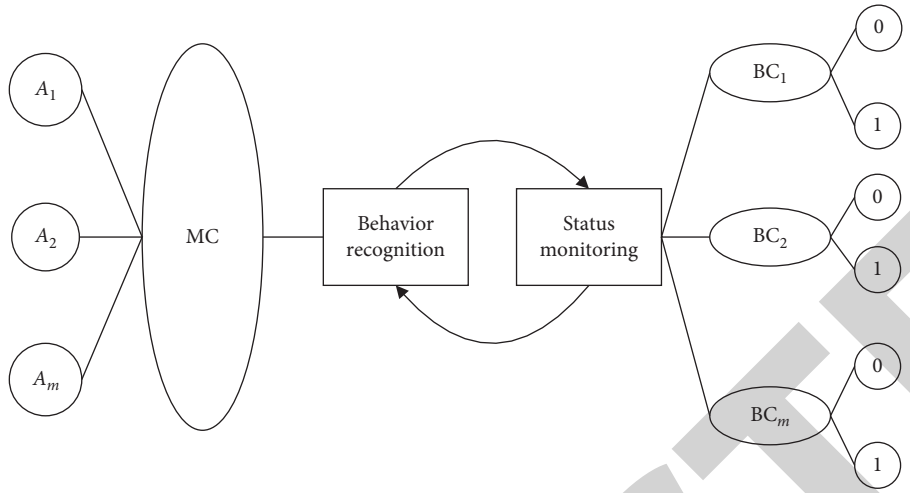

Figure 3: The user behavior sensing model.

Table 1: Multimodal sensor category.

Data set	Category	Symbol	Position
MHEALTH	Accelerometer	AR	Right wrist
	Gyro	GR	
	Magnetometer	MR	
	Accelerometer	AL	Left ankle
	Gyro	GR	
	Magnetometer	ML	
	Accelerometer	C	Chest
PAMAP2	Accelerometer 1	HAcc1	Dominant side wrist
	Accelerometer 2	HAcc2	
	Gyro	HGyro	
	Magnetometer	HMag	
	Accelerometer 1	CAcc1	Chest
	Accelerometer 2	CAcc2	
	Gyro	CGyro	
	Magnetometer	CMag	
	Accelerometer 1	AAcc1	Dominant side ankle
	Accelerometer 2	AAcc2	
	Gyro	AGyro	
	Magnetometer	AMag	

Table 2: Classifier category.

Symbol	Behavior status	Types	Purpose
Multi	Four behaviors	Multiclass classifier	Behavior recognition
U	Upright	Binary classifier	Status monitoring
S	Sit		
L	Lie down		
W	Walk		

The early symptoms of PD are prone to abnormalities in the limbs and trunk. The specific manifestations are hand tremor when sitting or resting, sleep disturbance, trunk stiffness when walking, inconvenience in turning, and hunchback. Therefore, it is related to four daily behaviors such as walking, sitting, lying, and standing that are usually continuous. Realizing the perception of user behavior is the key prerequisite for evaluating the status of motion. Thus, we mainly select four daily behaviors including standing, sitting, lying down, and walking from the two data sets for experiments, as shown in Table 2. In Table 2, the behavior recognition model based on multiclass modeling is used to identify four effective behaviors. The status monitoring model based on the binary classifier modeling is used to determine whether the user's behavior has changed. It is worth noting that in order to verify our behavior model, we use experimental results to determine the number of classifiers. When training multiclassifiers, k selects {5, 10, 20, 30, 40, 50, 60}, and the result of the constructed classifier on the validation set S_v is shown in Figure 4.

The abscissa of all subgraphs in Figure 4 represents the number of multiclassifiers, and the ordinate represents the recognition rate of behavior. It can be seen from Figure 4 that the recognition results of each classifier for walking, going upstairs, going downstairs, and stationary are roughly the same, and the interpolation of the recognition rate is within 1%. It can be seen from Figure 4(e) that when the number of classifiers is 30, the recognition result of the classifier for running has a small improvement. Combing the recognition rate of various behaviors, when the number of classifiers is 30, the classifier in the method designed in this paper has the best recognition effect on the verification set.

Data preprocessing: this paper uses a sliding window mechanism to frame the original data and uses the window as the smallest unit for feature extraction and behavior recognition. To ensure the accuracy of user behavior perception, the window size is set to 1 second; the overlap between windows is 50%; and the minimal time interval for sensing user behavior is 0.5 second. Aiming at the problem of data imbalance in the process of data collection, the down-sampling method is adopted in the experimental preprocessing process to ensure that the effective behavior and the quantity of other data are balanced during the model training process.

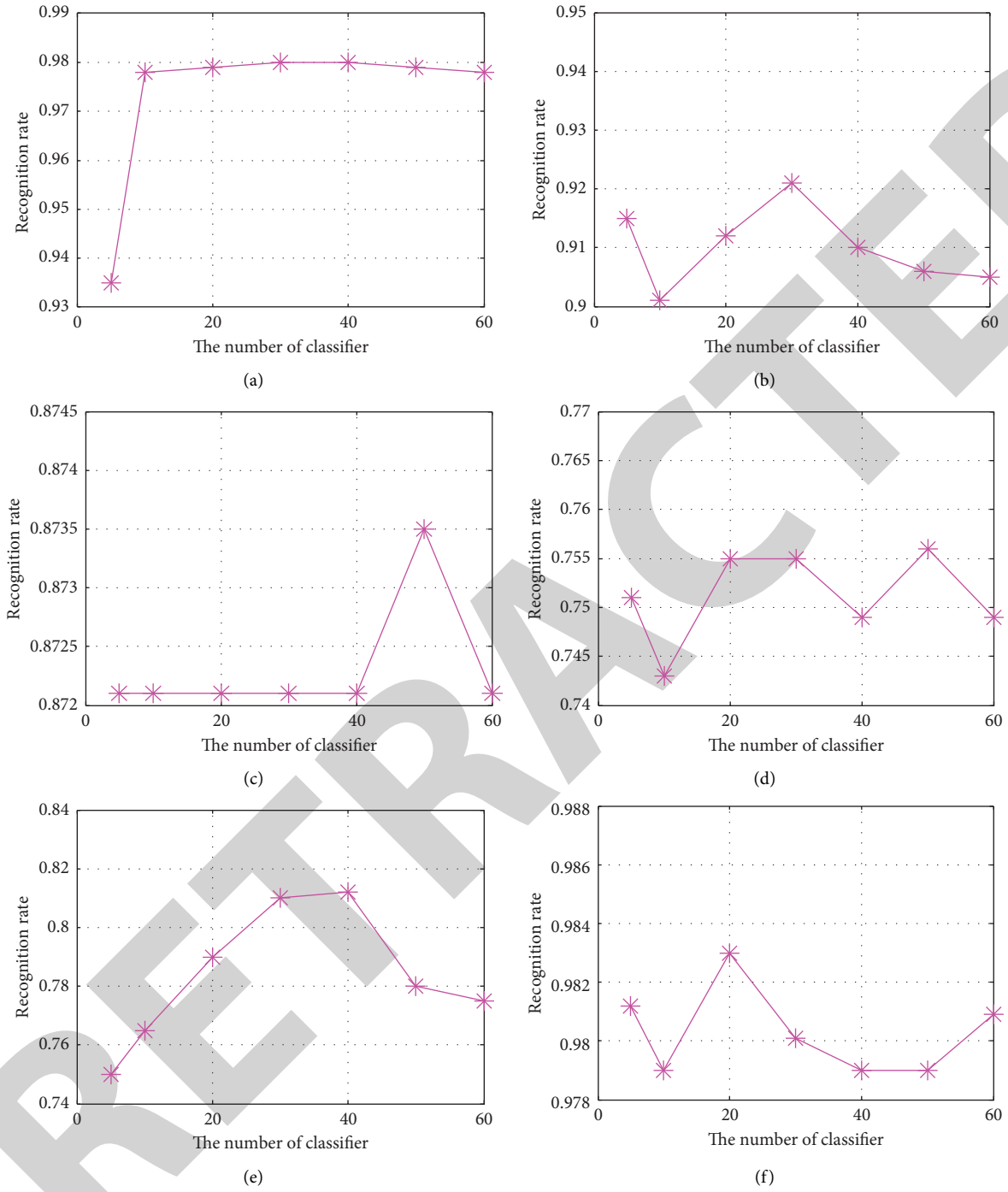

Figure 4: Experimental results: accuracy test of the classifier on the validation set. (a) Walk recognition rate. (b) Upstairs recognition rate. (c) Downstairs recognition rate. (d) Jump recognition rate. (e) Jogging recognition rate. (f) Stationary recognition rate.

Classifier selection: the multimodal collaborative perception method proposed in this paper divides behavior perception into two subtasks including behavior recognition and status monitoring, which are modeled by multiclassifiers and binary classifiers, respectively. In order to simplify the model training process, an extreme learning machine (ELM) [40] that supports multiclass classification and binary classification problems is selected as the classifier.

4.2. Effective Sensor Selection. The information gain calculation of the sensor is based on the information gain of related features, so common behavior statistical features are extracted in the sliding window, including mean, variance, standard deviation, zero-crossing rate, over-averaging rate, maximum value, and minimum value. Figure 5 shows the information gain of the multimodal sensor in the MHEALTH data set for the behavior recognition model and the status monitoring model (the results on the PAMAP2

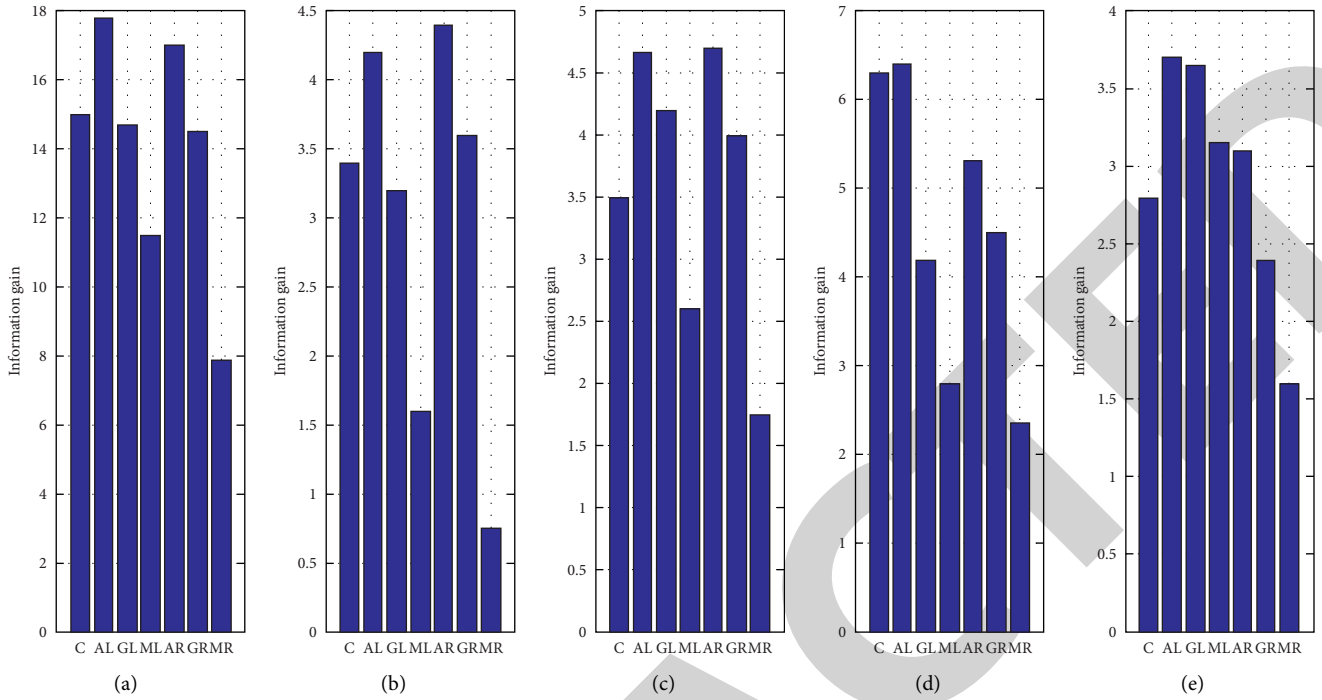

Figure 5: Information gain of multimodal sensors for each classification model in the MHEALTH. (a) Behavior recognition model. (b) Upright monitoring model. (c) Sitting monitoring model. (d) Lying down monitoring model. (e) Walking monitoring model.

Table 3: Optimal combination of multimodal sensors.

Data set	Model	Sensor combination	Number of hidden layer nodes
MHEALTH	Multi	AL, AR, C, GL	234
	Stand	AR	61
	Sit	AR, AL, GL	63
	Lie	AL, C	21
	Walk	AL, GL	112
PAMAP2	Multi	AAcc1, AAcc2, AMag, CAcc2, CAcc1, GMag	286
	Stand	AAcc1, AAcc2, AMag, CAcc1, CAcc2, CMag	21
	Sit	AAcc1, AAcc2, AMag	103
	Lie	CMag	306
	Walk	AAcc2, AAcc1, CAcc2, AGyro, CAcc1, AMag	126

data set are similar). It can be seen that the degree of contribution of the same sensor to different models is different, that is, it is scientific and necessary to select a targeted sensor combination for the behavior recognition model and the status monitoring model. In order to select the most effective sensor combination, multimodal sensors are greedily combined in descending order of information gain, and a tenfold cross-validation method is used for each combination to select the best sensor combination according to the best accuracy. According to the accuracy and time of model recognition, the optimal sensor combination is selected to achieve a balance between model performance and power consumption. The results are shown in Table 3. In the same data set, compared with the behavior recognition model, the status monitoring model needs either fewer sensors or a simpler model (with fewer hidden layer nodes), which reduces the energy consumption in terms of a number of sensor activations and computing resources consumption, respectively.

4.3. Low-Power Performance Evaluation. In the working process of WBSN, its power consumption mainly comes from data communication [41], and the energy consumption in the scheduling process comes from model calculations. On the two data sets of MHEALTH and PAMAP2, a leave-one-out cross-validation method is used to compare the method in this paper with the traditional method of multimodal sensor all working continuously. Comparing the perception accuracy, testing time, and the number of sensors, the results are shown in Figures 6 and 7. Compared with the traditional continuous working method, the method in this paper has a decrease in the accuracy of behavior perception due to the mutual scheduling between the behavior recognition model and the status when the behavior changes, but the method in this paper can be effective on the recognition of daily behavior of related users. Since only fewer sensors need to be activated in the status monitoring process and compared with the multiclass classifier, the binary classifier consumes less resources in the

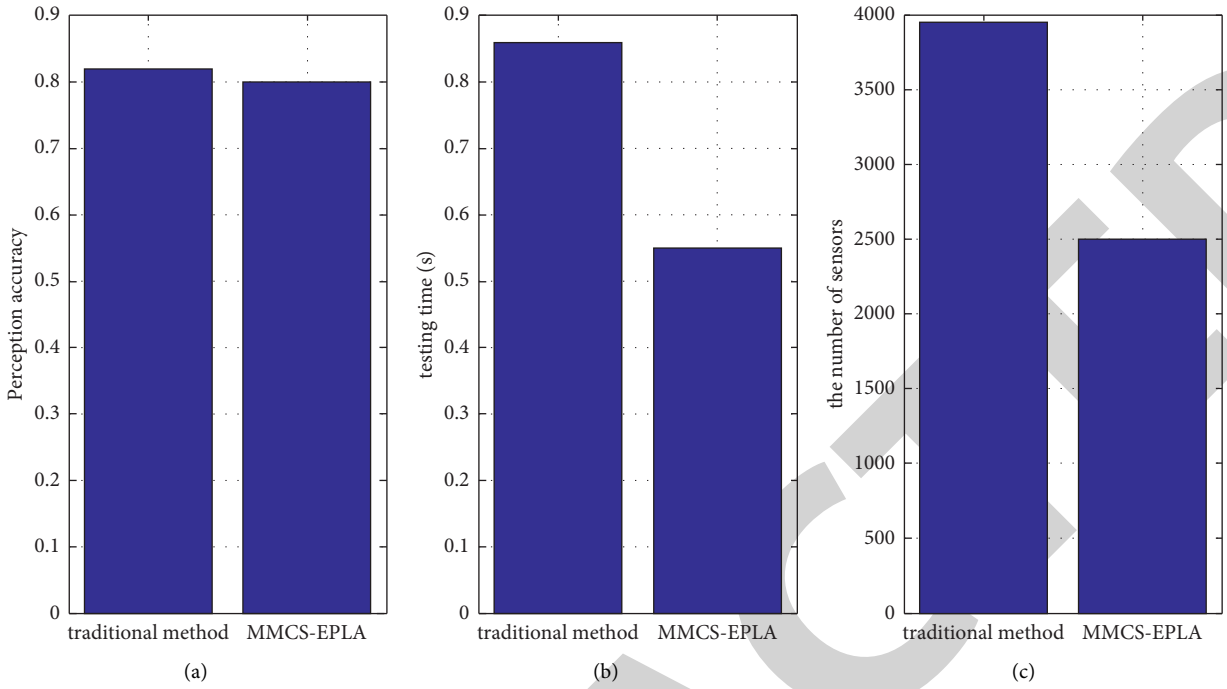

Figure 6: Performance comparison between MMCS-EPLA and traditional method in MHEALTH data set.

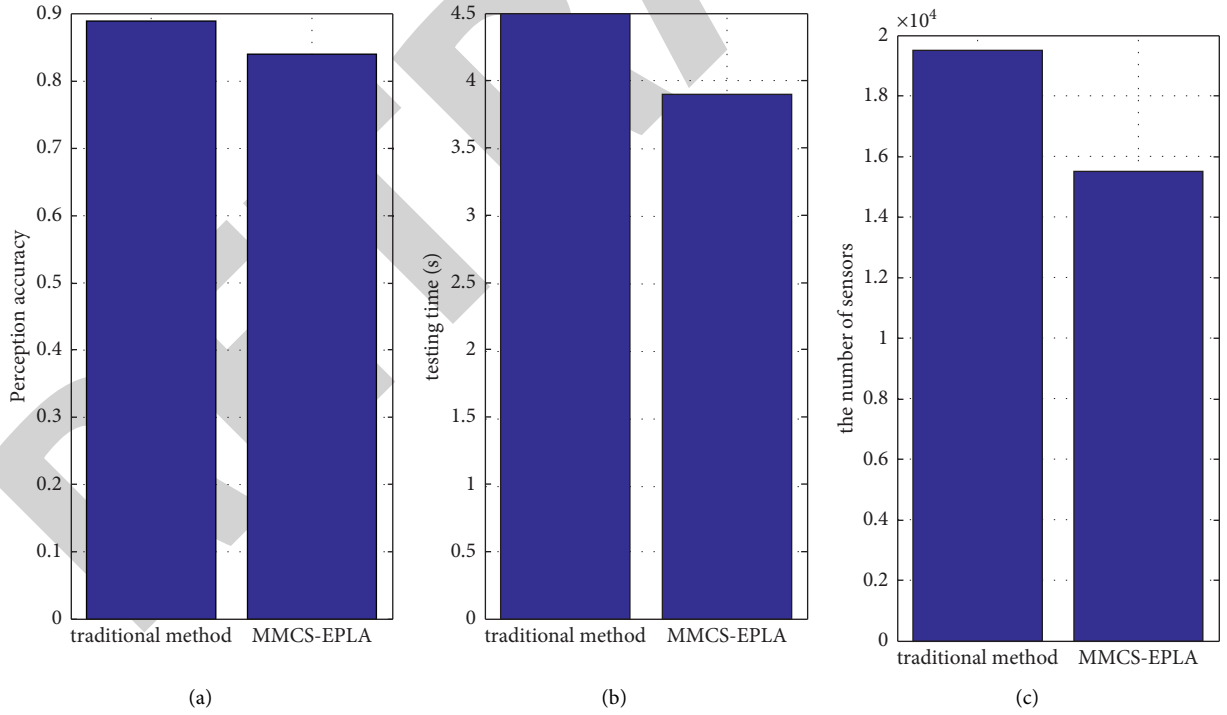

Figure 7: Performance comparison between MMCS-EPLA and traditional method in the PAMAP2 data set.

model calculation process, so the test time and the number of sensors showed better performance.

5. Conclusions

Based on the investigation of the research progress of WBSN perception, this paper proposes a multimodal collaborative perception method in order to reduce the energy consumption related to the daily behavior of WBSN perceiving the elderly living people. This method uses a multiclass classifier and binary classifier to perform behavior recognition and status monitoring of users' daily behaviors and perform collaborative scheduling of sensors. In addition, this paper proposes a sensor selection method based on information gain, which selects the minimum sensor combination that guarantees the sensing performance. Through experiments, the method proposed in this paper can effectively perceive the four behaviors required for the perception of PD motor symptoms. MMCS-EPLA uses the pertinence and low complexity of the binary classifier in the modeling process to reduce the power consumption of data transmission and model calculation in the behavioral perception process, thereby extending the perception lifetime of WBSN.

Data Availability

The experimental data used to support the findings of this study are available from the corresponding author upon request.

Conflicts of Interest

The authors declare that they have no conflicts of interest regarding the present study.

References

[1] M. D. Rugg and A. P. Yonelinas, "Human recognition memory: a cognitive neuroscience perspective," *Trends in Cognitive Sciences*, vol. 7, no. 7, pp. 313–319, 2003.

[2] M. D. Rugg and T. Curran, "Event-related potentials and recognition memory," *Trends in Cognitive Sciences*, vol. 11, no. 6, pp. 251–257, 2007.

[3] J. Kim, D. Yeom, and Y. Joo, "Fast and robust algorithm of tracking multiple moving objects for intelligent video surveillance systems," *IEEE Transactions on Consumer Electronics*, vol. 57, no. 3, pp. 1165–1170, 2011.

[4] D. A. Guttentag, "Virtual reality: applications and implications for tourism," *Tourism Management*, vol. 31, no. 5, pp. 637–651, 2010.

[5] C. Wilson, T. Hargreaves, and R. Hauxwell-Baldwin, "Benefits and risks of smart home technologies," *Energy Policy*, vol. 103, pp. 72–83, 2017.

[6] J. P. Difiori, H. J. Benjamin, J. S. Brenner et al., "Overuse injuries and burnout in youth sports: a position statement from the American medical society for sports medicine," *British Journal of Sports Medicine*, vol. 48, no. 4, pp. 287-288, 2014.

[7] L. Clifton, D. A. Clifton, M. A. F. Pimentel, P. J. Watkinson, and L. Tarassenko, "Gaussian processes for personalized e-health monitoring with wearable sensors," *IEEE Transactions on Biomedical Engineering*, vol. 60, no. 1, pp. 193–197, 2012.

[8] J. Edwards, "Wireless sensors relay medical insight to patients and caregivers [special reports]," *IEEE Signal Processing Magazine*, vol. 29, no. 3, pp. 8–12, 2012.

[9] T. H. Lin, W. J. Kaiser, and G. J. Pottie, "Integrated low-power communication system design for wireless sensor networks," *IEEE Communications Magazine*, vol. 42, no. 12, pp. 142–150, 2004.

[10] A. Sangwan and P. P. Bhattacharya, "Wireless body sensor networks: a review," *International Journal of Hospitality Information Technology*, vol. 8, no. 9, pp. 105–120, 2015.

[11] F. T. Zuhra, K. A. Bakar, A. Ahmed, and M. A. Tunio, "Routing protocols in wireless body sensor networks: a comprehensive survey," *Journal of Network and Computer Applications*, vol. 99, pp. 73–97, 2017.

[12] D. Bharadia, K. R. Joshi, M. Kotaru, and S. Katti, "BackFi," *ACM SIGCOMM—Computer Communication Review*, vol. 45, no. 4, pp. 283–296, 2015.

[13] P. Zhang, D. Bharadia, K. Joshi, and S. Katti, "Hitchhike: practical backscatter using commodity WiFi," in *Proceedings of the 14th ACM Conference on Embedded Network Sensor Systems*, pp. 259–271, Stanford, CA, USA, November 2016.

[14] J. Su, Z. Sheng, A. X. Liu, Z. Fu, and Y. Chen, "A time and energy saving-based frame adjustment strategy (TES-FAS) tag identification algorithm for UHF RFID systems," *IEEE Transactions on Wireless Communications*, vol. 19, no. 5, pp. 2974–2986, 2020.

[15] J. Su, Y. Chen, Z. Sheng, Z. Huang, and A. X. Liu, "From M-ary query to bit query: a new strategy for efficient large-scale RFID identification," *IEEE Transactions on Communications*, vol. 68, no. 4, pp. 2381–2393, 2020.

[16] J. Su, Z. Sheng, A. X. Liu, Y. Han, and Y. Chen, "Capture-aware identification of mobile RFID tags with unreliable channels," *IEEE Transactions on Mobile Computing*, p. 1. In press, 2020.

[17] J. Su, Z. Sheng, A. X. Liu, Y. Han, and Y. Chen, "A group-based binary splitting algorithm for UHF RFID anti-collision systems," *IEEE Transactions on Communications*, vol. 68, no. 2, pp. 998–1012, 2020.

[18] J. Su, Z. Sheng, A. X. Liu, Z. Fu, and C. Huang, "An efficient missing tag identification approach in RFID collisions," *IEEE Transactions on Mobile Computing*, p. 1. In press, 2021.

[19] T. Shany, S. J. Redmond, M. R. Narayanan, and N. H. Lovell, "Sensors-based wearable systems for monitoring of human movement and falls," *IEEE Sensors Journal*, vol. 12, no. 3, pp. 658–670, 2012.

[20] Y.-C. Kan and C.-K. Chen, "A wearable inertial sensor node for body motion analysis," *IEEE Sensors Journal*, vol. 12, no. 3, pp. 651–657, 2012.

[21] L. T. D'Angelo, J. Neuhaeuser, Y. Zhao, and T. C. Lueth, "SIMPLE-use-sensor set for wearable movement and interaction research," *IEEE Sensors Journal*, vol. 14, no. 4, pp. 1207–1215, 2014.

[22] K. V. Laerhoven, A. Schmidt, and H. W. Gellersen, "Multi-sensor context aware clothing," in *Proceedings of the 6th International Symposium on Wearable Computers*, pp. 49–56, Seattle, WA, USA, October 2002.

[23] N. Kern, S. Antifakos, B. Schiele, and A. Schwaninger, "A model for human interruptability: experimental evaluation and automatic estimation from wearable sensors," in *Proceedings of the 8th International Symposium on Wearable Computers*, pp. 158–165, Arlington, VA, USA, 2004.

Hindawi
International Journal of Antennas and Propagation
Volume 2023, Article ID 9810256, 1 page
https://doi.org/10.1155/2023/9810256

Retraction

Retracted: DOA Estimation of an Enhanced Generalized Nested Array with Increased Degrees of Freedom and Reduced Mutual Coupling

International Journal of Antennas and Propagation

Received 19 December 2023; Accepted 19 December 2023; Published 20 December 2023

This article has been retracted by Hindawi following an investigation undertaken by the publisher [1]. This investigation has uncovered evidence of one or more of the following indicators of systematic manipulation of the publication process:

(1) Discrepancies in scope

(2) Discrepancies in the description of the research reported

(3) Discrepancies between the availability of data and the research described

(4) Inappropriate citations

(5) Incoherent, meaningless and/or irrelevant content included in the article

(6) Manipulated or compromised peer review

The presence of these indicators undermines our confidence in the integrity of the article's content and we cannot, therefore, vouch for its reliability. Please note that this notice is intended solely to alert readers that the content of this article is unreliable. We have not investigated whether authors were aware of or involved in the systematic manipulation of the publication process.

Wiley and Hindawi regrets that the usual quality checks did not identify these issues before publication and have since put additional measures in place to safeguard research integrity.

We wish to credit our own Research Integrity and Research Publishing teams and anonymous and named external researchers and research integrity experts for contributing to this investigation.

The corresponding author, as the representative of all authors, has been given the opportunity to register their agreement or disagreement to this retraction. We have kept a record of any response received.

References

[1] Y. Zhang, G. Hu, J. Shi, H. Zhou, C. Zhan, and F. Zhao, "DOA Estimation of an Enhanced Generalized Nested Array with Increased Degrees of Freedom and Reduced Mutual Coupling," *International Journal of Antennas and Propagation*, vol. 2021, Article ID 7233651, 13 pages, 2021.

Hindawi
International Journal of Antennas and Propagation
Volume 2021, Article ID 7233651, 13 pages
https://doi.org/10.1155/2021/7233651

Research Article

DOA Estimation of an Enhanced Generalized Nested Array with Increased Degrees of Freedom and Reduced Mutual Coupling

Yule Zhang[1,2] **Guoping Hu**[2] **Junpeng Shi**[3] **Hao Zhou**[2] **Chenghong Zhan**[1,2] **and Fangzheng Zhao**[1,2]

[1]*Graduate College, Air Force Engineering University, Xi'an 710051, China*
[2]*Air and Missile Defense College, Air Force Engineering University, Xi'an 710051, China*
[3]*College of Electronic Countermeasure, National University of Defense Technology, Hefei 230037, China*

Correspondence should be addressed to Guoping Hu; guoping_hu6068@163.com

Received 8 May 2021; Accepted 25 September 2021; Published 14 October 2021

Academic Editor: Liangtian Wan

Aiming at low degrees of freedom (DOF) and high mutual coupling (MC) of the existing sparse arrays, an enhanced generalized nested array (EGNA) is proposed in this paper. Specifically, the proposed array adds a single antenna on the basis of generalized nested array (GNA), and the difference of coprime factors is employed as the spacing between the second subarray and the additional antenna. Then, the values of the coprime factors are analyzed in detail, which indicates that Yang-NA can be explained as a special case. Compared with the majority of the existing sparse arrays, EGNA not only has the closed-form expressions of the physical antenna locations, consecutive lags, and unique lags, but also significantly increases DOF and reduces MC. In view of the above advantages, EGNA can obtain superior performance in direction of arrival (DOA) estimation. Numerical simulation results verify the rationality and superiority of the proposed nested array.

1. Introduction

A basic technology of array signal processing is the direction of arrival (DOA) estimation, which is also one of the essential research tasks in the fields of communications, radar, sonar, and electronic countermeasures in the past decades and future [1–4]. The conventional DOA estimation generally considers uniform linear array (ULA) in theoretical research and engineering applications, whereas the antenna spacing is no more than half wavelength. Hence, the following problems arise. On one hand, when the signal frequency is too high, the arrangement of physical antennas is difficult to be realized due to the smaller interelement spacing, and large mutual coupling (MC) [5–7] will occur. On the other hand, high resolution means larger array aperture and more physical antennas, which will further increase the cost and complexity of the system.

Over the years, sparse arrays (e.g., the minimum redundancy array (MRA) [8–10], nested array (NA) [11], and coprime array (CPA) [12–14]) have attracted a lot of interest due to the concept of difference coarray (DCA) [15, 16] and significant degrees of freedom (DOF). Furthermore, compared with ULA, the larger interelement spacing of sparse arrays can further expand the virtual aperture and effectively suppress the MC of antennas, thereby increasing the number of detectable sources and angular resolution and improving the estimation accuracy.

BouDaher et al. [17] analyzed the influence of MC on DOA estimation, proving that MRA is least affected by MC, but it is difficult to obtain the effective closed-form expressions of DOF. CPA is alternately composed of two sparse uniform linear arrays with coprime interelement spacing, which has low MC as a result of the large interelement spacing, whereas the staggered distribution of the two subarrays leads to a smaller array aperture and lower DOF. By contrast, NA has definite physical antenna positions and closed-form expressions of DOF and can obtain more DOF. However, the interelement spacing of the first-level subarray of NA is still half wavelength, which causes serious MC. To this end, several modified configurations

have been derived. Zhao et al. [18] and Iizuka et al. [19] adjusted the interelement spacing of NA and obtained optimized nested configurations with higher DOF. Yang et al. [20] established an improved nested array by introducing an additional antenna, which has higher DOF than NA, and its DCA is a virtual uniform linear array without holes. Simultaneously, the increase of the subarrays interelement spacing alleviates MC between the antennas. Liu et al. [21, 22] constructed a super nested array (SNA) by designing a specific system program to determine the location of antennas, which has less MC due to fewer adjacent antennas. Chen et al. [23] proposed a loosely distributed nested array (LoDiNA) that generate greater DOF with higher robustness against MC. Shi et al. [24] flexibly adjusted the interelement spacing of NA and obtained a generalized nested array (GNA) with lower MC, but it does not enhance DOF. Nevertheless, these modifications only consider one of the DOF and MC, which limits DOA estimation performance.

With the intention of ulteriorly increasing DOF and reducing MC at the same time, we propose an enhanced generalized nested array (EGNA) in this paper. In short, EGNA exploits two coprime factors to increase the interelement spacing of two-level nested array and takes the difference of these two coprime integers as the spacing between the second subarray and the additional antenna. The closed-form expressions of the consecutive lags, and DOF are deduced. Then, according to different coprime factors, the DCA of EGNA is analyzed from the maximizing consecutive lags and maximizing unique lags. In general, EGNA has the following superiorities.

(a) By introducing the coprime factors, EGNA can flexibly adjust the interelement spacing according to actual needs. In addition, Yang-NA [20] can be considered as a special case of EGNA.

(b) EGNA has the same DOF as Yang-NA, but with less MC, especially for the larger coprime factors.

(c) Both EGNA and GNA [24] have less MC, but DOF of EGNA is higher than that of NA, ENA [18], Iizuka-NA [19], SNA, CPA, LoDiNA, and GNA.

The remainder of this paper is organized as follows. Several preliminaries are briefly reviewed in Section 2. Section 3 describes the signal model with MC. Section 4 elaborates on EGNA and compares it with the existing linear array. Section 5 evaluates the DOA performances of EGNA based on the simulation experiments. The conclusion is presented in Section 6.

1.1. Notations. In this paper, we use boldfaced italic uppercase and boldfaced italic lowercase letters to denote matrices and vectors, respectively. $(\cdot)^T$, $(\cdot)^H$, and $(\cdot)^*$ represent a matrix/vector transpose operator, the conjugate transpose operator, and the complex conjugate operator, respectively. $\odot$ and $\otimes$ stand for the Khatri–Rao product and Kronecker product. $|\cdot|$ represents absolute value. $\|\cdot\|_0$, $\|\cdot\|_1$, and $\|\cdot\|_2$ denote the l_0-norm, l_1-norm, and l_2-norm, respectively. $\mathrm{diag}(\cdot)$ is the diagonal matrix operator. $E[\cdot]$ and $vec(\cdot)$ represent the expectation and the vectorization operator, respectively. $\mathbb{Z}^+$ denotes the set of positive integers.

2. Preliminaries

In order to facilitate the discussion of our proposed EGNA, we will briefly review some preliminary knowledge of DCA, DOF, weight value, Yang-NA, and GNA in this section.

2.1. DCA, DOF, and Weight Value

Definition 1 (difference coarray). Let us consider two sets of integers $P = \{p_1, p_2, \ldots, p_m\}$ and $D = \{d_1, d_2, \ldots, d_n\}$.

Define the self-difference coarray S_s as

$$S_s = \{p_i - p_j | 1 \le i, j \le m\} \cup \{d_i - d_j | 1 \le i, j \le n\}. \quad (1)$$

Define the cross-difference coarray S_c as

$$S_c = \{\pm(p_i - d_j) | 1 \le i \le m,\ 1 \le j \le n\}. \quad (2)$$

The difference coarray S is the union set of the self-difference coarray S_s and the cross-difference coarray S_c.

$$S = S_s \cup S_c. \quad (3)$$

Definition 2 (degrees of freedom). In (3), if duplicate elements are allowed in the difference coarray S, the total number of disparate elements is defined as degrees of freedom.

Definition 3 (weight value). The weight value $\omega(\cdot)$ refers to the number of virtual array elements appearing in the DCA.

2.2. Yang-NA. As depicted in Figure 1, Yang-NA [20] is composed of two ULAs and an additional antenna, where the first level has M_1 antennas, and the interelement spacing is d; the second level has M_2 antennas, and the interelement spacing is $(M_1 + 2)d$; and the spacing between the second level and the additional antenna is $(M_1 + 1)d$. Herein, $d = \lambda/2$ is the unit interelement spacing and λ denotes the signal wavelength.

Then, the antenna positions set can be given as

$$P_{Yang-NA} = \{0, 1, \ldots, M_1 - 1, M_1, M_1 + (M_1 + 2), \ldots, M_1 + (M_2 - 1)(M_1 + 2), M_1 + (M_2 - 1)(M_1 + 2) + M_1 + 1\}. \quad (4)$$

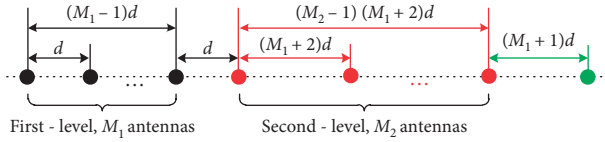

Figure 1: Yang-NA configuration.

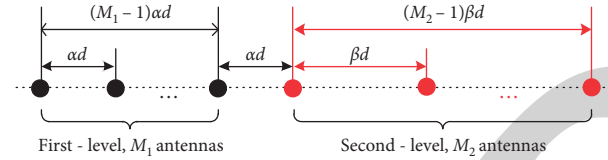

Figure 2: GNA configuration.

Yang-NA has the closed-form expressions of the antenna locations and DOF, and a lager DCA without holes can be provided than NA..

2.3. GNA. The original intention of GNA [24] is to alleviate mutual coupling. As presented in Figure 2, the interelement spacing is two coprime integers.

Then, the antenna positions set can be expressed as

$$P_{GNA} = \{0, \alpha, \ldots, \alpha M_1, \alpha M_1 + \beta, \ldots, \alpha M_1 + \beta(M_2 - 1)\}. \tag{5}$$

GNA has the closed-form expressions for the unique lags, which greatly reduces the mutual coupling while maintaining the DOF as NA.

3. Signal Model with Mutual Coupling

Assume that there are K far-field narrowband uncorrelated target incidents on a sparse array with G antennas from $\theta = \{\theta_k = k = 1, 2, \ldots, K\}$. Then, the signal with mutual coupling can be modeled as

$$\mathbf{x}(t) = \mathbf{CAs}(t) + \mathbf{n}(t), \tag{6}$$

where $\mathbf{A} = [\mathbf{a}(\theta_1), \mathbf{a}(\theta_2), \ldots, \mathbf{a}(\theta_K)]$ is the steering matrix and $\mathbf{a}(\theta_k) = [1, e^{-j2\pi d_2 d \sin \theta_k/\lambda}, \ldots, e^{-j2\pi d_G d \sin \theta_k/\lambda}]^T$ is the steering vector of the k-th source. d_i is the spacing between the i-th and the first antenna, where $d_1 = 0$. $\mathbf{s}(t) = [s_1(t), s_2(t), \ldots s_K(t)]^T$ denotes the target vector and $s_k(t)$ is the baseband waveform of the k-th source. $\mathbf{n}(t)$ represents the independent and identically distributed white Gaussian noise vector. $\mathbf{C}$ is the mutual coupling matrix introduced in [21], which can be approximated as a Toeplitz matrix with B-banded symmetry [25].

$$\mathbf{C}_{ij} = \begin{cases} c_{|d_i - d_j|}, & |d_i - d_j| \le B, \\ 0, & |d_i - d_j| > B, \end{cases} \tag{7}$$

where $\mathbf{C}_{ij}$ is the element in the i-th row and the j-th column of $\mathbf{C}$, and $1 = c_0 > |c_1| \cdots > |c_B| > |c_{B+1}| = 0$.

For the convenience of measuring the influence of mutual coupling, it can be defined as

$$\Omega = \frac{\|C - \mathrm{diag}(C)\|_2}{\|C\|_2}, \tag{8}$$

where $[\mathrm{diag}(C)]_{ij} = \mathbf{C}_{ij}\delta_{ij}$, and δ_{ij} is the Dirichlet function. It can be seen from (8) that the smaller the Ω is, the weaker the mutual coupling effect will be.

Afterwards, the signal covariance matrix under the condition of mutual coupling can be calculated as

$$\mathbf{R} = E\left[\mathbf{x}(t)\mathbf{x}^H(t)\right] = \mathbf{CAR}_s\mathbf{A}^H\mathbf{C}^H + \sigma_n^2\mathbf{I}_G, \tag{9}$$

where $\mathbf{R}_s = E[\mathbf{s}(t)\mathbf{s}^H(t)] = \mathrm{diag}[\sigma_1^2, \sigma_2^2, \ldots, \sigma_K^2]$ represents the source covariance matrix. σ_k^2 is the signal power of the k-th source. σ_n^2 is the noise power. $\mathbf{I}_G$ is the $G \times G$-dimensional identity matrix.

In practical application, $\mathbf{R}$ can usually be estimated by

$$\hat{\mathbf{R}} = \frac{1}{L}\sum_{t=1}^{L}\mathbf{x}(t)\mathbf{x}^H(t), \tag{10}$$

where L denotes the number of snapshots and $\hat{\mathbf{R}}$ is an estimate of $\mathbf{R}$.

Next, the observing vector $\mathbf{r}$ can be obtained by vectorizing the covariance matrix $\mathbf{R}$.

$$\begin{aligned} \mathbf{r} &= \mathrm{vec}(\mathbf{R}) = \left((\mathbf{CA})^* \odot (\mathbf{CA})\right)\mathbf{p} + \sigma_n^2\mathrm{vec}(\mathbf{I}_G) \\ &= \mathbf{C}_0(\mathbf{A}^* \odot \mathbf{A})\mathbf{p} + \sigma_n^2\mathrm{vec}(\mathbf{I}_G), \end{aligned} \tag{11}$$

where $\mathbf{C}_0 = \mathbf{C}^* \otimes \mathbf{C}$. $\mathbf{p} = [\sigma_1^2, \sigma_2^2, \ldots, \sigma_K^2]^T$.

$$\mathbf{A}^* \odot \mathbf{A} = [\mathbf{a}^*(\theta_1) \otimes \mathbf{a}(\theta_1), \mathbf{a}^*(\theta_2) \otimes \mathbf{a}(\theta_2), \ldots, \mathbf{a}^*(\theta_K) \otimes \mathbf{a}(\theta_K)] \tag{12}$$

is the virtual steering array matrix of single snapshot measurement $\mathbf{r}$.

Therefore, the virtual array positions of matrix $\mathbf{A}^* \odot \mathbf{A}$ are composed of the DCA of the physical antenna positions.

4. Enhanced Generalized Nested Array

GNA exploits two coprime extension factors to increase the interelement spacing of the nested array to reduce mutual coupling, while Yang-NA adds an additional antenna on the basis of NA and sets different interelement spacing for the subarray to improve the DOF. Therefore, we can introduce the idea of generalization into Yang-NA and establish an enhanced generalized nested array to achieve joint optimization of degrees of freedom and mutual coupling, as shown in Figure 3. EGNA can be obtained by introducing the interelement spacing coprime extension factors into the basic configuration of Yang-NA, where the interelement spacing of the first subarray is αd, and the number of antennas is M_1; the second subarray has M_2 antennas with the interelement spacing of βd; and the spacing between the second subarray and the additional antenna is $(\beta - \alpha)d$. α and β are two coprime integers.

Then, the positions of antennas can be given as

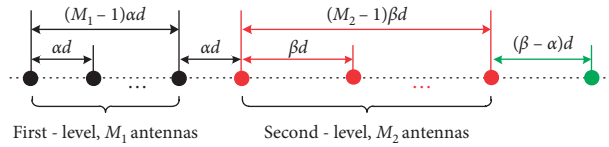

Figure 3: Enhanced generalized nested array.

$$P_{EGNA} = \{0, \alpha, \ldots, \alpha M_1, \alpha M_1 + \beta, \alpha M_1 + 2\beta, \ldots, \alpha M_1 + \beta(M_2 - 1), \alpha(M_1 - 1) + \beta M_2\}. \quad (13)$$

Subsequently, combining Figure 3 and (13), we can get the following definition.

Definition 4. The DCA of EGNA can be defined as

$$\begin{aligned} S_{EGNA} &= S^{+}_{EGNA} \cup S^{-}_{EGNA}, \\ S^{+}_{EGNA} &= \{x_n - x_{\tilde{n}}, \mid x_n \geq x_{\tilde{n}}, x_n, x_{\tilde{n}} \in P_{EGNA}\}, \end{aligned} \quad (14)$$

where S^{+}_{EGNA} and S^{-}_{EGNA} denote the positive elements set and negative elements set of S_{EGNA}, respectively.

Combined with Definition 4, the characteristics of S_{EGNA} can be derived as the following lemma.

Lemma 1. *The configuration of EGNA and the corresponding DCA set are presented in Figure 3 and (14), respectively. Then, S_{EGNA} has the following characteristics:*

(a) *When $1 \leq \alpha \leq M_2$, $2 \leq \beta \leq M_1 + 2$, and $\alpha < \beta$, the range of consecutive lags in S^{+}_{EGNA} can be expressed as $[(\alpha - 1)(\beta - 1) - \alpha, \alpha(M_1 - 1) + \beta M_2 - (\alpha - 1)(\beta - 1) + \alpha]$.*

(b) *When $1 \leq \alpha \leq M_2$, $2 \leq \beta \leq M_1 + 2$, and $\alpha < \beta$, the DOF of the set S_{EGNA} is equal to $2g + 1$, where $g = \alpha(M_1 - 1) + \beta M_2 - (\alpha - 1)(\beta - 1) + 2\alpha - 2$.*

Proof

(a) From Definition 4, the DCA S^{+}_{EGNA} includes the self-difference coarray S^{+}_{s-EG} and the cross-difference coarray S^{+}_{c-EG}. Then, S^{+}_{EGNA} can be expressed as

$$\begin{aligned} S^{+}_{EGNA} &= S^{+}_{s-EG} \cup S^{+}_{c-EG}, \\ S^{+}_{s-EG} &= \{\alpha m_1 \mid m_1 \in [0, M_1 - 1]\} \cup \{\beta m_2 \mid m_2 \in [0, M_2 - 1]\}, \\ S^{+}_{c-EG} &= \{\alpha m_1 + \beta m_2 \mid m_1 \in [0, M_1 - 1], m_2 \in [0, M_2]\}. \end{aligned} \quad (15)$$

Due to $S^{+}_{s-EG} \subset S^{+}_{c-EG}$, (15) can be restated as

$$\begin{aligned} S^{+}_{EGNA} &= S^{+}_{s-EG} \cup S^{+}_{c-EG} \\ &= \{\alpha m_1 + \beta m_2 \mid m_1 \in [0, M_1 - 1], m_2 \in [0, M_2]\}. \end{aligned} \quad (16)$$

According to Definition 4 and (16), we need to prove that there are $m_1 \in [0, M_1 - 1]$ and $m_2 \in [0, M_2]$ so that $s = \alpha m_1 + \beta m_2$ contains all the consecutive lags from $(\alpha - 1)(\beta - 1) - \alpha$ to $\alpha(M_1 - 1) + \beta M_2 - (\alpha - 1)(\beta - 1) + \alpha$, where $1 \leq \alpha \leq M_2$, $2 \leq \beta \leq M_1 + 2$, $\alpha < \beta$, α and β are two coprime integers.

Firstly, we can rewrite the condition $0 \leq m_1 \leq M_1 - 1$ as

$$0 \leq \alpha m_1 \leq \alpha(M_1 - 1). \quad (17)$$

Secondly, by substituting $\alpha m_1 = s - \beta m_2$ and $(\alpha - 1)(\beta - 1) - \alpha \leq s \leq \alpha(M_1 - 1) + \beta M_2 - (\alpha - 1)(\beta - 1) + \alpha$ into (17), we can obtain

$$\begin{aligned} &\alpha(\beta - M_1 - 2) + \alpha - \beta + 1 \leq \beta m_2 \\ &\leq \alpha(M_1 + 2 - \beta) + \beta M_2 - \alpha + \beta - 1. \end{aligned} \quad (18)$$

On account of $2 \leq \beta \leq M_1 + 2$, we have $\beta - M_1 - 2 \leq 0$, $M_1 + 2 - \beta \geq 0$. Hence, (18) can be represented as

$$\begin{aligned} &\alpha - \beta + 1 \leq \beta m_2 \leq \beta M_2 - (\alpha - \beta + 1) \\ &\Rightarrow \frac{(\alpha - \beta + 1)}{\beta} \leq m_2 \leq M_2 - \frac{(\alpha - \beta + 1)}{\beta}. \end{aligned} \quad (19)$$

Since $\alpha < \beta$, $\beta \geq 2$, we can obtain

$$\frac{(\alpha - \beta + 1)}{\beta} < \frac{1}{\beta} < 1. \quad (20)$$

Thus, $0 \leq m_2 \leq M_2$.

(b) We take the positive integer set S^{+}_{EGNA} as an example; i.e., it is necessary to prove that there exist $g + 1$ virtual array elements in S^{+}_{EGNA}, where $g = \alpha(M_1 - 1) + \beta M_2 - (\alpha - 1)(\beta - 1) + 2\alpha - 2$.

The maximum value of S^{+}_{EGNA} can be obtained from (16):

$$g_{\max} = \alpha(M_1 - 1) + \beta M_2. \quad (21)$$

The distribution of virtual array elements in S^{+}_{EGNA} is shown in Figure 4. The virtual array elements are composed of three parts, namely, discrete part 1, consecutive part, and discrete part 2.

From (21), it can be seen that the number of virtual array elements g_2 of discrete part 2 satisfies

$$\begin{aligned} &0 \leq g_2 \leq (g_{\max} + \alpha) - (\alpha(M_1 - 1) + \beta M_2 - (\alpha - 1)(\beta - 1) + \alpha) \\ &\Rightarrow 0 \leq g_2 \leq (\alpha - 1)(\beta - 1). \end{aligned} \quad (22)$$

In order to determine the size of g_2, the geometric distribution of α and β is established in Figure 5. Since D_1 and D_2 are symmetric, the two parts contain the same

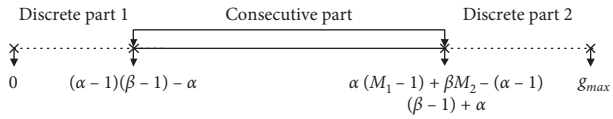

Figure 4: Schematic diagram of virtual array element distribution.

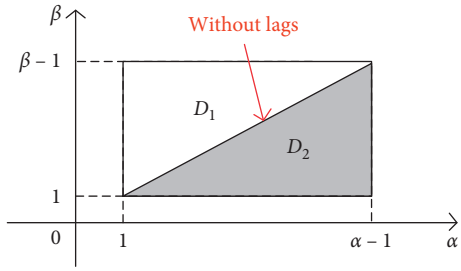

Figure 5: Geometric distribution of α and β.

number of virtual array elements. In addition, α and β are two coprime integers, so there are no virtual array elements on the diagonal. Thus, the total number of virtual array elements is $g_2 = (\alpha-1)(\beta-1)/2 - 1$.

Similarly, the number of virtual array elements g_1 contained in discrete part 1 also satisfies

$$g_1 = (\alpha-1)(\beta-1)/2 - 1. \tag{23}$$

As a result, the total number of S^+_{EGNA} satisfies

$$\begin{aligned} g &= [\alpha(M_1-1) + \beta M_2 - (\alpha-1)(\beta-1) + \alpha] \\ &\quad - [(\alpha-1)(\beta-1)+\alpha] + g_1 + g_2 = \alpha(M_1-1) \\ &\quad + \beta M_2 - (\alpha-1)(\beta-1) + 2\alpha - 2. \end{aligned} \tag{24}$$

EGNA and GNA are generalizations of Yang-NA and NA, respectively. To better illustrate their differences, we will provide two types of special cases to understand the lemma, namely, maximizing consecutive lags and maximizing unique lags. □

4.1. Maximizing Consecutive Lags. It can be known from (23) that the number of discrete virtual array elements in S^+_{EGNA} is equal to $(\alpha-1)(\beta-1)-2$. Consequently, only when $\alpha = 1$, $\beta \in [2, M_1+2]$ or $\alpha = 2$, $\beta = 3$, there are no holes in the DCA of EGNA; i.e., the number of unique lags is the same as the consecutive lags. Next, we will detailedly analyze the above two cases, in which GNA is provided for comparison.

(a) Case 1 ($\alpha = 1$, $\beta \in [2, M_1+2]$).

The ranges of the consecutive lags in S^+_{EGNA} and S^+_{GNA} [24] are $[(\alpha-1)(\beta-1)-\alpha, \alpha(M_1-1)+\beta M_2-(\alpha-1)(\beta-1)+\alpha]$ and $[(\alpha-1)(\beta-1), \alpha M_1+\beta M_2-\alpha\beta+\alpha-1]$, respectively. Therefore, when $\alpha = 1$, $\beta \in [2, M_1+2]$, we can get that the range of the consecutive lags in S^+_{EGNA} is $[-1, M_1+\beta M_2] \Rightarrow [0, M_1+\beta M_2]$. Besides, when $\alpha = 1$, $\beta \in [1, M_1+1]$, the range of the consecutive lags in S^+_{GNA} is $[0, M_1+\beta(M_2-1)]$. In addition, the total numbers of antennas for EGNA and GNA are M_1+M_2+1 and M_1+M_2, respectively, so we have $S^+_{EGNA} \geq S^+_{GNA}$.

Particularly, we can know from (4) and (13) that when $\alpha = 1$, $\beta = M_1+2$, we have $\beta-\alpha = M_1+1$. At the moment, EGNA is exactly equal to Yang-NA, whose DCA is kept as a ULA without holes. Hence, Yang-NA can be identified as a special case of EGNA. Similarly, for GNA, if $\alpha = 1$, $\beta = M_1+1$, the configuration of GNA is the same as NA. Moreover, it is proved that Yang-NA has a larger array aperture and better DOA estimation performance than NA [20].

(b) Case 2 ($\alpha = 2$, $\beta = 2k+1\,(k \in \mathbb{Z}^+)$).

It can be obviously known that when $\alpha = 2$, $\beta = 2k+1\,(k \in \mathbb{Z}^+)$, the ranges of the consecutive lags in S^+_{EGNA} and S^+_{GNA} are $[\beta-3, 2(M_1-1)+\beta M_2-(\beta-3)]$ and $[\beta-1, 2M_1+\beta M_2-2\beta+1]$, respectively.

The number of consecutive lags in S^+_{EGNA} is

$$2(M_1-1)+\beta M_2-(\beta-3)-(\beta-3)+1 = 2G+(\beta-2)M_2+3-2\beta = \begin{cases} \dfrac{[(\beta+2)G+6-4\beta]}{2} & G \text{ is Even}\left(M_2 = \dfrac{G}{2}\right) \\ \dfrac{[(\beta+2)G+4-3\beta]}{2} & G \text{ is Odd}\left(M_2 = \dfrac{(G+1)}{2}\right) \end{cases}. \tag{25}$$

The number of consecutive lags in S^+_{GNA} is

$$2M_1+\beta M_2-2\beta+1-(\beta-1)+1 = 2G+(\beta-2)M_2+3-3\beta = \begin{cases} \dfrac{[(\beta+2)G+6-6\beta]}{2} & G \text{ is Even}\left(M_2 = \dfrac{G}{2}\right) \\ \dfrac{[(\beta+2)G+4-5\beta]}{2} & G \text{ is Odd}\left(M_2 = \dfrac{(G+1)}{2}\right) \end{cases}. \tag{26}$$

Particularly, for EGNA, if $\alpha = 2$, $\beta = 3$, the discrete virtual holes will not appear in the DCA. However, for GNA, when $\alpha = 2, \beta = 3$, there are 2 holes in the S^{+}_{GNA} [24]; i.e., the number of unique lags will exceed that of consecutive lags.

Based on the above analysis, we can conclude that whether the number of antennas is even or odd, the range of consecutive lags in S^{+}_{EGNA} is larger than or equal to that of S^{+}_{GNA}.

4.2. Maximizing Unique Lags. In case of $\alpha \neq 1$ or $\alpha \neq 2, \beta \neq 3$, there are discrete virtual holes in the DCA of EGNA, whereas, for GNA, there exist discrete virtual holes as long as $\alpha \neq 1$ or $\beta \neq 1$. The holes will increase with the increase of α and β, resulting in fewer consecutive lags. Nevertheless, we can greatly reduce the MC by flexibly changing α and β.

According to (8), MC is mainly determined by the interelement spacing. Specifically, when $\alpha > B, \beta > B$, and $\beta - \alpha > B$, $\Omega = 0$; when $\alpha \leq B$, $\beta \leq B$ or $\beta - \alpha \leq B$, $\Omega > 0$. Supposing $M_1 > B, M_2 > B$, and $G = M_1 + M_2 + 1$, the joint optimization model of DOF and MC can be established as follows:

$$\begin{aligned} &\max_{\alpha,\beta} g = \alpha(M_1 - 1) + \beta M_2 - (\alpha - 1)(\beta - 1) + 2\alpha - 2 \\ &s.t.\ B < \alpha \leq M_2, \\ &\quad B < \beta \leq M_1 + 2, \\ &\beta - \alpha > B,\ G = M_1 + M_2 + 1. \end{aligned} \tag{27}$$

conditiodition of GNA. We can see that when the number of antennas is small, the optimization The optimization results of (27) are given in Table 1.

Proof. Firstly, we calculate the partial derivative of the variable g with respect to the parameters α and β.

$$\begin{aligned} \frac{\partial g}{\partial \alpha} &= M_1 + 2 - \beta \geq 0, \\ \frac{\partial g}{\partial \beta} &= M_2 + 1 - \alpha \geq 0. \end{aligned} \tag{28}$$

Therefore, the variable g is a monotonically increasing function. Therefore, when α or β reaches the maximum value, the variable g reaches the maximum. To determine its exact range, the variable g can be reexpressed.

$$\begin{aligned} g &= \alpha(M_1 - 1) + \beta M_2 - (\alpha - 1)(\beta - 1) + 2\alpha - 2 \\ &= \alpha(M_1 + 2 - \beta) + \beta(M_2 + 1) - 3 \\ &= \beta(M_2 + 1 - \alpha) + \alpha(M_1 + 2) - 3. \end{aligned} \tag{29}$$

From (29), we can see that when $\beta = M_1 + 2, \alpha \in (B, M_2]$, the variable g can take the maximum value; i.e., $g = M_1 M_2 + M_1 + 2M_2 - 1$. Then, according to the Arithmetic Mean–Geometric Mean (AM-GM) inequalities, the antenna configuration results are shown in Table 1.

To facilitate comparison, we first summarize the closed-form expressions of DOF of various array geometries (namely, NA, ENA, Iizuka-NA, Yang-NA, CPA, LoDiNA, GNA, and EGNA) in Table 2.

Compared with maximizing consecutive lags, maximizing unique lags can obtain a larger DOF and effective array aperture. In addition, a more flexible α makes the configuration of EGNA more realistic. It can be also found that when α takes a larger value, the interelement spacing of the first subarray becomes larger, which greatly reduces MC. However, when the maximizing consecutive lags is achieved, the smaller α causes no significant improvement in the MC of the first subarray. □

4.2.1. Remarks. After the joint optimization of DOF and MC, the excellent characteristics of EGNA can be listed as follows: (1) We can see that EGNA retains the original advantages of Yang-NA, which has the simple closed-form expressions with physical antennas and DOF. (2) In case of $\alpha \in [1, M_2], \beta = M_1 + 2$, EGNA has the same DOF as Yang-NA and has more DOF than NA, ENA, Iizuka-NA, SNA, CPA, LoDiNA, and GNA. (3) In terms of MC, both GNA and EGNA exploit two coprime extension factors to expand the interelement spacing, so their MC is much lower than the existing sparse arrays. Moreover, $\beta - \alpha$ is employed as the spacing between the second level and the single antenna of EGNA to mitigate MC, which is distinct from the optimization condition of GNA. We can see that when the number of antennas is small, the optimization condition of $\beta - \alpha > B$ cannot be satisfied. Once the number of antennas is large, it is not necessary to consider. (4) Compared with CPA, EGNA does not need the prerequisite that the number of two subarrays is coprime, but only the interelement spacing is coprime. Thus, the array arrangement will be more flexible. (5) From the perspective of configuration, the number of antennas of EGNA is less restrictive than SNA and LoDiNA. EGNA only requires $M_1 \geq 1$, $M_2 \geq 2$, while SNA and LoDiNA needs to meet $M_1 \geq 4$, $M_2 \geq 3$ and $M_1 \geq 3$, $M_2 \geq 3$, respectively. This means that SNA and LoDiNA are ineffective when the number of antennas is less than 7 and 5, respectively, while EGNA can obtain a valid configuration when the number of antennas exceeds 4.

In order to have a more explicit understanding of antenna and virtual element positions for different array geometries, Figure 6 depicts the physical antenna distribution and virtual array element expansion of various array structures, where the number of physical antennas is 10. It can be clearly seen that the DOF of NA, ENA, Iizuka-NA, Yang-NA, SNA, CPA, LoDiNA, GNA, and EGNA are 59, 61, 61, 67, 59, 39, 61, 59, and 67, respectively. The DOF of EGNA is the same as Yang-NA and higher than the other arrays, while EGNA can overcome the influence of MC by flexibly adjusting the interelement spacing. Moreover, the ranges of the consecutive lags of GNA and EGNA are [20, 29] and [15, 30], respectively. Both GNA and EGNA adopt the generalized idea, but EGNA can obtain more consecutive lags than those of GNA.

Table 1: Optimal configuration structure for EGNA.

G	Optimal M_1, M_2	Optimal α, β	g	$g_{\max}$
Even	$M_1 = G/2 - 1, M_2 = G/2$	$B < \alpha \le M_2, \beta = M_1 + 2$	$M_1M_2 + M_1 + 2M_2 - 1$	$(G^2 + 4G - 8)/4$
Odd	$M_1 = (G-1)/2 - 1, M_2 = (G+1)/2$	$B < \alpha < M_2, \beta = M_1 + 2$	$M_1M_2 + M_1 + 2M_2 - 1$	$(G^2 + 4G - 9)/4$

Table 2: Comparison of DOF for different arrays.

Total number of antennas	NA	ENA	Iizuka-NA	Yang-NA	CPA	LoDiNA	GNA	EGNA	
8	39	41	41	45	27	41	39	45	
9	49	49	51	55	29	51	49	55	
12	83	85	85	93	53	85	83	93	
14	111	113	113	123	69	113	111	123	
17	161	161	163	175	93	163	161	175	
19	199	199	201	215	117	201	199	215	
DOF	G is even	$(G^2 + 2G - 2)/2$	$(G^2 + 2G + 2)/2$	$(G^2 + 2G + 2)/2$	$(G^2 + 4G - 6)/2$	$M_1M_2 + M_1 + M_2 - 2$	$(G^2 + 2G + 2)/2$	$(G^2 + 2G - 2)/2$	$(G^2 + 4G - 6)/2$
	G is odd	$(G^2 + 2G - 1)/2$	$(G^2 + 2G - 1)/2$	$(G^2 + 2G + 3)/2$	$(G^2 + 4G - 7)/2$		$(G^2 + 2G + 3)/2$	$(G^2 + 2G - 1)/2$	$(G^2 + 4G - 7)/2$

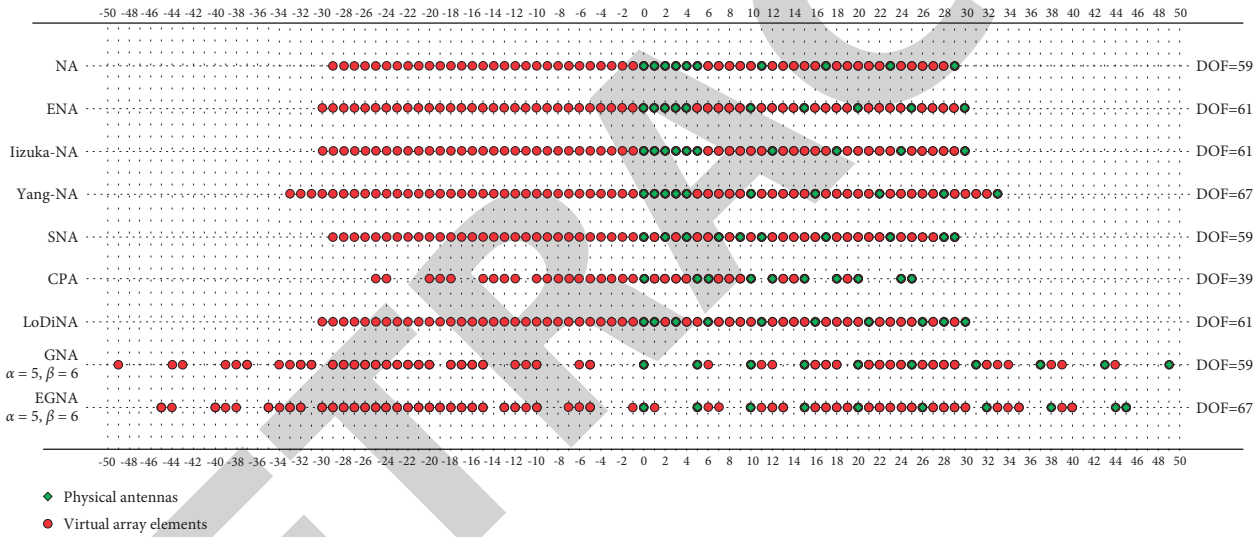

Figure 6: Schematic diagram of antenna distribution and virtual array element expansion of various arrays (the number of physical antennas is 10).

Then, we can utilize a spatial signal recovery method based on Lasso optimization proposed in [26] for DOA estimation, specifically as follows:

$$\widehat{q}_0 = \arg\min\left[\frac{1}{2}\left\|\mathbf{r} - \widetilde{B}\mathbf{q}_0\right\|_2 + \lambda_t\left\|\mathbf{q}_0\right\|_1\right], \tag{30}$$

where l_1-norm denotes a spatial constraint, l_2-norm represents the least square cost function, and λ_t is a penalty parameter used to balance the estimation of the least square error of nonzero, which is set as 2.15 based on experience. The above objective function can be optimized using the CVX toolkit.

5. Simulation Experiments

In this section, we employ the CS algorithm for DOA estimation and several numerical experiments to evaluate the performance of the proposed nested array, where NA, ENA, Iizuka-NA, Yang-NA, SNA, CPA, LoDiNA, and GNA are provided for comparison.

5.1. Experiment Setting. Suppose that the total number of physical antennas is 16; i.e., $M_1 = 7$, $M_2 = 8$. The parameters in the mutual coupling matrix $\mathbf{C}$ are set as $c_0 = 1$, $c_1 = 0.5e^{j\pi/4}$, $c_2 = 0.5e^{j0.7\pi}/2$, $c_3 = 0.5e^{j0.7\pi}/3$, $B = 3$ [24].

Table 3: Comparison of MC for different geometries.

Array structure	Physical antenna positions	MC
NA	{0, 1, 2, 3, 4, 5, 6, 7, 8, 17, 26, 35, 44, 53, 62, 71}	0.6987
ENA	{0, 1, 2, 3, 4, 5, 6, 7, 16, 24, 32, 40, 48, 56, 64, 72}	0.6857
Iizuka-NA	{0, 1, 2, 3, 4, 5, 6, 7, 8, 18, 27, 36, 45, 54, 63, 72}	0.6987
Yang-NA	{0, 1, 2, 3, 4, 5, 6, 7, 16, 25, 34, 43, 52, 61, 70, 78}	0.6857
SNA	{0, 2, 4, 5, 7, 10, 12, 15, 17, 26, 35, 44, 53, 62, 70, 71}	0.4876
CPA	{0, 8, 9, 16, 18, 24, 27, 32, 36, 40, 45, 48, 54, 56, 63, 64}	0.3574
LoDiNA	{0, 4, 8, 12, 16, 20, 24, 28, 32, 41, 50, 59, 68, 77, 86, 95}	0.4855
GNA	{0, 4, 8, 12, 16, 20, 24, 28, 32, 41, 50, 59, 68, 77, 86, 95}	0
EGNA	{0, 4, 8, 12, 16, 20, 24, 28, 37, 46, 55, 64, 73, 82, 91, 96}	0

According to the optimization results, we assume $\alpha = 4$, $\beta = 9$.

5.2. Degrees of Freedom and Mutual Coupling. Table 3 shows a comparison of antenna positions and MC between different array geometries at 16 antennas. It can be seen from Figure 7 and Table 3 that NA and Iizuka-NA have the largest MC due to the densely distributed subarrays and CPA has the lowest DOF owing to the coprime relationship between the number of antennas. Though ENA, Yang-NA, and LoDiNA have higher DOF than NA, the dense subarrays still have higher MC. Even though SNA, CPA, LoDiNA, and GNA have lower MC than NA, their DOF are limited. Compared with the above sparse array geometries, EGNA can increase DOF while reducing MC by improving the interelement spacing.

Figure 7 plots the relationship between the number of DOF and physical antennas for different array structures. We can clearly see that EGNA and Yang-NA can obtain more DOF than that of CPA and the gap between them increases with the number of physical antennas, while the DOF curves of other array structures slowly change between these two sets of curves.

Figure 8 depicts the relationship between the positions and weight values of the DCA for different array structures. It can be seen that NA, ENA, Iizuka-NA, Yang-NA, SNA, and LoDiNA can all obtain continuous virtual array elements, while CPA, GNA, and EGNA have discrete virtual array elements. ENA, Iizuka-NA, Yang-NA, SNA, and LoDiNA retain the original advantages of NA, and their DCA are ULA without holes. Since the interelement spacing and the number of subarrays of CPA are both coprime integers, the DCA has discrete holes. The DCA of GNA and EGNA are not ULAs without holes due to the coprime of the interelement spacing. It should be pointed out that EGNA and GNA have a larger interelement spacing and fewer virtual array elements near the zero position ($\omega(1) = \omega(-1) = \omega(2) = \omega(-2) = \omega(3) = \omega(-3) = 0$). Thus the mutual coupling is the smallest. NA and Iizuka-NA have more virtual array elements near the zero position and larger weight value ($\omega(-1) = \omega(1) = 8, \omega(-2) = \omega(2) = 7, \omega(-3) = \omega(3) = 6$) than other array structures, so the mutual coupling is the largest.

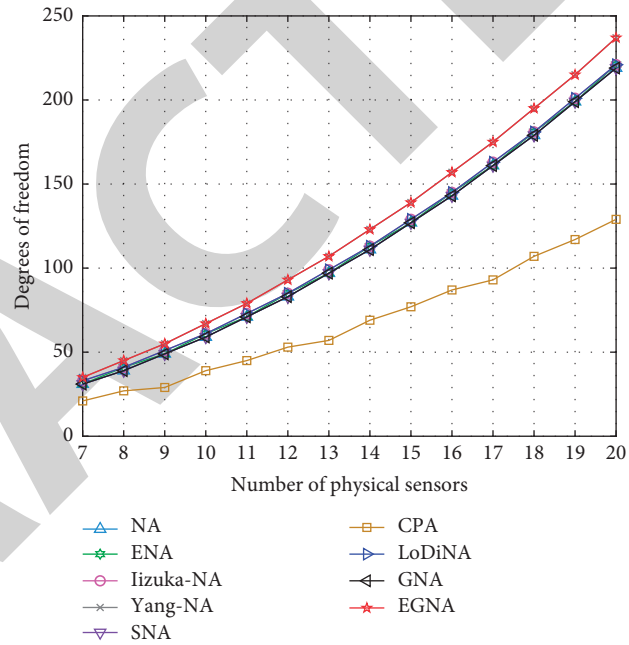

Figure 7: DOF versus the number of physical antennas.

5.3. CS Spectrum. To further illustrate the estimation performance of the proposed nested array, Figure 9 shows the CS spectrum of various array configurations, where SNR = 0 dB and the number of snapshots L is set as 100. 21 far-field narrowband uncorrelated targets are located at [−30°: 3°: 30°], and the red dash-dotted line represents the true angle direction. The search range is −35° to 35°, and the searching grid is 0.1°. As can be seen from Figure 9, NA, ENA, Iizuka-NA, and Yang-NA have the weakest estimation performance due to the highest MC. SNA, CPA, and LoDiNA can estimate 17, 20, and 16 targets, respectively, while GNA and EGNA can identify all targets. Although GNA has the same DOF as NA, lower MC makes its CS spectrum estimation performance better than that of other array structures. Moreover, EGNA has a better CS spectrum than GNA. Therefore, EGNA can obtain better DOA estimation performance than existing sparse arrays by joint optimizing DOF and MC.

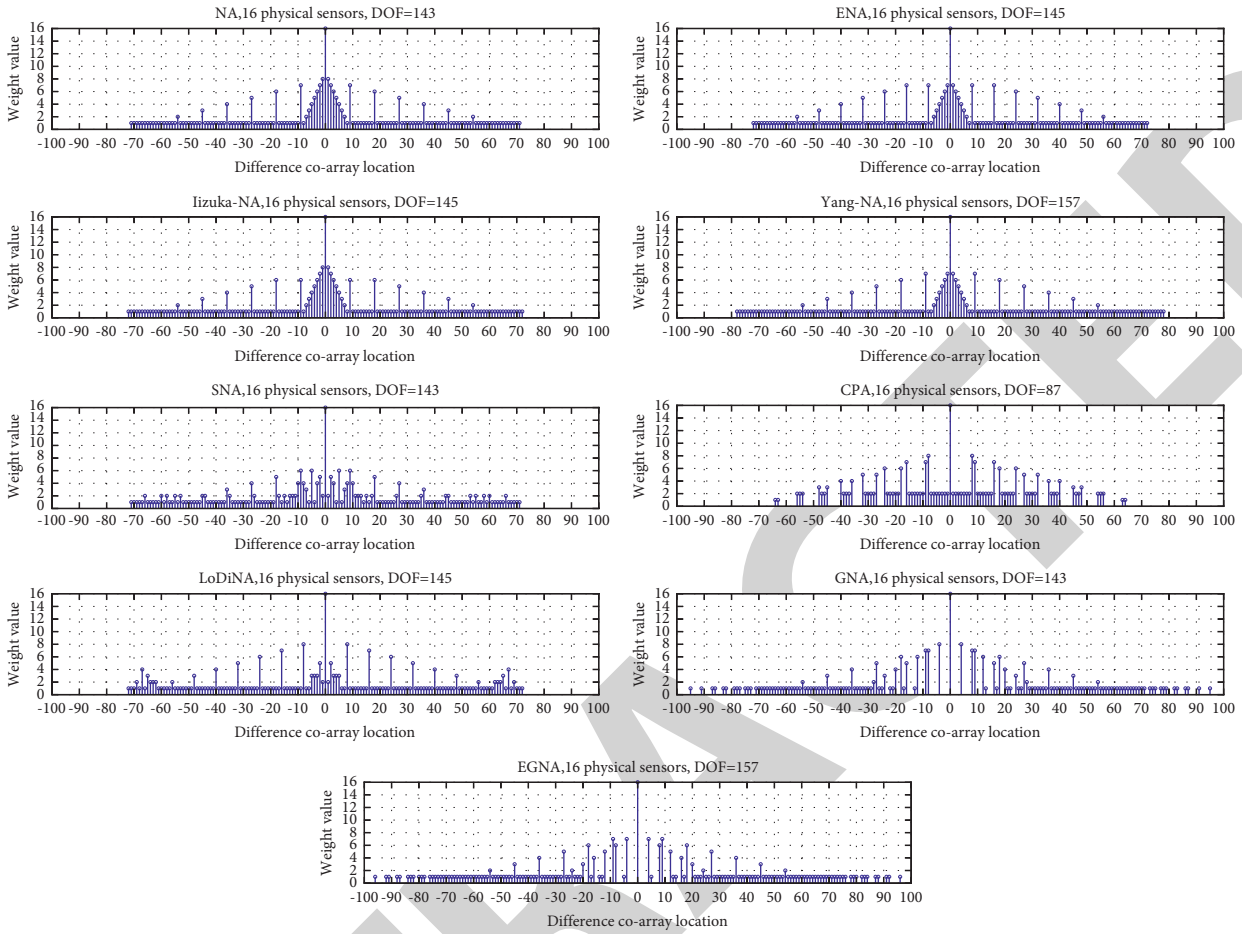

Figure 8: Comparison of difference coarray location for different array structures.

5.4. Root Mean Square Error (RMSE). In this part, RMSE of DOA estimation for EGNA and other arrays are compared via Monte Carlo experiments. Figure 10 describes the relationship between RMSE of DOA estimation and SNR, where the number of snapshots L is 100. Figure 11 shows the relationship between RMSE and the number of snapshots, where SNR = 0 dB. Assume that the sources are located at [5°, 8°, 11°]. The search range is 0° to 15°, and the searching grid is 0.01°. The RMSE of DOA estimation can be calculated as

$$RMSE = \sqrt{\frac{1}{TK}\sum_{i=1}^{T}\sum_{k=1}^{K}\left(\widehat{\theta}_k^i - \theta_k\right)^2}, \tag{31}$$

where $T = 200$ is the total number of Monte Carlo experiments, θ_k denotes the true DOA, and $\widehat{\theta}_k^i$ denotes the estimated DOA in the i-th experiments.

As can be seen from Figures 10 and 11, the estimation performance of each array geometry is gradually improved with the increase of SNR and the number of snapshots. In particular, EGNA has the optimal estimation performance by increasing DOF and reducing MC of antennas. Furthermore, although the DOF of CPA is lower, it has better estimation performance than NA owing to the smaller MC. Therefore, reducing MC is of great significance for improving array estimation performance.

5.5. Resolution Performance. Figure 12 depicts the close targets resolution performance of different array geometries. Here, the definition of resolution can be found in [27]. Suppose two nearby targets are distributed in 5° and 6°, where SNR = −10 dB and the number of snapshots is 50. The search range is [1°, 10°], and the searching grid is 0.01°. It can be seen from Figure 12 that NA, ENA, Iizuka-NA, Yang-NA, SNA, and CPA can only estimate one target, and the CS spectrums obviously deviate from the true angle. LoDiNA, GNA, and EGNA can distinguish the above two targets, whereas EGNA has a higher precision CS spectrum than LoDiNA and GNA.

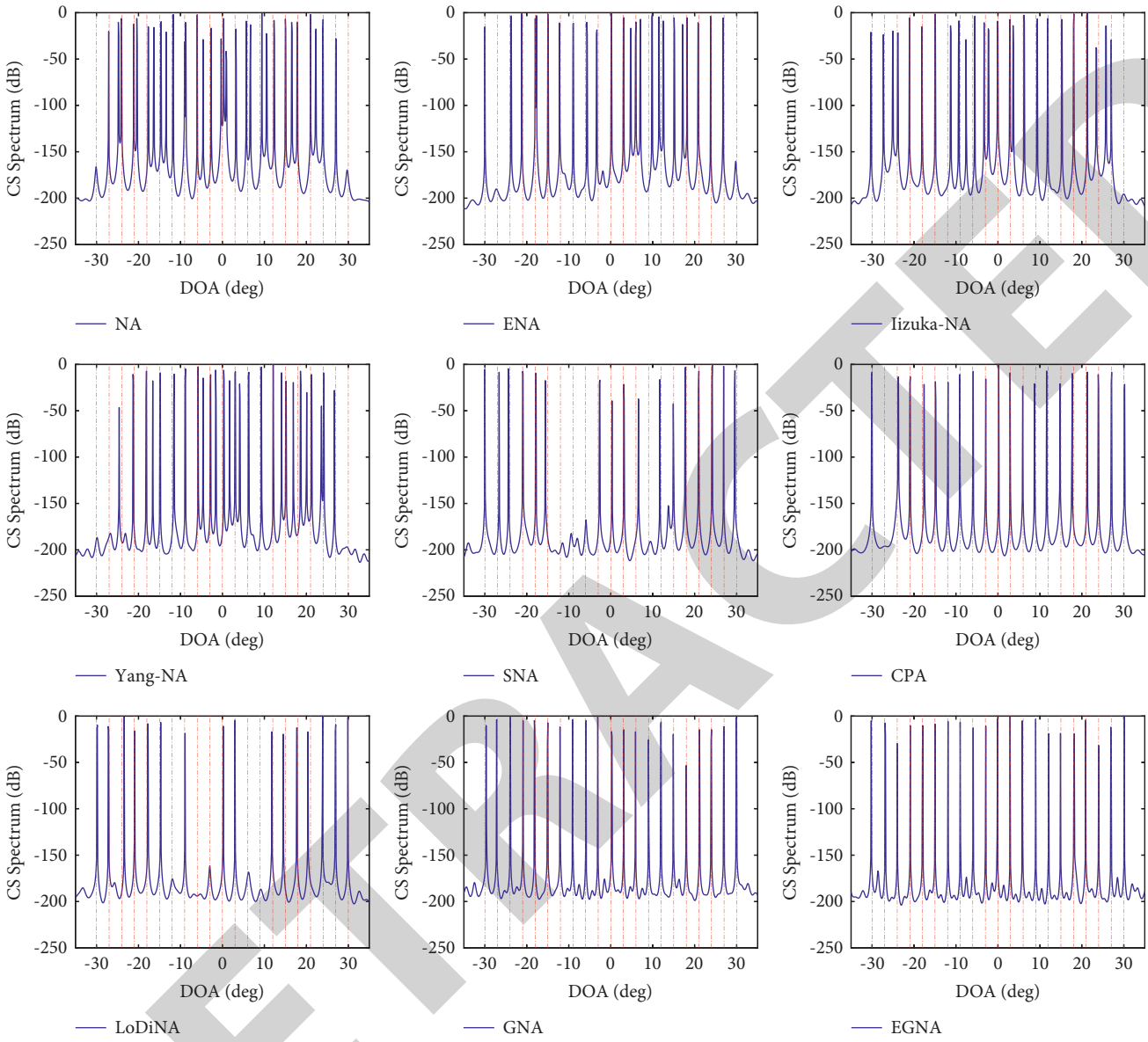

Figure 9: Comparison of CS spectrum for different array configurations.

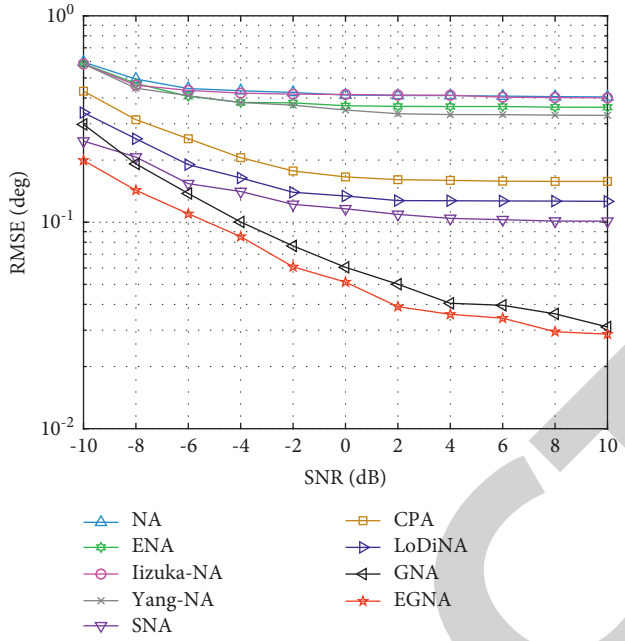

Figure 10: RMSE versus SNR for different array geometries.

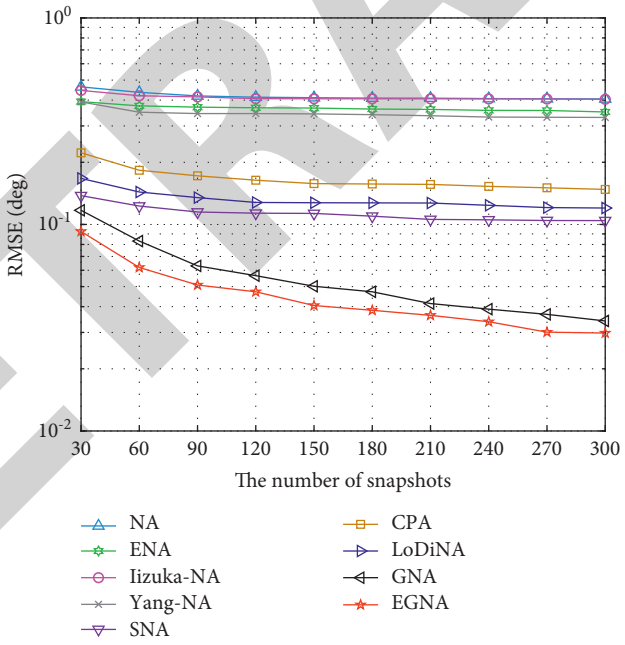

Figure 11: RMSE versus the number of snapshots for different array geometries.

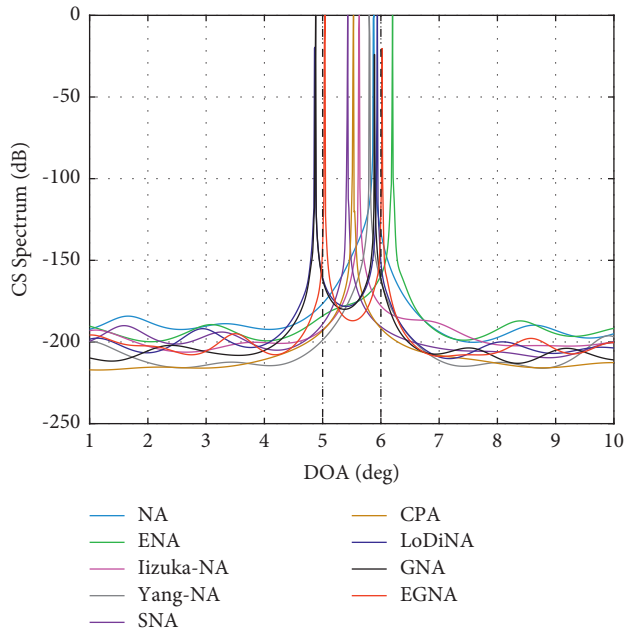

Figure 12: CS spectrum of two nearby targets for different array geometries.

6. Conclusion

In this paper, we have proposed an enhanced generalized nested array, and Yang-NA can be considered as a special case. By adjusting the interelement spacing, EGNA can achieve joint optimization of degrees of freedom and mutual coupling, which has explicit physical antenna positions and closed-form expressions. It was proved that EGNA can obtain the same degrees of freedom as Yang-NA and higher degrees of freedom than GNA, but with lower mutual coupling. Simulation experiments show that the more degrees of freedom and less mutual coupling lead to significant advantages over the existing sparse array structures in terms of spatial spectrum and DOA estimation accuracy.

Data Availability

The data supporting the conclusion of the study are shown in the research paper.

Conflicts of Interest

The authors declare that there are no conflicts of interest regarding the publication of this paper.

Acknowledgments

The authors would like to appreciate Mingming Zhu and Shijie Yue of Air and Missile Defense College, Air Force Engineering University, for their theoretical guidance and assistance with the experiments. This work was supported by the National Natural Science Foundation of China under Grant no. 61871395.

References

[1] H. Abeida and J. P. Delmas, "Robustness of subspace-based algorithms with respect to the distribution of the noise: application to DOA estimation," *Signal Processing*, vol. 164, pp. 313–319, 2019.

[2] F. Wen, J. Shi, and Z. Zhang, "Closed-form estimation algorithm for EMVS-MIMO radar with arbitrary sensor geometry," *Signal Processing*, vol. 186, no. 8, 2021.

[3] P. Chen, Z. Cao, Z. Chen, and X. Wang, "Off-Grid DOA estimation using sparse bayesian learning in MIMO radar with unknown mutual coupling," *IEEE Transactions on Signal Processing*, vol. 67, no. 1, pp. 208–220, 2019.

[4] J. Shi, F. Wen, and T. Liu, "Nested MIMO radar: coarrays, tensor modeling and angle estimation," *IEEE Transactions on Aerospace and Electronic Systems*, vol. 57, no. 1, pp. 573–585, 2021.

[5] Z. Zhongfu Ye, J. Jisheng Dai, X. Xu Xu, and X. Xiaopei Wu, "DOA estimation for uniform linear array with mutual coupling," *IEEE Transactions on Aerospace and Electronic Systems*, vol. 45, no. 1, pp. 280–288, 2009.

[6] S. Cai, J. Zhang, G. Wang, H. Zhu, and K. K. Wong, "Subspace methods for self-calibration of ULAs with unknown mutual coupling: a false-peak analysis," *Signal Processing*, vol. 174, 2020.

[7] X. Zhang, T. Jiang, Y. Li, and Y. Zakharov, "A novel block sparse reconstruction method for DOA estimation with unknown mutual coupling," *IEEE Communications Letters*, vol. 23, no. 10, pp. 1845–1848, 2019.

[8] A. Moffet, "Minimum-redundancy linear arrays," *IEEE Transactions on Antennas and Propagation*, vol. 16, no. 2, pp. 172–175, 1968.

[9] D. A. Linebarger, I. H. Sudborough, and I. G. Tollis, "Difference bases and sparse sensor arrays," *IEEE Transactions on Information Theory*, vol. 39, no. 3, pp. 716–721, 1993.

[10] C. S. Ruf, "Numerical annealing of low-redundancy linear arrays," *IEEE Transactions on Antennas and Propagation*, vol. 41, no. 1, pp. 85–90, 1993.

[11] P. Pal and P. P. Vaidyanathan, "Nested arrays: a novel approach to array processing with enhanced degrees of freedom," *IEEE Transactions on Signal Processing*, vol. 58, no. 8, pp. 4167–4181, 2010.

[12] P. P. Vaidyanathan and P. Pal, "Sparse sensing with Co-prime samplers and arrays," *IEEE Transactions on Signal Processing*, vol. 59, no. 2, pp. 573–586, 2011.

[13] P. Pal and P. P. Vaidyanathan, "Coprime sampling and the MUSIC algorithm," in *Proceedings of the 14th IEEE DSP/SPE Workshop*, pp. 289–294, Sedona, AZ, USA, January 2011.

[14] P. P. Vaidyanathan and P. Pal, "Sparse sensing with coprime arrays," in *Proceedings of the 44th Asilomar Conference Signals, System Computation*, pp. 1405–1409, Pacific Grove, CA, USA, November 2010.

[15] W.-K. Ma, T.-H. Hsieh, and C.-Y. Chi, "DOA estimation of quasi-stationary signals with less sensors than sources and unknown spatial noise covariance: a khatri-rao subspace approach," *IEEE Transactions on Signal Processing*, vol. 58, no. 4, pp. 2168–2180, 2010.

[16] Q. Shen, W. Cui, W. Liu, S. Wu, Y. D. Zhang, and M. G. Amin, "Underdetermined wideband DOA estimation of off-grid sources employing the difference co-array concept," *Signal Processing*, vol. 130, pp. 299–304, 2017.

[17] E. BouDaher, F. Ahmad, M. G. Amin, and A. Hoorfar, "Mutual coupling effect and compensation in non-uniform

Hindawi
International Journal of Antennas and Propagation
Volume 2023, Article ID 9768912, 1 page
https://doi.org/10.1155/2023/9768912

Retraction

Retracted: Research on Interactive Art Online Teaching System Based on BS Mode and Internet of Things

International Journal of Antennas and Propagation

Received 15 August 2023; Accepted 15 August 2023; Published 16 August 2023

This article has been retracted by Hindawi following an investigation undertaken by the publisher [1]. This investigation has uncovered evidence of one or more of the following indicators of systematic manipulation of the publication process:

(1) Discrepancies in scope

(2) Discrepancies in the description of the research reported

(3) Discrepancies between the availability of data and the research described

(4) Inappropriate citations

(5) Incoherent, meaningless and/or irrelevant content included in the article

(6) Peer-review manipulation

The presence of these indicators undermines our confidence in the integrity of the article's content and we cannot, therefore, vouch for its reliability. Please note that this notice is intended solely to alert readers that the content of this article is unreliable. We have not investigated whether authors were aware of or involved in the systematic manipulation of the publication process.

Wiley and Hindawi regrets that the usual quality checks did not identify these issues before publication and have since put additional measures in place to safeguard research integrity.

We wish to credit our own Research Integrity and Research Publishing teams and anonymous and named external researchers and research integrity experts for contributing to this investigation.

The corresponding author, as the representative of all authors, has been given the opportunity to register their agreement or disagreement to this retraction. We have kept a record of any response received.

References

[1] Y. Ying and W. Hongyan, "Research on Interactive Art Online Teaching System Based on BS Mode and Internet of Things," *International Journal of Antennas and Propagation*, vol. 2021, Article ID 7391634, 9 pages, 2021.

Hindawi
International Journal of Antennas and Propagation
Volume 2021, Article ID 7391634, 9 pages
https://doi.org/10.1155/2021/7391634

Research Article

Research on Interactive Art Online Teaching System Based on BS Mode and Internet of Things

Yang Ying[1] **and Wang Hongyan**[2]

[1]*School of Preschool Education, Shanghai Normal University Tianhua College, Shanghai 201815, China*
[2]*Computing Center of Anshan Normal University, Anshan 114007, China*

Correspondence should be addressed to Yang Ying; yy2251@sthu.edu.cn

Received 17 August 2021; Revised 18 September 2021; Accepted 29 September 2021; Published 12 October 2021

Academic Editor: Fangqing Wen

Traditional online art teaching system has problems such as poor score improvement and low system throughput. Therefore, this paper designs an interactive online art teaching system based on BS mode and IoT. Design the overall structure of the art teaching system according to THE B/S structure, build the interactive art online teaching model according to the system role use cases, introduce the RFID technology in the Internet of Things to control the information transmission of the interactive art online teaching system, and complete the code development of interactive art online teaching function. Complete the interactive art online teaching system based on BS mode and the Internet of Things. The experimental results show that the designed system can improve the scores of students in art colleges and improve the throughput of the system.

1. Introduction

Art courses require strong learning ability from the very beginning; the school established the fine arts course website, and teachers can use the traditional classroom teaching and modern multimedia teaching, through the method of combining the classroom by adopting the combination of electronic lesson plans and blackboard writing way, and according to the needs of curriculum content with some animation, audio, and video, giving full play to learn students' interests in learning [1]. At the same time, the construction of the course website has the following significance. The development and construction of the art course website are one of the important contents of our school's art course construction, but there are few special art course websites present, and many things are related to art, including some art interest schools. Moreover, these websites have the problems of low click rate and low usage rate [2]. This is mainly because the website construction is not perfect, the content is monotonous, there is not enough system, and there is no website construction according to the needs of specific groups of people. They are greatly limiting the effectiveness of these course websites. If some websites do not have an online communication platform, it is not conducive to the exchange of students and teachers. As a course website, it must be curricular as the center, provide services for classroom teaching, and provide support for extracurricular and in-class teaching interaction. From the perspective of web-based autonomous learning mode, it should be student-centered and provide help for autonomous learning.

The teaching website spreads the information related to the course through the network to realize the sharing of course resources, so the course website is required to operate and play a leading role in the actual teaching [3]. But throughout the existing course website it is not difficult to find that most of the course website construction still has many problems, mainly in the following aspects.

1.1. The Construction Quality of the Website Is Not High, and There Is a Lack of Overall Understanding and Planning for the Construction of Network Courses. There is disorderly page

production in the website's construction, and style is not unified, in addition to other problems. Such website construction did not form a unified style, giving a chaotic feeling, and it is difficult to form independent modules, which seriously affect the expansion of the system and reduce the flexibility of the system. Secondly, the content organization of the website is cumbersome. Content is the soul of the course website, and the quality of the content determines the website's success. However, many course websites are just conventional piles of simple content, monotonous, and boring, lack diversity and flexibility, and give little consideration to the actual needs of learners, which cannot really attract the use and participation of students and teachers.

1.2. The Interactivity of the Site Is Not High. In order to realize the interaction between teachers and students, interactive communication spaces such as a question-answering mailbox and teacher-student garden should be built on the course website. Interactivity is one of the basic requirements of website construction, so it is a goal of course website to build interactivity website. In order to make the course website have the interactive function of network teaching, the most common ways of website design include online communication, E-mail, and electronic announcement, through which the interaction between teachers and students can be realized [4]. However, the author found that in many websites, of course, this interactive function application is not good. Secondly, the course website should be interesting and entertaining. In order to improve students' initiative and enthusiasm, in the course website construction process, we should play the role of modern information technology and make full use of animation and other image modes and means, to deepen students' understanding and cognition, let students be more interested in using the course website to learn knowledge, so as to achieve better teaching effect. But in reality, many course websites do not have this function, and the form of website implementation is relatively single and boring. As a result, the website's utilization rate and visiting rate are not high, which does not play the role that the course website should play.

By analyzing the research results and study cases of online teaching reforms of arts courses, Reference [5] also interprets the purposes, meaning, and value of online teaching of arts courses. Meanwhile, according to the talent training objectives of colleges, policy guidelines, economic effect, and technical measures involved, this paper explored the challenges facing online teaching reforms of arts courses and attempted to make a breakthrough in terms of the development direction and ways of the reforms based on statistical analysis, students analysis, and major development analysis. Reference [6] collected large amounts of log data, based on the technology of data mining in the fine arts professional learning in the process of learning behavior data, through the study of artificial intelligence algorithm analysis to construct characteristic model, to recommend learning path, the object, and effectively use the established online learning system to improve the learning efficiency of learners.

Internet of Things (IoT) refers to the real-time collection of any object or process that needs to be monitored, connected, and interacted with through various devices and technologies, including information sensors, RADIO frequency identification (RFID) technology, global positioning system (GPS), infrared sensors, laser scanners, and so on. Collect the sound, light, heat, electricity, mechanics, chemistry, biology, location, and other required information, through all kinds of possible network access, realize the ubiquitous connection between objects and objects, and objects and people, and realize the intelligent perception, recognition, and management of objects and processes. The Internet of Things is an information carrier based on the Internet, traditional telecommunications networks, etc. It enables all ordinary physical objects that can be independently addressed to form an interconnected network.

Aiming at the above problems, this paper designs an interactive art online teaching system based on BS mode and Internet of Things.

The contributions of this paper include the following three points:

(1) Traditional online art teaching system has problems such as poor score improvement and low system throughput. Therefore, this paper designs an interactive online art teaching system based on BS mode and Internet of Things.

(2) Design the overall structure of the art teaching system according to THE B/S structure, build the interactive art online teaching model according to the system role use cases, and introduce the RFID technology in the Internet of Things to control the information transmission of the interactive art online teaching system.

(3) Complete the interactive art online teaching system based on BS mode and Internet of Things. The experimental results show that the designed system can improve the scores of students in art colleges and improve the throughput of the system.

2. Overall Design of Interactive Art Online Teaching System

2.1. B/S Structure of Art Teaching System Overall Structure Design. B/S structure has certain advantages in system design, development, and implementation. The information system based on B/S structure has good openness and expansibility. B/S structure is easy to realize in modular design and management. The B/S structure (browser/server) is widely used in the development and utilization of modern information technology and is a kind of network structure mode that emerged after the development of the Web [7]. Used in the installation of a Web browser and other related database software, you can input every aspect of the information in the system to achieve operations. Its main features are simple maintenance and upgrade and low development and use costs.

B/S structure has a strong operation and is conducive to the maintenance of the system; the system is open and a little

more prominent and in view of ASP.NET technology has flexibility, security, scalability, user-friendly access, and browser independent characteristics. This test adopts the browser server structure, composed of client and database servers [8]. As the system adopts Internet related technologies, the art teaching and research system based on B/S mode adopts the Web solution proposed by Microsoft based on ASP.NET technology, which is shown in Figure 1.

In the process of designing the art teaching system, this paper fully examines the characteristics of art teaching and integrates the characteristics of art teaching into the design of each module. The specific design module is shown in Figure 2.

2.1.1. Registration Module. Art teaching and research system can provide students and teachers with two identities of registration; students and teachers must be set according to the school of learning number or teacher's number of registrations; if it does not meet the registration it will fail; students need to fill in their basic information in the registration.

2.1.2. Student Management Module. Log in to the web system in the background of the student management module, the student background page will automatically pop up in the system, students can view the teacher's courseware, as well as the homework assigned by the teacher, and, according to the content of the homework, complete the related homework and works but also can modify the registration information and communicate with teachers and students through the forum.

2.1.3. Teacher Management Module. After a teacher logs in as a teacher, a teacher background page will pop up in the web system, where the teacher can issue courseware or not, assign homework, and view students' works or homework [9]. Teachers can check homework at any time according to the list of students and also can publish relevant information on the website, assign homework, and communicate through the forum.

2.1.4. Administrator Module. After the administrator successfully logs in as the administrator, the administrator background page will automatically pop up in the system. As the administrator, the administrator has the right to view and manage the website information and data information [10]. First, the administrator can view the relevant information of the website and has the permission to delete the information. Second, administrators can publish relevant information. Third, administrators can post relevant links to the relevant web pages or systems. Administrators can also publish related courseware and learning videos.

2.1.5. Online Test Module. This system includes the function of online test. Testing plays an important role in education and teaching. The traditional test is a paper-based test with low efficiency and requires many steps. Students cannot take the test at any time and can only examine their learning status through their usual homework [11]. And realize the online examination of the information system to help students pass timely examinations and understand their own learning situation, both pertinent and comprehensive. To develop interactive, dynamic, and efficient online testing function, we must rely on the support of database technology.

2.1.6. Forum Management Module. Forum management module is the main platform for students and teachers to communicate; its function is mainly to provide a real-time communication platform for teachers and students, through the way of posting-reply communication.

2.2. System Role Use Case Analysis. In the art teaching and research system, there are three login identities authorized by the system: system administrator, teacher, and examinee. Next, we use UML to describe the roles of the system, as shown in Figure 3.

According to the three methods of system client, the total subsystem can be divided into three subsystems: administrator, teacher, and student. The administrator's functions are mainly login and management of teaching. The teacher subsystem mainly realizes the management of teacher login, information release, and forum. The main functions of the student subsystem are login, online learning, viewing homework, forum communication, and other functions [12]. Based on the above analysis, the three roles of the system are students, teachers, and administrators, and each role has its own different functional requirements.

The system administrator plays an important role in the entire art teaching information system. As the administrator of the whole system, the main roles are user management, role management, grade management, class management, and course management. An example for system administrators is shown in Figure 4.

3. Interactive Art Online Teaching System Software Design

3.1. Interactive Art Online Teaching Model Design. Throughput the new system through the whole information is the key to coping with the increasing complexity of dynamic web pages. The design process of the whole system model is divided into presentation, business logic, and data access layers, as shown in Figure 5. In terms of deployment, the presentation layer corresponds to the server, the logical layer corresponds to the application layer server, and the data layer corresponds to the data layer server.

Presentation layer: the presentation layer realizes the function of providing customers with dynamic Web pages, and customers can easily access the dynamic web pages. This layer is in the form of Web projects in the system, and all pages are deployed under the Web folder.

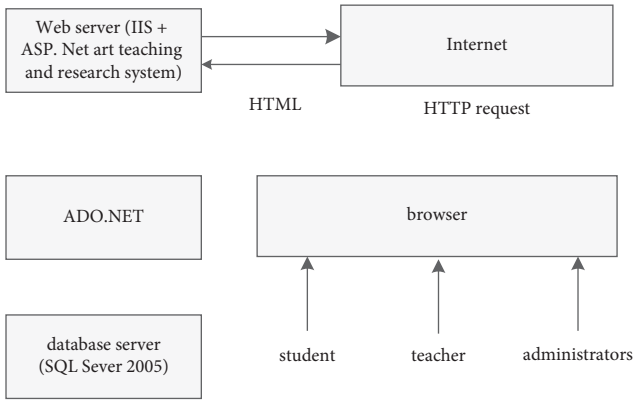

Figure 1: Structure design of the overall functional modules of the system.

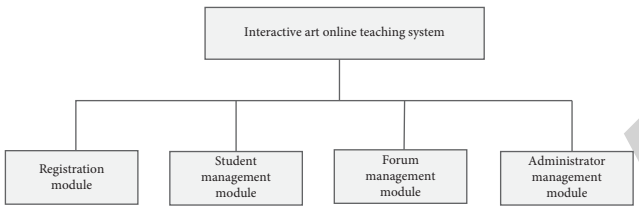

Figure 2: Overall structure module of the system.

Business logic layer: some business functions of the system can be realized in the form of BLL suffix in the system.

Data access layer: this layer provides related data access services for the above two layers.

3.2. Interactive Art Online Teaching Function Design. In the learning system, certain navigation and search functions can be provided, such as arranging the location of the network courseware in a certain order and providing the search function of the subject words according to certain knowledge points, so that users of the system can easily and quickly find the learning resources they need [13]. The learning system can also record the individual learning situation of learners at any time so that learners and teachers can master the relevant learning progress and make teaching arrangements. The most important design of the online learning function module is the upload of the course resource function, and the technology used for the production function of the course resource is ASP.NE. ASP.NET is a programming framework, which is a new framework based on the operation of the common language and can realize the establishment and generation of Web programs. Web programs have powerful functions [14]. Net under the condition of building generated Web program compared to the traditional Web program in the function and operation has a great progress:

(1) Simplicity: ASP.NET makes it easier to perform a variety of common tasks.

(2) Security: within ASP.NET, there is a Windows authentication that greatly improves application security.

(3) Power and flexibility: SP.NET is built on the common language runtime, and software developers can use its power and flexibility to develop powerful Web applications. And, in solving Microsoft.NET framework class library and other operations it can be very good. Realize seamless connection with the Web. In addition, ASP.NET ends programming language restrictions and can operate in any programming language, thus greatly enhancing the programming staff's choice of programming language tools [15]. In addition, the common language runtime's tomb-house feature ensures that ASP.NET maintains existing investments in COM-based development to a large extent.

(4) Enhanced performance: ASP.NET is a common language runtime code that has greatly improved performance even before the lines of code are written.

(5) Manageability: one of the biggest characteristics of ASP.NET is that it belongs to a text-based hierarchical configuration system. This configuration system greatly simplifies the program's development process and facilitates management when setting up the application server environment and Web applications. Since ASP.NET stores configuration information in plain text, we can deploy ASP.NET framework applications to the server by simply copying the necessary files to the server, which has the benefit of not having to repeatedly restart the server, greatly improving management performance [16].

(6) World-class tool support: the ASP.NET framework has been supplemented by a number of toolkits and designers from the Visual Studio integrated development environment. ASP.NET provides many powerful features, including drag-and-drop server controls, WYSIWYG editing, and automated deployment.

(7) Scalability and usability: ASP.NET was designed with scalability in mind and added a feature to improve performance in a variety of application environments.

3.3. The Transmission of Art Teaching Information Based on Internet of Things. The Internet of Things is the third wave in the development of the world's information industry. Generally speaking, the Internet of Things is a network that connects objects and objects based on the Internet. It can connect any object to the Internet through sensors, positioning systems, and other information devices according to certain protocols, realize all kinds of information exchange and communication between interconnected objects, and finally realize intelligent management of objects [17]. A typical RFID system consists of three parts: (1) a reader,

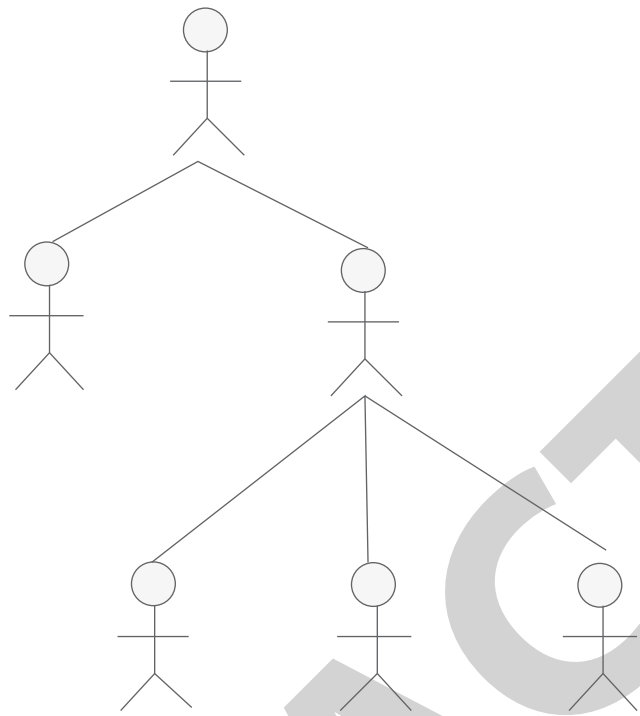

Figure 3: System roles use case diagram.

composed of a control module and an antenna, is used to read and write the information of the RFID tag and control its communication with the RFID tag, with signal encoding and decoding, data encryption and decryption, anticollision algorithm, authentication, and other functions; (2) RFID tag, which consists of a chip and a coupling element and contains a built-in antenna that can communicate with the RADIO frequency antenna; (3) a host mainly processes the RFID tag information obtained by the reader. The basic workflow of the RFID system is shown in Figure 6.

In practical application, the data of each artwork will be input into the tag in advance, and the reader can automatically identify the target object of the artwork by reading the tag information through the RADIO frequency signal and then transmit it to the control center wirelessly, so as to complete the fast tracking of the artwork and the fast exchange of data. It should be pointed out that RFID can identify the tags of artworks and identify multiple artworks at a time. When RFID technology identifies tags, if there are more than one electronic tag in the area, it will respond at the same time, and the signal will overlap, and the reader cannot accurately read the data. The anticollision algorithm can solve this problem. There are two types of collisions in RFID: the collision of multiple readers and the collision of multiple tags. The former is relatively easy to solve: just put the reader in the right place. The latter cannot read the information correctly because multiple tags are responding to the reader instruction at the same time.

Art teaching information needs multi-layer transmission. In order to realize the length value of the Internet of Things module, it is represented by M. Multi-layer linear art teaching information needs to be encrypted. The data encryption test length is M. Art teaching information is designed through the use of algorithms linear programming binary bit sequence programming design bit sequence flow can be divided into $N = \lfloor n/M \rfloor$ time window. The binarization P value of multilayer transmission control of art teaching information is defined as follows by using the block-feature matching technology:

$$\begin{aligned} P\,\text{value} &= \text{igamc}\left(\frac{N}{2}, \frac{\chi^2(\text{obs})}{2}\right) \\ &= \frac{1}{\Gamma(N/2)} \int_{\chi^2(obs)/2}^{\infty} e^{-t} t^{N/2-1} \mathrm{d}t, \end{aligned} \tag{1}$$

where $\Gamma(N/2) = \int_0^{\infty} t^{N/2-1} e^{-t} \mathrm{d}t$. Assuming that the plaintext number of art teaching information pieces to be transmitted is $X = (0, 1/M, 2/M, \ldots, 1)$, the random distribution probability of packet forwarding is $X = (0, 1/M, 2/M, \ldots, 1)$, the detection characteristic quantity of coding sequence is $P = (p_0, p_1, p_2, \ldots, p_M)$, and the transmission function of art teaching information can be obtained:

$$\begin{pmatrix} a & b & c & d \\ d & a & b & c \\ c & d & a & b \\ b & c & d & a \end{pmatrix} \begin{pmatrix} a & b & c & d \\ d & a & b & c \\ c & d & a & b \\ b & c & d & a \end{pmatrix} = \begin{pmatrix} 1 & 0 & 0 & 0 \\ 0 & 1 & 0 & 0 \\ 0 & 0 & 1 & 0 \\ 0 & 0 & 0 & 1 \end{pmatrix}. \tag{2}$$

Using the elliptic curve block encryption method, we can get $\begin{cases} a^2 + c^2 = 1, \\ b^2 + d^2 = 0 \end{cases}$; that is, $\begin{cases} g^{2\alpha} + g^{2\gamma} = 1, \\ g^{2\beta} + g^{2\rho} = 0 \end{cases}$. Since the first character of the plaintext sequence satisfies $g^{2\beta} + g^{2\rho} = 0$,

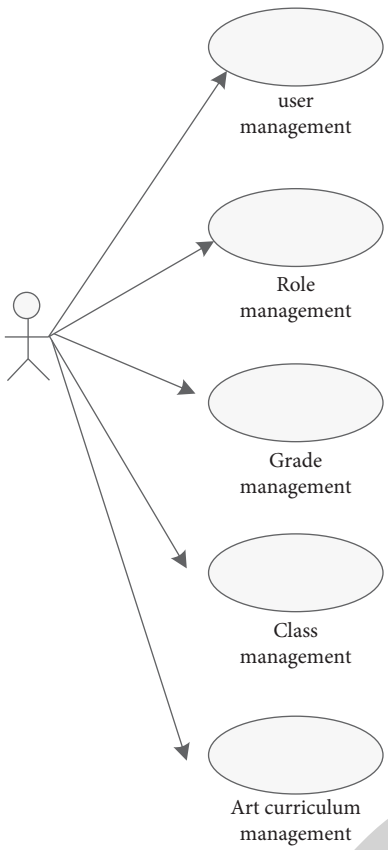

Figure 4: System administrator use case diagram.

$1 \le \beta$, the chaotic key state characteristic equation is constructed, and the big data of the basic art teaching information communication of the Internet of things is loaded into the chaotic key state characteristic equation to obtain the chaotic key state characteristic equation:

$$c = z \cdot \lfloor \frac{x_0}{2} \rfloor = \left(q_p(z)p + r_p(z)\right) \cdot \lfloor \frac{x_0}{2} \rfloor = q_p(z)p \cdot \lfloor \frac{x_0}{2} \rfloor + r_p(z) \cdot \lfloor \frac{x_0}{2} \rfloor. \quad (3)$$

The art teaching information is applied to the art online teaching system, and a feature group matches each group of information to realize the data transmission of art teaching information.

3.4. Interactive Art Online Teaching Function Implementation Code. The FileUpload control can be used to upload the art works file. Through the setting of the code, the program can upload the art works to the file. The main code is shown as follows:

```
try
{if (Filep Uploadl.PostedFile.FileName.Length = = 0)
{Response.Write ("<seript>alert (\"The upload path cannot be empty!\");</seript>");
return;
}
String filename = this.File Uploadl.PostedFile.FileName.Substring (
this.FileUploadl.PostedFile.FileNaxne.LastIndexOf ("\\") + 1);
String art = File Uploadl.PostedFile.FileName.Substring (
this.File UPloadl.PostedFile.FileName.LastIndexOf (".") + 1):
if (art = = "gif"‖art = = "jpg," ‖art = = "bmp")
{File Uploadl.PostedFile.SaveAs (Server.MapPath (,·, image/,·, +filename));
Response.Write ("<script>alert (\,·, Uploading the file succeeded!\,·, );</seript>"):
}
else
{Response.write("<seript>alert(\"Upload files must be IN GIF, JPG, BMP format!\):</scriPt>"):
relurn;
}
}
eateh (Exeeptionex)
{ResPonse.Write ("<seript>alert (\"+ex.Message+"\"); seriPt>"):}
```

The file type can be changed slightly according to your needs. On the basis of the above code, the interactive art online teaching system is completed, as shown in Figure 7.

4. Experiment

4.1. Testing Environment. In order to ensure the true and effective test results, the real campus network environment and school hardware and software resources are used in the system test. The device configuration is as follows:

(1) Hardware configuration: I5 series database server, CPU frequency above 2.8G, and memory capacity 4G. The hard disk capacity is greater than 500 GB, and Windows server operating system and gigabit network adapter are installed.

Two client computers: one requires E5300 series 2.6G processor, 2G or more memory capacity, 250G or more hard disk, Windows 7 operating system, and 100 m nic. The other one requires E2180 series 2.0G processor, 2 GB or more memory capacity, 160 GB or more hard disk, WinXP operating system, and 100 m nic.

(2) Network environment: art colleges teaching network.

4.2. Improving Effect of Art Teaching Credits. In order to verify the performance of the design system, literature [7] system, literature [8] system, and design system are used to verify the teaching effect of the online art teaching system.

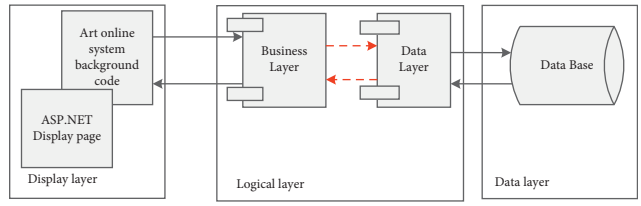

Figure 5: B/S pattern design model.

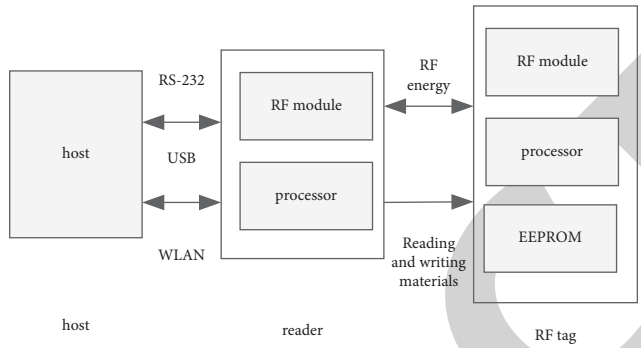

Figure 6: Working principle of RFID system.

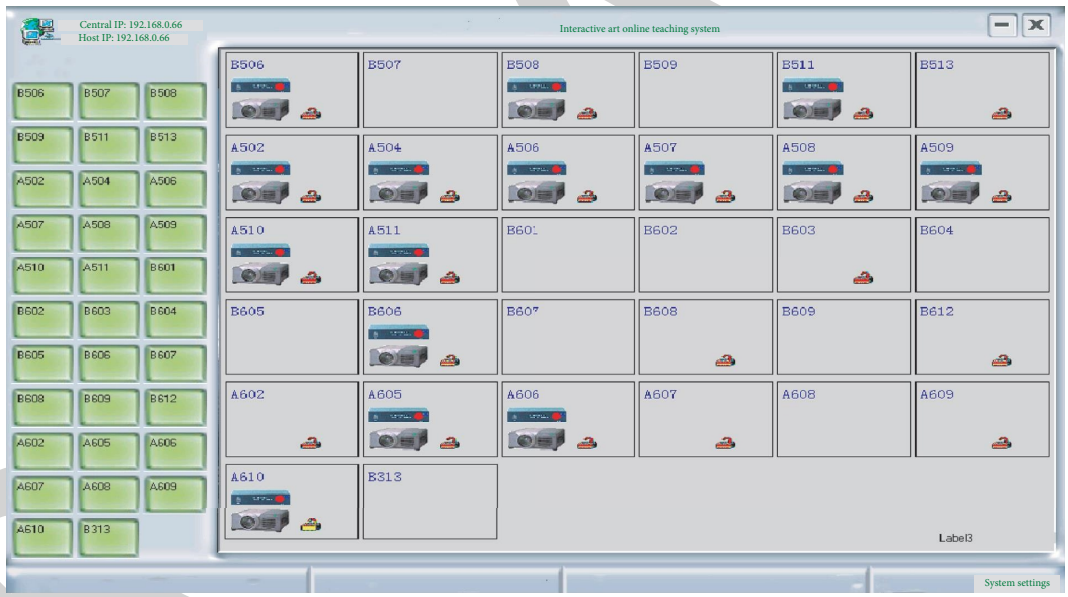

Figure 7: Interactive art online teaching system.

The teaching scores of art courses are compared, and the results are shown in Figure 8.

The improvement effect of online teaching system for art students is different under different methods. For the first group of students, the score before the application of the teaching system was 67, after the application of the literature [7] system was 76, after the application of the literature [8] system was 76, and after the application of the paper system was 96. For the third group of students, the score before the application of the teaching system was 65, after the application of the literature [7] system was 68, after the application of the literature [8] system was 85, and after the application of the paper system was 95. In the eighth group, the score was 76 before applying the teaching system, 79 after applying the literature [7] system, 79 after applying the literature [8] system, and 96 after applying the paper system. After the application of this system, the improvement effect of the online teaching system for art students is obviously better than other methods.

4.3. System Throughput. In order to verify the effectiveness of the designed system and the throughput of the literature [7] system, literature [8] system, and the designed system, the results are shown in Figure 9.

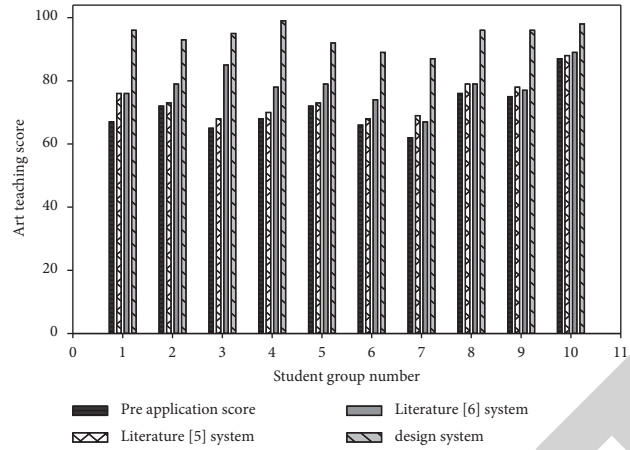

Figure 8: Improvement effect of online teaching system for art students.

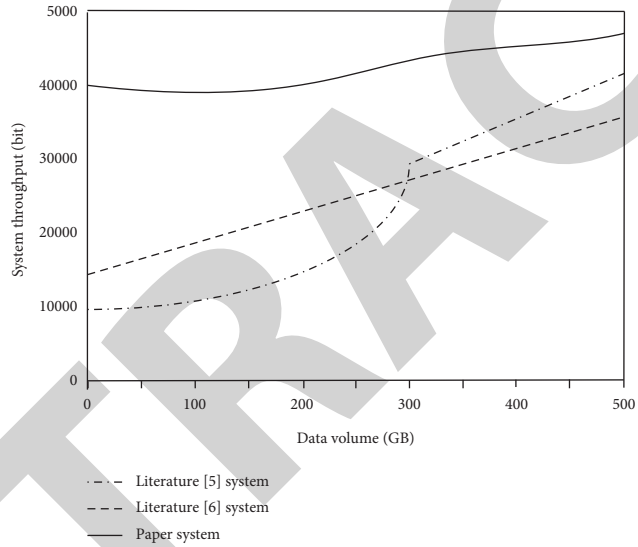

Figure 9: Data throughput of different systems.

As can be seen from Figure 9, when the data volume is 100 GB, the system data throughput of literature [7] is 10021 bits, the system data throughput of literature [8] is 20000 bits, and the system data throughput of the designed system is 38700 bits. When the amount of data is 200 GB, the system data throughput of literature [7] is 15200 bits, the system data throughput of literature [8] is 24000 bits, and the system data throughput of the designed system is 38700 bits. When the data amount is 500 GB, the system data throughput of literature [7] is 40000 bits, and that of literature [8] is 35000 bits, and the system data throughput of the designed system is 47700 bits. The data throughput of the designed system is much higher than that of other systems, which indicates that the system in this paper has good compression resistance and strong load capacity and can simultaneously meet the online teaching ability of students in more art colleges.

5. Conclusion

This paper designs an interactive art online teaching system based on BS mode and Internet of Things. The overall structure of the art teaching system was designed according to THE B/S structure, the interactive art online teaching model was designed, the RFID technology in the Internet of Things was introduced to control the information transmission of the interactive art online teaching system, and the interactive art online teaching system based on BS mode and the Internet of Things was completed. The following conclusions were drawn through the experiment:

(1) The eighth group got 96 points after applying this system. After applying this system, the improvement effect of the online teaching system for art students is obviously better than other methods.

Hindawi
International Journal of Antennas and Propagation
Volume 2024, Article ID 9867141, 1 page
https://doi.org/10.1155/2024/9867141

Retraction

Retracted: Risk Prediction Algorithm of Social Security Fund Operation Based on RBF Neural Network

International Journal of Antennas and Propagation

Received 23 January 2024; Accepted 23 January 2024; Published 24 January 2024

This article has been retracted by Hindawi following an investigation undertaken by the publisher [1]. This investigation has uncovered evidence of one or more of the following indicators of systematic manipulation of the publication process:

(1) Discrepancies in scope

(2) Discrepancies in the description of the research reported

(3) Discrepancies between the availability of data and the research described

(4) Inappropriate citations

(5) Incoherent, meaningless and/or irrelevant content included in the article

(6) Manipulated or compromised peer review

The presence of these indicators undermines our confidence in the integrity of the article's content and we cannot, therefore, vouch for its reliability. Please note that this notice is intended solely to alert readers that the content of this article is unreliable. We have not investigated whether authors were aware of or involved in the systematic manipulation of the publication process.

In addition, our investigation has also shown that one or more of the following human-subject reporting requirements has not been met in this article: ethical approval by an Institutional Review Board (IRB) committee or equivalent, patient/participant consent to participate, and/or agreement to publish patient/participant details (where relevant).

Wiley and Hindawi regrets that the usual quality checks did not identify these issues before publication and have since put additional measures in place to safeguard research integrity.

We wish to credit our own Research Integrity and Research Publishing teams and anonymous and named external researchers and research integrity experts for contributing to this investigation.

The corresponding author, as the representative of all authors, has been given the opportunity to register their agreement or disagreement to this retraction. We have kept a record of any response received.

References

[1] L. Yang, "Risk Prediction Algorithm of Social Security Fund Operation Based on RBF Neural Network," *International Journal of Antennas and Propagation*, vol. 2021, Article ID 6525955, 8 pages, 2021.

Hindawi
International Journal of Antennas and Propagation
Volume 2021, Article ID 6525955, 8 pages
https://doi.org/10.1155/2021/6525955

Research Article

Risk Prediction Algorithm of Social Security Fund Operation Based on RBF Neural Network

Linxuan Yang

University College London (UCL), London, UK

Correspondence should be addressed to Linxuan Yang; linxuan.yang.16@ucl.ac.uk

Received 16 August 2021; Revised 17 September 2021; Accepted 21 September 2021; Published 30 September 2021

Academic Editor: Fangqing Wen

In order to ensure the benign operation of the social security fund system, it is necessary to understand the social security fund facing all aspects of the risk, more importantly to know the relationship between different risks. Based on RBF, the interpretative structure model is applied to draw the risk correlation hierarchy diagram, which provides a scientific risk management method for the social security fund. RBF neural network is used to build the risk warning model of social security fund operation. Then, put forward the corresponding risk treatment scheme to the warning signal. Finally, the RBF neural network is used for comprehensive risk warning. In this paper, the risk warning of social security fund operation is the research object, and the corresponding risk treatment scheme is put forward for the warning signal. This paper uses an improved ant colony algorithm to optimize the parameters of the RBF neural network, which overcomes the shortcomings of the traditional RBF neural network such as slow convergence, ease of falling into local extremes, and low accuracy, and improves the generalization ability of the RBF neural network. It has the characteristics of good output stability and fast convergence speed. On this basis, the prediction model based on the improved ANT colony-RBF neural network is established, and the MATLAB software calculation tool is used for accurate calculation, which makes the prediction results of coal mine safety risk more accurate and provides more reliable decision basis for decision makers. The results show that the network has small calculation error, fast convergence, and good generalization ability.

1. Introduction

The elements of a system form a structure that determines the function and efficiency of the system. Interpretive structure model is a widely used method to analyze system structure in modern systems engineering. Interpretive structural models can be used to describe and analyze the interrelationships between system elements. It uses the known relationship between system elements to build the adjacencies matrix and then generate the reachability matrix and finally generate the hierarchy diagram [1]. It reveals the relationship between system elements through the form of hierarchy, including direct relationship, indirect relationship, membership relationship, and relative status. The operation of social security fund is a complex system, and various risks will be encountered in the operation. This paper tries to analyze the risk structure of social security fund operation from the perspective of system engineering by using the interpretive structure model [2].

China's insurance industry is in an unprecedented transition period. With the deepening of the reform of the national economic system, the living environment of China's insurance companies has undergone drastic changes, and some deep-level problems previously hidden have gradually been exposed. According to Standard & Poor's 2003 assessment of China's insurance market, the main risk facing China's property and casualty insurance industry is inadequate solvency, mainly due to insufficient liability reserves drawn and large capital gaps due to rapid business growth. Therefore, it is necessary to establish a comprehensive risk early warning system for property insurance companies in China [3]. The research on the risk early warning system of property insurance company is relatively few, and it mainly draws lessons from the banking risk early warning method.

Only Zeng Zhongdong, a domestic scholar, has put forward an early warning system of property insurance company's business risk based on fuzzy optimization and neural network [4]. Whether starting from artificial neural network technology or other technologies, want to go to, or technically is a breakthrough and innovation of traditional early warning system, it solves the traditional model is difficult to deal with high degree of nonlinear model, adaptive ability, lack of access to information and knowledge of indirect, time consuming and low ability of difficulties, so as to lay the foundations for the early warning go to practical [5–8].

Small- and medium-sized enterprises are an indispensable part of my country's national economic structure. They are of great significance to the stable and sustainable development of my country's economy and are gradually becoming the main force in the development of social productive forces. In recent years, many high-tech SMEs have risen rapidly, which has played a role in optimizing my country's economic structure. However, small- and medium-sized enterprises have weak financial strength, poor antirisk ability, and low creditworthiness. This makes banks more inclined to invest funds in large enterprises, and they are not very enthusiastic about lending to small- and medium-sized enterprises [9]. In the case of unbalanced sample data, the prediction of traditional risk analysis model has tendentious defects, so [10] analyzes the factors affecting the financial crisis and establishes a preliminary financial early warning index system of listed manufacturing companies in China. Then, the particle swarm optimization algorithm is used to improve the parameters of support vector machine, and the optimal financial crisis warning index set is selected. Combined with the theory and algorithm of empirical research, determine the financial early warning indicators of listed companies in China, and use SVM and PSO optimization parameters to establish an effective early warning model.

At present, the multilayer feedforward network is based on back propagation (BP), but most of the learning algorithms of this network must be based on some nonlinear optimization technology. Therefore, its application is limited due to the large amount of computation and slow learning speed [11–13].

2. Explain the Overview of the Structural Model

Interpretive structure model was developed by the American Professor Walter in 1973 to analyze the problem of element structure in complex social and economic system. The characteristic of this model is that the complex system is decomposed into several subsystems first, and then a multistage hierarchical structure model is constructed according to the relationship of the system elements with the help of computer and people's practical experience and knowledge [14–16].

The analysis procedure is as follows. (1) Form an analysis team. The number of team members is generally about 10, and each member is required to have relevant professional background in the research system and try to absorb professionals with different views into the team. (2) Design the questionnaire [17]. Design problems according to the interrelationships between system elements. The questionnaire design should pay attention to neutrality and avoid guiding the answer. (3) Gather panelists' opinions. All responses will be summarized, and a second round of consultation will be conducted for those who have serious differences in the relationship between system elements until a more uniform list of system elements is formed. (4) On the basis of the relation table of elements, the adjacency matrix and reachability matrix are established. (5) The skeleton matrix was established after the interlevel division of the reachable matrix. (6) The interpretation structure model was established according to the skeleton matrix.

2.1. The Construction of Social Security Fund Risk Structure Steps. Social security fund refers to the funds set up in various ways to implement the social security system in accordance with national legislation. Safety is the number one thing in the social security fund [18]. The collection, management, and payment of social security fund are facing systemic and nonsystemic risks. If the operation of social Security fund is regarded as a financial activity of institutional investors in the capital market, then it is possible to identify the major risk factors affecting the operation of the social security fund and to find the interrelationships between these risk factors [19]. This will help strengthen risk management in the operation of social security funds.

2.1.1. The Main Risk Factors of Social Security Fund Operation. (1) Credit risk (A1): The operation link of social security fund not only has credit risk of entrusted financial institutions and investment managers, but also will face credit risk in financial markets. Credit risk is broadly defined. Refer to the process of a transaction defined by a credit relationship. The possibility that one party in a transaction fails to fulfill its payment promise and causes losses to the other party is mainly caused by two aspects: subjectively, the existence of moral hazard and adverse selection; objectively, the existence of business cycles or the occurrence of other special events.

(2) Liquidity risk (A2): The social security fund should maintain sufficient liquidity in the investment process. If you do not have enough money and a certain short-term investment set aside in advance to cover your expenses, this may cause social security fund capital turnover difficulty, thus affecting the social security fund function play.

(3) Inflation risk (A3): Due to inflation, the real purchasing power of the operation results of the social insurance fund decreases, causing the depreciation of the fund. For pension funds, because of the long-term nature of its operations, the cumulative effect of inflation on the quality of life of retirees can not be ignored.

(4) Market interest rate risk (A4): The use of social security funds to buy securities will face a variety of risks. Among them, market interest rate risk refers to the fluctuation of security price caused by the change of market interest rate. This brings uncertainty to the buyer's earnings. Interest rates and security prices generally move in opposite

directions. When interest rates generally rise in the market, security prices will fall (both stocks and bonds) and vice versa. The price of the security will go up. Interest rate risk is the main risk of fixed income securities and bonds. A country's interest rate policy is determined by the central bank. Market interest rates will move in response to policy. So, the social security fund must take into account fluctuations in market interest rates in its investment operations.

(5) Asset allocation risk (A5): The social security fund aims to maintain and increase its value. You have to choose a reasonable mix of different asset classes. Due to the limitations of individual and institutional investors' own investment ability, allocate between different asset classes according to investment needs.

(6) Bankruptcy risk (A6): The management institution and trustee institution of the social security fund will be liquidated due to insolvency, leading to the loss of social security funds if they are broken up for other reasons.

(7) Financial risk (A7): Due to the social security fund's main business income and profit fluctuations, unreasonable liability structure leads to the increase of liabilities beyond the fund manager and fund custodians' bearing capacity. Or the change of financing conditions and environment leads to the loss of financial cost control.

(8) Economic environmental risk (A8): National macroeconomic weather and domestic and foreign economic background (including the position of the business cycle, economic policy, and adjustment of industrial structure) will affect the asset allocation choice of social security fund investment. And that leads to risk.

(9) Policy and legal risks (A9): Due to changes in various relevant systems, policy adjustments, or imperfections in regulations, risks will arise directly. Because social security is at a critical time for reform, formal social security regulations have not yet been promulgated. The uncertainty of reform makes various systems and policies have relatively large space for change.

(10) Overseas investment risk (A10): Overseas investment risk refers to the possibility of losses caused by changes in national sovereignty, political fluctuations, or economic crises in international economic activities of the social security fund. Based on the above analysis, after comprehensively considering the special security points and the realistic influencing factors of the current capital market, finally, 10 risk factors affecting the operation fund are determined as the object of analysis and research. In this way, the risk factor matrix A of the social security fund is obtained.

2.2. Adjacencies Matrix of Risk Factors of Social Security Fund Operation. The function of the adjacency matrix is to describe the direct relationship between the elements. It is the result of one by one comparison of each element. The rows are the elements that exert influence and the columns are the elements that are affected: 1 if there is a direct relationship between the two elements, and 0 if there is no relationship [20].

The 10 risk factors of the operation of social security fund are organically linked together, and the relationship of mutual influence can be expressed by the adjacent matrix. After many discussions with the analysis team members, the following adjacency matrix is established (see Table 1).

2.3. Generate the Reachable Matrix from the Known Adjacent Matrix

2.3.1. After the Generation of the Adjacent Matrix A. You sum it with the identity matrix I, A plus I, and then you power the matrix A plus I over A whole number n. The reachable matrix can be used to describe all the influences between the elements. The element M_{ij} of the reachable matrix M is 1, which means that there is a one-step or one-step reachable path between element A_i and element A_j. The reachable matrix completely expresses the direct and interconnection relationship between elements.

2.3.2. Interstage Division. The so-called interstage division is to divide the risk factors into different levels according to the structure of the above calculation. The manager of the social security fund will have a theoretical framework for managing risks.

The following concepts are involved in the process of interlevel division:

(1) Reachable set: The set of elements affected by element a_i is defined as the reachable set $R(a_i)$ of element a_i.

(2) Antecedent set: The set of factors affecting factor a_i is defined as antecedent set $A(a_i)$ of factor a_i.

(3) Superlative factor: For $R(a)$ and $A(a)$, a_i is the superlative factor. The elements in question are the risk factors mentioned in this article.

According to the reachability matrix, you can find the reachability set of any risk factor in the system starting with the reachability matrix. Through the list, find its superlative set of elements, and then cross them out of the reachable matrix. Then make the table from there. Find the highest level prime set in the new matrix. In this way, the different risks can be divided into different levels.

In order to be more concise and beautiful, the hierarchical diagram drawn by the computer is optimized to get the optimization hierarchy as shown in Figures 1 and 2.

3. Structure of RBF Neural Network

The structure of RBF neural network is shown in Figure 3.

For the mapping relation of RBF neural network, consider

$$y_j = f_n(x) = \sum_{j=1}^{m} v_{jk} R_j(x), \quad k = 1, 2, \ldots, p, \tag{1}$$

where p is the number of nodes; m is number of hidden layer nodes; n indicates the number of layer nodes; $R_j(x)$is the

action function of the j-th neuron in the hidden layer (radial basis function).

The basic idea of forming radial basis function is to realize the transformation from input layer to hidden layer by using hidden layer element. In this way, the vector maps directly to the hidden space without connecting weights. As long as the cluster center of RBF is determined, this nonlinear relationship will be determined accordingly. The Gaussian function is the most commonly used in the RBF neural network model:

$$R_j(x) = \exp\left(-\frac{\left\|x - c_j\right\|}{2\delta^2}\right), \quad j = 1, 2, \ldots, m, \tag{2}$$

where m is the number of nodes in the hidden layer; x-n is the dimension input vector; c is the center (vector) of the j-th basis function, which has the same dimension as x; δ is center radius or width of neuron node in the j-th hidden layer; $\|x - c_j\|$ is vector norm of $x - c_j$, usually said x with c_j distance; for $R_j(x)$, there is a maximum of only c_j; along with the $\|x - c_j\|$ increases, $R_j(x)$ decay to zero.

The advantages of using the Gaussian basis function are as follows:

(1) The representation form is simple and convenient, and the complexity of the algorithm will not be increased too much even if multiple variables are input

(2) radial symmetry

(3) There is strong smoothing performance and existence of arbitrary derivative

(4) The Expression of Gaussian basis function is simple and analytic, so it is conducive to theoretical analysis

3.1. Realization of RBF Neural Network Algorithm. Suppose there are P training sample sets $X = X^1, X^2, \ldots, X^p$; when the input vector of the P training sample is given as $X^p = x_1, x_2, \ldots, x_m^T$, the corresponding expected output is $Y^p = \{Y_1, Y_2, \ldots, Y_m\}$, and the excitation is "basis function" $\Phi(||x - c_j||)$, where $c_j = c_{j1}, c_{j2}, \ldots, c_{jm}^T$ represents the clustering center point (or center vector) of the hidden node base function, $y^p = \{y_1, y_2, \ldots, y_m\}$ represents the actual output of the system, and then the objective function of the total error of the system for P training samples is

$$J = \sum_{p=1}^{P} J^p = \frac{1}{2} \sum_{p=1}^{P} \sum_{n=1}^{N} \left(Y^p - y^p\right)^2. \tag{3}$$

RBF neural network is a nonlinear mapping relationship, which has the energy to cover the receiving domain, and the output layer is the weighted sum of the outputs of the basis function of the hidden layer. Therefore, as long as the number of nodes and basis functions of the scientific and reasonable hidden layer are determined, the problem to be solved before can be transformed into a classification problem. That is to say, the design process of RBF neural network can be transformed into a linearly separable mapping problem of high dimensional space.

In the application of RBF neural network, three kinds of adjustable parameters need to be determined: center vector c_j, connection weight v, and threshold θ of the network. The process of learning algorithm has two stages, that is, the stage of learning without teachers and the stage of learning with teachers. In the first stage, teacher-free learning is based on all input sample sets $X = X^1, X^2, \ldots, X^p$, and cluster analysis method is used to solve the center vector c_j.

Table 1: Adjacency matrix.

	A1	A2	A3	A4	A5	A6	A7	A8	A9	A10
A1	1	1	0	0	1	1	1	0	0	0
A2	1	1	0	0	1	1	1	0	0	0
A3	1	1	1	0	0	0	1	0	0	0
A4	1	1	0	1	0	0	1	0	0	0
A5	0	0	0	0	1	1	1	0	0	0
A6	0	0	0	0	0	1	1	0	0	0
A7	0	0	0	0	0	1	1	0	0	0
A8	0	0	1	1	0	1	1	1	0	0
A9	0	0	1	1	0	1	1	0	1	0
A10	1	1	0	0	0	0	0	0	0	1

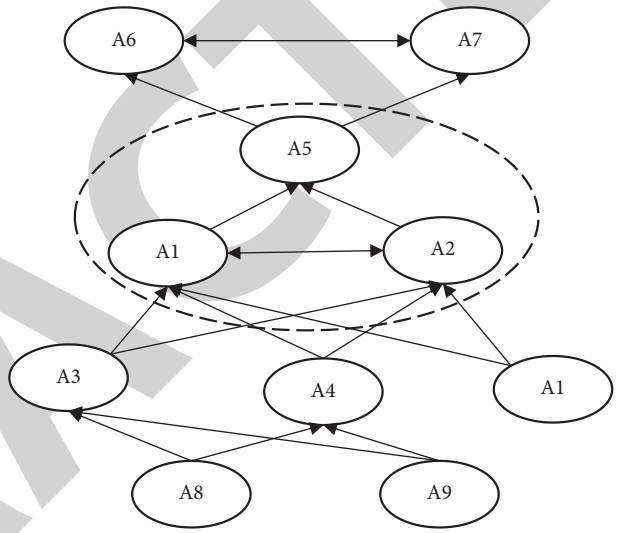

Figure 1: Optimization hierarchy.

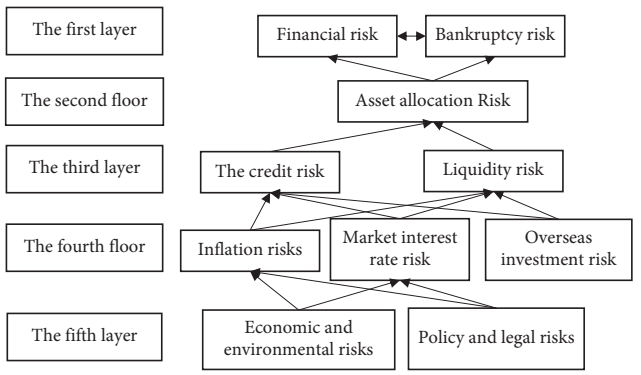

Figure 2: Optimization hierarchy.

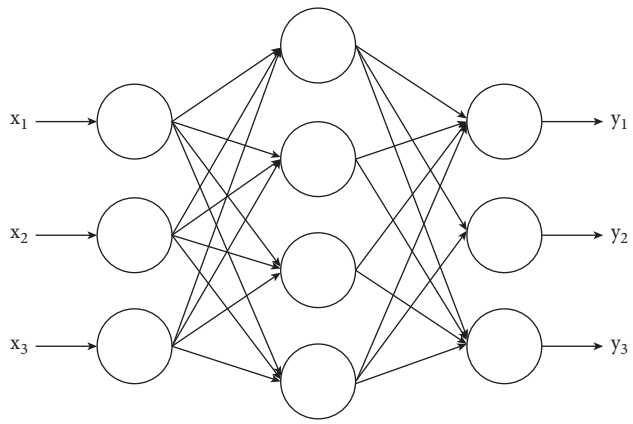

Figure 3: RBF neural network structure.

The second stage refers to the use of teacher learning algorithm to train and adjust the connection weight v_{jk} or threshold θ_k.

3.1.1. Learning without a Teacher. Teacher-free learning, also called unsupervised learning, is based on the clustering of all input sample sets to obtain the RBF center vector c_j of each hidden layer node. The k-means algorithm is a common clustering method, which is used to realize real-time adjustment of the center vector c_j. The training samples are clustered into several classes, and the center vector of the radial basis function is found by taking the minimum clustering distance as the index. The specific steps of the algorithm of k-means adjusting the central point are as follows:

(1) Consider the random initial value $c_j(0)$, $(j = 1, 2, \ldots, a)$, the initial value of the learning rate $\beta(0)$, and the limiting value of the error function of the total objective *xx*.

(2) Calculate the current Euclidean distance:

$$d_j(t) = \left\| x(t) - c_j(t-1) \right\|,$$
$$d_{\min}(t) = \min d_j(t) = d_r(t), \tag{4}$$

where r is the node with the smallest distance between input sample $x(t)$ and center vector $c_j(t-1)$.

(3) Center adjustment: the specific operation is

$$c_j(t) = c_j(t-1), \quad (j = 1, 2, \ldots, a),$$
$$c_j(t) = c_j(t-1) + \beta(t)\left[x(t) - c_r(t-1)\right]. \tag{5}$$

(4) After the operation of hidden layer nodes in a certain sample, the center vector and learning rate are modified according to the following formula:

$$\beta(t+1) = \frac{\beta(t)}{\sqrt{1 + \operatorname{int}(t/a)}}, \tag{6}$$

where $\beta(t)$ is the learning rate $(0 \le \beta(t) \le 1)$ and int$(\cdot)$ is the integer function.

(5) For the next sample $p(p = 1, 2, \ldots, p)$, repeat the calculation of step 2. When the error function $J = \sum_{p=1}^{p} J^p \le \varepsilon$ of the total criterion is satisfied, the clustering is terminated.

3.1.2. There Are Teachers to Learn. When the center vector c_j of each node of the hidden layer is determined, the connection weight v or threshold θ is trained and adjusted. Since the output layer is similar to the basis function output of a hidden layer, and it belongs to the linear optimization operation, updating its weight is similar to solving the linear optimization problem, and various linear optimization algorithms can be used to achieve the purpose, without the existence of minimum problem in the BP neural network.

There are many methods to correct the weight, such as least mean square algorithm and least square algorithm. This paper takes the least square recursive method as an example to correct the weight. The objective function is defined as

$$J = \sum_{p=1}^{p} J^p = \frac{1}{2} \sum_{p=1}^{p} \Lambda(p)\left[Y^p - y^p\right]^2, \tag{7}$$

where $\Lambda(p)$ represents the weighted factor matrix.

In order to solve a set of weight estimation values v_{jk} and minimize the objective function, let

$$\frac{\partial J(t)}{\partial V} = 0^T. \tag{8}$$

Using the least squares recursive method, the recursive formula of weight is expressed as

$$v_{jk}(t) = v_{jk}(t-1) + K(t)\left\{Y^p - \left[\phi^p(t)\right]^T w_{jk}(t-1)\right\},$$
$$K(t) = P(t-1)\phi^p(t)\left\{\phi^p(t)P(t-1)\phi^p(t) + \frac{1}{\Lambda(p)}\right\}^{-1},$$
$$P(t) = \left\{I - K(t)\left[\phi^p(t)\right]^T\right\}P(t-1). \tag{9}$$

3.2. Characteristics of RBF Neural Network. RBF neural network has the following characteristics:

(1) Like BP neural network, I strong F neural network also belongs to feedforward neural network.

(2) In general, the activation function of the RBF neural network is a function with a local accepting domain; that is, the vector falls in a specified minimal region, and the hidden node will produce a meaningful nonzero response (the response value is (0,11)).Therefore, in general, we can call RBF divine network local receptive domain neural network.

(3) Influenced by the regional nature of localized acceptance, RBF neural network has taken the concept of distance into consideration when making decisions. That is to say, the vector is close to the

acceptance domain of RBF neural network, the Divine network will make a meaningful non-zero response to it. However, BP neural network has the characteristic of arbitrary partition caused by hyperplane segmentation. The advantage of this method is that it can avoid this shortcoming.

(4) Some experimental studies have proved, in general, the key factor affecting the performance of the neural network, rather than the form of the nonlinear activation function used by the neural network. Both RBF and BP belong to forward neural network, and the above description of the characteristics of RBF shows that the RBF avoids some defects of BP neural network in many aspects.

4. Experimental Analysis

The property insurance company can get the final warning result according to the warning signal of RBF neural network, take the corresponding risk management measures, and coordinate the solvency, reinsurance ability, and the temperature profit of the insurance company and other indicators.

(1) The green warning signal (1, 0, 0) indicates that the property insurance company operates in a good condition and there is basically no risk. On the one hand, the company can continue to consolidate its existing business and enhance its core competitiveness. On the other hand, it can actively expand new business and improve the efficiency of capital use through active asset and debt management, so as to constantly adapt to improve the solvency and reinsurance ability of the company.

(2) Yellow warning signals (0, 1, 0) indicate that there are problems in the operation of the property insurance company, but they are still under control and there are certain risks. On the one hand, the company should take measures to check all financial indicators as soon as possible, handle all capital outflow business carefully, and strengthen measures to ensure the capital return as soon as possible. On the other hand, we should strengthen the monitoring of business processes, find out the possible problems in the organizational structure, operation mechanism, and governance mechanism of the company, and actively prepare solutions to deal with the possible financial crisis in the future.

(3) Red warning signals (0, 0, 1) indicate that the property insurance company has made major mistakes in operation, faces huge risks, and may have an existential crisis. The company takes emergency measures to implement centralized control and dispatch of funds, integrates stability funds through various channels, sells assets such as national bonds and short-term bills, and actively recovers funds through various channels to reduce losses. At the same time, the China Insurance Regulatory Commission and other regulatory authorities should be notified as soon as possible to seek emergency financial assistance from regulatory authorities and the industry to prevent bankruptcy.

Table 2: Test results.

Company	Ideal output value	Actual output value
1	(1, 0, 0)	(0.995, 0.023, 0.008)
2	(1, 0, 0)	(0.987, 0.002, 0.009)
3	(1, 0, 0)	(0.993, 0.007, 0.001)
4	(0, 1, 0)	(0.002, 0.992, 0.027)
5	(0, 1, 0)	(0.002, 0.983, 0.0009)
6	(0, 1, 0)	(0.010, 0.979, 0.013)
7	(0, 0, 1)	(0.0001, 0.0006, 0.981)
8	(0, 0, 1)	(0.0005, 0.014, 0.984)
9	(0, 0, 1)	(0.0001, 0.0001, 0.9934)

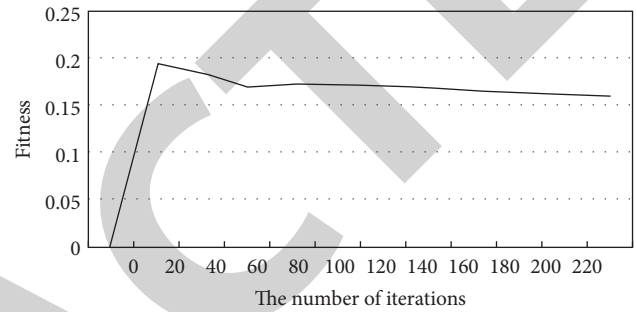

Figure 4: Improved ant colony algorithm optimization objective function convergence process.

First of all, the error index is err = 0.02; using the normalized data of the training set after 30 times of training, the error can meet the requirements. Secondly, the test is carried out using test set data, and the results are shown in Table 2. With a few exceptions, the actual output is very close to the expected output.

4.1. Simulation of Prediction Model. The parameters of RBF neural network are optimized by using the improved ant colony algorithm, and the convergence process is shown in Figure 4.

Figure 4 shows the adaptive convergence process of the objective function of RBF neural network optimized. It can be seen from the figure that the fitness rose in a straight line at the beginning, and the speed of rise was extremely fast. Although there were fluctuations when the iteration reached 34–95, it was difficult to decline after 130 generations when the fitness reached a certain value. After the iteration reached 210 generations, it was basically completely convergent, stabilized and finally reached the optimal.

4.2. Analysis of Experimental Results. In this paper, MATLAB software is selected for the analysis and design of RBF. According to the risk index data, samples 1–26 are selected as training samples to train the RBF neural network model optimized by ant colony algorithm. After the training is completed and the results meet the allowable error, samples

Table 3: The simulation results compared with the actual result.

Sample number	The actual results	RDF	Traditional ant colony algorithm	Traditional ant colony algorithm
27	0.6296	0.6220	0.6342	0.6318
28	0.6555	0.6619	0.6509	0.6574
29	0.8639	0.8754	0.8569	0.8612
30	0.4985	0.4937	0.5022	0.4970

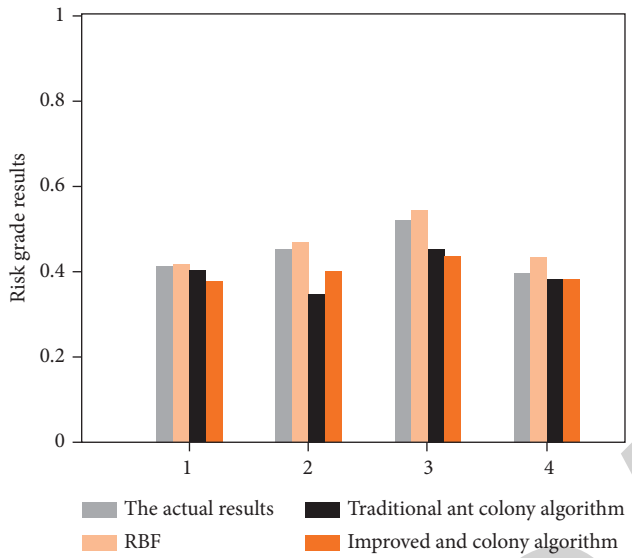

Figure 5: The actual value compared with the predicted results.

no. 27–30 are used to detect the RBF. The simulation results and actual results are shown in Table 3 and Figure 5.

As can be seen from Table 3 and Figure 5, the relative error between the predicted result of coal mine safety risk and the actual value through RBF neural network is 1.332% at most and 1.118% at least, and the average error is 0.746%. Through traditional ant colonies, the relative error between the prediction result of RBF neural network and the actual value of coal mine safety risk is the maximum 0.802% and minimum 0.735%, and the average error is 0.746%. By improving the ant colony, the maximum relative error result of RBF neural network, and the actual value of coal mine safety risk is 0.353%. The average error is 0.311%. So by improving the ant colony, RBF neural network model has a good prediction effect on the safety risk of coal mine, and the test has high accuracy and credibility, which can accurately reflect the overall safety situation of coal mine.

5. Conclusion

The nonsystemic risk and systemic risk of the social security fund investment operation: unsystematic risk (diversifiable risk) refers to the possibility that a particular cause will affect the return on a particular asset. It is a risk that can be eliminated with an efficient portfolio. Systemic risk (market risk, nondispersed risk) affects all assets (risks that cannot be eliminated by asset portfolio). This part of the risk is caused by risk factors that affect the market as a whole, for example, economic and environmental risks, policy and legal risks, foreign investment risks, market interest rate risk, and inflation risk. Therefore, systemic risk and nonsystemic risk form a whole and affect each other. Risk management theory and practice should not be separated from their internal relationship. By using RBF model method, a structural model of social security fund risk system with clear hierarchy and context is obtained, which provides a complete frame for the comprehensive risk management of social security fund investment. It provides theoretical basis for risk transformation model. Take bankruptcy risk and financial risk as the highest goal of risk management in the operation of social security fund. The interlinkage between risks requires the managers of the social security fund to manage the various risks under a comprehensive risk management. Attention should also be paid to the enterprise environment, market environment, economic environment, and policy laws that produce market risks in the operation of social security funds.

Data Availability

The data used to support the findings of this study are available from the corresponding author upon request.

Conflicts of Interest

The authors declare that they have no known competing financial interests or personal relationships that could have appeared to influence the work reported in this paper.

References

[1] Asbeck and Y. Y. Haimes, "The partitioned multi objective risk method (PMRM)," *Large Scale Systems Theory Application*, vol. 6, no. 1, pp. 13–38, 1984.

[2] T. L. Saaty, *The Analytic Hierarchy Process*, McGraw Hill, New York, NY, USA, 1980.

[3] J. H. M. Tah and V. Carr, "Information modelling for a construction project risk management system," *Engineering, Construction and Architectural Management*, vol. 7, no. 2, pp. 107–119, 2000.

[4] P. X. W. Zou, G. Zhang, and J. Wang, "Understanding the key risks in construction projects in China," *International Journal of Project Management*, no. 25, pp. 601–614, 2007.

[5] A. Chateauneuf and M. Cohen, "Risk seeking with diminishing marginal utility in a non-expected utility model," *Journal of Risk & Uncertainty*, no. 09, pp. 77–91, 2004.

[6] Z. Chen and H. Li, "Discussion of risks in Chinese construction market-contractors perspective," *Journal of Construction Engineering and Management*, vol. 132, no. 3, pp. 327-328, 2006.

[7] O. Moselhi and B. Deb, "Project selection considering risk," *Civil Engineering Practice*, vol. 11, pp. 45–53, 2003.

Hindawi
International Journal of Antennas and Propagation
Volume 2024, Article ID 9853970, 1 page
https://doi.org/10.1155/2024/9853970

Retraction

Retracted: Design of English Mobile Learning Platform Based on GSM-R Wireless Network Communication System

International Journal of Antennas and Propagation

Received 23 January 2024; Accepted 23 January 2024; Published 24 January 2024

This article has been retracted by Hindawi following an investigation undertaken by the publisher [1]. This investigation has uncovered evidence of one or more of the following indicators of systematic manipulation of the publication process:

(1) Discrepancies in scope
(2) Discrepancies in the description of the research reported
(3) Discrepancies between the availability of data and the research described
(4) Inappropriate citations
(5) Incoherent, meaningless and/or irrelevant content included in the article
(6) Manipulated or compromised peer review

The presence of these indicators undermines our confidence in the integrity of the article's content and we cannot, therefore, vouch for its reliability. Please note that this notice is intended solely to alert readers that the content of this article is unreliable. We have not investigated whether authors were aware of or involved in the systematic manipulation of the publication process.

In addition, our investigation has also shown that one or more of the following human-subject reporting requirements has not been met in this article: ethical approval by an Institutional Review Board (IRB) committee or equivalent, patient/participant consent to participate, and/or agreement to publish patient/participant details (where relevant).

Wiley and Hindawi regrets that the usual quality checks did not identify these issues before publication and have since put additional measures in place to safeguard research integrity.

We wish to credit our own Research Integrity and Research Publishing teams and anonymous and named external researchers and research integrity experts for contributing to this investigation.

The corresponding author, as the representative of all authors, has been given the opportunity to register their agreement or disagreement to this retraction. We have kept a record of any response received.

References

[1] X. Liu and H. Liu, "Design of English Mobile Learning Platform Based on GSM-R Wireless Network Communication System," *International Journal of Antennas and Propagation*, vol. 2021, Article ID 9944169, 9 pages, 2021.

Hindawi
International Journal of Antennas and Propagation
Volume 2021, Article ID 9944169, 9 pages
https://doi.org/10.1155/2021/9944169

Research Article

Design of English Mobile Learning Platform Based on GSM-R Wireless Network Communication System

Xiaowei Liu[1] **and Hongjin Liu**[2]

[1]*School of Culture and Tourism, Wuxi Vocational College of Science and Technology, Wuxi 214000, Jiangsu, China*
[2]*Wuxi Hengding Supercomputing Co. Ltd., Wuxi 214000, Jiangsu, China*

Correspondence should be addressed to Xiaowei Liu; 3101015@wxsc.edu.cn

Received 16 August 2021; Revised 14 September 2021; Accepted 20 September 2021; Published 30 September 2021

Academic Editor: Fangqing Wen

Because the traditional English mobile learning platform has low student satisfaction and a long learning time, an English mobile learning platform based on the GSM-R wireless network communication system is designed. A GSM-R wireless network communication system is built through existing facilities, new facilities, and business-side facilities. Platform function modules are designed based on the communication system, including course resource management module, online examination management module, online Q&A management module, platform management module, and user login. Based on this module, the platform software is designed according to the three steps of database design, platform encryption technology, and learning recommendation algorithm to create the English mobile learning platform. The simulation experiment results show that the application of the designed platform can improve student satisfaction and improve student learning efficiency.

1. Introduction

English is one of the most common languages in the world. Learning English well will help us communicate and cooperate with foreigners. Moreover, since China's entry into the WTO, various fields have been continuously in line with the world, and the foreign language ability requirements of talents will become higher and higher in the future. Therefore, it is of great significance to offer college English courses in colleges and universities. However, there are various problems in college English teaching at present, and the overall effect is not satisfactory. To a large extent, the teaching process is still the three centers of "class," "teacher," and "books," basically in "teaching—accept the one-way transmission status." In addition, although college English is taught in small classes, there are still dozens of students in each class, who raise a series of problems. Students with good foundation hope that teachers can add extra learning content in the classroom, and the pace is fast point, and the students with poor foundation hope that the teacher will speak more basic knowledge in the classroom, and the pace will be slower [1]. In addition, the English learning needs of college students are also different (such as some like reading, some like writing, some like listening, and some like speaking), so different college students hope that teachers will explain the knowledge points in class. It can be seen that unified teaching content can no longer meet the different needs of college students, and it is impossible to teach students in accordance with their aptitude. In addition, students hope that they can get guidance and help from teachers in time when they encounter problems in the learning process and also hope that they can contact teachers anytime and anywhere to obtain learning information on weekends and holidays. The problems mentioned above all pose a huge challenge to the traditional teaching mode of college English. The traditional teaching mode has gradually failed to meet the daily teaching requirements. College English needs a new learning method to cultivate students' relearning ability. Students' individual learning needs should be met, information literacy should be improved, teacher-student relationships should be improved, and teaching effects should be optimized [2].

Use the computer and classroom-based English teaching mode to improve the single teaching mode that focuses on teachers' lectures. The new teaching model should be supported by modern information technology, especially network technology, so that the teaching and learning of English can be developed in the direction of individualization and independent learning without being restricted by time and place to a certain extent. As an emerging online learning model, mobile learning is an informal learning. It can be combined with formal learning, that is, classroom teaching, to meet the English learning needs of college students. Therefore, the mobile learning platform of Big English has practical significance [3]. Literature [4] designed an English learning platform based on web technology and mobile terminals. This platform further expanded and improved college English textbooks. Students' learning is no longer restricted by location and time, and students have greater choice. A more superior learning environment has helped students obtain more and more learning opportunities. In terms of media selection, they have met their needs for effectiveness and individualization. The three basic frameworks of the software platform are the user layer, resource layer, and system layer. They explain the platform design process and finally research and learn platform resources in different ways. However, student satisfaction on this platform is low. Literature [5] designed an Android-based mobile learning platform for college English. According to the characteristics of Android applications, platform development principles and platform-related design requirements, starting from the overall platform architecture, login management module, learning module, video module, vocabulary learning module, etc., specific design discussions are carried out, and finally from the mobile learning based on Android University English, the platform's video playback and video learning processes are analyzed. The authors of [6] designed a mobile grammar learning platform based on the Android platform. When designing, based on software engineering theory for demand analysis, it includes grammatical content release, grammatical content management, data analysis, audio and video management, and platform management, which are the five levels of functional modules, to ensure the completeness of the platform functions. Through in-depth research on the Android operating mechanism, the article determines the platform architecture of the Model-ViewerPresenter (MVP), reducing platform coupling by 70% and improving operational stability by 29%. The database design of the platform is based on the SQLite lightweight database embedded in the Android ecosystem, which guarantees the access efficiency of the platform data model under the premise of meeting the storage overhead of the platform. From the perspective of English vocabulary deep learning, the study of [7] investigates the main mobile vocabulary learning in functional architecture and its advantages and disadvantages in promoting English vocabulary and designs and develops a mobile platform-oriented English vocabulary deep learning system. The purpose of the study of [8] is to analyze student supporting and inhibiting factors, the effectiveness of m-learning, and preventing the spread and impact of COVID-19.

However, the English mobile learning on the above two platforms takes a long time, which reduces students' learning efficiency in learning English. Aiming at the problems of the abovementioned platforms, this paper designs an English mobile learning platform based on the GSM-R wireless network communication system, verifies the effectiveness of the platform designed in this paper through simulation experiments, and provides convenient services for students' English learning.

2. GSM-R Wireless Network Communication System

2.1. System Composition. According to requirements, the system includes equipment and network parts, which can be divided into 3 areas: existing facilities, new facilities, and business-side facilities as shown in Figure 1.

Existing facilities include existing base stations, core networks, access routing, and other existing GSM-R infrastructures of the railway GSM-R network. These existing facilities are the foundation for the construction of this system and the origin of all English mobile learning services.

Newly built facilities include newly built facilities are important for providing users with controllable GSM-R network access capabilities. The objectives and main content of this system include modules, security servers, and authentication servers [9].

Business-side facilities: business-side facilities are facilities that use English mobile learning content, including terminals and business servers.

2.2. Way of Communication. As shown in Figure 2, the terminal equipment and the service platform are located on the user side, and the secure channel provides a safe and reliable communication method for the user.

Module: connect and communicate with terminal equipment through pins to provide terminal equipment with GSM-R network access capability. By establishing an encrypted channel based on the national secret algorithm and the security server, safe and reliable transmission of English mobile learning data is ensured [10].

Security service: a secure channel is established between encryption technology and the built-in security client of the module to ensure data security. The proxy gateway provides transparent communication services from the platform to the module for access to the management platform.

Access management platform: through the security service through proxy gateway or transparent transmission, communication with the module is realized. The access management platform provides terminal learning management and control services, student learning behavior analysis, and course business release. It enables communication with the business platform through the SDK or interface released to provide business services [11]. A schematic diagram of communication mode is shown in Figure 2.

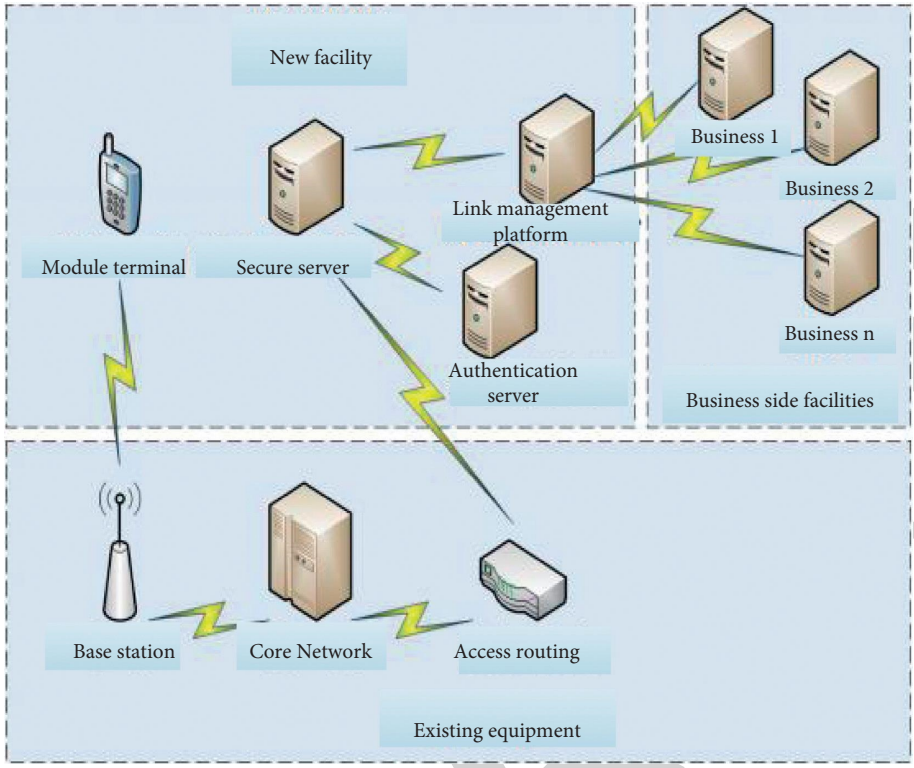

Figure 1: GSM-R wireless network communication system composition.

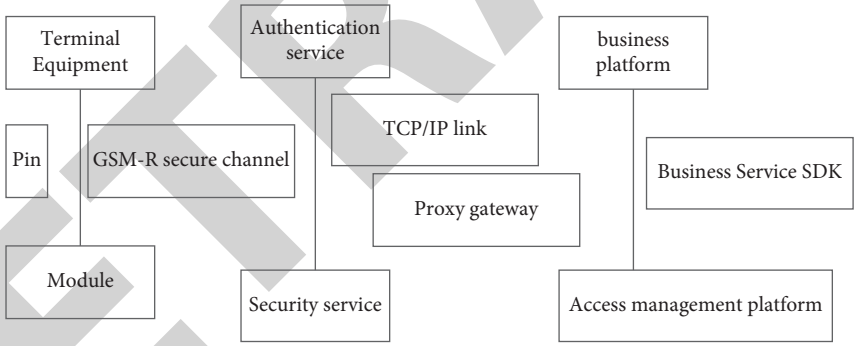

Figure 2: Schematic diagram of the communication mode.

3. English Mobile Learning Platform Design

3.1. Functional Module Design

3.1.1. Course Resource Management Module. The English mobile learning course resource management module is a functional management module, which mainly includes relevant teaching materials and courseware for teachers. Students can view the course resource information uploaded by the teacher through the English mobile learning platform. It has the function of online learning. Figure 3 shows the flow chart of the course resource management module of the mobile learning platform.

3.1.2. Online Exam Management Module. Teachers can use the online test management module in the English mobile learning platform to inspect students' learning conditions and evaluate students' autonomous learning conditions through the online test mode. The test papers used in the online test process are all issued by the teacher. According to the course of study, select the corresponding test paper in the English mobile learning platform. After the paper is handed in within the specified time, the system will score according to the correct answers and display the scoring results on the display interface. The workflow of the online exam management module in the English mobile learning platform is shown in Figure 4.

3.1.3. Online Q&A Management Module. The main function of the online Q&A management module is to provide a communication platform for teachers and students in the English mobile learning platform. In the English mobile learning platform, students can ask the teacher the questions

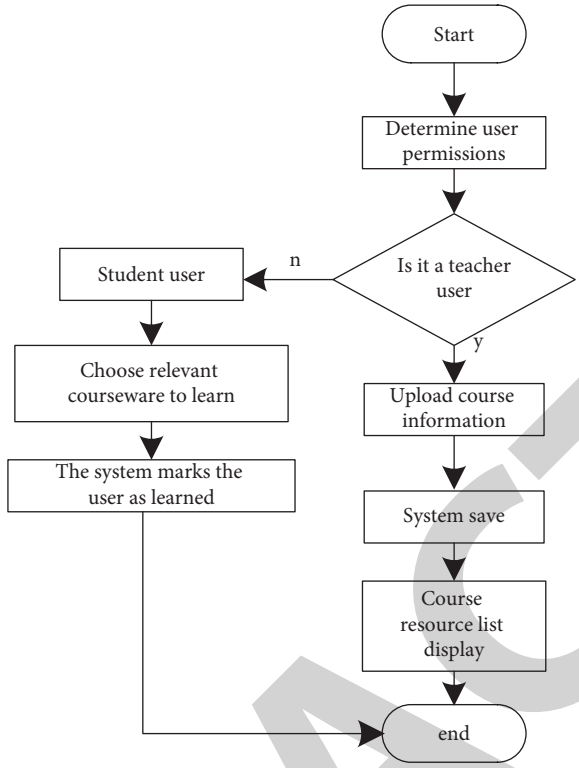

Figure 3: Course resource management process.

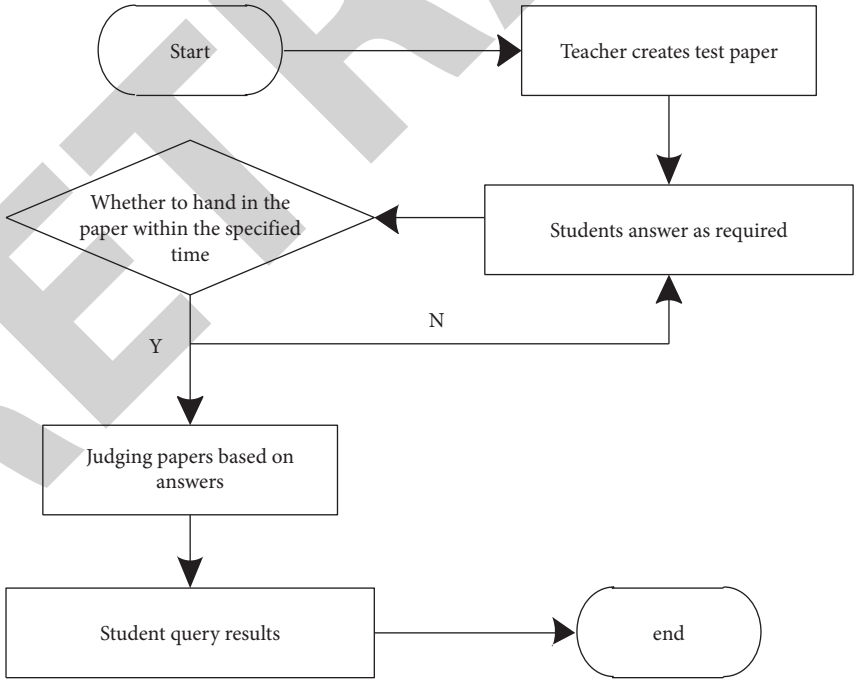

Figure 4: Online test process.

they do not know during the online learning process, and the teacher can use the online Q&A module. For students to answer, the workflow is shown in Figure 5.

3.1.4. Platform Management Module. The platform administrator manages the English remote self-learning system through the platform management module. In the platform

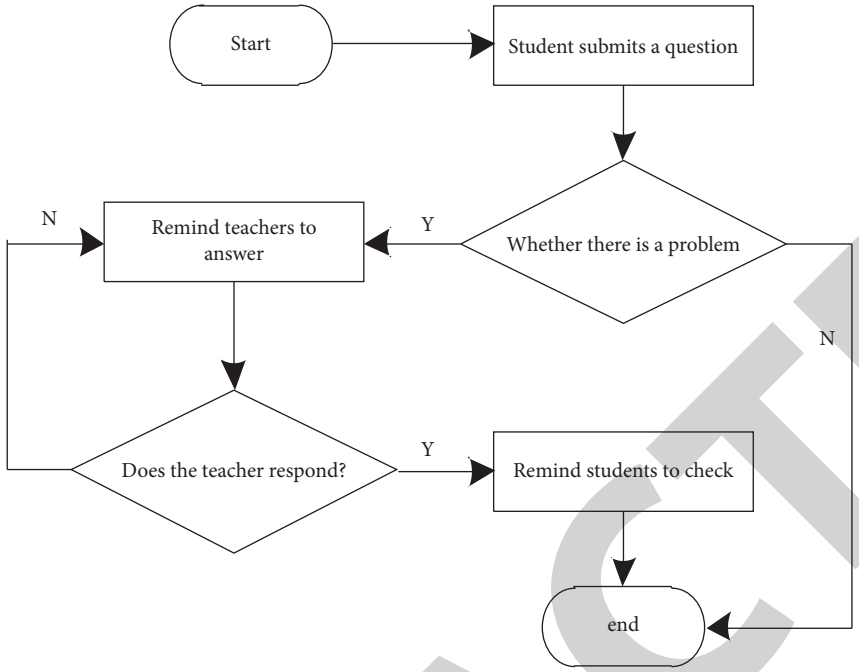

Figure 5: Online Q and A management module.

management module, the administrator first needs to determine the user's corresponding authority. According to the English mobile learning platform's functional module design and demand analysis, log in to the administrator account [12]. The workflow of the platform management module in the English mobile learning platform is shown in Figure 6.

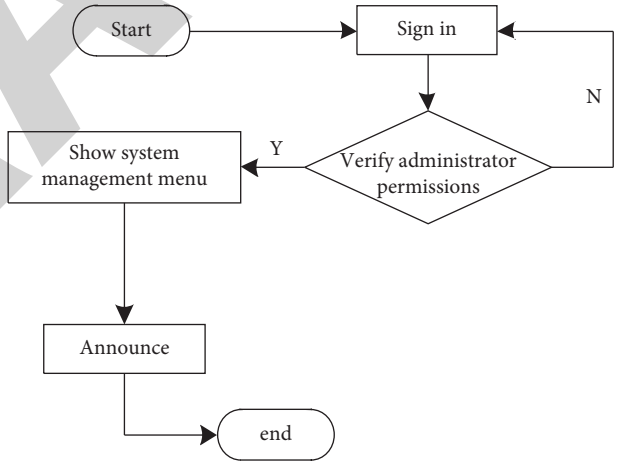

Figure 6: System management process.

3.1.5. User Login Module. The user login system is the prerequisite for realizing various functional operations, so the basis for operating various functional modules is the user login system. Designing the user login module in the English mobile learning platform mainly includes password verification and user account verification. The main target of the English mobile learning platform is students and teachers, but the login process of students and teachers is the same when logging on to the English mobile learning platform [13]. According to the characteristics of ordinary software passwords and account authentication, combined with the actual situation of the English mobile learning platform, the work flow chart is shown in Figure 7.

3.2. Platform Software Design. Through the GSM-R wireless network communication system constructed above, the platform function module is designed according to the course resource management module, online examination management module, online Q&A management module, platform management module, and user login module [14].

3.2.1. Database Design. The user management function is the most basic function of each online English mobile learning platform. Its main purpose is to manage all registered personnel who use this website, confirm user roles, assign corresponding permissions, and effectively manage the entire online English teaching process from all aspects. The registered personnel include administrators, teachers, and students. The administrators can use all the functions of this website. The course administrator assigns the identities of teachers and students. Teachers have the authority to manage course content, monitor student learning, and judge student performance. Students can use any learning resources provided on the website for online learning activities [15]. In the platform of this article, the user data table format in the database is shown in Table 1:

Visitors must register as a user before performing various operations. Each visitor can create his own account in the English mobile learning platform and participate in online English courses. If the registered user does not

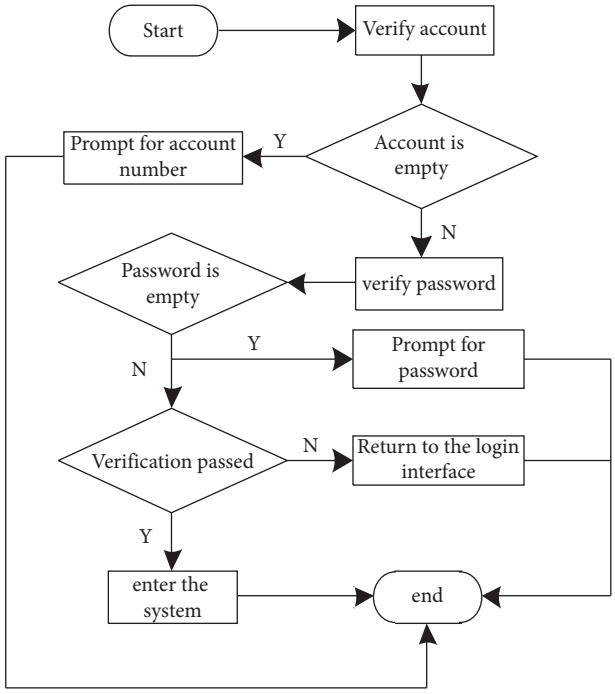

Figure 7: User login module.

Table 1: User data sheet.

Field name	Data type	Is it empty	Length
Number	Int	N	10
User name	Varchar	N	100
Use password	Varchar	N	32
Personal e-mail	Varchar	N	100
Name	Varchar	N	100
Surname	Varchar	N	100
City	Varchar	N	20
Country	Char	N	2
First login time	Int	N	10
Last login time	Int	N	10
Login IP address	Varchar	N	15
Modification time	Int	N	10

participate in activities for a period of time, the administrator will record [16]. This platform supports any electronic documents, PPT, flash animation, and video and sound files, and the platform administrator can upload files and manage files. The list of files uploaded by users and the operation of existing files are realized through directory functions and file system functions.

In addition to viewing and obtaining information related to directories in the resource management module of the database, we can also obtain information about files on the web server and interact with these files [17].

3.2.2. Platform Encryption Technology. In this English mobile learning platform, the encryption technology uses MD5 technology. The full name of MD5 is message-digest algorithm 5 (message-digest algorithm), and its function is to enable large-capacity information to be "compressed" into a confidential format before signing the private key with digital signature software (that is, to put an arbitrary length, the byte string is transformed into a large integer of a certain length). The implementation process of the one-way MD5 encryption algorithm is to add the Security. cs class to the system card project and define the Security. Encrypt() method in the class. When we are registering a user, the Security. Encrypt (passtex. Text) method can be called in the Regist Click event to realize the encryption of the password, and finally, a fixed-length string is stored in the database.

The verification code is generated to prevent attackers from using harmful programs to register many web service accounts in vain and then use these accounts to create trouble for other users, such as sending spam or logging in multiple accounts at the same time slow down the service. The verification code technology is used to prevent users from using robots to register, log in, and fill water in vain. The so-called verification code generates a picture from a string of randomly generated numbers or symbols, adds some interfering pixels to the picture (to prevent OCR), and the user can visually recognize the verification code information, enter the form, and submit it to the website for verification. The verification is successful. Then, you can use a function.

3.2.3. Learning Recommendation Algorithm. Suppose U represents the user set; T represents the user resource tag set; and C represents the user access thing set.

Based on the user resource tag set T, count the number of times $T_{u,k}$ of each tag of user u and the total number of times in the English mobile learning platform. Let $\Phi_u(k)$ represent the feature vector corresponding to the state, and its calculation formula is as follows:

$$\Phi_u(k) = \frac{1 + x_{u,k}}{\sum_{s=1}^{M} 1 + x_{u,k}}. \quad (1)$$

In the formula, M represents the total number of users; $x_{u,k}$ describes the number of times the kth tag corresponding to user u existing in the English mobile learning platform.

Use a user resource tag set T to count the total number of resource tags appearing in the system, according to the statistics of the total number $\sum_{j=1}^{n} N_j$ of the tags appearing on the basis of the user u's visit collection, where N_j describes the total number of tags j appearing in the English mobile learning platform when user u_t is accessed by user u in the English mobile learning platform.

Sort the user u in the user-visited thing set C in the order of time from the nearest to the farthest, obtain the sorting result C_u', set the time attenuation factor λ according to the empirical value, and set the initial function value to zero. The weight of each dimension of the user label vector and the initial user value function is set to zero.

The learning vector of the user u learns according to the sorting result C_u', and the transition set of the resource a is obtained according to the resource a accessed by the user u at each moment $i + 1$. Let $\widehat{V}_{i+1}(s)$ represent the user value function, and its calculation formula is as follows:

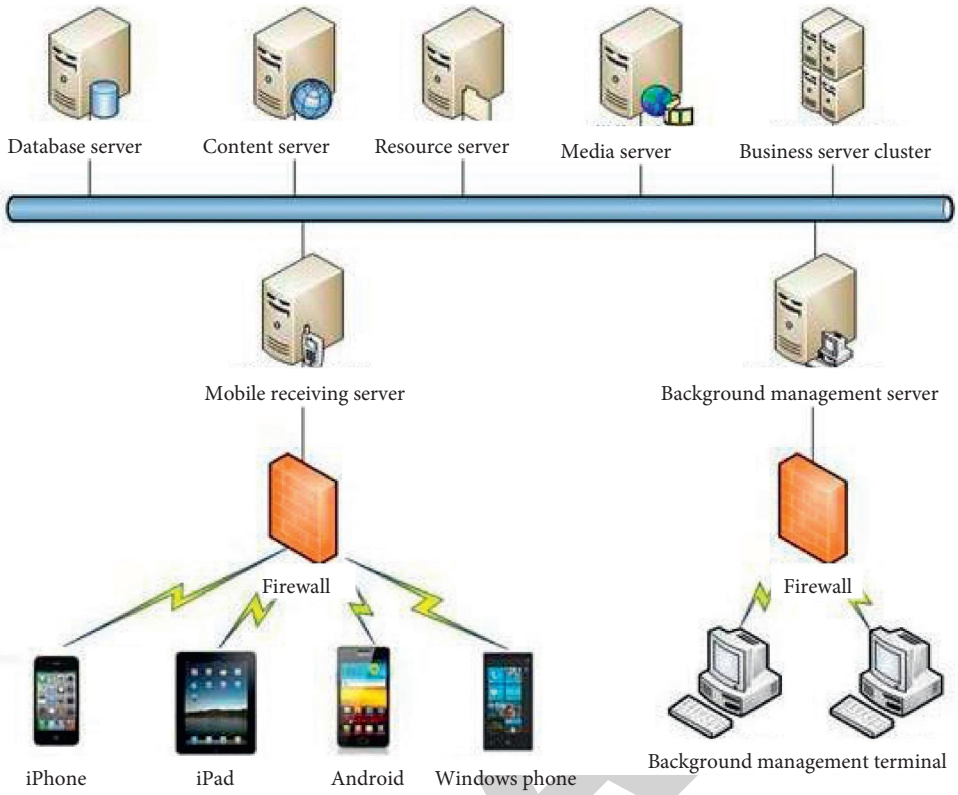

Figure 8: English mobile learning network terminal structure.

$$\hat{V}_{i+1}(s) = W_i \Phi_u. \tag{2}$$

In the formula, W_i describes the corresponding weight of the k-th dimension label after processing the user's step $i+1$ access to the data.

According to the calculation result of formula (2), the weight corresponding to the tag existing in resource a_t is updated by the following formula:

$$W_{i+1,k} = W_{i,k} + \alpha \lambda^{n-i} \frac{N_k}{\sum_{j=1}^{n} N_j} \cdot \left(R_{i+1} + \gamma \hat{V}(s_{i+1}) - \hat{V}(s_i)\right) \nabla \hat{V}(s_i), \tag{3}$$

In the formula, $\hat{V}(s_i)$ describes the actual state value function; α describes the parameters of convergence speed and control stability, that is, the convergence factor; and R_i describes the immediate reward value.

Simplify the resource set. When a resource appears in the historical access records of the user to be predicted, delete the resource, and use the remaining resources to form a candidate resource set.

For any candidate resource, the user scores its level, calculates the current need to predict the similarity between user s and user s_i that has visited, combined with the actual score obtained by user's nearest neighbor user's evaluation of the predicted resource, and scores $\mathrm{per}(s, a)$ for resource a. For prediction, the expression of $\mathrm{per}(s, a)$ is as follows:

$$\mathrm{per}(s, a) = \frac{1}{\sum_{i|a_i=a} \mathrm{sim}(s_i, s)} \sum_{i|a_i=a} \mathrm{sim}(s_i, s) R_i. \tag{4}$$

In the formula, $\mathrm{sim}(s_i, s)$ describes the similarity between user s and user s_i; $\sum_{i|a_i=a} \mathrm{sim}(s_i, s)$ describes the sum of similarity between user s who has visited resource a and the nearest neighbor user.

According to the calculation result of the recommendation score $\mathrm{per}(s, a)$, the resources existing in the candidate set are sorted to realize the recommendation of English mobile learning resources.

4. Simulation Experiment Analysis

In order to verify the performance of the English mobile learning platform based on the GSM-R wireless network communication system designed in this paper in practical applications, a simulation experiment is performed. The structure of the English mobile learning network terminal is shown in Figure 8.

Using the English mobile learning platform based on the GSM-R wireless network communication system designed in this paper, the English learning platform based on web technology and mobile terminal designed by literature [4] and the college English mobile learning platform based on Android designed by literature [5], a comparative analysis of student satisfaction is carried out, and the comparison result is shown in Figure 9.

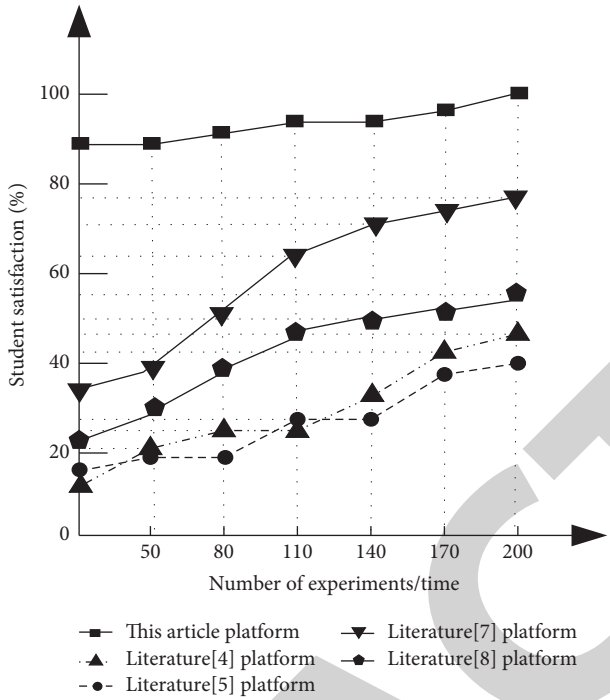

Figure 9: Comparison results of student satisfaction.

Table 2: Comparison results of students' study time.

Experiment times/time	Literature [4] platform	Literature [5] platform	Literature [7] platform	Literature [8] platform	This article platform
10	55.22	45.23	57.63	37.13	30.67
20	56.04	45.42	57.76	37.51	30.23
30	55.87	45.07	57.07	37.07	30.22
40	55.44	45.88	57.11	37.88	30.12
50	55.96	45.09	57.09	37.09	30.42
60	56.23	45.32	57.36	37.31	30.42
70	56.66	45.20	57.60	37.10	30.66
80	56.85	45.62	57.66	37.81	30.78
90	56.22	45.56	57.56	37.58	30.99
100	57.21	45.99	57.99	37.99	30.99

According to Figure 9, the student satisfaction of the English mobile learning platform based on the GSM-R wireless network communication system designed in this paper can reach up to 100%, which is better than the English learning platform and literature based on web technology and mobile terminals designed in the literature [4, 5]. The Android-based mobile learning platform for college English has high student satisfaction.

In order to further verify the effectiveness of the platform in this article, the English mobile learning platform based on the GSM-R wireless network communication system designed in this article, the English learning platform based on Web technology and mobile terminal designed by literature [4] and the English learning platform designed by literature [5], an Android-based mobile learning platform for college English, a comparative analysis of students' learning time, and the comparison results are shown in Table 2.

According to Table 2, the students' learning time of the English mobile learning platform based on the GSM-R wireless network communication system designed in this paper is about 30 min, which is lower than that of the English learning platform based on web technology and mobile terminal designed in document [4] and the College English mobile learning platform based on Android designed in document [5], which shows that the platform designed in this paper can improve students' learning efficiency.

5. Conclusion

Mobile learning is a means of learning in spare time. With the development of China's distance education and the rapid advancement of modern communication technology, mobile learning content and methods are becoming more and more abundant. From the initial way of learning by mailing teaching materials in correspondence teaching to now-

Hindawi
International Journal of Antennas and Propagation
Volume 2024, Article ID 9869817, 1 page
https://doi.org/10.1155/2024/9869817

Retraction

Retracted: Design of Chinese-English Wireless Simultaneous Interpretation System Based on Speech Recognition Technology

International Journal of Antennas and Propagation

Received 23 January 2024; Accepted 23 January 2024; Published 24 January 2024

This article has been retracted by Hindawi following an investigation undertaken by the publisher [1]. This investigation has uncovered evidence of one or more of the following indicators of systematic manipulation of the publication process:

(1) Discrepancies in scope
(2) Discrepancies in the description of the research reported
(3) Discrepancies between the availability of data and the research described
(4) Inappropriate citations
(5) Incoherent, meaningless and/or irrelevant content included in the article
(6) Manipulated or compromised peer review

The presence of these indicators undermines our confidence in the integrity of the article's content and we cannot, therefore, vouch for its reliability. Please note that this notice is intended solely to alert readers that the content of this article is unreliable. We have not investigated whether authors were aware of or involved in the systematic manipulation of the publication process.

In addition, our investigation has also shown that one or more of the following human-subject reporting requirements has not been met in this article: ethical approval by an Institutional Review Board (IRB) committee or equivalent, patient/participant consent to participate, and/or agreement to publish patient/participant details (where relevant).

Wiley and Hindawi regrets that the usual quality checks did not identify these issues before publication and have since put additional measures in place to safeguard research integrity.

We wish to credit our own Research Integrity and Research Publishing teams and anonymous and named external researchers and research integrity experts for contributing to this investigation.

The corresponding author, as the representative of all authors, has been given the opportunity to register their agreement or disagreement to this retraction. We have kept a record of any response received.

References

[1] F. Liu, "Design of Chinese-English Wireless Simultaneous Interpretation System Based on Speech Recognition Technology," *International Journal of Antennas and Propagation*, vol. 2021, Article ID 7346984, 9 pages, 2021.

Hindawi
International Journal of Antennas and Propagation
Volume 2021, Article ID 7346984, 9 pages
https://doi.org/10.1155/2021/7346984

Research Article

Design of Chinese-English Wireless Simultaneous Interpretation System Based on Speech Recognition Technology

Fengzhen Liu

Huanghuai University, Zhumadian 463000, China

Correspondence should be addressed to Fengzhen Liu; 20070479@huanghuai.edu.cn

Received 21 August 2021; Revised 12 September 2021; Accepted 19 September 2021; Published 30 September 2021

Academic Editor: Jin He

A Chinese-English wireless simultaneous interpretation system based on speech recognition technology is suggested to solve the problems of low translation accuracy and a high number of ambiguous terms in current Chinese-English simultaneous interpretation systems. The system's general structure and hardware architecture are summarized. The chairman unit, representative unit, transliteration unit, and auditing unit are the four basic components of the simultaneous interpretation system. The CPU is the nRF24E1 hardware wireless radio frequency transceiver chip, while the chairman machine, representative machine, translator, and auditorium are all created separately. Speech recognition technology is used by the system software to create a speech recognition process that properly produces speech-related semantics. The input text is used as the search criteria, a manual interactive synchronous translation program is created, and the results for the optimum translation impact are trimmed. The experimental findings reveal that this system's sentence translation accuracy rate is 0.9–1.0, and the number of ambiguous terms is minimal, which is an improvement on previous systems' low translation accuracy.

1. Introduction

International conferences are becoming increasingly common as the frequency of international interactions and collaboration grows. Representatives from many nations and areas talk and debate in the languages they are most comfortable with. To speak material, a simultaneous Chinese-English interpretation system is required. At present, the Chinese-English simultaneous interpretation system has become an indispensable facility in an international conference hall. The Chinese-English simultaneous interpretation system is a device that simultaneously translates the speaker's language (original language) by the interpreter (translated language) and transmits it to the audience in conference occasions where different languages are used at the same time [1]. According to the transmission mode, the Chinese-English simultaneous interpretation system may be classified as a wired Chinese-English simultaneous interpretation system or a wireless Chinese-English simultaneous interpretation system. The wireless Chinese-English simultaneous interpretation system can be divided into infrared radiation type, wireless induction type, and frequency modulation transmission type according to the signal transmission mode. Because the FM transmitter has the advantages of strong anti-interference ability, large coverage area, and lower cost, the system adopts the FM transmitter.

According to the target language's transmission mode, the Chinese-English simultaneous interpretation system may be split into a wired Chinese-English simultaneous interpretation system and a wireless Chinese-English simultaneous interpretation system. The wireless communication method can be divided into infrared radiation type, Bluetooth transmission method, and radio frequency transmission method according to the signal transmission method. The mainstream communication method of the current Chinese-English simultaneous interpretation system is infrared radiation instead of radio frequency transmission [2, 3]. The main reason is that the infrared radiation type has better confidentiality performance, while the radio frequency transmission type has poor confidentiality. However, this design adopts the radio frequency transmitting type.

This is because the radio frequency transmitting type has the advantages of strong anti-interference ability, large coverage area, and low cost, and the radio frequency transmitting type used in this design can encrypt the signal and play a good secret.

Simultaneous Chinese-English interpretation is an important component of today's digital conference system. The Chinese-English wireless simultaneous interpretation system is now being researched by relevant academics. Based on the wireless sensor network structure of ZigBee transmission, literature [4] created an audio conference simultaneous interpretation system. Each microphone serves as a node in the wireless sensor network, which is made up of all of the microphones. The sound data collected by the microphones is transmitted to the sink node through ZigBee and then forwarded to the sound reinforcement system by the sink node. This design efficiently addresses the issue of excessive transmission distance and the inability to transmit in some blind regions. Literature [5] investigates intelligent computer-assisted interpretation (CAI) tools that analyze spoken language and detect terms that may not be translated by the interpreter, that is, predict which terms the simultaneous interpreter will not translate, and investigates the method of performing this task using a supervised sequence marker.

We provide a number of task-specific functions that are clearly designed to notify when the interpreter is having trouble translating words.

Speech recognition is a technique that allows machines to recognize and understand speech signals and translate them into equivalent messages or commands. English has long been a vital tool for individuals to communicate with one another in today's economic globalization. However, the level of spoken English among Chinese people is often low due to constraints in learning mode and context. This paper designs and implements a Chinese-English wireless simultaneous interpretation system based on speech recognition technology and completes a set of simultaneous interpretation systems for small, medium, and ad hoc conferences.

2. Chinese-English Wireless Simultaneous Interpretation System Hardware Design

2.1. Hardware Overall Design Framework. The entire Chinese-English wireless simultaneous interpretation system consists of a chairman unit, a representative unit, a transliteration unit, an auditing unit, and others.

The basic structure of auxiliary equipment is shown in Figure 1.

The chairman unit, delegate unit, translator unit, and listener unit's related entities are the chairman unit, delegate unit, translator, and auditor. They use the nRF24E1 chip to carry out wireless speech and control signal transmission. The chairman unit, delegate unit, and translator all have similar basic circuits; however, the auditorium does not include a voice sending module; only a voice receiving module is included.

The basic hardware parts of chairman machine, delegate machine, and translator are as follows:

(1) nRF24E1 transceiver chip and basic peripheral circuit;
(2) Microphone input filter amplifier circuit;
(3) PWM demodulation circuit;
(4) Keyboard and LCD or LED;
(5) Memory EEPROM.

2.2. Wireless Radio Frequency Transceiver Chip nRF24E1. The chairman unit, the delegate unit, and the translator are used for data communication through the nRF24E1 wireless transceiver chip. Their basic circuits are all similar [6], as shown in Figure 2.

The nRF24E1 chip is the core of the wireless data acquisition and transceiver part. Through the embedded 8051 single-chip core, the *A*/*D* conversion module and the wireless transceiver module nRF2401 in the chip are controlled to realize the functions of data acquisition, transmission, and processing. The EEPROM part is the program memory of the nRF24E1 chip, with a capacity of 4 KB, which stores the programs required for system operation. When the module is powered on, first transfer the program in the EEPROM into the RAM of the chip, and then run the program. EEPROM is connected with nRF24E1 chip through SPI (Serial Peripheral Interface). The nRF24E1 chip includes a 9-channel 10-bit ADC module that can convert the analog audio signal sent by the microphone to digital audio. A programmable PWM output is available on the nRF24E1 chip. The PWM can be designed to work in 6, 7, or 8 bits during use. The PWM modulator in the nRF24E1 chip has a maximum carrier frequency of 64 KHz, which makes data reception easier to filter. The system's man-machine interface function is realized by the keyboard and LCD display screen [7]. The instruction system of the nRF24E1 microprocessor is compatible with the industry standard 8051 instruction system, but the instruction execution time of the two is somewhat different. Generally, the execution time of each instruction of nRF24E1 is 4 to 20 clock cycles, while the execution time of each instruction of the industry standard 8051 is 12 to 48 clock cycles. In addition, compared with the industry standard 8051, nRF24E1 adds ADC, SPI, RF receiver 1, RF receiver 2, wake-up timer 5 interrupt sources, and 3 timers the same as 8052. The nRF24E1 contains a UART that is the same as the 8051. In the traditional asynchronous communication mode, Timer 1 and Timer 2 can be used as the baud rate generator of the UART. In order to facilitate data transfer with the external RAM area, the CPU of nRF24E1 also integrates 2 data pointers. The clock of the nRF24E1 microcontroller comes directly from the crystal oscillator [8].

2.3. Chairman Machine Design. The meeting host is usually assigned the chairman unit. The chairman machine is primarily in charge of controlling and managing the entire conference process. The central control unit is integrated into the chairman machine in this system. The central control unit is the system's command and control center, allowing for unified management and control of the entire

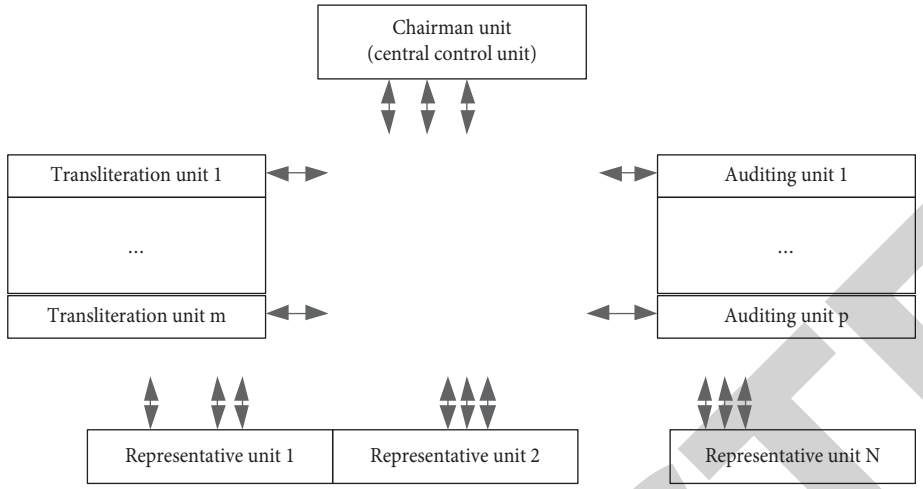

Figure 1: Overall hardware design framework.

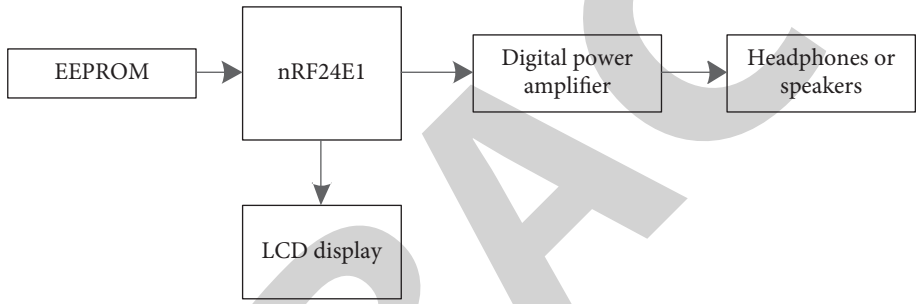

Figure 2: Communication principle of nRF24E1 transceiver chip.

system (including the representative unit, chairman unit, transliteration unit, and audio interface equipment). The following are its primary functions:

(1) The chairman unit has the priority function of full control of the conference order.

(2) Switch the conference mode. The meeting can be conducted under the management and control of the chairman unit; it can also be free to speak without being controlled and managed by the chairman unit. Of course, at the very beginning of the conference, the chairman unit can switch the conference mode.

(3) Allow the application to speak before approving or rejecting the representative's application. After the chairman unit has given the representative unit permission to apply for speech, the representative unit can do so by pressing the key; the chairman unit then approves or refuses these applications in the order listed.

(4) It has buttons for selecting transliteration in multiple languages. By pressing the button, you can change the receiving channel so that you can receive transliteration in multiple languages.

(5) You can adjust the microphone input level and the total volume of the audio (there is a headphone jack), and you can adjust the headphone volume.

(6) A PA power amplifier can be connected to amplify and output the speaker's speech. The speech of the representative unit cannot be directly connected to an external speaker. The voice signal must be sent to the chairman unit first and then amplified by the PA power amplifier. The chairman machine is mainly composed of the main controller, microphone, A/D converter, encoder, modulator, wireless transmitting module, wireless receiving module, demodulator, decoder, D/A converter, speaker, LCD display, light-emitting diode, keyboard, and other components. The structure block diagram of the chairman unit is shown in Figure 3.

Press the button to set the chairman unit to "host speaking" status and display the status on the display when the host speaks. According to the switch, the host chooses whether to broadcast the voice through the speaker or the transmitter, allowing the representative to use it. The host can switch on the authorization to talk by pushing the button when the conference is in the stage of representative speaking. At this time, the representative unit can send a request to the chairman unit, and the number of the representative units is displayed on the display of the chairman unit, and the host decides which representative speaks and sends a confirmation signal to the corresponding representative machine. The representative who receives the confirmation signal can speak on the representative

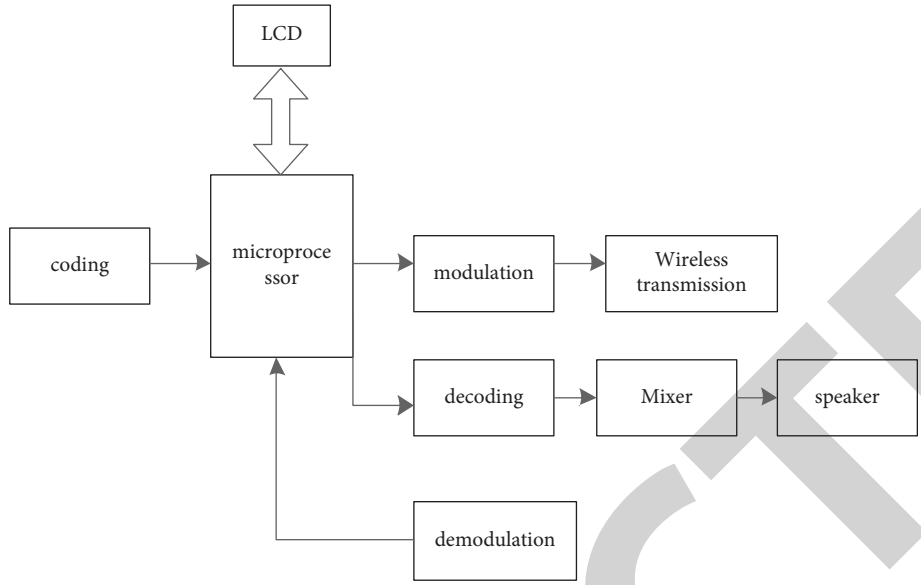

Figure 3: Block diagram of chairman machine structure.

machine; after the representative speaks, the chairman machine can select the next representative to speak.

2.4. Representative Machine Design. The representative machine is a critical component of the overall system. To complete the speech, all delegates participating in the conference can use the delegate's microprocessor to decode and demodulate the wireless reception *A*/*D* code *D*/*A* microphone LCD keyboard modulation wireless transmission mixer speaker LED 30 and can also receive statements from other representatives through the delegate machine. Delegates who want to speak can transmit a request to speak signal by pushing the want to speak button on the delegate machine when the conference enters the delegate speech stage. After receiving the confirmation signal, they will speak through the microphone. After the speech is finished, the chairman machine will reset; at the same time, other representatives can select the original sound of the representative's speech or the transliteration translated by the translator by selecting the channel. Its main functions are as follows:

(1) There is a button for selecting multilingual transliteration. By pressing the button, you can change the receiving channel so that you can receive transliteration in multiple languages.

(2) The microphone input level can be adjusted, with a headphone jack, and the headphone volume can be adjusted.

(3) There is a highly directional microphone with a speaking indicator circle (green). When the green light is on, you can speak; when the speech is over, the green light is off; while waiting to speak, the green light flashes.

The main controller, microphone, *A*/*D* converter, encoder, modulator, wireless transmitting module, wireless receiving module, demodulator, decoder, *D*/*A* converter, earphone, light-emitting diode, keyboard, and other components make up the representative machine. Figure 4 depicts the system block diagram of the typical machine.

2.5. Transliteration Machine Design. The most crucial component of the system is the transliteration machine. The translator is in charge of translating the conference chairperson's or delegates' language into the languages of various countries, as well as sending out the translator's voice. A channel is assigned to each translator (i.e., each language). The translator's settings remain essentially unchanged throughout the conference, although the chairman's speech and each participant's speech are broadcast on their own channels.

Its main functions are as follows:

(1) Indirect and direct translation functions can be performed: direct translation is the direct translation of the speech of the delegate; indirect translation is the second translation of another transliterator's transliteration (an understandable language) when the translator does not understand the language represented by the spoken language.

(2) It has buttons for selecting transliteration in multiple languages. By pressing the button, you can change the receiving channel so that you can receive transliteration in multiple languages.

(3) It has the interlock function of the same channel; that is, the same channel can only have one transliteration transmission. When a translation unit is fixed on a certain channel and the microphone is turned on, other translation units cannot turn on the microphone on the same channel. The number of channels is 4–6.

(4) One translation unit can be used by two translators in turn.

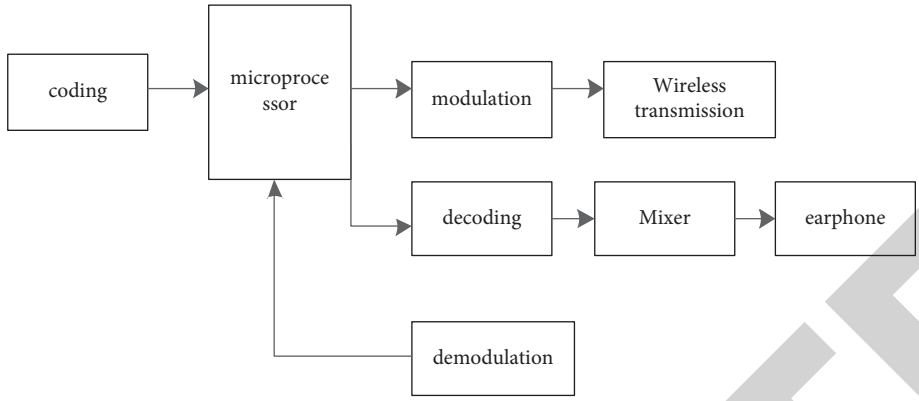

Figure 4: Block diagram of chairman machine structure.

The main controller, microphone, *A*/*D* converter, encoder, modulator, wireless transmitting module, wireless receiving module, demodulator, decoder, *D*/*A* converter, earphone, light-emitting diode, keyboard, and other components make up the translator. Figure 5 depicts the translator's system block diagram.

2.6. Design of Auditor. The listening machine is a wireless receiving device. Compared with the chairman machine, the delegate machine, and the translator, its function is simple. It can only receive voice signals but cannot send voice signals. Its specific functions are as follows:

(1) There is a button for selecting multilingual transliteration. By pressing the button, you can change the receiving channel so that you can receive transliteration in multiple languages.

(2) It has a headphone jack, and the headphone volume can be adjusted.

The auditorium is mainly composed of wireless receiving modules, demodulators, decoders, *D*/*A* converters, earphones, light-emitting diodes, keyboards, and other equipment.

3. Chinese-English Wireless Simultaneous Interpretation System Software Design Based on Speech Recognition Technology

Pattern recognition is a sort of speech recognition technology. The machine translates speech impulses into text by processing and analyzing them, as well as by recognizing and interpreting them. Many fields are involved in speech recognition technology. It can be integrated with other natural language processing technologies such as spoken language recognition, speech synthesis, and machine translation to create more complicated and intelligent applications, in addition to basic applications.

3.1. Wireless way. The Chinese-English wireless simultaneous interpretation method does not require cable transmission for transmission. The receiver only requires one receiver and is free to roam around. However, as compared to a connected connection, the reliability, security, and potential to be intercepted are all inferior. Furthermore, the general receiver is powered by a battery that must be replaced on a regular basis, which is more bothersome. The degree of complexity in achieving two-way transmission varies depending on the medium, although they are all more challenging than wired techniques. Radio waves refer to electromagnetic waves in the radio frequency band which propagate in free space (including air and vacuum). Radio frequency is an abbreviation for high-frequency alternating electromagnetic waves. Generally, alternating current with a change of less than 1000 times per second is called low-frequency current, and one with more than 10000 times is called high-frequency current, and radio frequency is such a high-frequency current. The wireless radio frequency data transmission module uses radio frequency as the transmission medium to achieve noncontact data transmission. It is appropriate for situations when there is a modest amount of data to exchange, the data transmission rate is low, and the power consumption is minimal. In the sphere of wireless communications, radio frequency technology plays a critical and indispensable role.

3.2. Chinese-English Wireless Simultaneous Interpretation Process Design Based on Speech Recognition Technology

3.2.1. Voice Recognition Function Design. The speech (original language) of the delegates in the conference is picked up by the microphone and transmitted to the transliteration unit through wireless frequency modulation and then translated into various prescribed languages by the translator, and then the transliteration is sent to each representative unit through wireless frequency modulation. There is a 9-channel 10-bit ADC embedded in the nRF24E1 chip. Its sampling frequency is 8 kHz, which means sampling once every 125 μm; meanwhile, the output value of PWM is also updated once every 125 μm. Before data communication in nRF24E1 must be synchronized (handshaking). In ShockBurst communication mode, each piece of RF data contains 24 bytes or 3 ms audio sampling signal [9].

The speech recognition process is shown in Figure 6.

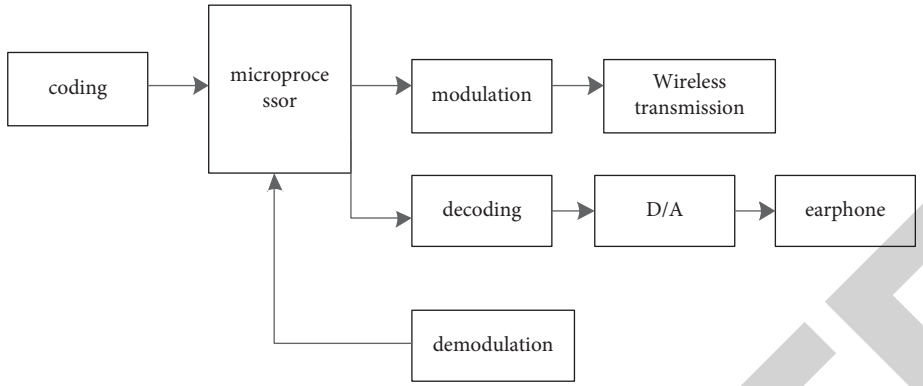

Figure 5: Block diagram of transliteration machine.

The voice recognition system may accomplish speech recognition based on the four following working principles, as shown in Figure 6. First, use antialiasing band-pass filtering technology to efficiently reduce individual voice variances, sampling equipment, and noise in the sample environment; then extract the average energy and vibration peaks of the voice, as well as the average zero crossing. Speech acoustic metrics, such as frequency, can be used to quickly and precisely represent sound quality attributes [10]. Following that, the speech pattern database is created. The main goal of language repetition training is to allow the speaker to repeat the pronunciation while also removing redundant speech data from the original speech samples one by one, keeping only a portion of the key speech data, and scientifically classifying the key speech data according to the relevant scheme. Finally, the relevant semantics of the voice are determined based on voice similarity.

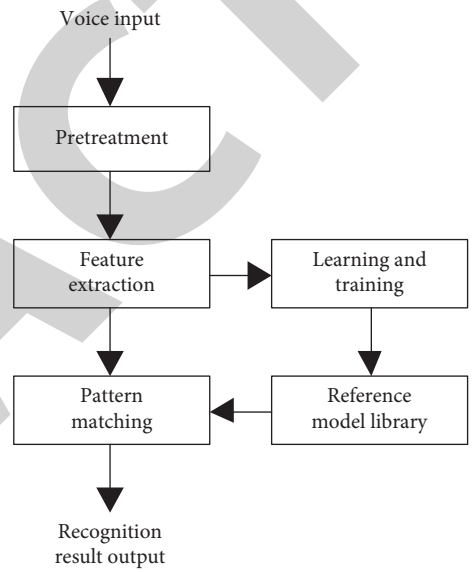

Figure 6: Speech recognition process.

3.2.2. Manual Interactive Simultaneous Translation. The machine translation method of human-computer interaction function includes the following steps:

Step 1: read the machine translation model and select the corresponding domain according to the user of the translation domain.

Step 2: after reading the text, divide the text into a series of sentences to facilitate the processing of subsequent modules.

Step 3: by inputting text as the search condition, after receiving the user input text, search the matching translation on the search network, and different users can get the corresponding different translation results of the input [11].

Since the number of states in the W_n set increases exponentially with the increase of n, it will take a lot of time if the set is not pruned. Therefore, pruning processing is required. The pruning process is as follows:

For the determined source language sentence $R_1, R_2, \ldots, R_n$, there is a phrase model (f, g, s, d), and the four elements in the model, respectively, represent the phrase library, grammar model, distortion limit, and distortion parameter.

Suppose that W_n translates n words into m sets. If one element of m sentences in W_2 consists of 2 words, it means that only two words are translated into sentences. For each state of W_i, there is a transition state, and all possible states will be added to the corresponding set and finally return to the state with the highest score [12].

Let β be the search parameter and let p be the transfer parameter; the resulting grammar model is

$$g = \text{next}(p, d). \tag{1}$$

After the search parameters are determined, all the unsatisfied in the collection are set:

$$a(g) > a(d) - \beta. \tag{2}$$

After removing all the parameters that do not satisfy formula (2), the purpose of pruning is achieved.

Step 4: when translating a source language sentence, read the source language sentence's translation possibilities first, and then expand the translation hypothesis

from a small to a large container. If the difference between a score and the highest score in the container is greater than the threshold at each transition stage, the state will be dropped; if the state remains the same, all available conversion options will be expanded; if the old and new assumptions are the same, the score will be increased. Finding the translated sentence with the highest score in the largest container yields the best translation result [13].

3.3. The Key Technology of System Realization

3.3.1. Switching between Single-Channel Transceiver Mode and Dual-Channel Reception Mode. The communication between the various devices of the simultaneous interpretation system is mainly the voice signal. The original language is sent to the representative unit and transliteration unit through wireless frequency modulation; the transliteration unit translates the received speech signal into the specified language and then sends it to the representative unit and other transliteration units. Therefore, it is the most basic requirement to realize the voice signal communication between various devices. The nRF2401 wireless transceiver module in the nRF24E1 chip allows for transliteration communication between various devices. nRF24E1 is currently in ShockBurst transceiver mode. The nRF2401 wireless transceiver module works in single-channel mode, sending and receiving data across a single channel. While each device maintains voice communication, it also maintains control signal communication on occasion. For example, if the representative unit wishes to apply for speech and the interpreter suggests that the speaker slow down, the button must be pressed to transmit a request signal to the chairman unit; the chairman unit should also give a response signal according to the situation. In this way, there will be situations in which voice signals and control signals are communicated simultaneously between various devices. They occupy one channel, respectively, which requires the nRF24E1 chip to work in ShockBurst dual-channel receiving mode. Through one antenna, nRF24E1 can receive data sent by two 1 Mbps transmitters (such as nRF24E1, nRF2401, or nRF24E2) with a frequency difference of 8 MHz (8 frequency channels). The data of these two different channels are sent to two different sets of interfaces: data channel 1 is CLK1, DATA, and DR1; and data channel 2 is CLK2, DOUT2, and DR2. Therefore, in voice communication, nRF24E1 works in ShockBurst single-channel transceiver mode; when voice signals and control signals are communicating at the same time, nRF24E1 works in ShockBurst dual-channel receiving mode. This requires constant switching between the two modes [14].

3.3.2. Improve Confidentiality. Wireless FM coverage is relatively wide; as long as there is a wireless receiving device, you can receive wireless FM signals [15]. Most of the current wireless simultaneous interpretation system products are based on infrared and seldom use wireless frequency modulation. One of the reasons is that its confidentiality is not good.

Then there is the question of how to increase the simultaneous interpretation system's confidentiality via wireless frequency modulation. This difficulty is effectively solved by the nRF24E1 chip utilized in this system. First and foremost, the nRF24E1 chip operates at a frequency of 2.4–2.5 GHz. General wireless reception equipment (such as a radio) cannot reach this range due to its operating frequency band. Secondly, it is possible to assign an address to each nRF24E1 chip through a program, and only the nRF24E1 chip that has been assigned an address can communicate. What is transmitted between nRF24E1 chips is a 248-bit RF data packet, including 8-bit prefix + 32-bit address + 24 bytes of useful data + 16-bit CRC, and its structure is shown in Figure 5. The address refers to the address of the receiving end nRF24E1. Only the receiving address of the receiving end matches the address in the data packet, and the nRF24E1 chip of the receiving end can receive the data packet; otherwise, it will not be received. In this way, the confidentiality of the system can be improved, and the eavesdropping can be avoided.

4. Experimental Analysis

4.1. Analysis of the Experimental Environment. In the DPDK environment, where the automatic translation system is installed, two hosts supporting IPv4 and two IPv6 are connected to four routers, and then they are connected to a repeater. The resulting system test topology is shown in Figure 7.

Select 123,425 sentences in English from the translation library, of which 1,000 sentences come from translation materials in the news field. Divide the 1000 into 5 data sets, each of which contains 200 English sentences. The methods in literature [4] and literature [5] are used as experimental comparison methods to test the effectiveness of the Chinese-English wireless simultaneous interpretation system.

4.2. Experimental Results and Analysis. After registering and completing the system login, ambiguous words in the data set in the above table are the research objects, indicating that the Chinese-English wireless simultaneous interpretation system can give multiple meanings to ambiguous words, based on the experimental test environment and corpus data set set up above. The number of uncertain words recognized by three automatic Chinese-English wireless simultaneous interpretation systems should be recorded and summarized. Table 1 shows the outcomes of the experiment.

The experimental results in Table 1 reveal that, for the same experimental data set, the three Chinese-English wireless simultaneous interpretation systems have varied levels of ambiguous word recognition. The comparison standard is the number of unclear words displayed during the experimental preparation stage. [4] The system's ability to recognize ambiguous words is the poorest. The average number of ambiguous words identified is 400 to 500, with the lowest number of recognition. Literature [5] has a strong ability to systematically translate uncertain words, with between 500 and 600 recognitions.

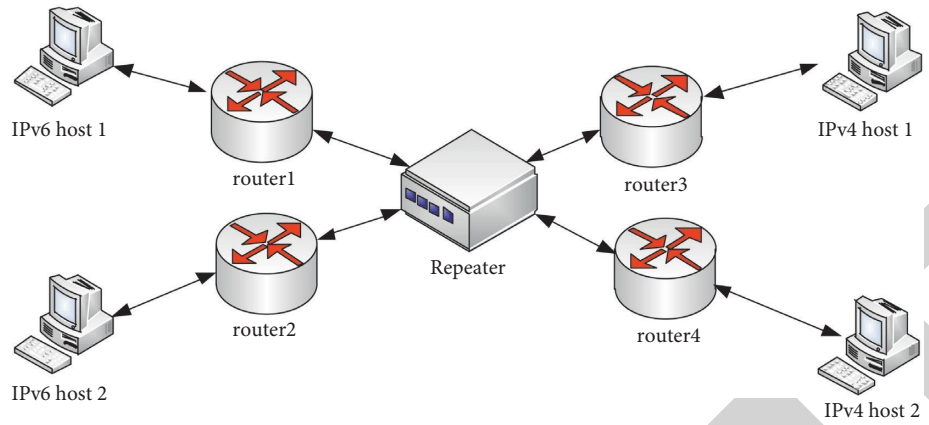

Figure 7: Topology of the test environment.

Table 1: The number of ambiguous words identified by three Chinese-English wireless simultaneous interpretation systems.

Data set name	Recognize the number of ambiguous words/*a*		
	Literature [4] system	Literature [5] system	Design system
Data set 1	441	574	995
Data set 2	424	525	897
Data set 3	457	565	903
Data set 4	452	572	908
Data set 5	463	581	852

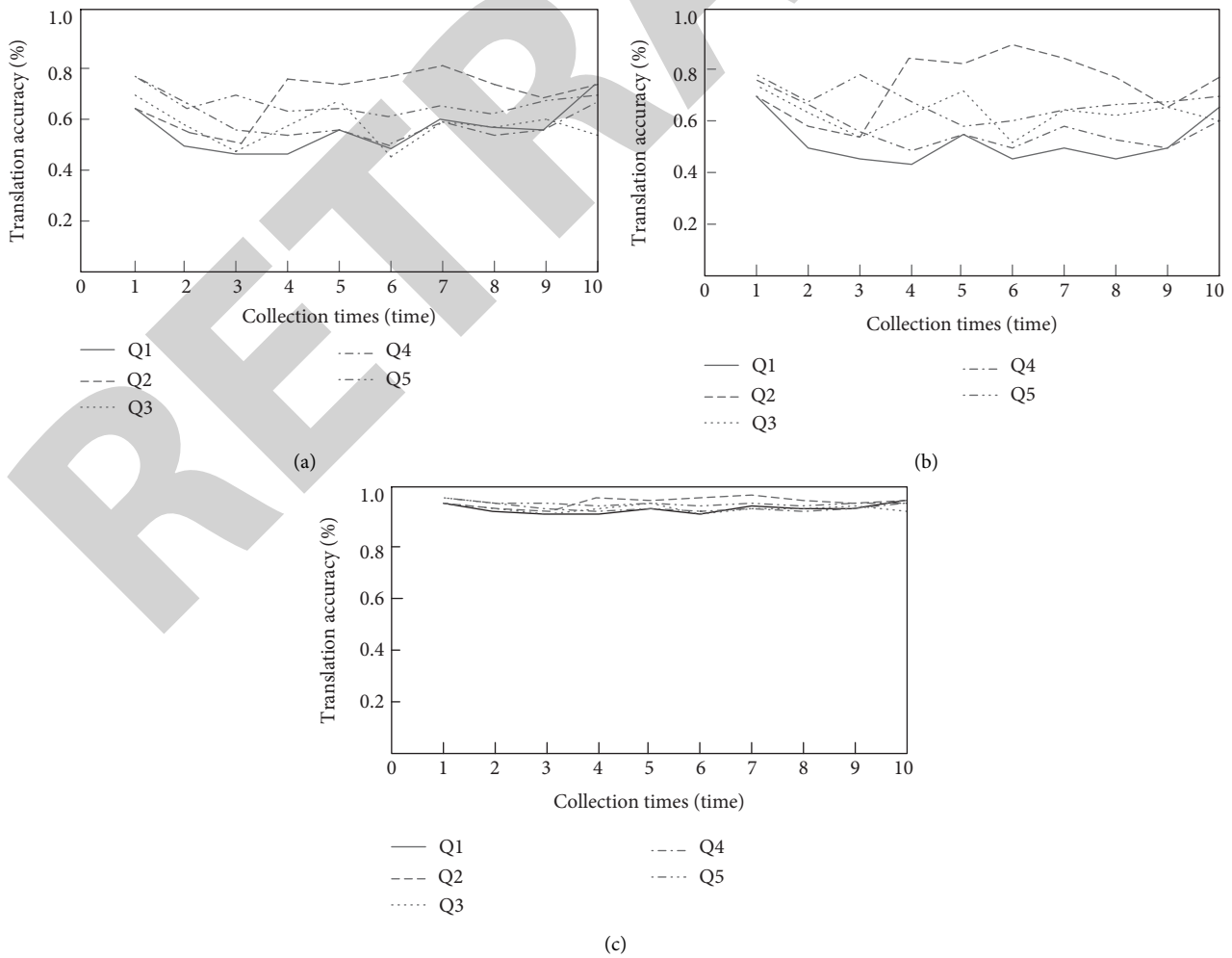

Figure 8: Comparison and analysis of translation accuracy of three Chinese-English wireless simultaneous interpretation systems. (a) Literature [4] system. (b) Literature [5] system. (c) This text's system.

Hindawi
International Journal of Antennas and Propagation
Volume 2023, Article ID 9769872, 1 page
https://doi.org/10.1155/2023/9769872

Retraction

Retracted: Research on Quantization Error Influence of Millimeter-Wave Phased Array Antenna

International Journal of Antennas and Propagation

Received 19 December 2023; Accepted 19 December 2023; Published 20 December 2023

This article has been retracted by Hindawi following an investigation undertaken by the publisher [1]. This investigation has uncovered evidence of one or more of the following indicators of systematic manipulation of the publication process:

(1) Discrepancies in scope

(2) Discrepancies in the description of the research reported

(3) Discrepancies between the availability of data and the research described

(4) Inappropriate citations

(5) Incoherent, meaningless and/or irrelevant content included in the article

(6) Manipulated or compromised peer review

The presence of these indicators undermines our confidence in the integrity of the article's content and we cannot, therefore, vouch for its reliability. Please note that this notice is intended solely to alert readers that the content of this article is unreliable. We have not investigated whether authors were aware of or involved in the systematic manipulation of the publication process.

Wiley and Hindawi regrets that the usual quality checks did not identify these issues before publication and have since put additional measures in place to safeguard research integrity.

We wish to credit our own Research Integrity and Research Publishing teams and anonymous and named external researchers and research integrity experts for contributing to this investigation.

The corresponding author, as the representative of all authors, has been given the opportunity to register their agreement or disagreement to this retraction. We have kept a record of any response received.

References

[1] H. Yang, L. Zhu, Z. Xia et al., "Research on Quantization Error Influence of Millimeter-Wave Phased Array Antenna," *International Journal of Antennas and Propagation*, vol. 2021, Article ID 1874537, 19 pages, 2021.

Hindawi
International Journal of Antennas and Propagation
Volume 2021, Article ID 1874537, 19 pages
https://doi.org/10.1155/2021/1874537

Research Article

Research on Quantization Error Influence of Millimeter-Wave Phased Array Antenna

Haigen Yang,[1] **Linqun Zhu**,[1] **Zhun Xia**,[1] **Yanqing Chen**,[1] **Luohao Dai**,[1] **Ruotian Xu**,[1] **YuanHao Chen**,[1] **Luyang Li**,[1] **GuiYing Sun**,[2] **Hongyang Yu**,[3] **and Wenting Xu**[3]

[1]*Engineering Research Center of Wider and Wireless Communication Technology of Ministry of Education, Nanjing University of Posts and Telecommunications, Nanjing 21003, China*
[2]*Chinese People's Liberation Army, No. 61416, Beijing 100089, China*
[3]*Beijing Electro-Mechanical Engineering Institute, Beijing 100074, China*

Correspondence should be addressed to Haigen Yang; yhg@njupt.edu.cn

Received 24 July 2021; Revised 23 August 2021; Accepted 13 September 2021; Published 25 September 2021

Academic Editor: Fangqing Wen

The millimeter-wave phased array antenna is a higher integration system that is composed of different subarray modules, and in actual engineering, the existing amplitude, phase errors, and structural errors will change the performance of the array antenna. This paper studies the influence of the random amplitude and phase errors of the antenna array in the actual assembly process and the actual position errors between the subarrays on the electrical performance of the antenna. Based on the planar rectangular antenna array-electromagnetic coupling model, we propose a method of verifying the effect of random errors on the phased array antenna. The simulation result shows that the method could obtain the critical value of the error generated by the antenna subarray during processing and assembly. To reduce the error factor, it is necessary to ensure that the random phase and amplitude error should not exceed $(10^{\circ}, 0.5\,\mathrm{dB})$. The error in the X-direction during assembly should be $\leq 0.05\lambda$, and the error in the Y-direction should be $\leq 0.1\lambda$. When symmetrical deformation occurs, the maximum deformation should be less than 0.05λ.

1. Introduction

The antenna is an important part of radar, and the advancement of radar technology is inseparable from reliable and stable radar signals, which will directly affect the detection effect of radar [1]. However, the directivity of a single antenna is limited, to use antennas for electrical scanning in space, several antennas can be arranged together regularly to produce a directional pattern, which is called an antenna array [2]. The millimeter wave has a short wavelength and has the comprehensive advantages of microwave and light waves. The antenna array using millimeter wave has the advantages of extremely wide bandwidth, small size, compact system structure, and electromagnetic energy focusing [3], which is especially suitable for radar and other equipment.

Driven by the rapid development of mobile communication systems, in order to better apply this multi-antenna array element structure to radar equipment, phased array systems and multiple input multiple output (MIMO) systems have emerged. Among them, the phased array system has been widely used on ground radars as early as the 1850s, and the MIMO concept was first introduced into radar technology in 2004, mainly using beam diversity to analyze and study the angle of arrival of the signal. Although the theories are similar, the application scenarios are quite different. MIMO radar is mostly used in civilian applications, such as the Industrial Internet of Things (IoT), due to its high packet loss rate and decreased multiplexing gain in high-speed conditions, and it is used in conjunction with the 5G technology being deployed to meet the needs of industrial communication systems [4]. In order to improve its performance, the model and algorithm need to be continuously improved. The so-called quaternion noncircular MUSIC (QNC-MUSIC) algorithm was proposed to improve the accuracy of DOA estimation in [5]. Shi et al. constructed

a generalized tensor model in [6] and optimized the tensor by maximizing the number of detection targets, and finally derived the Cramér–Rao Bound (CRB) of nested radars, which proves the superiority of the method. A bistatic coprime EMVS-MIMO radar framework was proposed in [7], and the work in [8] proposed a new closed-form estimation algorithm for EMVS-MIMO radar, constructed a new rotation invariant characteristic, and achieved better estimation than existing algorithms.

Compared with MIMO radar, phased array radar has a huge cost, larger volume and weight, a long history of development, and relatively complete technology, and it is mostly used in large-scale shipborne and airborne radars [9]. The antenna element spacing at the transmitting end of a phased array radar is usually on the order of wavelength. In order to prevent grating lobes from appearing, the spacing is usually set to half a wavelength. In MIMO radar, the sensor spacing should not exceed half a wavelength to avoid phase ambiguity [10]. Compared with conventional arrays, active phased array antennas have the advantages of multifunction, high reliability, and high detection and tracking capabilities [11]. Vollbracht determined the optimal phase excitation distribution through the study of the single-feed antenna array, and it was confirmed on the 4×8 antenna subarray [12]. Sharma also proposed a new phased array composed of antijamming antennas [13]. Recently, a highly efficient polarized 8×8 millimeter-wave antenna array in the 60 GHz frequency band was proposed in [14]. Compared with the traditional array, its impedance bandwidth, stable gain, and radiation within the bandwidth are improved. Ortiz et al. used a mathematical model based on diffraction theory to evaluate the influence of mutual coupling between polarized antennas [15].

Conventional phased array antennas have problems such as greater complexity and high cost [16]; we can use digital technologies splice digital array unit formed of different sizes and form fronts to reduce design difficulty [17]. However, in practical engineering, there are extensive excitation errors caused by amplitude and phase changes [18], as well as deformation errors caused by processing and using. Therefore, in order to achieve the expected antenna sidelobe requirements and obtain a stable array design, it is necessary to perform error analysis on the assembled antenna array [19]. Wang analyzed the influence of random feeding errors such as the failure rate of the array element and the feeding amplitude and phase error on the electrical performance of the phased array antenna, which analyzed the bowl surface deformation and bending deformation of both systematic errors impact the electrical properties of a phased array antenna [20]. Chen and Zhou proposed a mathematical model of the thermal deformation error of the active phased array to analyze the influence of such errors on the antenna pattern [21].

The current research on the performance of phased array radar mainly focuses on the influence of various factors on the electrical performance of the antenna when the radar is used, and the errors caused by the production process and assembly accuracy are often ignored. This article is mainly based on the error theory modeling of the millimeter-wave array antenna. The model is composed of two 16×8 rectangular subarrays and works in the 24.25 GHz~27.5 GHz frequency band. Based on the array antenna algorithm of this model, we can introduce random amplitude and phase errors of each channel and structural errors caused by array deformation [22]. Observe its influence on the performance of antenna gain, sidelobe level, beam width, etc. [23–25], realize the rapid analysis of the influence of the two types of errors on the electrical performance of the antenna array, establish the interval model of the relevant input parameters, and give the fluctuation interval of the relevant index, to provide support for the robust design of the millimeter-wave phased array antenna array.

2. Research of Active Phased Array Antennas

As a special type of antenna, the phased array antenna is composed of many identical independent antenna elements to form an antenna array. By controlling the radiation energy and phase relationship between each unit and using different array arrangements for each antenna unit in the array, the excitation feedback relationship affects the radiation field of the entire array, and accurate and predictable radiation patterns and beam directions are obtained, to improve the gain, scanning frequency, and anti-interference of the array [26].

Compared with the traditional passive array, the active array adopts a distributed feedback structure, that is, each unit in the antenna array has a complete transmit/receive (T/R) unit to achieve high-power amplification and high-sensitivity reception [27]. Compared with other arrays, the active phased array has flexibility in beam direction, can form and independently control multiple beams, and search, identify, and track multiple targets. At the same time, because the active phased array antenna adopts millimeter wave with high power, its anti-interference ability is greatly increased [28].

Phased array antennas are usually divided into two types: linear array and area array. The linear array only has one-dimensional scanning capability. If you want to have two-dimensional scanning capability, you need to combine multiple one-dimensional linear arrays to form a planar array antenna.

Figure 1 shows a rectangle of $M \times N$ antenna elements of the grid planar array antenna; the center position of the antenna element is $r_{m,n} = \hat{x}md_x + \hat{y}nd_y$. Assuming that the antenna element patterns are the same, and the analysis method is similar to a linear array, the array factor of the planar array antenna can be obtained as

$$F(\theta, \phi) = \sum_{m,n} |a_{m,n}| \exp\left\{jk\left[md_x(u - u_0) + nd_y(v - v_0)\right]\right\}, \tag{1}$$

where $u = \sin\theta\cos\phi$, $v = \sin\theta\sin\phi$, $u_0 = \sin\theta_0\cos\phi_0$, and $v_0 = \sin\theta_0\sin\phi_0$. The pencil beam is a typical feature of the planar antenna array pattern. When the excitation amplitude of each antenna element is equal, a uniform planar

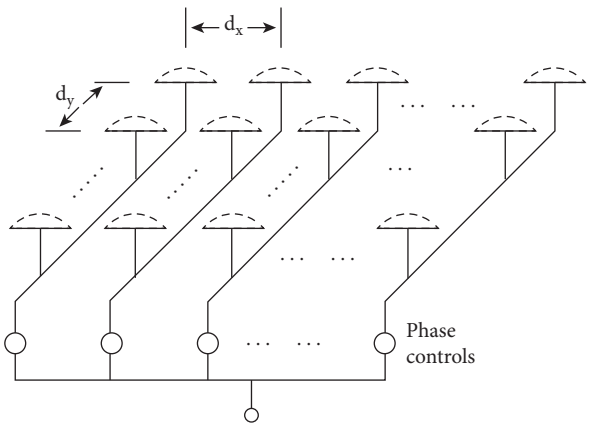

Figure 1: Planar array antenna diagram [29].

array is obtained. Normalize the above formula to get the matrix factor of the uniform plane array:

$$F(\theta,\phi)=\frac{\sin\left[M\pi d_x(u-u_0)/\lambda\right]}{M\,\sin\left[\pi d_x(u-u_0)/\lambda\right]}+\frac{\sin\left[N\pi d_y(v-v_0)/\lambda\right]}{N\,\sin\left[\pi d_y(v-v_0)/\lambda\right]}. \tag{2}$$

3. Error Modeling Theory

In the actual design process, the influence of various errors on the active phased array antenna must be considered. These errors have both random errors and systematic errors, which may be caused by component defects, or they may be caused by the feeder network, or other factors. These errors may cause the antenna gain to decrease, the sidelobe level to increase, the beam width to expand, the radiation efficiency to decrease, and even affect the antenna's beam pointing, which largely determines the performance of active phased array radar [30]. The errors mentioned above are all random errors, which cannot be eliminated due to their contingency and unpredictability, and the performance of all large antenna arrays is affected by random errors such as element position and amplitude and phase changes [31].

3.1. Planar Array Antenna Modeling. In order to facilitate the simulation calculation of the two-dimensional phased array antenna pattern, using the coordinate system is usually chosen to express the direction in the simulation. In order to facilitate multidimensional process analysis and experimental verification, the representation method adopted is as follows: the two-dimensional pattern is represented by the antenna coordinate system, and the three-dimensional pattern is represented by the sinusoidal coordinate system [32].

This article revolves around two-dimensional array pattern modeling. In the antenna coordinate system, the coordinate of R can be characterized by the parameter θ and the parameter ϕ. Among them, θ is the angle from the z-axis to the point $R\,(0^0 \le \theta \le 180^0)$, ϕ, and ϕ is the angle between the x-axis and the projection line of R on the XY-plane. Normalize the amplitude of R, and the coordinate value corresponding to R_0 is $(\sin\theta\cos\phi,\ \sin\theta\sin\phi,\ \cos\theta)$. The antenna coordinate system of the array direction diagram is shown in Figure 2.

The sine space is a hemispherical mapping from a three-dimensional space to a two-dimensional plane, represented by three variables U, V, and W, which can more intuitively characterize the antenna coordinate system. The transformation formula from antenna coordinate system to sine space is as follows:

$$\begin{aligned} U &= \sin\theta\cos\phi,\\ V &= \sin\theta\sin\phi,\\ W &= \cos\theta. \end{aligned} \tag{3}$$

For the visible space of a two-dimensional planar phased array antenna, the value range of U and V is $[-1, 1]$, and the value range of W is $[0, 1]$. For an ideal planar array, there is no z-component in the position function of the array element, so there is no need to consider the influence of W on the array.

Assuming the two-dimensional planar phased array has $M \times N$ radiation channels [33], the rectangular grid arrangement, the channel spacing is d_x and d_y, respectively, the phase center position of the radiation unit is $r_{m,n} = \hat{x}md_x + \hat{y}nd_y$. The array arrangement can be seen in Figure 1.

Then, the array factor pattern of the planar array antenna is

$$AF=\sum_{m,n}^{M,N} A_{mn}\exp\left[jk\left(md_xu+nd_yv\right)\right],\quad k=\frac{2\pi}{\lambda}. \tag{4}$$

Among them, M and N, respectively, represent the number of azimuth and elevation dimensions of the planar phased array antenna, and u and v, respectively, represent the coordinates of the UV-plane in the sine space representation, where the corresponding point of the incident angle is located, $u = \sin\theta\cos\phi$, $v = \sin\theta\sin\phi$. θ and ϕ are two parameters representing the spatial angle in the antenna coordinate system; A_{mn} is the complex excitation signal of radiation channels (m, n):

$$\begin{aligned} A_{mn} &= I_{mn}\exp\left(-jk\left(md_xu_0+nd_yv_0\right)\right),\\ u_0 &= \sin\theta_0\cos\phi_0,\\ v_0 &= \sin\theta_0\sin\phi_0. \end{aligned} \tag{5}$$

I_{mn} is the weighted amplitude of radiation channels (m, n), and (θ_0, φ_0) is the beam direction of the antenna. Then, the pattern of the two-dimensional array antenna can be expressed as

$$AF=\sum_{m,n} I_{mn}\exp\left\{jk\left[md_x(u-u_0)+nd_y(v-v_0)\right]\right\}. \tag{6}$$

According to the principle of pattern product, considering the influence of the element pattern on the array pattern, the expression of the two-dimensional array antenna can be expressed as

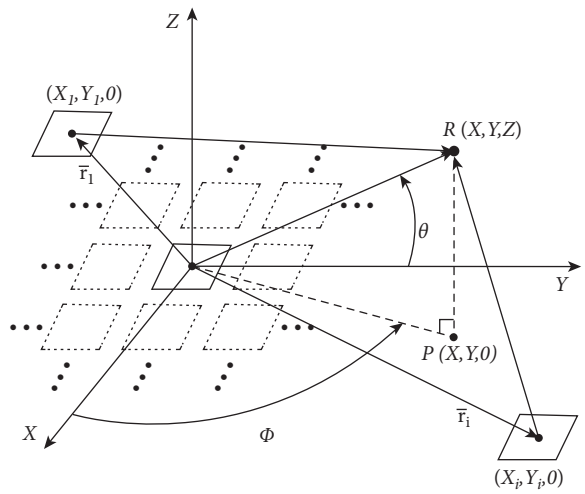

Figure 2: Antenna coordinate system [29].

$$E(\theta,\phi) = EP * AF = f(\theta,\phi) * AF, \tag{7}$$

where $EP = f(\theta,\phi)$ is the pattern of the antenna elements in the array.

3.2. Random Error of Amplitude and Phase. In actual engineering, there will be some errors in the amplitude and phase of the array element. Assume that the amplitude error of array element (m, n) is ΔI_{mn} and the phase error is $\Delta\phi_{mn}$, where $\Delta\phi_{mn}$ is a smaller amount after being converted to the radian system. Then, the array factor of the array antenna becomes

$$AF = \sum_{m,n} I_{mn}(1+\Delta\delta_{mn})\exp\{jk[md_x(u-u_0) + nd_y(v-v_0)]\}\exp(j\Delta\phi_{mn}). \tag{8}$$

According to Taylor's expansion,

$$\exp(j\Delta\phi_{mn}) = 1 + j\Delta\phi_{mn} + (1+j) * o(\Delta\phi_{mn}). \tag{9}$$

After finishing the expression of the antenna array factor, we can get

$$\begin{aligned} AF &= \sum_{m,n} I_{mn}(1+\Delta\delta_{mn})\exp\{jk[md_x(u-u_0) + nd_y(v-v_0)]\} * [1 + j\Delta\phi_{mn}], \\ &= \sum_{m,n} I_{mn}\exp\{jk[md_x(u-u_0) + nd_y(v-v_0)]\} + \sum_{m,n}\Delta\delta_{mn}\exp\{jk[md_x(u-u_0) + nd_y(v-v_0)]\} \\ &\quad + j\Delta\phi_{mn}\sum_{m,n} I_{mn}\exp\{jk[md_x(u-u_0) + nd_y(v-v_0)]\} \\ &\quad + j\Delta\phi_{mn}\sum_{m,n}\Delta\delta_{mn}\exp\{jk[md_x(u-u_0) + nd_y(v-v_0)]\} = AF_0 + \Delta AF_1 + \Delta AF_2 + \Delta AF_3. \end{aligned} \tag{10}$$

Among them, the elements are

$$\begin{aligned} \Delta AF_1 &= \sum_{m,n}\Delta\delta_{mn}AF_0, \\ \Delta AF_2 &= j\Delta\phi_{mn}AF_0, \\ \Delta AF_3 &= j\Delta\phi_{mn}\sum_{m,n}\Delta\delta_{mn}\exp\{jk[md_x(u-u_0) + nd_y(v-v_0)]\}. \end{aligned} \tag{11}$$

Since ΔAF_3 is the product of two minimal errors, it is ignored here. The array factor can be simplified as

$$AF = AF_0 + \Delta AF_1 + \Delta AF_2, \tag{12}$$

where AF_0 is the array factor of the two-dimensional array antenna under the ideal amplitude and phase distribution; ΔAF_1 is the amount of change caused by the amplitude error; and ΔAF_2 is the amount of change caused by the phase error.

$$E(\theta,\phi) = EP * AF = f(\theta,\phi) * AF. \tag{13}$$

The ideal power lobe function is

$$P_0 = E_0(u) * E_0^*(u). \tag{14}$$

Theoretically, the sidelobes of $E_0(u)$ and $P_0(u)$ can be designed to be arbitrarily low, but due to the existence of amplitude and phase errors, the reduction of the sidelobe level is limited. When there is amplitude and phase error between each unit, column and column, the lobe function is

$$E(\theta,\phi) = f(\theta,\phi)\sum_{m,n} I_{mn}(1+\delta_{mn})\exp(j\Delta\varphi_{mn}) * \exp\{jk[md_x(u-u_0) + nd_y(v-v_0)]\}, \tag{15}$$

where δ_{mn} and φ_{mn} are the amplitude and phase distributions of radiating element (m, n) in the antenna array. The amplitude and phase error can be expressed by Gaussian distribution, the mean value is 0, and the variance is δ_{mn}^2,

φ_{mn}^2. According to the central limit theorem, it can be proved that the sidelobe level R after considering the error obeys the Rician distribution; namely,

$$P(R) = \frac{R}{\delta^2} = \exp\left(-\frac{R^2 + S_m}{2\delta^2}\right) * I_0\left(\frac{RS_m}{\delta^2}\right),$$
$$I_0(x) = \frac{1}{2\pi}\int_{-\pi}^{\pi} e^{x\cos\varphi}\mathrm{d}\varphi,$$
$$\delta_E^2 = \frac{\delta_{ae}^2 + \delta_{\varphi e}^2}{MN\eta}, \tag{16}$$
$$\eta = \frac{\left(\sum\sum I_{mn}\right)^2}{MN\sum\sum I_{mn}^2}.$$

I_0 is the zero-order modified Bessel function; S_m is the sidelobe level value under ideal conditions; $\delta^2 = \delta_E^2/2$, δ_E^2 is the variance of the lobe, which represents the degree of agreement between the actual lobe and the theoretical design band; and η characterizes the aperture efficiency of the array weight. Therefore, the probability that the sidelobe is lower than the given value RT is

$$P(R < RT) = \int_0^{RT} P(R)\mathrm{d}R,$$
$$\text{limit sidelobe level} \approx 11\,\text{dB} + 101\,g\left(\frac{\delta_E^2}{2}\right). \tag{17}$$

In practical applications, in order to facilitate the implementation of the project, according to the modular design requirements of the antenna array, the array is usually divided into multiple small subarrays or modules, which are cascaded through the feed network. In the cascading process, random errors are generated in units of subarrays. The following formula is the expression of the antenna pattern when the array is used as a subarray to construct the array. The division of other subarrays is similar:

$$E(\theta,\phi) = f(\theta,\phi)\sum_n (1+\delta_n)\exp\left(j\Delta\varphi_n\right) * \sum_m I_{mn}(1+\delta_{mn})\exp\left(j\Delta\varphi_{mn}\right) \cdot \exp\left\{jk\left[md_x(u-u_0) + nd_y(v-v_0)\right]\right\}, \tag{18}$$

where δ_n and φ_n are the amplitude and phase distribution of the nth column of radiating elements in the antenna array.

3.3. Structural Error. The structural error of the antenna array includes the processing error of the array, the installation error of the radiating element, the antenna frame and the subarray, and the structural deformation error caused by the deformation of the antenna. In the active phased array, processing, assembly, and other links will cause the deformation of the array and generate random errors. In the actual working environment, the factors such as vibration, impact, and high and low temperature will also cause the deformation of the planar array and finally change the position of the element to produce deformation errors, which will reduce the electromagnetic performance of the antenna [34]. As a result, the active phased array has raised sidelobes, decreased gain, and worsened pointing accuracy. Therefore, the study of the relationship between the coupling active phased array structure and electromagnetic analysis antenna electrical properties varies with structural changes in the error active phased bursts of the same size curve surface [35, 36], to obtain the critical value wavefront deformation and random error combined, can provide quantitative theoretical guidance for structural design and reasonable allocation of tolerances.

4. Simulation Analysis of Random Error in Amplitude and Phase

4.1. Random Error Simulation Analysis. The amplitude and phase errors in the simulation analysis process of amplitude and phase random errors are random values. The random error probability distribution obeys the Gaussian distribution, and the error value range is defined by the variance.

In the simulation process, taking a 16 × 16 planar phased array antenna as an example, the element spacing $dx = 0.43\lambda$, $dy = 0.52\lambda$, and the antenna element pattern uses Gaussian beams. In the process of random error analysis, the error source includes quantization error. The minimum quantization step size of the numerically controlled attenuator is 0.5 dB, and the digital phase shifter adopts a 6-phase shifter.

Let us take the random phase and amplitude errors with variances of $(0^\circ, 0\,\text{dB}\backslash 0.3\,\text{dB}\backslash 0.5\,\text{dB}\backslash 1\,\text{dB}\backslash 2\,\text{dB})$ and $(10^\circ, 0\,\text{dB}\backslash 0.3\,\text{dB}\backslash 0.5\,\text{dB}\backslash 1\,\text{dB}\backslash 2\,\text{dB})$ as an example to simulate the array pattern under the influence of random error. The simulation results of random amplitude and phase antenna without scanning and scanning -45° are shown in Figures 3 and 4. In the same way, the simulation result data under the conditions of $(5^\circ, 0\,\text{dB}\backslash 0.3\,\text{dB}\backslash 0.5\,\text{dB}\backslash 1\,\text{dB}\backslash 2\,\text{dB})$ and $(20^\circ, 0\,\text{dB}\backslash 0.3\,\text{dB}\backslash 0.5\,\text{dB}\backslash 1\,\text{dB}\backslash 2\,\text{dB})$ are plotted and analyzed with the above experimental data.

Table 1 shows the statistical results of technical indicators under the abovementioned random error conditions. Random errors have a significant impact on antenna gain, sidelobe level, and beam width and have little impact on beam pointing. As the error value increases, the antenna gain gradually decreases, the sidelobe level gradually increases, and the beam width gradually expands. When the error value is large, the beam direction will also change to a certain extent.

According to the simulation results in Table 1, under the influence of random errors, the gain, sidelobe level, etc., change, which affects the array antenna gain and overall performance. As the random error variance increases, the average sidelobe level and the first sidelobe level of the array pattern also increase. When the amplitude random error variance exceeds 0.5 dB and the

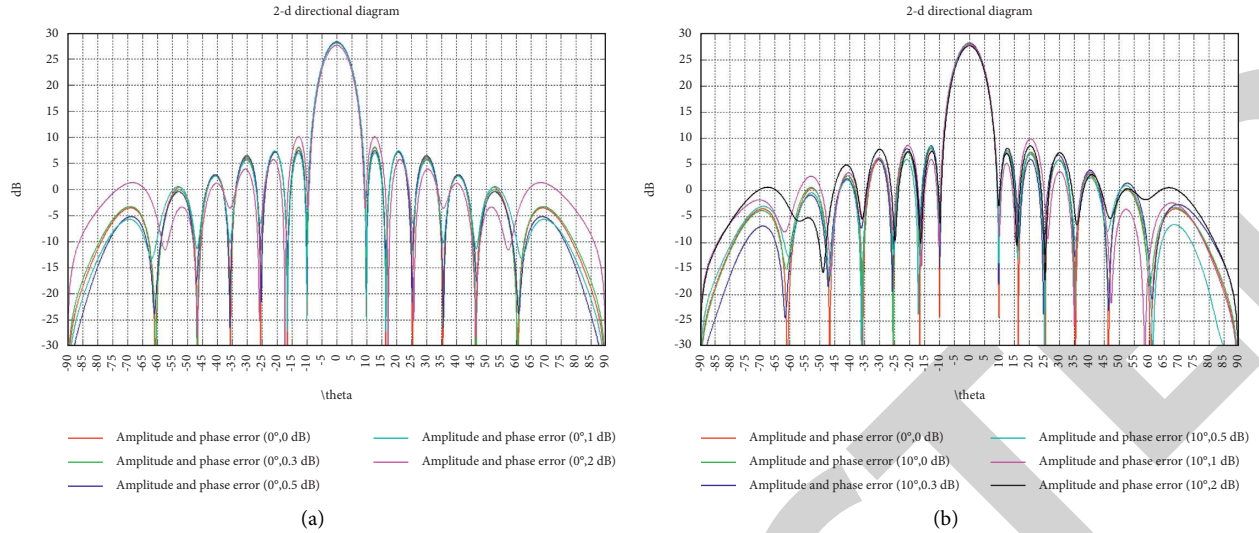

Figure 3: Simulation results of random amplitude and phase antenna without scanning pattern: (a) phase is $^{0^\circ}$; (b) phase is 10°.

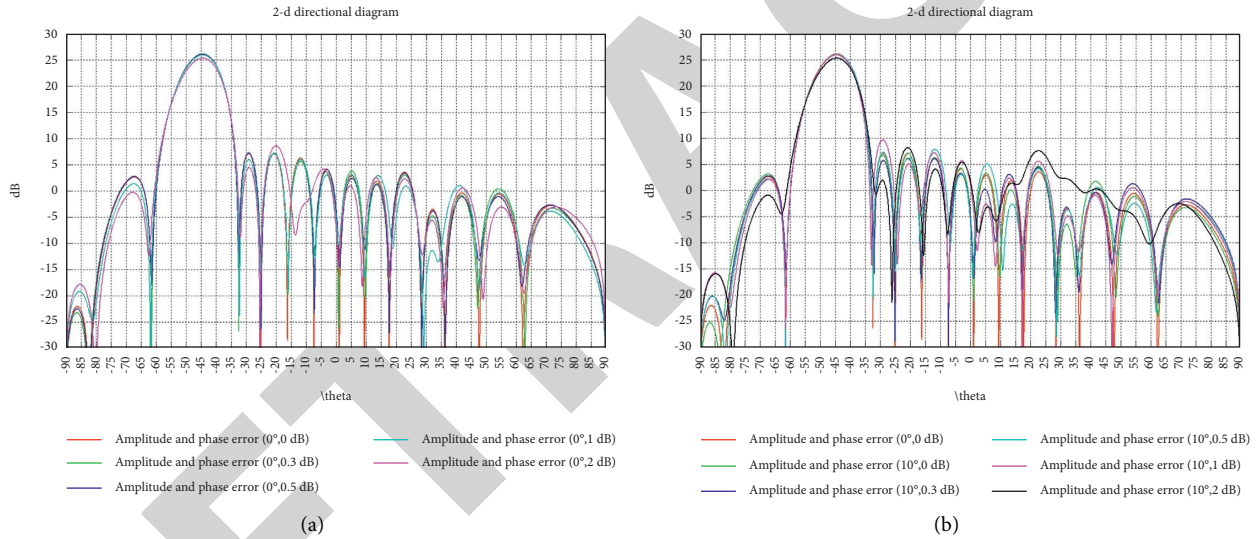

Figure 4: Random amplitude and phase antenna scanning −45° pattern simulation results: (a) phase is $^{0^\circ}$; (b) phase is 10°.

phase random error variance exceeds 10°, not only will the energy of the array pattern become more dispersed, the randomness of the sidelobe positions will increase, and the level of the first sidelobe will increase significantly compared to ideal conditions. In addition, the effect of random error on antenna beam scanning is like that when it is not scanning.

4.2. Verification of Multiple Random Results. The following is to verify the conclusion that the amplitude and phase random error is not greater than (0.5 dB, 10°). The simulation result of the antenna pattern with five random amplitude and phase errors is shown in Figure 5.

Table 2 counts the main technical indicators of antenna azimuth and elevation antennas with 5 different random errors. After comparison, the gain drop is less than or equal to 0.2 dB, the sidelobe level is less than or equal to 1 dB on average, the beam width changes up to 0.2°, and the influence of beam pointing is small.

5. Simulation Analysis of Structural Error

Figure 6 is a schematic diagram of a millimeter-wave antenna array and the center number of the array unit, where the x-axis is the azimuth direction, and the y-axis is the distance direction. The related data of the array is as follows:

(a) Working frequency: 24.25 GHz–27.5 GHz

(b) Model boundary size: 100 mm (azimuth direction) ∗ 112 mm (range direction)

(c) Rectangular array unit arrangement: 16 (azimuth direction) ∗ 16 (azimuth direction)

Table 1: Technical index statistics under the condition of random amplitude and phase error.

Random phase error (variance (°))	Scan angle	Random amplitude error (variance (dB))	Gain	Sidelobe level	3 dB beam width	Beam pointing
0	0	0	28.22	−20.25	8.00	0.00
		0.3	28.24	−19.61	8.00	0.00
		0.5	28.17	−20.77	8.00	0.00
		1	28.05	−20.22	8.00	0.00
		2	27.51	−17.92	8.20	0.00
	−45	0	26.08	−18.95	11.10	−44.40
		0.3	26.02	−18.56	11.20	−44.40
		0.5	25.94	−18.17	11.30	−44.40
		1	25.66	−17.56	11.40	−44.40
		2	25.66	−17.56	11.40	−44.40
5	0	0	28.20	−20.08	8.00	0.00
		0.3	28.18	−20.02	8.00	0.00
		0.5	28.17	−19.82	8.00	0.00
		1	28.02	−18.86	8.20	0.00
		2	27.70	−19.36	8.10	0.00
	−45	0	26.07	−18.55	11.20	−44.40
		0.3	26.04	−19.38	11.30	−44.40
		0.5	26.00	−18.82	11.30	−44.40
		1	25.98	−17.17	11.10	−44.40
		2	25.62	−17.03	11.00	−44.50
10	0	0	28.14	−20.04	8.00	−0.10
		0.3	28.13	−19.61	8.00	0.00
		0.5	28.08	−19.65	8.00	−0.10
		1	27.96	−18.14	8.10	0.00
		2	27.67	−19.18	7.90	0.00
	−45	0	26.00	−18.91	11.20	−44.50
		0.3	25.99	−19.92	11.20	−44.40
		0.5	25.98	−18.12	11.20	−44.40
		1	25.91	−16.27	11.10	−44.50
		2	25.30	−17.16	11.50	−44.40
20	0	0	27.84	−17.83	8.00	0.10
		0.3	27.90	−20.03	8.00	−0.10
		0.5	27.84	−17.77	8.10	0.10
		1	27.76	−16.42	8.00	0.00
		2	27.27	−19.62	8.00	0.10
	−45	0	25.80	−19.07	11.20	−44.50
		0.3	25.81	−18.87	11.20	−44.40
		0.5	25.72	−18.84	11.30	−44.40
		1	25.65	−17.19	11.10	−44.30
		2	25.27	−19.22	11.30	−44.30

(d) Antenna unit center spacing: 5 mm (azimuth direction) ∗ 6 mm (azimuth direction)

(e) Substrate material: Rogers 4350B. The thickness is 2.5 mm.

5.1. Subarray Assembly Error. In the actual antenna design, $16 \times 8 = 128$ units are used as a subarray, and errors in the position of the subarray must be considered during the assembly process.

This paper takes 16×16 planar phased array antenna, that is, two subarrays, as an example. The element spacing is $dx = 0.43\lambda$, $dy = 0.52\lambda$, the antenna element pattern uses Gaussian beam, and the element pattern function is $EP = \cos(\theta)^{EF/2}$. Among them, EF determines the gain of the radiating element. Here, 1.2 is selected, and the gain is about 6.4 dB. The position error of the left and right half arrays is simulated by MATLAB programming simulation, and the influence of the subarray error in the XY-direction on the antenna performance is analyzed.

5.1.1. Subarray Error in the X-Direction. When there is an 0.2λ error in the X-direction of the left and right half of the array, the array element grid is shown in Figure 7. The experiment simulated the changes of the antenna pattern with an error value of 0: 0.05λ: 0.2λ.

Figure 8 shows the projection of the three-dimensional pattern in the UV space when there is a 0.2λ error in the left and right half of the antenna. Figure 9 shows the simulation results of the directional pattern of the antenna azimuth

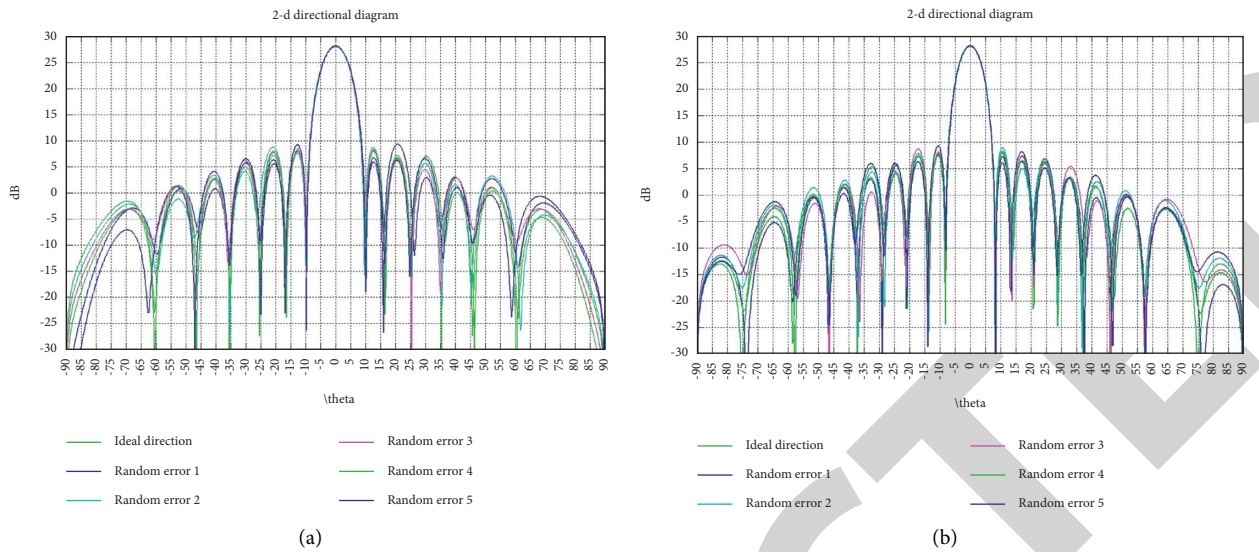

Figure 5: Simulation results of antenna pattern with five random amplitude and phase errors. (a) Azimuth plane. (b) Elevation plane.

Table 2: Five-order random amplitude and phase error antenna technical index statistics.

No.	Directional map section	Random times	Gain	Sidelobe level	3 dB beam width	Beam pointing
1	Azimuth plane	Ideal situation	28.22	−20.34	8.00	0.00
2		1	28.07	−18.76	7.80	0.00
3		2	28.13	−19.40	7.80	0.00
4		3	28.11	−19.84	8.00	0.00
5		4	28.12	−19.73	7.80	0.00
6		5	28.11	−18.89	8.00	0.00
7	Elevation plane	Ideal situation	28.22	−20.29	6.40	0.00
8		1	28.09	−20.56	6.60	0.00
9		2	28.15	−19.25	6.40	0.00
10		3	28.14	−19.44	6.60	0.00
11		4	28.12	−19.97	6.60	0.00
12		5	28.11	−18.88	6.60	0.00

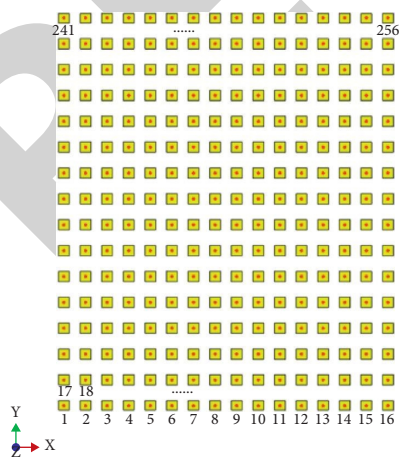

Figure 6: Schematic diagram of a millimeter-wave antenna array.

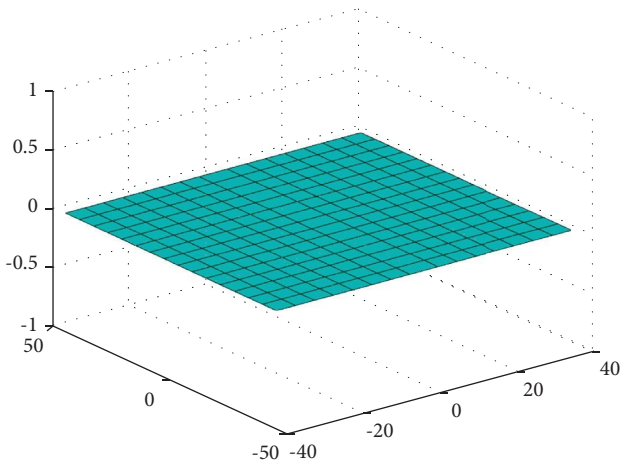

Figure 7: Position error of the left and right half arrays in the X-direction.

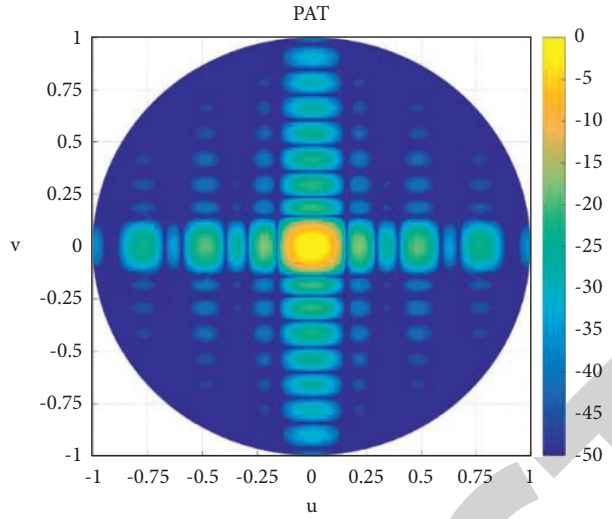

Figure 8: Change of the position error pattern of the left and right half arrays in the X-direction (0.2λ).

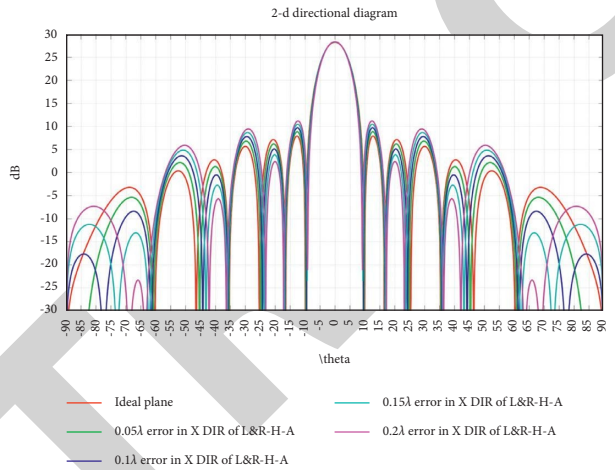

Figure 9: The change of the azimuth pattern caused by the position error of the left and right half arrays in the X-direction.

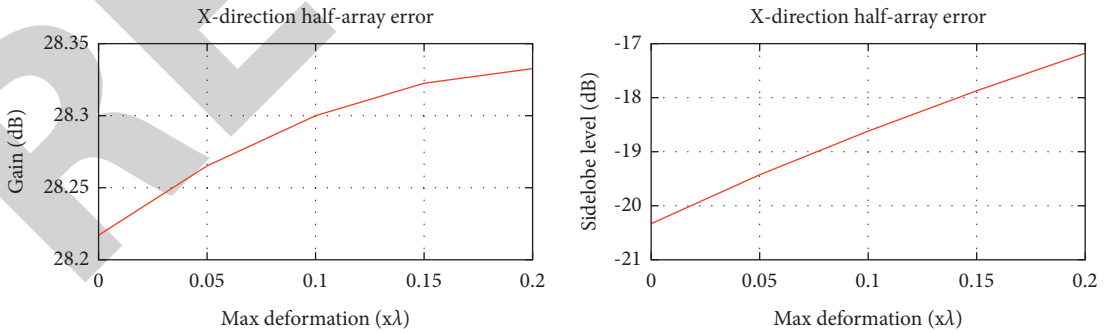

Figure 10: Continued.

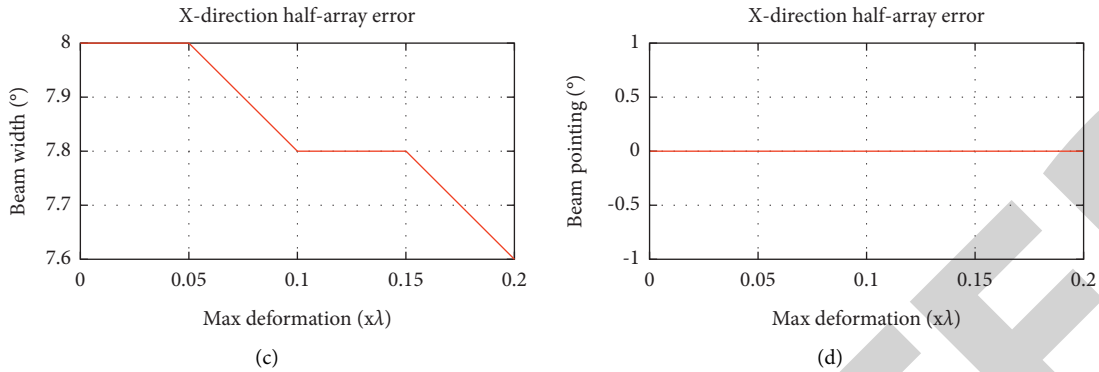

Figure 10: Changes in technical indicators caused by the position error of the left and right half arrays in the X-direction. (a) Gain. (b) Sidelobe level. (c) Beam width. (d) Beam pointing.

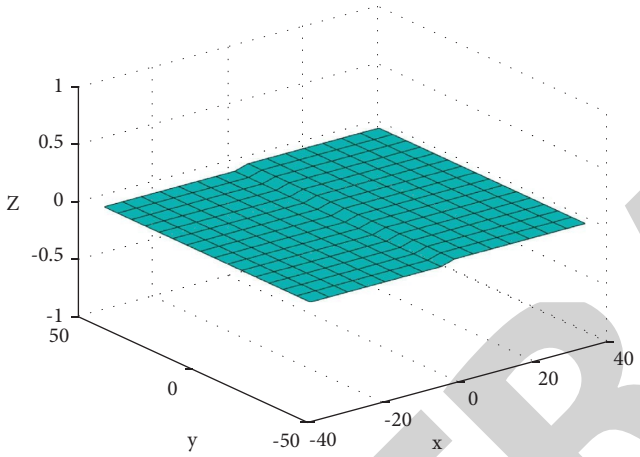

Figure 11: Position error of the left and right half arrays in the Y-direction.

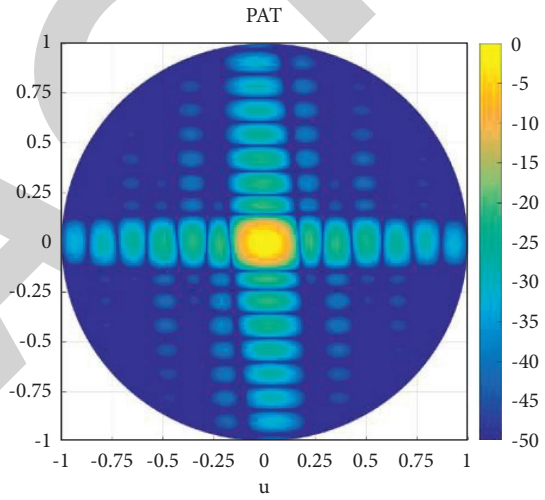

Figure 12: Change of the position error pattern of the left and right half arrays in the Y-direction (0.2λ).

plane when the left and right half arrays have different errors in the X-direction. The elevation plane has almost no effect. Figure 10 shows the changes in the technical indicators of the antenna azimuth plane when the left and right half arrays have different errors in the X-direction.

5.1.2. Subarray Error in the Y-Direction. When there is a 0.2λ error in the Y-direction of the left and right half of the array, the array element grid is shown in Figure 11. The experiment simulated the changes of the antenna pattern with an error value of 0: 0.05λ: 0.2λ.

Figure 12 shows the projection of the three-dimensional pattern in the UV space when there is a 0.2λ error in the left and right half of the antenna. Figure 13 shows the simulation results of the antenna elevation plane pattern when the left and right half arrays have different errors in the Y-direction. The azimuth plane has little influence. Figure 14 shows the changes in the technical indicators of the antenna azimuth plane when the left and right half arrays have different errors in the Y-direction.

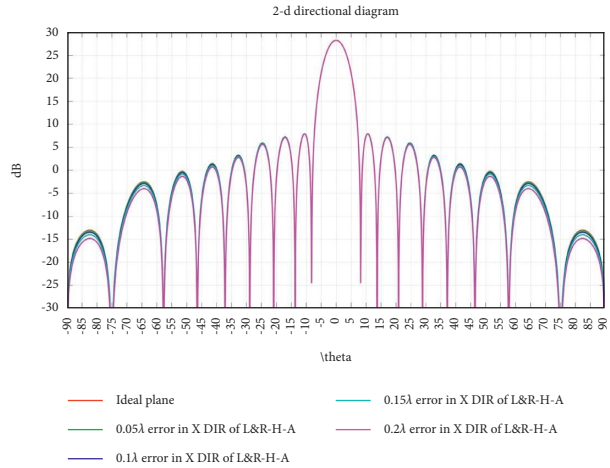

Figure 13: Change of the azimuth pattern caused by the position error of the left and right half arrays in the Y-direction.

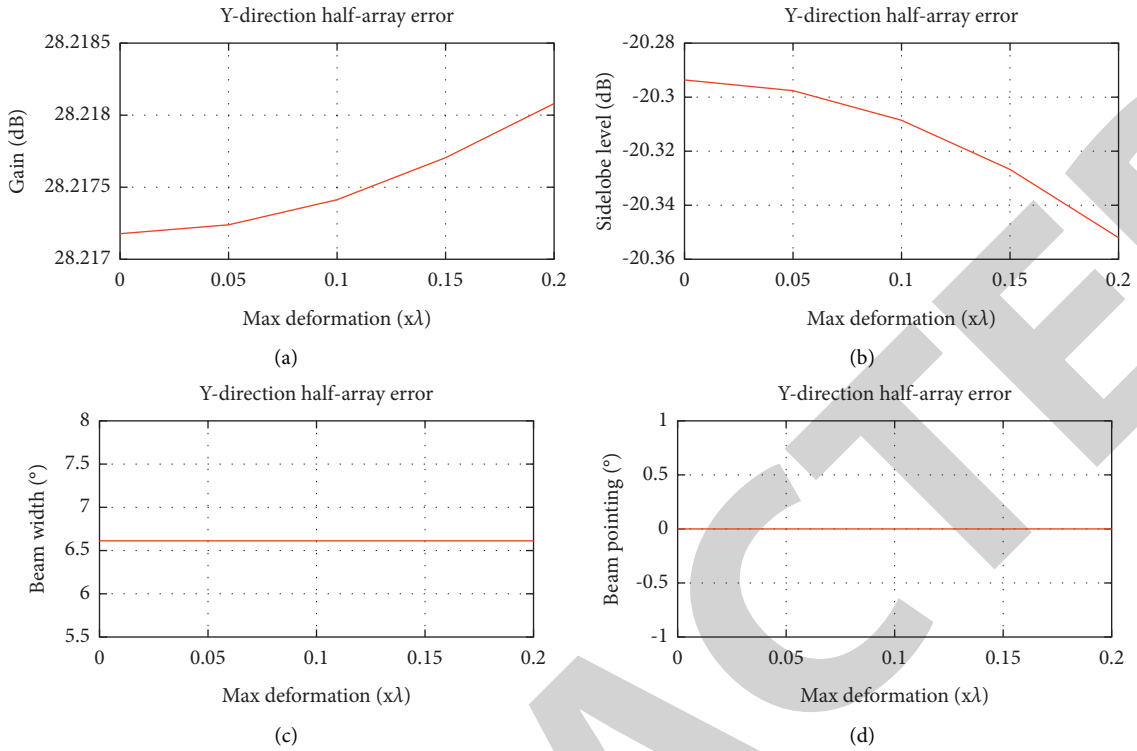

Figure 14: Changes in technical indicators caused by the position error of the left and right half arrays in the *Y*-direction. (a) Gain. (b) Sidelobe level. (c) Beam width. (d) Beam pointing.

5.1.3. Subarray Error in XY-Direction. Figure 15 shows the projection of the three-dimensional pattern in the *UV* space when there is a 0.1λ error in the left and right half of the antenna.

Table 3 shows the statistics of technical indicators such as antenna gain and sidelobe level when the *XY*-directions change at the same time.

From the above simulation results, it can be concluded that the gaps produced by the left and right half arrays in the *X*-direction will affect the distribution of antenna radiation power in space, and the impact on the sidelobe level is more obvious. As the gap increases, the electrical aperture of the planar array becomes larger, the gain becomes larger, the beam width becomes narrower, and the beam direction does not change. The gaps produced by the left and right half arrays in the *Y* direction will affect the distribution of antenna radiation power in space, causing tilt rotation, which has a significant impact on the far-area sidelobe level. As the gap increases, the electrical aperture of the planar array becomes larger, the gain becomes larger, the beam width becomes narrower, and the beam direction does not change. When the *XY*-direction changes at the same time, it is a combination of the above two situations.

In practical applications, according to the principle that the sidelobe level deterioration is not greater than 1 dB, the error in the *X*-direction should be $\leq 0.05\lambda$, and the error in the *Y*-direction should be $\leq 0.1\lambda$.

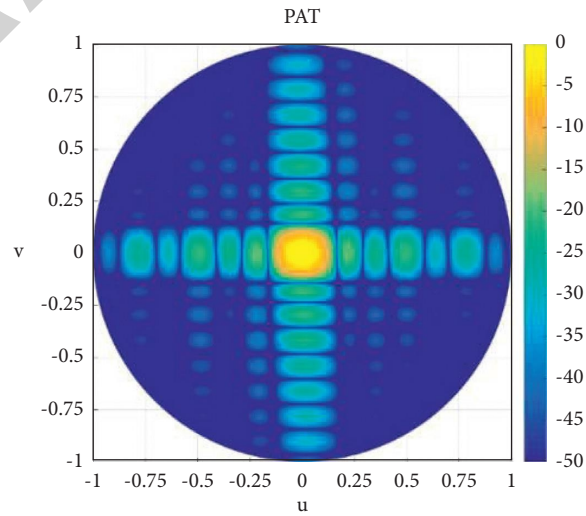

Figure 15: Position error pattern changes of the left and right half arrays in the *XY*-direction (0.1λ).

5.2. Subarray Deformation Error. Assuming that a vibration load is applied during the operation of the radar, under the constraints of the four corners, the antenna array will undergo symmetrical and asymmetrical deformation. For the planar rectangular active phased array antenna, the deformation of its subarray is usually saddle-shaped deformation.

Table 3: *XY*-direction changes at the same time technical indicator statistics.

No.	Directional map section	*X*-axis	*Y*-axis	Gain	Sidelobe level	3 dB beamwidth	Beam pointing
1			0	28.22	−20.33	8	0
2		0	0.05	28.22	−20.33	8	0
3			0.1	28.22	−20.33	8	0
4			0	28.26	−19.43	8	0
5	Azimuth plane	0.05	0.05	28.26	−19.43	8	0
6			0.1	28.26	−19.43	8	0
7			0	28.30	−18.62	7.8	0
8		0.1	0.05	28.30	−18.62	7.8	0
9			0.1	28.30	−18.62	7.8	0
10			0	28.22	−20.29	6.6	0
11		0	0.05	28.22	−20.30	6.6	0
12			0.1	28.22	−20.31	6.6	0
13			0	28.26	−20.29	6.6	0
14	Elevation plane	0.05	0.05	28.26	−20.30	6.6	0
15			0.1	28.26	−20.31	6.6	0
16			0	28.30	−20.29	6.6	0
17		0.1	0.05	28.30	−20.30	6.6	0
18			0.1	28.30	−20.31	6.6	0

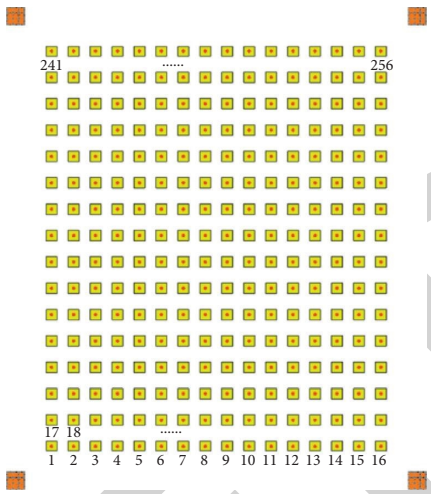

Figure 16: Matrix constraint condition.

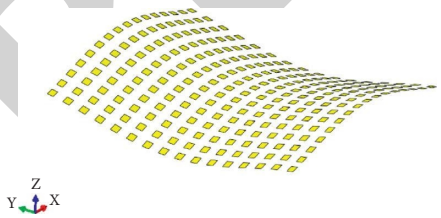

Figure 17: Saddle deformation.

The constraints are shown in Figure 16. A typical saddle-shaped deformation is listed below, the effect of antenna deformation on the antenna pattern is simulated and analyzed, and the main technical indicators of the antenna are counted.

Table 4: Normalized deformation data at the center of the antenna element.

Unit no.	Normalized data
1	0.0559
2	0.21
3	0.384
4	0.56
5	0.722
6	0.855
7	0.951
8	1
9	1
10	0.951
11	0.855
12	0.722
13	0.56
14	0.384
15	0.21
16	0.0559
17	−0.065
18	0.0901
19	0.257
20	0.423
21	0.575
22	0.701
23	0.791
24	0.837
25	0.837
26	0.791
27	0.701
28	0.575
29	0.423
30	0.257
31	0.0901
32	−0.065
33	−0.217
34	−0.0543
35	0.113
36	0.275
37	0.422

Table 4: Continued.

Unit no.	Normalized data
38	0.543
39	0.629
40	0.673
41	0.673
42	0.629
43	0.543
44	0.422
45	0.275
46	0.113
47	−0.0543
48	−0.217
49	−0.381
50	−0.209
51	−0.0381
52	0.124
53	0.269
54	0.388
55	0.472
56	0.515
57	0.515
58	0.472
59	0.388
60	0.269
61	0.124
62	−0.0381
63	−0.209
64	−0.381
65	−0.538
66	−0.358
67	−0.182
68	−0.0176
69	0.128
70	0.245
71	0.328
72	0.371
73	0.371
74	0.328
75	0.245
76	0.128
77	−0.0176
78	−0.182
79	−0.358
80	−0.538
81	−0.672
82	−0.485
83	−0.305
84	−0.138
85	0.0083
86	0.126
87	0.209
88	0.251
89	0.251
90	0.209
91	0.126
92	0.0083
93	−0.138
94	−0.305
95	−0.485
96	−0.672
97	−0.769

Table 4: Continued.

Unit no.	Normalized data
98	−0.578
99	−0.395
100	−0.225
101	−0.0781
102	0.0402
103	0.123
104	0.166
105	0.166
106	0.123
107	0.0402
108	−0.0781
109	−0.225
110	−0.395
111	−0.578
112	−0.769
113	−0.821
114	−0.627
115	−0.442
116	−0.271
117	−0.123
118	−0.0048
119	0.0781
120	0.121
121	0.121
122	0.0781
123	−0.0048
124	−0.123
125	−0.271
126	−0.442
127	−0.627
128	−0.821
129	−0.821
130	−0.627
131	−0.442
132	−0.271
133	−0.123
134	−0.0048
135	0.0781
136	0.121
137	0.121
138	0.0781
139	−0.0048
140	−0.123
141	−0.271
142	−0.442
143	−0.627
144	−0.821
145	−0.769
146	−0.578
147	−0.395
148	−0.225
149	−0.0781
150	0.0402
151	0.123
152	0.166
153	0.166
154	0.123
155	0.0402
156	−0.0781
157	−0.225

Table 4: Continued.

Unit no.	Normalized data
158	−0.395
159	−0.578
160	−0.769
161	−0.672
162	−0.485
163	−0.305
164	−0.138
165	0.0083
166	0.126
167	0.209
168	0.251
169	0.251
170	0.209
171	0.126
172	0.0083
173	−0.138
174	−0.305
175	−0.485
176	−0.672
177	−0.538
178	−0.358
179	−0.182
180	−0.0176
181	0.128
182	0.245
183	0.328
184	0.371
185	0.371
186	0.328
187	0.245
188	0.128
189	−0.0176
190	−0.182
191	−0.358
192	−0.538
193	−0.381
194	−0.209
195	−0.0381
196	0.124
197	0.269
198	0.388
199	0.472
200	0.515
201	0.515
202	0.472
203	0.388
204	0.269
205	0.124
206	−0.0381
207	−0.209
208	−0.381
209	−0.217
210	−0.0543
211	0.113
212	0.275
213	0.422
214	0.543
215	0.629
216	0.673
217	0.673

Table 4: Continued.

Unit no.	Normalized data
218	0.629
219	0.543
220	0.422
221	0.275
222	0.113
223	−0.0543
224	−0.217
225	−0.065
226	0.0901
227	0.257
228	0.423
229	0.575
230	0.701
231	0.791
232	0.837
233	0.837
234	0.791
235	0.701
236	0.575
237	0.423
238	0.257
239	0.0901
240	−0.065
241	0.0559
242	0.21
243	0.384
244	0.56
245	0.722
246	0.855
247	0.951
248	1
249	1
250	0.951
251	0.855
252	0.722
253	0.56
254	0.384
255	0.21
256	0.0559

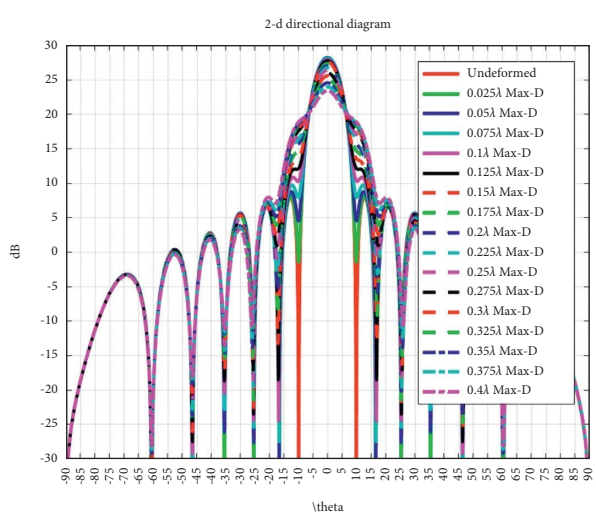

Figure 18: Azimuth plane of saddle-shaped deformation.

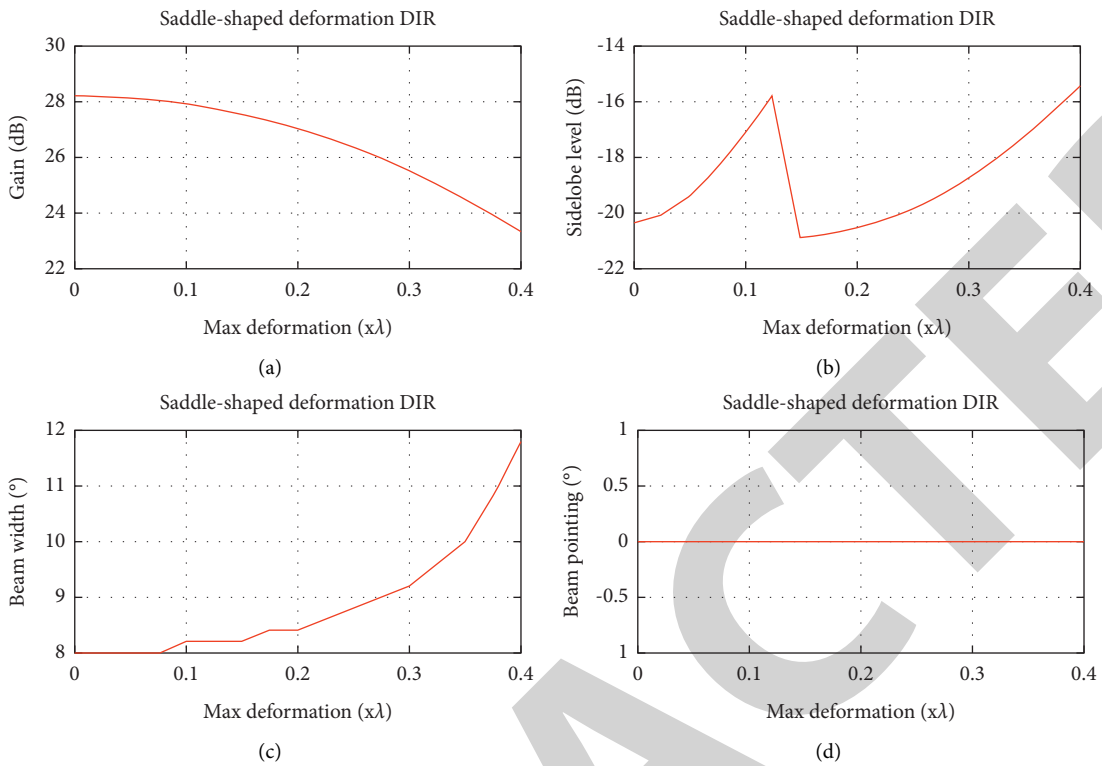

Figure 19: Changes in technical indicators of azimuth plane caused by saddle-shaped deformation. (a) Gain. (b) Sidelobe level. (c) Beam width. (d) Beam pointing.

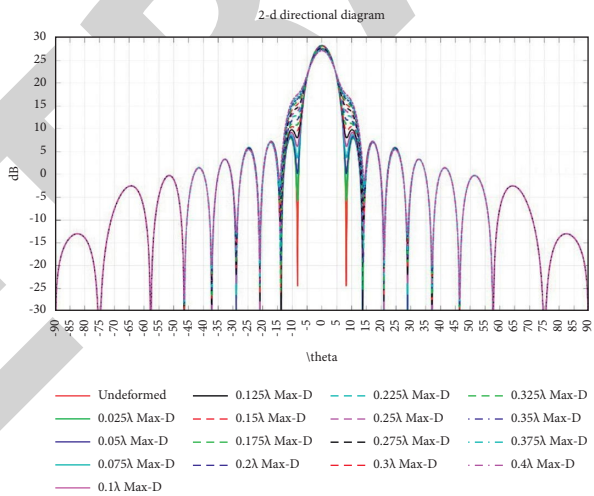

Figure 20: Elevation plane of saddle-shaped deformation.

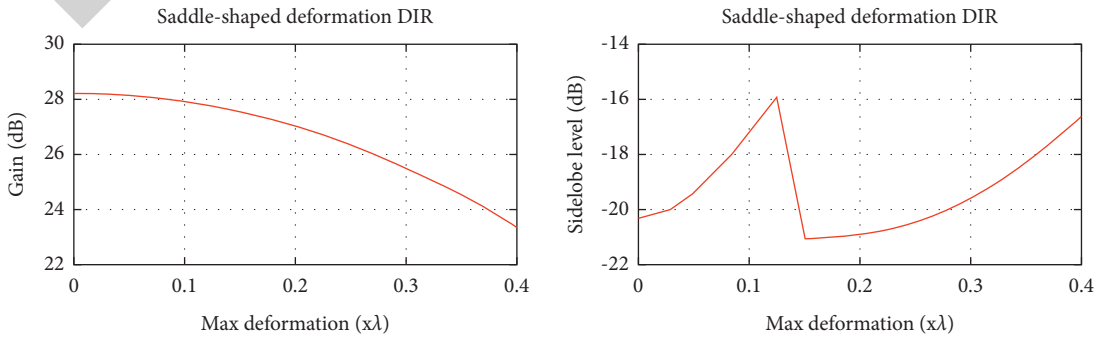

Figure 21: Continued.

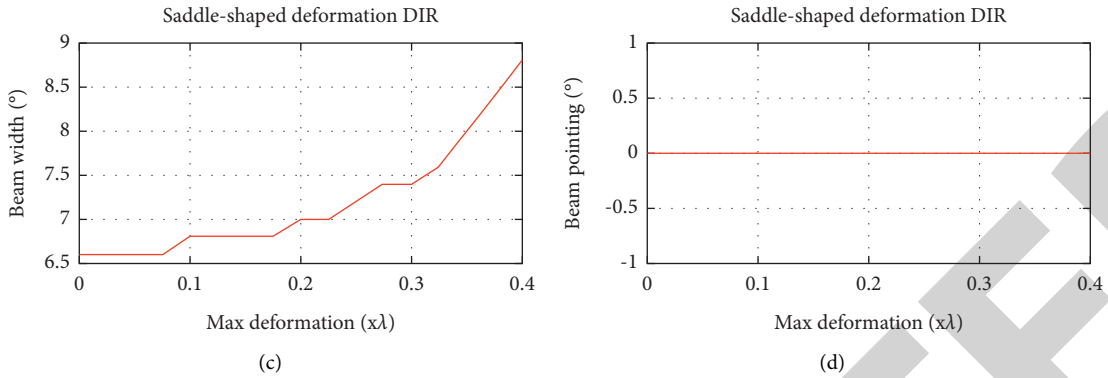

Figure 21: Changes in technical indicators of elevation plane caused by saddle-shaped deformation. (a) Gain. (b) Sidelobe level. (c) Beam width. (d) Beam pointing.

Table 5: Statistics of saddle-shaped deformation technical indicators.

No.	Directional map section	Max deformation	Gain	Sidelobe level	3 dB beam width	Beam pointing
1		0	28.22	−20.33	8.00	0.00
2		0.025	28.20	−20.09	8.00	0.00
3		0.05	28.14	−19.40	8.00	0.00
4		0.075	28.05	−18.37	8.00	0.00
5		0.1	27.92	−17.12	8.20	0.00
6		0.125	27.75	−15.73	8.20	0.00
7		0.15	27.55	−20.90	8.20	0.00
8		0.175	27.31	−20.75	8.40	0.00
9	Azimuth plane	0.2	27.02	−20.54	8.40	0.00
10		0.225	26.71	−20.24	8.60	0.00
11		0.25	26.35	−19.86	8.80	0.00
12		0.275	25.95	−19.37	9.00	0.00
13		0.3	25.51	−18.78	9.20	0.00
14		0.325	25.04	−18.09	9.60	0.00
15		0.35	24.52	−17.30	10.00	0.00
16		0.375	23.96	−16.43	10.80	0.00
17		0.4	23.37	−15.47	11.80	0.00
18		0	28.22	−20.29	6.60	0.00
19		0.025	28.20	−20.06	6.60	0.00
20		0.05	28.14	−19.39	6.60	0.00
21		0.075	28.05	−18.40	6.60	0.00
22		0.1	27.92	−17.21	6.80	0.00
23		0.125	27.75	−15.91	6.80	0.00
24		0.15	27.55	−21.05	6.80	0.00
25		0.175	27.31	−20.99	6.80	0.00
26	Elevation plane	0.2	27.02	−20.89	7.00	0.00
27		0.225	26.71	−20.71	7.00	0.00
28		0.25	26.35	−20.44	7.20	0.00
29		0.275	25.95	−20.07	7.40	0.00
30		0.3	25.51	−19.59	7.40	0.00
31		0.325	25.04	−18.99	7.60	0.00
32		0.35	24.52	−18.29	8.00	0.00
33		0.375	23.96	−17.49	8.40	0.00
34		0.4	23.37	−16.61	8.80	0.00

5.2.1. Saddle-Shaped Deformation of Arrays. Figure 17 shows the saddle-shaped deformation of the antenna array. The normalized deformation data of the center of each antenna element is shown in Table 4.

Based on the normalized deformation, the maximum deformation of the antenna array was set, and the azimuth and elevation patterns of the antenna were simulated when the maximum deformation became 0: 0.025λ: 0.4λ. Figure 18 shows the changes in the pattern of the array azimuth plane under saddle-shaped deformation. Figure 19 shows the changes in the main technical indicators of the array azimuth under saddle-shaped deformation. Figure 20 shows

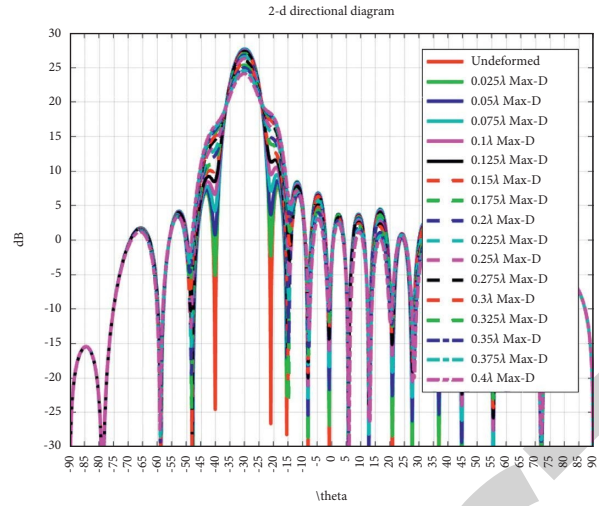

Figure 22: Saddle-shaped deformation azimuth scanning −30° direction map.

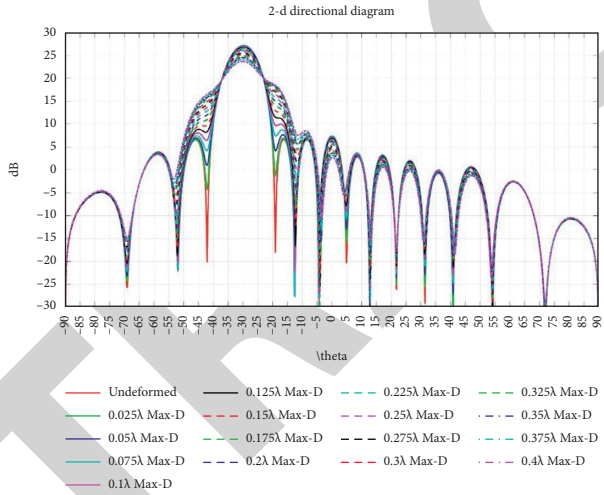

Figure 23: Saddle-shaped deformation elevation scanning −30° direction map.

the changes in the pattern of the array elevation plane under saddle-shaped deformation. Figure 21 shows the changes in the main technical indicators of the array elevation plane under saddle-shaped deformation. Table 5 shows the changes in the main technical indicators of the antenna under the saddle-shaped deformation of the array.

From Figures 18–21 and Table 5, the saddle-shaped deformation has a great influence on the azimuth plane and the elevation plane pattern of the planar array. As the amount of deformation increases, the antenna gain gradually decreases, the sidelobe level gradually increases, and the beam width gradually expands, which has almost no effect on the antenna beam direction. When the deformation amount is greater than or equal to 0.15λ, the azimuth plane and the elevation plane pattern begin to defocus, the pattern is no longer focused, and the first zero point disappears.

5.2.2. Analysis of Deformation Error Impact. In order to verify whether the saddle-shaped deformation will affect the scanning beam of the antenna, the azimuth plane and the elevation plane, respectively, scan the directional patterns of −30° under different maximum deformation variables, as shown in Figures 22 and 23. It can be seen from the figure that the influence of saddle-shaped deformation on antenna beam scanning is basically the same as when the antenna is not scanning.

Integrating the technical indicators of the azimuth plane and the elevation plane, the maximum deformation error of the saddle-shaped deformation is $\leq 0.05\lambda$ and the deterioration of the technical indicators is acceptable. In engineering practice, the maximum deformation error value should be controlled to be $\leq 0.05\lambda$.

6. Conclusions

Taking a 16×16 two-dimensional array antenna as an example, this paper constructed a millimeter-wave antenna array error theoretical model. The influence of random errors caused by production, XY-direction errors caused by assembly, and saddle-shaped deformation of the front on the electrical performance of the antenna under the condition

that the size of the front is unchanged is analyzed. Through a large amount of data calculation, we have given the quantitative relationship between the influence of the error and the electrical performance of the antenna, drawn the influence relationship curve, and finally obtained the critical value. Engineers can refer to the analysis methods and conclusions in the article to estimate the antenna performance and put forward reasonable requirements for the processing tolerance of the antenna array within the allowable range of electrical performance. In follow-up research, we will further analyze the impact of other forms of errors on the electrical performance of the antenna and find the best correction method so that engineers can get a more optimized antenna design and assembly plan. The specific indicators obtained from the experiment are as follows:

(1) In engineering practice, we should try to eliminate the possible factors that produce random errors. At the same time, strictly control the production process and flow during the production and development process, so that the variance of the random phase and amplitude error does not exceed $(10^{\circ}, 0.5\,\text{dB})$, to ensure a small impact on the array antenna pattern and meet the performance requirements of the array antenna.

(2) The errors caused by the assembly of the left and right half arrays, the gaps in the X-direction, have a more obvious impact on the sidelobe level, and the gaps in the Y-direction will affect the distribution of antenna radiation power in space, causing tilt rotation. When the XY-direction changes at the same time, it is a combination of the two situations. According to the sidelobe level deterioration being not more than 1 dB, the error in the X-direction should be $\leq 0.05\lambda$, and the error in the Y-direction should be $\leq 0.1\lambda$.

(3) Symmetrical deformations such as saddle-shaped deformations mainly affect the gain and energy distribution of the antenna and will not affect the beam direction. In engineering practice, to ensure that the sidelobe level deterioration is better than 1 dB, the maximum deformation should be better than 0.05λ.

Data Availability

All data, models, and codes generated or used during the study are included within this article.

Conflicts of Interest

The authors declare that they have no conflicts of interest regarding the publication of this paper.

Acknowledgments

This work was supported by the National Defense Basic Scientific Research Program of China under Grants JCKY2019210B005, JCKY2018204B025, and JCKY2017204B011, the Key Scientific Project Program of National Defense of China under Grant ZQ2019D20401, and the Open Program of National Engineering Laboratory for Modeling and Emulation in E-Government under Grant MEL-20-02, and the Foundation Strengthening Project of China under Grant no. 2019JCJZZD13300.

References

[1] J. Ou, J. Zhang, and R. Zhan, "Processing technology based on radar signal design and classification," *International Journal of Aerospace Engineering*, vol. 2020, Article ID 4673763, 19 pages, 2020.

[2] F. Zhang, *Research and Analysis of Millimeter-Wave Phased Array Antenna Array*, Nanjing University of Science and Technology, Nanjing, China, 2009.

[3] G. Federico, D. Caratelli, G. Theis, and A. B. Smolders, "A review of antenna array technologies for point-to-point and point-to-multipoint wireless communications at millimeter-wave frequencies," *International Journal of Antennas and Propagation*, vol. 2021, Article ID 5559765, 18 pages, 2021.

[4] H. Wang, L. Xu, Z. Yan, and T. A. Gulliver, "Low-complexity MIMO-FBMC sparse channel parameter estimation for industrial big data communications," *IEEE Transactions on Industrial Informatics*, vol. 17, no. 5, pp. 3422–3430, 2021.

[5] L. Wan, K. Liu, Y.-C. Liang, and T. Zhu, "DOA and polarization estimation for non-circular signals in 3-D millimeter wave polarized massive MIMO systems," *IEEE Transactions on Wireless Communications*, vol. 20, no. 5, pp. 3152–3167, 2021.

[6] J. Shi, F. Wen, and T. Liu, "Nested MIMO radar: coarrays, tensor modeling, and angle estimation," *IEEE Transactions on Aerospace and Electronic Systems*, vol. 57, no. 1, pp. 573–585, 2021.

[7] X. Wang, M. Huang, and L. Wan, "Joint 2D-DOD and 2D-DOA estimation for coprime EMVS-MIMO radar," *Circuits, Systems, and Signal Processing*, vol. 40, no. 6, pp. 2950–2966, 2021.

[8] F. Wen, J. Shi, and Z. Zhang, "Closed-form estimation algorithm for EMVS-MIMO radar with arbitrary sensor geometry," *Signal Processing*, vol. 186, Article ID 108117, 2021.

[9] X. Yu, "Functional characteristics and application analysis of phased array radar," *China New Telecommunications*, vol. 21, no. 6, p. 168, 2019.

[10] J. He, L. Li, and T. Shu, "Sparse nested arrays with spatially spread orthogonal dipoles: high accuracy passive direction finding with less mutual coupling," *IEEE Transactions on Aerospace and Electronic Systems*, vol. 57, no. 4, pp. 2337–2345, 2021.

[11] C. Luison, A. Landini, P. Angeletti et al., "Aperiodic arrays for spaceborne SAR applications," *IEEE Transactions on Antennas and Propagation*, vol. 60, no. 5, pp. 2285–2294, 2012.

[12] D. Vollbracht, "Optimum phase excitations and probe- feed positions inside antenna arrays for the reduction of cross polarization radiation in demanding phased array weather radar applications," in *Proceedings of the 2016 10th European Conference on Antennas and Propagation (EuCAP)*, pp. 1–5, Davos, Switzerland, April 2016.

[13] S. K. Sharma, "Design and development of some novel phased arrays and anti-jamming antennas," in *Proceedings of the 2017 IEEE Radio and Antenna Days of the Indian Ocean (RADIO)*, p. 1, Cape Town, South Africa, September 2017.

[14] K. Wu, Y. Yao, X. Cheng, J. Yu, and X. Chen, "Design of high efficiency linearly polarized 8 × 8 millimeter-wave antenna

Hindawi
International Journal of Antennas and Propagation
Volume 2023, Article ID 9895714, 1 page
https://doi.org/10.1155/2023/9895714

Retraction

Retracted: Three-Dimensional Inversion of Borehole-Surface Resistivity Method Based on the Unstructured Finite Element

International Journal of Antennas and Propagation

Received 19 December 2023; Accepted 19 December 2023; Published 20 December 2023

This article has been retracted by Hindawi following an investigation undertaken by the publisher [1]. This investigation has uncovered evidence of one or more of the following indicators of systematic manipulation of the publication process:

(1) Discrepancies in scope

(2) Discrepancies in the description of the research reported

(3) Discrepancies between the availability of data and the research described

(4) Inappropriate citations

(5) Incoherent, meaningless and/or irrelevant content included in the article

(6) Manipulated or compromised peer review

The presence of these indicators undermines our confidence in the integrity of the article's content and we cannot, therefore, vouch for its reliability. Please note that this notice is intended solely to alert readers that the content of this article is unreliable. We have not investigated whether authors were aware of or involved in the systematic manipulation of the publication process.

Wiley and Hindawi regrets that the usual quality checks did not identify these issues before publication and have since put additional measures in place to safeguard research integrity.

We wish to credit our own Research Integrity and Research Publishing teams and anonymous and named external researchers and research integrity experts for contributing to this investigation.

The corresponding author, as the representative of all authors, has been given the opportunity to register their agreement or disagreement to this retraction. We have kept a record of any response received.

References

[1] Z. Wang and S. Fang, "Three-Dimensional Inversion of Borehole-Surface Resistivity Method Based on the Unstructured Finite Element," *International Journal of Antennas and Propagation*, vol. 2021, Article ID 5154985, 13 pages, 2021.

Hindawi
International Journal of Antennas and Propagation
Volume 2021, Article ID 5154985, 13 pages
https://doi.org/10.1155/2021/5154985

Research Article

Three-Dimensional Inversion of Borehole-Surface Resistivity Method Based on the Unstructured Finite Element

Zhi Wang[1] **and Sinan Fang**[2]

[1]*Electronics and Information School, Yangtze University, Jingzhou 434023, China*
[2]*College of Geophysics and Petroleum Resources, Yangtze University, Wuhan 430100, China*

Correspondence should be addressed to Zhi Wang; 1324385898@qq.com

Received 11 August 2021; Revised 25 August 2021; Accepted 12 September 2021; Published 24 September 2021

Academic Editor: Jin He

The electromagnetic wave signal from the electromagnetic field source generates induction signals after reaching the target geological body through the underground medium. The time and spatial distribution rules of the artificial or the natural electromagnetic fields are obtained for the exploration of mineral resources of the subsurface and determining the geological structure of the subsurface to solve the geological problems. The goal of electromagnetic data processing is to suppress the noise and improve the signal-to-noise ratio and the inversion of resistivity data. Inversion has always been the focus of research in the field of electromagnetic methods. In this paper, the three-dimensional borehole-surface resistivity method is explored based on the principle of geometric sounding, and the three-dimensional inversion algorithm of the borehole-surface resistivity method in arbitrary surface topography is proposed. The forward simulation and calculation start from the partial differential equation and the boundary conditions of the total potential of the three-dimensional point current source field are satisfied. Then the unstructured tetrahedral grids are used to discretely subdivide the calculation area that can well fit the complex structure of subsurface and undulating surface topography. The accuracy of the numerical solution is low due to the rapid attenuation of the electric field at the point current source and the nearby positions and sharply varying potential gradients. Therefore, the mesh density is defined at the local area, that is, the vicinity of the source electrode and the measuring electrode. The mesh refinement can effectively reduce the influence of the source point and its vicinity and improve the accuracy of the numerical solution. The stiffness matrix is stored with Compressed Row Storage (CSR) format, and the final large linear equations are solved using the Super Symmetric Over Relaxation Preconditioned Conjugate Gradient (SSOR-PCG) method. The quasi-Newton method with limited memory (L_BFGS) is used to optimize the objective function in the inversion calculation, and a double-loop recursive method is used to solve the normal equation obtained at each iteration in order to avoid computing and storing the sensitivity matrix explicitly and reduce the amount of calculation. The comprehensive application of the above methods makes the 3D inversion algorithm efficient, accurate, and stable. The three-dimensional inversion test is performed on the synthetic data of multiple theoretical geoelectric models with topography (a single anomaly model under valley and a single anomaly model under mountain) to verify the effectiveness of the proposed algorithm.

1. Introduction

Owing to the need for energy development and the development of remote sensing technology, the research of electromagnetic wave propagation and its application in communication and detection has made significant progress. It has been used in radio communications in mine tunnels, railway tunnels, and military tunnels; communications with submarines, command, and navigation; and the electromagnetic wave detection of mineral resources and crustal structures [1, 2] (including faults, glaciers, caves, pipelines, water sources, and objects in the ocean). The wave-field structure is an important problem for communication and detection systems [3–9]. Electromagnetic exploration is based on the electrical differences between different rocks in the Earth's crust (such as differences in electrical conductivity,

magnetic permeability, dielectric, and electrochemical properties). The electromagnetic field signal sent by the field source passes through the underground medium to reach the target geological body and then generates an induction signal. These electromagnetic waves containing the induction signal of the target geological body are received by the receiver arranged in the well or on the ground. In this paper, the influence of geometric and electromagnetic characteristics of various geological structures (including man-made structures) on electromagnetic wave propagation is studied. The time and space distributions of artificial or natural electromagnetic fields are observed and analyzed to determine useful underground mineral resources, identify underground geological structures, and solve the geological problems [1]. Electromagnetic exploration methods are mainly divided into direct current method based on the principle of geometric sounding, magnetotelluric method (MT/AMT/CSAMT) based on the principle of frequency domain sounding, and transient electromagnetic method (TEM) based on the principle of time-domain sounding [2]. The direct current (DC) resistivity method is one of the classic methods of geoelectric exploration. It has been widely and effectively applied in mineral resources (metallic and nonmetallic minerals, coal fields, oil, and gas), environmental engineering (groundwater, geological landslides, and environmental monitoring), geotechnical engineering (tunnel construction and mine water inrush), and other fields. Moreover, the DC resistivity method has been expanded to hydrology, archaeology, and other fields that are closely related to national economic construction and human social life. The DC resistivity method has a variety of flexible observation methods such as the electrical profile method and electrical sounding method with different electrode arrays, pole-pole, dipole-dipole, and multipole. The high-density electrical method has been introduced, which can efficiently obtain large observation data, making it possible for the three-dimensional resistivity inversion of underground fine structures [10]. The borehole-surface resistivity method is a type of electrical method in which electrodes are placed in the well and on the ground. The electrode in the well is the source electrode and the electrode on the ground receiving the electromagnetic field is measured. The source electrode is always placed in the deep part of the borehole to make it close to the object to be detected, thereby increasing the current intensity or the received abnormal response [11]. The borehole-surface resistivity method is mainly used for secondary resource exploration in metal mines and the prediction of oil reservoir boundaries [12]. Data are collected on a grid along parallel lines with different electrode arrays, and a 3D inversion algorithm is used. With the development of computer and numerical computing technology, the three-dimensional electromagnetic forward and inversion algorithms have made significant progress in the mesh design (structured [13–16] and unstructured [17–25]), as well as the numerical method in the forward solution (finite difference [26–30] and finite element [31, 32]), solving the objective function (Gauss–Newton (GN) method [33–37], quasi-Newton (QN) method [38–50], nonlinear conjugate gradient (NLCG) method [51–53], etc.).

The unstructured finite element method (FEM) has achieved promising success in the three-dimensional numerical simulation of resistivity in complex topography. The unstructured grid allows local densification and can simulate complex geometric models. The structure also has controllable element quality and its solution efficiency significantly increases in the three-dimensional unstructured FEM. The calculation time and the storage capacity of the unstructured grid can be reduced by about an order of magnitude retaining the same calculation accuracy as the structured grid [10]. Owing to a large number of inversion parameters and a vast amount of data in the three-dimensional resistivity inversion, the Jacobian matrix (partial derivative matrix) has huge calculation and storage requirements. Many inversion algorithms have been proposed which can avoid the calculation of the Jacobian matrix. Zhang et al. [26] and Wu and Xu [54] introduced the conjugate gradient method to achieve fast and effective three-dimensional resistivity inversion and resolve the issues of solution and storage of the Jacobian matrix in the three-dimensional inversion to improve the efficiency. The optimization methods used in 3D data inversion mainly include the nonlinear conjugate gradient (NLCG) method, the Gauss-Newton (GN) method, and the quasi-Newton (QN) method. Both the NLCG and the QN only need the gradient information of the objective function, and no explicit sensitivity matrix is needed. The GN method has second-order sensitivity information, and the inversion convergence speed is better but the calculation speed is lower than that of the QN and the NLCG methods. The QN method approximately computes the inverse Hessian matrix in the iterative process and is more efficient than the NLCG method in the step size search. In the large-scale 3D data inversion, the QN method still has the problem of occupying memory. Therefore, the limited memory quasi-Newton method (L_BFGS) has been developed. The L_BFGS method only needs to store the last m iterations information to generate the inverse Hessian matrix, which significantly reduces the required memory. With the expansion of the application range of the DC resistivity method, the study of inversion accuracy and inversion speed in the 3D resistivity inversion method has important practical significance and theoretical value.

In the above-mentioned studies, the L_BFGS method has the advantages of fast convergence, less memory, and better inversion efficiency than the other inversion algorithms. The L_BFGS is also more suitable for solving large-scale 3D electromagnetic inversion problems. Therefore, an inversion algorithm for the three-dimensional resistivity method with the undulating terrain is developed in this paper by combining the L_BFGS method, the borehole-to-surface observation method, and the FEM with unstructured tetrahedrons. Numerical results of the theoretical model inversion validate the effectiveness of the proposed method.

2. Forward Modeling Theory

2.1. Base Equation. The partial differential equation and its boundary-value problem satisfied by the total potential of the three-dimensional point current source field are given by the following equation with mixed boundary conditions [14, 55]:

$$\nabla \cdot (\sigma(x,y,z)\nabla u(x,y,z)) = -\frac{4\pi}{\omega_A} I\delta(\mathbf{r}_A), \quad \text{in } \Omega,$$
$$\frac{\partial u}{\partial \mathbf{n}} = 0, \quad \text{on } \Gamma_s, \tag{1}$$
$$\frac{\partial u}{\partial \mathbf{n}} + \frac{\cos\theta}{r} u = 0, \quad \text{on } \Gamma_\infty,$$

where σ is the conductivity distribution on the surface, $\mathbf{u}$ is the electrical potential, $\mathbf{I}$ is the strength of the source, δ is the Dirac delta function, $\mathbf{r_A}$ is the coordinate of the source electrode $\mathbf{A}$, ω_A is the opening angle of the source to the underground Earth by Ω, $\mathbf{n}$ is the outward normal to the boundary surface Γ_∞ of the modal domain, r is the location of an arbitrary potential electrode from the source point, Γ_s and Γ_∞ are the natural boundary condition (surface-air interface) and the infinite boundary condition (artificially cut off the interface), respectively, and θ is the angle between the radial distance $\mathbf{r}$ from the source point and the outward normal spatial coordinate n on the boundary. If the source point is on the ground, then $\omega_A = 2\pi$, while if the source point is underground, then $\omega_A = 4\pi$. The weighted residual method can be used to derive the integral equation of the variational problem corresponding to equation (1) [15, 55]:

$$F(u) = \int_\Omega \left[\frac{1}{2}\sigma(\nabla u)^2 - \frac{4\pi}{\omega_A}\delta(A)u\right] d\Omega + \int_{\Gamma_\infty} \frac{1}{2}\sigma u^2 \frac{\cos(\mathbf{r},\mathbf{n})}{r} d\Gamma, \tag{2}$$
$$\delta F(u) = 0.$$

The calculation area adopts tetrahedral division and linear difference and finally forms a large sparse symmetric linear equation system. The matrix expression is as follows:

$$\mathbf{Ku} = \mathbf{P}, \tag{3}$$

where $\mathbf{K}$ is an $n \times n$ symmetric matrix, $\mathbf{u}$ is an $n \times 1$ column vector representing the potential vector on the three-dimensional grid node, and $\mathbf{P}$ is a column vector containing field source information. In order to save memory, the Compressed Sparse Row or Compressed Row Storage is used to store the coefficient matrix $\mathbf{K}$, and the Super Symmetric Over Relaxation Preconditioned Conjugate Gradient (SSOR-PCG) algorithm [16, 25] is used to solve equation (3).

2.2. Algorithm Verification. In order to verify the correctness of the proposed algorithm, a buried spherical model in a uniform half-space is selected. All calculations in this article are done on a computer consisting of an Intel i7-4712 MQ CPU with a frequency of 2.3 GHz and 16 G memory. Both forward and inversion programs are compiled and run by Intel Fortran. Gmsh 4.8.4 [56] and ParaView 5.6.0 [57] are used for generating and visualizing the unstructured tetrahedral meshes, respectively.

Figure 1 shows the model for the spherical anomaly embedded in a uniform half-space (Ren and Tang [20]). The

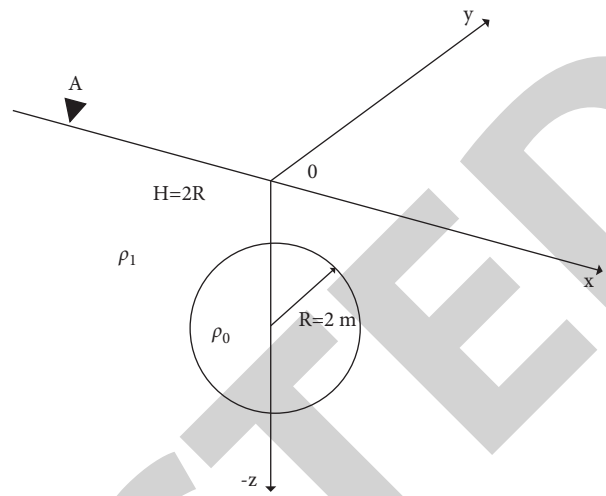

Figure 1: The geometric structure of the sphere model.

radius, the center coordinates, and the resistivity of the sphere are $R = 2.25$ m, (0, 0, −4.5), and $\rho_0 = 1\,\Omega$m, respectively, the resistivity of the half-space is $\rho_1 = 10\,\Omega$m, the point current source electrode A is at (−5, 0, 0), and a current source of strength 1A is injected into the Earth. The measuring electrodes M are along the X direction with spacing of 0.25 m. The spatiality of the entire calculation area is 500 m × 500 m × 500 m.

The target area size is 100 m × 100 m × 100 m. The meshes at the source and the measurement points are refined, the total number of grid nodes is 56737, and the total number of grid cells is 277375. Figure 2 shows the partial magnification effect of the mesh division. The source point, the measuring point, and the anomalous body were refined meshes. The potential value at the measuring point is calculated by the finite element forward modeling program in this article with the pole-pole device and compared with the analytical solution given by Cook and Van Nostrand [58]. Figure 3 compares the analytical and numerical solutions of apparent resistivity of an underground spheroid. Figure 4 presents the relative error of the analytical and numerical solutions of apparent resistivity in the sphere model. It can be seen from Figure 4 that the maximum error is less than 1.4%.

3. Inversion Theory

3.1. Objective Function. According to Tikhonov's regularization theory, the inversion objective function in the sense of least squares is used. The objective function is described as [10, 18]

$$\Phi(m) = \Phi_d(\mathbf{m}) + \lambda\Phi_m(\mathbf{m}) = \left\|\mathbf{W}_d(\mathbf{d}_{\text{obs}} - F(\mathbf{m}))\right\|_2^2 + \lambda\left\|\mathbf{W}_m(\mathbf{m} - \mathbf{m}_{\text{ref}})\right\|_2^2, \tag{4}$$

where $F(\mathbf{m})$ is the forward response function, m is the model parameter $(m_i, i = 1, 2, \ldots, M)$, $\mathbf{d}_{\text{obs}}$ is the observation data, $\mathbf{W}_d$ is an $N \times N$ data weighting matrix (N is the number of data) in which the diagonal elements are the measured data

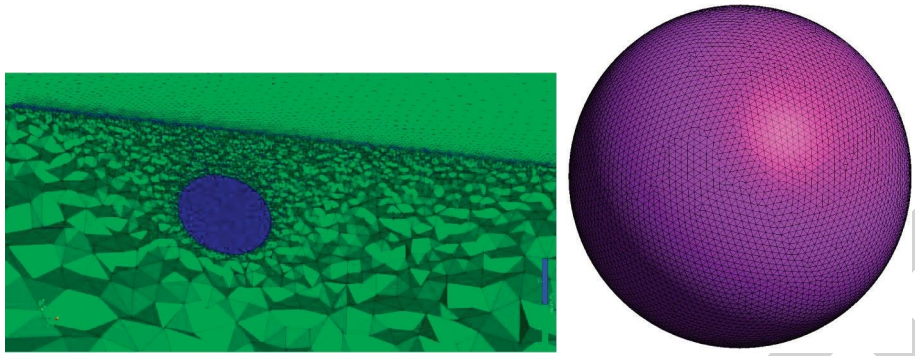

Figure 2: Partial magnification effect of the mesh division.

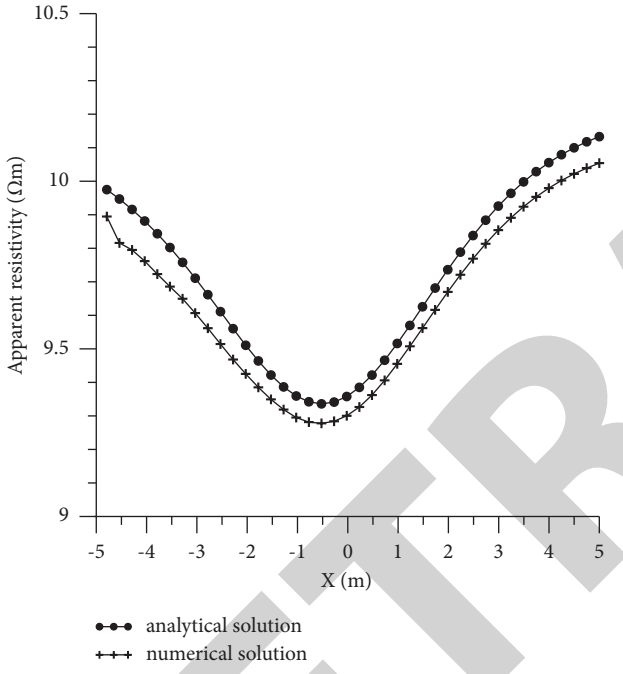

Figure 3: Comparison of analytical and numerical solutions of apparent resistivity of the underground spheroid.

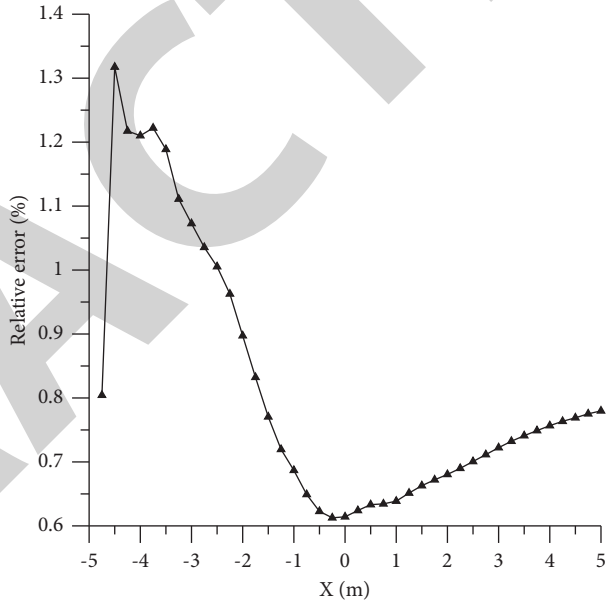

Figure 4: Relative error.

and the remaining elements are zero, σ_i is the standard deviation of the i-th measured data, $\mathbf{W}_m$ is the model-weighted matrix usually defined by the discrete difference operator of the model unit and generally takes the first-order regularization constraint, λ is the regularization parameter used to balance the weight of data fitting and model smoothness, and $\mathbf{m}_{\text{ref}}$ is a reference model containing prior information about the model parameters. The inverted measured data $\mathbf{d}_{\text{obs}}$ are the pole-pole potential value and the model parameter is the conductivity value of the element. Usually, the logarithm is used to calibrate the measured data and the model parameters mainly due to the large variation range and to invert the stability. The logarithm is defined as $d = \ln \phi_{\text{obs}}, m = \ln \sigma$. The resistivity inversion problem is generally a mixed problem, which often leads to equation (4) as an ill-conditioned equation. To solve this problem, smooth constraints are introduced into the inversion equation. Unstructured grid with disorderly arrangement was used in the forward modeling, so we adopt smooth constraint method, that is, judge the adjacency of the grid according to whether the grid unit has contact surface to determine the adjacency of the grid unit. For adjacency to generate matrix W_m, $W_m(i, j)$ represents the contribution of the j-th unit to the smoothness of the i-th unit, which is generated according to the following formula:

$$W_m = \begin{cases} -\dfrac{\left(1/x_{ij}\right)}{\sum_{j=1}^{k_i}\left(1/x_{ij}\right)}, & i \text{ and } j \text{ are adjacent units,} \\ 1, & i = j, \\ 0, & \text{other,} \end{cases} \tag{5}$$

where $x_{ij} = |x_i - x_j|$, and it is the distance in the X direction between the center of the i-th unit and the j-th unit, and k_i is the number of adjacent units to the i-th unit.

3.2. Inversion Framework. For the large-scale inversion problem, the traditional BFGS method requires a large

amount of memory. Nocedal [50] improved the BFGS method and proposed a limited memory BFGS (L_BFGS) method to solve the nonlinear optimization problem. In the L_BFGS method, the inverse Hessian matrix approximation formula is defined as

$$\begin{aligned}
\mathbf{H}_{k+1} &= \left(V_{k-1}^T, \ldots, V_{k-m}^T\right)\mathbf{H}_k^0\left(V_{k-m}, \ldots, V_{k-1}\right) \\
&\quad + \rho_{k-m}\left(V_{k-1}^T, \ldots, V_{k-m+1}^T\right)s_{k-m}s_{k-m}^T\left(V_{k-m+1}, \ldots, V_{k-1}\right) \\
&\quad + \rho_{k-m+1}\left(V_{k-1}^T, \ldots, V_{k-m+2}^T\right)s_{k-m+1}s_{k-m+1}^T\left(V_{k-m+2}, \ldots, V_{k-1}\right) + \cdots + \rho_{k-1}s_{k-1}s_{k-1}^T, \\
\rho_k &= \frac{1}{y_k^T s_k}, \\
V_k &= \left(I - \rho_k y_k s_k^T\right), \\
s_k &= m_{k+1} - m_k, \\
y_k &= g_{k+1} - g_k,
\end{aligned} \tag{6}$$

where m is the number of previous iterations with a value between 3 and 20. The previous iteration information of gradient and the model modification is used to modify the inverse Hessian matrix. $\mathbf{H}_k^0$ defined by Nocedal and Wright [59] gives an update method as

$$\mathbf{H}_k^0 = \gamma_k \mathbf{I}. \tag{7}$$

In this paper, the identity matrix I is selected to initialize matrix $\mathbf{H}_k^0$ and γ_k can be defined as

$$\gamma_k = \frac{s_{k-1}^T y_{k-1}}{y_{k-1}^T y_{k-1}}. \tag{8}$$

The inversion steps of the L_BFGS method are defined in Algorithm 1 as follows [49, 59].

In the algorithm, g_k is the gradient of the objective function (4), and it is expressed as

$$g_k = \nabla\Phi\left(m_k\right) = -2J_m^T W_d^T W_d\left(d_{\text{obs}} - F\left(m_k\right)\right) + 2\lambda W_m^T W_m m_k, \tag{9}$$

where J represents the Jacobian matrix. It can be seen from formula (9) that the calculation of the gradient lies in the calculation of the Jacobian matrix. The explicit calculation requires massive computation and memory storage. Therefore, it is necessary to avoid directly calculating the Jacobian matrix and calculate the product of the transpose of the Jacobian matrix and any one-dimensional vector. Thus, there is no need for storing the Jacobian matrix, and the calculation can be obtained together after the forwarding in each inversion, which significantly speeds up the inversion calculation. The calculation details are provided by Zhanget al. [26].

Nocedal and Wright [59] presented a double-loop recursive method to update Step 2 in Algorithm 1. The detailed calculation process can be found in the literature [59]. In the process of minimizing the objective function, in contrast to the CG's method in which the step size is obtained using an analytical method, both the NLCG and the L_BFGS methods need to obtain the iterative step size through an inexact one-dimensional linear search method. In this article, the iterative step size is required to meet the sufficient descent condition and the curvature condition. The Wolfe-Powell criterion can be obtained as

$$\begin{aligned}
&\Phi\left(m_k + \alpha_k p_k\right) \le \Phi\left(m_k\right) + c_1\alpha_k\nabla\Phi\left(m_k\right)^T p_k, \\
&\nabla\Phi\left(m_k + \alpha_k p_k\right)^T p_k \ge c_2\nabla\Phi\left(m_k\right)^T p_k,
\end{aligned} \tag{10}$$

where Φ is the forward operator, m_k is the model parameter of the k-th inversion iteration, α_k is the iteration step length, c_1 and c_2 are constants satisfying $0 < c_1 < c_2 < 1$, and p_k is the search direction. The search methods product can be calculated using the process described in the work of Nocedal and Wright [59]. In general, the smaller c_2 is, the more accurate the linear search will be. If $c_2 = 0.1$, a fairly accurate linear search will be obtained, while $c_2 = 0.9$ will result in a relatively weak linear search. The smaller c_2, the longer the search time. According to the literature, the commonly used values c_1 and c_2 in the L_BFGS method are $c_1 = 10^{-4}$ and $c_2 = 0.9$.

4. Synthetic Data Inversion

In actual exploration, the influence of topography is unavoidable and will cause deviations in the inversion results. Topography correction is usually used to eliminate the impact. However, since the underground structure is complex, the topography correction can only be approximated and will still have large errors. Therefore, regardless of the topography correction in the data or the model space, the resistivity inversion under undulating topography conditions cannot eliminate the influence of the terrain. The influence of the topography can be accurately eliminated

(1) Set $k = 1$, choose initial model $\mathbf{m}_0$, integer $m > 0$ and initial matrix $\mathbf{H}_k^0$ (the identity matrix);
(2) Compute $p_k = -H_k g_k, m_{k+1} = m_k + \alpha_k p_k$, where α_k is selected to satisfy the Wolfe-Powell conditions;
(3) If $k > m$ then
    Discard the vector pair $\{s_{k-m}, y_{k-m}\}$ from the storage
    Compute and save $s_k = m_{k+1} - m_k, y_k = g_{k+1} - g_k$;
    end
(4) Update $\mathbf{H}_k^0$ using formula (7) for m times to obtain $\mathbf{H}_{k+1}$ from formula (6);
(5) Set $k = k + 1$, go to step 2.

Algorithm 1: Limited Memory BFGS.

only by incorporating the topography into the inversion algorithm [10]. In this paper, the topography information is directly introduced in the inversion and the three-dimensional resistivity inversion with topography is conducted. Numerical examples over different scenarios are provided to illustrate the validity of the inversion algorithm proposed in this paper. A single low-resistance anomaly model is embedded with measured data for three-dimensional inversion under the flat, valley, and mountain topographies.

4.1. Inversion of Buried Cuboid Model under Flat Topography. The rectangular model is shown in Figure 5. The resistivities of the background half-space and the low-resistance body are $\rho_0 = 100\,\Omega$m and $\rho_1 = 10\,\Omega$m, respectively. The size of the low-resistance cuboid is $10\,\text{m} \times 10\,\text{m} \times 5\,\text{m}$. The buried depths of the cuboid from the top to the ground and from the bottom to the ground are $h = 5$ m and 10 m, respectively. The blue triangles represent the locations of the two wellheads (40, 50, 0) and (60, 50, 0). The red five-pointed star represents the origin of the Cartesian coordinate system (50, 50, 0), and the horizontal distance between the anomalous body and the drilling on both sides is $d = 5$ m. The survey line range used in inversion is 1~99 m and the spacing between survey lines is 1 m. The number of selected measuring points in each survey line is 99, and the position coordinates of measuring point M (measuring electrode) along the X direction are $x = 1$~99 m and $y = 1$~99 m, while the spacing is 1 m. The range of the source point A (source electrode) is from −5 m to −25 m downhole, with an interval of 5 m. Figures 6(a) and 6(b) are the unstructured tetrahedral grids used in forward modeling and inversion, respectively. In order to improve the accuracy of forward modeling and reduce the numerical simulation errors near the source point, the forward modeling grids are measured, the source point and the vicinity of the anomalous body are refined meshes, and the total number of tetrahedra grids is 1706788. The inversion grid is refined at the source and the measurement points, and the total number of tetrahedra grids is 1512967. A total of 98,010 pieces of "potential measured data" of the primary field were obtained by using a pole-pole array and the three-dimensional finite element forward modeling program. In order to verify the stability of the proposed inversion algorithm, 3% Gaussian noise was added to the theoretical measured data. The selection of the inversion parameters is as follows: the regularization parameter$\lambda = 0.05$, which remains unchanged during the inversion process, the convergence coefficient of the inversion termination, and the number of inversion iterations is 12 times. Figures 7(a) and 7(b) show the objective function fitting and the root mean square (RMS) error during the inversion process, respectively. It can be seen from the figures that the data fitting is poor and the objective function decreases steadily, indicating that the L_BFGS in this paper has good convergence for the three-dimensional borehole-surface resistivity method. Figures 8(a) and 8(b) show the inversion result profiles of XOZ and YOZ, respectively. It can be seen that the inversion result of the synthetic model data is still in good agreement with the real model in the presence of noise, and the location of the underground low-resistance anomaly is the same as the resistivity value, which verifies the effectiveness of the inversion method proposed in this paper.

4.2. Inversion of Buried Cuboid Model under Valley. The model of the buried anomaly under the valley is shown in Figure 9. The lowest part of the valley is 10 m above the ground, and the entire depression is symmetrical about the minimum. The horizontal span is 45 m. The resistivities of the background half-space and the low-resistance body are $\rho_0 = 100\,\Omega$m and $\rho_1 = 10\,\Omega$m, respectively. The size of the low-resistance cuboid is $10\,\text{m} \times 10\,\text{m} \times 5\,\text{m}$. The buried depths of the cuboid from the top to the ground and from the bottom to the ground are $h = 5$ m and 10 m, and the horizontal distance between the anomalous body and the drilling on both sides is $d = 5$ m. The blue triangles represent the locations of the two wellheads (40, 50, −8) and (60, 50, −8). The red five-pointed star represents the origin of the Cartesian coordinate system (50, 50, 0). There are a total of 5 survey lines in the survey area in inversion. The distance between survey lines is 5 m. The number of measuring points selected in each survey line is 79. The position coordinates of measuring point M (measuring electrode) along the X direction are $x = 11$~89 m and $y = 40$~60 m with an interval of 1 m. The total measuring points are 395. The range of the source point A (source electrode) is from −5 m to −25 m downhole, with an interval of 5 m. Figure 10 shows the unstructured tetrahedral meshes used in the forwarding and inversion of the model. In order to improve the accuracy of the forward modeling and reduce the numerical simulation error near the source point, the forward meshes are refined in the vicinity of the survey point, the source point, and the anomalous body. The inversion mesh is at the source point. The total number of tetrahedral cells is 1247660. Encrypted

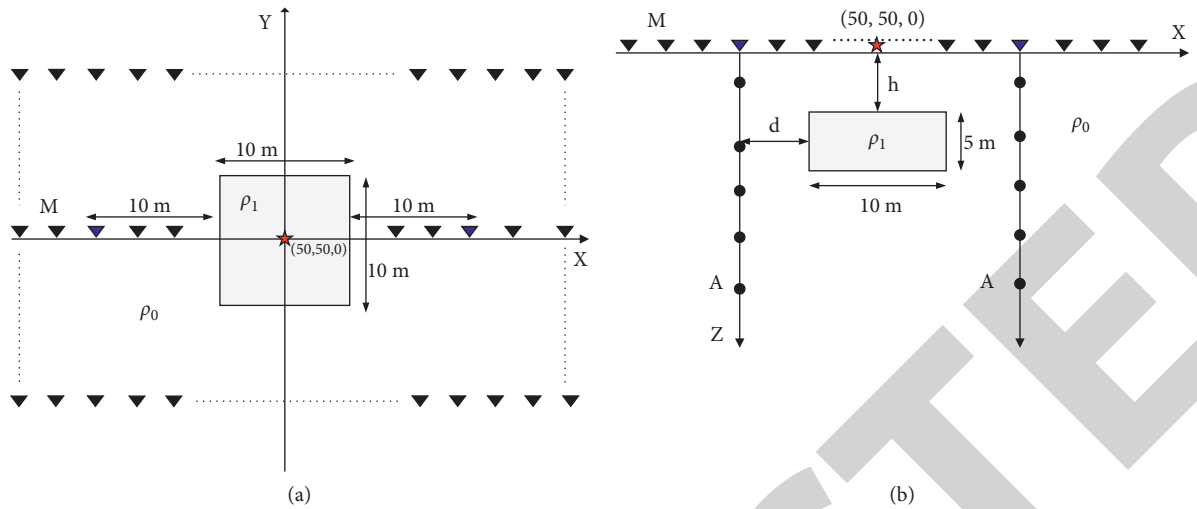

Figure 5: Geometrical model of a flat surface with a cube. (a) XOY plane view of the model; (b) XOZ cross-sectional view of the model.

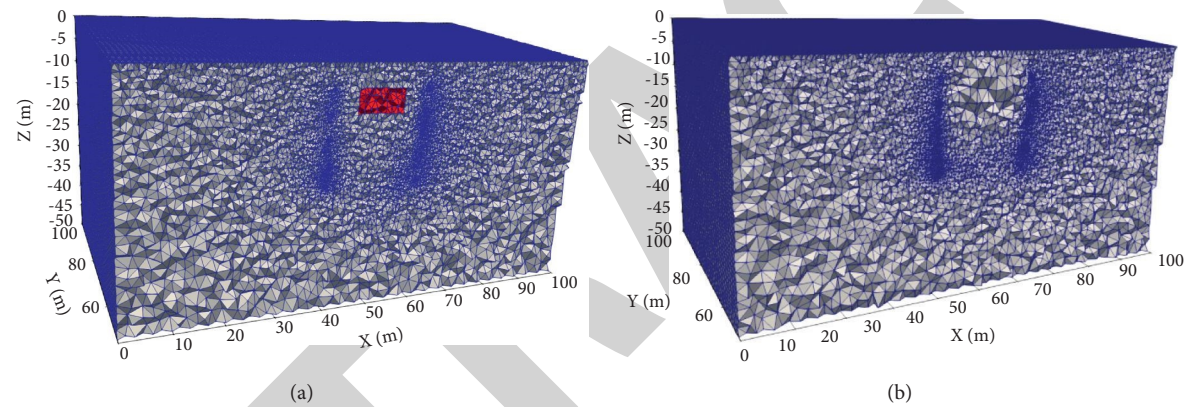

Figure 6: Forward and inversion grid of the buried rectangular model under the flat surface. (a) Forward mesh and (b) inversion mesh.

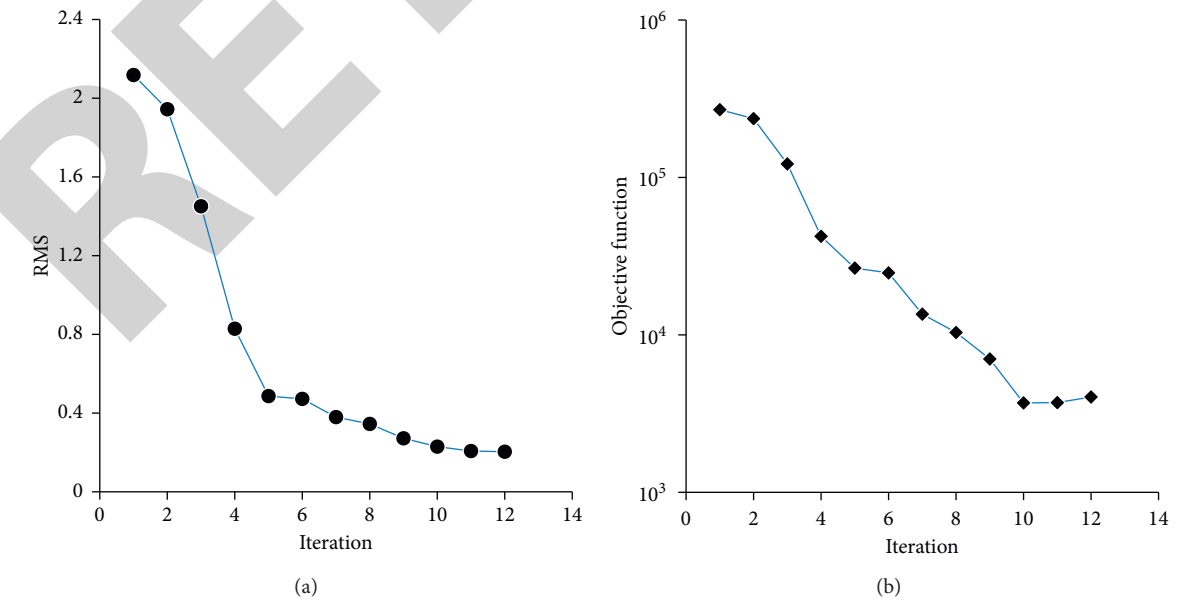

Figure 7: The relationship between inversion parameters and the number of iterations. (a) Data relative fit difference RMS; (b) fitting of objective function.

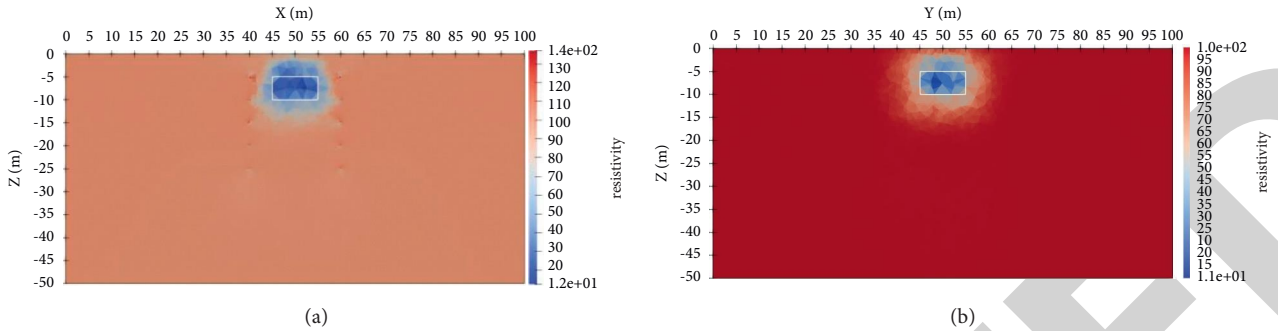

Figure 8: Inversion results of anomalous bodies under the flat surface. (a) Slice of resistivity inversion result at XOZ profile; (b) slice of resistivity inversion result at YOZ profile. The outline of the true model is indicated by the white rectangles.

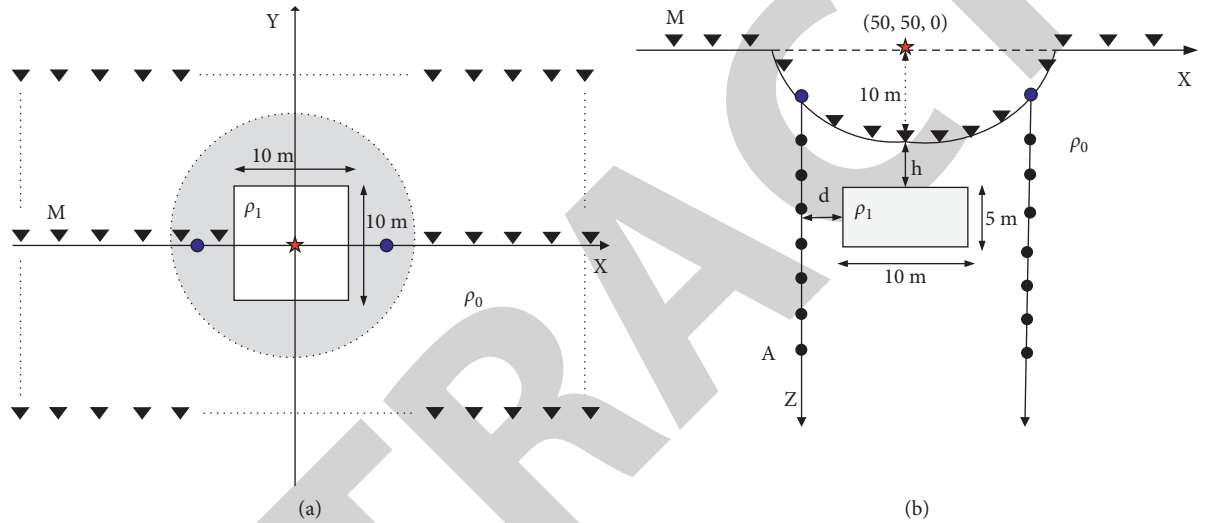

Figure 9: The geometry of valley topographical model with a cube. (a) XOY plane view; (b) XOZ cross-sectional view.

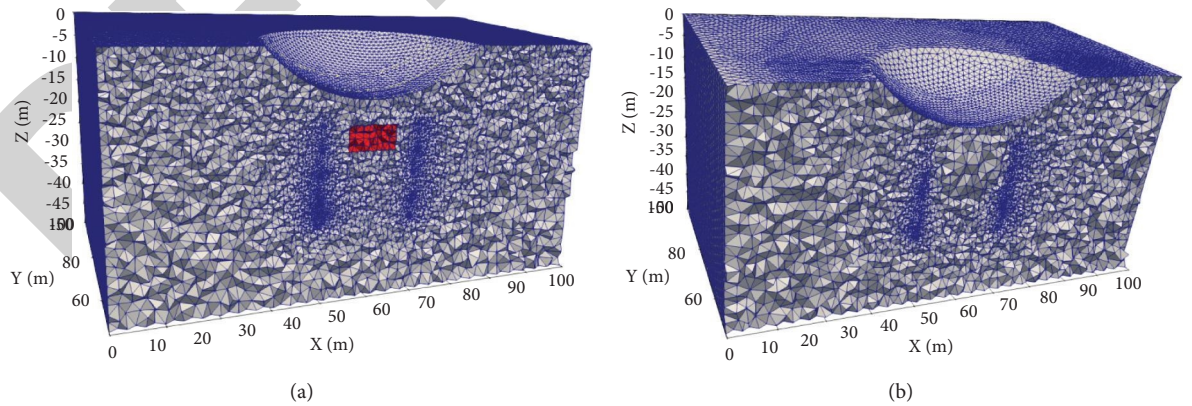

Figure 10: Forward and inversion grid of buried rectangular model under valley topography. (a) Forward mesh; (b) inversion mesh.

with the measuring point, the total number of inversion grid tetrahedral cells is 1169531. The selection of the inversion parameters is consistent with the inversion model under a flat surface. The number of inversion iterations is 17 times. The relative fitting error RMS of the data during the inversion process is shown in Figure 11(a). It can be seen from the figure that the data fitting is poor. The steady decline indicates that the L_BFGS inversion method has good convergence in this paper. Figure 11(b) shows the slice of resistivity 3D inversion result, while Figures 11(c) and 11(d) show the results of slices

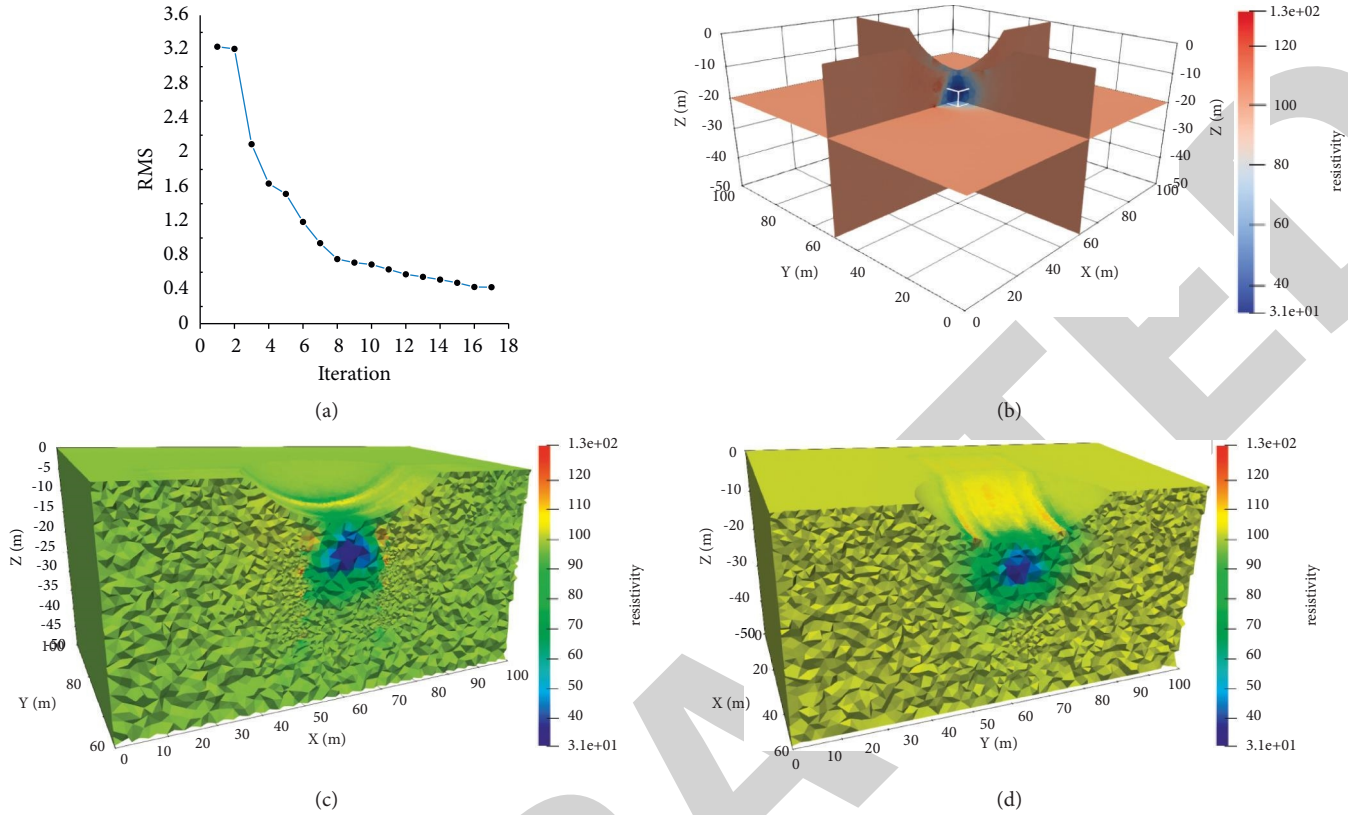

Figure 11: Inversion results of anomalous bodies under valley topographical model. (a) The relative fitting error RMS during the inversion process; (b) slice of resistivity 3D inversion result; (c) slice of resistivity inversion result at XOZ profile; (d) slice of resistivity inversion result at YOZ profile. The outline of the true model is indicated by the white boxes.

at XOZ and YOZ profiles, respectively, under valley topography. The topography effects can be seen in the figures. Under the circumstances, the inversion result of the synthetic model data is in good agreement with the real model, and the location of the underground low-resistance anomaly is the same as the resistivity value, which effectively eliminates the influence of topography and verifies the effectiveness of the proposed inversion method.

4.3. Inversion of the Buried Cuboid Model under Mountain. The buried rectangular model under the mountain is shown in Figure 12. The highest part of the mountain relative to the ground is 10 m high, the entire uplift is symmetrical about the maximum, and the horizontal span is 45 m. The resistivities of the background half-space and the low-resistance body are $\rho_0 = 100\ \Omega$m and $\rho_1 = 10\ \Omega$m, respectively. The size of the low-resistance rectangular block is 10 m × 10 m × 5 m. The buried depths of the cuboid from the top to the ground and from the bottom to the ground are $h = 5$ m and 10 m, respectively. The horizontal distance between the abnormal body and the drilling on both sides is $d = 5$ m. The blue triangles represent the locations of the two wellheads (40, 50, 8) and (60, 50, 8). The red five-pointed star represents the origin of the Cartesian coordinate system (50, 50, 0). There are a total of 5 survey lines in the survey area of inversion. The survey lines are laid on the ground. The measuring device is placed along the positive direction of the x-axis with 99 measuring electrodes separated by 1 m to pass through the top of the mountain. The distance between the survey lines is 5 m. The position coordinates of measuring point M (measuring electrode) are $x = 1$~99 m and $y = 40$~60 m, and the total number of measuring points is 495. The range of the source point A (source electrode) is from −5 m to −25 m downhole, with an interval of 5 m. Figure 13 shows the unstructured tetrahedral meshes used in the forwarding and inversion of the model. In order to improve the accuracy of the forward modeling and reduce the numerical simulation error near the source point, the forward meshes are refined in the vicinity of the measuring point, the source point, and the anomalous body. The total number of tetrahedral cells is 1105427. The inversion mesh is refined at the source and the measuring points. The total number of tetrahedral cells is 732012. The selection of inversion parameters is consistent with the inversion model under a flat surface. The number of inversion iterations is 9 times. The RMS change during the inversion process is shown in Figure 14(a). It can be seen from the figure that the relative RMS of the data is poorly fitted. The steady decline of RMS indicates that the L_BFGS inversion method in this paper has good convergence. Figure 14(b) shows the slice of resistivity 3D inversion result, while Figures 14(c) and 14(d) show the results slices at XOZ and YOZ profiles, respectively, under mountain topography. It can be seen from the figures that the inversion result of the

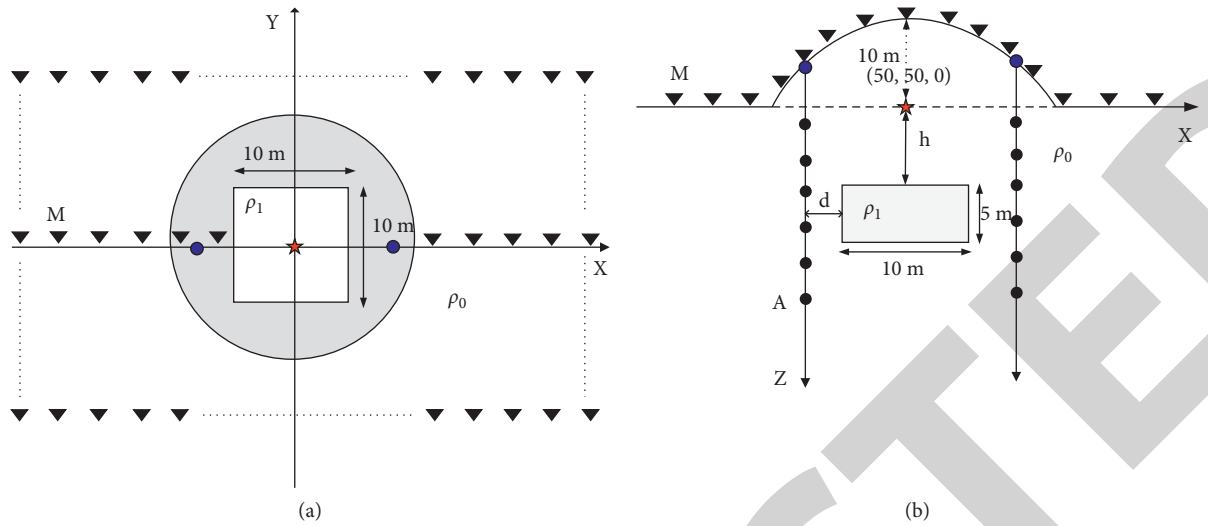

Figure 12: The geometry of mountain topographical model with a cube. (a) XOY plane view; (b) XOZ cross-sectional view.

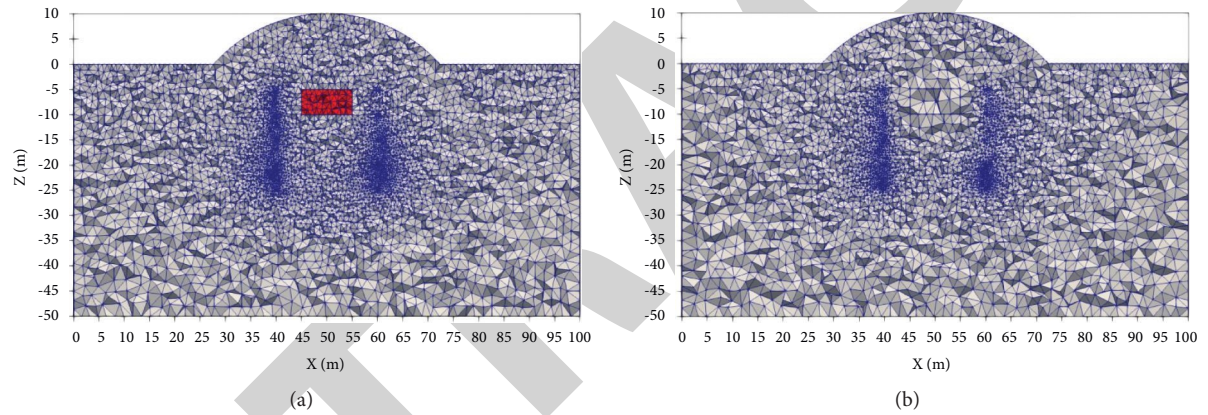

Figure 13: Forward and inversion grid of buried rectangular model under mountain topography. (a) Forward mesh; (b) inversion mesh.

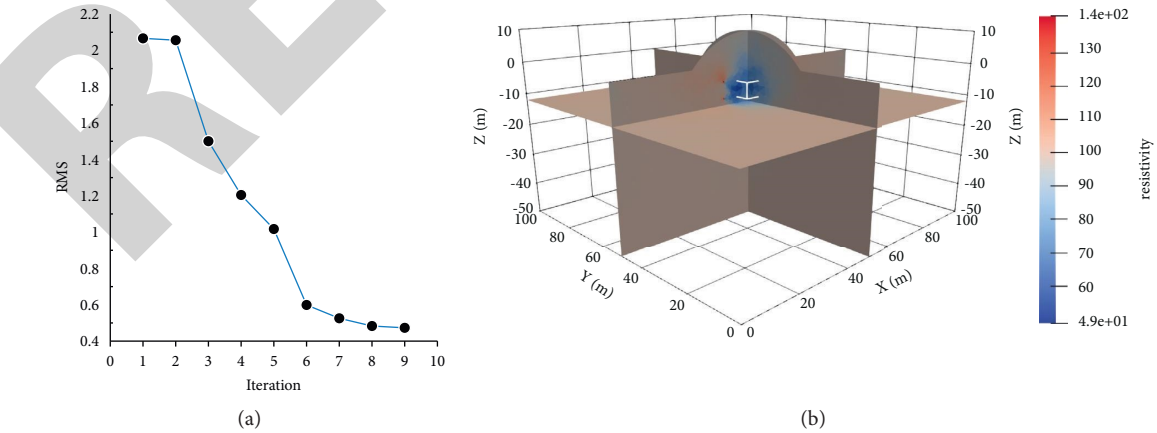

Figure 14: Continued.

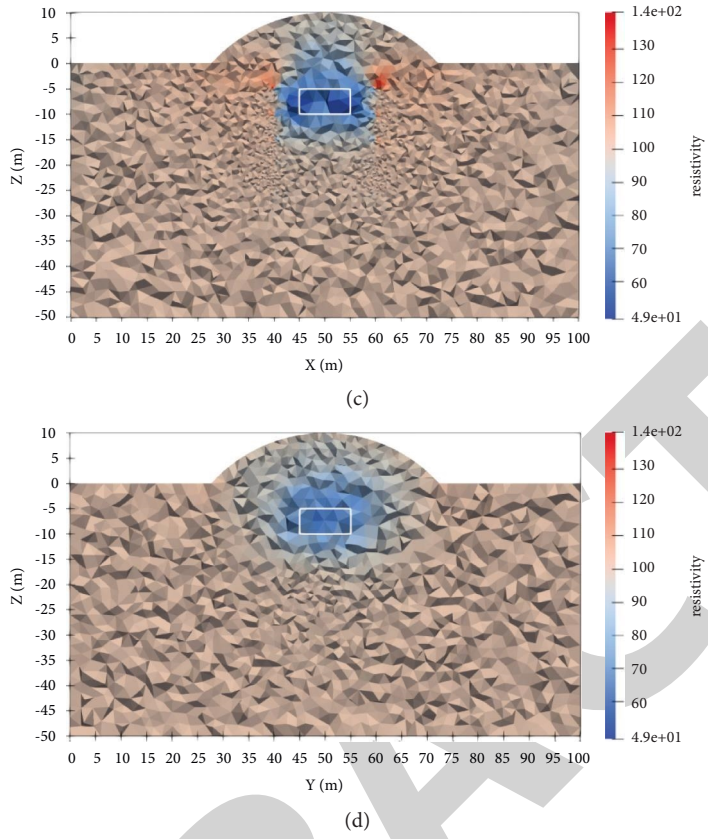

Figure 14: Inversion results of anomalous bodies under mountain topographical model. (a) The change in the relative RMS during the inversion process; (b) slice of resistivity 3D inversion result; (c) slice of resistivity inversion result at XOZ profile; (d) slice of resistivity inversion result at YOZ profile. The outline of the true model is indicated by the white rectangles.

synthetic model data is in good agreement with the real model. The location of the underground low-resistance anomaly is the same as the resistivity value, which effectively eliminates the influence of topography and verifies the effectiveness of the inversion method proposed in this paper.

5. Conclusion

This paper successfully realizes and develops the three-dimensional inversion of the borehole-to-surface resistivity method in nonflat surface topography based on the unstructured finite element method and the limited memory L_BFGS method. In order to verify the effectiveness of the proposed algorithm, numerical simulations of inversion of synthetic data for flat, valley, and mountain topographies are conducted. The obtained results validate that the proposed algorithm has high stability, and the inversion results better restore the distribution characteristics of low-resistance anomalies under various topography conditions. Future research will focus on utilizing the algorithm proposed in this paper to carry out the inversion of field-data applications resistivity. A reasonable application of a variety of information constraints can improve the accuracy of the position and shape of anomalies in the imaging results. Future research plan also includes the use of regularization and related techniques to achieve high-precision underground imaging with prior information.

Data Availability

No data were used to support this paper.

Conflicts of Interest

The authors declare that they have no conflicts of interest.

References

[1] J. X. Liu, R. Zhao, and Z. W. Guo, "Research progress of electromagnetic methods in the exploration of metal deposits," *Progress in Geophysics*, vol. 34, pp. 151–160, 2019.

[2] Q. T. Lv, X. P. Zhang, J. T. Tang et al., "Review on advancement in technology and equipment of geophysical exploration for metallic deposits in China," *Chinese Journal of Geophysics*, vol. 62, pp. 3629–3664, 2019.

[3] X. Wang, M. Huang, and L. Wan, "Joint 2D-DOD and 2D-DOA estimation for coprime EMVS-MIMO radar," *Circuits, Systems, and Signal Processing*, vol. 40, no. 6, pp. 2950–2966, 2021.

[4] J. He, L. Li, and T. Shu, "Sparse nested arrays with spatially spread orthogonal dipoles: high accuracy passive direction finding with less mutual coupling," *IEEE Transactions on Aerospace and Electronic Systems*, vol. 57, no. 4, pp. 2337–2345, 2021.

[5] F. Wen, J. Shi, and Z. Zhang, "Closed-form estimation algorithm for EMVS-MIMO radar with arbitrary sensor geometry," *Signal Processing*, vol. 186, pp. 108–117, 2021.

[6] H. Wang, X. Li, R. H. Jhaveri et al., "Sparse Bayesian learning based channel estimation in FBMC/OQAM industrial IoT networks," *Computer Communications*, vol. 176, pp. 40–45, 2021.

[7] J. Shi, F. Wen, and T. Liu, "Nested MIMO radar: coarrays, tensor modeling and angle estimation," *IEEE Transactions on Aerospace and Electronic Systems*, vol. 57, pp. 573–585, 2020.

[8] H. Wang, L. Xu, Z. Yan, and T. A. Gulliver, "Low-complexity MIMO-FBMC sparse channel parameter estimation for industrial big data communications," *IEEE Transactions on Industrial Informatics*, vol. 17, no. 5, pp. 3422–3430, 2021.

[9] L. Wan, K. Liu, Y. C. Liang, and Z. Tong, "DOA and polarization estimation for non-circular signals in 3-D millimeter wave polarized massive MIMO systems," *IEEE Wireless Communications*, vol. 20, pp. 3152–3167, 2017.

[10] X. P. Wu, Y. Liu, and W. Wang, "3D resistivity inversion incorporating topography based on unstructured meshes," *Chinese Journal of Geophysics*, vol. 58, pp. 2706–2717, 2015.

[11] Z. Wang, A. P. Wu, and G. Li, "Forward modeling of borehole-ground induced polarization method under undulating topography," *Geophysical Prospecting for Petroleum*, vol. 57, no. 6, pp. 927–935, 2018.

[12] J. T. Tang, J. F. Zhang, B. Feng, J.-Y. Lin, and C.-S. Liu, "Determination of borders for resistive oil and gas reservoirs by deviation rate using the hole-to-surface resistivity method," *Chinese Journal of Geophysics*, vol. 50, pp. 926–931, 2007.

[13] Y. Li and K. Spitzer, "Finite element resistivity modelling for three-dimensional structures with arbitrary anisotropy," *Physics of the Earth and Planetary Interiors*, vol. 150, no. 1-3, pp. 15–27, 2005.

[14] X. Wu, "A 3-D finite-element algorithm for DC resistivity modelling using the shifted incomplete Cholesky conjugate gradient method," *Geophysical Journal International*, vol. 154, no. 3, pp. 947–956, 2003.

[15] X. P. Wu and T. T. Wang, "A 3-D finite-element resistivity forward modeling using conjugate gradient algorithm," *Chinese Journal of Geophysics*, vol. 46, pp. 428–432, 2003.

[16] Y. Li and K. Spitzer, "Three-dimensional DC resistivity forward modelling using finite elements in comparison with finite-difference solutions," *Geophysical Journal International*, vol. 151, no. 3, pp. 924–934, 2002.

[17] M. Blome, H. R. Maurer, and K. Schmidt, "Advances in three-dimensional geoelectric forward solver techniques," *Geophysical Journal International*, vol. 176, no. 3, pp. 740–752, 2009.

[18] T. Günther, C. Rücker, and K. Spitzer, "Three-dimensional modelling and inversion of dc resistivity data incorporating topography - II. Inversion," *Geophysical Journal International*, vol. 166, no. 2, pp. 506–517, 2006.

[19] C. Rücker, T. Günther, and K. Spitzer, "Three-dimensional modelling and inversion of dc resistivity data incorporating topography-I Modelling," *Geophysical Journal International*, vol. 166, no. 2, pp. 495–505, 2006.

[20] Z. Ren and J. Tang, "3D direct current resistivity modeling with unstructured mesh by adaptive finite-element method," *Geophysics*, vol. 75, no. 1, pp. H7–H17, 2010.

[21] Z. Ren and J. Tang, "A goal-oriented adaptive finite-element approach for multi-electrode resistivity system," *Geophysical Journal International*, vol. 199, no. 1, pp. 136–145, 2014.

[22] Z. Ren, L. Qiu, J. Tang, X. Wu, X. Xiao, and Z. Zhou, "3-D direct current resistivity anisotropic modelling by goal-oriented adaptive finite element methods," *Geophysical Journal International*, vol. 212, no. 1, pp. 76–87, 2018.

[23] Y. Sasaki, "3-D resistivity inversion using the finite-element method," *Geophysics*, vol. 59, no. 12, pp. 1839–1848, 1994.

[24] W. Wang, X. Wu, and K. Spitzer, "Three-dimensional DC anisotropic resistivity modelling using finite elements on unstructured grids," *Geophysical Journal International*, vol. 193, no. 2, pp. 734–746, 2013.

[25] B. Zhou and S. A. Greenhalgh, "Finite element three dimensional direct current resistivity modelling: accuracy and efficiency considerations," *Geophysical Journal International*, vol. 145, pp. 679–688, 2001.

[26] J. Zhang, R. L. Mackie, and T. R. Madden, "3-D resistivity forward modeling and inversion using conjugate gradients," *Geophysics*, vol. 60, no. 5, pp. 1313–1325, 1995.

[27] K. Spitzer, "A 3-D finite-difference algorithm for DC resistivity modelling using conjugate gradient methods," *Geophysical Journal International*, vol. 123, no. 3, pp. 903–914, 1995.

[28] X. Wu, Y. Xiao, C. Qi, and T. Wang, "Computations of secondary potential for 3D DC resistivity modelling using an incomplete Choleski conjugate-gradient method," *Geophysical Prospecting*, vol. 51, no. 6, pp. 567–577, 2003.

[29] S. Zhao and M. J. Yedlin, "Some refinements on the finite-difference method for 3-D dc resistivity modeling," *Geophysics*, vol. 61, no. 5, pp. 1301–1307, 1996.

[30] X. P. Wu, G. M. Xu, and S. C. Li, "The calculation of three-dimensional geoelectric field of point source by incomplete cholesky conjugate gradient method," *Chinese Journal of Geophysics*, vol. 41, pp. 848–855, 1998.

[31] J. T. Tang, F. Y. Wang, and Z. Y. Ren, "2.5 D resistivity modeling by adaptive finite-element method with unstructured triangulation," *Chinese Journal of Geophysics*, vol. 53, pp. 708–716, 2010.

[32] Z. Y. Ren and J. T. Tang, "Finite element modeling of 3-D DC resistivity using locally refined unstructured meshes," *Chinese Journal of Geophysics*, vol. 52, pp. 2627–2634, 2009.

[33] N. Y. Gundogdu and M. E. Candansayar, "Three-dimensional regularized inversion of DC resistivity data with different stabilizing functionals," *Geophysics*, vol. 83, pp. E399–E407, 2018.

[34] L. G. Guo, G. L. Dai, and B. C. Yang, "3D resistivity inversion with multiple priori-information constraint," *Oil Geophysical Prospecting*, vol. 53, pp. 1333–1340, 2018.

[35] R. H. Peng, X. Y. Hu, and B. Han, "3D inversion of frequency-domain CSEM data based on Gauss-Newton optimization," *Chinese Journal of Geophysics*, vol. 59, pp. 3470–3481, 2016.

[36] D. W. Oldenburg, E. Haber, and R. Shekhtman, "Three dimensional inversion of multisource time domain electromagnetic data," *Geophysics*, vol. 78, no. 1, pp. E47–E57, 2013.

[37] A. Pidlisecky, E. Haber, and R. Knight, "RESINVM3D: a 3D resistivity inversion package," *Geophysics*, vol. 72, no. 2, pp. H1–H10, 2007.

[38] X. Cao, X. Huang, C. Yin, L. Yan, and B. Zhang, "3D MT anisotropic inversion based on unstructured finite- element method," *Journal of Environmental & Engineering Geophysics*, vol. 26, pp. 46–60, 2021.

[39] Z. J. Hui, C. C. Yin, Y. H. Liu, B. Zhang, X. Y. Ren, and C. Wang, "3D inversion of time-domain marine EM data based on unstructured finite-element method," *Chinese Journal of Geophysics*, vol. 63, pp. 3167–3179, 2020.

[40] H. Yu, J. Z. Deng, H. Chen et al., "Three-dimensional magnetotelluric inversion under topograpkic relief based on the limited-memory quasi-Newton algorithm(L_BFGS)," *Chinese Journal of Geophysics*, vol. 62, pp. 3175–3188, 2019.

Hindawi
International Journal of Antennas and Propagation
Volume 2023, Article ID 9838045, 1 page
https://doi.org/10.1155/2023/9838045

Retraction

Retracted: Channel Estimation for Switch-Based Millimeter-Wave Communications via Atomic Norm

International Journal of Antennas and Propagation

Received 19 December 2023; Accepted 19 December 2023; Published 20 December 2023

This article has been retracted by Hindawi following an investigation undertaken by the publisher [1]. This investigation has uncovered evidence of one or more of the following indicators of systematic manipulation of the publication process:

(1) Discrepancies in scope

(2) Discrepancies in the description of the research reported

(3) Discrepancies between the availability of data and the research described

(4) Inappropriate citations

(5) Incoherent, meaningless and/or irrelevant content included in the article

(6) Manipulated or compromised peer review

The presence of these indicators undermines our confidence in the integrity of the article's content and we cannot, therefore, vouch for its reliability. Please note that this notice is intended solely to alert readers that the content of this article is unreliable. We have not investigated whether authors were aware of or involved in the systematic manipulation of the publication process.

Wiley and Hindawi regrets that the usual quality checks did not identify these issues before publication and have since put additional measures in place to safeguard research integrity.

We wish to credit our own Research Integrity and Research Publishing teams and anonymous and named external researchers and research integrity experts for contributing to this investigation.

The corresponding author, as the representative of all authors, has been given the opportunity to register their agreement or disagreement to this retraction. We have kept a record of any response received.

References

[1] T. Ma, X. Fan, and X. Wu, "Channel Estimation for Switch-Based Millimeter-Wave Communications via Atomic Norm," *International Journal of Antennas and Propagation*, vol. 2021, Article ID 7356963, 9 pages, 2021.

Hindawi
International Journal of Antennas and Propagation
Volume 2021, Article ID 7356963, 9 pages
https://doi.org/10.1155/2021/7356963

Research Article

Channel Estimation for Switch-Based Millimeter-Wave Communications via Atomic Norm

Tao Ma,[1,2] **Xiangning Fan**,[1] **and Xiaohuan Wu**[3]

[1]*School of Information Science and Engineering, Southeast University, Nanjing 210096, China*
[2]*NARI Group Corporation, Nanjing, China*
[3]*School of Telecommunication and Information Engineering, Nanjing University of Posts and Telecommunications, Nanjing 210003, China*

Correspondence should be addressed to Tao Ma; 230198982@seu.edu.cn

Received 15 July 2021; Revised 16 August 2021; Accepted 31 August 2021; Published 13 September 2021

Academic Editor: Fangqing Wen

Channel estimation is a challenging issue in millimeter-wave massive multiple-input-multiple-output (MIMO) communication systems due to the large number of antennas in the transceiver. Existing methods are usually based on phase shifters which may not be a simple circuit at mmWave band. In this paper, we construct a switch-based architecture for analog processors from the coarray point of view and then propose an atomic ℓ_0-norm minimization problem. We then propose an efficient algorithm to solve this problem based on Wirtinger projection. Since the proposed method requires no angle discretization, it does not suffer from grid mismatch effect that greatly deteriorates the estimation performance of grid-based channel estimation methods. Compared to the atomic norm minimization (ANM) method, our method does not involve vectorization of the channel matrix and hence the dimensionality of the problem is much less than that of ANM. We show that our method is able to provide comparable estimation performance to ANM but with much less computational time. Extensive simulations are carried out to verify the effectiveness of our proposed method.

1. Introduction

Millimeter-wave (mmWave) communications is a key technology for the 5th generation (5G) mobile communication system. Compared to the sub-6 GHz communication system, the main differentiating factor for mmWave communication systems is the tenfold increase in carrier frequency. This difference can provide multigigabit services which are able to meet future traffic demand [1]. However, the mmWave signals in the high-frequency band suffer from large pathloss; thus, the power of the received signal to be detected by the receiver can be negligible and reliable communication cannot be achieved. To solve this problem, high-resolution beamforming by using massive multiple-input-multiple-output (MIMO) is essential in combating the large pathloss for mmWave communication systems. By using massive MIMO, the transmitter can concentrate the transmitted power on a specific direction to highly improve the power of the received signal. On the other hand, the small wavelength of mmWave signal allows hundreds of antennas to be accommodated within a reasonable physical size, e.g., the 8×8 antenna array in a hand-hold unit, making high-resolution beamforming with large-scale antenna arrays possible.

Nevertheless, high-resolution beamforming requires accurate full channel state information (CSI) which is difficult to obtain due to the large number of antennas. Conventional channel estimation methods suffer from high training overhead and complexity [2, 3]. To address this issue, a codebook-based beam searching strategy is proposed to find the correct pair between the beamformer and combiner [4, 5]. Although the hierarchical search can be incorporated to reduce complexity to some extent, the performance heavily depends on the predefined training beam codebook [6]. Another approach is to exploit the sparse nature of the mmWave channel. Due to large

pathloss, there only exist a few ray components between the transmitter and receiver, i.e., the channel is sparse in space [7, 8]. With a high degree of freedom provided by a large number of antennas, we are able to find the angle of arrival (AoA) and angle of departure (AoD) as well as the complex gain of each ray [9, 10]. Then, the channel estimation problem can be formulated as an angle estimation one. Existing methods include compressive sensing- (CS-) based methods [11–13] and subspace-based methods [14–17]. CS-based methods formulate the channel estimation problem as a sparse signal recovery one and utilize the CS recovery methods such as orthogonal matching pursuit (OMP) [18] to retrieve the sparse signal where the indices of nonzero elements indicate the AoAs and AoDs. The subspace method in [14, 19] employs beamspace 2-D MUSIC to estimate the channel. However, for CS-based methods, formulating the sparse model requires discretizing the angle space into a set of predefined angle grids and then assuming that the AoAs and AoDs exactly lie on the grids [20, 21]. Since the angle space is continuous rather than discrete, this discretizing procedure will bring in nonnegligible bias between the true angle and the closest grid. We call this the grid mismatch effect. Thus, a dense grid set is appealing since its bias can be small. However, since the dimensionality of the sparse model is proportional to the size of the grid set, a dense grid set may suffer from high computational cost. Moreover, a dense grid may conflict the restricted isometry property (RIP), and thus, it is not easy to find the balance between accuracy and efficiency. For 2-D MUSIC, finding the angles also require discretizing, and thus, it may also encounter computational issues when the grid set is large.

Recently, a gridless method which does not require angle discretization is proposed [22–26]. It employs the atomic norm minimization (ANM) concept into angle estimation and then reformulates the channel estimation problem as the semidefinite programming (SDP) which can be solved by CVX [27]. The ANM method does not suffer from the accuracy and efficiency issues caused by gridding. Theoretical analysis shows that the ANM method is an asymptotic maximum likelihood (ML) estimator [28] and its complexity is also immune to the size of the grid set. Although ANM shows excellent estimation performance in angle estimation [29] or channel estimation [24, 25], the main obstacle of the ANM estimator is the computational issue since solving SDP by CVX is time-consuming. Especially, in the full-dimensional MIMO case, ANM requires to solve an n^2-dimensional SDP, where n denotes the number of antennas on the transmitter or receiver which may be large [24]. Thus, it is urgent to derive a new algorithm for ANM methods to reduce computational complexity.

The ANM-based channel estimation method [24] only considers the phase shifters in hybrid architecture of the mmWave system. The hybrid architecture can achieve near-optimal performance compared to the fully digital transceivers [1]. However, the phase shifter-based network is not a simple circuit at the mmWave band [30]. Another type of architecture is to employ switch-based networks [31]. It is shown that the switch-based network is preferred in a range of operating conditions [30]. From the viewpoint of array structures, antenna selection is relative to sparse arrays. Different selection strategies result in different sparse array architectures. From the coarray perspective [32], the antenna selection strategy having the longest uniform coarray part enjoys the best estimation performance. Several recently proposed sparse arrays such as coprime array [32], nested array [33, 34], and fractal array [35] have good coarray property and can be used in competitive antenna selection strategies for mmWave channel estimation. The coprime array has been incorporated into mmWave channel estimation in [36], and the nested array has been used in channel estimation and tracking in [37]. However, these papers only consider a single user with one antenna rather than multiuser or multiantenna.

In this paper, we consider the switch architecture for the analog processor in channel estimation of mmWave massive MIMO systems. We first exploit the antenna selection from the coarray point of view and then propose an atomic ℓ_0-norm minimization problem. Compared to ANM, our method has much less dimensionality of the problem and hence is much more efficient than ANM. We also propose an efficient algorithm to solve this problem based on Wirtinger projection. Our method requires no angle discretization and hence is immune to the grid mismatch effect. We also carry out simulations to show the superiority of our method.

Notations: $\mathbb{C}$ and $\mathbb{Z}$ denote the sets of complex numbers and integers, respectively. $\mathbf{A}^*$, $\mathbf{A}^T$, and $\mathbf{A}^H$ denote the conjugate, transpose, and conjugate transpose of matrix $\mathbf{A}$, respectively. $\mathrm{vec}(\mathbf{A})$ denotes the vectorization operator that stacks matrix $\mathbf{A}$ column by column. $\mathbf{A} \odot \mathbf{B}$ and $\mathbf{A} \otimes \mathbf{B}$ are the Khatri–Rao and Kronecker products of matrices $\mathbf{A}$ and $\mathbf{B}$, respectively. $\mathrm{tr}(\bullet)$ and $\mathrm{rank}(\bullet)$ denote the trace and rank operators. $\mathbf{I}_N$ denotes the identity matrix of size $N \times N$. $\|\mathbf{A}\|_1$, $\|\mathbf{A}\|_2$, and $\|\mathbf{A}\|_F$ denote the ℓ_1-norm, ℓ_2-norm, and Frobenius norm of $\mathbf{A}$, respectively. $\mathbf{A} \geq 0$ means that matrix $\mathbf{A}$ is positive semidefinite (PSD). For a vector $\mathbf{x}$, $\mathrm{diag}(\mathbf{x})$ denotes a diagonal matrix with the diagonal elements being the elements of vector $\mathbf{x}$ in turn.

The rest of this paper is organized as follows: Section 2 introduces the coarray concept and the system model. Section 3 provides our proposed method. Extensive simulations are provided in Section 4, and Section 5 concludes the whole paper.

2. Preliminary and System Model

2.1. Coarray Concept. In array signal processing, the aperture of an array is an important factor for angle estimation. A larger array aperture can bring in high estimation accuracy and super resolution. But, increasing the inter-element spacing is not a positive way to extend the aperture because a uniform linear array (ULA) with interelement spacing being greater than half-wavelength suffers from angle ambiguity. In this case, pseudo AoAs or AoDs will prevent us from correctly identifying the true positions. Fortunately, we can exploit the coarray concept to solve this problem. It is shown that we can construct a sparse linear array (SLA) with much larger aperture if its coarray has a long uniform part without holes [32]. Denote $\Omega = \{\Omega_1, \Omega_2, \ldots, \Omega_M\}$ as the antenna

indices where $\Omega_1 < \Omega_2 < \cdots < \Omega_M$ and each element is a positive integer. Then, the coarray is defined as

$$\mathscr{D} = \{m_1 - m_2 + 1: \quad m_1, m_2 \in \mathbf{\Omega}, m_1 \geq m_2\}. \tag{1}$$

For instance, denote the array $\Omega = \{1, 2, 5, 7\}$; then, its coarray $\mathscr{D} = \{1, 2, 3, 4, 5, 6, 7\}$ which can be regarded as a 7-element ULA and has a large aperture without angle ambiguity. Thus, some special SLAs such as coprime array and nested array having a larger aperture can provide super resolution and satisfying performance.

2.2. System Model. Consider the mmWave massive MIMO communication system with a single user shown in Figure 1, where the transmitter is equipped with M_t RF chains and $N_t > M_t$ antennas and the receiver is equipped with M_r RF chains and $N_r > M_r$ antennas. The interelement spacing of each array is set to half-wavelength to avoid angle ambiguity. The analog architectures of both the transmitter and receiver are implemented by using switches. In particular, each switch is connected to a specific RF chain and can build connection between the RF chain and any antenna. The antennas selected by the switches are activated to transmit data, while other antennas remain idle. The selection strategy can be specified by a $\{0, 1\}$ matrix denoted by $\mathbf{F} \in \mathbb{C}^{N_t \times M_t}$ for the transmitter and $\mathbf{W} \in \mathbb{C}^{N_r \times M_r}$ for the receiver. Let $\Omega_F = \{\Omega_1, \Omega_2, \ldots, \Omega_{M_t}\}$ and $\mathbf{\Phi}_W = \{\Phi_1, \Phi_2, \ldots, \Phi_{M_r}\}$ denote the element indices of the transmit antennas and receiver antennas, respectively, where $\Omega_1 < \Omega_2 < \cdots < \Omega_{M_t} \leq N_t$, $\Phi_1 < \Phi_2 < \cdots < \Phi_{M_r} \leq N_r$, and each element is a positive integer. In the following, we provide a simple example to better demonstrate the selection matrix. For simplicity, we only consider the transmitter. Let $N_t = 7$ and $M_t = 4$; if we select the antenna indexed by $\mathbf{\Omega}_F = \{1, 2, 5, 7\}$, then the antenna array is an SLA and the selection matrix $\mathbf{F}$ is as follows:

$$\mathbf{F} = \begin{bmatrix} 1 & 0 & 0 & 0 \\ 0 & 1 & 0 & 0 \\ 0 & 0 & 0 & 0 \\ 0 & 0 & 0 & 0 \\ 0 & 0 & 1 & 0 \\ 0 & 0 & 0 & 0 \\ 0 & 0 & 0 & 1 \end{bmatrix}. \tag{2}$$

From equation (2), it can be seen that the m-th column of matrix $\mathbf{F}$ contains all zeros but a single one at the Ω_m-th position. Note that if we let $\mathbf{\Omega}_F = \{1, 2, 3, 4\}$, the transmitted antenna array is a short ULA having a shorter aperture than the SLA case. The discrete-time transmitted signal is therefore given by

$$\mathbf{x} = \mathbf{F}\mathbf{s}, \tag{3}$$

where $\mathbf{s} \in \mathbb{C}^{M_t}$ denotes the signal after the digital processor. For simplicity, we consider a narrowband block-fading propagation channel which gives that

$$\mathbf{y}_s = \mathbf{W}^H\mathbf{H}\mathbf{F}\mathbf{s} + \mathbf{W}^H\mathbf{n}, \tag{4}$$

where $\mathbf{y}_s \in \mathbb{C}^{M_r}$ denotes the received signal at the RF chains, $\mathbf{H} \in \mathbb{C}^{N_r \times N_t}$ denotes the channel matrix, and $\mathbf{n} \in \mathbb{C}^{N_r}$ is the additive Gaussian noise with zero mean. During M_t successive time slots, the received signal at the receiver can be given as

$$\mathbf{Y} = \mathbf{W}^H\mathbf{H}\mathbf{F}\mathbf{S} + \mathbf{W}^H\mathbf{N}, \tag{5}$$

where $\mathbf{S}$ is the transmitted signal and $\mathbf{N}$ is the noise matrix. For the training phase, we assume $\mathbf{S} = \mathbf{I}_{M_t}$, and therefore,

$$\mathbf{Y} = \mathbf{W}^H\mathbf{H}\mathbf{F} + \mathbf{W}^H\mathbf{N}. \tag{6}$$

Our goal is to estimate $\mathbf{H}$ given $\mathbf{Y}$.

2.3. Channel Model. In the mmWave massive MIMO system, the number of rays between the transmitter and receiver is limited. The channel $\mathbf{H}$ can be expressed as

$$\mathbf{H} = \sum_{k=1}^{K} \alpha_k \mathbf{a}_r(\theta_k)\mathbf{a}_t^H(\phi_k), \tag{7}$$

where α_k, θ_k, and ϕ_k denote the complex gain, AoA, and AoD of the k-th ray, respectively, and $\mathbf{a}_t(\phi_k)$ and $\mathbf{a}_r(\theta_k)$ denote the steering vectors of the transmitter and receiver arrays with respect to the k-th ray, respectively, and can be given as

$$\begin{aligned} \mathbf{a}_t(\phi_k) &= \left[1, e^{j\cdot 1\cdot((2\pi\, d)/\lambda)\sin(\phi_k)}, \ldots, e^{j\cdot(N_t-1)\cdot((2\pi\, d)/\lambda)\sin(\phi_k)}\right]^T, \\ \mathbf{a}_r(\theta_k) &= \left[1, e^{j\cdot 1\cdot((2\pi\, d)/\lambda)\sin(\theta_k)}, \ldots, e^{j\cdot(N_r-1)\cdot((2\pi\, d)/\lambda)\sin(\theta_k)}\right]^T, \end{aligned} \tag{8}$$

where λ and d denote the wavelength and the spacing between adjacent antennas, respectively. Equation (7) can be compactly rewritten as

$$\mathbf{H} = \mathbf{A}_r\mathbf{\Sigma}\mathbf{A}_t^H, \tag{9}$$

where $\mathbf{A}_t = [\mathbf{a}_t(\phi_1), \mathbf{a}_t(\phi_2), \ldots, \mathbf{a}_t(\phi_K)]$, $\mathbf{A}_r = [\mathbf{a}_r(\theta_1), \mathbf{a}_r(\theta_2), \ldots, \mathbf{a}_r(\theta_K)]$, and $\mathbf{\Sigma} = \mathrm{diag}([\alpha_1, \ldots, \alpha_K])$. Substituting equation (9) into model (6), we have

$$\mathbf{Y} = \mathbf{W}^H\mathbf{A}_r\mathbf{\Sigma}\mathbf{A}_t^H\mathbf{F} + \mathbf{W}^H\mathbf{N}. \tag{10}$$

Vectorizing $\mathbf{Y}$ results in,

$$\begin{aligned} \mathbf{y} &= \mathrm{vec}(\mathbf{Y}) \\ &= \left(\mathbf{F}^T \otimes \mathbf{W}^H\right)\mathbf{h} + \mathrm{vec}\left(\mathbf{W}^H\mathbf{N}\right) \\ &= \left(\mathbf{F}^T \otimes \mathbf{W}^H\right)\left(\mathbf{A}_t^* \odot \mathbf{A}_r\right)\mathbf{z} + \mathrm{vec}\left(\mathbf{W}^H\mathbf{N}\right), \end{aligned} \tag{11}$$

where $\mathbf{h} = \mathrm{vec}(\mathbf{H})$ and $\mathbf{z} = [\alpha_1, \ldots, \alpha_K]^T$.

3. The Proposed Channel Estimation Method

3.1. The Proposed Method. Different from the ANM-based method in [23], we directly operate on model (10) rather than its vectorized version. First, we set up the following atom set:

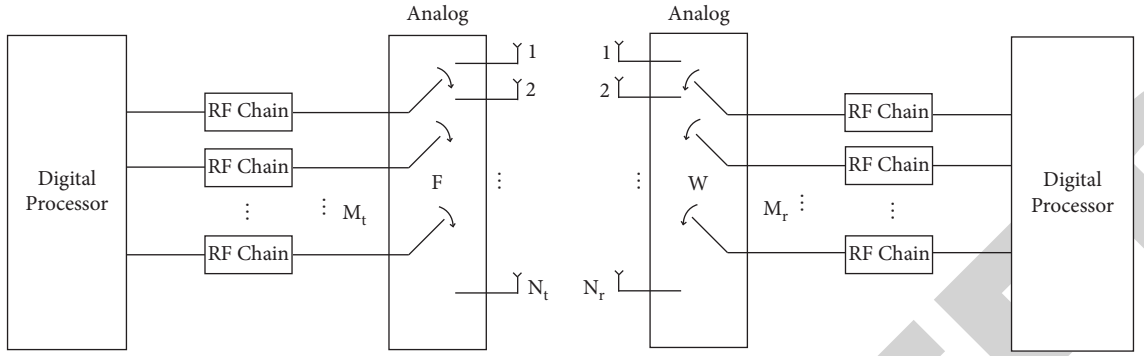

Figure 1: Block diagram of the mmWave massive MIMO communication system with an analog processor implemented using switches.

$$\widetilde{\mathscr{A}} = \left\{ \mathbf{a}_r(\theta)\mathbf{a}_t^H(\phi): \quad \theta, \phi \in (-90^\circ, 90^\circ] \right\}, \tag{12}$$

based on which we can formulate the atomic ℓ_0-norm of the channel matrix $\mathbf{H}$ as

$$\|\mathbf{H}\|_{\widetilde{\mathscr{A}},0} = \inf\left\{ K: \mathbf{H} = \sum_{k=1}^{K} \alpha_k \widetilde{\mathbf{A}}, \quad \widetilde{\mathbf{A}} \in \widetilde{\mathscr{A}}, \alpha_k \in \mathbb{C} \right\}. \tag{13}$$

We then propose the following optimization problem:

$$\min_{\mathbf{H}} \|\mathbf{H}\|_{\widetilde{\mathscr{A}},0} \text{ s.t. } \left\|\mathbf{Y} - \mathbf{W}^H\mathbf{H}\mathbf{F}\right\|_F \le \beta. \tag{14}$$

However, the above problem is a semi-infinite programming (SIP) which cannot be efficiently solved in polynomial time. To solve this problem, we have the following theorem.

Theorem 1. *Assume that* $K < \min(N_t, N_r)$, *then* $\|\mathbf{H}\|_{\widetilde{\mathscr{A}},0}$ *equals the optimal value of the following rank minimization problem:*

$$\begin{aligned} &\min_{\mathbf{u},\mathbf{v},\mathbf{W}} \quad \operatorname{rank}[\mathbf{W}], \\ &\text{s.t.} \quad \mathbf{W} = \begin{bmatrix} \mathbf{T}(\mathbf{v}) & \mathbf{H}^H \\ \mathbf{H} & \mathbf{T}(\mathbf{u}) \end{bmatrix} \ge 0, \end{aligned} \tag{15}$$

where $\mathbf{T}(\mathbf{u})$ *and* $\mathbf{T}(\mathbf{v})$ *are Toeplitz matrices.*

Proof. First, for arbitrary decomposition of $\mathbf{H}$ as $\mathbf{H} = \sum_{k=1}^{K} \alpha_k \mathbf{a}_r(\theta_k)\mathbf{a}_t^H(\phi_k)$, we can construct matrices $\mathbf{T}(\mathbf{u}) = \sum_{k=1}^{K} |\alpha_k|^2 \mathbf{a}_r(\theta_k)\mathbf{a}_r^H(\theta_k)$ and $\mathbf{T}(\mathbf{v}) = \sum_{k=1}^{K} \mathbf{a}_t(\phi_k)\mathbf{a}_t^H(\phi_k)$ and then we have

$$\begin{aligned} \widetilde{\mathbf{W}} &= \begin{bmatrix} \mathbf{T}(\mathbf{v}) & \mathbf{H}^H \\ \mathbf{H} & \mathbf{T}(\mathbf{u}) \end{bmatrix} \\ &= \sum_{k=1}^{K} \begin{bmatrix} \mathbf{a}_t(\phi_k)\mathbf{a}_t^H(\phi_k) & \alpha_k^H \mathbf{a}_t(\phi_k)\mathbf{a}_r^H(\theta_k) \\ \alpha_k \mathbf{a}_r(\theta_k)\mathbf{a}_t^H(\phi_k) & |\alpha_k|^2 \mathbf{a}_r(\theta_k)\mathbf{a}_r^H(\theta_k) \end{bmatrix} \\ &= \sum_{k=1}^{K} \begin{bmatrix} \mathbf{a}_t(\phi_k) \\ \alpha_k \mathbf{a}_r(\theta_k) \end{bmatrix} \begin{bmatrix} \mathbf{a}_t(\phi_k) \\ \alpha_k \mathbf{a}_r(\theta_k) \end{bmatrix}^H \ge 0. \end{aligned} \tag{16}$$

It follows that the optimal solution of (15) $K^\circ \le \operatorname{rank}(\widetilde{\mathbf{W}}) = K = \|\mathbf{H}\|_{\widetilde{\mathscr{A}},0}$. On the other hand, if we find the optimal solution of (15) as $\{\mathbf{H}^\circ, \mathbf{u}^\circ, \mathbf{v}^\circ\}$, then we have $\operatorname{rank}(\mathbf{W}^\circ) = K^\circ \le K$. It follows from the Vandermonde decomposition [38] that $\mathbf{T}(\mathbf{u}^\circ) = \sum_{k=1}^{K^\circ} |\alpha_k|^2 \mathbf{a}_r(\theta_k^\circ)\mathbf{a}_r^H(\theta_k^\circ)$ and $\mathbf{T}(\mathbf{v}^\circ) = \sum_{k=1}^{K^\circ} \mathbf{a}_t(\phi_k^\circ)\mathbf{a}_t^H(\phi_k^\circ)$. Then, since $\mathbf{H}^\circ$ lies in the column space of $\mathbf{T}(\mathbf{u}^\circ)$ and row space of $\mathbf{T}(\mathbf{v}^\circ)$, there exists $\widetilde{\alpha}^\circ$ such that $\mathbf{H}^\circ = \sum_{k=1}^{K^\circ} \widetilde{\alpha}_k^\circ \mathbf{a}_r(\theta_k^\circ)\mathbf{a}_t^H(\phi_k^\circ)$. Hence, $\|\mathbf{H}\|_{\widetilde{\mathscr{A}},0} \le K^\circ$. Therefore, it can be concluded that $\|\mathbf{H}\|_{\widetilde{\mathscr{A}},0} = K^\circ$. □

According to Theorem 1, model (14) can be rewritten as

$$\begin{aligned} &\min_{\mathbf{H},\mathbf{u},\mathbf{v},\mathbf{W}} \quad \operatorname{rank}[\mathbf{W}], \\ &\text{s.t.} \quad \mathbf{W} = \begin{bmatrix} \mathbf{T}(\mathbf{v}) & \mathbf{H}^H \\ \mathbf{H} & \mathbf{T}(\mathbf{u}) \end{bmatrix} \ge 0, \\ &\qquad \left\|\mathbf{Y} - \mathbf{W}^H\mathbf{H}\mathbf{F}\right\|_F \le \beta. \end{aligned} \tag{17}$$

It can be seen that, compared to the ANM model [23], the proposed model in (17) has much smaller problem dimensionality.

However, directly solving this model is difficult due to the nonconvex rank operator. One possible approach is to relax the rank operator to the trace operator. The relaxed problem is convex and can be solved by CVX. Nevertheless, CVX is also an inefficient solver. In the following, we propose an efficient method to solve (17) based on Wirtinger projection.

First, we define two matrices sets as

$$\begin{aligned} &\mathscr{M} = \{\mathbf{M}: \operatorname{rank}(\mathbf{M}) \le K\}, \\ &\mathscr{N} = \left\{ \mathbf{N}: \mathbf{N} = \begin{bmatrix} \mathbf{V} & \mathbf{H}^H \\ \mathbf{H} & \mathbf{U} \end{bmatrix} \ge 0, \left\|\mathbf{Y} - \mathbf{W}^H\mathbf{H}\mathbf{F}\right\|_F \le \beta \right\}, \end{aligned} \tag{18}$$

where $\mathbf{U}$ and $\mathbf{V}$ have Toeplitz structure. Solving model (17) is equivalent to finding a matrix that both in $\mathscr{M}$ and $\mathscr{N}$ or solving the following problem:

$$\min_{\mathbf{M}\in\mathscr{M},\mathbf{N}\in\mathscr{N}} \|\mathbf{M} - \mathbf{N}\|_F^2. \tag{19}$$

One effective way is to alternatively update $\mathbf{M}$ and $\mathbf{N}$ until convergence. Based on the Wirtinger strategy [39], we formulate the following update rule to solve problem (19):

$$\begin{aligned}\mathbf{M}^{(t+1)} &= \mathscr{P}_{\mathscr{M}}\left(\mathbf{M}^{(t)} - \delta_1\left(\mathbf{M}^{(t)} - \mathbf{N}^{(t)}\right)\right),\\ \mathbf{N}^{(t+1)} &= \mathscr{P}_{\mathscr{N}}\left(\mathbf{N}^{(t)} - \delta_2\left(\mathbf{N}^{(t)} - \mathbf{M}^{(t+1)}\right)\right),\end{aligned} \tag{20}$$

where the superscript (t) denotes the t-th iteration, $\mathscr{P}_{\mathscr{M}}(\bullet)$ and $\mathscr{P}_{\mathscr{N}}(\bullet)$ denote the projection procedures onto matrices sets $\mathscr{M}$ and $\mathscr{N}$, respectively, and δ_1 and δ_2 are two user-defined parameters. The next target is to find the two projection operators $\mathscr{P}_{\mathscr{M}}(\bullet)$ and $\mathscr{P}_{\mathscr{N}}(\bullet)$.

Projection $\mathscr{P}_{\mathscr{M}}(\mathbf{X})$ is to find the best rank-K approximation that can be formulated as follows. We first apply singular value decomposition onto $\mathbf{X}$ as $\mathbf{X} = \mathbf{U}_{\mathbf{X}}\Sigma_{\mathbf{X}}\mathbf{V}_{\mathbf{X}}^H$; then, projection $\mathscr{P}_{\mathscr{M}}(\mathbf{X})$ is

$$M_{\mathscr{M}}(\mathbf{X}) = \mathbf{U}_K\mathbf{\Sigma}_K\mathbf{V}_K^H, \tag{21}$$

where $\mathbf{U}_K$ and $\mathbf{V}_K$ are the first K columns of $\mathbf{U}_{\mathbf{X}}$ and $\mathbf{V}_{\mathbf{X}}$, respectively, and Σ_K is the corresponding singular value matrix.

Denoting $\widetilde{\mathbf{X}} = \begin{bmatrix} \widetilde{\mathbf{V}} & \text{amp;}\, \widetilde{\mathbf{H}}^H \\ \widetilde{\mathbf{H}} & \text{amp;}\, \widetilde{\mathbf{U}} \end{bmatrix}$, projection $M_{\mathscr{N}}(\widetilde{\mathbf{X}})$ contains four sequential subprojections: $\mathscr{P}_{\mathscr{N}_1} \longrightarrow \mathscr{P}_{\mathscr{N}_2} \longrightarrow \mathscr{P}_{\mathscr{N}_3} \longrightarrow \mathscr{P}_{\mathscr{N}_4}$ where $\mathscr{P}_{\mathscr{N}_1}$ and $\mathscr{P}_{\mathscr{N}_2}$ are to project $\widetilde{\mathbf{U}}$ and $\widetilde{\mathbf{V}}$ onto the set of Toeplitz matrix, respectively, $\mathscr{P}_{\mathscr{N}_3}$ is to project $\widetilde{\mathbf{H}}$ onto the ball defined by $\{\mathbf{H}\colon \|\mathbf{Y} - \mathbf{W}^H\mathbf{H}\mathbf{F}\|_F \le \beta\}$, and $\mathscr{P}_{\mathscr{N}_4}$ is to project $\widetilde{\mathbf{X}}$ onto a positive semidefinite matrix set. In particular, $M_{\mathscr{N}_1}(\mathbf{U})$ is defined as

$$\mathscr{P}_{\mathscr{N}_1}(\mathbf{U}) = \mathbf{T}(\mathbf{u}), \tag{22}$$

where the i-th element of $\mathbf{u}$ is $\mathbf{u}_i = (1/(N_r - i + 1))\sum_i \mathbf{U}_{m,n}$ where $i = n - m + 1$, $n \ge m$, and $m, n = 1, \ldots, N_r$. Similarly, $\mathscr{P}_{\mathscr{N}_2}(\mathbf{V})$ is

$$\mathscr{P}_{\mathscr{N}_2}(\mathbf{V}) = \mathbf{T}(\mathbf{v}), \tag{23}$$

where the i-th element of $\mathbf{v}$ is $\mathbf{v}_i = (1/(N_t - i + 1))\sum_i \mathbf{V}_{m,n}$ where $i = n - m + 1$, $n \ge m$, and $m, n = 1, \ldots, N_t$. Projection $\mathscr{P}_{\mathscr{N}_3}$ is to project $\mathbf{W}^H\widetilde{\mathbf{H}}\mathbf{F}$ onto a ball with center $\mathbf{Y}$ and radius β. To realize $\mathscr{P}_{\mathscr{N}_3}$, we first define

$$\widetilde{\mathbf{H}}^{\text{proj}} = \mathbf{W}\left(\mathbf{Y} + \frac{\mathbf{W}^H\widetilde{\mathbf{H}}\mathbf{F} - \mathbf{Y}}{\left\|\mathbf{W}^H\widetilde{\mathbf{H}}\mathbf{F} - \mathbf{Y}\right\|_F}\beta\right)\mathbf{F}^H. \tag{24}$$

Then, $M_{\mathscr{N}_3}$ can be given as

$$\left[\mathscr{P}_{\mathscr{N}_3}\right]_{m,n} = \begin{cases} \left[\widetilde{\mathbf{H}}^{\text{proj}}\right]_{m,n}, & \text{if } m \in \mathbf{\Phi}_W, n \in \mathbf{\Omega}_F, \\ \widetilde{\mathbf{H}}_{m,n}, & \text{otherwise.} \end{cases} \tag{25}$$

For $\mathscr{P}_{\mathscr{N}_4}$, we first apply eigen-decomposition to $\widetilde{\mathbf{X}}$ and have $\widetilde{\mathbf{X}} = \mathbf{U}_{\widetilde{\mathbf{X}}}\text{diag}(\boldsymbol{\sigma}_{\widetilde{\mathbf{X}}})\mathbf{U}_{\widetilde{\mathbf{X}}}^H$. Then, projection $\mathscr{P}_{\mathscr{N}_4}$ can be given as

$$\mathscr{P}_{\mathscr{N}_4}(\widetilde{\mathbf{X}}) = \mathbf{U}_{\widetilde{\mathbf{X}}}^{+}\text{diag}\left(\boldsymbol{\sigma}_{\widetilde{\mathbf{X}}}^{+}\right)\left(\mathbf{U}_{\widetilde{\mathbf{X}}}^{+}\right)^H, \tag{26}$$

where $\boldsymbol{\sigma}_{\widetilde{\mathbf{X}}}^{+}$ denotes the positive part of $\boldsymbol{\sigma}_{\widetilde{\mathbf{X}}}$ and $\mathbf{U}_{\widetilde{\mathbf{X}}}^{+}$ denotes the corresponding eigen-vectors.

The proposed method converges when $(\|\mathbf{N}^{(t+1)} - \mathbf{N}^{(t)}\|_F / \|\mathbf{N}^{(t)}\|_F) \le \varepsilon$, where ε is a predefined threshold.

3.2. The Case of $N_t > \Omega_{M_t}$. It should be noted that, given the number of RF chains M_t at the transmitter (we take the transmitter as an example.), the array aperture is limited by its maximum tag Ω_{M_t} which may not equal N_t. If $N_t > \Omega_{M_t}$, finding the accurate channel matrix $\mathbf{H}$ from model (17) is difficult since there may exist too many variables to be determined in (17). Thus, instead of directly obtaining $\mathbf{H}$, we alternatively first retrieve the angle information based on which we can find the channel gain. And then, the channel matrix $\mathbf{H}$ can be well estimated. Specifically, we first let $\Omega_1 = 1$ and replace $\mathbf{F} \in \mathbb{Z}^{N_t \times M_t}$ by $\overline{\mathbf{F}} \in \mathbb{Z}^{\Omega_{M_t} \times M_t}$. Similarly, we obtain $\overline{\mathbf{W}} \in \mathbb{Z}^{\Phi_{M_r} \times M_r}$. Then, received signal model (10) can be rewritten as

$$\mathbf{Y} = \overline{\mathbf{W}}^H\overline{\mathbf{A}}_r\mathbf{\Sigma}\overline{\mathbf{A}}_t^H\overline{\mathbf{F}} + \overline{\mathbf{W}}^H\overline{\mathbf{N}}, \tag{27}$$

where $\overline{\mathbf{A}}_t = [\overline{\mathbf{a}}_t(\phi_1), \overline{\mathbf{a}}_t(\phi_2), \ldots, \overline{\mathbf{a}}_t(\phi_K)]$ and $\overline{\mathbf{A}}_r = [\overline{\mathbf{a}}_r(\theta_1), \overline{\mathbf{a}}_r(\theta_2), \ldots, \overline{\mathbf{a}}_r(\theta_K)]$ with

$$\begin{aligned}\overline{\mathbf{a}}_t(\phi_k) &= \left[1, e^{j\cdot 1\cdot \frac{2\pi d}{\lambda}\sin(\phi_k)}, \ldots, e^{j\cdot(\Omega_{M_t}-1)\cdot \frac{2\pi d}{\lambda}\sin(\phi_k)}\right]^T,\\ \overline{\mathbf{a}}_r(\theta_k) &= \left[1, e^{j\cdot 1\cdot \frac{2\pi d}{\lambda}\sin(\theta_k)}, \ldots, e^{j\cdot(\Phi_{M_r}-1)\cdot \frac{2\pi d}{\lambda}\sin(\theta_k)}\right]^T.\end{aligned} \tag{28}$$

It is easy to see that $\overline{\mathbf{a}}_t(\phi_k)$ and $\overline{\mathbf{a}}_r(\theta_k)$ are subvectors of $\mathbf{a}_t(\phi_k)$ and $\mathbf{a}_r(\theta_k)$, respectively. Based on truncated model (27), we propose the following truncated problem:

$$\begin{aligned}&\min_{\overline{\mathbf{H}},\overline{\mathbf{u}},\overline{\mathbf{v}},\overline{\mathbf{W}}} \quad \text{rank}[\overline{\mathbf{W}}],\\ &\text{s.t.} \quad \overline{\mathbf{W}} = \begin{bmatrix} \mathbf{T}(\overline{\mathbf{v}}) & \overline{\mathbf{H}}^H \\ \overline{\mathbf{H}} & \mathbf{T}(\overline{\mathbf{u}}) \end{bmatrix} \ge 0,\\ &\qquad \left\|\mathbf{Y} - \overline{\mathbf{W}}^H\overline{\mathbf{H}}\mathbf{F}\right\|_F \le \beta.\end{aligned} \tag{29}$$

The optimal solution $\overline{\mathbf{H}}^{\circ} \in \mathbb{C}^{\Phi_{M_r} \times \Omega_{M_t}}$ is only a submatrix of the full channel matrix $\mathbf{H}$. To estimate $\mathbf{H}$, we should first find the AoAs and AoDs from (29). From the proof of Theorem 1, we can see that $\mathbf{T}(\overline{\mathbf{u}})$ and $\mathbf{T}(\overline{\mathbf{v}})$ contain the AoAs and AoDs information, respectively, and the two Toeplitz matrices can be regarded as the noiseless covariance matrices of a ULA. Thus, the traditional ESPRIT method can be applied to find the angle estimates. Alternatively, we can also find the angle estimates from the Vandermonde decomposition theorem [40]. The channel matrix can then be constructed according to (7) after finding the channel gain by the LS method.

4. Simulation Results

In this section, we evaluate the channel estimation performance of our proposed method on the switch-based mmWave massive MIMO system. We also consider other

methods including MUSIC [41], OMP [18], $L1$ minimization [42], ANM [22], and decoupled ANM (DANM) [43] for comparison. It should be pointed out that DANM is applied with the alternating direction method of multipliers (ADMM) [44] which is a fast solver. We assume that $N_t = 16$, $N_r = 32$, $M_t = 6$, and $M_r = 10$ and the antennas are placed with half-wavelength spacing. The channel estimation performance is evaluated by

$$\text{NMSE} = \mathbb{E}\left[\frac{\|\mathbf{H} - \mathbf{H}^{\circ}\|_F^2}{\|\mathbf{H}\|_F^2}\right], \tag{30}$$

based on 400 independent trials. The number of paths is set to $K = 3$. The AoAs and AoDs are randomly generated from $[-90^{\circ}, 90^{\circ})$ for each path. The SNR is defined as $\text{SNR} = (P_t/\sigma^2)$, where P_t and $\sigma^2 = 1$ denote the transmitted power and noise power, respectively. For our method, we assume $\delta_1 = \delta_2 = 0.8$ and $\beta = \sqrt{M_t M_r + 2\sqrt{M_t M_r}}\sigma$ to the upper bound of noise energy.

4.1. Convergence Performance. We first evaluate the convergence of our method. Denote $\Delta\mathbf{U}^{(t+1)} = (\|\mathbf{H}^{(t+1)} - \mathbf{H}^{(t)}\|_F^2/\|\mathbf{H}^{(t)}\|_F^2)$ as the variation of the estimated channel matrices between the $(t+1)$-th and t-th iterations. The threshold ε is set to 10^{-3}. We consider different SNR scenarios and show the relationship between $\Delta\mathbf{U}$ and the iteration in Figure 2, from which we can observe that for different SNRs, $\Delta\mathbf{U}$ decreases rapidly and our method converges after about 300 iterations.

4.2. Different Antenna Selection Strategies. In this section, we compare the performance of different antenna selection strategies. We select two representative SLA structures, nested and coprime arrays, and random selection strategy is also taken into consideration. In particular, we set $\mathbf{\Omega}_F^{\text{nested}} = \{1, 2, 3, 4, 8, 12\}$ and $\mathbf{\Phi}_W^{\text{nested}} = \{1, 2, 3, 4, 5, 10, 15, 20, 25, 30\}$ for the nested structure and $\mathbf{\Omega}_F^{\text{nested}} = \{1, 3, 4, 5, 7, 10\}$ and $\mathbf{\Phi}_W^{\text{nested}} = \{1, 4, 6, 7, 10, 11, 13, 16, 21, 26\}$ for the coprime structure. For random selection strategy, we always first select the first antenna and then randomly select $M_t - 1$ antennas from $\{2, \ldots, 16\}$ for the transmitter and $M_r - 1$ antennas from $\{2, \ldots, 32\}$ for the receiver. The NMSEs of our proposed method based on these three strategies are shown in Figure 3 with the SNR varying from -10 dB to 8 dB. It can be seen that the nested array enjoys the best estimation performance. The coprime array shows inferior performance compared to nested array since it has shorter successive uniform part in its coarray. The random strategy shows the worst performance.

4.3. Performance Comparison. Next, we evaluate the channel estimation performance of our proposed method with other representative methods. For MUSIC, OMP, and $L1$ which require discretizing the angle space, we consider two grid resolutions 2° and 3°. The NMSEs of these methods are shown in Figure 4(a). We can see that ANM enjoys the best estimation performance in the compared SNR region. The

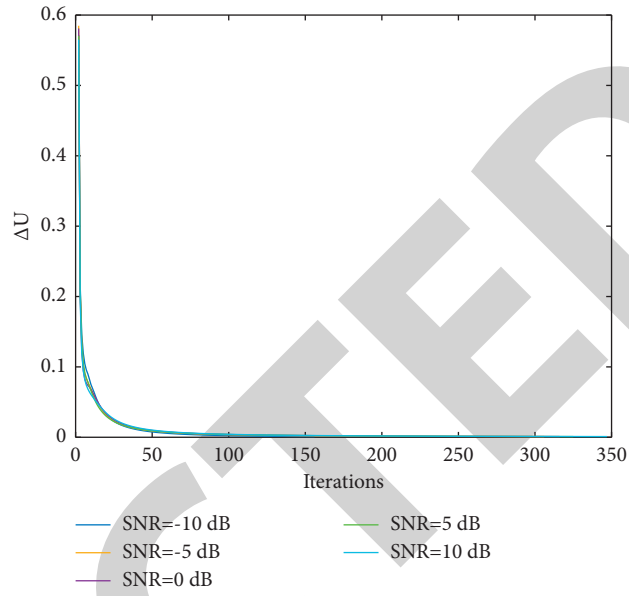

Figure 2: Convergence of the proposed method.

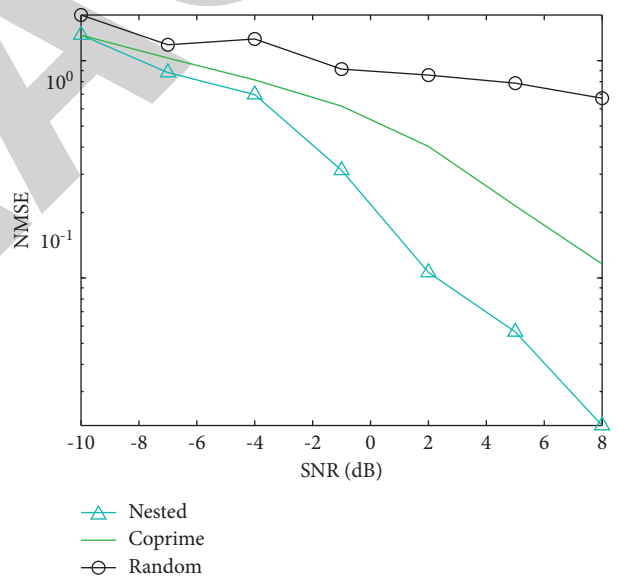

Figure 3: NMSE comparison of three different antenna selection strategies.

proposed method is superior to other methods except ANM in most cases. For the three grid-based methods with grid resolution 3°, they show unsatisfying accuracy in the low SNR region while suffer from grid effect when SNR becomes large. Thus, we can see that when SNR is larger than 4 dB, the gaps between these methods and our method become large. For grid resolution 2°, these methods show better performance than for the case of grid resolution 3°. This is because reducing the grid interval can relieve the grid mismatch effect, yielding higher estimation accuracy. We also show the running time of these methods in Figure 4(b). Since ANM requires to solve a large-dimensional SDP, it has the largest running time as compared to other methods. The $L1$ method

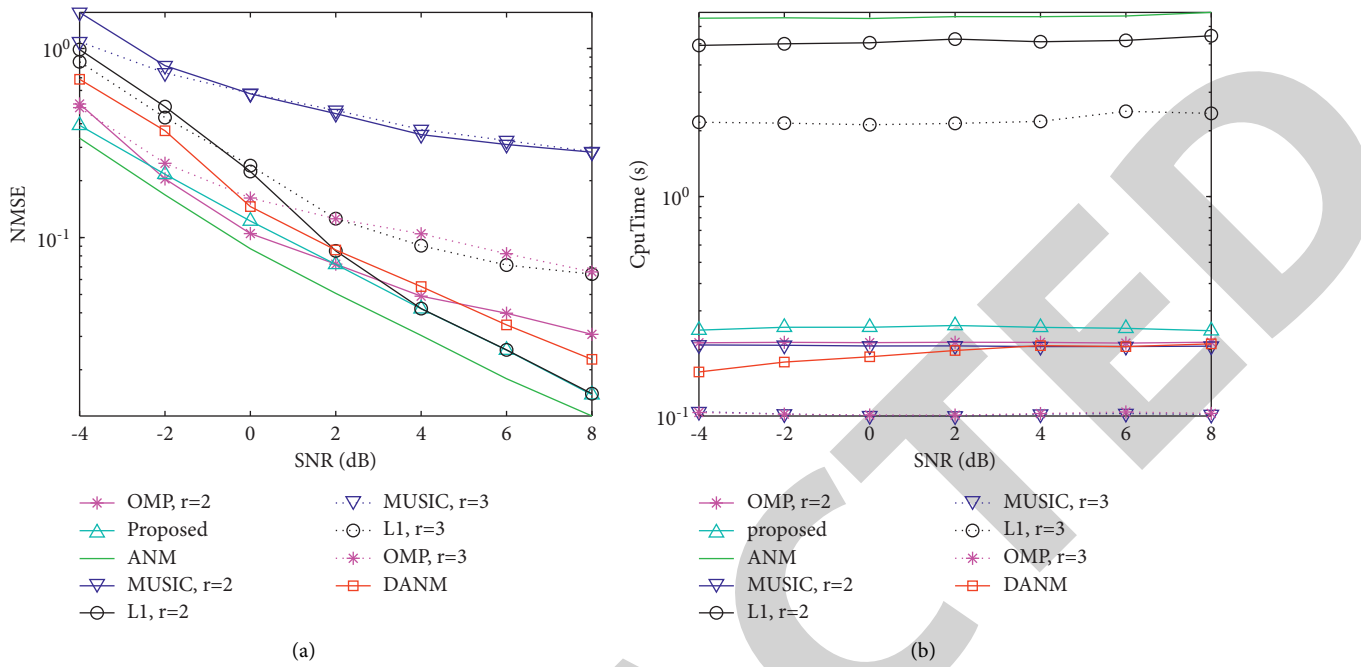

Figure 4: Channel estimation performance comparison with respect to the SNR. Two grid resolutions 2° and 3° are considered. (a) NMSE comparison. (b) CPU time comparison.

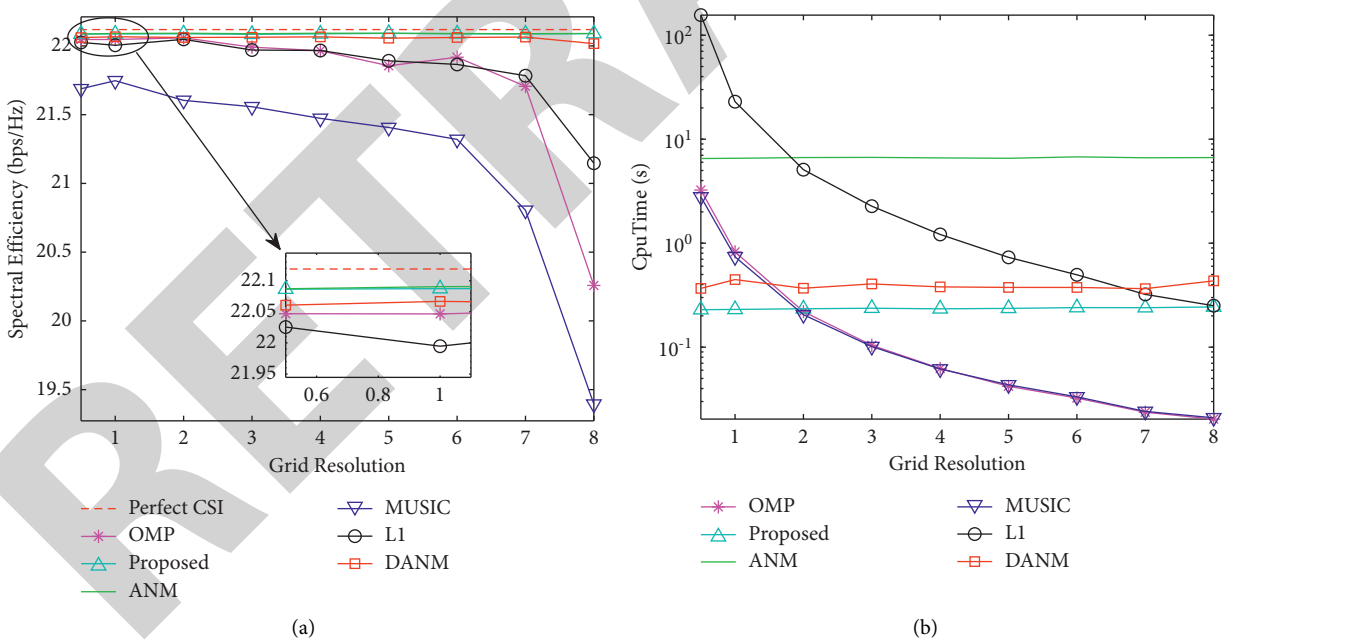

Figure 5: Spectral efficiency comparison with respect to the grid resolution. SNR = 5 dB. (a) Spectral efficiency comparison. (b) CPU time comparison.

requires solving a BPDN problem by CVX, and hence, it also suffers from high computational complexity, with respect to the two grid resolutions. DANM, MUSIC, and OMP are much faster than the ANM and $L1$ method, especially in the case of grid resolution 2°. Our method shows comparable computational efficiency to OMP and MUSIC with grid resolution 3° but has better estimation performance as shown in Figure 4(a).

We also evaluate the spectral efficiency of these methods and show the simulation results in Figure 5 with different grid resolutions ranging from 0.5° to 8°. The spectral efficiency with perfect CSI is also considered as the upper

bound. From Figure 5(a), it can be seen that since ANM, DANM, and our method are immune to the angle discretization, they are not affected by the grid resolution and can coincide with the perfect CSI. For OMP, MUSIC, and $L1$ methods, their performance deteriorates as the grid becomes sparser. Although the spectral efficiency of the $L1$ method and OMP can approach our method, DANM and ANM in dense grid cases, from Figure 5(b), it can be seen that their computational times increase exponentially as the grid resolution decreases and are several times slower than our proposed method if the grid resolution is less than 1°.

5. Conclusion

In this paper, we proposed an atomic ℓ_0-norm-based channel estimation method for switch-based mmWave massive MIMO communication systems. The proposed method exploits the coarray property of sparse arrays to select antennas and then formulates an atomic ℓ_0-norm minimization problem which is efficiently solved based on Wirtinger projection. The proposed method is shown to have higher computational efficiency than ANM at comparable estimation performance. Compared to grid-based methods such as OMP, MUSIC, and $L1$, our method does not require angle discretization and hence is immune to the grid mismatch effect, leading to higher estimation accuracy.

Data Availability

All data, models, or codes used to support the findings of this study are available from the corresponding author upon request.

Conflicts of Interest

The authors declare that they have no conflicts of interest.

Acknowledgments

This work was supported by the Science and Technology Project of SGCC (State Grid Corporation of China): "Development and Application of Power 5G Terminal based on Modular Design" (SGZJXT00JSJS2000454).

References

[1] O. E. Ayach, S. Rajagopal, S. Abu-Surra, Z. Pi, and R. W. Heath, "Spatially sparse precoding in millimeter wave mimo systems," *IEEE Transactions on Wireless Communications*, vol. 13, no. 3, pp. 1499–1513, 2014.

[2] H. Wang, L. Xu, Z. Yan, and T. A. Gulliver, "Low-complexity mimo-fbmc sparse channel parameter estimation for industrial big data communications," *IEEE Transactions on Industrial Informatics*, vol. 17, no. 5, pp. 3422–3430, 2021.

[3] H. Wang, X. Li, R. H. Jhaveri et al., "Sparse Bayesian learning based channel estimation in fbmc/oqam industrial iot networks," *Computer Communications*, vol. 176, pp. 40–45, 2021.

[4] J. Zhang, Y. Huang, Q. Shi, J. Wang, and L. Yang, "Codebook design for beam alignment in millimeter wave communication systems," *IEEE Transactions on Communications*, vol. 65, no. 11, pp. 4980–4995, 2017.

[5] Z. Xiao, T. He, P. Xia, and X. Xia, "Hierarchical codebook design for beamforming training in millimeter-wave communication," *IEEE Transactions on Wireless Communications*, vol. 15, no. 5, pp. 3380–3392, 2016.

[6] M. Xiao, S. Mumtaz, Y. Huang et al., "Millimeter wave communications for future mobile networks," *IEEE Journal on Selected Areas in Communications*, vol. 35, no. 9, pp. 1909–1935, 2017.

[7] M. K. Samimi and T. S. Rappaport, "3-d millimeter-wave statistical channel model for 5G wireless system design," *IEEE Transactions on Microwave Theory and Techniques*, vol. 64, no. 7, pp. 2207–2225, 2016.

[8] T. A. Thomas, H. C. Nguyen, G. R. MacCartney, and T. S. Rappaport, "3d mmwave channel model proposal," in *Proceedings of the 2014 IEEE 80th Vehicular Technology Conference (VTC2014-Fall)*, pp. 1–6, Vancouver, Canada, September 2014.

[9] X. Wang, M. Huang, and L. Wan, "Joint 2d-dod and 2d-doa estimation for coprime emvscmimo radar," *Circuits, Systems, and Signal Processing*, vol. 40, no. 6, pp. 1–17, 2021.

[10] F. Wen, J. Shi, and Z. Zhang, "Closed-form estimation algorithm for emvs-mimo radar with arbitrary sensor geometry," *Signal Processing*, vol. 186, no. 8, Article ID 108117, 2021.

[11] A. Alkhateeb, O. E. Ayach, G. Leus, and R. W. Heath, "Channel estimation and hybrid precoding for millimeter wave cellular systems," *IEEE Journal of Selected Topics in Signal Processing*, vol. 8, no. 5, pp. 831–846, 2014.

[12] A. Alkhateeb, G. Leus, and R. W. Heath, "Compressed sensing based multi-user millimeter wave systems: how many measurements are needed?" in *Proceedings of the 2015 IEEE International Conference on Acoustics, Speech and Signal Processing (ICASSP)*, pp. 2909–2913, South Brisbane, Australia, April 2015.

[13] S. Sun and T. S. Rappaport, "Millimeter wave mimo channel estimation based on adaptive compressed sensing," in *Proceedings of the 2017 IEEE International Conference on Communications Workshops (ICC Workshops)*, pp. 47–53, Paris, France, May 2017.

[14] Z. Guo, X. Wang, and W. Heng, "Millimeter-wave channel estimation based on 2-d beamspace music method," *IEEE Transactions on Wireless Communications*, vol. 16, no. 8, pp. 5384–5394, 2017.

[15] C. Tsai, Y. Liu, and A. Wu, "Efficient compressive channel estimation for millimeter-wave large-scale antenna systems," *IEEE Transactions on Signal Processing*, vol. 66, no. 9, pp. 2414–2428, 2018.

[16] F. Dong, W. Wang, Z. Huang, and P. Huang, "High-resolution angle-of-arrival and channel estimation for mmwave massive mimo systems with lens antenna array," *IEEE Transactions on Vehicular Technology*, vol. 69, no. 11, pp. 12963–12973, 2020.

[17] L. Wan, K. Liu, Y.-C. Liang, and T. Zhu, "Doa and polarization estimation for non-circular signals in 3-d millimeter wave polarized massive mimo systems," *IEEE Transactions on Wireless Communications*, vol. 20, no. 5, pp. 3152–3167, 2021.

[18] J. Tropp and A. Gilbert, "Signal recovery from random measurements via orthogonal matching pursuit," *IEEE Transactions on Information Theory*, vol. 53, no. 12, pp. 4655–4666, 2007.

[19] J. Shi, F. Wen, and T. Liu, "Nested mimo radar: coarrays, tensor modeling, and angle estimation," *IEEE Transactions on Aerospace and Electronic Systems*, vol. 57, no. 1, pp. 573–585, 2021.

Hindawi
International Journal of Antennas and Propagation
Volume 2023, Article ID 9864861, 1 page
https://doi.org/10.1155/2023/9864861

Retraction

Retracted: 2D-DOA Estimation for EMVS Array with Nonuniform Noise

International Journal of Antennas and Propagation

Received 19 December 2023; Accepted 19 December 2023; Published 20 December 2023

This article has been retracted by Hindawi following an investigation undertaken by the publisher [1]. This investigation has uncovered evidence of one or more of the following indicators of systematic manipulation of the publication process:

(1) Discrepancies in scope

(2) Discrepancies in the description of the research reported

(3) Discrepancies between the availability of data and the research described

(4) Inappropriate citations

(5) Incoherent, meaningless and/or irrelevant content included in the article

(6) Manipulated or compromised peer review

The presence of these indicators undermines our confidence in the integrity of the article's content and we cannot, therefore, vouch for its reliability. Please note that this notice is intended solely to alert readers that the content of this article is unreliable. We have not investigated whether authors were aware of or involved in the systematic manipulation of the publication process.

Wiley and Hindawi regrets that the usual quality checks did not identify these issues before publication and have since put additional measures in place to safeguard research integrity.

We wish to credit our own Research Integrity and Research Publishing teams and anonymous and named external researchers and research integrity experts for contributing to this investigation.

The corresponding author, as the representative of all authors, has been given the opportunity to register their agreement or disagreement to this retraction. We have kept a record of any response received.

References

[1] C.-X. Cai, G.-J. Huang, F.-Q. Wen, X.-H. Wang, and L. Wang, "2D-DOA Estimation for EMVS Array with Nonuniform Noise," *International Journal of Antennas and Propagation*, vol. 2021, Article ID 9053864, 9 pages, 2021.

Hindawi
International Journal of Antennas and Propagation
Volume 2021, Article ID 9053864, 9 pages
https://doi.org/10.1155/2021/9053864

Research Article

2D-DOA Estimation for EMVS Array with Nonuniform Noise

Chang-Xin Cai,[1] Guan-Jun Huang,[1] Fang-Qing Wen,[2] Xin-Hai Wang,[3] and Lin Wang[4]

[1]*National Demonstration Center for Experimental Electrical and Electronic Education, Yangtze University, Jingzhou 434200, China*
[2]*College of Computer and Information Technology, China Three Gorges University, Yichang 443002, China*
[3]*Nanjing Marine Radar Institute, Nanjing 211153, China*
[4]*The 723 Institute of CSIC, Yangzhou 225000, China*

Correspondence should be addressed to Guan-Jun Huang; 201971326@yangtzeu.edu.cn

Received 21 June 2021; Revised 24 July 2021; Accepted 9 August 2021; Published 19 August 2021

Academic Editor: Jin He

Electromagnetic vector sensor (EMVS) array is one of the most potential arrays for future wireless communications and radars because it is capable of providing two-dimensional (2D) direction-of-arrival (DOA) estimation as well as polarization angles of the source signal. It is well known that existing subspace algorithm cannot directly be applied to a nonuniform noise scenario. In this paper, we consider the 2D-DOA estimation issue for EMVS array in the presence of nonuniform noise and propose an improved subspace-based algorithm. Firstly, it recasts the nonuniform noise issue as a matrix completion problem. The noiseless array covariance matrix is then recovered via solving a convex optimization problem. Thereafter, the shift invariant principle of the EMVS array is adopted to construct a normalized polarization steering vector, after which 2D-DOA is easily estimated as well as polarization angles by incorporating the vector cross-product technique and the pseudoinverse method. The proposed algorithm is effective to EMVS array with arbitrary sensor geometry. Furthermore, the proposed algorithm is free from the nonuniform noise. Several simulations verify the improvement of the proposed method.

1. Introduction

Sensor array is one of the most important infrastructures in wireless communication and radar detection [1–4]. Among the various branches in array signal processing, direction-of-arrival (DOA) estimation is the most canonical one and has aroused much attention. The principle of DOA estimation is to estimate the direction of the incoming source via the phase characteristics between sensors, and it is a highly nonlinear problem. Many efforts have been devoted to tackling this issue, for instance, an estimation approach to signal parameters with the rotational invariance technique (ESPRIT) [5, 6], Capon, multiple signal classification (MUSIC) [7–9], propagator method (PM) [10], maximum-likelihood (ML) [11], and tensor method [12–14]. Usually, the spectrum search counterparts, such as MUSIC, are always inefficient. Besides, they hardly avoid the off-grid problem. ESPRIT, however, is much more efficient than the spectrum search frameworks because it can acquire closed-form solutions to the parameter estimation issue.

A majority of the current studies focus on how to estimate the one-dimensional (1D) DOA from the scalar sensor arrays, e.g., uniform linear array (ULA). In practice, two-dimensional (2D) DOA may be more attractive. To pursue 2D-DOA estimation with the traditional scalar sensors, nonlinear sensor geometries are necessary [15–17], e.g., L-shape array, circular geometry, and rectangular manifold. Unfortunately, scalar sensor arrays often suffer from the sensor position error. Thus, complex array calibration is indispensable. Unlike scalar sensors, a single electromagnetic vector sensor (EMVS) is capable of providing 2D-DOA estimation [18]. Moreover, it is able to offer additional polarization angles of the source, and such characteristic may be very helpful in detecting stealth source [19]. Besides, an EMVS array with N sensors occupies more degree of freedom (DOF) than a scalar array, and thus, it

provides more accurate estimation result than the latter. Furthermore, it has been proven that parameter estimation using EMVS array is insensitive to sensor positions [20], giving rise to the fact that the EMVS is more flexible than the traditional scalar sensor arrays.

It should be emphasized that the angle estimation issue using EMVS array is often more complex than that using the scalar sensors, since it involves 2D-DOA (azimuth angle and elevation angle) and 2D polarization angle (polarization phase difference and auxiliary polarization angle). In [19], the vector cross product was proposed, and the angles therein were obtained from the Poynting vector of the polarization steering vector. In [20], the ESPRIT-like algorithm was introduced. Therein, the concept of normalized Poynting vector was proposed to estimate the 2D-DOA, which was insensitive to the sensor positions and free from the sensor position error. In [21], the ULA-configured EMVS architecture was presented, and another ESPRIT estimator was derived. Unlike [20], the elevation angle was achieved by using ESPRIT, and the azimuth angle was estimated by using vector cross product. Likewise, in [22–26], the methods of combining the subspace approach and vector cross product were investigated. To avoid the eigendecompositon in the subspace approaches, a PM-like algorithm was presented in [27]. To further exploit the multidimensional structure in EMVS array, tensor algorithms were also been investigated in [28]. Besides, some efforts have been devoted to the active radar system with EMVS arrays [29–31], which brings new insights to target detection.

Nevertheless, it should be noticed that the subspace-based approaches achieve good performance with Gaussian white noise. In practice, the array noise may be nonuniform due to hardware nonideality. The nonuniform noise issue has been extensively stressed in scalar sensor array [32–35], but little attention has been paid to EMVS array. Therefore, we revisit the 2D-DOA estimation in EMVS array with nonuniform noise in this paper. An improved ESPRIT algorithm is presented. It eliminates the nonuniform noise via constructing a reduced covariance matrix, after which both noise covariance and parts of the signal covariance are removed. The recovery of the noiseless covariance matrix is recast as a matrix completion issue and is accomplished via solving a convex optimization problem. Thereafter, the ESPRIT idea is adopted to construct the normalized polarization steering vector. 2D-DOA, as well as polarization parameters, is then achieved by combining the vector cross product and the least squares (LS) technique. Our algorithm is effective in the scenario with arbitrary array geometry. Numerical simulations are designed to verify its effectiveness.

2. Preliminaries and the Data Model

2.1. EMVS Preliminaries. For a complete EMVS, it consists of six colocated antennas: three electric dipoles, and three magnetic loops. The dipoles and loops, respectively, sense the information of the electric field and magnetic field. Considering that a far-field source signal impinges on a single EMVS, the polarization responses of the six components can be expressed as

$$b = \left[\underbrace{b(1)\ b(2)\ b(3)}_{e \in \mathbb{C}^{3\times 1}} \ \underbrace{b(4)\ b(5)\ b(6)}_{m \in \mathbb{C}^{3\times 1}} \right]^T, \quad = Dp\ , \tag{1}$$

where $(\cdot)^T$ denotes transpose. D and p are, respectively, given by

$$D = \begin{bmatrix} \cos\phi\cos\theta & -\sin\phi \\ \sin\phi\cos\theta & \cos\phi \\ -\sin\theta & 0 \\ -\sin\phi & -\cos\phi\cos\theta \\ \cos\phi & -\sin\phi\cos\theta \\ 0 & \sin\theta \end{bmatrix} \tag{2}$$

and

$$p = \begin{bmatrix} \sin\gamma e^{j\eta} \\ \cos\gamma \end{bmatrix}, \tag{3}$$

where e and m denote the electric steering vector and the magnetic steering vector, respectively; θ, ϕ, γ, and η denote, respectively, the elevation angle, the azimuth angle, the auxiliary polarization angle, and the polarization phase difference. $D \in \mathbb{C}^{6\times 2}$ denotes the direction-only matrix, and $p \in \mathbb{C}^{2\times 1}$ denotes the polarization-only vector, respectively. Moreover, the Poynting vector between e and p satisfies [20]

$$\frac{e}{|e|} * \frac{p^*}{|p|} = \begin{bmatrix} \sin\theta\cos\phi \\ \sin\theta\sin\phi \\ \cos\theta \end{bmatrix}, \tag{4}$$

where $(\cdot)^*$ denotes the conjugate, $|\cdot|$ returns the absolute value, and $*$ denotes the vector cross product.

2.2. Data Model. Let us consider an N-element EMVS array. Without loss of generality, let the coordinate of the n-th EMVS be $r_n = [x_n, y_n, z_n]^T$. Suppose that K far-field signals appear in the array. Let θ_k, ϕ_k, γ_k, and η_k stand for the k-th $(k = 1, 2, \ldots, K)$ angle parameters. The array signal can be written as [19]

$$y(t) = \sum_{k=1}^{K} [a_k \otimes b_k] s_k(t) + n(t), \tag{5}$$

where t is the time index; $\otimes$ denotes the Kronecker product, $a_k = [e^{-j\pi\tau_{1,k}}, e^{-j\pi\tau_{2,k}}, \ldots, e^{-j\pi\tau_{N,k}}]^T$, where $\tau_{n,k} = r_n^T g_k / \lambda \in \mathbb{C}^{N\times 1}$ denotes the k-th spatial response (steering) vector with $g_k = [\cos(\phi_{t,k})\sin(\theta_{t,k}),\ \sin(\phi_{t,k})\sin(\theta_{t,k}),\ \cos(\theta_{t,k})]^T$ and λ is the carrier wavelength; and $b_k = D_k v_k$ denotes the polarization response vector associated with the k-th target. $s_k(t)$ accounts for the k-th signal; $n(t)$ denotes the array noise. Let $A = [a_1, a_2, \ldots, a_K] \in \mathbb{C}^{N\times K}$ and $B = [b_1, b_2, \ldots, b_K] \in \mathbb{C}^{6\times K}$. Equation (6) can also be formulated as

$$\begin{aligned} y(t) &= [A \odot B]s(t) + n(t), \\ &= Cs(t) + n(t), \end{aligned} \tag{6}$$

where the symbol $\odot$ stands for the Khatri–Rao product, $s(t) = [s_1(t), s_2(t), \ldots, s_K(t)]^T$, and $C = A \odot B$. Suppose that the noise $n(t)$ is uncorrelated with the signal $s(t)$; then, the covariance matrix of $y(t)$ is given by

$$\begin{aligned} R &= E\{y(t)y^H(t)\}, \\ &= CR_sC^H + R_n, \\ &= \widetilde{R} + R_n, \end{aligned} \tag{7}$$

where $E\{\cdot\}$ is to acquire the mathematical expectation and $(\cdot)^H$ denotes Hermitian transpose.$R_s = E\{s(t)s^H(t)\}$, $R_n = E\{n(t)n^H(t)\}$, and $\widetilde{R} = CR_sC^H$. In the presence of uncorrelated source signals, $R_s = \mathrm{diag}\{\lambda_1, \lambda_2, \ldots, \lambda_K\}$, where diag{·} accounts for the diagonalization operation and λ_k is the power of the k-th source. Moreover, since the noise is nonuniform, its covariance matrix is then given by

$$R_n = \mathrm{diag}\{\sigma_1^2, \sigma_2^2, \ldots, \sigma_{6N}^2\}, \tag{8}$$

where $\sigma^2_{6(n-1)+q}$ denotes the noise power corresponding to the q-th component of the n-th EMVS. In practical applications, we can estimate R via L samples as

$$\widehat{R} = \frac{1}{L}\sum_{t=1}^{L} y(t)y^H(t). \tag{9}$$

Our objective here is to estimate the angles from $\widehat{R}$.

3. The Proposed Approach

3.1. Principle of Traditional Eigendecompositon. It is well known that when Gaussian white noise (uniform noise) exists, the noise powers fulfill

$$\sigma_1^2 = \sigma_2^2 = \cdots = \sigma_{6N}^2 = \sigma^2, \tag{10}$$

where σ^2 is a constant, and then, the noise covariance becomes

$$R_n = \sigma^2 I_{6N}, \tag{11}$$

where I_M stands for the $M \times M$ identity matrix. If we ignore the noise item in equation (7), the eigendecomposition of R is given by

$$\begin{aligned} \widetilde{R} &= \sum_{n=1}^{K} \alpha_k u_k u_k^H, \\ &= U_s \Sigma_s U_s^H, \end{aligned} \tag{12}$$

where α_k is the k-th eigenvalue, u_k is the associated eigenvector, and $u_{k1}^H u_{k2} = 0$ is for any $k_1 \neq k_2$; $\Sigma_s = \mathrm{diag}\{\alpha_1, \alpha_2, \ldots, \alpha_K\}$ denotes the eigenvalue matrix, and $U_s = [u_1, u_2, \ldots, u_K] \in \mathbb{C}^{6N \times K}$ is called the signal subspace, which spans the same subspace as $A \odot B$. Namely, there is a full-rank matrix $T \in \mathbb{C}^{K \times K}$ such that

$$U_s = CT. \tag{13}$$

Also, the noiseless covariance matrix can be expressed as

$$\begin{aligned} \widetilde{R} &= \sum_{n=1}^{K} \alpha_k u_k u_k^H + \sum_{n=1}^{6N-K} 0 \cdot v_n v_n^H, \\ &= U_s \Sigma_{s1} U_s^H + U_n 0_{(6N-K)(6N-K)} U_n^H, \end{aligned} \tag{14}$$

where v_n is the eigenvector from the null subspace of U_s, i.e., $v_n^H U_s = 0_{1\times K}$, and $0_{M\times N}$ represents the $M \times N$ full zero matrix. $\Sigma_{s1} = \mathrm{diag}\{\alpha_1 + \sigma^2, \alpha_2 + \sigma^2, \ldots, \alpha_K + \sigma^2\}$, and $U_n = [v_1, v_2, \ldots, v_{6N-K}] \in \mathbb{C}^{6N\times(6N-K)}$ is called the noise subspace. Since the identity matrix can be formulated as the product of arbitrary unitary matrix and its Hermitian transpose, the noisy R can be written as

$$\begin{aligned} R &= \sum_{n=1}^{K} (\alpha_k + \sigma^2) u_k u_k^H + \sum_{n=1}^{6N-K} \sigma^2 u_n u_n^H, \\ &= U_s \Sigma_{s1} U_s^H + U_n \Sigma_n U_n^H, \end{aligned} \tag{15}$$

where $\Sigma_n = \mathrm{diag}\{\sigma^2, \sigma^2, \ldots, \sigma^2\} \in \mathbb{C}^{(6N-K)\times(6N-K)}$. The results in equation (15) reveal that the uniform noise would not destroy the eigendistribution of the signal. However, in the presence of nonuniform noise, the noise power is not unique, so the conclusion in equation (15) will be untenable. It is necessary for us to denoise before further processing.

3.2. Denoising. Let Ω be a set that records the nonzero entities of R_n, i.e.,

$$\Omega = \{(m, m) | m = 1, 2, \ldots, 6N\}. \tag{16}$$

We define a sampling operator $S_\Omega\{\cdot\}$ that picks up the elements of the matrix in the blanket with indexes in Ω, for example, $S_\Omega\{R\} = \overline{R} \in C^{6N\times 6N}$ such that

$$\overline{R}(m, n) = \begin{cases} R(m, n), & (m, n) \in \Omega, \\ 0, & (m, n) \notin \Omega, \end{cases} \tag{17}$$

where $R(m, n)$ denotes the (m, n)-th entity of R and is similar to others. Since R_n is a diagonal matrix, we have $R_n = S_\Omega\{R_n\}$. The effect of the noise can be easily removed via the following reduced covariance matrix:

$$\begin{aligned} \breve{R} &= R - S_\Omega\{R\}, \\ &= \widetilde{R} - S_\Omega\{\widetilde{R}\}. \end{aligned} \tag{18}$$

The abovementioned denoising procedure is illustrated in Figure 1. However, the abovementioned denoising procedure can also destroy the structure of $\widetilde{R}$, so we need to recover $\widetilde{R}$ from $\breve{R}$. Next, let us focus on the diagonal element of $\widetilde{R}$. It can be deduced that the m-th $(m = 6(n-1) + q)$ diagonal entity of $\widetilde{R}$ is

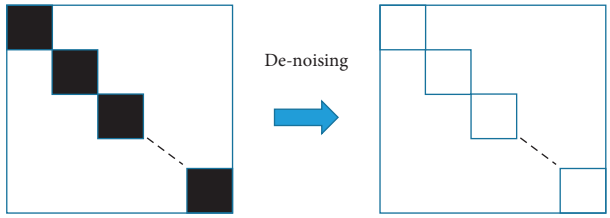

Figure 1: Illustration of the proposed denoising principle.

$$\begin{aligned}\widetilde{R}(m,m) &= \sum_{k=1}^{K} C(m,k)\lambda_k C^H(m,k),\\ &= \sum_{k=1}^{K} |C(m,k)|^2\lambda_k,\\ &= \sum_{k=1}^{K} \left|e^{-j\pi\tau_{n,k}}B(q,k)\right|^2\lambda_k,\\ &= \sum_{k=1}^{K} |B(q,k)|^2\lambda_k.\end{aligned} \tag{19}$$

We define $\chi_q = \sum_{k=1}^{K} |B(q,k)|^2\lambda_k$ and let $\chi = \mathrm{diag}\{\chi_1, \chi_q, \ldots, \chi_q\} \in \mathbb{C}^{6\times 6}$, and then, we have

$$\breve{R} = R_s - I_6 \otimes \chi. \tag{20}$$

Since R_s is a low-rank matrix, the noiseless recovery problem can be formulated as [32]

$$\begin{aligned}&\min \mathrm{rank}\{R\}\\ &\text{s.t. } S_\Omega(R) = \breve{R},\end{aligned} \tag{21}$$

where $\mathrm{rank}\{R\}$ returns the rank of R. To recover, the noiseless covariance coincides with the concept of matrix completion. Noting that the rank optimization is a non-convex issue, it is usually replaced by the relaxed nuclear norm constraint $\|\cdot\|_*$, i.e.,

$$\begin{aligned}&\min \|R\|_*\\ &\text{s.t. } S_\Omega(R) = \breve{R}.\end{aligned} \tag{22}$$

In practice, $\breve{R}$ is replaced by its estimation, denoted by $\widehat{R}_1$. Since there exists error between $\breve{R}$ and $\widehat{R}_1$, a bound ε is usually set, and the issue in equation (22) is transformed into

$$\begin{aligned}&\min \|R\|_*\\ &\text{s.t.} \left\|S_\Omega(R) - \widehat{R}_1\right\| \le \varepsilon.\end{aligned} \tag{23}$$

In practice, ε is usually chosen according to the noise tolerance; in this paper, it is set to 10^{-4}. The abovementioned optimization can be easily accomplished via the convex toolboxes, e.g., cvx. After that, the eigendecompositon can be performed, and then, the estimation of the signal subspace U_s is accomplished.

3.3. Parameter Estimation. Actually, the following rotational invariance relations exist:

$$\begin{cases} AD_1\{B\} = AD_2\{B\}\Phi^{(1,2)},\\ AD_1\{B\} = AD_3\{B\}\Phi^{(1,3)},\\ \vdots\\ AD_1\{B\} = AD_6\{B\}\Phi^{(1,6)},\end{cases} \tag{24}$$

where $D_n\{B\}$ returns a diagonal matrix, the diagonals of which are the n-th row of B, and $\Phi^{(1,q)} = \mathrm{diag}\{\beta_1^{(1,q)}, \beta_2^{(1,q)}, \ldots, \beta_K^{(1,q)}\}$, $q = 2, 3, \ldots, 6$, $\beta_k^{(1,q)} = b_k(q)/b_k(1)$. Next, we define

$$J_q = I_M \otimes i_{6,q}, \tag{25}$$

where $i_{6,q}$ accounts for the q-th column of I_6. The relations in equation (24) become

$$\begin{cases} J_1[A\odot B] = J_2[A\odot B]\Phi^{(1,2)},\\ J_1[A\odot B] = J_3[A\odot B]\Phi^{(1,3)},\\ \vdots\\ J_1[A\odot B] = J_6[A\odot B]\Phi^{(1,6)}.\end{cases} \tag{26}$$

Inserting equation (26) into equation (13) yields

$$\begin{cases} J_1U_s = J_2U_sT^{-1}\Phi^{(1,2)}T,\\ J_1U_s = J_3U_sT^{-1}\Phi^{(1,3)}T,\\ \vdots\\ J_1U_s = J_6U_sT^{-1}\Phi^{(1,6)}T,\end{cases} \tag{27}$$

where $(\cdot)^{-1}$ denotes the inverse. In other words, we have

$$\begin{cases} (J_2U_s)^\dagger J_1U_s = T^{-1}\Phi^{(1,2)}T,\\ T(J_3U_s)^\dagger J_1U_sT^{-1} = \Phi^{(1,3)},\\ \vdots\\ T(J_6U_s)^\dagger J_1U_sT^{-1} = \Phi^{(1,6)},\end{cases} \tag{28}$$

where the superscript $(\cdot)^\dagger$ denotes the pseudoinverse. Performing eigendecomposition on $(J_2U_s)^\dagger J_1U_s$, we can get the eigenvalues of the matrix and the associated eigenvectors, which reveal the estimation of $\Phi^{(1,2)}$ and the estimation of T (denoted as $\widehat{T}$). Calculating the left parts of equation (28) (except the first row), one can get the estimation of $\Phi^{(1,3)}$, $\Phi^{(1,4)}$, $\Phi^{(1,5)}$, and $\Phi^{(1,6)}$, respectively.

It has been pointed out in [20] that b_k can be written as

$$b_k = b_k(1)\begin{bmatrix}1\\ \beta_k^{(1,2)}\\ \vdots\\ \beta_k^{(1,6)}\end{bmatrix}. \tag{29}$$

It is easy to find that

$$\left(b_k(1)\begin{bmatrix}1\\ \beta_k^{(1,2)}\\ \beta_k^{(1,3)}\end{bmatrix}\right) * \left(b_k(1)\begin{bmatrix}\beta_k^{(1,4)}\\ \beta_k^{(1,5)}\\ \beta_k^{(1,6)}\end{bmatrix}\right)^* = \left\|b_k(1)\right\|^2 \left(\begin{bmatrix}1\\ \beta_k^{(1,2)}\\ \beta_k^{(1,3)}\end{bmatrix} * \begin{bmatrix}\beta_k^{(1,4)}\\ \beta_k^{(1,5)}\\ \beta_k^{(1,6)}\end{bmatrix}^*\right). \tag{30}$$

Let $e_k = [b_k(1), b_k(2), b_k(3)]^T$ and $h_k = [b_k(4), b_k(5), b_k(6)]^T$. Then, we have

$$\frac{e_k}{\|e_k\|} * \frac{h_k^*}{\|h_k\|} = \begin{bmatrix}\sin\theta_k\cos\phi_k\\ \sin\theta_k\sin\phi_k\\ \cos\theta_k\end{bmatrix}. \tag{31}$$

According to equation (30), we can get

$$\begin{aligned}\begin{bmatrix}u_k\\ v_k\\ w_k\end{bmatrix} &\triangleq \left(\frac{b_k(1)b_k^*(1)}{\|b_k(1)\|\|b_k^*(1)\|}\right)\cdot\frac{\begin{bmatrix}1\\ \beta_k^{(1,2)}\\ \beta_k^{(1,3)}\end{bmatrix}}{\left\|\begin{bmatrix}1\\ \beta_k^{(1,2)}\\ \beta_k^{(1,3)}\end{bmatrix}\right\|} * \frac{\begin{bmatrix}\beta_k^{(1,4)}\\ \beta_k^{(1,5)}\\ \beta_k^{(1,6)}\end{bmatrix}^*}{\left\|\begin{bmatrix}\beta_k^{(1,4)}\\ \beta_k^{(1,5)}\\ \beta_k^{(1,6)}\end{bmatrix}\right\|},\\ &\triangleq \frac{\begin{bmatrix}1\\ \beta_k^{(1,2)}\\ \beta_k^{(1,3)}\end{bmatrix}}{\left\|\begin{bmatrix}1\\ \beta_k^{(1,2)}\\ \beta_k^{(1,3)}\end{bmatrix}\right\|} * \frac{\begin{bmatrix}\beta_k^{(1,4)}\\ \beta_k^{(1,5)}\\ \beta_k^{(1,6)}\end{bmatrix}^*}{\left\|\begin{bmatrix}\beta_k^{(1,4)}\\ \beta_k^{(1,5)}\\ \beta_k^{(1,6)}\end{bmatrix}\right\|},\\ &= \begin{bmatrix}\sin\theta_k\cos\phi_k\\ \sin\theta_k\sin\phi_k\\ \cos\theta_k\end{bmatrix}.\end{aligned} \tag{32}$$

Obviously, $\|b_k(1)\|^2$ is a constant, and it has been removed by normalizing calculation. Let the estimations of u_k, v_k, and w_k be $\hat{u}_k$, $\hat{v}_k$, and $\hat{w}_k$, respectively. 2D-DOA can be estimated by

$$\begin{cases}\hat{\theta}_k = \arccos(\hat{w}_k),\\ \hat{\phi}_k = \arctan(\hat{v}_k/\hat{u}_k).\end{cases} \tag{33}$$

Once the 2D-DOA estimation has been accomplished, the polarization parameters can be estimated via the least squares approach in [30]. The details are omitted for simplicity.

4. Algorithmic Analyses

4.1. Important Remarks

Remark 1: as described in the context, the proposed method is insensitive to the r_n, which means it is suitable for arbitrary sensor geometry. Besides, it is insensitive to the sensor position error as well.

Remark 2: it is well known that the uniform noise is a special case of the nonuniform noise. Therefore, the proposed algorithm is effective in the white noise scenario.

Remark 3: as explained in [30], all the estimated parameters $\theta_k, \phi_k, \eta_k, \gamma_k$ are one-to-one paired.

Remark 4: since the matrix completion would not hurt the rank and the dimension of the covariance matrix, the proposed algorithm can identify the same number of sources in [20].

4.2. Stochastic CRB. Let $R_n = Q(q)$, where $q = [q_1, q_2 \cdots q_P]^T$ is a real vector that parameterizes R_n. From the derivations in [35], we can get the stochastic CRB on 2D-DOA and polarization angle, which are given by

$$\mathrm{CRB} = \frac{1}{L}\left[H - MT^{-1}M^T\right]^{-1}, \tag{34}$$

with

$$\begin{cases}H = 2\mathrm{Re}\left\{\left(\tilde{D}^H\prod_{\tilde{F}}^{\perp}\tilde{D}\right)\oplus\left(\left(R_c\tilde{F}^H\tilde{R}^{-1}\tilde{F}R_c\right)\right)\otimes 1_{4\times 4}\right)\right\},\\ M = 2\mathrm{Re}\left\{\begin{bmatrix}J^T\left(\left(\tilde{D}_d^H\prod_{\tilde{F}}^{\perp}\right)\otimes\left(\tilde{R}^{-1}\tilde{F}R_c\right)^T\right)\tilde{Q}^*\\ J^T\left(\left(\tilde{D}_p^H\prod_{\tilde{F}}^{\perp}\right)\otimes\left(\tilde{R}^{-1}\tilde{F}R_c\right)^T\right)\tilde{Q}^*\end{bmatrix}\right\},\\ T = 2\mathrm{Re}\left\{\tilde{Q}^H\left(\tilde{R}^{-T}\otimes\prod_{\tilde{F}}^{\perp}\right)\tilde{Q}\right\} - \tilde{Q}^H\left(\left(\prod_{\tilde{F}}^{\perp}\right)^T\otimes\prod_{\tilde{F}}^{\perp}\right)\tilde{Q},\end{cases} \tag{35}$$

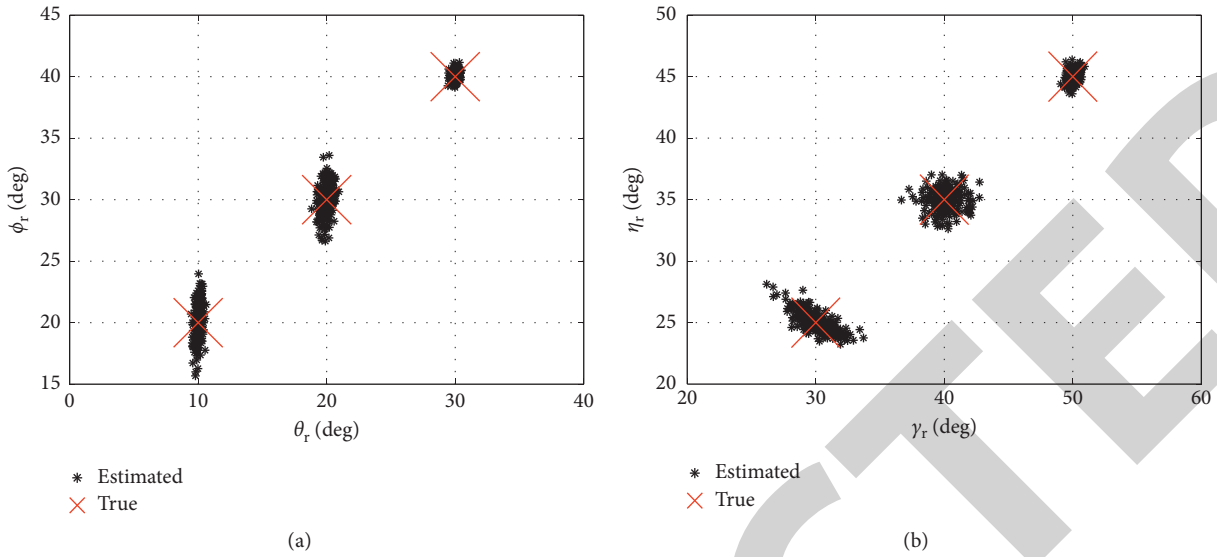

FIGURE 2: Scattering figures of our algorithm with $N = 4$, $L = 500$, and SNR = 20 dB: (a) 2D-DOA estimation; (b) polarization parameter estimation.

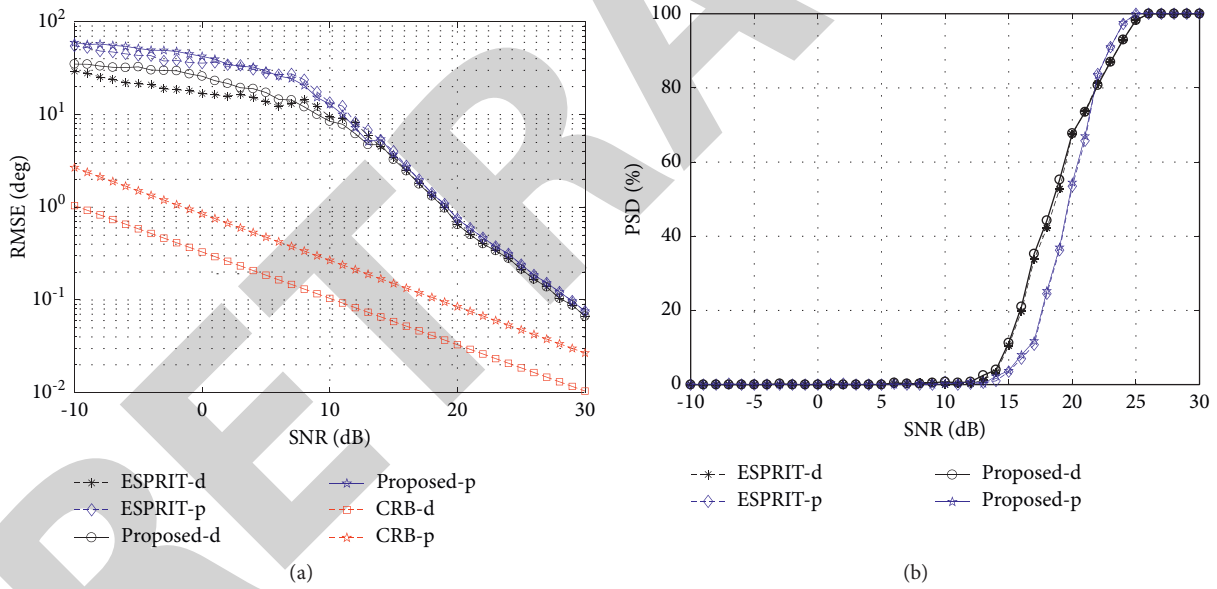

FIGURE 3: RMSE performance and PSD performance versus SNR (a) RMSE vs. SNR (b) PSD vs. SNR.

where $\widetilde{F} = Q^{-1/2}C$, $\prod_{\widetilde{F}}^{\perp} = I_{6N} - \prod_{\widetilde{F}}$ with $\prod_{\widetilde{F}} = \widetilde{F}\widetilde{F}^{\dagger}$, And $\widetilde{D} = [\widetilde{D}_d, \widetilde{D}_p]$, where $\widetilde{D}_d = Q^{-1/2}D_d$ and $\widetilde{D}_p = Q^{-1/2}D_p$ with $D_d = [\partial f_1/\partial\theta_1, \ldots, \partial f_K/\partial\theta_K, \partial f_1/\partial\phi_1, \ldots, \partial f_K/\partial\phi_K]$ and $D_p = [\partial f_1/\partial\eta_1, \ldots, \partial f_K/\partial\eta_K, \partial f_1/\partial\gamma_1, \ldots, \partial f_K/\partial\gamma_K]$, respectively, where f_k denotes that with the k-th column of C. $\widetilde{R} = Q^{-1/2}RQ^{-1/2}$. $J = [\mathrm{vec}\{e_1e_1^T\}, \mathrm{vec}\{e_2e_2^T\}, \ldots, \mathrm{vec}\{e_Ke_K^T\}]$, where e_k denotes the k-th column of I_K and vec$\{\cdot\}$ denotes the vectorization. $\widetilde{Q} = [vec\{\widetilde{Q}_1'\}, vec\{\widetilde{Q}_2'\}, \ldots, vec\{\widetilde{Q}_P'\}]$ with $\widetilde{Q}_p' = Q^{-1/2}Q_p'Q^{-1/2}$, $\widetilde{Q}_p' = \partial Q/\partial q_p$.

5. Simulation Results

In this subsection, the Monte Carlo simulation is utilized to assess the estimation accuracy. We consider an arbitrary N-element EMVS receives array configuration, and we assume that $K = 3$ far-field sources impinge on the array, whose parameters are $\theta = (10^\circ, 20^\circ, 30^\circ)$, $\phi = (20^\circ, 30^\circ, 40^\circ)$, $\gamma = 3\,(0^\circ, 40^\circ, 50^\circ)$, and $\eta = (25^\circ, 35^\circ, 45^\circ)$. Moreover, we suppose that L snapshots have been collected. Each result

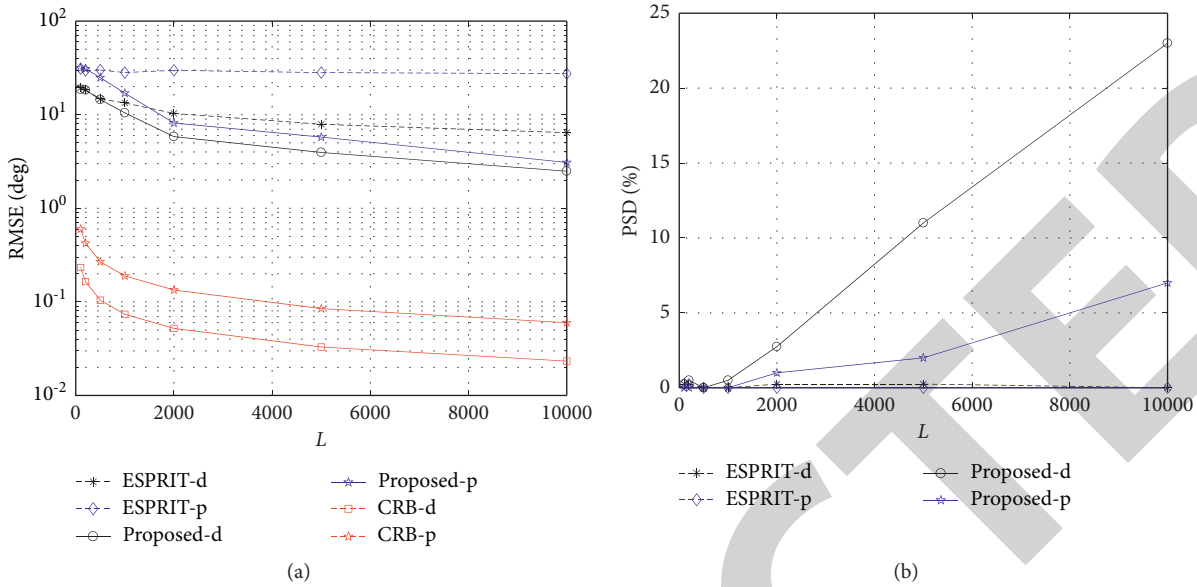

Figure 4: RMSE performance and PSD performance versus L (a) RMSE vs. L (b) PSD vs. L.

relies on 200 experiments. In the simulation, the signal-to-noise ratio (SNR) is defined as the ration of the power of the two components in equation (6). Two measures are adopted: one is the root mean square error (RMSE), and the other is the probability of successful detection (PSD). In all the simulations, the noise is randomly generated with powers which are uniformly chosen from [1 100000].

Example 1. We give the scattering figures of the proposed algorithm with $N = 4$ and $L = 500$, where the SNR is set to 20 dB. Herein, the EMVS is randomly placed in a three-dimensional space with (x_n, y_n, z_n) fulfilling a uniform distribution with interval $[-0.5\lambda, 0.5\lambda]$. Figure 2 shows the results of direction angle estimation and polarization parameters estimation. Clearly, all the angles can be correctly estimated and automatically paired. It is evident that our estimator is effective in a nonuniform noise scenario.

Example 2. We present the RMSE and PSD curves of the proposed estimator. Herein, a successful trial is recognized if the absolute error of the estimated angle is smaller than 1°. In Figure 3, we plot the average estimation performance on the direction angle estimate (labelled with the suffix "$-d$") and polarization angle estimate (labelled with the suffix "$-p$"), where $N = 4$ and $L = 500$. In contrast, the RMSE results of ESPRIT in [20] as well as the CRB are added. From the result, we can observe that the RMSE performance of both the proposed estimator and ESPRIT is improved with the increasing SNR, while the PSD of both estimators reaches 100%, once SNR is larger than a threshold (e.g., 25 dB). Besides, it depicts that the proposed estimator provides more accurate parameter estimation performance for direction angle estimation when SNR <10 dB. However, the improvement is not obvious as for polarization parameter estimation.

Example 3. We plot the average RMSE performance and the average PSD curves with different snapshot number L in Figure 4, while N and SNR are set to 4 and 10 dB, respectively. Notably, both the proposed estimator and ESPRIT provide better estimation performance with larger L. Similar to the previous observation, the proposed algorithm outperforms the ESPRIT algorithm. The improvement benefits from the fact that the proposed algorithm can eliminate the noise, while traditional ESPRIT algorithm cannot avoid the effect of nonuniform noise.

6. Conclusions

In this paper, we investigate the issue of angle estimation using EMVS array with arbitrary sensor geometry and nonuniform noise. A matrix completion-based algorithm has been proposed, which first eliminates the effect of nonuniform via solving a convex problem. After the noiseless covariance matrix has been recovered, the traditional subspace method is utilized to estimate the signal subspace, and the ESPRIT idea is adopted for 2D-DOA estimation. Our algorithm is robust to nonuniform noise and sensor position error. It should be pointed out that the tensor structure has not been exploited. More attention should be paid to this topic to further increase the estimation accuracy.

Data Availability

No data were used in this study.

Conflicts of Interest

The authors declare no conflicts of interest.

Acknowledgments

This work was supported by the National Natural Science Foundation of China under Grant no. 62071476.

References

[1] G. Gui, M. Liu, F. Tang, N. Kato, and F. Adachi, "6G: opening new horizons for integration of comfort, security, and intelligence," *IEEE Wireless Communications*, vol. 27, no. 5, pp. 126–132, 2020.

[2] H. Wang, L. Xu, Z. Yan, and T. A. Gulliver, "Low-complexity MIMO-FBMC sparse channel parameter estimation for industrial big data communications," *IEEE Transactions on Industrial Informatics*, vol. 17, no. 5, pp. 3422–3430, 2021.

[3] H. Wang, X. Li, R. H. Jhaveri et al., "Sparse bayesian learning based channel estimation in FBMC/OQAM industrial IoT networks," *Computer and Communications*, vol. 17, pp. 40–45, 2021.

[4] L. Wan, K. Liu, Y.-C. Liang, and T. Zhu, "DOA and polarization estimation for non-circular signals in 3-D millimeter wave polarized massive MIMO systems," *IEEE Transactions on Wireless Communications*, vol. 20, no. 5, pp. 3152–3167, 2021.

[5] D. Chen, B. Chen, and G. Qin, "Angle estimation using ESPRIT in MIMO radar," *Electronics Letters*, vol. 44, no. 12, pp. 770-771, 2008.

[6] J. Chen, H. Gu, and W. Su, "Angle estimation using ESPRIT without pairing in MIMO radar," *Electronics Letters*, vol. 44, no. 24, pp. 1422-1423, 2008.

[7] I. Bekkerman and J. Tabrikian, "Target detection and localization using MIMO radars and sonars," *IEEE Transactions on Signal Processing*, vol. 54, no. 10, pp. 3873–3883, 2006.

[8] H. Yan, J. Li, and G. Liao, "Multitarget identification and localization using bistatic MIMO radar systems," *EURASIP Journal on Applied Signal Processing*, vol. 2008, Article ID 8828610, 2008.

[9] X. Zhang, L. Xu, L. Xu, and D. Xu, "Direction of departure (DOD) and direction of arrival (DOA) estimation in mimo radar with reduced-dimension music," *IEEE Communications Letters*, vol. 14, no. 12, pp. 1161–1163, 2010.

[10] Z. D. Zheng and J. Y. Zhang, "Fast method for multi-target localisation in bistatic MIMO radar," *Electronics Letters*, vol. 47, no. 2, pp. 138-139, 2011.

[11] B. Tang, J. Tang, Y. Zhang, and Z. Zheng, "Maximum likelihood estimation of DOD and DOA for bistatic MIMO radar," *Signal Processing*, vol. 93, no. 5, pp. 1349–1357, 2013.

[12] Y. Cheng, R. Yu, H. Gu, and W. Su, "Multi-SVD based subspace estimation to improve angle estimation accuracy in bistatic MIMO radar," *Signal Processing*, vol. 93, no. 7, pp. 2003–2009, 2013.

[13] X. Zhang, Z. Xu, L. Xu, and D. Xu, "Trilinear decomposition-based transmit angle and receive angle estimation for multiple-input multiple-output radar," *IET Radar, Sonar & Navigation*, vol. 5, no. 6, pp. 626–631, 2011.

[14] J. Shi, F. Wen, and T. Liu, "Nested MIMO radar: coarrays, tensor modeling and angle estimation," *IEEE Transactions on Aerospace and Electronic Systems*, vol. 57, no. 1, pp. 573–585, 2021.

[15] W. Rao, D. Li, and J. Q. Zhang, "A tensor-based approach to L-shaped arrays processing with enhanced degrees of freedom," *IEEE Signal Processing Letters*, vol. 25, no. 2, pp. 234–238, 2018.

[16] R. Goossens and H. Rogier, "A hybrid UCA-RARE/Root-MUSIC approach for 2-D direction of arrival estimation in uniform circular arrays in the presence of mutual coupling," *IEEE Transactions on Antennas and Propagation*, vol. 55, no. 3, pp. 841–849, 2007.

[17] M. D. Zoltowski, M. Haardt, and C. P. Mathews, "Closed-form 2-D angle estimation with rectangular arrays in element space or beamspace via unitary ESPRIT," *IEEE Transactions on Signal Processing*, vol. 44, no. 2, pp. 316–328, 1996.

[18] J. He, L. Li, and T. Shu, "Sparse nested arrays with spatially spread orthogonal dipoles: high accuracy passive direction finding with less mutual coupling," *IEEE Transactions on Aerospace and Electronic Systems*, 2021.

[19] K. T. Wong and X. Yuan, ""Vector cross-product direction-finding" with an electromagnetic vector-sensor of six orthogonally oriented but spatially noncollocating dipoles/loops," *IEEE Transactions on Signal Processing*, vol. 59, no. 1, pp. 160–171, 2011.

[20] K. T. Wong and M. D. Zoltowski, "Closed-form direction finding and polarization estimation with arbitrarily spaced electromagnetic vector-sensors at unknown locations," *IEEE Transactions on Antennas and Propagation*, vol. 48, no. 5, pp. 671–681, 2000.

[21] A. Nehorai and E. Paldi, "Vector-sensor array processing for electromagnetic source localization," *IEEE Transactions on Signal Processing*, vol. 42, no. 2, pp. 376–398, 1994.

[22] J. Li, "Direction and polarization estimation using arrays with small loops and short dipoles," *IEEE Transactions on Antennas and Propagation*, vol. 41, no. 3, pp. 379–387, 1993.

[23] K. T. Wong and M. D. Zoltowski, "Uni-vector-sensor ESPRIT for multisource azimuth, elevation, and polarization estimation," *IEEE Transactions on Antennas and Propagation*, vol. 45, no. 10, pp. 1467–1474, 1997.

[24] K. T. Wong and M. D. Zoltowski, "Self-initiating music-based direction finding and polarization estimation in spatio-polarizational beamspace," *IEEE Transactions on Antennas and Propagation*, vol. 48, no. 8, pp. 1235–1245, 2000.

[25] M. D. Zoltowski and K. T. Wong, "ESPRIT-based 2-D direction finding with a sparse uniform array of electromagnetic vector sensors," *IEEE Transactions on Signal Processing*, vol. 48, no. 8, pp. 2195–2204, 2000.

[26] S. Miron, N. Le Bihan, and J. Mars, "Vector-sensor MUSIC for polarized seismic sources localization," *EURASIP Journal on Applied Signal Processing*, vol. 48, no. 8, Article ID 280527, 2005.

[27] J. He and Z. Liu, "Computationally efficient 2D direction finding and polarization estimation with arbitrarily spaced electromagnetic vector sensors at unknown locations using the propagator method," *Digital Signal Processing*, vol. 19, no. 3, pp. 491–503, 2009.

[28] T. Ahmed, Z. Xiaofei, and Z. Wang, "DOA estimation for coprime EMVS arrays via minimum distance criterion based on PARAFAC analysis," *IET Radar, Sonar & Navigation*, vol. 13, no. 1, pp. 65–73, 2019.

[29] S. Chintagunta and P. Palanisamy, "2D-DOD and 2D-DOA estimation using the electromagnetic vector sensors," *Signal Processing*, vol. 147, pp. 163–172, 2018.

[30] F. Wen, J. Shi, and Z. Zhang, "Closed-form estimation algorithm for EMVS-MIMO radar with arbitrary sensor geometry," *Signal Processing*, vol. 186, Article ID 108117, 2021.

[31] X. Wang, M. Huang, and L. Wan, "Joint 2D-DOD and 2D-DOA estimation for coprime EMVS-MIMO radar," *Circuits, Systems, and Signal Processing*, 2021.

Hindawi
International Journal of Antennas and Propagation
Volume 2023, Article ID 9834050, 1 page
https://doi.org/10.1155/2023/9834050

Retraction

Retracted: The System Research and Implementation for Autorecognition of the Ship Draft via the UAV

International Journal of Antennas and Propagation

Received 19 December 2023; Accepted 19 December 2023; Published 20 December 2023

This article has been retracted by Hindawi following an investigation undertaken by the publisher [1]. This investigation has uncovered evidence of one or more of the following indicators of systematic manipulation of the publication process:

(1) Discrepancies in scope

(2) Discrepancies in the description of the research reported

(3) Discrepancies between the availability of data and the research described

(4) Inappropriate citations

(5) Incoherent, meaningless and/or irrelevant content included in the article

(6) Manipulated or compromised peer review

The presence of these indicators undermines our confidence in the integrity of the article's content and we cannot, therefore, vouch for its reliability. Please note that this notice is intended solely to alert readers that the content of this article is unreliable. We have not investigated whether authors were aware of or involved in the systematic manipulation of the publication process.

Wiley and Hindawi regrets that the usual quality checks did not identify these issues before publication and have since put additional measures in place to safeguard research integrity.

We wish to credit our own Research Integrity and Research Publishing teams and anonymous and named external researchers and research integrity experts for contributing to this investigation.

The corresponding author, as the representative of all authors, has been given the opportunity to register their agreement or disagreement to this retraction. We have kept a record of any response received.

References

[1] W. Zhan, S. Hong, Y. Sun, and C. Zhu, "The System Research and Implementation for Autorecognition of the Ship Draft via the UAV," *International Journal of Antennas and Propagation*, vol. 2021, Article ID 4617242, 11 pages, 2021.

Hindawi
International Journal of Antennas and Propagation
Volume 2021, Article ID 4617242, 11 pages
https://doi.org/10.1155/2021/4617242

Research Article

The System Research and Implementation for Autorecognition of the Ship Draft via the UAV

Wei Zhan, Shengbing Hong, Yong Sun, and Chenguang Zhu

School of Computer Science, Yangtze University, Jingzhou 434023, China

Correspondence should be addressed to Wei Zhan; zhanwei814@yangtzeu.edu.cn

Received 8 June 2021; Revised 16 July 2021; Accepted 4 August 2021; Published 17 August 2021

Academic Editor: Jin He

The reading of the ship draft is an important step in the process of weighing and pricing. The traditional detection method is time-consuming and labor-consuming, and it is easy to lead to misdetection. In order to solve the above problems, this paper introduces the computer image processing technology based on deep learning, and the specific process is divided into three steps: first, the video sampling is carried out by the UAV to obtain a large number of pictures of the ship draft reading face, and the images are preprocessed; then, the deep learning target detection algorithm of improved YOLOv3 is used to process the images to predict the position of the waterline and identify the draft characters; finally, the prediction results are analyzed and processed to obtain the final reading results. The experimental results show that the ship draft reading method proposed in this paper has obvious effects. The method has a good detection effect on high-quality images, and the accuracy rate can reach 98%. The accuracy rate can also reach 73% for the images with poor quality caused by improper capture, character corrosion, bad weather, etc. This method is a kind of artificial intelligence method with safe measurement process, high measurement effect, and accuracy, providing a new idea for related research.

1. Introduction

The ship draft reading is an important method widely used in measuring the ship cargo load and identifying the weight of import and export commodities. According to the statistics of 2021 Express, the cargo throughput of China's ports above designated size has reached 2.3 billion tons, with a year-on-year growth of 6.4%, the container throughput has increased by 2.27% to 8.3%, and the growth rate is significantly faster than that of the cargo throughout of 6.4%. Among them, the import volume of foreign trade coal has increased significantly, and the growth rate exceeds the expected value [1].

Accurate results of draft weight measurement are of great significance to the protection of the interests of carriers, consignors, and consignees. The current mainstream method is artificial observation. However, with the increasingly close economic exchanges among countries, the efficiency of manual observation is difficult to support the rapid growth of ship freight demand. In recent years, most of the new draft weight measurement methods have higher requirements on the cost and maintenance of weight measurement equipment.

There are a variety of existing draft detection methods [2], mainly including (1) artificial observation, which is vulnerable to interference from subjective factors and objective condition [3]. The observation results have a large deviation from the actual real value and need a large amount of manpower and time consumption. (2) The pressure sensor detection, using the pressure sensor installed in advance on the outside of the ship hull, obtains the change of water depth through the pressure before and after loading, with high accuracy. However, due to the high density and accuracy of the instrument, the installation is inconvenient, and the later maintenance cost is high, so it is not easy to popularize. (3) Sonar detection [4]: because of the slow attenuation speed of ultrasonic energy transfer in water and strong penetration, sonar detection uses this characteristic to measure the waterline of the ship. However, due to the accuracy of the instrument and since the installation

position is usually underwater, there are also problems of difficult installation and high maintenance cost in the later stage. (4) Computer image detection: with the current rapid development of artificial intelligence technology, its application scope spreads to various fields, among which the image processing technology is particularly vigorous. In fields such as UAV [5] and medicine [6], a lot of automatic image recognition technologies based on the principle of image processing [7] have been produced. There has been some exploration based on the image detection technology in the field of ship draft reading. Table 1 is the comparison of the parameters for the above water gauge detection methods.

As can be seen from Table 1, deep learning image detection technology based on computer vision has the best effect, and the popularity of high-precision and low-cost camera equipment in the market also provides the possibility of draft reading based on computer vision. At present, the existing deep learning method is to use semantic segmentation algorithm to segment the target area in the image [8], obtain the waterline position, and then obtain the final draft according to the traditional method. At the same time, target detection technology has become more and more mature in recent years, such as Faster R-CNN, SSD, YOLO, and other deep learning algorithms, which have achieved good results in the field of target detection. Therefore, this paper carries out research from the direction of computer vision and proposes a deep learning object detection algorithm based on improved YOLOv3 [9] to conduct research on the draft reading. By preprocessing the sampled data in the early stage and inputting the YOLOv3 network for training, the position of the waterline and the draft character can be predicted. Then, the accuracy of the results can be judged according to the loss of the network. Finally, the draft reading formula can be obtained according to the processing of some fitting functions.

2. Materials and Methods

2.1. Experimental Materials

2.1.1. Experimental Equipment and Environment. This paper is to study the application of deep learning target detection algorithm in ship draft reading. Because it is an image processing technology based on deep learning, it has high requirements on equipment. The hardware device used in this paper is Intel Core i9 9900k, 32 GB RAM, and GPU is RTX 2080Ti; the software experimental environment is Python 3.6.8 and PyCharm 2020.3 professional edition, using NumPy, OpenCV, and Matplotlib module package to process videos and images, and using PyTorch to build the neural network.

2.1.2. Image Acquisition of the Ship Draft Surface. The ship draft surface video is shot at a customs office in Suzhou by F450 UAV with a resolution of 1920×1080. There are 50 videos (in different weather conditions), each of which lasts for 5 minutes, with a total of 250 minutes. Figure 1 shows the effect of video shooting.

2.2. Basic Principle of Ship Draft Logarithmic Detection. The process of reading the draft mainly involves two parts: one is the character of the draft on the ship and the other is the position of the waterline. The position of the waterline can be detected by image background subtraction or edge detection. However, considering the fluctuation of the water surface and various factors affecting the color difference, the deep learning detection algorithm using YOLOv3 will have a better effect. For the draft character, it is actually the process of target detection, which can be realized by using Faster R-CNN, SSD, YOLOv3, and other detection methods. However, since the first two algorithms are behind YOLOv3 in both mAP and detection speed, both parts are implemented by using YOLOv3 detection algorithm in the end.

3. Experimental Principle and Process

In this paper, the improved YOLOv3 network is used to detect the waterline and draft character. Its network structure is shown in Figure 2. Its backbone network is Darknet53, which contains 53 convolution layers and is a feature extraction network. Darknet contains a series of residual structures that are the residual modules. The convolutional layer in the network actually includes three parts: Conv2d layer, BN layer, and LeakyReLu layer. Considering that the waterline in the draft image is clear and the draft character is also relatively easy to detect the character, it is unnecessary to use such a deep Darknet53 network as the feature extraction network. This paper designs a light feature extraction network S-Net (small network) for this detection task. After the feature extraction network, the prediction output of three branches is followed. The first prediction output corresponds to the prediction of a large target; the second prediction output is the fusion of a medium-sized feature map, predicting a medium-sized target; the third prediction output is the fusion of a large-sized feature map and, finally, is the prediction of a small target. Please refer to Figure 2 for specific information.

3.1. Image Preprocessing. OpenCV library is used to read the captured ship video images. According to the change of the ship position in the video, we finally decided to take a frame every 3 seconds. A total of 250 minutes of the video can be sampled to 5000 pictures. In the shooting video, the characters and numbers on the hull are not on a vertical line due to the shooting angle and hull shaking, which will greatly affect the training effect. Therefore, this paper is looking for a better processing method and finally decided to use the principle of image affine transformation to process the image in order to get the image of vertical characters and numbers. Image affine transformation is a linear transformation from two-dimensional coordinates (x, y) to two-dimensional coordinates (u, v), and the mathematical formula is as follows:

$$\begin{cases} u = a_1 x + b_1 y + c_1, \\ v = a_2 x + b_2 y + c_2. \end{cases} \tag{1}$$

Table 1: Parameters of existing draft reading methods.

Contrast parameters	Artificial observation	Pressure sensor detection	Sonar detection	Traditional image recognition technology detection	Deep learning model detection
Detection accuracy	Average	Higher	Higher	Low	Higher
Maintenance cost	Lower	Higher	Higher	Average	Average
Distance from the ship	Average	Unreachable	Higher	Higher	Higher
Human resources	Higher	Low	Low	Low	Low

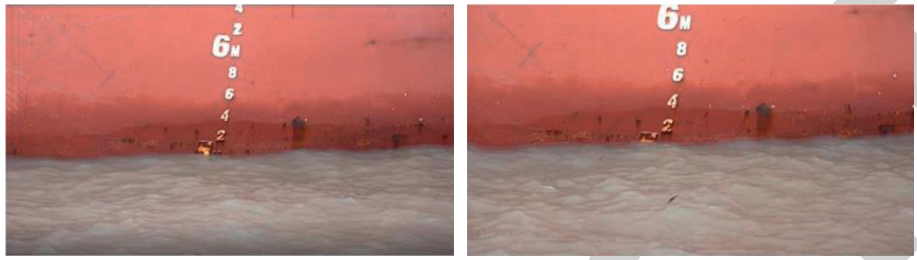

Figure 1: Video capture of the ship draft surface.

Affine transformation maintains the straightness and parallelism of the two-dimensional image. In other words, the original straight line still remains the same, as well as the original parallel line, but the position coordinates of each point have changed considerably. The inclined straight line can be turned into vertical so that the problem that the hull characters are not in the vertical line can be solved. The image after affine processing is shown in Figure 3.

3.2. Waterline Detection. The YOLOv3 grid is used to detect the waterline. Although the whole waterline can contain more waterline information, the final recognition result obtained based on this information cannot fit the waterline, so it is necessary to restore the water wave in the actual shipping process. Therefore, the YOLOv3 network can be used to mark and optimize the waterline in the actual shipping process. Due to different styles of each picture, this paper uses the artificial tagging, which is mainly to frame the picture of the ship dataset manually, use multiple squares to mark the waterline [6], transfer the manually marked picture to the YOLOv3 network for training, and then forecast the new picture to obtain the predicted waterline position of the new picture. The effect is shown in Figure 4, which corresponds to the waterline marked manually and detected by YOLOv3, respectively.

3.3. Draft Character Recognition. The recognition of the draft character in this paper is also detected using the target detection algorithm of YOLOv3. The numbers and characters are manually labeled and input into the network for training.

As the main network of YOLOv3 uses the Darknet network, it is a kind of convolutional neural network as shown in Figure 5. The three characteristics of the convolutional neural network [10] are that it has local receptive field, weight sharing, and downsampling, greatly reduces the complexity of the network model and the number of parameters, and has a better processing effect on the grid data than the traditional DNN. Therefore, it is widely used in image classification and target recognition field.

Assuming that layer L is a convolution layer and layer $L+1$ is a pooling layer, the calculation process of the j feature map of layer L is shown in formula (2), where k is the convolution kernel.

$$x_j^L = f\left(\sum_{i\in M_j} i_x^{l-1} * k_{ij}^L + b_j^L\right). \tag{2}$$

The residual calculation formula of the j feature map in layer L is as follows:

$$\delta_j^l = \beta_j^{l+1}\left(f'\left(u_j^l\right)\odot \mathrm{up}\left(\delta_j^{l+1}\right)\right). \tag{3}$$

YOLO algorithm adopts a single convolutional neural network model to achieve end-to-end target detection. The input image is adjusted to 448×448 and then input into the CNN to process the network prediction results to obtain the detected target, as shown in Figure 6.

Specifically, the CNN of YOLO divides the input image into $S\times S$ grids [11], and each grid will detect the target whose center point falls in the grid and predict bounding boxes and the corresponding confidence score for the target, which is defined as

$$\text{confidence} = \Pr(\text{object}) * \mathrm{IOU}_{\text{pred}}^{\text{truth}}, \tag{4}$$

where $\Pr(\text{object})$ is the possibility that the bounding box contains the target, which is 1 when containing the target and 0, otherwise. $\mathrm{IOU}_{\text{pred}}^{\text{truth}}$ is the accuracy of the bounding box when it contains the target, which is expressed by the intersection and union ratio of the actual box and the prediction box.

This paper attempts to mark the draft character in 5000 pictures in different situations and obtains the effect as shown in Figure 7.

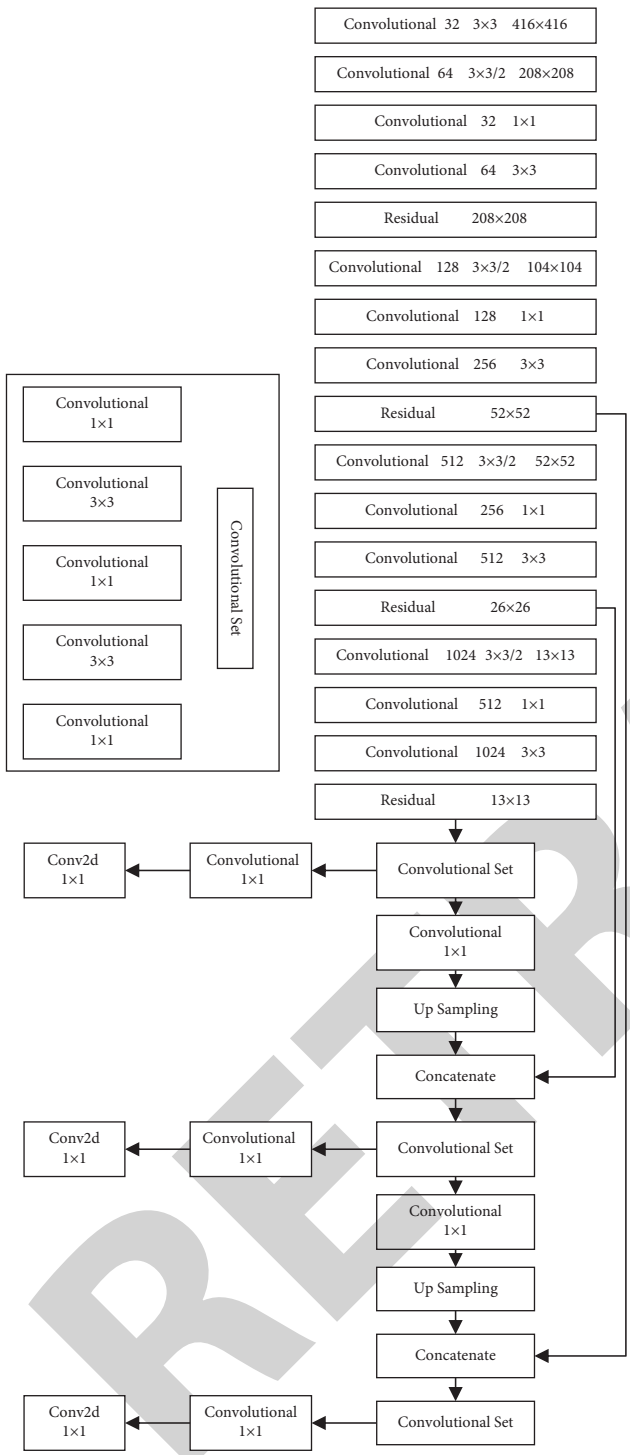

Figure 2: Network structure of improved YOLOv3.

Note that the left reading of the downmost character is "M," and the minimum centimeter reading is *C*. Due to the complexity of the real situation, the prediction value should be further cleaned according to the correlation of characters in the vertical direction to reduce the possibility of wrong prediction after obtaining the prediction results.

3.4. Acquisition of Reading Results. After the implementation of the first two parts, the prediction results of the waterline and the draft character are finally obtained. The next problem is how to obtain the final draft reading according to these prediction results. The specific method is shown in Figure 8, which requires a series of processing to obtain the final reading formula.

3.4.1. Fitting Function of the Draft Character. Combined with the reading rules of the ship draft, under ideal conditions shown in Figure 9, the draft is perpendicular to the water surface, and the number is 2, 4, 6, and 8 m counting characters and *M* characters, whose height is 10 cm, and the spacing between two adjacent characters is 10 cm.

Since the arrangement of the ship draft character will be curved because of the curvature of the ship, the coordinate system is established with the upper left corner of the picture as the origin. It is assumed that, in the recognition result of the draft character, the bottom ordinate and center abscissa of the character prediction box with the lowest y value (negative value) in the picture are (X_1^B, Y_1^B), with its top ordinate and center abscissa (X_1^T, Y_1^T). Because of the curvature of the hull, the pixel changes between the characters with more spacing are not consistent, and there is no predictive value. However, the pixel changes between the characters with shorter spacing are basically consistent, which can fit the curve. After the experiment, this paper takes three numbers with the actual total distance less than 1 m from bottom to top and records them in Table 2.

According to Table 2, the curve function $W(x)$ passing through the middle axis of the bottom three characters of the image is obtained by fitting the water ruler character curve with the least square method. When reading the draft, there will be an intersection point between this function and the waterline fitting function, and the draft reading can be obtained by obtaining the value of the ordinate of the intersection.

3.4.2. Fitting the Mapping Function of Pixels in Height. The relationship between the actual height and the pixel changes by the mapping function Y, and the result goes 0, which is recorded in Table 3.

According to Table 3, the mapping function $Z_1(y)$ of interval pixel changing at the actual height is deduced by using the least square method. The least square method is the basis of classification regression algorithm, which seeks the best function matching of data by minimizing the sum of squares of errors and is defined as

$$S_{\epsilon^2} = \min \sum_{i=1}^{n} \left(y_i - f(x_i)\right)^2. \tag{5}$$

The optimal value is y which makes S_{ϵ^2} the minimum.

When the independent variable of the polynomial is x_i, $f(x_i)$ is the predicted value and y_i is the real value. When the sum of squares between the two differences is the

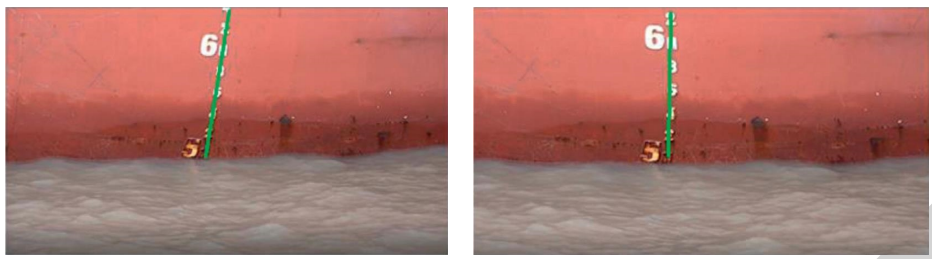

(a) (b)

Figure 3: (a) The image of ship draft before affine transformation. (b) The image after affine transformation.

(a) (b)

Figure 4: (a) Marked image by YOLOv3. (b) Detection image of waterline by YOLOv3.

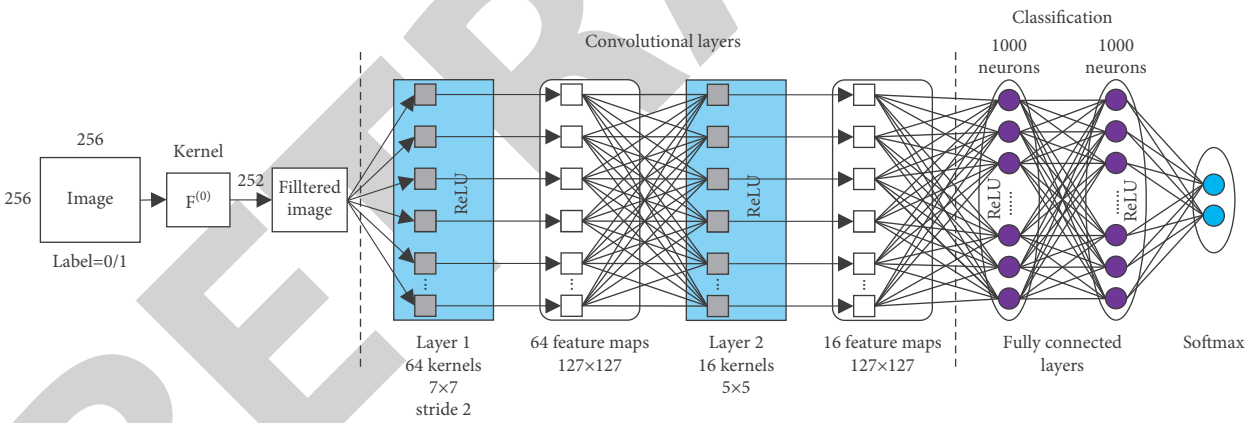

Figure 5: Convolutional neural network.

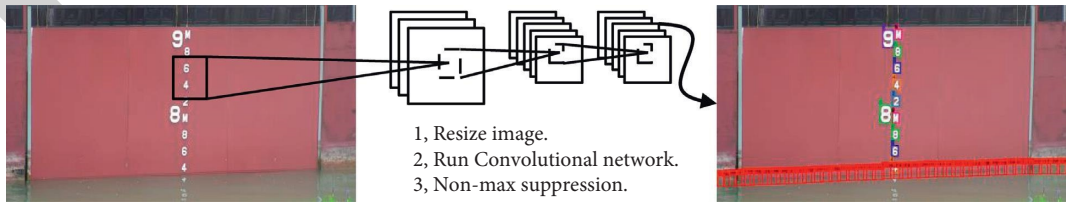

Figure 6: The result of prediction via the CNN of YOLO.

smallest, it can be considered that the deviation degree of all predicted values from the real value is to the least extent, which is the optimal fitting curve. The higher the degree of the polynomial is, the more fitting the curve will be, but the slower the fitting speed will be. After testing, eight groups of data and a six-degree polynomial can meet the needs.

The mapping function $Z_1(y)$ fitted by the least square method has a good anti-interference ability when the hull

(a) (b)

Figure 7: (a) Prediction result 1. (b) Prediction result 2.

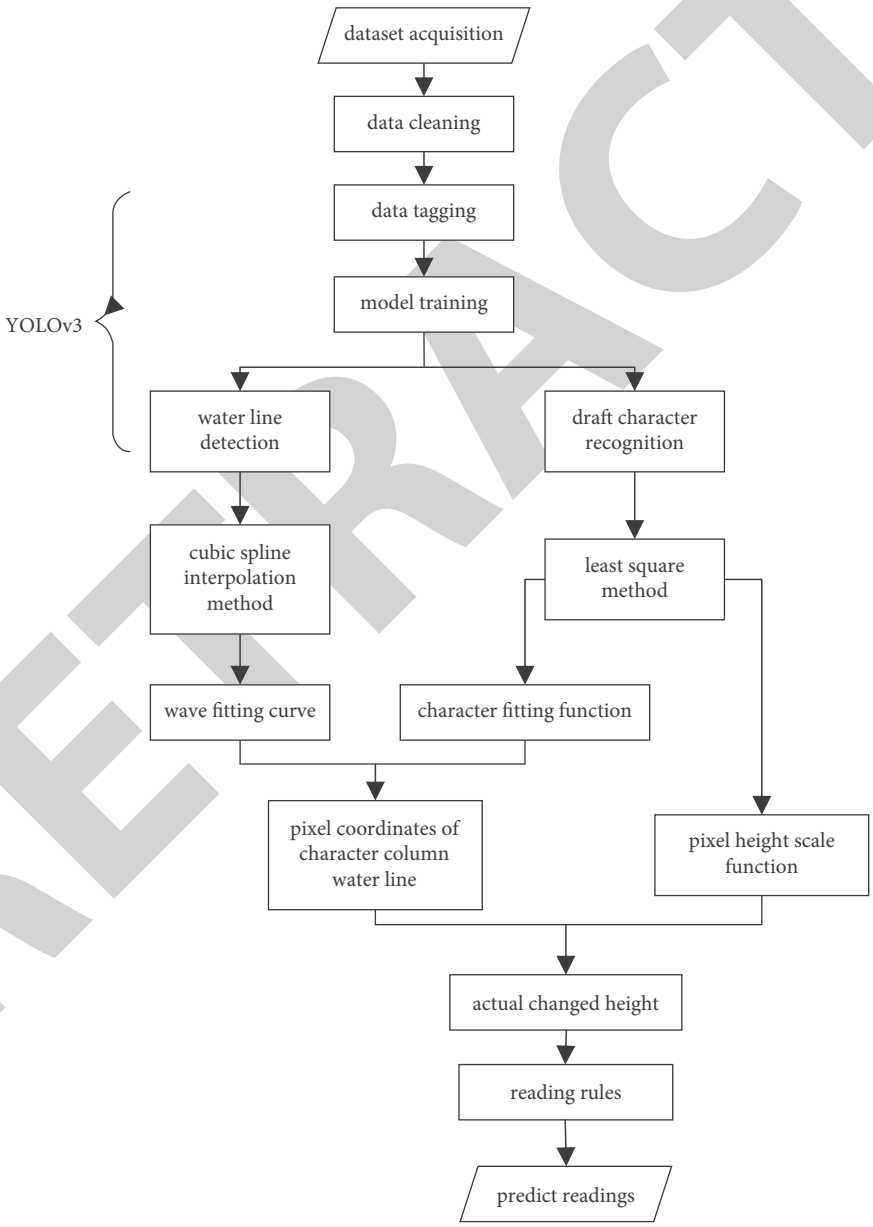

Figure 8: Flowchart of the draft reading.

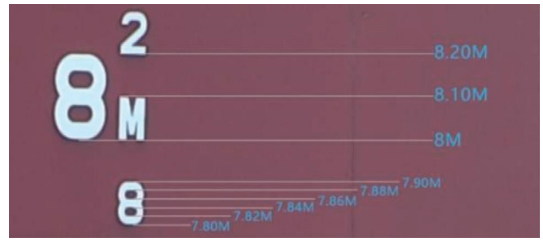

Figure 9: Draft reading rules.

Table 2: Variables of the character fitting function.

(X_1^B, Y_1^B)	(X_1^T, Y_1^T)	(X_2^B, Y_2^B)	(X_2^T, Y_2^T)	(X_3^B, Y_3^B)	(X_3^T, Y_3^T)	(X_4^B, Y_4^B)	(X_4^T, Y_4^T)

Table 3: Variables of the mapping function.

$(Y_1^B, 70)$	$(Y_1^T, 60)$	$(Y_2^B, 50)$	$(Y_2^T, 40)$	$(Y_3^B, 30)$	$(Y_3^T, 20)$	$(Y_4^B, 10)$	$(Y_4^T, 0)$

appears radian, but when the character recognition result box deviates, it will lead to a certain deviation of the mapping result. In this case, the mapping function $Z_2(y)$ needs to be calculated. According to the proportional relationship between the height of the character box at the bottom of the hull recognition and 10 cm, formulas (6) and (7) are obtained:

$$\frac{Y_1^B - Y_1^T}{10} = \frac{Y_{\text{join}} - Y_1^B}{u}, \tag{6}$$

$$Z_2(y) = \left(10 \times \left(Y_{\text{join}} - Y_1^B\right)\right) \div \left(Y_1^B - Y_1^T\right), \tag{7}$$

where u is the centimeter from the bottom of the lowest character to the surface of water. Compared with $Z_1(y)$, $Z_2(y)$ reduces the error caused by the deviation of the character recognition box, but it does not have the advantage of $Z_1(y)$ in hull radian detection. Therefore, after unifying the specifications of X and Y, let the manual label reading be the dependent variable H, the variation of X_1^B and X_4^T be n, $Z_1(y) - 70$ be m, and $Z_2(y)$ be u. The least square method of three variables [12] is used to further study the relationship between the above three and fit the mapping function $Z(y)$. The function reflects the relationship between the pixel height of the draft reading and the actual height, through which the actual draft reading can be obtained.

3.4.3. Fitting the Wave Curve. After the experiment of waterline prediction, the number of prediction boxes in a picture is usually about 20, and the central coordinate of the prediction box is taken. Here, two methods are tried to determine the waterline curve $S(x)$, and the fitting effect of the waterline is relatively good. The details are as follows:

(1) Fitting the wave curve with the least square method: Taking four center points as a set of data, the cubic polynomial is established, and the fitting function is calculated by using the least square method. Because the distribution of the prediction box is roughly uniform throughout the horizontal axis of the picture, the first coordinate of the latter set of data can be taken as the fourth coordinate of the previous set of data, and the final result is a fitting wave curve.

(2) Fitting the wave curve by cubic spline interpolation: In the real situation, the detected prediction box will show the phenomenon of misidentification. Thus, in the above method (1), the least square curve fitting is carried out in segments to reduce the error interference. Method (2) also uses the cubic spline difference method [13–18] to fit the curve based on the idea of segmentation.

Cubic spline interpolation method is to divide an interval (a, b) into n intervals of $x_0 = a < x_1, \ldots\ldots, x_{n-1} < b = x_n$ and use the known $n + 1$ points to simulate an unknown function $S(x)$. The function $S(x)$ satisfies the following conditions:

① $S(x_i) = f(x_i) = y_i$, $(i = 0, 1, 2, \ldots, n)$.

② $S(x)$ is a cubic polynomial on each subinterval $[x_i - x_{i+1}]$.

③ $S(x)$ is second-order continuously differentiable on $[a, b]$, and $S(x)$ satisfies

$$\begin{cases} S_{i-1}(x_i) = S_i(x_i), \\ S'_{i-1}(x_i) = S'_i(x_i), \\ S''_{i-1}(x_i) = S''_i(x_i). \end{cases} \tag{8}$$

The specific fitting method to fit the wave curve needs to be selected according to the actual dataset. The least square fitting curve is a polynomial form to determine myopia by tracing points. However, due to the error of given data, the mathematical model of fitting curve cannot be selected at the beginning, and it often needs multiple calculations and analyses to obtain a good fitting effect. Cubic spline interpolation method is related to the number of difference points, accuracy, and selection of difference points. The more the difference points, the better the result fitting. The dataset in this paper is limited, so the cubic spline interpolation method is used to fit the waterline. The fitting effect

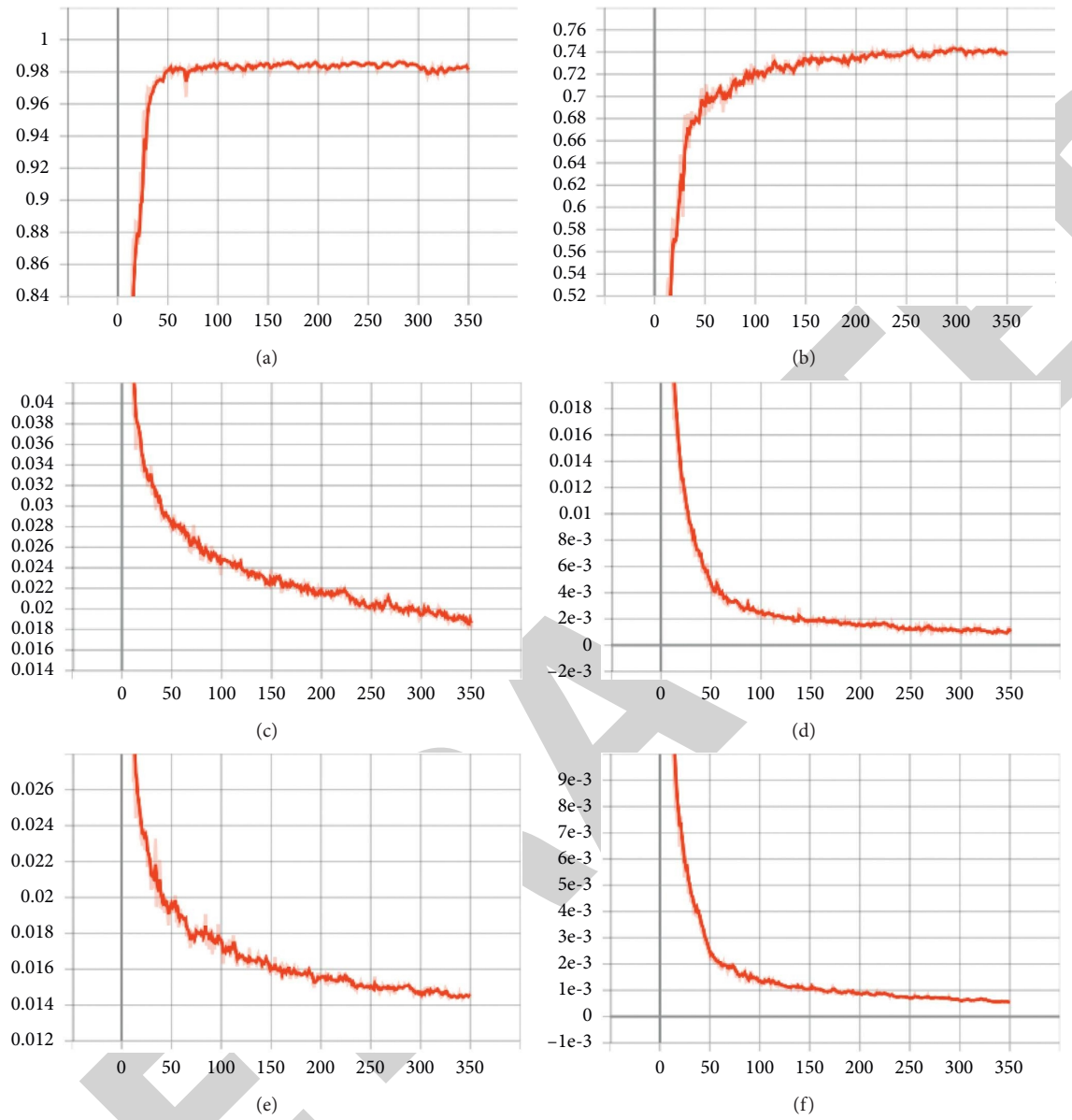

Figure 10: The curve of mAP and the loss of the training and verification set during training. (a) mAP@0.5 curve in the process of the training. (b) mAP@0.5 : 0.95 curve in the process of the training. (c) Loss curve of the training set bounding box. (d) Loss curve of the training set class. (e) Loss curve of the verification set bounding box. (f) Loss curve of the verification set class.

is good, and the speed is fast. Finally, the fitting function $S(x)$ is obtained.

3.4.4. Draft Reading Formula. According to the previous fitting steps, the calculation formula of draft reading can be obtained:

(1) Let $W(x) = S(x)$; then, Y_{join} is obtained

(2) Let $H_{\text{distance}} = Z(Y_{\text{join}})$ to obtain the actual height change

(3) Compare the height relationship between H_{distance} and the draft characters predicted by the network, and select the lowest draft meters M and centimeters C of the height H_{distance} in the character coordinate set

(4) $\text{Predict}_{\text{reading}} = (M - 1) + C * 0.1 - 0.01 * (H_{\text{distance}})$ (unit: m)

3.4.5. Application of Reading Results. After the above series of processing, the final formula of the draft reading is obtained. Based on this formula, we can realize the system of this draft reading method in order to apply it in the actual measurement process. For instance, a set of ship draft reading system can be developed, which can be deployed on the intelligent UAV, intelligent HD camera, and server so as to realize the reading of the ship draft. On both sides of the channel, solar-powered cameras can be installed to collect the images of the ship's six-side draft through high-definition cameras. The data can be transmitted to the server

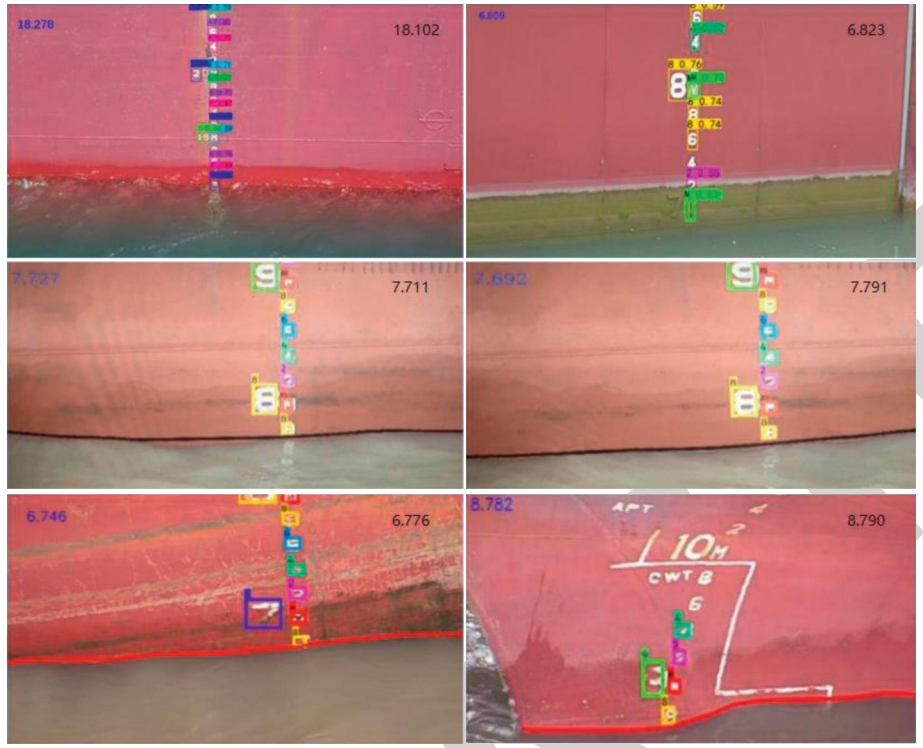

Figure 11: Sample diagram of experimental results.

through digital signals, and the system deployed on the server can be used to read the ship's draft.

In complicated ports, the UAV can be controlled on the shore or on the deck, and the high mobility and high zoom of the UAV can be used to collect the ship draft images. In addition, for the UAV equipped with DJI Onboard SDK custom programming, the cruise mode can be set to make the UAV fly according to the set inspection mode and automatically collect the draft images, further reducing the waste of human resources. In addition, if conditions permit, the UAV and intelligent camera with high chip performance can be deployed in the embedded system so that the UAV or camera can read the draft of the image while taking the image, reducing the calculation of the server and improving the reading speed.

4. Experimental Results and Analysis

According to the above experimental process and experimental steps, to train the experience, the mAP curve and loss curve during the training process and the loss curve during the verification process are obtained, as shown in Figure 10. Use the trained model to predict the new ship video or image, then fit the predicted result through the draft character fitting function and the waterline fitting function, and finally use the draft reading formula to read; one can obtain as shown in Figure 11. The results shown can clearly detect the position of the draft characters and the waterline, and the draft reading results are recorded in the upper left corner of the picture.

Based on the factors of time and data collection, this paper collected 5000 aerial draft images in different scenes (different weathers, waves, light, and other scenes), annotated the draft characters and waterline in the images, and selected 4000 of them randomly for training, and two test sets were tested, with the number of test sets in each group being 500 sheets. The experimental results are shown in Table 4.

Table 4: Statistical table of effective values of the two groups.

Group number	Error < 0.02 m	Error < 0.01 m
1	480	460
2	485	465

Compared with the manual observation results and the existing semantic segmentation methods, we can obtain the results in Table 5. In order to ensure the reliability of the contrast data, the semantic segmentation method uses the Fine-MobileNet [8] network improved based on the MobileNet V2 network and uses the same dataset and hardware environment for the experiment. The manual observation results are obtained by a number of professional meteorologists, respectively, reading the results and taking the average value. It can be seen that, in most cases, the error between the reading result of this method and the result of manual observation is within 0.3 cm. The semantic segmentation method can also control the error, but the average value of the absolute error of the method in this paper is small. In the actual ship draft reading, the robustness is good, and the detection accuracy and efficiency all satisfy the actual demand.

We also divided the images into two categories according to the quality of the photos, which are the image samples corresponding to clear hull characters in sunny weather and the image samples corresponding to fuzzy hull characters in

Table 5: Comparison of experimental results.

Serial number	Results of manual observation (m)	Results of semantic segmentation (m)	Results of this article (m)	Error (segmentation method/method of this article) (m)
a	18.280	18.282	18.278	0.002/−0.002
b	6.810	6.802	6.813	−0.008/0.003
c	7.751	7.756	7.727	0.005/−0.024
d	7.703	7.716	7.705	0.013/0.002
e	6.752	6.774	6.757	0.022/0.005
f	8.797	8.795	8.790	−0.002/−0.007
Mean absolute value of difference (m)			0.0087/0.0072	

Table 6: Prediction results of different quality images.

Picture quality	mAP@0.5 : 0.95	mAP@0.5
Better-quality images	0.74	0.98
Poor-quality images	0.62	0.73

bad weather. These two kinds of pictures were used to test the training model, and the corresponding results in Table 6 were finally obtained.

According to the above experimental results, it can be seen that the sample experimental effect chart is clear, and the position of the waterline and the recognized characters can be clearly given, the draft reading result is given, and the error can be basically stabilized within 0.03 m, generally within 0.01 m. Moreover, this article compares their prediction effects when the picture quality is relatively poor and relatively good. For pictures with better quality, such as those with clear hull characters and clear weather, their prediction accuracy is 98%. For poor quality pictures, such as pictures in which the hull characters had been blurred by corrosion or in bad weather, their test accuracy is only 73%. Comparing with manual estimation, the method in this article can basically control the error within the millimeter level. Therefore, the research in this article has achieved relatively good experimental results.

5. Conclusions

In this paper, based on computer vision technology, through the exploration and comparison of various image processing technologies, the results show that using deep learning technology to predict the draft reading, with artificial reading deviation within 0.01 meters, is valid. The prediction accuracy of this method is 98% in the case of good image quality and 73% in the case of poor image quality caused by bad weather, hull corrosion, and other reasons. In fact, this kind of error is normal; even if the manual reading is also biased, this method has greatly reduced the error. Moreover, the image processing method using deep learning has better effect in speed and accuracy both compared with the traditional manual reading method and the traditional image detection technology.

However, it cannot be ignored that there are still some errors in the experimental results, which are inseparable from the complex and changeable real navigation situation. And there will be various interferences in the actual detection, which requires further research to collect a large number of hull pictures in different environments, build a larger dataset, train the network, and enhance the robustness of the model. Meanwhile, the data preprocessing is also worthy of further investigation.

Data Availability

The dataset used in this paper was provided by a company of Jiangsu, China. It cannot be made freely available. We are only permitted to use some images in the article.

Conflicts of Interest

The authors declare that there are no conflicts of interest regarding the publication of this paper.

Acknowledgments

This research was funded by the China University Industry-University-Research Innovation Fund (New Generation Information Technology Innovation Project) (2019ITA03004).

References

[1] C. Liu and J. Li, "Self-correction ship tracking and counting with variable time window based on YOLOv3," *Complexity*, vol. 2021, Article ID 2889115, 9 pages, 2021.

[2] Y. Cao, Y. Zhang, W. Shi et al., "Water-jet erosion of grade-A ship steel: experimental research," *Shock and Vibration*, vol. 2021, Article ID 6617685, 8 pages, 2021.

[3] Xi Jiang, H. Mao, and H. Zhang, "Simultaneous optimization of the liner shipping route and ship schedule designs with time windows," *Mathematical Problems in Engineering*, vol. 2020, Article ID 3287973, 11 pages, 2020.

[4] P. Yuan, P. Wang, and Yu Zhao, "Innovative method for ship navigation safety risk response in landslide-induced wave," *Advances in Civil Engineering*, vol. 2021, Article ID 6640548, 10 pages, 2021.

[5] S. Wang, M. Bai, M. Gellert et al., "TorontoCity: seeing the world with a million eyes," 2016, https://arxiv.org/abs/1612.00423v1.

[6] Q. Dou, L. Yu, H. Chen et al., "3D deeply supervised network for automated segmentation of volumetric medical images," *Medical Image Analysis*, vol. 41, pp. 40–54, 2017.

[7] X. Zhu and Y. Luo, "Analysis and research on intelligent reading of ship draft based on image processing and deep learning," *Quality Safety Inspection and Testing*, vol. 30, no. 3, pp. 102–105, 2020.

[8] Y. Li, Y. Xue, H. Li, W. Zhang, and Y. Gao, "Ship waterline extraction strategy based on deep learning," *Control Theory & Applications*, vol. 37, no. 11, pp. 2347–2353, 2020.

Hindawi
International Journal of Antennas and Propagation
Volume 2024, Article ID 9785482, 1 page
https://doi.org/10.1155/2024/9785482

Retraction

Retracted: Iris Localization Algorithm based on Effective Area

International Journal of Antennas and Propagation

Received 23 January 2024; Accepted 23 January 2024; Published 24 January 2024

This article has been retracted by Hindawi following an investigation undertaken by the publisher [1]. This investigation has uncovered evidence of one or more of the following indicators of systematic manipulation of the publication process:

(1) Discrepancies in scope

(2) Discrepancies in the description of the research reported

(3) Discrepancies between the availability of data and the research described

(4) Inappropriate citations

(5) Incoherent, meaningless and/or irrelevant content included in the article

(6) Manipulated or compromised peer review

The presence of these indicators undermines our confidence in the integrity of the article's content and we cannot, therefore, vouch for its reliability. Please note that this notice is intended solely to alert readers that the content of this article is unreliable. We have not investigated whether authors were aware of or involved in the systematic manipulation of the publication process.

Wiley and Hindawi regrets that the usual quality checks did not identify these issues before publication and have since put additional measures in place to safeguard research integrity.

We wish to credit our own Research Integrity and Research Publishing teams and anonymous and named external researchers and research integrity experts for contributing to this investigation.

The corresponding author, as the representative of all authors, has been given the opportunity to register their agreement or disagreement to this retraction. We have kept a record of any response received.

References

[1] J. Yu, L. Zhang, and Z. Wang, "Iris Localization Algorithm based on Effective Area," *International Journal of Antennas and Propagation*, vol. 2021, Article ID 2049646, 11 pages, 2021.

Hindawi
International Journal of Antennas and Propagation
Volume 2021, Article ID 2049646, 11 pages
https://doi.org/10.1155/2021/2049646

Research Article

Iris Localization Algorithm based on Effective Area

Jinfeng Yu,[1] **Lei Zhang**,[2] **and Zhi Wang**[1]

[1]*School of Electronics and Information, Yangtze University, Jingzhou, Hubei 434000, China*
[2]*College of Computer and Information Technology, Three Gorges University, Yichang, Hubei 443000, China*

Correspondence should be addressed to Zhi Wang; 1324385898@qq.com

Received 7 May 2021; Revised 26 May 2021; Accepted 3 June 2021; Published 22 June 2021

Academic Editor: Jin He

Iris localization is the most crucial part of the iris processing because its accuracy can directly affect the accuracy of biometric identification in subsequent steps. Yet, the quality of iris images may be sharply degraded due to interference from eyelashes and reflections during image acquisition, which can affect the localization accuracy adversely. To solve the problem, an iris localization algorithm based on effective area is proposed. First, YOLOv4 is used to crop the image to obtain the effective iris area, which is beneficial in improving the accuracy of subsequent localization. Furthermore, a method to remove reflective noise is proposed, which can effectively avoid the problem of noise interference in the process of inner boundary determination. Finally, aiming at the edge deviation caused by eyelashes, an outer boundary adjustment method is proposed. The experimental results show that the proposed method achieves good performance in the localization of iris images of both good quality and noise interference and outperforms other state-of-the-art methods.

1. Introduction

With the rapid development of information security, the role of biometric technology in military, banking, e-commerce, security, and other fields is becoming increasingly more prominent. Among the different technologies available, such as fingerprints, faces, signatures, and the like, iris recognition has gained much attention because of its unique advantages in stability, uniqueness, and universality. As one of the key components of iris recognition systems [1], the purpose of iris localization is to accurately determine the ring area between the pupil and the sclera. However, in practical applications, this process is often accompanied by noise-generated interference, such as eyebrows, blinking, eyelashes, and uneven illumination, which affects the quality of iris images and increases the difficulty of localization, leading to high rates of iris recognition failure.

The integrodifferential operator (IDO) [2, 3], proposed by Daugman, and edge detection combined with the circular Hough transform (CHT) [4], proposed by Wildes, are classic algorithms used in iris localization, which have made great contributions to the research of iris localization. However, the classic algorithms have certain shortcomings usually: IDO is based on the difference in grayscale of adjacent pixels, so it is extremely sensitive to noise; CHT is based on voting on edge points, and it is difficult to set a universal threshold when the image is marginalized based on gradient information. At the same time, because the two classic algorithms calculate the entire image, it makes the calculation expensive. For these reasons, many scholars have made improvements on the basis of classic algorithms.

In the study by Sun et al. [5], pupil's segmentation according to gray projection and maximum between-class variance method was performed at first, followed by then segmented sector areas in different directions based on the center of the pupil and circle fitting according to the three groups of points with the largest grayscale change in the sector areas. However, this method relies on high-quality images, if there is a lot of noise in the image, the method cannot complete pupil segmentation correctly. In another study [6], a circular Gabor filter [7] was used to estimate the initial pupil center to limit the search range of the iris and pupil circles but did not give a noise solution when using IDO to locate the boundary. Therefore, good results can only be achieved in iris images with less noise.

A morphological method was used in previous studies [8, 9] to remove the reflective noise in the image before binarizing the image. Kumar et al. [8] assumed that the pupil and iris were located in the center of the image, filtered out the binary pixels close to the boundary directly to obtain the largest connected area, then estimated the center of the pupil, and used IDO to determine the iris boundaries finally. They [9] also performed edge detection on binary images, used CHT to locate the inner boundary of the iris, and a limited-angle IDO was used to locate the outer boundary according to the center of the inner boundary. However, method in this study [9] did not consider eyelashes noise.

In the study by Soliman et al. [10], a three-layer threshold system was proposed to solve the binarization problem of images with large differences in grayscale distribution. Then the pupil center was estimated based on the largest connected area and used IDO to accurately locate the boundaries of iris. But there was a problem: when there are large areas of low-gray pixels in the noniris area, the three-layer threshold system will break down. In another study [11], an iris localization method based on rough entropy and circular region analysis was proposed. However, this method is easily susceptible to a localization error of the pupil region because it does not take into account the potential presence of regions with lower gray values than the pupil in the iris image. In the study by Ma et al. [12], a localization method based on conformal geometry was proposed, which was similar to CHT. Firstly, the grayscale values of the whole image were divided into three values (0, 150, and 255) according to the set threshold. Then, the edge detection was performed on the image, and the boundaries of iris was obtained according to the inner product of the edge points in the conformal space. But when the difference in grayscale values of pupil and iris, and background is not obvious, the localization effect of this method is limited. Jan et al. [13] used the bilinear interpolation scheme to remove the reflective noise in image and set the threshold according to continuous low grayscale pixels to binarize the image. Then, the inner boundary of the iris was roughly identified using the largest connected area directly, and the outer boundary was roughly determined using the CHT. Finally, the Fourier series was used to adjust the localization boundaries. However, this method suffered from poor localization for low-quality images.

In recent years, the applications of deep learning in iris localization have gradually attracted researchers' attention. The authors of [14, 15] improved a deep learning network to locate human eyes in binocular images. In the study by Choudhary et al. [16], in order to distinguish living from forged irises, the region of interest (ROI) of the image was obtained using the YOLO [17] network, and a convolutional neural network [18] was used to extract the distinctive texture features. In practical applications, the effective iris area of an eye image usually occupies a small area of the entire image, while other areas are noniris area and can be disregarded, which reduce the localization accuracy of algorithms due to the presence of uneven illumination, hair, eyelids, glasses, and other interference, as shown in Figure 1. If the effective iris area can be accurately extracted, the localization accuracy will be greatly improved. Therefore, in this article, we propose an iris localization algorithm based on effective area. First of all, YOLOv4 [19] is used to crop the image to obtain the effective iris area, which improves the accuracy of subsequent localization. Furthermore, a method to remove reflective noise is proposed, which reduces the interference on the localization of the inner iris boundary. Finally, an outer boundary adjustment method is proposed to improve the accuracy of iris outer boundary localization.

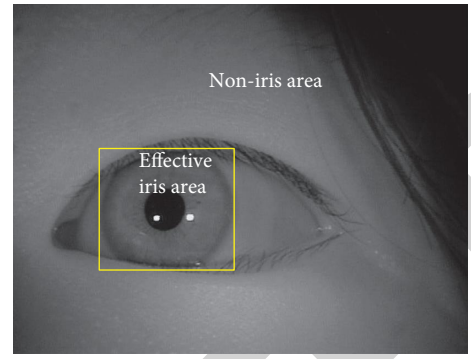

Figure 1: Effective iris area and noniris area.

2. Proposed Iris Localization Algorithm

The flowchart of the iris localization method proposed in this article is shown in Figure 2 and includes three parts:

(1) The effective area of the iris is detected using a YOLOv4 network, and the original image is cropped along the prediction box.

(2) The minimum grayscale average method [20] is used to binarize the image and roughly estimate the pupil center. A reflective noise removal method is proposed to eliminate the noise interference, while the IDO is used to identify the inner boundary of iris.

(3) In order to reduce the influence of the sudden grayscale changes in the pupil area and the upper eyelid area while the outer iris boundary is first coarsely identified using the IDO, the pixels around the pupil and the upper eyelid are fused, followed by an outer boundary adjustment method to improve the localization deviation caused by eyelashes.

2.1. Effective Iris Area Extraction using YOLOv4. Extracting the effective iris area accurately can effectively remove the interference from the noniris area and greatly improve the accuracy of subsequent iris localization. Because of their powerful feature extraction capabilities, existing deep learning algorithms [19, 21] have higher accuracy compared with traditional algorithms in target detection [22–24]. In particular, YOLOv4 uses the CIoU [25] loss function, which considers the distance, overlap rate, scale, and penalty items between the predicted frame and the real frame. It also ensures that the target frame has a more stable regression performance, effectively avoiding the divergence problem in the training process and thus has strong robustness to interference, leading to its excellent performance in target detection tasks.

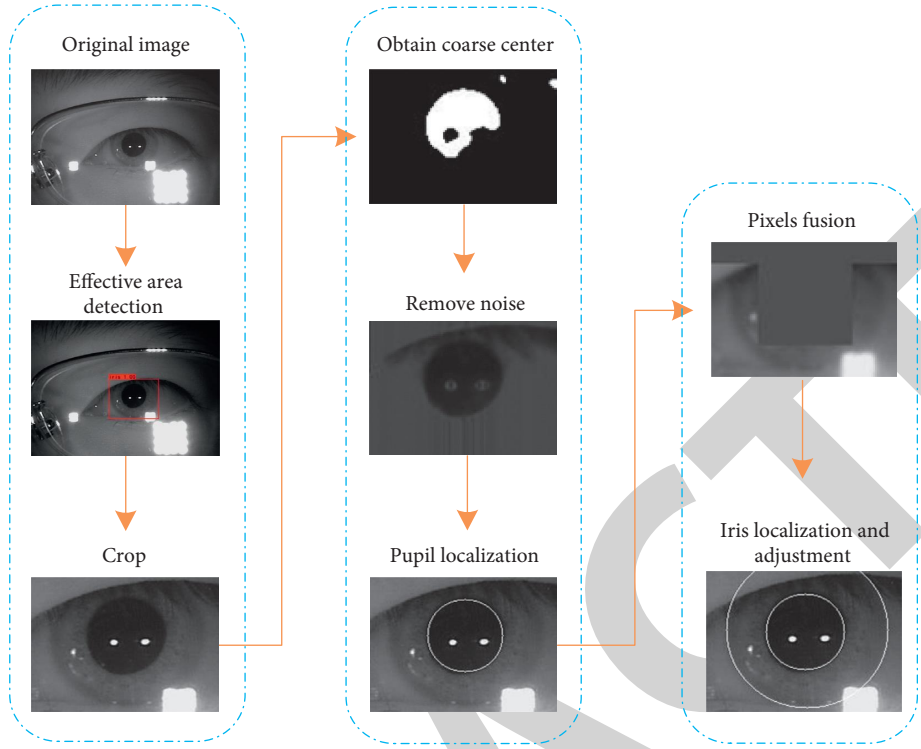

Figure 2: Flowchart of proposed iris localization method.

Annotate the effective iris area and use it for training the YOLOv4 model. A trained model is used to predict the effective iris area, and the coordinates of the target with the highest confidence are used to obtain the effective area of iris image. In order to protect the information of iris, the upper and lower borders of the predicted area are expanded by 10 pixels, and the left and right borders are expanded by 20 pixels when cropping. Figure 3(a) shows a prediction example, whereas Figure 3(b) shows the result of the effective iris area extraction.

2.2. Inner Boundary Identification. In the effective iris area, the boundary feature of the pupil (inner boundary of iris) is relatively obvious and easier to identify. Moreover, the successfully identification of inner boundary can reduce the difficulty of outer boundary's determination, so the pupil boundary is identified first. A rough estimation of the pupil center based on some prior knowledge can effectively limit the search range of the inner boundary and avoid blindness; hence, we can roughly estimate the location of the pupil center as follows. On the inner boundary between the pupil and the iris, there will usually be an obvious change in the pixels' grayscale values, and the grayscale of the pupil region's pixels that immune to interference will be relatively lower than that of the iris in the effective iris area.

At the same time, the pupil area is vulnerable to reflective noise, so it is necessary to remove the noise before accurate localization using the IDO. Therefore, in this article, we propose a global noise removal method to remove the reflective noise and improve the accuracy of inner boundary localization.

2.2.1. Rough Pupil Center Localization. Inevitably, reflective noise sometimes exists in the effective iris area, which makes the pupil area with low grayscale have high grayscale pixels and affects the traditional methods of coarse localization greatly (such as grayscale projection method and convolution method). Generally speaking, even if there is interference from reflective noise, there will be some normal pixels in the pupil area. Through the adaptive binarization threshold combined with the largest connected area, the minimum grayscale average method [20] can estimate the pupil center successfully. First, we divide the image into $m \times n$ rectangles of equal area according to the size of the effective iris area (Figure 4(a)). Then, we calculate the average grayscale value of each rectangular area and use the minimum average value as the threshold to binarize the image (Figure 4(b)). Finally, we roughly estimate the pupil center and the inner boundary radius from the largest connected area, as shown in equation (1).

$$\begin{aligned} r_p &= \frac{(H+W)}{4}, \\ x_p &= x_{\text{loc}} + r_p, \\ y_p &= y_{\text{loc}} + r_p, \end{aligned} \tag{1}$$

where H, W are the height and width of the largest connected area, respectively; $(x_{\text{loc}}, y_{\text{loc}})$ are the coordinates of the upper left corner of the largest connected area; (x_p, y_p) is the coarse position of the pupil center, and r_p is the initial radius of the inner boundary.

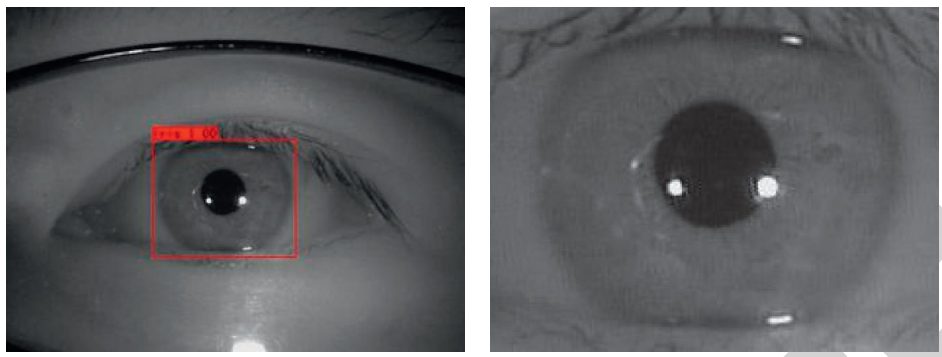

(a) (b)

Figure 3: Extraction of effective iris area by YOLOv4. (a) Iris area border predicted by YOLOv4. (b) Effective iris area extraction.

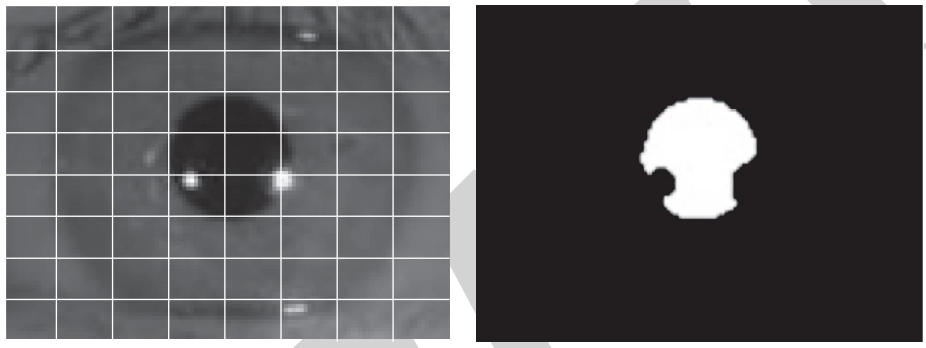

(a) (b)

Figure 4: Minimum grayscale average method. (a) Division in rectangular areas. (b) Binarization using the minimum average of all areas.

2.2.2. Reflective Noise Removal. The IDO method [2, 3] accumulates the grayscale difference of circumference, and there is no need to set an additional threshold when detecting the circle with grayscale difference, so it has strong adaptability, as shown in equation (2). However, the actual iris image often has reflective noise, which causes the grayscale difference of adjacent pixels to be too large, which greatly restricts the localization accuracy of the IDO method. For this reason, it is necessary to remove the influence of reflective noise before iris localization.

$$\max_{(r,x_0,y_0)}\left|G_\sigma(r) * \frac{\partial}{\partial r}\oint_{r,x_0,y_0}\frac{I(x,y)}{2\pi r}\mathrm{d}s\right|, \tag{2}$$

where $G_\sigma(r)$ is the Gaussian smoothing function with a scale of σ; $*$ represents convolution; r, x_0, y_0 are the integration radius and center, respectively; $I(x, y)$ is the original image of iris.

Existing methods generally use bilinear interpolation [13] or morphological methods [9] to avoid the interference of reflective noise. However, the essence of bilinear interpolation is to select the average grayscale value of four pixels in the vertical and horizontal directions according to a fixed distance to replace the current pixel, so it is susceptible to the interpolation distance when performing reflective noise filtering. If the distance is too small, the noise cannot be completely removed, while too large values may affect the effective boundary of the iris adversely. During reflective noise removal, morphological methods commonly damage the effective boundary of the iris due to the difficulty of setting the grayscale value for hole filling.

Even when affected by reflective noise, the normal pixels' grayscale value of the pupil area is lower than the average grayscale value of the entire iris area. For this reason, in this article, we propose a method of removing reflective noise based on global characteristics. First, we calculate the average grayscale value of the entire iris image as the global threshold, and use this as the basis for replacing the reflective noise. In view of the fact that the IDO is only sensitive to arc-shaped grayscale mutations, pixel replacement is performed on the square area with the coarse localization center of the pupil as the center point and a side length q column by column (that is, the area where the inner boundary of the iris may appear). If the current pixel is greater than the threshold, the pixel is judged as a reflective noise pixel, and it is replaced with the nearest effective pixel's grayscale value in the same column. Otherwise, the original pixel as the valid pixel is retained, and its grayscale value is stored. The replacement result is shown in Figure 5(a). On the one hand, the proposed method takes into account the global characteristics of pixels, which can better eliminate the interference of reflective noise. On the other hand, it can better retain the effective iris edge by replacing the reflective noise pixel value with an acceptable effective pixel's grayscale value

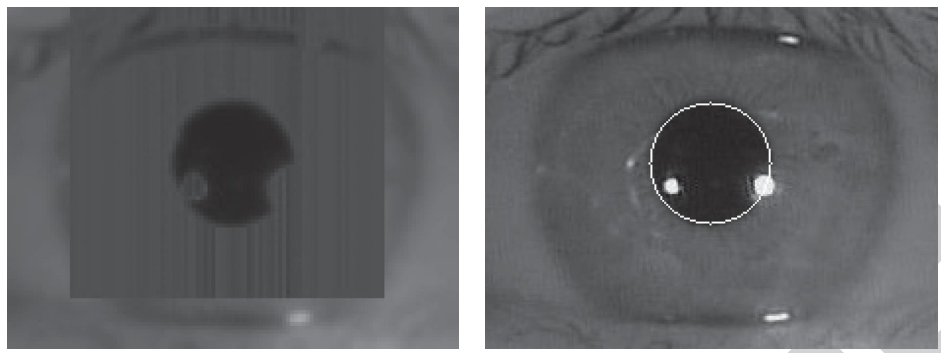

(a) (b)

Figure 5: Localization of inner boundary. (a) Reflective noise removal. (b) Precise localization of inner boundary.

Input: The obtained effective iris area, *img*; The first and last columns of the noise filled area, *L_c* and *R_c*; The first and last rows of the noise filled area, *U_r* and *D_r*;
Output: The image after reflective noise removal

```
(1) import numpy as np
(2) T_1 = np.mean (img) #calculate the average grayscale value of the image
(3) B_uff = T_1
(4) for j in range (L_c, R_c):
(5)         for i in range (U_r, D_r):
(6)             P_ix = img [i] [j]
(7)             if P_ix > T_1:        #is the current pixel a valid pixel?
(8)                 img [i] [j] = B_uff
(9)             else:
(10)                B_uff = P_ix
(11) return img
```

Algorithm 1: Pseudo code of reflective noise removal.

(i.e. below the threshold and nearest on the same column). The pseudo code of the reflective noise removal is shown in Algorithm 1.

2.2.3. Identification of Inner Boundary. The inner boundary is identified by follows:

(a) According to the pupil center (x_p, y_p) roughly estimated by the minimum grayscale average method, the search range of the inner boundary center is limited to a square area with the rough pupil center as the center point and a side length p. The value of p should ensure that the true inner boundary center of the iris can be located.

(b) Using the reflective noise removal method proposed in this article to remove the reflective noise in the area where the inner boundary of the iris may appear, and the area is set as a square area with the rough pupil center as the center point and a side length q. In this article, q is set according to the rough pupil center and the maximum radius of the inner boundary.

(c) Setting the radius range of the inner boundary (r_{p1}, r_{p2}), where r_{p1} is the initial radius of the inner boundary estimated by the minimum grayscale average method, and r_{p2} is set according to the long side of the effective iris area. Then, we obtain the inner boundary center (X_p, Y_p) and radius R_p using the IDO, and the localization result is shown in Figure 5(b).

2.3. Determination of Outer Boundary. The outer boundary of the iris refers to the boundary between the iris and the sclera, which is not always visible and may be occluded by the eyelid or eyelashes and affected by other types of noise. Therefore, the upper eyelid and the pupil regions are fused before boundary identification, so as to reduce the problem of the sudden grayscale changes caused by pupil and eyelashes effectively while using the IDO to identify the outer boundary. At the same time, for our eyes, the pupil is surrounded by the iris, so the center of the outer boundary can be defined according to the center of the inner boundary.

2.3.1. Regional Pixel Fusion. In order to reduce the influence of the inner boundary, as well as the problems of eyelashes and occlusion by the upper eyelid, the pupil region and upper eyelid are fused when identifying the outer boundary of the iris. The details are as follows. First, a pixel matrix in the lower right corner of the iris image is selected according to the center and radius of the acquired inner boundary and

its average grayscale value is calculated (a relatively mild grayscale value is needed to reduce sudden changes in grayscale leading to localization failure). Then, the pixels of the pupil region and the upper eyelid are replaced according to the iris inner boundary parameters. The pseudo code of the regional pixel fusion is shown in Algorithm 2, and the fusion result is shown in Figure 6(a).

2.3.2. Outer Boundary Adjustment. When the iris area occupies a small proportion of the overall image, the localization deviation of outer boundary caused by the eyelashes in existing algorithms is often difficult to detect, although the determined boundary does not fit the actual boundary accurately. Therefore, it is necessary to adjust the outer boundary of the iris to avoid localization deviation that affect the subsequent recognition results. The inaccurate outer boundary caused by eyelashes results in imperfect iris boundary fitting. So, in the area without eyelash interference (the lower part of the outer boundary), the grayscale difference between adjacent pixels in the same radial direction is small. Therefore, we can select several sets of IDO parameters with larger circumferential difference values to perform outer boundary comparison in areas with less eyelash interference and choose the optimal circle parameter. To this end, in this article, we propose an outer boundary adjustment method, as follows:

(a) The parameters acquired by IDO are composed of radius and center, and only a set of parameters with the largest grayscale difference value on circumference are retained. We keep z sets of IDO parameters with the largest difference values and compare them according to certain rules.

(b) Take the center of the circle as the center and make rays according to certain angles direction. The intersection points of the rays and the circle with angles of 0°, -20°, and -30° are a_1, b_1, and c_1, and the intersection points of the rays and the circle with angles of 180°, 200°, and 210° are a_2, b_2, and c_2.

(c) We extend the radius of the circle by Δn pixels and obtain the intersection points of the rays in the original angle's direction and the circle a_3, b_3, c_3 and a_4, b_4, c_4, as shown in Figure 6(b).

(d) Calculating the grayscale difference of two pixels in the same angle direction and getting the accumulated value. Because of the grayscale difference between the iris and the sclera, the accumulated value will be larger while the outer boundary fits well enough. Then, the optimal circle parameters is obtained by comparing the accumulated values. The pseudo code of the outer boundary adjustment is shown in Algorithm 3.

2.3.3. Determination of Outer Boundary. The outer boundary is determined by follows:

(a) According to the identified inner boundary's center (X_p, Y_p) and radius R_p, we remove the interference of pupil and upper eyelid through strategy of regional pixel fusion while determining the outer boundary and limit the outer boundary center within the square area centered at the center point of the inner boundary and with a side length of k (the area where the center of outer boundary may appear).

(b) In order to further remove the interference of eyelids, the IDO's integration angle is limited between $(-45^\circ, 30^\circ)$ and $(150^\circ, 225^\circ)$ [8], as shown in Figure 6(c). Setting the outer boundary radius range to $(R_p, 5R_p)$ according to the radius of inner boundary. Then, we keep z sets of IDO parameters with the largest difference values on circumference.

(c) Comparing the z sets of IDO parameters according to the outer boundary adjustment method proposed in this article, the optimal outer boundary parameters (X_I, Y_I, R_I) are obtained to adjust the localization deviation caused by eyelashes. Figure 6(d) shows the final boundary determination result.

3. Experimental Results

The experimental environment of this study is shown in Table 1. Select 3000 images from CASIA-IrisV4-thousand and 1000 images from CASIA-IrisV3-Interval to label the training set of YOLOv4 model. The software used to label the effective iris area was LabelImg, shown in Figure 7.

In order to verify the effectiveness of the improved algorithm, comparative experiments were carried out to determine whether the use of YOLOv4 to extract the effective iris area aids the proposed iris localization method, the effect of reflective noise removal, and that of outer boundary adjustment. At the same time, in order to verify the performance of the proposed algorithm, we compared with other excellent iris localization methods [8, 10, 13]. The algorithm parameters were set as follows: The area where the center of the inner boundary may appear was set as a square with a side length of $p = 100$, the maximum radius of the inner boundary r_{p2} was set to one-third of the long side of the effective iris area, the side length q of the reflective noise removing range was the sum of the inner boundary center range and the inner boundary diameter, and the center range of the outer boundary was $k = 20$. The sets of the IDO parameters reserved was $z = 3$, the extend distance of radius $\Delta n = 2$. We randomly selected 2000 images from each of CASIA-IrisV4-thousand and CASIA-IrisV3-Interval data sets for localization. In this article, the localization accuracy on the corresponding data set is used as the evaluation index:

$$\text{Acc} = \frac{N_s}{N_t} \times 100\%, \tag{3}$$

where N_s refers to the number of images accurately located, and N_t is the total number of images.

3.1. Effective Iris Area Extraction Using YOLOv4. In order to verify the effectiveness of extracting the effective iris area using YOLOv4, comparative experiments are carried out. The purpose of the experiments was to determine whether the use

Input: The obtained effective iris area, *IMG*; The center of the inner boundary, (X_p, Y_p); the radius of the inner boundary, R_p;
Output: The image after regional pixel fusion **1 import** math **2** $Pix\_block = IMG[(Y_p + R_p - 1): (Y_p + R_p + 1), (X_p + R_p + 4): (X_p + R_p + 6)]$ #get pixel matrix
(3) $p_a, p_b, p_c, p_d = Pix\_block\ [0]\ [0], Pix\_block\ [0]\ [1], Pix\_block\ [1]\ [0], Pix\_block\ [1, 1]$
(4) P_aver = math.floor $(p_a/4 + p_b/4 + p_c/4 + p_d/4)$ # calculate the average grayscale value
(5) $IMG\ [Y_p - R_p - 5: Y_p + R_p + 5, X_p - R_p - 5: X_p + R_p + 5] = P\_aver$ #fuse the pupil
(6) $IMG\ [0 : Y_p - R_p, :] = P\_aver$ #fuse the upper eyelid
(7) **return** *IMG*

Algorithm 2: Pseudo code of regional pixel fusion.

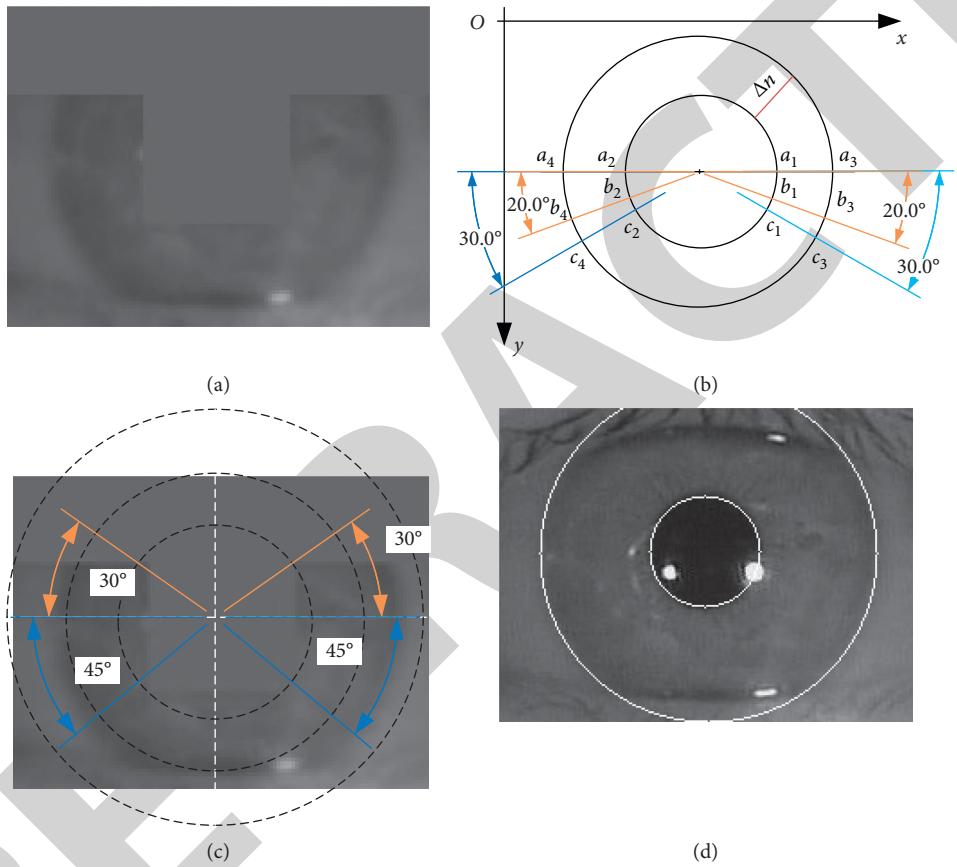

Figure 6: Determination of outer boundary. (a) Regional pixels fusion. (b) Outer boundary adjustment. (c) Integral angle limits. (d) Boundary determination result.

Input: The z sets of IDO parameters with the largest difference values, *para_1*, *para_2*,...,*para_z*; the pixels in six directions were obtained according to each set of parameters, $a_{1i}, a_{2i}, a_{3i}, a_{4i}, b_{1i}, b_{2i}, b_{3i}, b_{4i}, c_{1i}, c_{2i}, c_{3i}, c_{4i}$, where $i = 1, 2,...,z$;
Output: The optimal parameters, *Opt_para*;
(1) $Para = (para\_1, para\_2,...,para\_z)$
(2) $val\_1 = (a_{11} - a_{31})^2 + (a_{21} - a_{41})^2 + (b_{11} - b_{31})^2 + (b_{21} - b_{41})^2 + (c_{11} - c_{31})^2 + (c_{21} - c_{41})^2$

(3) $val\_2 = (a_{12} - a_{32})^2 + (a_{22} - a_{42})^2 + (b_{12} - b_{32})^2 + (b_{22} - b_{42})^2 + (c_{12} - c_{32})^2 + (c_{22} - c_{42})^2$
(4) ...
(5) $val\_z = (a_{1z} - a_{3z})^2 + (a_{2z} - a_{4z})^2 + (b_{1z} - b_{3z})^2 + (b_{2z} - b_{4z})^2 + (c_{1z} - c_{3z})^2 + (c_{2z} - c_{4z})^2$
(6) $Value = [val\_1, val\_2,...,val\_z]$
(7) $Index = Value$.index (max $(Value)$) #get the index of maximum
(8) $Opt\_para = Para\ [Index]$
(9) **return** *Opt_para*

Algorithm 3: Pseudo code of outer boundary adjustment.

Table 1: Experimental environment.

Environment	Configuration
Operating system	Ubuntu16.04
GPU	NVIDIA GeForce RTX2080
GPU RAM	8 Gb
CPU	Core i7
RAM	16 Gb
Programming environment	Python 3.7

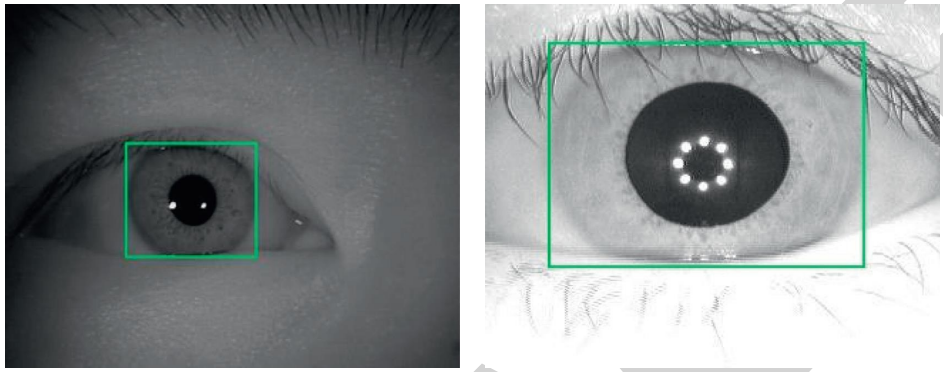

(a) (b)

Figure 7: Training set labeling. (a) Labeling a CASIA-IrisV4-thousand image. (b) Labeling a CASIA-IrisV3-Interval.

of YOLOv4 to extract the effective iris area aids the iris localization method proposed in this article. The comparative experimental results are shown in Table 2 and Figure 8.

As shown in Table 2, after using YOLOv4 to extract the effective iris area in CASIA-IrisV4-thousand data set, the iris localization accuracy was greatly improved. It can be seen from Figure 8(b) that when the effective iris area is not extracted using YOLOv4, the pupil region may not the area of lowest grayscale because of the black area around the image of the human eye. This results in an error when using the grayscale levels directly to roughly estimate the center of the pupil, which in turn leads to the wrong determination of the iris boundary to the upper right corner of the image. From Figure 8(c), we see that after when YOLOv4 is used to extract the effective iris area, there are fewer invalid pixels interfering with the pupil center estimation process, so the localization accuracy is greatly improved. The above experimental results verify the effectiveness of extracting the effective area of the iris using YOLOv4.

Table 2: Comparison of proposed iris localization accuracy with and without YOLOv4 to extract the effective iris area.

YOLOv4-crop	CASIA-IrisV4-thousand (%)	CASIA-IrisV3-interval (%)
No	39.80	97.15
Yes	98.60	98.85

3.2. Reflective Noise Removal. In order to verify the effectiveness of the strategy of reflective noise removal proposed in this article, a comparative experiment is carried out to determine whether the reflective noise removal method proposed aids the iris localization accuracy. The comparison results are shown in Table 3 and Figure 9.

As shown in Table 3, after the removal of reflective noise points, the localization accuracy of was improved to a certain extent in both data sets. As can be seen from Figure 9(b), when there is reflective noise in the effective area of the iris, the grayscale levels of the pupil area are lower, while the grayscale levels of the reflective noise are higher in general. If the reflective noise is not removed, the application of IDO for difference accumulation is adversely affected, and this eventually results in localization error. It can be seen from Figure 9(c) that removing the reflective points under the condition of protecting the effective edges can reduce the impact of reflective noise on the inner boundary localization effectively and ultimately improve the localization accuracy. The experimental results verify the effectiveness of the proposed reflective noise removal strategy.

3.3. Outer Boundary Adjustment. In order to verify the effectiveness of the proposed outer boundary adjustment method, a comparative experiment was carried out to determine whether the adjustment improves the accuracy of the iris localization method proposed in this article. The comparative experiment results are shown in Table 4 and Figure 10.

As indicated in Table 4, the outer boundary adjustment method can improve the localization accuracy to a certain extent. In the case shown in Figure 10(b), there are dense eyelashes in the upper eyelid area, and many long eyelashes cover the upper part of the outer boundary after extracting the effective iris area. This makes the grayscale difference of the eyelashes more obvious than that of the true outer boundary of the iris and results in a slight deviation in the

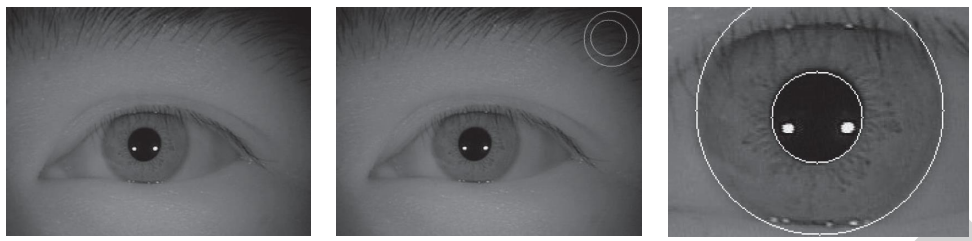

(a) (b) (c)

Figure 8: Iris localization result without and with YOLOv4 to extract effective iris area. (a) Original image. (b) Localization without YOLOv4. (c) Localization with YOLOv4.

Table 3: Comparison of localization accuracy between without and with reflective noise removal.

Noise removal	CASIA-IrisV4-thousand (%)	CASIA-IrisV3-interval (%)
No	86.40	96.10
Yes	98.60	98.85

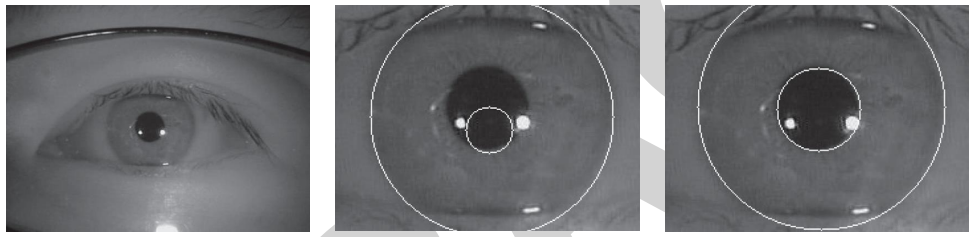

(a) (b) (c)

Figure 9: Iris localization result without and with reflective noise removal. (a) Original image. (b) Localization without reflective noise removal. (c) Localization with reflective noise removal.

Table 4: Comparison of localization accuracy without and with outer boundary adjustment.

Adjustment	CASIA-IrisV4-thousand (%)	CASIA-IrisV3-interval (%)
No	98.40	98.70
Yes	98.60	98.85

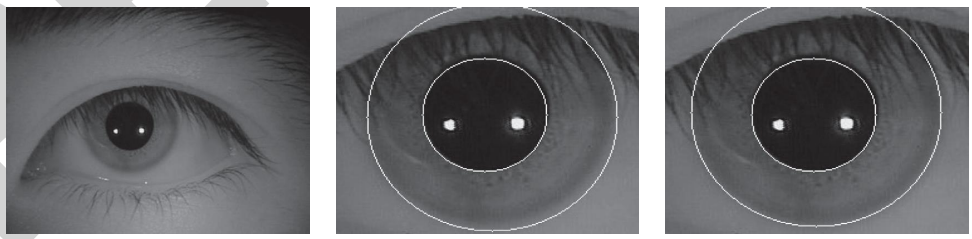

(a) (b) (c)

Figure 10: Iris localization result without and with outer boundary adjustment. (a) Original image. (b) Localization without adjustment. (c) Localization with adjustment.

determination of the outer boundary. At the same time, because the deviating outer boundary of the iris does not correspond to the actual boundary, the radial grayscale difference value at the lower part of the outer boundary of the iris is small. It can be seen from Figure 10(c) that the localization error caused by long eyelashes is adjusted effectively through the radial difference comparison of several groups of parameters with the largest integral value obtained via IDO, and the iris localization accuracy is ultimately improved. The above experimental results verify the effectiveness of the proposed outer boundary adjustment method.

Table 5: Comparison of localization accuracy of several algorithms.

Method	CASIA-IrisV4-thousand (%)	CASIA-IrisV3-interval (%)
Kumar et al. [8]	97.95	98.30
Soliman et al. [10]	94.60	97.95
Jan et al. [13]	94.00	96.65
Proposed	98.60	98.85

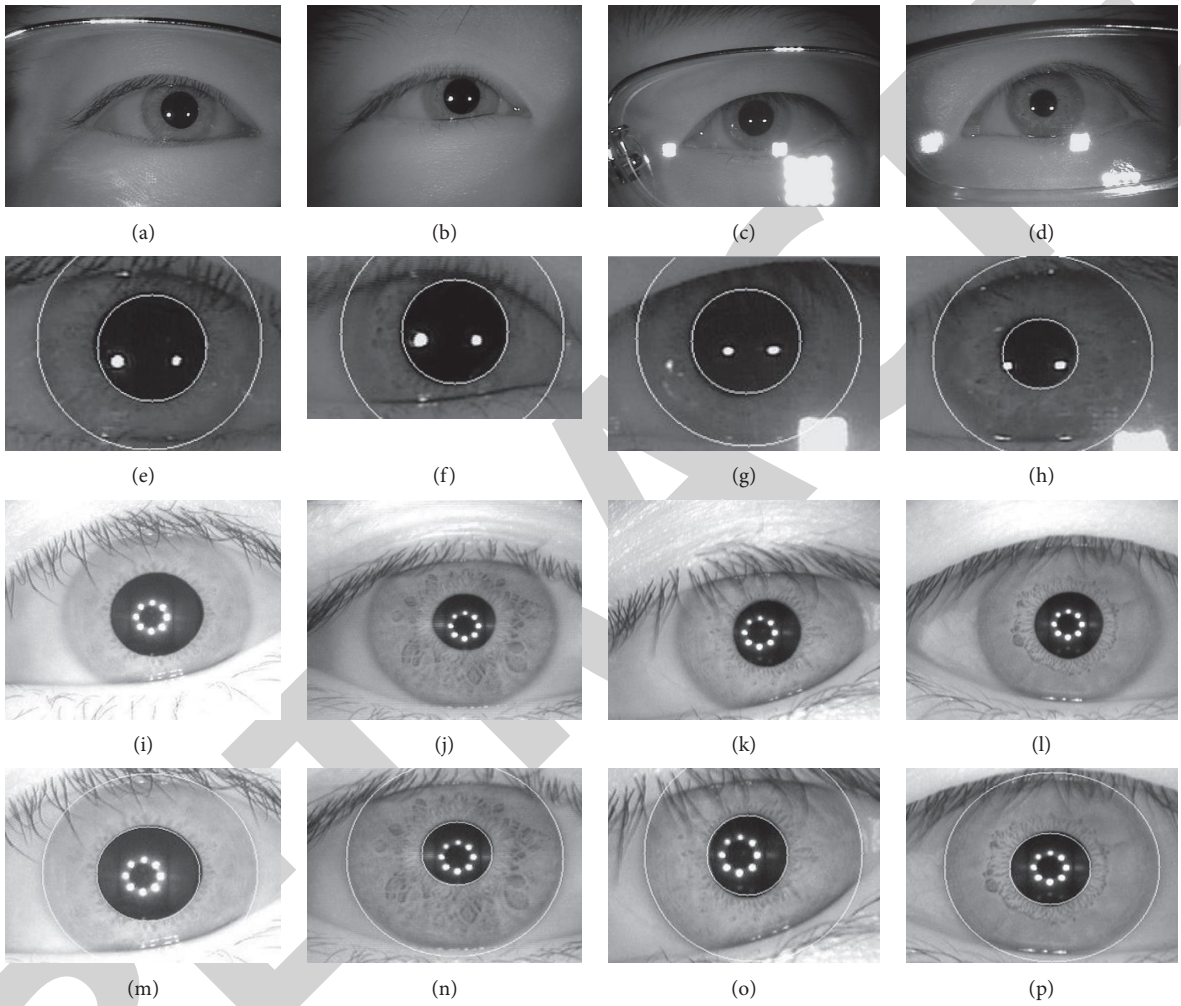

Figure 11: Examples of the iris localization results of the proposed algorithm.

3.4. Comparison with Other Algorithms. In order to verify the performance of the proposed algorithm, we compared it with the algorithms presented in the literature [8, 10, 13]. All algorithms completed localization based on the effective iris area extracted by YOLOv4. The experimental results are shown in Table 5 and Figure 11. The first and second lines of Figure 11 are partial CASIA-IrisV4-thousand images and their iris localization results, while the third and the fourth lines are partial CASIA-IrisV3-Interval images and their localization results.

As can be seen from Table 5, the proposed method has better results when compared with other localization methods. As can be seen from Figure 11, when the iris area accounts for a small proportion of the whole image, there is a lot of interference in the image, and the proposed algorithm can effectively remove the interference caused by the eyeglass frame, reflections, the eyebrows, hair, etc. and obtain the effective iris area to achieve accurate localization. The quality of images is higher when the iris area accounts for a large proportion of the whole image, and the proposed algorithm still yields better performance than other state-of-the art methods. At the same time, the proposed method also suffers localization errors when the iris area is severely obscured, which shows that this method has some room for improvement when the effective edges are fewer.